ANNUAL REPORTS ON NMR SPECTROSCOPY

Volume 27

ANNUAL REPORTS ON

NMR SPECTROSCOPY

This Page Intentionally Left Blank

ANNUAL REPORTS ON

NMR SPECTROSCOPY

Edited by

G. A. WEBB

Department of Chemistry, University of Surrey, Guildford, Surrey, England

VOLUME 27

ACADEMIC PRESS

Harcourt Brace & Company, Publishers

London • San Diego • New York
Boston • Sydney • Tokyo • Toronto

ACADEMIC PRESS LIMITED
24–28 Oval Road,
LONDON NW1 7DX

U.S. Edition Published by

ACADEMIC PRESS INC.
San Diego, CA 92101

This book is printed on acid free paper

A catalogue record for this book is available from the British Library

ISBN 0-12-505327-4
ISSN 0066-4103

Phototypesetting by Keyset Composition, Colchester, Essex
Printed by Hartnolls Limited, Bodmin, Cornwall

List of Contributors

John Cavanagh, *Department of Molecular Biology, The Scripps Research Institute, 10666 North Torrey Pines Road, La Jolla, California 92037, USA.*

R. H. Contreras, *Departamento de Fisica, Facultad de Ciencias Exactas y Naturales, Universidad de Buenos Aires, Ciudad Universitaria, Pabellon 1, (1428) Buenos Aires, Argentina.*

J. C. Facelli, *Utah Supercomputing Institute and Department of Chemistry, University of Utah, Salt Lake City, Utah 84112, USA.*

Yoshio Inoue, *Department of Biomolecular Engineering, Tokyo Institute of Technology, 4259 Nagatsuta, Midori-ku, Yokohama 227, Japan.*

Cynthia L. Lean, *Membrane-NMR Unit, Department of Cancer Medicine, University of Sydney, NSW 2006, Australia.*

Wanda B. Mackinnon, *Membrane-NMR Unit, Department of Cancer Medicine, University of Sydney, NSW 2006, Australia.*

Carolyn E. Mountford, *Membrane-NMR Unit, Department of Cancer Medicine, University of Sydney, NSW 2006, Australia.*

Takuhei Nose, *Department of Polymer Chemistry, Tokyo Institute of Technology, Ookayama, Meguro-ku, Tokyo 152, Japan.*

K. G. Orrell, *Department of Chemistry, The University, Exeter, EX4 4QD, UK.*

Mark Rance, *Department of Molecular Biology, The Scripps Research Institute, 10666 North Torrey Pines Road, La Jolla, California 92037, USA.*

Peter Russell, *Department of Anatomical Pathology, Royal Prince Alfred Hospital, Missenden Road, Camperdown, NSW 2050, Australia.*

V. Šik, *Department of Chemistry, The University, Exeter, EX4 4QD, UK.*

This Page Intentionally Left Blank

Preface

The present collection of reports serve to demonstrate the extensive purview of NMR and its applications. The pellucid presentations provided include accounts of sensitivity-enhanced techniques in the study of biomolecules, NMR studies of the structure and properties of cyclodextrins and their inclusion complexes, dynamic NMR spectroscopy in inorganic and organometallic chemistry, the use of proton NMR in cancer pathology, pulsed-field-gradient NMR studies of the diffusion of chain molecules in polymer matrices, and advances in theoretical aspects of spin–spin couplings. Taken together with reviews in other volumes of this series, the present accounts ably demonstrate that NMR is *facile princeps* when it comes to problem solving in most areas of science, including medicine.

It is a very great pleasure for me to be able to thank all of the contributors, and the production team, for their diligence and kind cooperation in the creation of this volume of *Annual Reports on NMR Spectroscopy*. It is their efforts that ensure the continuing success of this series.

University of Surrey
Guildford, Surrey
England

G. A. WEBB

This Page Intentionally Left Blank

Contents

This Page Intentionally Left Blank

Sensitivity-Enhanced NMR Techniques for the Study of Biomolecules

JOHN CAVANAGH and MARK RANCE

Department of Molecular Biology, The Scripps Research Institute, La Jolla, California 92037, USA

ANNUAL REPORTS ON NMR SPECTROCOPY
VOLUME 27 ISBN 0-12-505327-4

1. INTRODUCTION

Nuclear magnetic resonance spectroscopy is one of the most powerful tools available for obtaining detailed information on the structure, dynamics and interactions of molecules. Unfortunately, in comparison with some other physical methods, NMR spectroscopy is a relatively insensitive technique in terms of the achievable signal-to-noise ratio per unit measuring time. Indeed, in many applications of NMR spectroscopy, particularly to systems of biochemical interest, the inherent sensitivity of the measurements is a significant limiting factor in the quality and quantity of experimental information obtainable. Thus the optimization of the sensitivity of experimental measurements is an extremely important area of research and development in the application of NMR spectroscopy.

As indicated above, the term "sensitivity" in this chapter refers to the experimental signal-to-noise (S/N) ratio achievable for a given amount of measuring time. Many factors contribute to the sensitivity of an NMR experiment, and thus there are numerous ways in which the sensitivity potentially can be enhanced. These methods can generally be classified into three broad categories:

(i) optimization of experimental apparatus;

(ii) spin physics;

(iii) post-acquisition data processing.

In the first category are factors such as the magnetic field strength, sample volume and concentration and spectrometer design and performance.[1] The second category comprises of NMR techniques designed for achieving sensitivity improvements, such as polarization transfer experiments[2] and indirect detection methods.[3] Also included in the second category are factors directly concerning the acquisition of NMR data, such as optimum timing of experiments[4] and sampling of free induction decays.[5–7] The third category, post-acquisition data processing, covers areas such as optimum weighting,[4,5] apodization[8] and digital filtration of the recorded FID, and alternatives to Fourier transformation for spectral analysis.[9–11] The purpose of this chapter is not to review the very broad field of sensitivity enhancement in NMR spectroscopy, but rather to report on a specific class of new techniques for sensitivity improvement in multidimensional experiments which falls into the second category above.

The basic principle underlying this new class of sensitivity-enhanced NMR experiments is the preservation of spectral information that is normally discarded in the corresponding conventional experiments. When this additional information is combined in an appropriate fashion with the data normally collected, the composite data sets provide improvements in sensitivity over conventional experiments by factors of up to $\sqrt{2}$.

For convenience of discussion, this new methodology will be referred to as PEP (preservation of equivalent pathways). The theory underlying the basic concept is described in Section 2. Subsequent sections discuss the implementation of the sensitivity-improvement scheme in various types of solution-state multidimensional NMR experiments, with applications demonstrated on systems of biochemical interest.

2. GENERAL METHODOLOGY

The sensitivity-improvement scheme discussed here is closely related to that employed in quadrature phase-sensitive detection[12,13] and cross-coil detection[14] to achieve $\sqrt{2}$ improvements in sensitivity in 1D NMR spectroscopy. Thus, as an introduction to the PEP methodology, these analogous techniques will be discussed briefly.

2.1. Quadrature detection

Owing to the relatively high frequencies present in most NMR signals in pulsed Fourier transform spectroscopy, it is usually necessary to convert these signals to the audio frequency range before passing them to the analogue-to-digital converter. To do this frequency conversion, it is necessary to mix the NMR signal with a suitable reference source in a phase-sensitive detector[1,13] (most spectrometer designs employ at least a two-step frequency conversion process, but this is irrelevant for the present discussion). One problem with the use of a single phase-sensitive detector is that the sign of the converted NMR signal is not determined, i.e. frequencies equidistant above and below the reference source are indistinguishable.[12,13] One solution to this problem is to choose a frequency such that all the NMR signals are either above or below this reference. Unfortunately, this solution is disadvantageous for several reasons:

(i) the maximum sampling rate in the ADC process is twice what it might otherwise be;

(ii) since common source frequencies are usually necessary for the transmitter and receiver sections of the spectrometer, four times the RF power is required to compensate for the reference offset;

(iii) unless special precautions are taken, noise imaging will occur.

For the present discussion it is the latter point which is of particular relevance. Noise imaging occurs in a single phase-sensitive detector owing to the inability to distinguish the sign of the frequencies; if the noise at frequencies above and below the reference source is statistically independent then the noise imaging will degrade the achievable sensitivity by a factor of $\sqrt{2}$. Fortunately, the inability to distinguish between frequencies above and below the reference source in a single phase-sensitive detector can be overcome by employing two phase-sensitive detectors with reference sources that have identical frequencies but orthogonal phases.[12,13] The signals from the two detectors can then be combined as the real and imaginary parts of a complex function, which can be Fourier transformed to yield the desired spectrum with frequency sign discrimination. A $\sqrt{2}$ improvement in sensitivity will be realized as a result of the elimination of noise imaging, in addition to the advantages gained by placing the reference frequency in the middle of the spectral range of interest rather than at one end. Use of dual phase-sensitive detectors allows all of the information contained in the signal picked up by the probe coil to be recorded, resulting in substantial improvement in sensitivity.

2.2. Cross-coil detection

Hoult and co-workers[14] pointed out some time ago that, in principle, a $\sqrt{2}$ improvement in sensitivity could be achieved through the use of two orthogonal detection coils; this improvement is in addition to that discussed above for quadrature phase-sensitive detection employing a single coil. The concept is very simple. If the two coils are orthogonally situated but otherwise identical, the NMR signals detected by them will be identical except for a relative 90° phase shift; on the other hand, the thermal noise in the receiver circuits (probe coil plus preamplifiers) will be uncorrelated. Therefore, when the signals from the two coils are combined after correcting for the relative phase shift, the coherent NMR signals will double in intensity while the noise level will only increase by $\sqrt{2}$, resulting in a net increase of $\sqrt{2}$ in sensitivity over a single-coil detection system.

2.3. Principles of PEP technology

The PEP technique is essentially an analogue of cross-coil detection for evolution periods[8] in multidimensional experiments. To illustrate the basic principle, the effect of the simple three-pulse sequence:

$$90^\circ_\beta\text{–}t_1\text{–}90^\circ_x\text{–}90^\circ_\phi\text{–}t_2 \quad \text{(detection)}$$

on an isolated spin ½ will be analysed.

2.3.1. *The signal*

Starting at thermal equilibrium, the net magnetization of the spin ½ is proportional to the z component of its angular momentum, I_z. The first 90° pulse rotates the magnetization to the transverse plane, and the subsequent evolution period results in the following density operator (assuming $\beta = y$ and ignoring constants of proportionality):

$$\sigma_y(t_1) = I_x \cos \Omega t_1 + I_y \sin \Omega t_1, \tag{1}$$

where Ω is the resonance offset in the rotating frame. The third 90° pulse is phase-cycled such that the pulse pair 90°_x–90°_ϕ results in net rotations of 0° ($\phi = -x$) or 180° ($\phi = x$) about the x axis. Thus, after the pulse pair, the density operator is given by

$$\sigma_y^{-x}(t_1) = I_x \cos \Omega t_1 + I_y \sin \Omega t_1 \tag{2a}$$

for $\phi = -x$ and

$$\sigma_y^{x}(t_1) = I_x \cos \Omega t_1 - I_y \sin \Omega t_1 \tag{2b}$$

for $\phi = x$. Subsequent evolution during the t_2 detection period of this simple 2D experiment results in the following density operators:

$$\begin{aligned}\sigma_y^{-x}(t_1, t_2) = {} & I_x(\cos \Omega t_1 \cos \Omega t_2 - \sin \Omega t_1 \sin \Omega t_2) \\ & + I_y (\sin \Omega t_1 \cos \Omega t_2 + \cos \Omega t_1 \sin \Omega t_2),\end{aligned} \tag{3a}$$

$$\begin{aligned}\sigma_y^{x}(t_1, t_2) = {} & I_x(\cos \Omega t_1 \cos \Omega t_2 + \sin \Omega t_1 \sin \Omega t_2) \\ & - I_y(\sin \Omega t_1 \cos \Omega t_2 - \cos \Omega t_1 \sin \Omega t_2).\end{aligned} \tag{3b}$$

These expressions can be rewritten as

$$f_y^{-x}(t_1, t_2) = \exp(i\Omega t_1) \exp(i\Omega t_2), \tag{4a}$$

$$f_y^{x}(t_1, t_2) = \exp(-i\Omega t_1) \exp(i\Omega t_2), \tag{4b}$$

where the real and imaginary components correspond to the I_x and I_y coefficients respectively. A two-dimensional Fourier transformation[8] of the signals represented by (4) (with appropriate damping factors included), will result in 2D spectra with a single resonance at frequencies $\omega_1 = \Omega(\phi = -x)$ or $\omega_1 = -\Omega(\phi = x)$ and $\omega_2 = \Omega$; unfortunately, this resonance will have a highly undesirable, mixed lineshape.[15,16] This phase-twisted lineshape results from the phase modulation with respect to t_1 of the detected NMR signal. As discussed by Keeler and Neuhaus,[16] pure absorption lineshapes can be obtained by converting the phase-modulated signal to an amplitude-modulated signal. In the example discussed here this can be accomplished by adding (or subtracting) the signals represented by (2). Adding the operators yields

$$\sigma_y^{a}(t_1) = 2I_x \cos \Omega t_1 \tag{5}$$

or

$$f_y^a(t_1, t_2) = 2 \cos \Omega t_1 \exp(i\Omega t_2), \tag{6}$$

while subtraction yields

$$\sigma_y^s(t_1) = 2I_y \sin \Omega t_1 \tag{7}$$

or

$$f_y^s(t_1, t_2) = 2i \sin \Omega t_1 \exp(i\Omega t_2). \tag{8}$$

When the signal $f_y^a(t_1, t_2)$ in (6) is subjected to a cosine Fourier transformation with respect to t_1 and a complex Fourier transformation with respect to t_2, a resonance with a pure absorption lineshape in both frequency dimensions of the 2D spectrum will be observed; likewise, if $f_y^s(t_1, t_2)$ in (8) is subjected to a sine Fourier transformation with respect to t_1 and a complex Fourier transformation with respect to t_2, an identical double absorption resonance will be observed. If the transformed spectra are added together, the resonance will double in intensity.

In conventional experiments only one of the signals, either addition or subtraction, is retained; the phase cycling of the RF pulses and receiver is engineered such that only one combination is accumulated in computer memory, i.e. the signal arising from only one of the orthogonal magnetization components present during t_1 is retained. However, it is clear from the discussion that retention of either component and use of appropriate data processing leads to identical spectra, in the absence of noise and pulse imperfections, which can be combined to enhance the signal. The key to the PEP technique is the behaviour of the spectral noise when the data are combined to enhance the signal; this issue will be discussed below.

Before proceeding to the discussion of noise, the analysis of the coherent signal behaviour will be extended somewhat for the sake of generality. In the procedure outlined above, a phase-modulated signal, for example (4a), is converted to an amplitude-modulated signal, for example (6). This process results in the loss of the ability to distinguish the sign of the resonance frequency in the ω_1 dimension. As discussed by Keeler and Neuhaus,[16] there are at least two related procedures for recovering the ability for ω_1 sign discrimination: (i) the so-called hypercomplex method,[17] also commonly referred to as the States method,[18] and (ii) the time-proportional phase-incrementation technique (TPPI).[19–21] For ease of discussion, the hypercomplex method for ω_1 sign discrimination will be included in the present example. If one considers the additive combination of the data for the two phase steps ($\phi = \pm x$) in the present example, the signal during the detection period is given by (6). If the experiment is repeated with the phase of the first pulse advanced by 90°, the corresponding signal during the detection period is

$$f_{-x}^a(t_1, t_2) = -2 \sin \Omega t_1 \exp(i\Omega t_2). \tag{9}$$

The signals in the two experiments, (6) and (9), can be combined as complex pairs with respect to t_1, and a complex Fourier transformation will yield an absorptive resonance with sign discrimination in the ω_1 dimension. If one considers the subtractive combination for the two phase steps ($\phi = \pm x$) with $\beta = -x$, the detected signal is

$$f^{s}_{-x}(t_1, t_2) = 2i \cos \Omega t_1 \exp(i\Omega t_2). \tag{10}$$

As for the case of the additive combination, (8) and (10) can be combined as complex pairs with respect to t_1, and a complex Fourier transformation performed to yield the desired spectral information.

The discussion above focused on the additive, (6) and (9), and subtractive, (8) and (10), data sets being processed separately and combined only at the end as 2D spectra to enhance the NMR resonance intensity. In practice, it is much simpler to combine the time domain data sets so that a single 2D Fourier transformation is required. Inspection of (6), (8), (9) and (10) indicates that the time domain data should be combined as follows:

$$f^{r}(t_1, t_2) = f^{a}_{y}(t_1, t_2) - i f^{s}_{-x}(t_1, t_2) \tag{11}$$

$$= 4 \cos \Omega t_1 \exp(i\Omega t_2) \tag{12}$$

$$f^{i}(t_1, t_2) = f^{a}_{-x}(t_1, t_2) + i f^{s}_{y}(t_1, t_2) \tag{13}$$

$$= -4 \sin \Omega t_1 \exp(i\Omega t_2). \tag{14}$$

The superscripts r and i indicate that these functions should be combined as complex pairs with respect to t_1 in the usual hypercomplex prescription[16–18] prior to the complex ω_1 Fourier transformation; a complex Fourier transformation with respect to t_2 should be performed separately on (11) and (13). The factor i in the second term of (11) indicates that the real and imaginary components of $f^{s}_{-x}(t_1, t_2)$ should be interchanged and one component negated[22] before being combined with $f^{a}_{y}(t_1, t_2)$; a similar operation is indicated in (13).

The signal enhancement in the PEP technique is clearly demonstrated in the analysis above. In a conventional experiment only the additive (or subtractive) combination of the two-step phase cycle ($\phi = \pm x$) would be accumulated, leading to the signals of (6) and (9) (or (8) and (10)); with the PEP technique, information from equivalent pathways is preserved and combined appropriately to double the signal intensity, as indicated in (12) and (14). It should be emphasized that this signal enhancement is achieved without any additional data being recorded. In conventional experiments the signal arising from only one of the two orthogonal transverse magnetization components present during the mixing time is retained, while in the PEP technique the signals from both transverse components, which contain equivalent spectral information, are preserved, in direct analogy to cross-coil detection in 1D spectroscopy.

2.3.2. *The noise*

The straightforward analysis presented above has indicated that the NMR signal intensity for a given experimental acquisition time can be doubled through the use of the PEP methodology. The key, therefore, to determining the sensitivity of the technique is the behaviour of the spectral noise. In the original description of the PEP technology[23] it was demonstrated via an analysis of the frequency domain spectra that the spectral noise increased by a factor of $\sqrt{2}$ in the enhanced spectra relative to the conventional spectra. An equivalent proof is provided here based on a simple inspection of the time domain data.

To determine the noise behaviour, it is sufficient to consider the data accumulated for a single value of t_1. In the example introduced above, four free induction decays are recorded and stored separately, corresponding to the two-step phase cycle ϕ and the two steps ($\beta = y, =x$) required for ω_1 sign discrimination. These four free induction decays can be designated as

$$F_y^x(t_2) = [\mathrm{Fr}]_y^x(t_2) + \mathrm{i}[\mathrm{Fi}]_y^x(t_2) \tag{15}$$

$$F_y^{-x}(t_2) = [\mathrm{Fr}]_y^{-x}(t_2) + \mathrm{i}[\mathrm{Fi}]_y^{-x}(t_2) \tag{16}$$

$$F_{-x}^x(t_2) = [\mathrm{Fr}]_{-x}^x(t_2) + \mathrm{i}[\mathrm{Fi}]_{-x}^x(t_2) \tag{17}$$

$$F_{-x}^{-x}(t_2) = [\mathrm{Fr}]_{-x}^{-x}(t_2) + \mathrm{i}[\mathrm{Fi}]_{-x}^{-x}(t_2) \tag{18}$$

where the superscripts refer to the phase ϕ, the subscripts to the phase β, and the Fr and Fi refer to the real and imaginary components of the free induction decays respectively. The additive combination of the free induction decays for the phase cycle ϕ are

$$\begin{aligned} F_y^{\mathrm{a}} &= F_y^x + F_y^{-x} \\ &= ([\mathrm{Fr}]_y^x + [\mathrm{Fr}]_y^{-x}) + \mathrm{i}([\mathrm{Fi}]_y^x + [\mathrm{Fi}]_y^{-x}), \end{aligned} \tag{19}$$

$$\begin{aligned} F_{-x}^{\mathrm{a}} &= F_{-x}^x + F_{-x}^{-x} \\ &= ([\mathrm{Fr}]_{-x}^x + [\mathrm{Fr}]_{-x}^{-x}) + \mathrm{i}([\mathrm{Fi}]_{-x}^x + [\mathrm{Fi}]_{-x}^{-x}) \end{aligned} \tag{20}$$

where the explicit reference to t_2 has been omitted for convenience. The subtractive combinations are

$$\begin{aligned} F_y^{\mathrm{s}} &= F_y^x - F_y^{-x} \\ &= ([\mathrm{Fr}]_y^x - [\mathrm{Fr}]_y^{-x}) + \mathrm{i}([\mathrm{Fi}]_y^x - [\mathrm{Fi}]_y^{-x}), \end{aligned} \tag{21}$$

$$\begin{aligned} F_{-x}^{\mathrm{s}} &= F_{-x}^x - F_{-x}^{-x} \\ &= ([\mathrm{Fr}]_{-x}^x - [\mathrm{Fr}]_{-x}^{-x}) + \mathrm{i}([\mathrm{Fi}]_{-x}^x - [\mathrm{Fi}]_{-x}^{-x}). \end{aligned} \tag{22}$$

Following the prescription outlined above for combining the additive and subtractive data sets, the composite time domain data are specified by

$$F_y^c = F_y^a - iF_{-x}^s, \tag{23}$$

$$F_{-x}^c = F_{-x}^a + iF_y^s. \tag{24}$$

Substituting (19–22) into (23) and (24) leads to

$$F_y^c = ([Fr]_y^x + [Fr]_y^{-x} + [Fi]_{-x}^x - [Fi]_{-x}^{-x}) + i([Fi]_y^x + [Fi]_y^{-x} - [Fr]_{-x}^x + [Fr]_{-x}^{-x}), \tag{25}$$

$$F_{-x}^c = ([Fr]_{-x}^x + [Fr]_{-x}^{-x} - [Fi]_y^x + [Fi]_y^{-x}) + i([Fi]_{-x}^x + [Fi]_{-x}^{-x} + [Fr]_y^x - [Fr]_y^{-x}). \tag{26}$$

The real and imaginary components of F_y^c and F_{-x}^c are each the sum of four statistically independent data sets (it is assumed for the present analysis that the free induction decays in (19)–(22) consist simply of random noise), whereas the additive data set, (19) and (20), and the subtractive data set, (21) and (22), are each the sum of only two statistically independent data sets. Therefore, since random noise increases by $n^{1/2}$ when n independent noise samples are combined, the composite data set represented by (25) and (26) will have a noise level $\sqrt{2}$ larger than either the additive or subtractive data sets in (19)–(22).

2.3.3. Sensitivity improvement

The analysis in Section 2.3.1 demonstrated that the NMR signal intensity in the example experiment could be doubled by making an appropriate combination of the data accumulated separately for distinct phase steps in the pulse sequence. In Section 2.3.2 it was demonstrated that the prescription for the combination of data that leads to the doubling of NMR intensities results in a $\sqrt{2}$ increase in noise compared to the conventional data set. Thus the net improvement in the signal-to-noise ratio is a factor of $\sqrt{2}$. Since this improvement is achieved with no increase in the experimental acquisition time, a significant sensitivity enhancement is realized.

2.3.4. General comments

The analysis presented above for a simple experiment was sufficient to demonstrate the general principle upon which the PEP methodology is based. By recording separately the data for phase-cycling steps normally incorporated to suppress one of the orthogonal transverse magnetization components during an evolution period of a multidimensional experiment, it is possible to obtain separate spectra from signals arising from the two components. If the nature of the experiment is such that the two spectra are

essentially equivalent, the spectra can be combined to achieve an improvement in sensitivity up to $\sqrt{2}$. This will be the case if the two transverse magnetization components are subjected to the same mixing process between the evolution and detection periods. In the simple example provided above the mixing process consisted only of a pair of 90° pulses. Strictly speaking, the mixing process was not identical for the two transverse magnetization components, since one was spin-locked along the rotation axis of the pulses while the other was being rotated. However, neglecting significant pulse imperfections and off-resonance effects, the two magnetization components could be treated, to a good approximation, as though they had experienced the same mixing processs. An example in which the process would be quite different for the two orthogonal magnetization components is a 2D NOESY experiment;[24] the pulse sequence is the same as above except that a finite mixing time τ_m is inserted between the second and third 90° pulses. In this case one of the transverse components during the evolution period will be rotated to the longitudinal axis during the mixing time, while the other will remain in the transverse plane; clearly, the coherent and relaxation behaviours of these two components during τ_m will be quite different, and the resulting spectra will not be equivalent.

In the following sections the application of PEP technology to various types of multidimensional NMR experiments will be described. The element in common to all of these experiments is that the mixing process essentially treats equally the two orthogonal transverse magnetization components present during an evolution period, so that if the NMR signals arising from both these components are retained, a sensitivity improvement can be achieved.

3. SENSITIVITY IMPROVEMENT IN ISOTROPIC MIXING (TOCSY) EXPERIMENTS

One of the most popular techniques currently employed for obtaining resonance assignments in high resolution ^{1}H NMR spectroscopy is the TOCSY experiment (sometimes referred to as HOHAHA).[25,26] In this experiment magnetization is transferred coherently from one spin to another belonging to the same scalar-coupled spin system during an extended mixing period. During this mixing period some RF pulse sequence is applied that, ideally, eliminates the chemical-shift terms from the nuclear spin Hamiltonian and leaves only the isotropic scalar coupling interactions. The TOCSY experiment derives its popularity from several advantages:

(i) coherence transfer through a spin system is a continuous process, allowing correlations to be established through an extended coupling network, subject to favourable relaxation rates;

(ii) a net transfer of magnetization is achieved more rapidly than via alternative, pulse-interrupted free precession techniques;

(iii) with a suitable implementation of the TOCSY experiment,[26–28] the spectra obtained have resonances with predominantly absorption lineshapes.

It is important to note that a net transfer of magnetization gives rise to NMR resonances for which the multiplet components are all in phase (i.e. have the same algebraic sign). This is a very advantageous feature in cases where the linewidth exceeds the size of the active scalar couplings, since then the antiphase multiplets are severely attenuated owing to the destructive interference of the antiphase multiplet components. Thus the TOCSY experiment is particularly useful in cases where the resonance linewidths are large because of molecular size or exchange effects.

The general scheme for the most flexible version of the 2D TOCSY experiment is[27,28]

$$\text{(equilibration)–90°–}t_1\text{–90°–(isotropic mixing)–90°–}t_2\text{(acquire)}.$$

During the t_1 evolution period the initial transverse magnetization created by the first 90° pulse evolves under the influence of both chemical-shift and scalar coupling interactions. At the end of the evolution period another 90° pulse prepares the system to enter the subsequent isotropic mixing period. The mixing period consists of a multipulse sequence designed to eliminate chemical-shift terms and give rise to a nuclear spin Hamiltonian consisting of only the isotropic scalar coupling terms. During the mixing period, magnetization is coherently transferred among spins belonging to the same coupling network. At the end of the mixing, a third 90° pulse generates the appropriate transverse magnetization to be detected, and the data are processed to provide a 2D correlation map. Any arbitrary coherence can be transferred under the isotropic mixing process to another of the same order; however, it is most common to focus on the transfer of net magnetization, $M_{i\phi} \rightarrow M_{j\phi}$($\phi = x$, y or z, and i and j are any two spins belonging to the same spin system), since all other coherences or multispin order will give rise to resonances that have antiphase multiplet structure. While such antiphase contributions can be observed in TOCSY spectra as distortions of the otherwise in-phase multiplet structures, their contribution is usually minimal owing to the destructive interference of the antiphase multiplet components, especially when the resonance linewidths are comparable to the active scalar couplings. This is very often the case in the study of large biomolecules. For this reason, the analysis here will focus on only the single spin order terms and those single quantum coherences that lead to resonances with in-phase multiplet structure.

3.1. Theory

To understand the origin of the sensitivity improvement in the TOCSY experiment,[23] it is sufficient to consider the behaviour of a weakly coupled two-spin system AX. The nuclear spin angular momentum operators for the spins A and X are denoted by I_ϕ and S_ϕ respectively, where $\phi = x$, y or z. At the end of the evolution period the density matrix will be given by (ignoring constants of proportionality and all relaxation effects)[29–31]

$$\begin{aligned}\rho(t_1) = & -I_y \cos \Omega_A t_1 \cos \pi J t_1 + 2I_x S_z \cos \Omega_A t_1 \sin \pi J t_1 \\ & + I_x \sin \Omega_A t_1 \cos \pi J t_1 + 2I_y S_z \sin \Omega_A t_1 \sin \pi J t_1 \\ & + \text{similar terms with } I \text{ and } \Omega_A \text{ replaced by } S \text{ and } \Omega_X, \end{aligned} \tag{27}$$

where J is the scalar coupling between A and X; Ω_A and Ω_X are the resonance offsets of spins A and X, and the first 90° pulse is assumed to have phase x. For convenience the terms with transverse S_ϕ components will be omitted. The two-spin terms in (27) will give rise to peaks that have antiphase multiplet structure in the ω_1 dimension of the 2D TOCSY spectrum and a mixture of both in-phase and antiphase character in the ω_2 dimension. For the reasons stated above, all antiphase contributions will be ignored in the present discussion, so that (27) simplifies to

$$\rho(t_1) = -I_y \cos \Omega_A t_1 \cos \pi J t_1 + I_x \sin \Omega_A t_1 \cos \pi J t_1. \tag{28}$$

A subsequent 90° pulse of phase x generates the terms

$$\rho(t_1, 90_x) = -I_z \cos \Omega_A t_1 \cos \pi J t_1 + I_x \sin \Omega_A t_1 \cos \pi J t_1. \tag{29}$$

Assuming that the effective nuclear spin Hamiltonian during the ensuing mixing period consists only of the isotropic scalar coupling term $2\pi \boldsymbol{I} \cdot \boldsymbol{S}$, the density matrix at the end of the mixing period τ will be given by[25]

$$\begin{aligned}\rho(t_1, 90_x, \tau) = & -I_z \cos \Omega_A t_1 \cos \pi J t_1 \cos \pi J \tau + I_x \sin \Omega_A t_1 \cos \pi J t_1 \cos \pi J \tau \\ & - S_z \cos \Omega_A t_1 \cos \pi J t_1 \sin \pi J \tau + S_x \sin \Omega_A t_1 \cos \pi J t_1 \sin \pi J \tau \\ & + \text{antiphase terms.} \end{aligned} \tag{30}$$

The antiphase terms are ignored, since they give rise to antiphase contributions in the final spectrum. The final 90° pulse of phase x then generates the following observable magnetization:

$$\begin{aligned}\rho(t_1, 90_x, \tau, 90_x) = & I_y \cos \Omega_A t_1 \cos \pi J t_1 \cos \pi J \tau \\ & + I_x \sin \Omega_A t_1 \cos \pi J t_1 \cos \pi J \tau \\ & + S_y \cos \Omega_A t_1 \cos \pi J t_1 \sin \pi J \tau \\ & + S_x \sin \Omega_A t_1 \cos \pi J t_1 \sin \pi J \tau. \end{aligned} \tag{31}$$

When the resulting NMR signal is detected during the t_2 period and subjected to 2D Fourier transformation, a diagonal peak for the I spin and a cross-peak to the S spin will be observed, as well as the diagonal peak for

the S spin and cross-peak to the I spin from terms that were dropped earlier. The lineshapes for all these peaks will be the highly undesirable phase twist, a mixture of two-dimensional absorption and dispersion. In order to obtain absorption mode spectra in the version of the TOCSY experiment described, one of the orthogonal components in (31) is removed by the use of phase cycling.[27] In other variants of the TOCSY experiment[26] RF field inhomogeneity ("trim" pulse) is used for the same purpose; sensitivity improvement via PEP technology is not possible in this case, since one of the necessary orthogonal magnetization components is destroyed.

Unlike many experiments, where the desired spectral information is obtained through a unique pathway, the isotropic mixing experiment allows equivalent information to be obtained simultaneously along two orthogonal axes. As noted above, the key to sensitivity improvement is to employ the PEP technology to retain the information obtained along both orthogonal axes and combine it in such a way that pure 2D absorption lineshapes result.

If the phase of the 90° pulse immediately prior to the isotropic mixing period is inverted i.e. changed from x to $-x$, the signal eventually detected evolves from the following density operator at the beginning of the t_2 period:

$$\begin{aligned}\rho(t_1, 90_{-x}, \tau, 90_x) = & -I_y \cos \Omega_A t_1 \cos \pi J t_1 \cos \pi J \tau \\ & + I_x \sin \Omega_A t_1 \cos \pi J t_1 \cos \pi J \tau \\ & - S_y \cos \Omega_A t_1 \cos \pi J t_1 \sin \pi J \tau \\ & + S_x \sin \Omega_A t_1 \cos \pi J t_1 \sin \pi J \tau. \end{aligned} \tag{32}$$

Rather than combining the two data sets represented by (31) and (32) in real time as the experiment proceeds, the data can be stored separately ready for combination later. By adding (31) and (32), only the I_x components are retained, while the difference retains only the I_y components. Ideally the two spectra that result will be identical except for a 90° phase shift in both dimensions. Thus, once the two spectra are each phased to give pure 2D absorption lineshapes, they can be co-added to double the size of all peaks. As shown above, in the PEP method, the noise from the two spectra combines as though statistically independent, giving an overall sensitivity improvement of $\sqrt{2}$ compared with the conventional method. The data can also be combined in the time domain, as discussed in Section 2.3, if the hypercomplex method has been employed for ω_1 frequency discrimination.

3.2. Experimental demonstration

Before proceeding with the experimental demonstration of the sensitivity-enhanced TOCSY procedure, it is important to note that there is an alternate method in which the data can be treated. From (31) and (32) it can be seen that the two orthogonal magnetization components M_x and M_y (which are proportional to I_x and I_y respectively) have sine and cosine

amplitude modulations respectively as functions of t_1. Thus these separated components may be combined in the manner referred to as the hypercomplex method to discriminate the signs of the ω_1 frequencies.[17,18] It can be demonstrated that the hypercomplex combination will result in a spectrum with the same signal-to-noise ratio as a spectrum obtained in the conventional way, where the orthogonal components are recorded in two separate experiments by phase-shifting the first 90° pulse by 90°. Since the modified experiment is completed in half the time of the conventional method (N scans per t_1 in the modified experiment versus $2N$ scans in the conventional experiment), a gain in sensitivity of $\sqrt{2}$ is realized. The drawback of the hypercomplex implementation of the sensitivity-improved experiment is that if the two quadrature magnetization components do not have exactly the same amplitude then ω_1 quadrature images will appear in the 2D TOCSY spectra. Owing to non-idealities in the mixing sequence, there will likely be some small amplitude differences in the orthogonal components, and so this implementation of the sensitivity improvement is not recommended. The conventional hypercomplex method for ω_1 quadrature detection can still be employed with the scheme described above for combining separate spectra to obtain the sensitivity improvement.

For the z-filtered TOCSY experiment[27,28] employed here the general scheme can be written as

$$\text{(equilibration)}\text{–}90^\circ_{\phi+\beta+\psi}\text{–}t_1\text{–}90^\circ_{\varepsilon}\text{–(mixing)}_\gamma\text{–}90^\circ_{\alpha}\text{–}t_2\text{(acq, rec} = \alpha+\beta).$$

At the end of the t_1 period, one of the orthogonal transverse in-phase magnetization components is rotated to the z axis by the pulse immediately preceding the mixing period. In the conventional z-filtered TOCSY experiment $\phi = \varepsilon$, and the first two 90° pulses are phase-cycled (i.e. ϕ and ε are advanced in increments of 90°) to eliminate the remaining transverse single-quantum components as well as higher-order coherences. For axial peak suppression $\beta = 0°$, 180°, and ψ is incremented to obtain ω_1 sign discrimination. In the modification proposed here two data sets are recorded; in both data sets the phase cycling of β and ψ is unchanged, but the remaining cycling is such that $\phi = \alpha$ is incremented in steps of 90° simply to remove ω_2 quadrature images and $\gamma = \phi + 90°$ for mixing sequences such as WALTZ[32] and DIPSI[33] (see below). The difference in the two acquisitions is that in one $\varepsilon = \phi$, while in the other $\varepsilon = \phi + 180°$. The result will be that the z component of the magnetization during the mixing period will be inverted between the two experiments, while the transverse component will be unaffected; thus addition and subtraction of the data sets will allow these two components to be separated. While the restricted phase cycling will not eliminate higher-order coherences, the contributions from these terms are minimal.

To show that virtually identical spectra can be obtained from the coherence pathways selecting the two orthogonal magnetization components

M_x and M_z during the mixing time, 2D TOCSY spectra were obtained for a 1 mM solution (D_2O) of the protein bovine pancreatic trypsin inhibitor (pD 4.7, 303 K). The mixing time was 69 ms; this value was chosen to enhance long-range coherence transfer.[34] The spectra were obtained at 500 MHz on a Bruker AM500 spectrometer using the modified z-filtered sequence and phase cycling described above. More explicitly, the basic phase cycling used was as follows:

For the first experiment: 1st 90° pulse: $+x$, $-x$; 2nd 90° pulse: $+x$, $+x$; mixing sequence: $+y$, $+y$; 3rd 90° pulse: $+x$, $+x$; receiver: $+x$, $-x$.

For the second experiment: 1st 90° pulse: $+x$, $-x$; 2nd 90° pulse: $-x$, $-x$; mixing sequence: $+y$, $+y$; 3rd 90° pulse: $+x$, $+x$; receiver: $+x$, $-x$.

Note the only change is the inversion of the second pulse. Furthermore, all phases were advanced in increments of 90° to eliminate quadrature images in the acquisition dimension, to give a total of eight steps for the complete phase cycle in each experiment. The TPPI scheme[21] was used for sign discrimination of the ω_1 frequencies. Although it is unnecessary in the conventional z-filtered TOCSY experiment,[35] RF phase coherence is required in the modified experiment to ensure that both magnetization components are kept orthogonal to the mixing sequence;[26] this is to avoid undesirable relaxation effects. A WALTZ-16[32] sequence was used for the isotropic mixing, with an 8 kHz field strength. When the two data sets are added together, the magnetization that was in the transverse plane at the beginning and the end of the mixing sequence is selected. The resulting phase-sensitive 2D spectrum is shown in Fig. 1. When the two data sets are subtracted, the magnetization that was longitudinal at the beginning and end of the mixing period is selected. The resulting spectrum is shown in Fig. 2 with exactly the same plotting parameters as for Fig. 1; this data set was processed identically to that in [illegible]. 1 except for a 90° phase shift in each dimension. Clearly the two data sets are virtually indistinguishable on this scale.

To demonstrate the improvement in sensitivity that results from adding the M_x (Fig. 1) and M_z (Fig. 2) spectra together, slices are shown in Fig. 3 that were taken parallel to the ω_1 axis through selected resonances in the three data sets M_x, M_z and $M_x + M_z$. Also included in Fig. 3 are the relevant slices taken from a spectrum obtained by combining the M_x and M_z data as quadrature pairs and performing a complex Fourier transformation in the ω_1 dimension; in this case only half of the experimental data was used, since every other FID recorded in the TPPI scheme is not required for the hypercomplex method. The data are plotted such that the r.m.s. noise level is the same for the corresponding slices from each data set; this required scaling down of the $M_x + M_z$ data by a factor of $\sqrt{2}$ relative to the other data sets. The factor of $\sqrt{2}$ is both that predicted theoretically above and

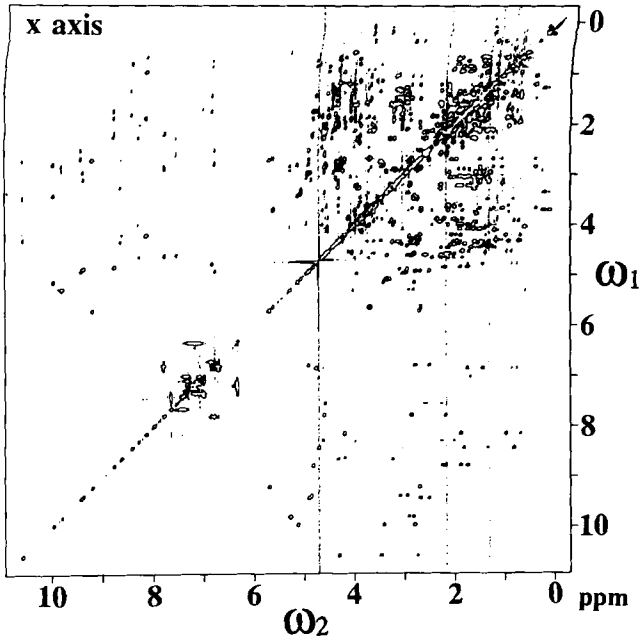

Fig. 1. Contour plot of a 2D phase-sensitive TOCSY spectrum for the protein BPTI (1 mM, in D_2O, pD 4.7, 303 K) recorded at 500 MHz (Bruker AM500) using the sensitivity-improved pulse sequence described in the text. The data shown arise from the magnetization that is aligned along the x axis of the rotating frame at the beginning and end of the mixing period (WALTZ-16 sequence has phases $+/-y$); the spectrum was generated by adding together the two data sets acquired. The WALTZ-16 sequence was applied for 69 ms, with an RF field strength of 8 kHz. The ω_2 spectral width was 12 500 Hz, 4096 data points were acquired (alternately in time) in each channel of the quadrature receiver, and 16 scans were signal-averaged for each of the two experiments needed to generate the spectrum shown. The ω_1 spectral width was 7143 Hz, and 640 t_1 values were used. A sine-bell window function, shifted by 60°, was applied in the ω_2 dimension and shifted by 45° in the ω_1 dimension. Only the positive contour levels are plotted. All data were processed using software provided by Hare Research. Suppression of t_1 ridges was accomplished by the method of Otting *et al.*[36]

that measured experimentally via numerical evaluation of the r.m.s. noise in ω_1 slices from the spectra. It can be seen in each example shown in Fig. 3 that the combined data have an improved signal-to-noise ratio compared with either the M_x or M_z data; quantitatively, the improvement in all cases is approximately $\sqrt{2}$, in agreement with theory. It is also apparent that the data treated as hypercomplex have the same signal-to-noise ratio as the M_x and M_z spectra, even though they were accumulated in half the time.

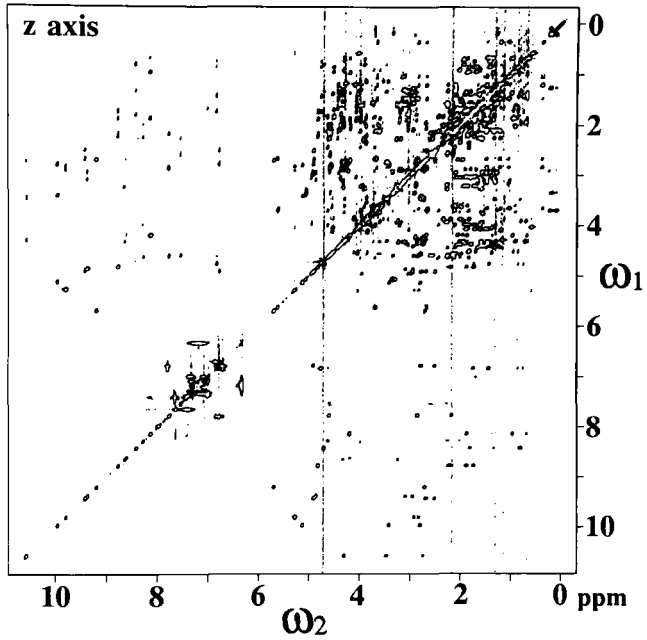

Fig. 2. Contour plot of a 2D TOCSY spectrum of BPTI, obtained from the same two data sets used to generate the spectrum in Fig. 1, except that the two sets were subtracted instead of added. The data shown arise from the magnetization that is aligned along the *z* axis of the rotating frame at the beginning and end of the mixing period. Processing parameters identical to those for the spectrum in Fig. 1 have been used, except that an additional 90° zeroth-order phase correction has been applied in both frequency dimensions.

3.2.1. Mixing sequences

The improvement in sensitivity of the TOCSY experiment as described here is based on the PEP methodology. In addition to the fact that the noise functions in the two orthogonally detected signals are uncorrelated, the sensitivity enhancement also requires that the two orthogonal magnetization components give rise to nearly identical spectra. In principle, this latter requirement would mean that the experimental mixing sequence should produce an effective Hamiltonian that retains only the isotropic scalar coupling terms. While the WALTZ-16 sequence does not produce a strictly isotropic mixing Hamiltonian,[38] the deviations are small enough to cause minimal problems. The so-called "17th pulse" proposed by Bax[26,39] to minimize the small loss in intensity due to intermixing of the orthogonal magnetization components during the mixing period is not compatible with the scheme described here for retaining two coherence transfer pathways. Mixing schemes based on the MLEV-16 sequence[26] are not useful for the sensitivity-improved TOCSY method because of non-isotropic behaviour

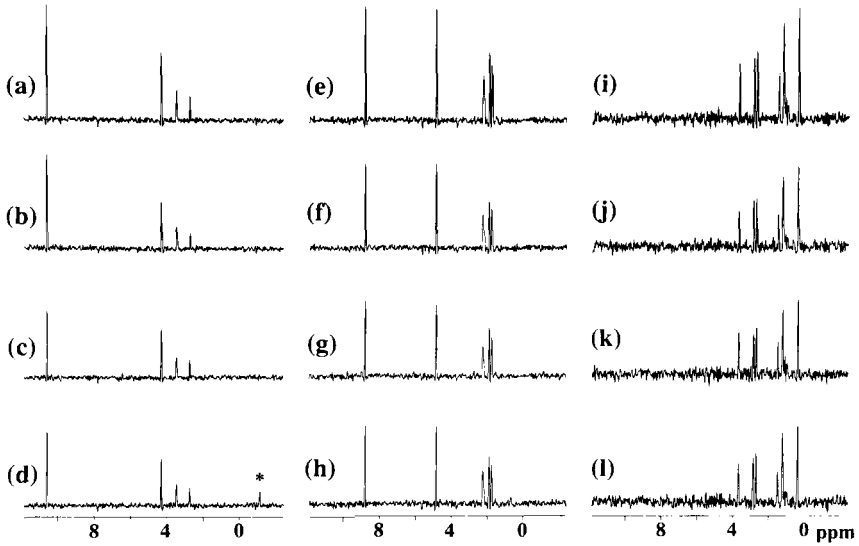

Fig. 3. Slices taken parallel to the ω_1 axis through 2D TOCSY spectra of BPTI. Slices (a)–(d) were taken at the ω_2 frequency (10.55 ppm) of the NH of tyrosine-23, slices (e)–(h) at the ω_2 frequency (8.77 ppm) of the NH of glutamine-31, and slices (i)–(l) at the ω_2 frequency (0.39 ppm) of one of the $C^{\beta}H$ of arginine-42.[37] The top row of data, slices (a), (e) and (i), was taken from the sensitivity-improved TOCSY spectrum obtained by adding together the M_x spectrum (Fig. 1) and the M_z spectrum (Fig. 2). The second row of data, slices (b), (f) and (j), was taken from the M_z spectrum, and the third row, slices (c), (g) and (k), was taken from the M_x spectrum. The bottom row of data, slices (d), (h) and (l), was taken from a data set generated by combining half of the M_x and M_z data as complex pairs before the ω_1 Fourier transformation (see text). The asterisk in slice (d) indicates an ω_1 "quadrature image" peak. Clearly the top row ($M_x + M_z$) has improved sensitivity over the M_x and M_z data, and the bottom row (complex combination) has equal sensitivity to the M_x and M_z spectra, even though the data were essentially acquired in half the time (i.e. only half the M_x and M_z data were used).

and unwanted relaxation effects. The DIPSI sequences reported by Shaka *et al.*[33] are very effective in the sensitivity-improved TOCSY experiment, since they were specifically designed to produce an isotropic mixing Hamiltonian. The DIPSI-2 and DIPSI-3 sequences are used in this context in our laboratory. One would predict that the FLOPSY sequences,[40] also introduced by Shaka, may not be applicable, for those reasons noted.

4. SENSITIVITY IMPROVEMENT IN ONE-BOND HETERONUCLEAR CORRELATION EXPERIMENTS

At present, information about the structure of proteins is mostly derived from proton NMR spectroscopy; bond connectivities are characterized by

the use of two-dimensional COSY[41,42] and TOCSY[25] experiments and interproton distances are determined by the use of two-dimensional NOESY[24] experiments. Although this approach has been fruitful for small proteins, the study of larger proteins by two-dimensional homonuclear NMR methods is limited in part by increased resonance overlap in the spectra.

One method that has been very useful in alleviating much of the resonance congestion is two-dimensional heteronuclear correlation spectroscopy.[43–45] Many assignment problems can be simplified by employing one-bond heteronuclear correlation methods, taking advantage of the larger chemical-shift dispersion of ^{13}C and ^{15}N heteronuclei. In addition to its inherent usefulness, the one-bond heteronuclear correlation experiment is also the basis for powerful heteronuclear relay experiments[46–50] and for heteronuclear relaxation measurements.[51–53] To obtain optimum sensitivity in these types of experiments, excitation and detection of proton magnetization is required.

Even with the introduction of proton-detected methods, sensitivity enhancement is always a prime concern in these types of experiments and maximizing the inherent sensitivity of the method, as in the case of the TOCSY experiment, is of paramount importance. In this section, the potential for an increase in sensitivity via PEP technology in various heteronuclear correlation methods is demonstrated. The size of the sensitivity enhancement can be as large as $\sqrt{2}$.

The principle behind the sensitivity increase for heteronuclear correlation experiments[22] is exactly the same as that described for the TOCSY experiment, by using the PEP methodology. However, modifications of the conventional sequences are required to obtain the enhancement, unlike in the TOCSY example, where only the phase cycling played a crucial part. Again, two orthogonal magnetization components are required to be detected, and it is in preserving these two components that the pulse sequences themselves need to be extended.

In Sections 4.1–4.3 methods are described for improving the sensitivity of each of the main classes of one-bond heteronuclear correlation experiments for heteronuclei with single geminal protons. An analysis of relaxation effects is presented along with experimental demonstration of the proposed methods.

4.1. Theory

The different classes of proton-detected one-bond heteronuclear correlation methods are conveniently categorized according to the form of the density operator after the initial excitation sequence and before the t_1 period. The methods can be classified as follows:

(i) sequences in which the density operator contains both I and S components that are unmodulated by chemical-shift evolution;

(ii) sequences in which the operator contains both I and S components that are encoded with the I-spin chemical shift;

(iii) sequences in which the operator contains only S-spin components.

The labels I and S refer to protons and heteronuclei respectively. The analysis below will consider the mosts popular methods belonging to each class, which are as follows:

class 1—the heteronuclear single-quantum coherence (HSQC) experiment;[44,54]

class 2—the heteronuclear multiple quantum coherence (HMQC) experiment;[44,55,56]

class 3—the double DEPT[44] and double refocused INEPT[44] experiments.

Although in the strictest definition, those experiments noted under class 3 involve the evolution of heteronuclear single quantum coherence during t_1; here they are differentiated from "conventional" HSQC experiments (class 1) by virtue of the fact that at the beginning of t_1 in-phase coherence evolves rather than antiphase coherence. (In practice, both class 1 and class 3 experiments would be referred to as HSQC methods.)

The PEP principle upon which the sensitivity-enhanced sequences are based is, of course, broadly applicable; however, the manner in which a given sequence must be modified depends on the particular nature of the experiment. Figure 4 shows the conventional pulse sequences for the HSQC, HMQC and double DEPT experiments, while Fig. 5 shows the sensitivity-enhanced versions of each of these methods. In the analysis below the spin system consists of a heteronucleus, denoted the S spin, that has one or more directly attached protons and any number of remotely connected protons, denoted the I spins. All spins are assumed to be weakly coupled, and the one-bond heteronuclear coupling between the I and S spins is assumed to be much larger than the homonuclear scalar couplings between the attached and remote I spins. In the following treatment only the product operator terms that illustrate the principles of the methods are given; other terms potentially giving rise to observable signal are experimentally suppressed by appropriate phase cycling, homospoil gradients or purge pulses.

As a fully worked example of PEP sensitivity enhancement technology in heteronuclear correlation experiments, the HSQC experiment is chosen because of its popularity in the study of proteins.[57,58] The conventional sequence (Fig. 4a) consists of an INEPT polarization transfer from the I to the S spins, a t_1 evolution period, a reverse INEPT polarization transfer

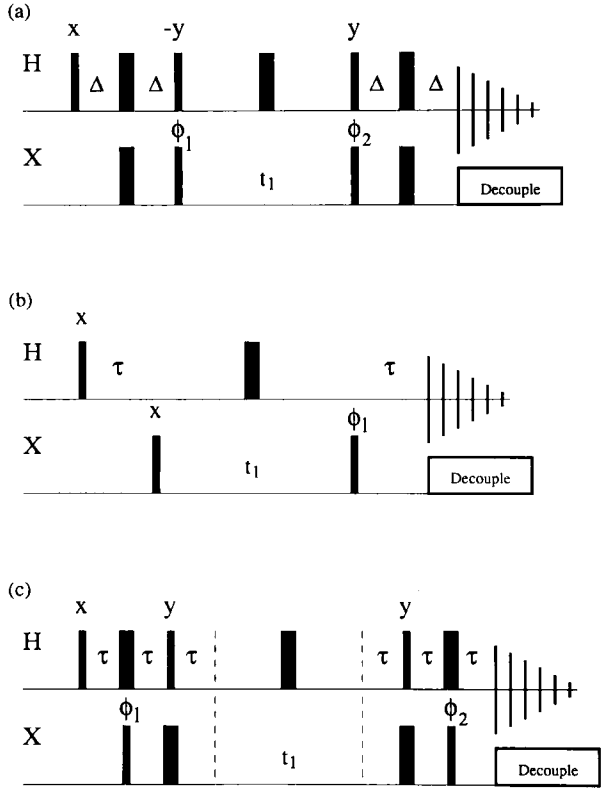

Fig. 4. Pulse sequences for recording conventional heteronuclear correlation spectra. The pulse sequences shown are for (a) the HSQC, (b) the HMQC and (c) the double DEPT methods of acquiring two-dimensional heteronuclear correlation spectra. The thin and thick vertical bars represent 90° and 180° pulses applied to the H (protons) or X (heteronucleus) spins; all 180° pulses in the sequences are applied along the y axis. The delays Δ and τ are $1/4J$ and $1/2J$ respectively, where J is the one-bond HX coupling constant. Decoupling of the X spins during acquisition is achieved by using an appropriate composite pulse decoupling sequence. Quadrature detection in the ω_1 dimension can be achieved by either the TPPI or hypercomplex methods (see text). The basic phase cycling is (a) $\phi_1 = (x, -x, x, -x)$, $\phi_2 = (x, x, -x, -x)$ and receiver = $(x, -x, -x, x)$; (b) $\phi_1 = (x, -x, -x, x)$ and receiver = $(x, -x, -x, x)$; (c) same as (a). In practice, composite 180° pulses may be used in place of the regular 180° pulses on the X spins. Heteronuclear zero- and double-quantum artefacts can be reduced by phase cycling of the 180° proton pulse in the middle of t_1.

from S to I spins, and a t_2 acquisition period. Beginning with equilibrium I-spin magnetization, the evolution up to the t_1 period is (see Figs 4a and 5a):

$$I_z \xrightarrow{\text{INEPT}} -2I_zS_y \tag{33}$$

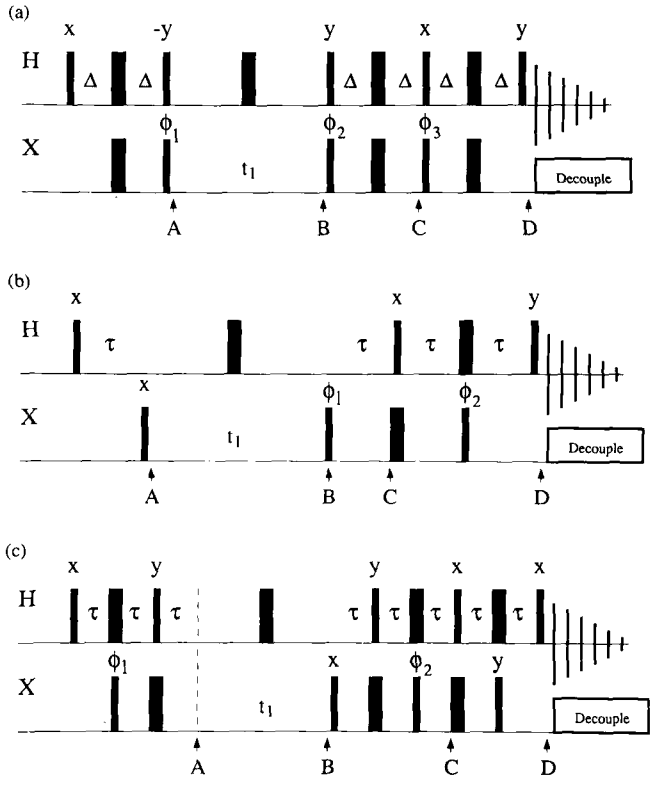

Fig. 5. Pulse sequences for recording heteronuclear correlation spectra with improved sensitivity. The pulse sequences shown are for improving the sensitivity of (a) the HSQC, (b) the HMQC and (c) the double DEPT methods of acquiring two-dimensional heteronuclear correlation spectra. The relevant product operators present at the points labelled A–D in the sequences are given in Table 1. The thin and thick vertical bars represent 90° and 180° pulses applied to the H (protons) or X (heteronucleus) spins; all 180° pulses in the sequences are applied along the y axis. The delays Δ and τ are $1/4J$ and $1/2J$ respectively, where J is the one-bond HX coupling constant. Decoupling of the X spins during acquisition is achieved by using an appropriate composite pulse decoupling sequence. Quadrature detection in the ω_1 dimension can be achieved by either the TPPI or hypercomplex methods (see text). The basic phase cycling is (a) $\phi_1 = (x, -x, x, -x)$, $\phi_2 = (x, x, -x, -x)$, $\phi_3 = (y, y, -y, -y)$ and receiver = $(x, -x, -x, x)$; (b) $\phi_1 = (x, -x, -x, x)$, $\phi_2 = (y, -y, y, -y)$ and receiver = $(x, -x, -x, x)$; (c) $\phi_1 = (x, -x, x, -x)$, $\phi_2 = (x, x, -x, -x)$ and receiver = $(x, -x, -x, x)$. In practice, composite 180° pulses may be used in place of the regular 180° pulses on the X spins. Heteronuclear zero- and double-quantum artefacts can be reduced by phase cycling of the 180° proton pulse in the middle of t_1. For sensitivity improvement, two experiments are recorded, the first with the phase cycle as noted above, the second with phase inversion of the pulse on the X spins immediately following the t_1 period. The two data sets are stored separately and then combined as described in the text.

where the delay Δ in the INEPT sequence is $1/4J_{IS}$, and J_{IS} is the one-bond heteronuclear scalar coupling constant (a factor of $\sin \pi J_{IS}\Delta$ has been dropped from (33) for convenience). During the t_1 period the antiphase operator evolves solely under the influence of the heteronuclear chemical shift because the 180° pulse on the I spins in the middle of t_1 decouples the I and S spins:

$$-2I_zS_y \xrightarrow{t_1/2-180°(I)-t_1/2} 2I_zS_y \cos \omega_S t_1 - 2I_zS_x \sin \omega_S t_1, \tag{34}$$

in which ω_S is the Larmor frequency of the decoupled S spins in the rotating reference frame. If the heteronucleus has a single attached proton, the reverse INEPT sequence gives (again dropping $\sin \pi J_{IS}\Delta$ factors),

$$2I_zS_y \cos \omega_S t_1 - 2I_zS_x \sin \omega_S t_1 \xrightarrow{\text{reverse INEPT}} I_y \cos \omega_S t_1 - 2I_xS_x \sin \omega_S t_1. \tag{35}$$

If the heteronucleus has more than one attached proton, evolution of the multiple quantum coherence term $2I_xS_x$ under heteronuclear scalar couplings to the passive spins I' occurs during the reverse INEPT sequence. In the case of two attached protons the reverse INEPT sequence would generate

$$2I_zS_y \cos \omega_S t_1 - 2I_zS_x \cos \omega_S t_1 \xrightarrow{\text{reverse INEPT}} I_y \cos \omega_S t_1 - 4I_xI'_zS_y \sin \omega_S t_1. \tag{36}$$

In (35) and (36), the $I_y \cos \omega_S t_1$ term represents I-spin magnetization that is labelled by the chemical shift of the heteronucleus during t_1 and is detected during t_2. The other terms represent multiple quantum coherences that are unobservable during t_2. For these types of experiments, where only one in-phase magnetization component is observed, the resulting two-dimensional data set can be processed into a single-bond heteronuclear correlation spectrum with peak shapes that are purely absorptive in both dimensions as expected. This is the case for the purely conventional HSQC experiment of Fig. 4(a).

The evolution of the density operator for the enhanced HSQC sequence (Fig. 5a) proceeds exactly as for the conventional HSQC experiment up to the point labelled C in Fig. 5(a), where the operators are given by the final terms in (35) and (36). For a heteronucleus with a single attached proton, (35), the evolution through the remainder of the sequence is

$$\begin{aligned} I_y \cos \omega_S t_1 - 2I_xS_x \sin \omega_S t_1 &\xrightarrow{90°_x(I)\,90°_y(S)} I_z \cos \omega_S t_1 - 2I_xS_z \sin \omega_S t_1 \\ &\xrightarrow{\Delta-180°_y(I,S)-\Delta} -I_z \cos \omega_S t_1 + I_y \sin \omega_S t_1 \\ &\xrightarrow{90°_y(I)} -I_x \cos \omega_S t_1 + I_y \sin \omega_S t_1. \end{aligned} \tag{37}$$

The resultant $-I_x \cos \omega_S t_1$ and $I_y \sin \omega_S t_1$ terms in (37) describe orthogonal

in-phase I-spin magnetization components that have evolved at the frequency of the S-spin during t_1. This state of affairs can be recognized as the basis for the sensitivity enhancement procedure, where two orthogonal in-phase magnetization components are detected simultaneously. It is also important to consider the fate of the heteronucleus with two attached protons, (36), during the final stage of the enhanced sequence:

$$\begin{aligned} I_y \cos\omega_S t_1 - 4I_x I_z' S_y \sin\omega_S t_1 &\xrightarrow{90^\circ_x(I)\,90^\circ_y(S)} I_z \cos\omega_S t_1 + 4I_x I_y' S_y \sin\omega_S t_1 \\ &\xrightarrow{\Delta\text{–}180^\circ_y(I,S)\text{–}\Delta} -I_z \cos\omega_S t_1 - 4I_x I_y' S_y \sin\omega_S t_1 \\ &\xrightarrow{90^\circ_y(I)} -I_x \cos\omega_S t_1 + 4I_z I_y' S_y \sin\omega_S t_1. \end{aligned} \quad (38)$$

The first term in the final expression of (38) represents in-phase I-spin magnetization, while the second term represents unobservable multiple quantum coherence. In this case, for a heteronucleus with two attached protons, the modified sequence does not generate the required two orthogonal components for sensitivity improvement; consequently, the extended sequences do not provide sensitivity enhancement for heteronuclei with two geminal protons. Similar conclusions hold for heteronuclei with more than two attached protons.

The resulting two terms in (37) give rise to the observable signals, which are 90° out of phase in both dimensions; processing of these data alone would generate a phase-twisted spectrum. As outlined in the basic PEP methodology, it is necessary to separate the two orthogonal terms and obtain purely absorptive spectra by recording a second experiment in which one of the detected terms in (37) changes sign. This is easily achieved by executing the extended sequence again, but with inversion of the phase of the 90° pulse on the heteronucleus immediately following the t_1 period. In this experiment the relevant operator terms are (beginning with the operators at the end of (34)),

$$\begin{aligned} &2I_z S_y \cos\omega_S t_1 - 2I_z S_x \sin\omega_S t_1 \\ &\xrightarrow{90^\circ_y(I)\,90^\circ_{-x}(S)\text{–}\Delta\text{–}180^\circ_y(I,S)\text{–}\Delta\text{–}90^\circ_x(I)\,90^\circ_y(S)\text{–}\Delta\text{–}180^\circ_y(I,S)\text{–}\Delta\text{–}90^\circ_y(I)} \\ &\qquad I_x \cos\omega_S t_1 + I_y \sin\omega_S t_1, \end{aligned} \quad (39)$$

for a single attached proton. For a heteronucleus with two attached protons the second experiment yields

$$\begin{aligned} &2I_z S_y \cos\omega_S t_1 - 2I_z S_x \sin\omega_S t_1 \\ &\xrightarrow{90^\circ_y(I)\,90^\circ_{-x}(S)\text{–}\Delta\text{–}180^\circ_y(I,S)\text{–}\Delta\text{–}90^\circ_x(I)\,90^\circ_y(S)\text{–}\Delta\text{–}180^\circ_y(I,S)\text{–}\Delta\text{–}90^\circ_y(I)} \\ &\qquad I_x \cos\omega_S t_1 + 4I_z I_y' S_y \sin\omega_S t_1. \end{aligned} \quad (40)$$

Following the above analysis, it is now possible to write general expressions to describe the observable operators at the beginning of the acquisition period for the modified experiment. For the first experiment the observable operators are

$$-I_x \cos \omega_S t_1 + \delta_{1n} I_y \sin \omega_S t_1, \tag{41}$$

and for the second experiment

$$I_x \cos \omega_S t_1 + \delta_{1n} I_y \sin \omega_S t_1 \tag{42}$$

in which δ_{1n} is the Kronecker delta and n is the number of protons directly attached to the heteronucleus. Addition of the two data sets (41) and (42) yields the single observable term

$$2\delta_{1n} I_y \sin \omega_S t_1, \tag{43}$$

while subtraction gives the single observable term

$$-2I_x \cos \omega_S t_1. \tag{44}$$

Neglecting relaxation effects and pulse imperfections in the longer sequences, the spectrum that results from the $-2I_x \cos \omega_S t_1$ term is identical to the spectrum obtained using the conventional HSQC sequence. When one neglects relaxation, mismatching between the one-bond heteronuclear coupling constants and the delay Δ, and pulse imperfections, the spectrum that results from the $2\delta_{1n} I_y \sin \omega_S t_1$ term produces a two-dimensional heteronuclear correlation spectrum that has been edited with a multiplicity filter.[55,59] In this spectrum the resonances that arise from heteronuclei with one attached proton have the same intensities as those in the conventional spectrum, but the resonances of other heteronuclei are nulled. These two spectra are obtained using the enhanced sequence of Fig. 5(a) in the same amount of time required to obtain one spectrum using the conventional HSQC sequence of Fig. 4(a).

The final sensitivity-enhanced spectrum is obtained by adding the two pure absorption spectra derived above. As described earlier for the PEP technique, the resultant spectrum has resonances that are coherent combinations of the two separate spectra, whereas the r.m.s. noise in this process combines as though statistically independent and increases only by $\sqrt{2}$. Neglecting relaxation effects, the theoretical increase in signal-to-noise ratio of the enhanced experiment over the conventional one is $\sqrt{2}$. For convenience in the discussion above the equivalent data sets were presumed to have been processed separately and then co-added as 2D spectra. As pointed out in Section 2.3.1, it is also possible to combine the data in the time-domain using the appropriate recipe if the hypercomplex method for ω_1 sign discrimination has been employed.

The other sensitivity-enhanced sequences shown in Fig. 5 work in virtually the same way as described for the HSQC sequence. First, the operator that

Table 1. Product operators for pulse sequences with enhanced sensitivity.[a]

Point	HSQC
A	$-2I_zS_y$
B	$2I_zS_y\cos\omega_S t_1 - 2I_zS_x\sin\omega_S t_1$
C	$I_y\cos\omega_S t_1 - 2I_xS_x\sin\omega_S t_1$
D	$-I_x\cos\omega_S t_1 + I_y\sin\omega_S t_1$
Point	**HMQC**
A	$-2I_xS_y\cos\omega_I\tau - 2I_yS_y\sin\omega_I\tau$
B	$2(I_x\cos\omega_I\tau - I_y\sin\omega_I\tau)(S_y\cos\omega_S t_1 - S_x\sin\omega_S t_1)$
C	$I_y\cos\omega_S t_1 - 2I_x\sin\omega_S t_1(S_x\cos\omega_S\tau + S_y\sin\omega_S\tau)$
D	$-I_x\cos\omega_S t_1 + I_y\sin\omega_S t_1$
Point	**Double DEPT**
A	S_x
B	$S_x\cos\omega_S t_1 + S_y\sin\omega_S t_1$
C	$-I_y\cos\omega_S t_1 - 2I_z\sin\omega_S t_1(S_x\cos\omega_S\tau + S_y\sin\omega_S\tau)$
D	$-I_y\cos\omega_S t_1 - I_x\sin\omega_S t_1$

[a]The table shows the principal product operators, for a heteronuclear S spin with a single geminal proton I spin, that are present at the points labelled A–D in Fig. 5 for the sensitivity-enhanced HSQC, HMQC and double DEPT pulse sequences. The terms at point D are detected during the acquisition period; the sign of one of the components can be negated by inverting the phase of the first 90° pulse on the S spins following the t_1 period in Fig. 5. The operators at point A and B are identical to the operators at the corresponding points in the conventional sequences shown in Fig. 4. The operators at point C are identical to the operators prior to acquisition in the conventional HSQC and HMQC sequences; for the conventional double DEPT sequence the operator terms are: $-I_y\cos\omega_S t_1 - 2I_x\sin\omega_S t_1 (S_X\cos\omega_S\tau + S_y\sin\omega_S\tau)$.

is cosine-modulated during t_1 is transferred to a single-quantum I-spin operator. Secondly, this operator is stored as longitudinal magnetization while the product operator that is sine-modulated during t_1 is refocused to transverse proton magnetization. Thirdly, the final proton 90° pulse rotates the longitudinal magnetization back to the transverse plane for detection. In all cases a second experiment is acquired in which the phase of the first 90° pulse on the heteronuclei after t_1 is inverted and the data are processed as described. The product operators present at the most informative points in each of the sequences in Fig. 5 are given in Table 1.

Unlike in the enhanced TOCSY experiment, the sensitivity-enhanced heteronuclear correlation sequences have been extended in duration. Consequently the maximum signal-to-noise enhancement of $\sqrt{2}$ is only achievable if relaxation of the density operator during the pulse sequences is negligible. In general, owing to additional relaxation processes during the longer pulse sequences, the magnitudes of the two orthogonal I-spin

operators that are acquired in the enhanced experiments will be less than the magnitudes of the I-spin operators present during the acquisition period in the conventional experiments. In addition, the magnitudes of the two orthogonal magnetization components in the enhanced sequences will not be equal, because the cosine- and sine-modulated operators present after the t_1 period follow different pathways during the reverse polarization transfer steps and relax at different rates. For these reasons, the sensitivity gains afforded by the methods described here will be reduced from the ideal value of $\sqrt{2}$ by amounts that depend on both the relative lengths of the conventional and enhanced pulse sequences and the particular product operator terms present during the polarization transfer from the heteronucleus back to proton.

4.2. Relaxation considerations

Once again, for illustrative purposes, the conventional and enhanced HSQC sequences are considered.[22] During the reverse INEPT transfer in the conventional experiment, the heteronuclear antiphase operator I_xS_z is refocused to I_y. The magnitude of the observable operator at the beginning of the t_2 acquisition period is, disregarding the chemical shift modulation,

$$I_y = I_y^0 \exp(-2R_{2I}\Delta), \tag{45}$$

in which R_{2I} is the average of the transverse relaxation rate constants of the in-phase and antiphase I-spin operators, and I_y^0 is the magnitude of the operator in the absence of relaxation.

In the enhanced experiment two consecutive reverse INEPT sequences, each of length 2Δ, are used to refocus the heteronuclear operators present after t_1 into orthogonal I_x and I_y operators. The magnitude of each of the I_x and I_y operators depends on the relaxation of the operators present during each of the reverse INEPT sequences. Inherent within the reverse INEPT portion of (35), a cosine-modulated I_xS_z term is refocused to an I_y term during the first INEPT transfer. The second INEPT sequence then simply stores this term as longitudinal magnetization, and it is finally converted to the I_x operator by the last 90° pulse for detection. In the second INEPT sequence the initial I_z operator relaxes toward the thermal equilibrium polarization during the first delay Δ; then the 180° pulse on the I spins inverts the I_z term to $-I_z$, which proceeds to relax towards thermal equilibrium during the second Δ delay. The operator prior to the final pulse of the sequence is

$$I_z = I_z^\infty - [2I_z^\infty - (I_z^\infty - I_z^0)\exp(-R_{1I}\Delta)]\exp(-R_{1I}\Delta), \tag{46}$$

in which I_z^∞ is the thermal-equilibrium value of the longitudinal magnetization, I_z^0 is the value of the longitudinal magnetization at the beginning of the

second reverse INEPT sequence, and R_{1I} is the longitudinal relaxation rate constant for the I spins. Because of the phase cycling of the 90° pulses on the S spins and of the receiver (Fig. 5a), the value of I_z^0 is inverted on alternate scans and the resulting signals are subtracted. The average relaxation of I_z over the phase cycle is found by changing the sign of I_z^0 in (46) and subtracting the new result from (46) to yield

$$I_z = -I_z^0 \exp(-2R_{1I}\Delta). \tag{47}$$

During the 2Δ period, cross-relaxation can also occur between I spins, which would be expected to produce NOESY peaks in the spectrum described by the term $-2I_x \cos \omega_S t_1$; however, since Δ is short, such peaks are expected to be extremely weak and very difficult to observe. Using (45) and (47), it is now possible to calculate the magnitude of the final observable cosine-modulated I_x operator, disregarding chemical-shift modulation,

$$I_x = I_x^0 \exp[-2(R_{2I} + R_{1I})\Delta], \tag{48}$$

in which I_x^0 is the magnitude of the operator in the absence of relaxation. The sine-modulated component, I_y, following t_1, is stored as I_xS_x multiple quantum coherence during the first reverse INEPT sequence (35) and refocused from I_xS_z to I_y during the second reverse INEPT transfer (37). The magnitude of the final observable operator is, disregarding chemical-shift modulation,

$$I_y = I_y^0 \exp[-2(R_{2I} + R_{2MQ})\Delta], \tag{49}$$

in which R_{2MQ} is the average of the transverse relaxation rates of the zero and double-quantum coherences present during the first INEPT sequence, and I_y^0 is the magnitude of the operator in the absence of relaxation.

The relative intensities of the conventional HSQC spectrum and the spectra that result from addition, (43), and subtraction, (44), of the two data sets acquired with the enhanced sequence can be determined from (45), (48) and (49). The relative intensities of the spectra that result from addition and subtraction compared with the conventional sequence are

$$E_{add} = \exp(-2R_{2MQ}\Delta), \tag{50}$$

$$E_{sub} = \exp(-2R_{1I}\Delta) \tag{51}$$

respectively. The relative intensity of the added spectrum compared with the subtracted spectrum is

$$E_r = \frac{E_{add}}{E_{sub}}, \tag{52}$$

Table 2. Effects of relaxation in pulse sequences with enhanced sensitivity.[a]

	ε_a	ε_s
HSQC	$\exp(-2R_{2MQ}\Delta)$	$\exp(-2R_{1I}\Delta)$
HMQC	$\exp(-2R_{2MQ}\tau)$	$\exp(-2R_{1I}\tau)$
DEPT	$\exp(-2R_{1S}\tau)$	$\exp(-2R_{1I}\tau)$

[a]The table shows the relative intensities of the two spectra obtained by deconvoluting the two orthogonal in-phase magnetization components that are obtained in the sensitivity-enhanced heteronuclear correlation experiments (Fig. 5), compared with the corresponding conventional spectra (Fig. 4). The relative intensities ε_a and ε_s refer to the ADD and SUBTRACT spectra respectively. The notation is described in the text.

where $E_r < 1$ since R_{2MQ} will generally be greater than R_{1I}. The achievable sensitivity enhancement is

$$E = \tfrac{1}{2}\sqrt{2}(E_{add} + E_{sub}), \tag{53}$$

compared with the maximum value of $\sqrt{2}$. The analysis of the effects of relaxation of the other sensitivity-enhanced pulse sequences follow similar lines. The results for the relative intensities of the two independent deconvoluted data sets are given in Table 2.

To estimate the expected sensitivity enhancement for a given molecule, the appropriate relaxation rates, given in (50) and (51) and Table 2, must be measured experimentally or calculated for a specific relaxation mechanism. In the following the I and S spins are assumed to relax solely by dipole–dipole interactions, and the spins are assumed to be rigidly attached to a molecule that undergoes isotropic rotational diffusion with a correlation time τ_c. The S spins relax only through interactions with the directly attached I spins; the I spins relax both with the S spins and with other nearby I spins. Other relaxation mechanisms are not considered. The I spins are assumed to be in the slow-motion limit with $\omega_I\tau_c \gg 1$ and $\omega_I \gg \omega_S$, where ω_I and ω_S are the Larmor frequencies of the I and S spins respectively.

The expressions for the dipolar relaxation rate constants for the longitudinal I_z and S_z operators and for the transverse multiple quantum operator are given by

$$R_{1I} = \frac{1}{10} D_{IS}^2[J(\omega_I - \omega_S) + 3J(\omega_I) + 6J(\omega_I + \omega_S)] + \frac{1}{10}\sum_k D_{IK}^2[J(0) + 3J(\omega_I) + 6J(2\omega_I)], \tag{54}$$

$$R_{1S} = \frac{1}{10} D_{IS}^2[J(\omega_I - \omega_S) + 3J(\omega_I) + 6J(\omega_I + \omega_S)], \tag{55}$$

$$R_{2MQ} = \frac{1}{20} D_{IS}^2[J(\omega_I - \omega_S) + 3J(\omega_I) + 3J(\omega_S) + 6J(\omega_I + \omega_S)]$$

$$+ \frac{1}{20} \sum_k D_{IK}^2[5J(0) + 9J(\omega_I) + 6J(2\omega_I)], \tag{56}$$

in which

$$D_{IJ} = \frac{h\gamma(I)\gamma(J)\mu_0}{8\pi^2 r_{IJ}^3}, \tag{57}$$

$$J(\omega) = \frac{\tau_c}{1 + \omega^2\tau_c^2} \tag{58}$$

where h is Planck's constant, $\gamma(I)$ and $\gamma(J)$ are the magnetogyric ratios of the spins I and J respectively, r_{IJ} is the length of the internuclear vector between the I and J spins, and μ_0 is the permeability of free space. The summation sign includes all of the homonuclear $K \neq I$ (proton) spins. The longitudinal relaxation rate constant of the S spins, R_{1S}, is required for the analysis of the double DEPT sequence. The terms containing D_{IS} arise from the heteronuclear dipolar coupling between the I and S spins, and the terms containing D_{IK} reflect the homonuclear dipolar coupling between I spins.

In the limit of slow overall tumbling, as is the case for most biomolecules, $J(0) > J(\omega_S) \gg J(\omega_I)$; therefore the relaxation rate constants are approximately given by

$$R_{1I} = D_{IS}^2 J(\omega_I) + \frac{1}{10} J(0) \sum_k D_{IK}^2, \tag{59}$$

$$R_{iS} = \frac{3}{10} D_{IS}^2 J(\omega_S), \tag{60}$$

$$R_{2MQ} = \frac{3}{20} D_{IS}^2 J(\omega_S) + \frac{1}{4} J(0) \sum_k D_{IK}^2. \tag{61}$$

As noted elsewhere,[43,60] the expressions for the heteronuclear dipolar contribution to R_{2MQ} do not depend on $J(0)$, and hence vanish as $\tau_c \to \infty$. However, R_{2MQ} can still be large, because the magnitudes of the homonuclear dipolar terms increase monotonically with τ_c. Typically, for molecules under conditions such that $\omega_S\tau_c \gg 1$, $R_{2MQ} > R_{1I} > R_{1S}$. Keeping this inequality in mind, the results in Table 2 suggest that the attainable sensitivity enhancement would be greatest for the double DEPT, followed by the HSQC and lastly the HMQC enhanced experiments. Although this is the case theoretically, it should be noted that the enhanced double DEPT

sequence is considerably longer than the other enhanced sequences, and in practice may not have a higher absolute sensitivity.

Substituting (59) and (61) in (50) and (51) gives, for the HSQC case under consideration,

$$E_{\text{add}} = \exp\left\{-2\Delta\left[\frac{3}{20}\ D_{IS}^2 J(\omega_S) + \ \frac{1}{4} J(0)\ \sum_k D_{IK}^2\right]\right\}, \tag{62}$$

$$E_{\text{sub}} = \exp\left\{-2\Delta\left[D_{IS}^2 J(\omega_I) + \ \frac{1}{10} J(0)\ \sum_k D_{IK}^2\right]\right\}. \tag{63}$$

Similar expressions can be found for the other sequences. The expressions for E_{add} and E_{sub} for the sensitivity-enhanced sequences are dominated by the term

$$J(0) \sum_k D_{IK}^2 = \left[\frac{h\gamma(I)^2 \mu_0}{8\pi^2}\right]^2 \tau_c \sum_k r_{IK}^{-6} \tag{64}$$

for large proteins with long rotational correlation times. In the absence of significant internal motions, the largest molecules for which the longer sensitivity-enhanced HSQC sequence will yield appreciable gains in the signal-to-noise ratio of the heteronuclear correlation spectra are determined by the values of the parameters in (64). Using a typical value of $\Sigma_k r_{IK}^{-6} = 0.027\ \text{Å}^{-6} \pm 0.009\ \text{Å}^{-6}$ for the distances from a backbone proton to the other protons in proteins,[22] enhancement factors of greater than 1.1 are estimated to be obtainable for molecules with molecular correlation times of the order of 20 ns. The average value of $\Sigma_k r_{IK}^{-6}$ was calculated from the atomic coordinates of the zinc finger Xfin-31, BPTI, french bean plastocyanin and sperm whale myoglobin obtained from the Brookhaven Protein Data Bank. Distances were calculated from each backbone amide or alpha proton (except for the alpha protons of glycines) to the other protons in the protein, and the summation executed.

4.3. Experimental demonstration

In the study of proteins, sensitivity-enhanced heteronuclear correlation experiments are most useful for correlating the backbone α-carbons or amide nitrogens with their attached protons. Except for the α-carbon of glycine, the imino nitrogen of proline, and the *N*-terminal amide, these heteronuclei all have a single geminal proton, as required for sensitivity enhancement. In addition, the multiplicity-filtered spectrum that can also be obtained in these experiments assists in distinguishing backbone resonances from side-chain resonances with similar chemical shifts.

The sensitivity gains predicted theoretically were verified experimentally by the acquisition of two-dimensional heteronuclear correlation spectra using the conventional HSQC pulse sequence and the corresponding sensitivity-enhanced sequence.[22] The relevant phase cycling schemes are given in the figure captions to Figs 4 and 5. All experiments were performed on a sample of the small globular protein BPTI (MW = 6500) at ^{15}N *natural abundance*. The experimental protocol is given in the caption to Fig. 6. The total acquisition was 20 h each for the conventional HSQC experiment and the sensitivity-enhanced HSQC experiment. A contour plot of the conventional HSQC spectrum is shown in Fig. 6(a). The two data sets acquired in the sensitivity-enhanced experiment are independent combinations of two orthogonal in-phase proton magnetization components, which, if processed independently, would generate spectra with unacceptable phase-twisted lineshapes. To deconvolute the two magnetization components, the two data sets were added to produce a new data set called ADD and subtracted to produce a second data set labelled SUBTRACT. Following two-dimensional Fourier transformation and appropriate phasing, two pure absorption HSQC spectra are obtained; these spectra are shown in Fig. 6(b) for the ADD spectrum and Fig. 6(c) for the SUBTRACT spectrum. The sensitivity-enhanced spectrum is produced by adding the ADD and SUBTRACT spectra. This spectrum is shown in Fig. 6(d), and is labelled ENHANCED. For comparison purposes, cross-sections taken parallel to the ω_2 dimension from all four types of spectra are shown in Fig. 7 for selected heteronuclear resonances.

On close inspection of the two-dimensional spectra and the cross-sections it is seen that the SUBTRACT and conventional HSQC spectra are virtually identical; however, some resonances in the ADD spectrum exhibit drastically reduced intensities relative to those of both the conventional and SUBTRACT HSQC spectra. These resonances, indicated by arrows in

---

Fig. 6. Contour plots of two-dimensional ^1H–^{15}N HSQC spectra of BPTI acquired using conventional and sensitivity-enhanced HSQC methods. All experiments were performed on a sample of BPTI (20 mM, 90% H_2O/10% D_2O, pH 4.6, 308 K) at natural ^{15}N abundance. Spectroscopy was performed on a Bruker AM500 spectrometer equipped with 451 MHz IF electronics. Data processing was performed using software provided by Hare Research. A conventional HSQC spectrum was acquired using the pulse sequence of Fig. 4(a). For this experiment 1024 scans were acquired per t_1 increment. The two data sets required to produce the sensitivity-enhanced HSQC spectrum (Fig. 5a) were acquired with 512 scans per t_1 increment. For all spectra 4096 real data points (2048 per quadrature channel) were acquired in t_2 and 100 real points were acquired in t_1. TPPI was used for frequency discrimination in the ω_1 dimension. The spectral width was 7042 Hz in ω_2 and 2500 Hz in ω_1. The delay Δ was set to 2.3 ms, which is slightly less than $1/4J$ to reduce relaxation losses. To

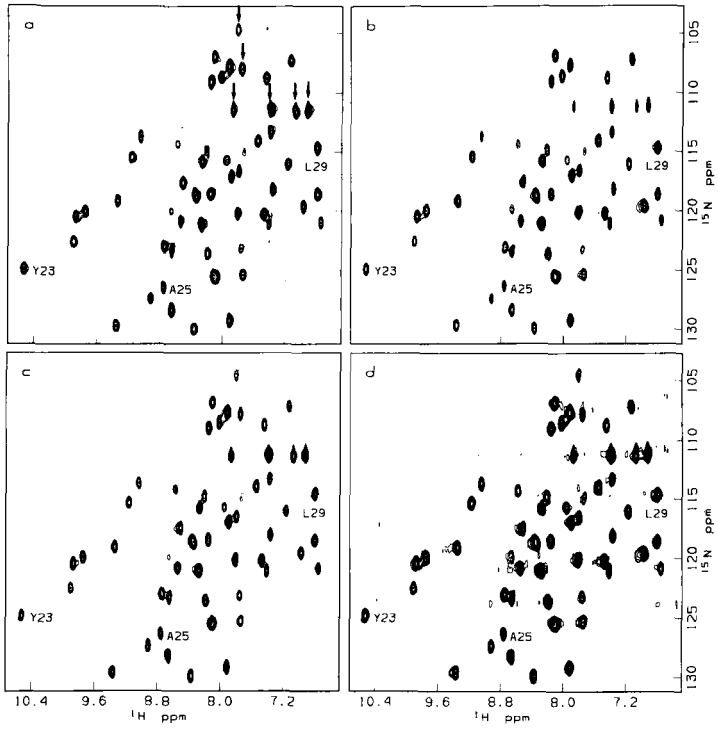

improve the suppression of magnetization from protons not bound to ^{15}N, a homospoil gradient pulse of 3 ms was applied directly after the second 90° proton pulse. The gradient pulse was followed by a delay of 7 ms to allow the magnetic field to stabilize prior to the first 90° heteronucleus pulse. The two data sets acquired using the sequence of Fig. 5(a) were added and subtracted to produce the new data sets, called respectively ADD and SUBTRACT, which were used for subsequent data manipulation. Spectra were processed using 8 Hz exponential line broadening in ω_2 and a Kaiser window in ω_1. Spectra were zero-filled before Fourier transformation to yield a final size of 2048 real points in each dimension. The spectra shown are (a) the conventional HSQC spectrum, (b) the ADD spectrum and (c) the SUBTRACT spectrum. The SUBTRACT spectrum was initially phased to be pure absorption in both dimensions; the ADD spectrum was also phased to be pure absorption in both dimensions by adding a 90° phase shift in both dimensions relative to the SUBTRACT spectrum. The ADD and SUBTRACT spectra were then added to produce the ENHANCED spectrum shown in (d). All two-dimensional spectra are shown on the same absolute scale. Arrows in (a) indicate resonances arising from the side-chain groups noted. The conventional and SUBTRACT spectra are virtually identical, while the ADD spectrum exhibits attenuated resonances in some regions (those indicated by arrows in (a)) due to the multiplicity filter. Assignments for selected resonances for comparison in Fig. 7 are also noted. For the 49 backbone amide resonances identified the ENHANCED HSQC spectrum displays a 1.32 sensitivity improvement over the conventional HSQC spectrum.

Fig. 6(a), were identified, using a conventional double-refocused INEPT experiment, as side-chain NH_2 groups (data not shown). As noted above, NH_2 resonances are suppressed in the ADD spectrum because only NH resonances are retained by the multiplicity filter in the sensitivity-enhanced sequences. In principle, these peaks should be completely absent in the ADD spectrum, but, because of mismatching of the Δ delays and the one-bond NH coupling, small residual components may remain. An example of the suppression of NH_2 resonances in the ADD spectrum is clearly demonstrated in the spectrum shown in Fig. 7(d). The ability to distinguish NH_2 side-chain groups from backbone NH groups within one experiment is a useful bonus to this methodology.

As discussed theoretically, the ideal sensitivity enhancement of $\sqrt{2}$ depends on the noise being uncorrelated in the ADD and SUBTRACT spectra, and the achievable sensitivity enhancement depends on the longitudinal and multiple quantum relaxation rates of the I and S spins. For the conventional HSQC spectrum, and the ADD, SUBTRACT and ENHANCED spectra, the magnitudes of the r.m.s. baseline noise were calculated and the intensities of 49 resolved amide peaks were determined. The levels of the r.m.s. noise in the ADD, SUBTRACT and ENHANCED spectra relative to the intensity in the conventional HSQC spectrum, the ADD spectrum and SUBTRACT spectrum were nearly identical. The ratio of the r.m.s. noise in the ENHANCED spectrum to that in the conventional HSQC spectrum was 1.35, in agreement with the expected $\sqrt{2}$. For each amide peak the values of E_{add}, E_{sub} and E were calculated as the ratios of the intensities of the resonance in the conventional HSQC spectrum respectively. A substantial sensitivity increase is realized, as seen in Fig. 7. The relative intensities and signal-to-noise enhancement are given for these selected resonances in the figure caption. The average values for all 49 resonances were $E_{add} = 0.88 \pm 0.09$, $E_{sub} = 0.99 \pm 0.07$ and $E_r = 0.89 \pm 0.08$. The average improvement in signal-to-noise ratio in the ENHANCED spectrum compared to that in the conventional HSQC spectrum was $E = 1.32 \pm 0.10$ on the basis of the theoretical increase in the r.m.s. noise.

In accordance with the described analysis of the effects of relaxation on the longer enhanced pulse sequences, the overall sensitivity enhancement obtained for the ^1H–^{15}N heteronuclear correlation spectra of BPTI was slightly less than $\sqrt{2}$. Theoretical values of $E_{add} = 0.92$, $E_{sub} = 0.97$ and $E = 1.34$ were estimated for BPTI using the details outlined above and a molecular correlation time of 4 ns.[62] The close correspondence between the empirical and calculated values suggests that pulse imperfections and evolution of homonuclear scalar couplings are not seriously detrimental to the performance of the sensitivity-enhanced method. In principle, amide proton exchange could also diminish the observed sensitivity enhancements; however, no correlation was seen between resonances having below average

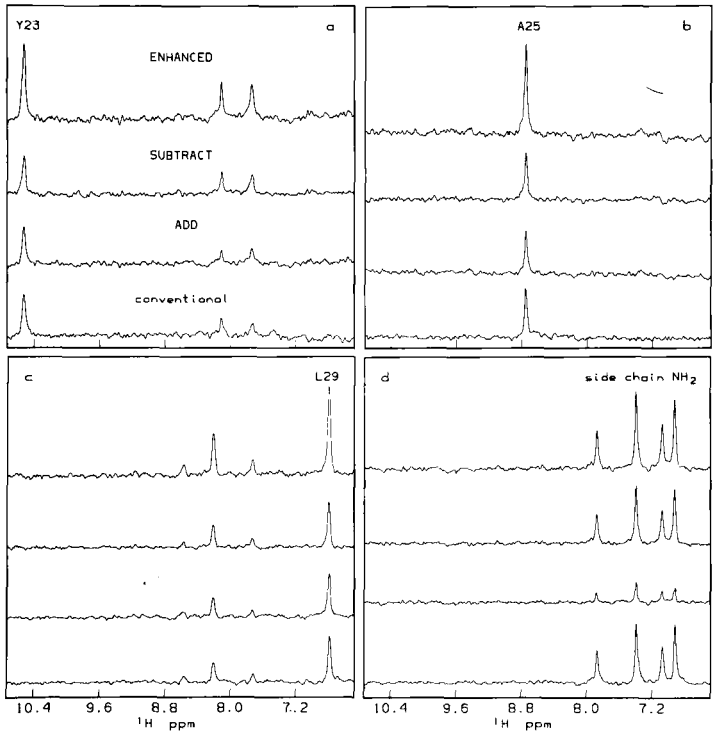

Fig. 7. Cross-sections taken parallel to the ω_2 axis, through selected N–H resonances, from the two-dimensional spectra shown in Fig. 6. Cross-sections are shown for the amide resonances of (a) Tyr 23, (b) Ala 25 and (c) Leu 29.[61] The NH_2 resonances with a ^{15}N chemical shift of 115 ppm, indicated by arrows in Fig. 6(a), are also shown. In each case the bottom trace is taken from the conventional HSQC spectrum, the second trace from the ADD spectrum, the third trace from the SUBTRACT spectrum, and the top trace from the ENHANCED spectrum. The slices are plotted on an absolute intensity scale to demonstrate clearly the noise combination characteristics. In each case the sensitivity improvement of the ENHANCED spectrum over the conventional spectrum is clear, and has been measured for the respective examples as (a) 1.26, (b) 1.31 and (c) 1.36. The slices in (d) illustrate the effect of the multiplicity filter of the ADD spectrum. In the conventional HSQC and SUBTRACT spectra four peaks are clearly visible, corresponding to two NH_2 groups, but these resonances have been suppressed in the ADD spectrum.

enhancements and amides that have been reported to undergo rapid exchange in BPTI.[63]

5. SENSITIVITY IMPROVEMENT IN PROTON-DETECTED TWO-DIMENSIONAL HETERONUCLEAR RELAY SPECTROSCOPY

Two-dimensional one-bond heteronuclear correlation NMR spectroscopy correlates a heteronucleus X with its directly connected protons H^c, as discussed above. In the proton-detected heteronuclear single-quantum coherence (HSQC)[54] version of this experiment polarization is transferred from H^c to X using an INEPT sequence,[59] allowed to evolve as heteronuclear single-quantum coherence during t_1, transferred back to H^c with a reverse INEPT sequence, and detected as proton magnetization. Two-dimensional Fourier transformation of these data generates peaks at the chemical shift of the X nucleus in the ω_1 dimension and H^c in the ω_2 dimension.

The heteronuclear NMR resonances of small biomolecules can often be assigned directly from one-bond correlation spectra if the proton resonances have been assigned previously; however, this approach alone is insufficient for larger molecules with complex proton NMR spectra. Two-dimensional heteronuclear relay spectroscopy allows the observation of correlations between a heteronucleus and protons H^r that are remotely connected, and can alleviate problems due to spectral overlap in the one-bond correlation spectra. In the proton-detected version the magnetization transfer pathway proceeds as $H^c \rightarrow X \rightarrow H^c \rightarrow H^r$, and relay peaks appear at the X nucleus chemical shift in the ω_1 dimension and the H^r chemical shift in the ω_2 dimension. Following the one-bond HSQC sequence, coherence transfer between the H^c and H^r scalar-coupled protons can be obtained by either appending a COSY-type sequence to allow the development of antiphase magnetization between the coupled protons[47,64] or, preferably, by a TOCSY-type isotropic mixing sequence.[48,49] In practice, the isotropic mixing-based heteronuclear relay experiment is by far the method of choice. The conventional pulse sequence to do this is shown in Fig. 8(a).

5.1. Theory

By simple inspection of Fig. 8(a) it is clear that the conventional heteronuclear relay pulse sequence is merely a direct combination of the two experiments described above; the one-bond HSQC experiment and the homonuclear TOCSY experiment. It is therefore not surprising that one can employ the same PEP procedures described above to increase the sensitivity of the relay method.[65]

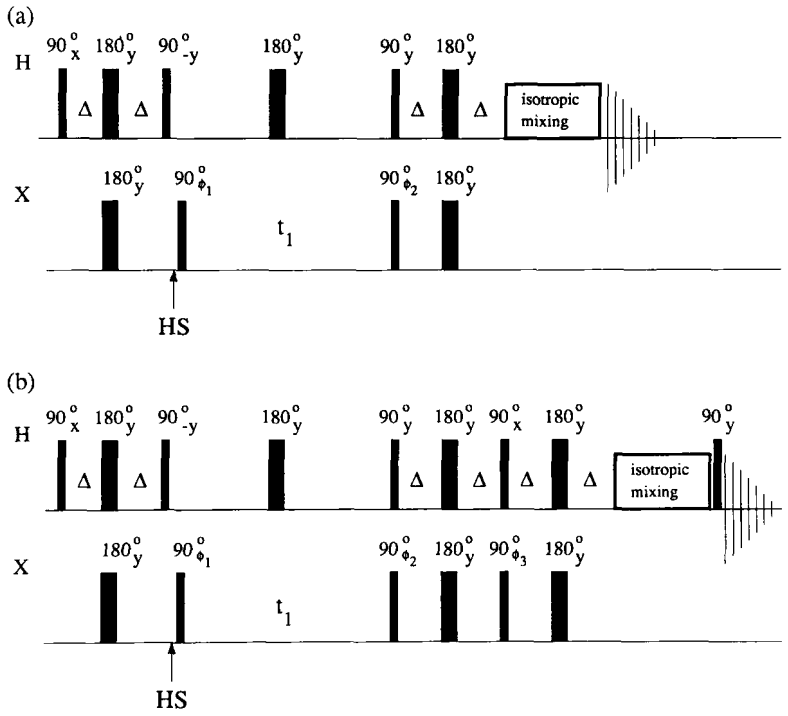

Fig. 8. Pulse sequences for heteronuclear relay correlation spectroscopy. (a) Pulse sequence to record a conventional two-dimensional ^{1}H-detected heteronuclear relay spectrum. Initially, an HSQC experiment establishes one-bond heteronuclear correlations, and then the resulting in-phase magnetization component passes into the isotropic mixing period for homonuclear coherence transfer. The phase cycling used is $\phi_1 = (x, -x, x, -x, -x, x, -x, x)$, $\phi_2 = (x, x, -x, -x)_2(-x, -x, x, x)_2$, and receiver = $(x, -x, -x, x, -x, x, x, -x, -x, x, x, -x, x, -x, -x, x)$. (b) Pulse sequence to record a sensitivity-enhanced two-dimensional ^{1}H-detected heteronuclear relay spectrum. Following the HSQC part of the sequence, two orthogonal in-phase magnetization components are refocused and both allowed to pass into the isotropic mixing scheme. Two data sets are acquired and deconvoluted to produce two pure absorption heteronuclear relay spectra that are added together to obtain a sensitivity-enhanced spectrum as described in the text. For the first data set the phase cycling is $\phi_1 = (x, -x, x, -x, -x, x, -x, x)$, $\phi_2 = (x, x, -x, -x)_2(-x, -x, x, x)_2$, $\phi_3 = (y, y, -y, -y)_2(-y, -y, y, y)_2$, and receiver = $(x, -x, -x, x, -x, x, x, -x, -x, x, x, -x, x, -x, -x, x)$; for the second data set the phase of ϕ_2 is inverted to yield $\phi_2 = (-x, -x, x, x)_2(x, x, -x, -x)_2$. In both sequences (a) and (b) the delay Δ is set to approximately 20% less than $1/4J_{XH}$ to reduce relaxation losses. A homospoil gradient pulse (HS) is applied, as shown, to reduce subtraction artefacts. In practice, composite heteronuclear 180° pulses of the form $90_x180_y90_x$ are used. Quadrature detection in the ω_1 dimension can be achieved by either the TPPI method or the hypercomplex method (see text).

Figure 8(b) shows the sensitivity-enhanced heteronuclear relay pulse sequence. A product operator analysis of the first part of this sequence has been given above for the HSQC experiment. The operators present following the second reverse INEPT sequence, just prior to the isotropic mixing period, are

$$+I_z \cos \omega_S t_1, \qquad -I_y \sin \omega_S t_1, \tag{65}$$

which are recognized as the orthogonal in-phase magnetization components required for the PEP method of sensitivity enhancement. These operators now pass into the isotropic mixing period. As discussed above, the isotropic mixing period gives rise to an effective Hamiltonian that is completely dominated by the scalar coupling interaction and commutes with any component of the total spin angular momentum. Thus evolution during the mixing period does not cause orthogonal magnetization components to mix. Coherence transfer occurs simultaneously and independently for the two terms in (65):

$$+I_z^c \cos \omega_S t_1 \rightarrow +I_z^r \cos \omega_S t_1 \tag{66}$$

via longitudinal magnetization, and

$$-I_y^c \sin \omega_S t_1 \rightarrow -I_y^r \sin \omega_S t_1 \tag{67}$$

via transverse magnetization, where I_k^c and I_k^r denote magnetization components of scalar-coupled I spins (protons) that are directly and remotely connected to the X spin (heteronucleus). At the end of the isotropic mixing the two orthogonal components are conserved. A final $90_y^\circ(I)$ pulse generates two observable terms of the forms (in addition to similar terms for the directly coupled protons)

$$+I_x^r \cos \omega_S t_1, \qquad -I_y^r \sin \omega_S t_1. \tag{68}$$

The accumulation of a second experiment with phase inversion of the 90° pulse on the heteronucleus immediately following the t_1 period generates the two observable terms

$$-I_x^r \cos \omega_S t_1, \qquad -I_y^r \sin \omega_S t_1. \tag{69}$$

Addition of the two data sets yields the single observable term

$$-2I_y^r \sin \omega_S t_1, \tag{70}$$

while subtraction on the other hand gives

$$-2I_x^r \cos \omega_S t_1. \tag{71}$$

The coefficient of 2 in (70) and (71) arises because two acquisitions have been used to produce them. Both the data sets represented by (70) and (71) can be phased to have pure absorption lineshapes in both dimensions. Addition of these phased spectra then yields a two-dimensional heteronuclear relay

spectrum in which, neglecting relaxation, the NMR resonances should be double in size. As has been described above, the noise increase from such a combination procedure is only $\sqrt{2}$, and a signal-to-noise ratio increase of $\sqrt{2}$ is expected compared with the conventional experiment. In practice, the sensitivity improvement is expected to be slightly less than $\sqrt{2}$ because of the previously analysed relaxation phenomena during the extended HSQC portion of the sequence.

5.2. Experimental demonstration

One of the most useful applications of the sensitivity-enhanced heteronuclear relay experiment is to provide through-bond correlations within each amino acid spin system in a protein, starting from the backbone amide. To demonstrate the experimental validity of the proposed enhanced sequence, two-dimensional heteronuclear relay spectra were acquired using the conventional sequence of Fig. 8(a) and the modified sequence of Fig. 8(b). Isotropic mixing was achieved using the DIPSI-2 sequence. The relevant phase-cycling information is given in the figure caption. All experiments were performed on a sample of the enzyme IIA^{glc}-like domain (previously referred to as enzyme III^{glc}) that was uniformly ^{15}N-labelled.[65] The total experimental time was 18 h for the conventional experiment and 18 h for the modified experiment.

For the conventional and ENHANCED spectra the r.m.s. baseline noise was calculated, and the intensities of 168 resolved relayed cross-peaks were determined. The ratio of the r.m.s. noise in the two spectra agreed with the expected value of $\sqrt{2}$. The average improvement in the signal-to-noise in the ENHANCED spectrum compared with the conventional spectrum was 1.27. As expected, the overall sensitivity enhancement is slightly less than the theoretical maximum of $\sqrt{2}$, owing to relaxation effects during the additional delays in the new pulse sequence. However, for a protein of this size (17.4 kDa) this is not surprising, and still represents a significant increase.

As in the cases described earlier, in addition to the conventional spectrum, ADD, SUBTRACT and ENHANCED spectra are shown in Fig. 9 for comparison purposes. The figure shows slices taken parallel to the ω_2 dimension through selected resonances of the two-dimensional spectra. Each cross-section shows the resonances through which magnetization has been relayed from the amide proton by the DIPSI-2 mixing sequence. The relevant ^1H assignments are noted on the figure; the ^{15}N frequency in each case is that of the backbone amide of that particular residue. As can be seen the ADD and SUBTRACT spectra are virtually identical to the conventional spectrum and the signal-to-noise ratio of the ENHANCED spectrum is superior to that of the conventional heteronuclear relay spectrum. Note that the slices are plotted on an absolute scale to show the increase in noise size for the ENHANCED spectrum compared to the others.

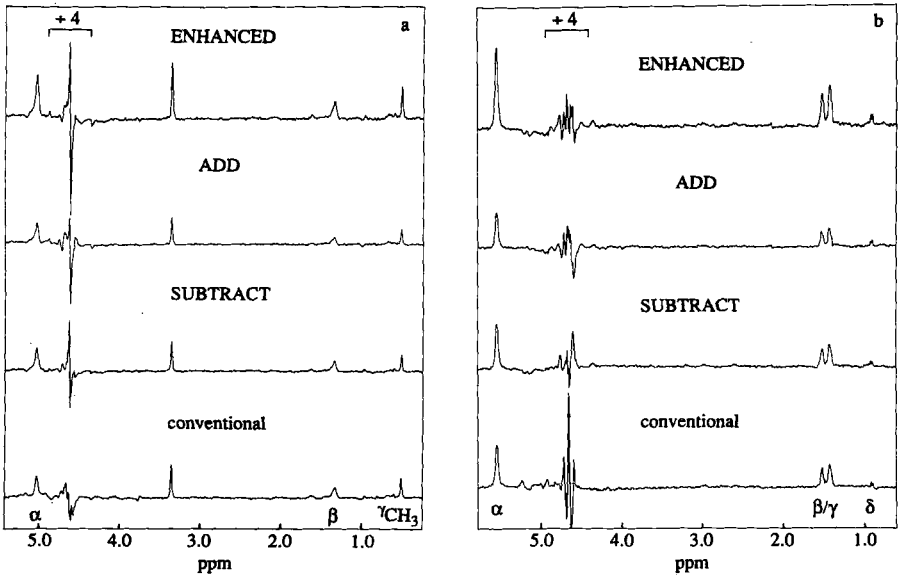

Fig. 9. Conventional and sensitivity-enhanced heteronuclear relay spectra of enzyme III^{glc}. All experiments were performed on a sample of the enzyme III^{glc}-like domain from *Bacillus subtilis* (0.8 mM, 90% H_2O/10% D_2O, pH 6.6 10 mM kP_i, 308 K), a 162-residue protein (MW = 17 400) that was uniformly labelled with $^{15}N > 95\%$.[65] Spectroscopy was performed on a Bruker AM600 spectrometer equipped with an Aspect 3000 computer and digital phase-shifting hardware. Data processing was performed using software supplied by Hare Research. The conventional heteronuclear relay spectrum was acquired using the pulse sequence of Fig. 8(a) and a Hahn echo. Sixty-four scans were acquired per t_1 increment. The two data sets required to produce the sensitivity-enhanced spectrum were acquired using the pulse sequence of Fig. 8(b) and a Hahn echo.[66,67] Each data set was acquired with 32 scans per t_1 increment. For all spectra, 4K real data points (2K per quadrature channel) were acquired in t_2 and 448 real points were acquired in t_1. TPPI was used for frequency discrimination in the ω_1 dimension. The spectral width was 12 500 Hz in the ω_2 dimension and 3333 Hz in the ω_1 dimension. The proton carrier was placed on the H_2O resonance and the ^{15}N carrier was placed at 107.5 ppm. The delay Δ was set to 2.3 ms. The homospoil gradient pulse was 3 ms, and was followed by a 7 ms delay to allow the magnetic field to stabilize. The two data sets acquired using the sequence of Fig. 8(b) were alternately added and subtracted to produce the two new data sets, called ADD and SUBTRACT respectively, which were then used for subsequent data reduction. Spectra were processed using exponential weighting in ω_2 and a

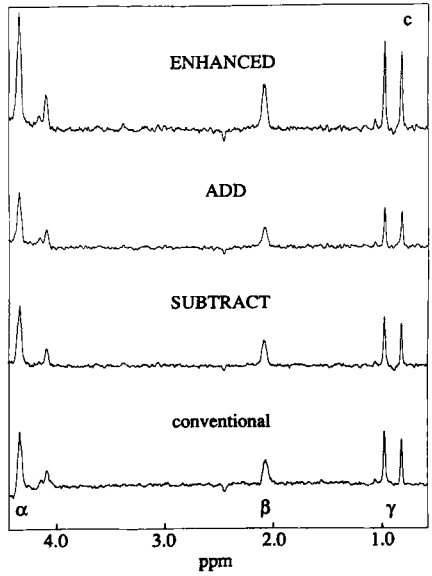

Kaiser window in ω_1. Prior to Fourier transformation, the data were zero-filled to 8K and 4K real points in t_2 and t_1 respectively. The conventional and SUBTRACT were phased to be purely absorptive in both dimensions; the ADD spectrum was also phased to be purely absorptive by adding a 90° phase shift in both dimensions relative to the SUBTRACT spectrum. The cross-sections shown are parallel to the ω_2 axis at the backbone amide ^{15}N shift in ω_1 for (a) Ile 80, (b) Leu 113 and (c) Val 63.[65] In each case the bottom trace is taken from the conventional heteronuclear relay spectrum, the second trace from the SUBTRACT spectrum, the third trace from the ADD spectrum, and the top trace from the ENHANCED spectrum. The slices are plotted on the same absolute intensity scale; as indicated, the intensities of the residual water resonances in (a) and (b) have been reduced by a factor of four. For each spin system the peaks resulting from the relay of magnetization from the amide proton are noted; the amide resonances are not shown. Peaks that are from other spin systems are not labelled. As expected, the conventional spectrum, the ADD spectrum, and the SUBTRACT spectrum are nearly identical in all cases. The sensitivity enhancement for a given peak in the ENHANCED spectrum compared to the conventional spectrum is calculated as the ratio of the relative peak intensities to the theoretical increase in the r.m.s. baseline noise, $\sqrt{2}$, for the two spectra. The average enhancements for each of the spin systems shown are (a) 1.27, (b) 1.28 and (c) 1.25.

6. SENSITIVITY IMPROVEMENT IN THREE-DIMENSIONAL HETERONUCLEAR CORRELATION SPECTROSCOPY

Three-dimensional NMR spectroscopy has been shown to offer significant improvements in spectral resolution compared with the 2D techniques commonly employed for biomolecular structural investigations. Combining two of the most powerful two-dimensional homonuclear methods for structure elucidation (TOCSY and NOESY) with the resolving power of the (generally) larger chemical-shift dispersion of ^{13}C and ^{15}N heteronuclei into three-dimensional experiments has proved a remarkably successful procedure for alleviating resonance overlap.[68–71]

The application of PEP technology to achieve sensitivity improvements of up to $\sqrt{2}$ in the 3D TOCSY–HMQC[68] and 3D NOESY–HMQC[72–74] experiments is demonstrated in Sections 6.1 and 6.2. The same enhancement can, of course, be obtained in the HSQC versions of these experiments.

6.1. 3D TOCSY–HMQC

The same pulse sequence, shown in Fig. 10(a), is used for the conventional and sensitivity-enhanced (SE) TOCSY–HMQC experiments. The principle of the method can be seen for a spin system consisting of two scalar-coupled protons A and B, with their mutual coupling constant denoted by J, and a heteronucleus S that is scalar-coupled to at least one of the protons, say B, with a one-bond coupling constant J_{SB}. Beginning with equilibrium magnetization of the A spin, evolution of coherence during the pulse sequence is easily followed by using the product operator formalism. Coherence transfer from proton A to proton B occurs independently during the isotropic mixing period for the two orthogonal single-spin operators present following the t_1 period:

$$-\text{sgn}(\phi_2)\, A_z \cos \omega_A t_1 \cos \pi J t_1 \rightarrow -\text{sgn}(\phi_2)\, B_z \cos \omega_A t_1 \cos \pi J t_1, \quad (72)$$

$$A_x \sin \omega_A t_1 \cos \pi J t_1 \rightarrow B_x \sin \omega_A t_1 \cos \pi J t_1, \quad (73)$$

in which ω_A is the resonance frequency of the A spin, t_1 is the duration of the first incrementable time period, and sgn (ϕ_2) is the sign of the initial phase for ϕ_2. One-half of the number of transients recorded per increment is obtained with sgn $(\phi_2) = 1$ and the other half is obtained with sgn $(\phi_2) = -1$ by inverting the phase ϕ_2. Multi-spin terms have been excluded for the usual reasons. Again, we assume complete coherence transfer to occur from spin A to spin B.

Concentrating on the B-proton terms, the remainder of the pulse sequence constitutes an HMQC isotope filter. The B-operator terms in (72) and (73) are labelled with the chemical shift of the heteronucleus, ω_S, during t_2;

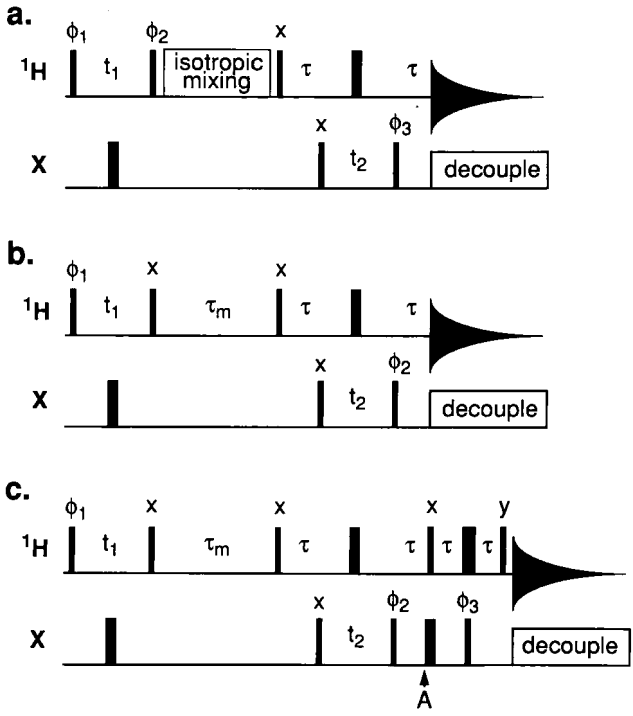

Fig. 10. Pulse sequences for recording three-dimensional (a) conventional and SE–TOCSY–HMQC, (b) conventional NOESY–HMQC, and (c) SE–NOESY–HMQC experiments. The thin and thick vertical lines represent 90° and 180° pulses applied to the H (protons) or X (heteronucleus) spins; the delay τ is set to $1/2J_{XH}$. Decoupling is accomplished by an appropriate composite pulse sequence. Quadrature detection in the ω_1 dimension can be achieved by either the TPPI method or the hypercomplex method. Isotropic mixing is achieved by DIPSI-2 or a similar pulse scheme. The basic phase cycle for (a) is $\phi_1 = (x, -x)$, $\phi_2 = x$, $\phi_3 = (x, x, -x, -x)$ and receiver = $(x, -x, -x, x)$. For the conventional TOCSY–HMQC experiment the phases of ϕ_2 and the receiver are inverted after four scans. For the SE–TOCSY–HMQC experiment the phase of ϕ_2 is inverted after four scans, and the two halves of the data are stored separately. The basic phase cycle for (b) is $\phi_1 = (x, -x)$, $\phi_2 = (x, x, -x, -x)$ and receiver = $(x, -x, -x, x)$. The basic phase cycle for (c) is $\phi_1 = (x, -x)$, $\phi_2 = (x, x, -x, -x)$, $\phi_3 = (y, y, -y, -y)$ and receiver = $(x, -x, -x, x)$. In (c) the phase of ϕ_2 is inverted after four scans, and the two halves of the data are stored separately.

consequently the observable terms detected during the acquisition period t_3 are

$$\tfrac{1}{2}(-B_y \cos \omega_A t_1 + B_x \sin \omega_A t_1) \cos \pi J t_1 \cos \omega_S t_2 \cos \pi J t_2 \tag{74}$$

for the data acquired with sgn $(\phi_2) = 1$, and

$$\tfrac{1}{2}(B_y \cos \omega_A t_1 + B_x \sin \omega_A t_1) \cos \pi J t_1 \cos \omega_S t_2 \cos \pi J t_2 \tag{75}$$

for the data acquired with sgn $(\phi_2) = -1$.

In the conventional TOCSY–HMQC experiment the two halves of the data represented by (74) and (75) are subtracted by inverting the phase of the receiver in synchrony with ϕ_2. The recorded signal is then given by

$$-B_y \cos \omega_A t_1 \cos \pi J t_1 \cos \omega_S t_2 \cos \pi J t_2. \tag{76}$$

The data represented by (76) can be Fourier-transformed to give a 3D spectrum with absorptive lineshapes in all three dimensions. In the SE–TOCSY–HMQC experiment the two halves of the data are recorded separately. Subsequently the two data sets are alternately added to give

$$B_x \sin \omega_A t_1 \cos \pi J t_1 \cos \omega_S t_2 \cos \pi J t_2, \tag{77}$$

and subtracted to yield the same result as (76). The data set represented by (77) is 90° out of phase with respect to that of (76), in the t_1 and t_3 periods, but both can be individually phased to generate two 3D TOCSY–HMQC with pure absorption lineshapes in all three dimensions. The spectra would have the form of homonuclear TOCSY spectra correlating A and B spins, separated by the chemical shift of the appropriate heteronucleus S.

Addition of the two 3D data sets doubles the size of the resonances, while the r.m.s. noise increases only by the factor of $\sqrt{2}$, and a sensitivity improvement of $\sqrt{2}$ is obtained compared with the conventional method.[75]

6.2. 3D NOESY–HMQC

A similar approach can be used to obtain sensitivity enhancement of the 3D NOESY–HMQC experiment; however, modification of the conventional pulse sequence is required.[75] Figures 10(b, c) show the 3D conventional and SE–NOESY–HMQC pulse sequences respectively. The principles of the experiment can be illustrated for a system of two protons A and B that are close enough in space to cross-relax via their mutual dipolar interaction. The heteronucleus S is again scalar coupled to proton B.

Beginning with equilibrium magnetization of the A spin, the product-operator term of interest following the t_1 period cross-relaxes with proton B during the mixing period to give

$$-A_z \cos \omega_A t_1 \cos \pi J t_1 \rightarrow -B_z \cos \omega_A t_1 \cos \pi J t_1 \tag{78}$$

for molecules in the slow motion limit. For the conventional experiment (Fig. 10b) the remainder of the pulse sequence comprises an HMQC isotope filter. The final detectable term is

$$-B_y \cos \omega_A t_1 \cos \pi J t_1 \cos \omega_S t_2, \tag{79}$$

which yields a 3D NOESY–HMQC spectrum with pure absorptive lineshapes in all dimensions.

For the SE–NOESY–HMQC sequence the isotope filter extends to the point labelled A in Fig. 10(c), at which the operators present are

$$[-\text{sgn}(\phi_2)\, B_y \cos \omega_S t_2 + B_x \sin \omega_S t_2\, (S_x \cos \omega_S \tau + S_y \sin \omega_S \tau)] \cos \omega_A t_1 \cos \pi J t_1. \tag{80}$$

One-half of the number of transients per t_2 increment is recorded with each value of sgn (ϕ_2). During the remainder of the sequence, the second term in (80) is refocused to a single-quantum proton operator. The resultant observable operators immediately prior to acquisition are

$$\tfrac{1}{2}(-B_x \cos \omega_S t_2 - \delta_{1N} B_y \sin \omega_S t_2) \cos \omega_A t_1 \cos \pi J t_1 \tag{81}$$

for the data acquired with sgn $(\phi_2) = 1$, and

$$\tfrac{1}{2}(B_x \cos \omega_S t_2 - \delta_{1N} B_y \sin \omega_S t_2) \cos \omega_A t_1 \cos \pi J t_1 \tag{82}$$

for the data acquired with sgn $(\phi_2) = -1$. The Kronecker delta δ_{1N} is used to indicate that the second term in (80) can be refocused only for heteronuclei with $N = 1$ directly attached protons. The two halves are alternately added to yield

$$-\delta_{1N} B_y \sin \omega_S t_2 \cos \omega_A t_1 \cos \pi J t_1 \tag{83}$$

and subtracted to yield

$$-B_x \cos \omega_S t_2 \cos \omega_A t_1 \cos \pi J t_1. \tag{84}$$

The two data sets represented by (83) and (84) are 90° out of phase with respect to each other in the t_2 and t_3 periods, and are in-phase in the t_1 period. As before for the PEP method, the two data sets can be processed independently to give purely absorptive lineshapes in all three dimensions. Addition of the two spectra yields an overall signal-to-noise increase of up to $\sqrt{2}$ in the enhanced spectrum for heteronuclei with a single directly attached proton, compared with the conventional NOESY–HMQC experiment. As described above, the actual improvement in the 3D SE–NOESY–HMQC experiment will be slightly less than the theoretical value of $\sqrt{2}$ due to relaxation effects during the longer pulse sequence of Fig. 10(c). As in the 2D experiments, the data can also be combined in the time-domain according to the PEP prescription of Section 2.3.1, provided that the hypercomplex

method has been employed for frequency discrimination in the affected dimension.

6.3. Experimental demonstration

The above analysis was verified experimentally by recording ^{1}H–^{15}N–^{1}H 3D conventional and sensitivity-enhanced TOCSY–HMQC and NOESY–HMQC spectra using the pulse sequences given in Figs 10(a–c). Experiments were performed on a 2.5 mM solution of calbindin D_{9k} in 90% H_2O/10% D_2O at 300 K. Calbindin D_{9k} is a 75 amino acid calcium-binding protein;[76] the sample used for NMR studies was uniformly labelled with ^{15}N to >95%. Examples of the processed 3D spectra obtained for the TOCSY–HMQC and NOESY–HMQC experiments are shown in Figs 11 and 12 respectively. Figure 11 illustrates the sensitivity improvement obtained for TOCSY transfer through the spin systems of Lys 12 and Glu 35 in calbindin D_{9k}. The experimentally measured increase in sensitivity between the enhanced and conventional TOCSY–HMQC spectra are 42% for Lys 12 and 38% for Glu 35, across the whole spin system. Figure 12 illustrates the sensitivity improvement obtained for magnetization transfer via cross-relaxation with the amide proton of the spin systems of Lys 12 and Glu 35 is calbindin D_{9k}. The average enhancement across each cross-section in Fig. 12(a) is 41% while that across the cross-section of Fig. 12(b) is 39%. The enhancement for the SE–TOCSY–HMQC experiment agrees well with the theoretical value of $\sqrt{2}$, as expected since the pulse sequence remains unmodified. Although in the case of the SE–NOESY–HMQC experiment, a $\sqrt{2}$ improvement in signal-to-noise ratio is also seen, this is unlikely always to be the case. The pulse sequence for this experiment has been extended from the conventional sequence, and relaxation effects will become more important as the biomolecule under investigation becomes larger. As noted earlier, sensitivity enhancement is most strongly affected by relaxation in experiments that use the HMQC isotope filter; consequently, for proteins larger than calbindin the SE–NOESY–HSQC experiment may be preferable.

7. SENSITIVITY IMPROVEMENT IN PROTON-DETECTED HETERONUCLEAR SPIN RELAXATION MEASUREMENTS

An expanding body of theoretical and experimental results indicate that intramolecular, dynamical processes are intimately involved in protein function.[77–80] Furthermore, the interpretation of NMR data used to generate constraints for structure calculations should ideally encompass intramolecular dynamics.[81–83] Dipolar nuclear magnetic spin relaxation of

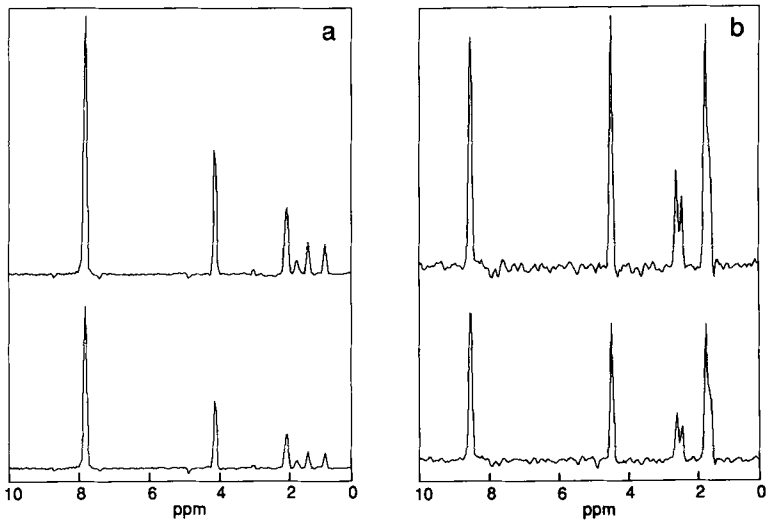

Fig. 11. Comparison of conventional and SE–TOCSY–HMQC spectra recorded on the ^{15}N-enriched calcium binding protein calbindin (see text). A single data set was recorded on a Bruker AM600 spectrometer with the pulse sequence of Fig. 10(a). The conventional spectrum was obtained by subtracting the two halves of the data set represented by (67) and (68) after acquisition. A total of eight transients were recorded per (t_1, t_2) data point; the data matrix consisted of $256 \times 64 \times 2048$ real points in the $t_1 \times t_2 \times t_3$ dimensions respectively. The spectral widths were 7812 Hz in the t_1 and t_3 proton dimensions and 1506 Hz in the t_2 nitrogen dimension. The isotropic mixing period was 60 ms. The cross-sections shown are taken from the 3D TOCSY–HMQC spectra parallel to the ω_1 axis at the ω_2, ω_3 frequencies of the backbone amide ^{15}N and proton resonances for the spin systems of (a) Lys 12 and (b) Glu 35. The top and bottom traces show sensitivity-enhanced and conventional spectra respectively. The spectra are plotted on an absolute intensity scale, and it is noted that the increase in the r.m.s. baseplane noise seen here for the enhanced spectrum compared with the conventional one agrees with the theoretical value of $\sqrt{2}$. The average signal-to-noise improvements between the enhanced and conventional spectra are (a) 1.42 and (b) 1.38.

protonated heteronuclei, such as ^{13}C and ^{15}N, is mediated by overall rotational tumbling of the molecule and by internal motions of X—H bond vectors;[84] consequently, heteronuclear NMR spectroscopy is a powerful technique for experimental investigation of dynamics in biological macromolecules.[85] The measurement of spin–lattice and spin–spin relaxation rate constants (R_1 and R_2 respectively) and the steady-state {^{1}H}–X nuclear Overhauser effect (NOE), is proving to be viable for a growing number of proteins.[51–53,86–95]

Basic methods for the determination of X-nucleus relaxation parameters by proton-detected heteronuclear correlation experiments have been described elsewhere,[51–53,96,97] as have techniques for minimizing systematic

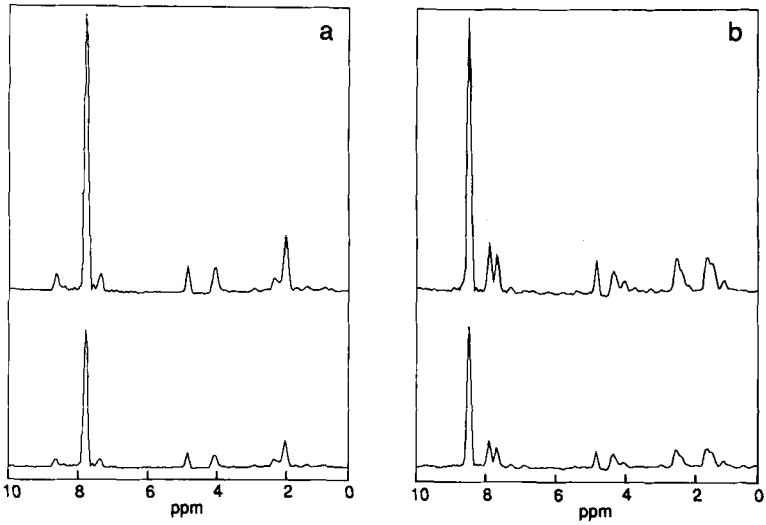

Fig. 12. Comparison of conventional and SE–NOESY–HMQC spectra recorded on the ^{15}N-enriched calcium binding protein calbindin (see text). The data sets were recorded on a Bruker AMX500 spectrometer using the pulse sequences of Figs 10(b, c). A total of 16 transients were recorded per (t_1, t_2) data point; the data matrix consisted of 100 complex × 32 complex × 2048 real points in the $t_1 \times t_2 \times t_3$ dimensions respectively. The spectral widths were 7042 Hz in the t_1 and t_3 proton dimensions and 1250 Hz in the t_2 nitrogen dimension. The NOESY mixing time was 150 ms. Both experiments were recorded in the same overall time. The cross-sections shown are taken from the 3D NOESY–HMQC spectra parallel to the ω_1 axis at the ω_2, ω_3 frequencies of the backbone amide ^{15}N and proton resonances for the spin systems of (a) Lys 12 and (b) Glu 35. The top and bottom traces show sensitivity-enhanced and conventional spectra respectively. The spectra are plotted on an absolute intensity scale, and it is noted that the increase in the r.m.s. baseplane noise seen here for the enhanced spectrum compared with the conventional one agrees with the theoretical value of $\sqrt{2}$. The average signal-to-noise improvements between the enhanced and conventional spectra are (a) 1.41 and (b) 1.39.

contributions from dipole–CSA cross-correlation effects,[98–100] and from evolution of antiphase terms during R_2 measurements.[98,99,101]

7.1. Theory

Using the same principles as described and demonstrated above for increasing the signal-to-noise ratio in heteronuclear correlation experiments, it is possible to enhance the sensitivity of heteronuclear relaxation methods for AX systems.[87,91,102]

The modified pulse schemes used to measure R_1, R_2 and the {^{1}H}–XNOE, along with the conventional sequence to measure R_1, are shown in

Fig. 13 (although in the figure ^{15}N is shown as the heteronucleus, the sequences are, of course, applicable to other heteronuclei, such as ^{13}C). As in the other cases, the R_1 and R_2 sensitivity-enhancement sequences consist of an initial refocused INEPT transfer from ^1H to X, the relaxation period t, the t_1 evolution period, and the now familiar extended reverse polarization transfer scheme that allows phase-sensitive detection of the orthogonal magnetization components produced during t_1. Proton decoupling is performed using a composite pulse decoupling sequence during the relaxation delay of the inversion recovery sequence (Fig. 13b) to suppress the time-dependent effects of dipolar X–^1H cross-relaxation and of cross-correlation between dipolar and CSA relaxation mechanisms.[100] In order to suppress the time-dependent effects of cross-correlation between dipolar and CSA relaxation mechanisms in the CPMG experiments (Fig. 13c), proton decoupling is performed using synchronous proton 180° hard pulses during the relaxation delay t.[98,99] The spin-echo delay in CPMG experiments must be short to minimize effects from evolution under the heteronuclear scalar coupling Hamiltonian; $\tau = 0.5$ ms is sufficient for this purpose.[99] Inversion recovery and CPMG[103,104] decay curves are obtained by recording a series of 2D heteronuclear correlation spectra in which the relaxation period t is varied parametrically. The steady-state NOE[105] pulse sequence consists of the t_1 evolution period and the extended reverse polarization transfer segment. The NOE enhancements are measured by recording pairs of spectra with and without saturation of protons during the recycle time between transients (Fig. 13d). Saturation of protons during the recovery delay is performed using a composite pulse decoupling sequence. In all sequences the H_2O resonance is suppressed by short spin-lock purge pulses during the INEPT transfer steps to minimize the effects of saturation transfer from the solvent protons.[106]

In the sensitivity-enhancement heteronuclear correlation sequences two data sets are recorded differing only by inversion of the phase of the first heteronuclear pulse after the t_1 period (Figs 13b–d). If each data set is recorded with n scans per increment, two independent pure-phase spectra with $2n$ scans per increment are obtained by adding and subtracting the recorded data, as described above. The peak intensities in the spectra obtained by addition (I^a) and subtraction (I^s) of the recorded data sets are given by

$$I^a = I^c\varepsilon_a = I^c \exp(-2R_1\Delta), \tag{85}$$

$$I^s = I^c\varepsilon_s = I^c \exp(-2R_1^H\Delta), \tag{86}$$

in which I^c is the intensity that would be obtained in the equivalent conventional experiment, ε_a and ε_s are the fractional losses of signal due to the additional delays and pulses in the enhanced sequences compared with the conventional experiments, R_1 is the ^{15}N spin–lattice relaxation rate

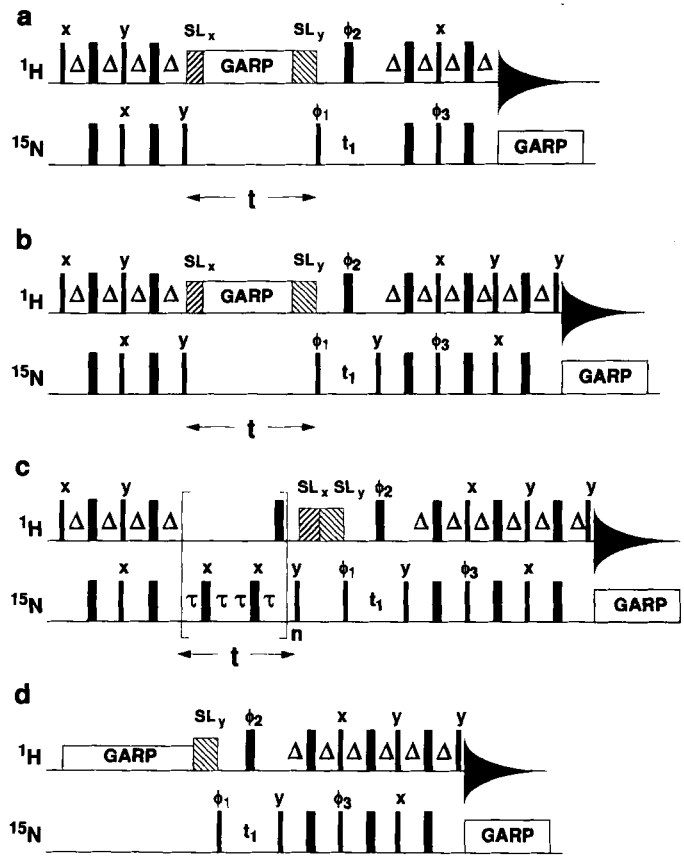

Fig. 13. Pulse schemes used to measure (a, b) ^{15}N R_1, (c) ^{15}N R_2 and (d) $\{^1H\}$–^{15}N NOE with indirect proton detection. Sensitivity enhancement schemes are shown in (b)–(d) and the conventional inversion recovery sequence is shown in (a). Thin bars represent 90° pulses and thick bars 180° pulses. The phase cycling used for R_1 and R_2 experiments is $\phi_1 = (x, -x, x, -x)$, $\phi_2 = (y)_4(-y)_4$, $\phi_3 = (y, y, -y, -y)$ and receiver = $(x, -x, -x, x)$. In the case of the $\{^1H\}$–^{15}N NOE experiments the following phase cycle is suggested: $\phi_1 = (x, -x, x, -x, -x, x, -x, x)_2$, $\phi_2 = (y)_{16}(-y)_{16}$, $\phi_3 = (y, y, -y, -y)_2(-y, -y, y, y)_2$ and receiver = $(x, -x, -x, x, -x, x, x, -x, -x, x, x, -x, x, -x, -x, x)$. In all cases, for sensitivity enhancement, each t_1 experiment is recorded twice with the phase of the ^{15}N 90° pulse immediately after t_1 differing by 180°. Linear combination of these two experiments produces sensitivity enhancement. The 180° pulses without phase designations are applied along the y axis. The value of Δ is set to $1/4J_{NH}$. For (a), (b) and (c) the delay t is parametrically varied in a series of 2D experiments; for (d) pairs of spectra are acquired with and without proton saturation.

constant, R_1^H is the proton spin–lattice relaxation rate constant, $\Delta = 1/4J$, and J is the one-bond N—H scalar coupling constant. The second equalities in (85) and (86) are obtained if the effects of pulse imperfections are negligible. For the inversion recovery and CPMG experiments I^a and I^s are combined to yield

$$I(t) = [I_\infty^c - (I_\infty^c - I_0^c)\exp(-t/R_1)](\varepsilon_a + \varepsilon_s) = I_\infty - (I_\infty - I_0)\exp(-t/R_1), \quad (87)$$

$$I(t) = [I_0^c \exp(-t/R_2) + I_\infty^c](\varepsilon_a + \varepsilon_s) = I_0 \exp(-t/R_2) + I_\infty \quad (88)$$

respectively. In (87) and (88) I_0 is the peak intensity for $t = 0$ while I_∞ is the limiting peak intensity as $t \to \infty$. Peak intensities may decay to a non-zero limiting value in CPMG experiments as a consequence of pulse imperfections.[107] Thus the time series for both experiments have the same forms as for the conventional experiments; however, the signal-to-noise ratio in the final enhanced spectrum is proportional to $[2n(\varepsilon_a + \varepsilon_s)]^{1/2}$, unlike the conventional case where it is proportional to $(2n)^{1/2}$. Since $2R_1\Delta \ll 1$ and $2R_1^H\Delta \ll 1$ for proteins with molecular masses less than 20 kDa, $\varepsilon_a + \varepsilon_s \approx 2$ and the signal-to-noise ratio in the enhanced spectrum is nearly equivalent to that in a conventional experiment acquired with $4n$ scans per increment. For the NOE experiments the NOE is calculated independently for the ADD and SUBTRACT linear combinations of data sets:

$$\text{NOE} = \frac{I_{sat}^a}{I_{unsat}^a} = \frac{I_{sat}^s}{I_{unsat}^s} = \frac{I_{sat}}{I_{unsat}}, \quad (89)$$

in which I_{sat} and I_{unsat} are the peak intensities in spectra recorded with and without saturation of protons during the recycle delay. Thus two independent measurements of the NOE enhancement are obtained in the same time required for a single conventional measurement with the same total number of scans per increment. Alternatively, the data can be combined as usual to yield a sensitivity-improved spectrum.

As a consequence of incorporating PEP technology, relaxation data with a given signal-to-noise ratio can be acquired in approximately one-half of the measurement time required by the conventional pulse sequences.[102]

7.2. Experimental demonstration

To demonstrate the sensitivity improvement that can be achieved by applying PEP technology in heteronuclear relaxation experiments, data are shown in Fig. 14 for a sample of the Pro43Gly mutant of calbindin D_{9k} (in D_2O) that has been uniformly isotropically enriched in ^{13}C to a level of approximately 15% abundance. The data (Rance, Chazin and Palmer, unpublished results) presented in Fig. 14 are 1D slices (displaying proton

chemical shifts) taken from 2D ^{1}H–^{13}C heteronuclear correlation spectra recorded using the T_1 pulse sequence of Fig. 13(b); the inversion–recovery delay for these data was 1.06 s. The top slice was taken from a spectrum in which the two separately collected data sets (for the two halves of the phase cycle) were added together, the middle slice from the spectrum for the subtracted data (with a 90° phase correction in both dimensions relative to the "add" spectrum), and the bottom slice from the composite spectrum in which the "add" and "subtract" have been combined. The slices intersect peaks for the $^{\alpha}C^{\alpha}H$ correlations of Val 61 (5.10 ppm), Thr 45 (4.43 ppm), Tyr 13 (4.00 ppm) and Lys 25 (3.46 ppm). The three slices are plotted on a scale such that the r.m.s. noise levels are the same, which required the composite slice to be reduced by a factor of $\sqrt{2}$ relative to the component slices, as expected on theoretical grounds. The data in Fig. 14 clearly demonstrate the improved sensitivity afforded by incorporating PEP technology into the heteronuclear relaxation experiments.

8. SENSITIVITY ENHANCEMENT IN GRADIENT-ENHANCED HETERONUCLEAR CORRELATION SPECTROSCOPY

Until recently, the selection of desired coherence transfer pathways[108,109] in solution-state NMR experiments has relied almost solely on the use of phase-cycling procedures or radiofrequency pulse inhomogeneity to eliminate unwanted pathways. In principle, a third alternative—pulsed magnetic field gradient technology—also provides a very powerful means for coherence transfer pathway selection, but was seldom employed in NMR spectroscopy in the past owing to hardware limitations. However, recent developments in probe technology and related hardware have greatly facilitated the use of pulsed field gradients, and as a result a number of new or improved experiments have been proposed that rely on gradient methodology. These developments are very important because of the significant advantages offered by gradient methodology for coherence pathway selection. One of the principal advantages is that pathway selection can be achieved within a single scan, as opposed to the multiple scans required for phase-cycling procedures. In addition, an extremely important advantage in biological applications in aqueous solution is the possibility of suppressing the enormous water resonance with appropriate field gradients in a single scan; alternative methods for solvent suppression are usually compromised by problems with saturation transfer, non-uniform spectra excitation or dynamic range limitations in the receiver.

Recently, Kay and co-workers[110] have incorporated PEP technology into a pulsed field gradient variation of the HSQC experiment. Their new method allows pure absorption heteronuclear correlation spectra to be recorded with the use of pulsed field gradients for eliminating undesired

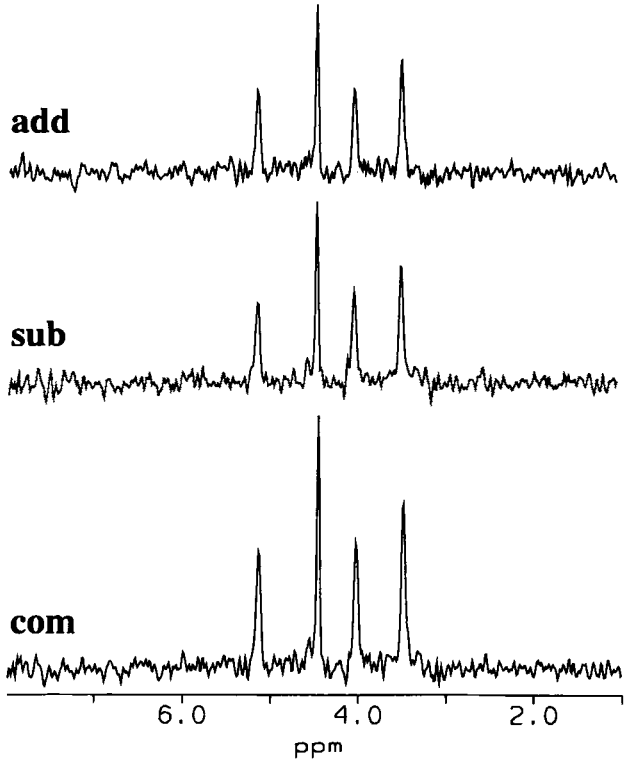

Fig. 14. One-dimensional slices (displaying proton chemical shifts) taken from 2D ^{1}H–^{13}C heteronuclear correlation spectra recorded using the T_1 pulse sequence of Fig. 13(b); the inversion-recovery delay for these data was 1.06 seconds. The top slice was taken from a spectrum in which the two separately collected data sets (for the two halves of the phase cycle) were added together, the middle slice from the spectrum for the subtracted data (with a 90° phase correction in both dimensions relative to the "add" spectrum), and the bottom slice from the composite spectrum in which the "add" and "subtract" have been combined. The slices intersect peaks for the $^{\alpha}C^{\alpha}H$ correlations of Val 61 (5.10 ppm), Thr 45 (4.43 ppm), Tyr 13 (4.00 ppm) and Lys 25 (3.46 ppm). The three slices are plotted on a scale such that the r.m.s. noise levels are the same, which required the composite slice to be reduced by a factor of $\sqrt{2}$ relative to the component slices, as expected on theoretical grounds.

coherence transfer pathways; in particular, the advantage of suppressing the water with field gradients is clearly demonstrated. This gradient-enhanced experiment employs a pulse sequence similar to that discussed in detail in Section 4.1 for the sensitivity-enhanced non-gradient HSQC experiment. PEP technology is employed in the gradient-enhanced experiment to extract separate signals, which are cosine- and sine-modulated as a function of the evolution time t_1; these data are then used to generate a hypercomplex data set, which can be Fourier-transformed to yield a pure absorption spectrum with

ω_1 frequency discrimination. Kay *et al.* demonstrate that the use of both PEP and gradient technology can yield significant improvements in sensitivity for moderately sized proteins or other biomolecules.

9. ADDITIONAL APPLICATIONS

The PEP technology for sensitivity enhancement can be incorporated into a wide variety of NMR experiments; two papers have appeared recently describing additional applications. Madsen and Sørensen[111] have described very useful modifications to a variety of "constant-time" experiments to achieve optimum spectral resolution. The general principle of a "constant-time" experiment was first presented by Bax and co-workers[112] as a means of eliminating homonuclear scalar couplings in the indirectly detected frequency dimension of 2D correlated spectra. This principle has found important applications in many recent 2D and 3D heteronuclear NMR experiments of uniformly ^{13}C-enriched biomolecules. PEP technology for sensitivity enhancement was incorporated into the optimized "constant-time" experiments presented by Madsen and Sørensen in a straightforward manner following the principles described by Palmer *et al.*[22] and reviewed above.

The application of PEP technology in a homonuclear, 3D NOESY–TOCSY experiment has recently been described by Feng Ni.[113] In this experiment a NOESY element is simply prefixed to the sensitivity-improved TOCSY experiment described by Cavanagh and Rance.[23]

10. CONCLUSIONS

This report has described the basic principle of a general methodology for improving the sensitivity of a variety of multidimensional NMR experiments, and has discussed the means by which this so-called PEP technology can be incorporated into some of the most popular experiments in current use. The basic requirement that must be satisfied in order to incorporate PEP technology into a multidimensional NMR experiment is that the orthogonal magnetization components present during an evolution period be made to follow approximately equivalent coherence transfer pathways during the subsequent portion of the pulse sequence. It should be anticipated that PEP technology will be applicable in additional classes of experiments not specifically addressed in this chapter. The maximum achievable improvement in sensitivity (defined as signal-to-noise ratio per unit measuring time) for PEP technology applied to one evolution period of a multidimensional NMR experiment is $\sqrt{2}$. Such improvement is extremely important in applications where the sensitivity is limited by practical factors

such as low sample concentrations or inherent features such as the requirement for large numbers of experiments in 3D and 4D experiments or in relaxation rate measurements.

ACKNOWLEDGEMENTS

The authors wish to acknowledge the fundamental contributions of Professor A. G. Palmer III, who was a principal architect of the sensitivity-improved heteronuclear NMR experiments, and Dr R. A. Byrd. Professor L. E. Kay is thanked for providing a preprint of ref. 110. A very helpful discussion with Professor G. Bodenhausen in which he pointed out a useful definition of sensitivity as "signal-to-noise ratio per unit time" is acknowledged. The preparation of this report was supported in part by a grant from the National Institutes of Health (GM 40089).

REFERENCES

1. D. I. Hoult, *Prog. NMR Spectrosc.*, 1978, **12**, 41.
2. O. W. Sørensen, *Prog. NMR Spectrosc.*, 1989, **21**, 503.
3. A. Bax, S. W. Sparks and D. A. Torchia, *Meth. Enzymol.*, 1989, **176**, 134.
4. R. R. Ernst, *Adv. Magn. Reson.*, 1966, **2**, 1.
5. M. H. Levitt, G. Bodenhausen and R. R. Ernst, *J. Magn. Reson.*, 1984, **58**, 462.
6. M. A. Delsuc and J. Y. Lallemand, *J. Magn. Reson.*, 1986, **69**, 504.
7. (a) M. H. Levitt and R. Freeman, *J. Magn. Reson.*, 1980, **39**, 533.
   (b) J. C. J. Barna, E. D. Laue, M. R. Mayger, J. Skilling and S. J. P. Worrall, *J. Magn. Reson.*, 1987, **73**, 69.
8. R. R. Ernst, G. Bodenhausen and A. Wokaun, *Principles of Nuclear Magnetic Resonance in One and Two Dimensions*. Clarendon Press, Oxford, 1987.
9. D. S. Stephenson, *Prog. NMR Spectrosc.*, 1989, **20**, 515.
10. G. L. Bretthorst, C.-C. Hung, D. A. D'Avignon, J. J. H. Ackerman, *J. Magn. Reson.*, 1988, **79**, 369.
11. D. L. Donoho, I. M. Johnstone, A. S. Stein and J. C. Hoch, *Proc. Natl Acad. Sci. USA*, 1990, **87**, 5066.
12. A. G. Redfield and R. K. Gupta, *Adv. Magn. Reson.*, 1971, **5**, 82.
13. J. D. Ellett Jr, M. G. Gibby, U. Haeberlen, L. M. Huber, M. Mehring, A. Pines and J. Waugh, *Adv. Magn. Reson.*, 1971, **5**, 117.
14. C.-N. Chen, D. I. Hoult and V. J. Sank, *J. Magn. Reson.*, 1983, **54**, 324.
15. A. Bax, *Two-Dimensional Nuclear Magnetic Resonance in Liquids*. Delft University Press, Delft, 1982.
16. J. Keeler and D. Neuhaus, *J. Magn. Reson.*, 1985, **63**, 454.
17. L. Müller and R. R. Ernst, *Mol. Phys.*, 1979, **38**, 963.
18. D. J. States, R. A. Haberkorn and D. J. Ruben, *J. Magn. Reson.*, 1982, **48**, 286.
19. G. Drobny, A. Pines, S. Sinton, D. Weitekamp and D. Wemmer, *Symp Faraday Soc.*, 1979, **13**, 49.
20. G. Bodenhausen, R. L. Vold and R. R. Vold, *J. Magn. Reson.*, 1980, **37**, 93.
21. D. Marion and K. Wüthrich, *Biochem. Biophys. Res. Commun.*, 1983, **113**, 967.
22. A. G. Palmer, J. Cavanagh, P. E. Wright and M. Rance, *J. Magn. Reson.*, 1991, **93**, 151.

23. J. Cavanagh and M. Rance, *J. Magn. Reson.*, 1990, **88**, 72.
24. J. Jeener, B. H. Meier, P. Bachmann and R. R. Ernst, *J. Chem. Phys.*, 1979, **71**, 4546.
25. L. Braunschweiler and R. R. Ernst, *J. Magn. Reson.*, 1983, **53**, 521.
26. A. Bax and D. G. Davis, *J. Magn. Reson.*, 1985, **65**, 355.
27. M. Rance, *J. Magn. Reson.*, 1987, **74**, 557.
28. R. Bazzo and I. D. Campbell, *J. Magn. Reson.*, 1988, **76**, 358.
29. O. W. Sørensen, G. W. Eich, M. H. Levitt, G. Bodenhausen and R. R. Ernst, *Prog. NMR Spectrosc.*, 1983, **16**, 163.
30. K. J. Packer and K. M. Wright, *Mol. Phys.*, 1983, **50**, 797.
31. F. J. M. van de Ven and C. W. Hilbers, *J. Magn. Reson.*, 1983, **54**, 512.
32. A. J. Shaka, J. Keeler, T. Frenkiel and R. Freeman, *J. Magn. Reson.*, 1983, **52**, 335.
33. A. J. Shaka, C. J. Lee and A. Pines, *J. Magn. Reson.*, 1988, **77**, 274.
34. J. Cavanagh, W. J. Chazin and M. Rance, *J. Magn. Reson.*, 1990, **87**, 110.
35. M. Rance and J. Cavanagh, *J. Magn. Reson.*, 1990, **87**, 363.
36. G. Otting, H. Widmer, G. Wagner and K. Wüthrich, *J. Magn. Reson.*, 1986, **66**, 187.
37. G. Wagner and K. Wüthrich, *J. Mol. Biol.*, 1982, **155**, 347.
38. J. S. Waugh, *J. Magn. Reson.*, 1986, **68**, 189.
39. A. Bax, *Isr. J. Chem.*, 1988, **28**, 309.
40. M. Kadkhodaie, O. Rivas, M. Tan, A. Mohebbi and A. J. Shaka, *J. Magn. Reson.*, 1991, **91**, 473.
41. J. Jeener, Ampère International Summer School, Basko Polje, Yugoslavia, 1971.
42. W. P. Aue, E. Bartholdi and R. R. Ernst, *J. Chem. Phys.*, 1976, **64**, 2229.
43. R. H. Griffey and A. G. Redfield, *Q. Rev. Biophys.*, 1987, **19**, 51.
44. G. Wagner, *Meth. Enzymol.*, 1989, **176**, 93.
45. D. C. Muchmore, L. P. McIntosh, C. B. Russell, D. E. Anderson and F. W. Dahlquist, *Meth. Enzymol.*, 1989, **177**, 44.
46. P. H. Bolton, *J. Magn. Reson.*, 1982, **48**, 336.
47. P. H. Bolton, *J. Magn. Reson.*, 1985, **62**, 143.
48. A. Bax, D. G. Davis and S. K. Sarkar, *J. Magn. Reson.*, 1985, **63**, 230.
49. L. Lerner and A. Bax, *J. Magn. Reson.*, 1986, **69**, 375.
50. M. Rance, P. E. Wright, B. A. Messerle and L. D. Field, *J. Am. Chem Soc.*, 1987, **109**, 1591.
51. N. R. Nirmala and G. Wagner, *J. Am. Chem Soc.*, 1988, **110**, 7557.
52. N. R. Nirmala and G. Wagner, *J. Magn. Reson.*, 1989, **82**, 659.
53. L. E. Kay, D. A. Torchia and A. Bax, *Biochemistry*, 1989, **28**, 8972.
54. G. Bodenhausen and D. J. Ruben, *Chem. Phys. Lett.*, 1980, **69**, 185.
55. M. R. Bendall, D. T. Pegg and D. M. Doddrell, *J. Magn. Reson.*, 1983, **52**, 81.
56. A. Bax, R. H. Griffey and B. L. Hawkins, *J. Magn. Reson.*, 1983, **55**, 301.
57. A. Bax, M. Ikura, L. E. Kay, D. A. Torchia and R. Tschudin, *J. Magn. Reson.*, 1990, **86**, 304.
58. (a) T. J. Norwood, J. Boyd, J. E. Heritage, N. Soffe and I. D. Campbell, *J. Magn. Reson.*, 1990, **87**, 488.
    (b) T. J. Norwood, J. Boyd and I. D. Campbell, *FEBS Lett.*, 1989, **255**, 369.
59. G. A. Morris and R. Freeman, *J. Am. Chem Soc.*, 1979, **101**, 760.
60. A. Bax, L. E. Kay, S. W. Sparks and D. A. Torchia, *J. Am. Chem Soc.*, 1989, **111**, 408.
61. (a) J. Glushka, M. Lee, S. Coffin and D. J. Cowburn, *J. Am. Chem Soc.*, 1989, **111**, 7716.
    (b) J. Glushka, M. Lee, S. Coffin and D. J. Cowburn, *J. Am. Chem Soc.*, 1990, **112**, 2843.
62. R. Richarz, K. Nagayama and K. Wüthrich, *Biochemistry*, 1980, **19**, 5189.
63. G. Wagner, *Q. Rev. Biophys.*, 1983, **16**, 1.
64. D. Brühweiler and G. Wagner, *J. Magn. Reson.*, 1986, **69**, 546.
65. J. Cavanagh, A. G. Palmer, P. E. Wright and M. Rance, *J. Magn. Reson.*, 1991, **91**, 429.
66. M. Rance and R. A. Byrd, *J. Magn. Reson.*, 1983, **54**, 221.
67. D. G. Davis, *J. Magn. Reson.*, 1989, **81**, 603.

68. G. M. Clore and A. M. Gronenborn, *Ann. Rev. Biophys. Biophys. Chem.*, 1991, **20**, 29.
69. L. E. Kay, D. Marion and A. Bax, *J. Magn. Reson.*, 1989, **84**, 72.
70. L. E. Kay, M. Ikura, R. Tschudin and A. Bax, *J. Magn. Reson.*, 1990, **89**, 496.
71. S. W. Fesik and E. R. P. Zuiderweg, *Q. Rev. Biophys.*, 1990, **23**, 97.
72. S. W. Fesik and E. R. P. Zuiderweg, *J. Magn. Reson.*, 1988, **78**, 588.
73. D. Marion, L. E. Kay, S. W. Sparks, D. A. Torchia and A. Bax, *J. Am. Chem Soc.*, 1989, **111**, 1515.
74. E. R. P. Zuiderweg and S. W. Fesik, *Biochemistry*, 1989, **28**, 2387.
75. A. G. Palmer, J. Cavanagh, R. A. Byrd and M. Rance, *J. Magn. Reson.*, 1992, **96**, 416.
76. J. Kördel, S. Forsen and W. J. Chazin, *Biochemistry*, 1989, **28**, 7065.
77. M. Karplus and J. A. McCammon, *Ann. Rev. Biochem.*, 1983, **53**, 263.
78. R. J. P. Williams, *Eur. J. Biochem.*, 1989, **183**, 479.
79. H. Frauenfelder, F. Parak and R. D. Young, *Ann. Rev. Biophys. Biophys. Chem.*, 1988, **17**, 451.
80. F. R. N. Gurd and T. M. Rothgeb, *Adv. Prot. Chem.*, 1979, **33**, 73.
81. T. M. G. Konong, R. Boelens, G. A. van de Marel, J. H. van Boom and R. Kaptein, *Biochemistry*, 1991, **30**, 3787.
82. J. E. Mertz, P. Güntert, K. Wüthrich and W. Braun, *J. Biomol. NMR*, 1991, **1**, 257.
83. H. Liu, P. D. Thomas and T. L. James, *J. Magn. Reson.*, 1992, **98**, 163.
84. A. Abragam, *Principles of Nuclear Magnetism*. Clarendon Press, Oxford, 1961.
85. R. E. London, *Meth. Enzymol.*, 1989, **176**, 358.
86. G. M. Clore, P. C. Driscoll, P. T. Wingfield and A. M. Gronenborn, *Biochemistry*, 1990, **29**, 7387.
87. J. Kördel, N. J. Skelton, M. Akke, A. G. Palmer and W. J. Chazin, *Biochemistry*, 1992, **31**, 4856.
88. A. G. Palmer, M. Rance and P. E. Wright, *J. Am. Chem. Soc.*, 1991, **113**, 4371.
89. J. W. Peng and G. Wagner, *J. Magn. Reson.*, 1992, **98**, 308.
90. D. M. Schneider, M. J. Dellwo and A. J. Wand, *Biochemistry*, 1992, **31**, 3645.
91. M. J. Stone, W. J. Fairbrother, A. G. Palmer, J. Reizer, M. H. Saier and P. E. Wright, *Biochemistry*, 1992, **31**, 4394.
92. A. G. Palmer, R. Hochstrasse, D. P. Millar, M. Rance and P. E.. Wright, *J. Amer. Chem. Soc.*, 1993 (in press).
93. J. W. Peng and G. Wagner, *Biochemistry*, 1992, **31**, 8571.
94. G. Barbato, M. Ikura, L. E. Kay, R. W. Pastore and A. Bax, *Biochemistry*, 1992, **31**, 5269.
95. L. K. Nicholson, L. E. Kay, D. M. Baldisseri, J. Arango, P. E. Young and D. A. Torchia, *Biochemistry*, 1992, **31**, 5253.
96. V. Sklenar, D. A. Torchia and A. Bax, *J. Magn. Reson.*, 1987, **73**, 375.
97. L. E. Kay, T. L. Jue, B. Bangerter and P. C. Demou, *J. Magn. Reson.*, 1987, **73**, 558.
98. L. E. Kay, L. K. Nicholson, F. Delagio, A. Bax and D. A. Torchia, *J. Magn. Reson.*, 1992, **97**, 359.
99. A. G. Palmer, N. J. Skelton, W. J. Chazin, P. E. Wright and M. Rance, *Mol. Phys.*, 1992, **75**, 699.
100. J. Boyd, U. Hommel and I. D. Campbell, *Chem. Phys. Lett.*, 1990, **175**, 477.
101. J. W. Peng, V. Thanabal and G. Wagner, *J. Magn. Reson.*, 1991, **95**, 421.
102. N. J. Skelton, A. G. Palmer, M. Akke, J. Kördel, M. Rance and W. J. Chazin, *J. Magn. Reson.*, in press, 1993.
103. S. Meiboom and D. Gill, *Rev. Sci. Instrum.*, 1958, **29**, 688.
104. H. Y. Carr and E. M. Purcell, *Phys. Rev.*, 1954, **94**, 630.
105. J. H. Noggle and R. E. Shirmer, *The Nuclear Overhauser Effect: Chemical Applications*. Academic Press, New York, 1971.
106. B. A. Messerle, G. Wider, G. Otting, C. Weber and K. Wüthrich, *J. Magn. Reson.*, 1989, **85**, 608.

107. R. L. Vold, R. R. Vold and H. E. Simon, *J. Magn. Reson.*, 1973, **11**, 283.
108. A. D. Bain, *J. Magn. Reson.*, 1984, **56**, 418.
109. G. Bodenhausen, H. Kogler and R. R. Ernst, *J. Magn. Reson.*, 1984, **58**, 370.
110. L. E. Kay, P. Keifer and T. Saarinen, *J. Am. Chem. Soc.*, 1992, **114**, 10 663.
111. J. C. Madsen and O. W. Sørensen, *J. Magn. Reson.*, 1992, **100**, 431.
112. A. Bax, A. F. Mehlkopf and J. Smidt, *J. Magn. Reson.*, 1979, **35**, 167.
113. F. Ni, *J. Magn. Reson.*, 1992, **100**, 391.

NMR Studies of the Structure and Properties of Cyclodextrins and Their Inclusion Complexes

YOSHIO INOUE

Department of Biomolecular Engineering, Tokyo Institute of Technology, Yokohama 227, Japan

ANNUAL REPORTS ON NMR SPECTROCOPY
VOLUME 27 ISBN 0-12-505327-4

1. INTRODUCTION

1.1. Supramolecular chemistry and molecular inclusion phenomena

In the last two decades there have been great advances in supramolecular chemistry. As described by J.-M. Lehn[1] in his Nobel lecture, "supramolecular chemistry may be defined as chemistry beyond the molecule". In general, a supramolecular system has high structural complexity arising from the association of two or more chemical species held together through noncovalent, i.e. intermolecular, forces such as electrostatic interactions, hydrogen bonding and van der Waals forces. A stricter definition of supramolecular system must include processes of molecular recognition, transformation and translocation.[1] Thus supramolecular chemistry involves not only basic chemical, biological and physical questions but also various technological aspects.

A variety of molecules and molecular groups can form supramolecular systems through molecular inclusion processes. Molecular inclusion is of great intrinsic interest, as a phenomenon in which various types of intermolecular interactions play important roles. A molecular complex formed through molecular inclusion is called an inclusion complex or, frequently, an inclusion compound. In some cases it is also called a clathrate compound. Molecular inclusion phenomena have been well known for a long time in both inorganic and organic chemistry and in biology: examples are the iodine–starch reaction, and the formation of enzyme–substrate complexes, antigen–antibody complexes and urea–channel complexes or urea adducts. The intercalation found in layered inorganic materials and nucleic acids is also a well-known molecular inclusion phenomenon.

A molecular system having a molecular architecture that can form an inclusion complex with another molecular species, termed the "guest", is called the "host", and the chemistry of molecular inclusion phenomena is sometimes known as "host–guest chemistry".[2] The term "guest" also refers to a substrate or ligand, especially in biological and biomimetic chemistry. A number of natural and synthetic compounds of medium or relatively large size are known to act as hosts for molecular inclusion of a wide variety of guest compounds.[3–5] Most of the compounds that, as single molecules, can act as hosts have macrocyclic structures involving three-dimensional molecular cavities that can accommodate guest compounds. The oligopeptide valinomycin is a typical macrocyclic compound that acts as a monomolecular host. It is a natural product, and it transports actively and selectively a K^+ ion in biological membranes, resulting in antibiotic activity.[6] A group of macrocyclic antibiotics are known and have been termed "ionophores".[7] A variety of artificial host compounds that show natural ionophore-like activity have been also synthesized.[3–5,8–13] Some of these can form host–guest complexes not only with ions including metallic cations but also with a

variety of non-ionic molecular species. Examples include crown ethers,[14] cryptands,[15] cyclophanes[16] and spherands.[17]

As well as these synthesized host compounds, the group of cyclodextrins represents a particularly wide area of host–guest chemistry.

1.2. Cyclodextrins

Cyclodextrins (CDs) are a series of cyclic oligosaccharides composed of at least six (1→4)-linked α-D-glucopyranosyl residues. Their unique macrocyclic structure is a result of the stable chair conformation of the constituent D-glucopyranosyl residues and α-(1→4)-glycosidic bonds linking the residues with each other. According to conformational energy calculations, CDs with less than six D-glucopyranosyl residues cannot form owing to steric hindrance.[18] In order of increasing number of D-glucopyranosyl residues, they are termed α-CD (also called Schardinger's α-dextrin, cyclohexaamylose, or cyclomaltohexaose), β-CD (Schardinger's β-dextrin, cycloheptaamylose, or cyclomaltoheptaose), and so on.

The most common CDs are α-, β- and γ-CD, which are constructed of six, seven and eight D-glucopyranosyl units respectively. Figure 1 shows the molecular structures of a component D-glucopyranosyl unit and a typical CD, namely β-CD. The shape of α-, β- and γ-CD molecules can be represented as a toroidal hollow truncated cone, which is frequently compared to a bottomless bucket. The hollow-cone structure of macrocyclic rings of α-CD and β-CD is generally rather stable owing to the formation of intramolecular, interglycosyl hydrogen bonds between the secondary hydroxyl groups at C-2 on one residue and C-3 on the other. In contrast, the structures of γ-CD and CDs with more than nine D-glucopyranosyl residues are rather flexible, and may deviate from the cone-like form.

CDs with cone-like structure have many primary and secondary hydroxyl groups crowning the narrower and wider rims of the hollow cone respectively. Methine protons and glycosidic oxygen atoms are located inside the hollow cone, which will hereinafter be called the cavity. Hence the interior is relatively apolar and hydrophobic, whereas the exterior is relatively polar and hydrophilic. In the common CDs the cavity height is about 0.8 nm and its internal diameter is about 0.5 nm (α-CD) or more, depending on the number of D-glucopyranosyl residues forming the CD macrocycle.

Various branched CDs composed of CDs with one or more carbohydrate branches, which are D-glucopyranoses or (1→4)-linked α-D-glucooligosaccharides, are also well known. Since CDs have many functional groups, namely primary and secondary hydroxyl groups, a variety of chemically modified CDs have also been synthesized. All the primary hydroxyl groups are located on one of the two rims of the CD cavity, while all the secondary ones are on the other. Thus it is possible to introduce regioselectively

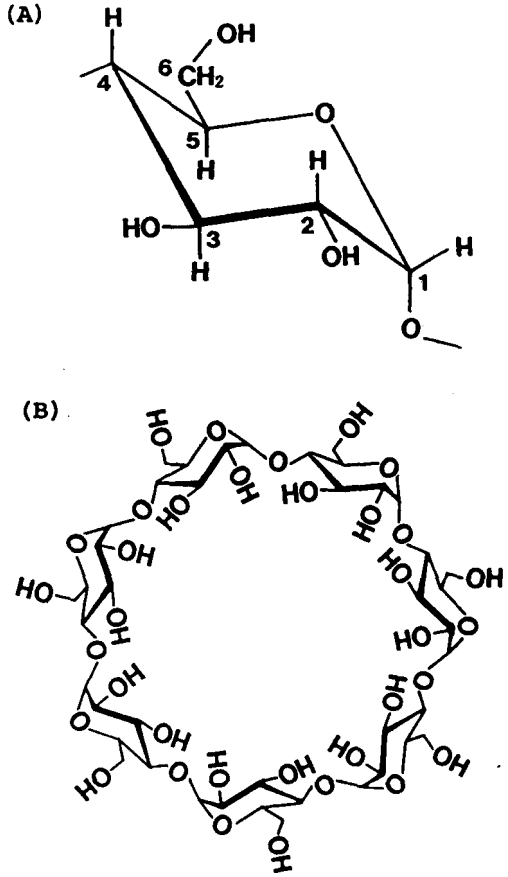

Fig. 1. Molecular structures of (A) D-glucopyranose residue and (B) β-CD.

various types of functional groups into the CD macrocycle. The carbohydrate branches as well as the chemical modifications alter the CD properties to a varying extent.

The most striking and important feature of a CD is its ability as a host to trap a variety of compounds as guest molecules inside its cavity, without the formation of any covalent bonds between the host and guest, resulting in the formation of host–guest inclusion complexes. CDs can form inclusion complexes with a variety of guest compounds, ranging from rare gases, nonpolar and polar organic and inorganic compounds and water to some organic and inorganic ions. The functions of CDs are not limited to their ability to become hosts. The CD molecule more or less modifies the physicochemical properties of the included guest molecules, and can

sometimes exhibit enzyme-like action on a guest molecule, converting it efficiently and selectively to another compound. These abilities of CDs depend on their types, i.e. their cavity size and whether or not they are chemically modified. Hence CDs have great possibilities for applications in a wide variety of fields. In fact, they are receiving increased attention in the scientific, industrial, biotechnological and especially pharmaceutical fields.

Cyclodextrins are typical of chemical compounds that can form supramolecular species in the strict sense. That is, CDs and their derivatives can recognize, transform and translocate guest molecules via the formation of molecular inclusion complexes as described in detail in this review.

It was just over a century ago that the field of cyclodextrin chemistry was opened up by Villiers,[19] who first isolated CDs as crystals from a culture medium of *Bacillus amylobacter* grown on a starch-containing medium. Since then, CD chemistry has been developed by many pioneering researchers, but it has been only in the last two decades that CDs have received so much attention from so many investigators in diverse fields. The main reason for this is that the biotechnological basis for the production of high-purity CDs on an industrial scale in a completely aqueous medium was established just 15–20 years ago. It is now possible to obtain several types of CDs at a reasonable price.

Up to now, significant effort has been devoted to identifying the mechanism leading to the formation of CD inclusion complexes and to describing clearly the structure of CD–guest complexes on the molecular level in solution as well as in the solid state. There are still several unresolved problems, especially concerning the driving force(s) for the formation of CD inclusion complexes. At present only the following is well established as a constraint for inclusion complexation: the guest must have a molecular size that fully or at least partially fits the cavity of CD.

In order to understand the formation mechanism of CD inclusion complexes, although these can provide information only on complex application of CDs, the spatial structures of inclusion complexes and the various interactions contributing to their formation must be well characterized. In the solid state the most direct and powerful method is X-ray diffraction for the determination of the three-dimensional structure of CD inclusion complexes if these are available in the form of single crystals. X-ray powder diffraction and some thermal analyses are also useful for solid complexes, although these can provide only information on complex formation, and the detailed structure of complexes cannot be obtained by either of these methods alone. In aqueous solution, since the physical and chemical properties of CDs and guests change on the formation of inclusion complexes, a variety of physical and chemical methods can be used for the detection and characterization of CD complexes. As described later in this chapter, almost all important intermolecular interactions leading to formation and stabilization of complexes occur between atoms or chemical groups

of the host CD and the guest situated within a few angstroms of each other. High-resolution NMR spectroscopy is one of the most useful methods for studies of CD inclusion complexes in solution, because NMR parameters such as chemical shift, spin coupling constant and relaxation time are sensitive to short-range intermolecular interactions. Thus, since Demarco and Thakkar[20] presented direct evidence for the inclusion nature of the complex formation of β-CD with aromatic guest molecules in aqueous solution by observing proton chemical-shift changes, NMR spectroscopy has been widely used for studies of CD inclusion phenomena. With the introduction of superconducting higher-field magnets, pulse techniques including multidimensional methods, and so on, NMR has become indispensable for the study of CD supramolecular chemistry in solution. High-resolution NMR spectroscopy is also useful for investigating CD inclusion complexes in the solid state.

The present chapter centres on several aspects of the application of high-resolution NMR in the study of CD inclusion phenomena in solution as well as in the solid state, based mainly on the results obtained by the author and co-workers. The experimental procedures for NMR determination of the structure of CD inclusion complexes in aqueous solution are discussed in detail in the first half of the chapter. Some results of theoretical studies are then given. Short reviews of the NMR study of CD inclusion complexes have been published elsewhere.[21,22] A very large number of papers describing such NMR studies have been published for a variety of CD–guest systems, and it has not been possible to cite many important papers here. General aspects of the basic science and the applications of CD inclusion phenomena have been described in some excellent books (e.g. refs 3–5 and 23) and reviews (e.g. ref. 24), and the many references cited therein.

2. NMR EXPERIMENTAL STUDY OF CYCLODEXTRIN INCLUSION PHENOMENA

2.1. NMR spectra of cyclodextrins and their inclusion complexes

Carbon, oxygen and hydrogen are essential constituents of CDs. For this reason, proton and carbon nuclei are potentially the most useful NMR probes for the study of CD inclusion phenomena. In order to extract information on CD molecular inclusion phenomena from NMR spectra, one needs the full assignments of all resonances of host CD and guest appearing in the spectra. ^{1}H and ^{13}C NMR spectra of unmodified CDs are rather simple to assign. As an example, Fig. 2(a) shows the ^{1}H NMR spectrum of β-CD in deuterium oxide solution observed at 500 MHz. The apparent sevenfold symmetry of the β-CD macrocyclic ring structure and rapid interconversion among several possible conformations of macrocyclic ring as

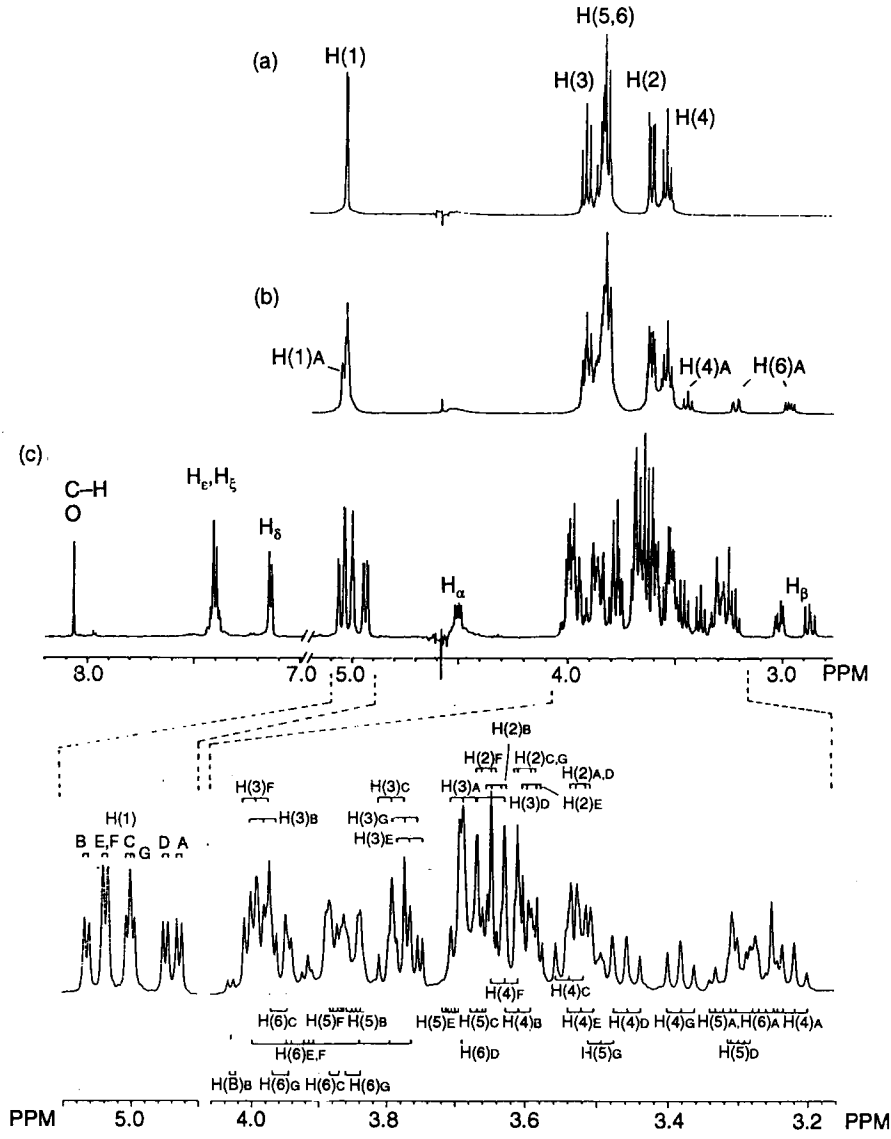

Fig. 2. 500 MHz ^{1}H NMR spectra of β-CD (a), amino-β-CD (b) and f-L-Phe-β-CD (c) in deuterium oxide solution at 40°C.[30] (Reproduced with permission from Saka *et al.*[30])

well as those of the respective glucopyranose rings in solution result in the appearance of a single set of resonances as if there were only one glucopyranosyl residue. Observation at higher field also simplifies the appearance of the spectrum. Generally, in the case of saccharides consisting of D-glucopyranosyl residues it is well known that their anomeric protons, namely the H-1s as shown in Fig. 1, exhibit characteristic low-field shifts (see e.g. ref. 25). On the basis of this, and using the ^{1}H–^{1}H homonuclear shift correlated two-dimensional spectroscopy (COSY) technique (reviewed e.g. in ref. 26), all resonances appearing in the ^{1}H NMR spectrum are straightforwardly assigned;[22,27] the results are also shown in Fig. 2(a). It is also possible to assign this spectrum using the following classical procedures as was first done by Demarco and Thakkar:[20] comparison of the chemical shifts of analogous series of linear chain sugars, analysis of individual splitting patterns and spin coupling constants, and selective spin decoupling experiments. Although the same procedures are also applicable to the assignments of ^{13}C NMR spectra of CDs, almost all ^{13}C resonances of protonated carbon nuclei of CDs could be unequivocally assigned on the basis of assignments of the ^{1}H spectrum. Once the full assignments of ^{1}H resonances of CDs have been made, the corresponding ^{13}C resonances can be assigned more easily and unambiguously from the ^{1}H assignments by ^{1}H–^{13}C heteronuclear COSY.[27,28] It is also easy to assign fully the ^{1}H and ^{13}C NMR spectra of some chemically modified CDs that retain their apparent symmetry, such as permethylated α- and β-CDs.[27,28]

In contrast to the simplicity of NMR spectra of unmodified and some symmetrically modified CDs, those of unsymmetrically modified CDs are generally too complex to be assigned completely using only empirical rules and COSY techniques.[21,29] An example is *N*-(*N*-formyl-L-phenylalanyl)-6-deoxy-6-amino-β-CD (f-L-Phe-β-CD, Fig. 3), which is a branched β-CD consisted of a β-CD macrocyclic skeleton together with an amino acid branch attached to one of the D-glucopyranosyl residues of the macrocycle through the 6-methylene group.[30] f-L-Phe-β-CD shows improved ability for chiral recognition, as described in detail in Section 2.3.3. Its 500 MHz ^{1}H NMR spectrum is shown in Fig. 2(c), in comparison with spectra of β-CD (Fig. 2a) and 6-deoxy-6-amino-β-CD (amino-β-CD, Fig. 2b). The ^{1}H NMR spectrum becomes more complex with increasing structural complexity of the branch. These complexities are due to the resolution of structural and magnetical degeneracy of the D-glucopyranosyl residues constituting the branched CDs. In the chemical structure of f-L-Phe-β-CD shown in Fig. 3 there are seven different types of D-glucopyranosyl residues, namely the residue A at the branched site, B and G next to the residue A, and so on. Hence seven sets of D-glucopyranosyl resonances must appear in addition to the branch resonances in the spectrum shown in Fig. 2(c). In fact, the anomeric protons of f-L-Phe-β-CD exhibit seven well-separated resonances. The combined use of some two-dimensional (2D) NMR techniques,

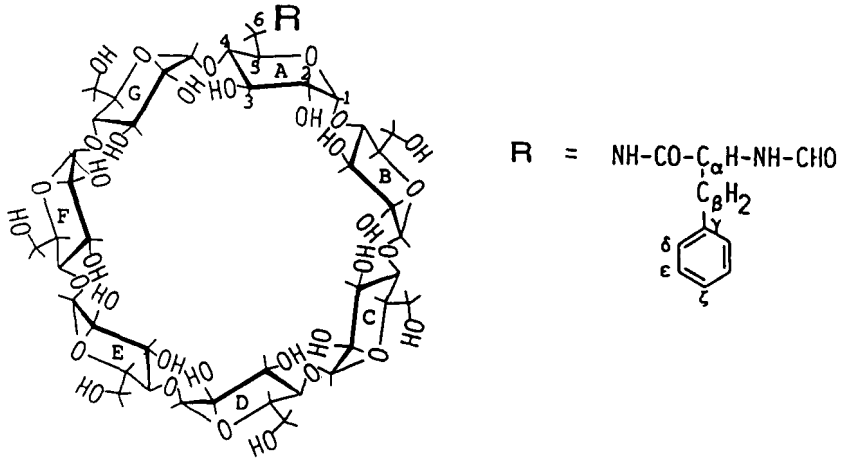

Fig. 3. Structure of f-L-Phe-β-CD, illustrating the ring-labelling sequence with the assignments of carbon atoms. (Reproduced with permission from Saka *et al.*[30])

especially 2D homonuclear Hartmann–Hahn spectroscopy (HOHAHA)[31–33] and 2D nuclear Overhauser effect (NOE) spectroscopy under spin-locked conditions (ROESY),[34–37] makes it possible to assign all these resonances reasonably. The detailed procedures for the assignments will be presented here.

By using the HOHAHA technique, it is possible to extract each set of resonances of protons belonging to the same D-glucopyranosyl residue. Part of the 2D HOHAHA spectrum of f-L-Phe-β-CD covering the anomeric proton region of the F_1 axis is shown in Fig. 4(A), and an example of the cross-section data along the F_2 axis of this experiment is shown in Fig. 4(B). Each anomeric proton H-1 resonance has crosspeaks with H-2 to H-6 resonances belonging to the same D-glucopyranosyl residue. At this stage it is still difficult to assign cross-peaks to each proton using only a single 2D HOHAHA experiment. However, in the HOHAHA experiment, by changing the mixing time,[33,38] it is possible to control the degree of magnetization transfer from a certain selectively irradiated proton (in the example presented here the anomeric proton) to other protons along the bonds. At the shortest mixing time only the resonance of the proton nearest to H-1, namely H-2, should be observed. With increasing mixing time, the resonances of more distant protons along the bonds, namely H-3, H-4, H-5 and finally H-6, appear. In this way, a set of resonances of protons constituting a whole D-glucopyranosyl residue, the so-called spin network, is picked up, and hence the all resonances appearing in Fig. 2(c) can be classified into seven spin-networks. Here only a spin-network whose H-6 resonance shifts largely to the higher field is identified as the D-glucopyra-

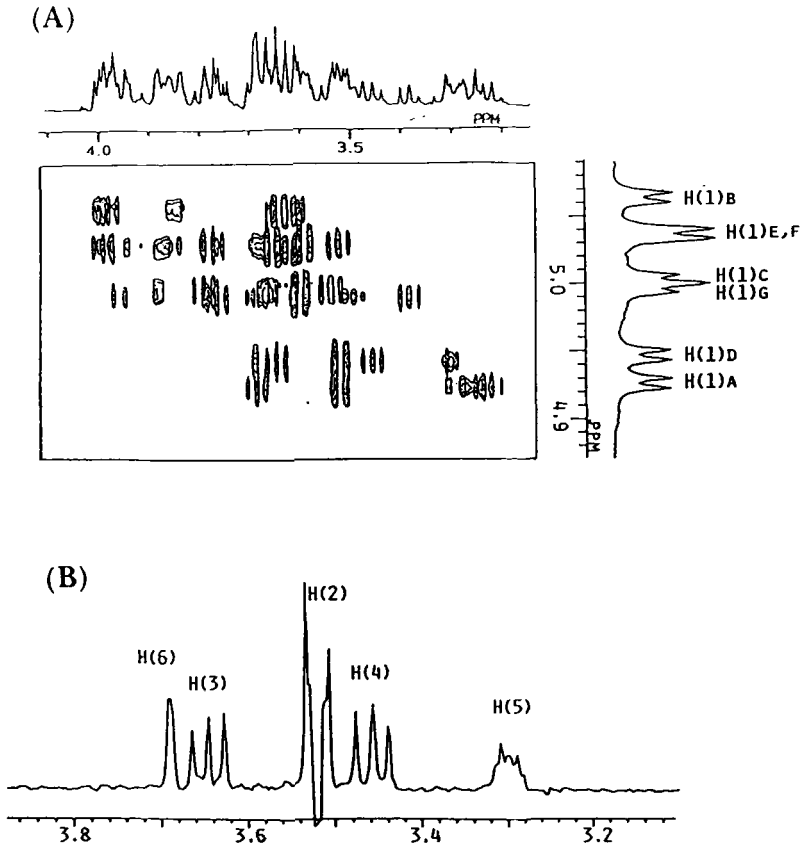

Fig. 4. (A) Part of the 2D HOHAHA spectrum of f-L-Phe-β-CD covering the anomeric proton resonance region of the F_1 axis. (B) An example of cross-section data along the F_2 axis of (A), sliced at δ = 4.947 ppm on the F_1 axis. (Reproduced with permission from Saka *et al.*[30])

nosyl residue substituted by the f-L-Phe moiety, i.e. the A unit. The chemical shift of this H-6 resonance is very close to that of the H-6 resonance of D-glucopyranosyl residue substituted by the amino group in amino-β-CD.

The next step of the assignments is to obtain information on sequence relation among the spin networks. This is provided by the 2D ROESY spectrum. The distance between H-1 of one D-glucopyranosyl residue and H-4 of its neighbouring residue across the common α-(1→4)-glycosidic linkage is short enough to increase the observable level of through-space NOE enhancement,[26] which allows sequence-specific interlinking of one residue with the neighbouring residue along the CD macrocycle[39]. The spin network of the D-glucopyranosyl residue whose H-4 resonance has an NOE

cross-peak with the H-1 resonance of the A residue is identified as the spin network of the B residue, and in a similar way all spin networks up to the G residue are successively identified, as shown in Fig. 5. The validity of this sequential assignment was confirmed, since the H-1 resonance of the G residue has an NOE cross-peak with the H-4 resonance of the A residue. Thus, at this point, ^{1}H resonances of f-L-Phe-β-CD are fully and sequence-specifically assigned as shown in Fig. 2(c). Some other 2D methods, such as relayed COSY,[40,41] may also be useful for assignment of complex ^{1}H NMR spectra of oligosaccharides, including CDs.

2.2. Formation and stoichiometry of cyclodextrin inclusion complexes in aqueous solution

Good knowledge of stoichiometry is indispensable for quantitative description and mechanistic investigation of host–guest inclusion phenomena. Any physical parameter that changes its magnitude with a change in host/guest molar ratio can provide stoichiometric information. A variety of spectroscopic methods, including NMR, have been used for the quantitative study of complex formation by cyclodextrins. In the case of NMR studies, complexation-induced changes in chemical shifts of both host CD and guest molecules are widely used for this purpose.

Figure 6 shows ^{1}H NMR spectral changes of permethylated α-CD (α-MCD) on complexation with *p*-nitrophenol (*p*NP) in aqueous solution at pH 10.[42] Large shifts in the resonances of H-3 and H-5 located inside the CD cavity induced by the addition of *p*NP indicate inclusion complexation and the effect of the magnetic field created by the benzene ring current of *p*NP. The resonances of the *ortho* and *meta* protons of *p*NP also show large shifts upon interaction with α-MCD. These shift changes allow determination of the stoichiometry and the association constant for complexation. Figure 7 shows plots of the changes in chemical shift of the *p*NP protons as functions of the molar ratio [α-MCD]/[*p*NP], clearly indicating that 1:1 complexation predominates. Since only a single set of resonances was observed for the host α-MCD and the guest *p*NP, and their chemical shifts changed monotonically as the host:guest molar ratio was varied, this host–guest complexation system is considered to be in the NMR chemical-shift fast-exchange limit.[43] In this case the observed chemical shifts of the guest (or host) resonances are the averages of the chemical shift of guest (or host) in the free state and that in the complexed state, weighted by the fraction of guest (host) molecules in each state.

By assuming 1:1 equilibrium complexation, expressed as

$$\alpha\text{-MCD} + p\text{NP} \rightleftarrows [\alpha\text{-MCD}, p\text{NP}] \quad (1)$$

where [α-MCD, *p*NP] is the host–guest complex, the value of the dissocia-

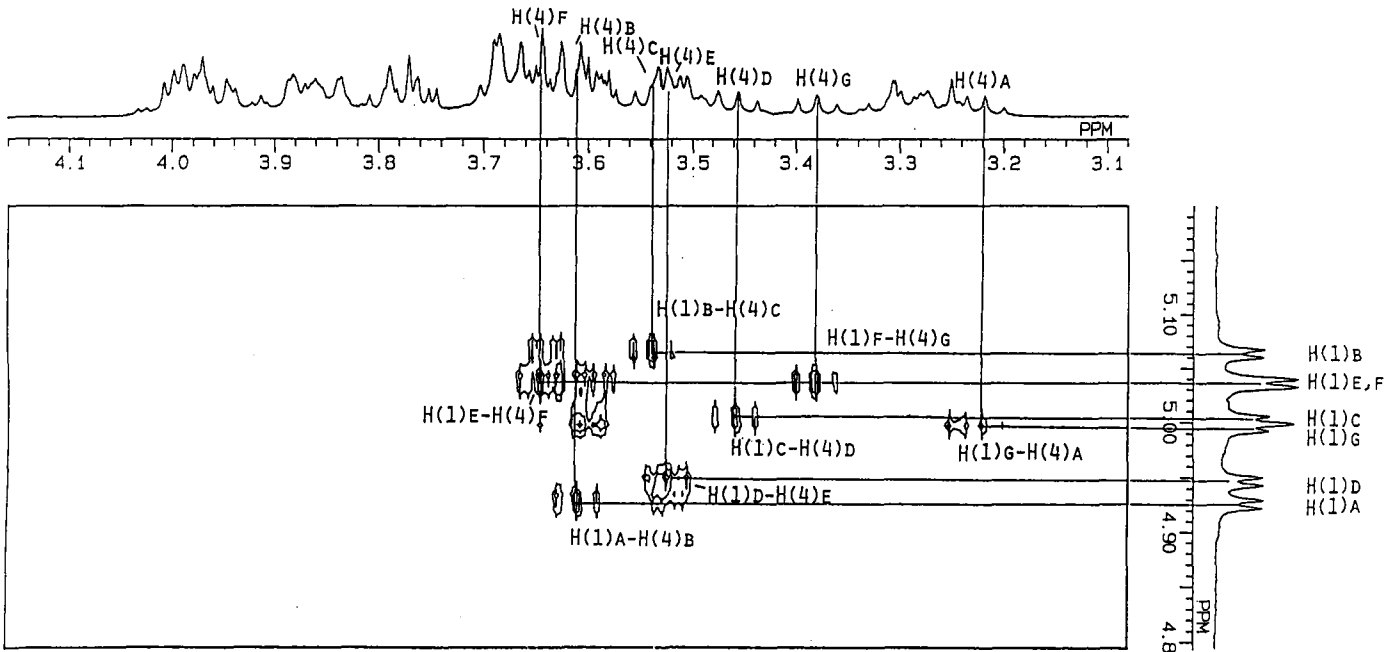

Fig. 5. Part of the ROESY spectrum of f-L-Phe-β-CD covering the H-1 resonance region of the F_1 axis, indicating the NOE connectivities between the H-1 and H-4 resonances of successive D-glucopyranosyl units. (Reproduced with permission from Saka *et al.*[30])

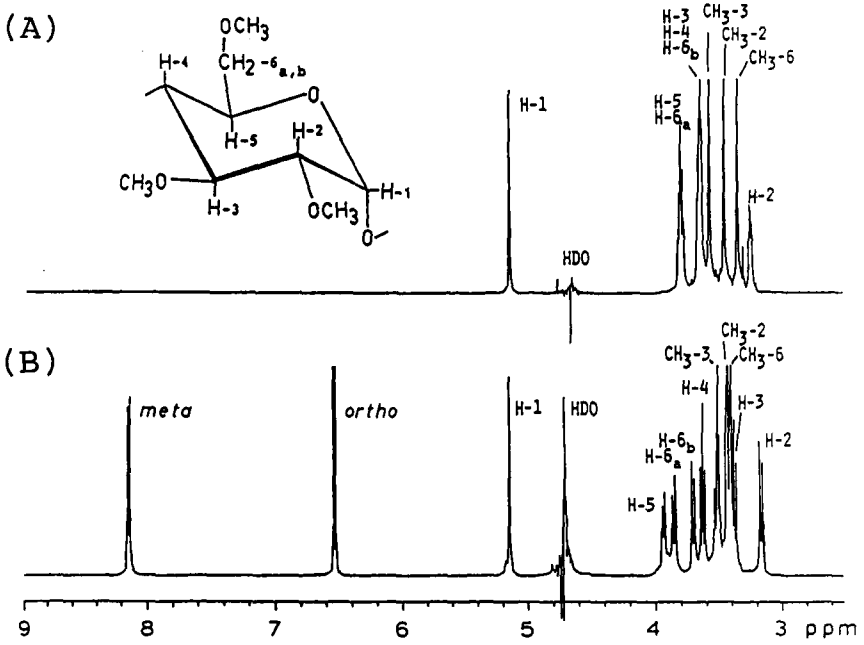

Fig. 6. 500 MHz ^{1}H NMR spectra of 0.1 M α-MCD (A), and a 0.03 M α-MCD/0.10 M *p*NP mixture (B) in deuterium oxide solution at pD 10 and 27°C. (Reproduced with permission from Yamamoto *et al.*[42])

tion constant K_d (the reciprocal of the association or binding constant) can be obtained by a least-squares fit of the Hildebrand–Benesi equation (modified for the treatment of NMR chemical-shift data[44]) to the observed chemical-shift data shown in Fig. 7. The K_d value from the NMR data for the α-MCD/*p*NP system at pH 10, where *p*NP is ionized to the phenolate anion, shown in Fig. 7 is 8.0×10^{-5} M. The corresponding value at pH 3, where *p*NP is not ionized, is about seven times larger, namely 5.5×10^{-4} M. The K_d values for the α-CD/*p*NP system are 6.1×10^{-4} and 5.8×10^{-3} M at pH 10 and 3 respectively. Similar K_d values have been obtained from ultraviolet (UV) spectra, although the sample concentration used for UV titration is at least three orders of magnitude smaller than that for NMR.[42]

At a given pH the K_d values for the α-MCD/*p*NP system are almost an order of magnitude less than those for the α-CD/*p*NP system. This means that permethylation increases the binding capability of α-CD. The results also indicate that for both α-MCD and α-CD the *p*NP anion binds in the CD cavity more strongly than the un-ionized *p*NP.

The stoichiometry of host CD complexation with a guest is not always limited to 1:1, but depends on the combination of host–guest pairs. For example, both ^{13}C NMR and conductimetric data[45] indicate that α-CD

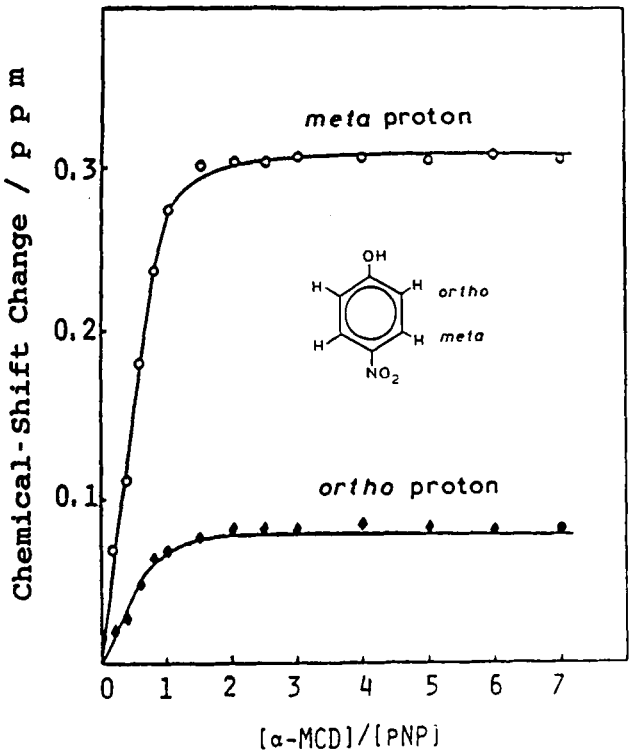

Fig. 7. Plots of the changes in chemical shifts of the *meta* and *ortho* proton resonances of *p*NP as functions of the molar ratio [α-MCD]/[*p*NP] at pD 10. (Reproduced with permission from Yamamoto *et al.*[42])

forms 1:1 and 2:1 stoichiometric complexes with *p*-methylcinnamate anion in aqueous solution. The data show binding of the carboxylate terminal of *p*-methylcinnamate by α-CD in the 1:1 complex, while in the 2:1 complex the structure involves occlusion of the *p*-methylcinnamate anion between two α-CD molecules in a head-to-head orientation. α-CD also forms 2:1 as well as 1:1 complexes with 4-biphenylcarboxylate anion.[46] α-MCD, too, forms 1:1 and 2:1 complexes with *p*-methylcinnamate and 4-biphenylcarboxylate anions.[47]

A special case is the complex formation between α-CD and the linear long-chain molecule poly(ethylene glycol) (PEG, average molecular weight 1000). The ^{1}H NMR spectrum indicates that the stable α-CD–PEG complex is composed of two ethylene glycol monomer units per α-CD molecule.[48] In contrast, ^{1}H and ^{13}C NMR spectral data for dynamically and statically stable through-ring complexes of α-CD with α-ω-alkanedicarboxylate anions, having a long spacer methylene chain of 7 to 12 carbon atoms, have been analysed on the basis of 1:1 stoichiometry.[49]

The stoichiometry of host CD complexation with guests in solution state is not always the same as that in the solid state, even for the same host–guest pair. According to ^{1}H and ^{13}C NMR,[50] methyl orange forms 1:1 complexes with α- and β-CD in aqueous solution, with the methyl orange being included predominantly from the *N*,*N*-dimethylamino side. On the other hand, X-ray crystallography[51] shows that sodium and potassium salts of methyl orange form 1:2 complexes with α-CD in the crystalline state, with the benzene rings and the azo group inside the cavity and the dimethylamino and sulphonyl groups outside. A particularly interesting case is the system of α-CD and *m*-nitrophenol (*m*NP). In aqueous solution ^{1}H and ^{13}C NMR data[52–54] indicate that α-CD and *m*NP form a 1:1 stoichiometric complex, as expected from the size of the *m*NP molecule relative to that of the α-CD cavity. However, in the solid state the crystal structure determined by the X-ray method consists of α-CD and *m*NP with a 1:2 molar ratio,[55] with the two *m*NP molecules in different environments: one located in a channel formed by a stack of α-CD molecules, and the other sandwiched between the α-CD molecules. The 1:2 α-CD–*m*NP complexation and the presence of two types of *m*NP molecules in the solid state are also confirmed by high-resolution solid-state ^{13}C NMR,[56] as described in Section 2.5.

2.3. Determination of structures of cyclodextrin inclusion complexes in aqueous solution

2.3.1. Geometrical structures determined on the basis of ^{1}H NMR chemical shifts

Kinetics and mechanisms have been studied for numerous CD-catalysed stereospecific reactions in solution.[23b,24a,d,g] In attempting quantitatively to explain the results of reaction, it is important to know the molecular geometry of CD–reactant complexes in solution—in particular the relative orientation and the position of the reactant in the CD cavity. Determination of the host–guest geometrical relation may provide insight into the mechanisms of CD-catalysed reactions and host–guest intermolecular interactions.

The solid-state geometry of CD inclusion complexes has been widely investigated by the X-ray method,[23c] in cases where crystals of good quality are available. Although the solid-state geometry can explain many of the characteristics of reactions in solution, the geometry of a CD inclusion complex in the solution state is not necessarily the same as that in the solid state. Thus it is necessary to independently investigate the geometry of a complex in solution, even if its counterpart in the solid state has been determined by the X-ray method.

NMR parameters such as chemical shifts and NOE can provide informa-

tion on the structure of CD complexes in solution. First, we shall describe the method of geometry determination on the basis of chemical-shift changes of the host CD induced by CD–aromatic guest interaction.[42,57–61]

As described in Section 1.2, the intrusion of an aromatic guest compound into the cavity of a CD induces ^{1}H chemical-shift changes[20] of the CD protons inside the cavity, i.e. H-3 and H-5. These shift changes are due to anisotropic shielding by the aromatic molecules, and their extent reflects the location of the corresponding protons with respect to the aromatic ring of the guest molecule. The changes in chemical shifts of the H-3 and H-5 resonances of CDs induced by an aromatic guest can be interpreted qualitatively in terms of the spatial relationship between these protons and the centre of the benzene ring of the guest, based on the Johnson–Bovey theory of the ring-current effect.[62] Here the observed difference $\Delta\delta$ between the chemical shifts of free and fully complexed states is used for comparison with the theoretical magnitudes of the anisotropic shielding effects due to the aromatic ring on the H-3 and H-5 resonances, which are calculated as functions of the depth of insertion of the aromatic ring of guest molecule into the CD cavity. The shift for the fully complexed state is obtained from a plot of chemical-shift change versus molar ratio, using the known K_d value.

The observed magnitudes of the ring-current effects on H-3 and H-5 are considered to be the time averages of those for several orientations of the aromatic plane with respect to H-3 and H-5, since only one set of H-3 and H-5 resonances appears, even for CD inclusion complexes at higher [guest]/[CD] molar ratios. This is supported by the evidence of ^{13}C relaxation times,[63] which indicate rapid rotational motion of phenyl compounds in CD cavities in solution, as shown in Section 2.4. Thus the theoretical $\Delta\delta$ values for H-3 and H-5 are calculated for every depth of guest insertion as the weighted averages of the changes in chemical shifts for, e.g., the 6(α-CD) and 7(β-CD), corresponding protons. As the macrocyclic ring of the CD molecule is rather flexible,[63,64] the induced-fit type conformational change should be also assumed. Hence the Johnson–Bovey theoretical $\Delta\delta$ values are calculated for H-3 and H-5 by taking account of the conformational change on the CD macrocyclic ring structure on complexation with an aromatic guest molecule. The location of the guest molecule in the CD cavity is determined as the position where the calculated $\Delta\delta$ values for both H-3 and H-5 show the best fit at the same time with the observed ones. The calculated $\Delta\delta$ values are very sensitive to the location of the aromatic ring, so its location can be precisely determined. For example, for the α-CD–*p*-nitrophenol (*p*NP) complex in aqueous solution at pH 10 and 27°C, from the observed $\Delta\delta$ values, −0.27 (high-field shift) and 0.00 ppm for H-3 and H-5 respectively, the most probable position of the centre of the benzene ring of *p*NP is determined to be 0.8 ± 0.1 Å from the plane comprising the six H-3 atoms and to be on the side of H-5 of α-CD, as shown schematically in Fig. 8.[61] The most probable position of the *p*NP phenyl ring determined

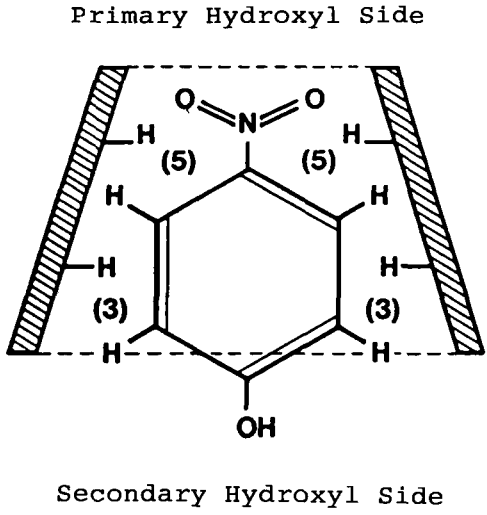

Fig. 8. Schematic representation of the host–guest orientation in the inclusion complex between α-CD (shaded) and *p*NP.

by the above procedure agrees well with that in the solid state determined by X-ray crystallography.[65]

Some other *para*-substituted phenols, such as *p*-cyanophenol and *p*-hydroxybenzaldehyde, were found to penetrate to almost the same position in the α-CD cavity as *p*NP at 100% binding, irrespective of the type of *p*-substituent.[60] Space-filling molecular models suggest that these phenol derivatives can penetrate to the position shown in Fig. 8 without any steric contact with atoms inside the α-CD cavity, although deeper penetration would induce severe steric interaction between the hydrogens of the guest *meta* to its hydroxyl group and H-5 of α-CD, since the radius of the circle formed by the six H-5 (about 3.2 Å) is smaller than that formed by the six H-3 (about 3.6 Å). Molecular models also indicate that significant portions of the included *para*-substituted phenols are exposed to the aqueous medium.

In the permethylated (α-MCD)–*p*NP complex the most probable position of *p*NP with respect to the H-3 circle is found to be quite similar to that in the α-CD–*p*NP complex, although the hydrophobic region inside the cavity should be greater in α-MCD than in α-CD because of the presence of methoxy groups in the former. The additive stabilization effects arising from the hydrophobic methoxy groups on the complex is reflected in the K_d values, as shown in Section 2.2.

In β-CD-*para*-substituted phenol complexes the guest-induced chemical shift changes of H-3 and H-5 were different in trend from those in α-CD complexes, in that not only H-3 but also H-5 resonances of β-CD were

induced to shift largely to high field.[60,61] For example, for the β-CD–*p*NP complex in aqueous solution at pH 10 and 27°C $\Delta\delta$ values of −0.14 and −0.21 ppm were observed for H-3 and H-5 respectively. For these values the most probable position of the centre of the benzene ring of *p*NP is determined to be 1.3 ± 0.1 Å from the plane comprising the seven H-3 atoms and to be on the side of H-5, indicating that deeper penetration of the *p*NP molecule into the cavity is attained in β-CD than in α-CD. This result is consistent with the relative sizes of the cavities: the diameter of the cavity of β-CD is about 1 Å larger than that of α-CD. The K_d value found for the β-CD–*p*NP system at pH 10 and 27°C was 1.5×10^{-3} M, which is 2.5 times larger than that (6.1×10^{-4} M, as shown in Section 2.2) for the α-CD–*p*NP system under the same conditions,[61] indicating the latter complex is more stable. Thus the stability of the complexes cannot be related simply to the depth of *p*NP penetration into the CD cavity. A more intimate van der Waals interaction between α-CD and *p*NP may contribute to the stabilization of the inclusion complex between them. As shown here, precise geometrical data can provide a wealth of information on the mechanism of CD–guest complexation.

Deuterium solvent-induced isotope effects on ^{19}F NMR chemical shifts have been used for the estimation of binding constants as well as the relative geometrical orientation in inclusion complexes of CDs with fluorophenols, fluorobenzenes and fluorobenzoic acid derivatives.[66]

2.3.2. *Geometrical structures determined on the basis of ^{1}H homonuclear Overhauser effects*

In determining the geometrical relationship between the host CD and the guest in the inclusion complex, measurements of ^{1}H spectral enhancement due to the homonuclear Overhauser effect (NOE) are expected to be very useful.[67–70] In this case the origin of the NOE is a host–guest intermolecular dipole–dipole interaction. The magnitude of the ^{1}H homonuclear NOE enhancement is small (maximum 50%), and depends critically on the mutual motion and the distance between relevant protons.[71] In solution the guest molecule included in the CD cavity is not at rest, but is in fairly rapid motion, as shown below. Thus it is not easy to observe NOE enhancement.

Under conditions in which more than 99% of the guest *p*NP was complexed with the host α-CD in an aqueous solution at pD 10 and room temperature, a small but obvious NOE enhancement was observed only in the *meta*-proton resonance of *p*NP when the H-5 resonance of α-CD was selectively irradiated.[72] Selective irradiation of the H-3 resonance of α-CD enhanced both *meta* and *ortho* resonances simultaneously. The same results were obtained more elegantly from two-dimensional NOE correlated spectroscopy (NOESY).[73] In the NOESY spectrum of the α-CD–*p*NP system the cross-peaks connecting the H-3 resonance to both *meta* and *ortho*

proton resonances of *p*NP and the H-5 resonance to just the *meta* one were observed. These NOE results clearly indicate that the *p*NP molecule is preferentially inserted into the α-CD cavity as shown in Fig. 8, i.e. the geometry deduced from the NOE agrees well with that determined from ^{1}H chemical-shift data.

Under experimental conditions similar or identical to those used for the measurement of the NOESY spectrum of the α-CD–*p*NP system, no cross-peak due to an intermolecular NOE was observed for the 6-*O*-(α-D-glucopyranosyl)-α-cyclodextrin (branched α-CD or G_1-α-CD)[74,75]–*p*NP system,[76] although analysis of ^{1}H chemical-shift data based on the Johnson–Bovey theory clearly indicated that the *p*NP molecule is inserted into the cavity of G_1-α-CD with almost the same insertion depth as for α-CD.[77–79] Thus an alternative two-dimensional NOE method, namely ROESY, was applied to this system. Measurements of NOE enhancement by ROESY[34–37] are particularly useful for molecules with a motional correlation time τ_c near to or just satisfying the condition $\omega\tau_c = 1$, where ω is the angular Larmor frequency. This condition corresponds to a rather larger molecular system, in which the magnitude of conventional NOE enhancement is very small, but an NOE enhancement observed in a rotating frame is always positive and quite large. For the α-CD–*p*NP system a set of ROESY cross-peaks connecting the H-3 and H-5 resonances of α-CD to the *p*NP resonances is observed, and is essentially identical with the NOESY spectrum.[76]

In the G_1-α-CD–*p*NP complex the CD molecule is formed from at least three types of D-glucopyranose residues, namely one in the branch, one at the branching site on the CD macrocycle, and the other five macrocyclic residues, which exhibit different resonances from each other, making the one-dimensional ^{1}H NMR spectrum complicated. By using various two-dimensional NMR techniques as described in Section 2.1, it is possible to assign all resonances appearing in the 500 MHz ^{1}H NMR spectrum of the G_1-α-CD–*p*NP complex.[79] According to these assignments, in the corresponding ROESY spectrum the cross-peaks due to the CD–*p*NP intermolecular NOEs are observed between the H-3 resonances of the D-glucopyranose residues constituting the macrocyclic ring and both *meta* and *ortho* resonances of *p*NP, and between H-5 resonances of the same residues and only the *meta* resonance of *p*NP.[76] Therefore the host–guest geometry in the G_1-α-CD–*p*NP complex is similar to that in α-CD–*p*NP complex.

In the NOESY spectrum of a α-CD–*m*NP mixture at pH 10 and 30°C[73] there are weak but clear cross-peaks connecting the resonance of H-3 of α-CD to the resonances of two protons *ortho* to the nitro group of *m*NP. As no cross-peak connecting *m*NP resonances with the H-5 resonance of α-CD was observed, the *m*NP molecule might be incorporated into the cavity of α-CD from the nitro group. The insertion depth of *m*NP into the α-CD cavity is less than that of *p*NP—at least partly because of the steric interaction between the hydroxyl group of *m*NP and the same atoms on the

wider rim of the α-CD cavity. The NOESY results are consistent with the geometry determined by the X-ray method,[55] but not with that proposed on the basis of NMR chemical-shift studies in aqueous solution,[80] in which the *m*NP molecule is assumed to be inserted into the α-CD cavity from the hydroxyl group.

Enantioselective binding of (*R*)- and (*S*)-tryptophan (Trp) by α-CD was studied using ^{1}H and ^{13}C NMR.[81] An intermolecular NOE between guest Trp and α-CD indicates that the Trp indole ring is situated near the secondary hydroxyl rim of CD for both enantiomers, suggesting similar modes of binding, although the changes in chemical shifts, ^{1}H coupling constants and ^{1}H spin–lattice relaxation times indicate tighter binding of the *R* enantiomer. Similar NOE methods should be applicable to the determination of the geometry of any CD inclusion complex.

2.3.3. Conformational changes on complex formation

In induced-fit type models (see e.g. ref. 82) both the enzyme and substrate are assumed to adopt specific conformations when they form a so-called "enzyme–substrate complex". One of the most important properties of CDs is their enzyme-like function. Thus it is interesting to investigate the conformations of CDs and their changes on complexation. In general, the molecular conformation is reflected in NMR parameters such as chemical shifts and spin-coupling constants.

The values of vicinal spin-coupling constants among the protons of the α-D-glucopyranosyl residues constituting the macrocycles of CDs, as well as some derivatives such as methylated and acetylated CDs, are almost identical with those in the monomeric analogue of CDs, methyl-α-D-glucopyranoside,[57,83–88] indicating that the time-averaged conformations of the α-D-glucopyranosyl rings of CDs in solution are not so different from the most stable chair conformation $^{4}C_{1}$. The C_{1} chair is also a predominant conformation in the CDs and their inclusion complexes in the crystalline states,[51,55,65,89] although there are a few exceptions. In the crystalline inclusion complex of permethylated β-CD with *m*-iodophenol[89f] one α-D-glucopyranosyl residue takes an unusual skew-boat conformation, which may contribute to relief of the repulsive interaction between methyl groups.

The conformation of the macrocyclic ring of a CD is determined by two dihedral angles, i.e. ϕ and ψ, which define the conformation around the bond between C-1 and the glycosidic oxygen and the bond between C-4 and the glycosidic oxygen respectively. For steric reasons, the possible values of these angles are limited to rather narrow ranges. The macrocyclic conformations and thus those about the glycosidic linkage may be reflected mainly in the chemical shifts of C-1 and C-4. In solution conformation-dependent chemical shifts of C-1 and C-4 are more or less time-averaged owing to the presence of rapid interconversion on the NMR time scale among several

possible macrocyclic conformations of unmodified CDs. At pH about 7 the C-1 and C-4 nuclei of α-, β- and γ-CD show remarkable downfield shifts of around 2 and 3–4 ppm respectively compared with amylose,[91,92] although the ^{13}C chemical-shift values of other carbon nuclei of CDs are almost the same with those of amylose. The results indicate the presence of some steric effects of the CD macrocycle on the chemical shifts of carbon atoms participating in the glycosidic linkage. As the ^{1}H and ^{13}C chemical shifts of CDs are delicately affected by the included guests, and because of the averaging effect of rapid interconversion of the macrocyclic ring in solution, it is difficult to estimate quantitatively the conformational change of the CD macrocycle upon complexation with guests on the basis of chemical-shift changes.

The highly symmetrical circular conformation of the macrocyclic ring of CDs is stabilized by the formation of intramolecular O-2---O-3 hydrogen bonds between adjacent α-D-glucopyranosyl residues.[3–5,23,24] The formation of the hydrogen bonds is demonstrated by ^{1}H NMR observation of hydrogen–deuterium exchange in dimethylsulphoxide.[90] The C-2 and C-3 hydroxyl groups in α- and β-CD are more resistant to hydrogen exchange than those in amylose. The temperature dependence of ^{1}H chemical shifts[93–95] and spin-coupling constants[94,95] reveal not only the existence of the intramolecular hydrogen bond between the secondary hydroxyl groups but also the fact that the C-3 hydroxyl is the dominant proton donor for this hydrogen bond in α- and β-CD, and 2,6-di-*O*-methyl-α- and -β-CD. Studies of the ^{2}H isotope effect on ^{1}H and ^{13}C chemical shifts also indicate that the C-3 hydroxyl is the dominant proton donor in α- and β-CD.[96,97]

The conformation about the C-5—C-6 bond of a pyranose is ordinarily analysed in terms of the fractional contributions from the three staggered, i.e. *gauche–gauche* (*gg*), *gauche–trans* (*gt*), and *trans–gauche* (*tg*) conformers. Here *gauche* and *trans* indicate the orientations of the two C-6—H-6 bonds with respect to the C-5—H-5 bond. The time-averaged fractions of these conformers can be estimated from the two observed spin-coupling constants between the H-5 and the two H-6 protons.[98] The magnitudes of these constants for α-CD are distinctively lower than those for the monomer methyl-α-D-glucopyranoside, but their values indicate that the preferred conformer in α-CD as well as in the monomer analogue is the *gg* one.[57] The trends in the C-5—C-6 bond in α-CD do not show any large change on the inclusion of aromatic guests.[57]

Observation of ^{1}H NOE enhancement can also give information on conformations, including that of the C-5—C-6 bond, in CDs. In the case of branched CDs determination of the orientation of the branch is important for understanding the influence of the branch on the ability of the CD to form inclusion complexes. The ^{1}H ROESY spectrum of f-L-Phe-β-CD, whose chemical structure and normal ^{1}H NMR spectrum are shown in Figs 3 and 2 respectively, exhibits NOE cross-peaks between the resonances of the

side-chain phenyl protons and those of H-3 and H-5 of several D-glucopyranosyl residues, clearly indicating that the side-chain Phe phenyl group is inserted into the β-CD cavity from the primary-hydroxyl group side of the CD macrocyclic ring.[30] The chemical-shift values of the H-3 and H-5 resonances also indicate the self-inclusion of the Phe phenyl group into the CD cavity. The orientation of the Phe group should contribute to the potential for chiral recognition of f-L-Phe-β-CD.[99]

In the cases of branched CDs, i.e. G_1-α-CD[76] and 6-*O*-(α-maltosyl)-α- and β-CDs[100] in the free states as well as in the complexed states with the guest *p*NP, ^{1}H ROESY spectra indicate that the glucopyranosyl and maltosyl branches orient not towards the entrance of the CD cavity but to the aqueous surroundings. This preferential orientation of the branches explains well the experimental observation that these branches improve the solubility of the CD molecules in water without significant modification of their ability to form inclusion complexes or of the geometrical structure of these complexes.[76,78,79,100] The ROESY result concerning the preferential orientation of the glucosyl branch of G_1-α-CD is consistent with the orientation found in the G_1-α-CD · $8H_2O$ crystal by X-ray analysis.[101]

On complexation with CDs, a conformational change is also induced in a guest molecule. According to analysis of ^{1}H spin-coupling constants, the populations for the side-chain conformers around the α-methine–β-methylene bond of the amino acids phenylalanine (Phe) and tyrosine as well as those of Phe residue of Phe-containing dipeptides change upon formation of CD inclusion complexes, in which the aromatic group is included in the CD cavity.[102–104] The conformational change depends on the cavity size of the CD and also on the amino acid sequence of the dipeptide. These results can be explained using space-filling molecular models. The conformational change was found to occur for the Phe side chain of the sweetener aspartame (*N*-L-aspartyl-L-phenylalanine methyl ester) on the formation of a complex with β-CD, although its main chain conformation was suggested to be unchanged.[105]

2.4. Molecular dynamics of cyclodextrin inclusion complexes in solution

The strength of the host–guest dynamic coupling is one of the most important properties involved in inclusion phenomena. Important information on the mechanism of the molecular inclusion process can be obtained by studying the molecular dynamics of the host and the guest. Host–guest complexation in solution leads to alterations in the dynamic properties of both components. The strength of the host–guest dynamic coupling can be directly related to the stability of the host–guest complex in solution as well as to the host-mediated reaction of the guest. The host–guest dynamic

coupling can be estimated from analyses of the molecular motion of both host and guest by using the spin–lattice relaxation time T_1.

First, the physical meaning of ^{13}C T_1 in the CD–guest complexation system will be discussed briefly, since measurements of ^{13}C T_1 values are common and are useful in the study of CD–guest dynamic coupling. As stated in Section 2.2, if the CD–guest complexation reaction

$$\text{free-CD} + \text{free-guest} \rightleftarrows \text{CD–guest complex} \tag{2}$$

is assumed to be rapid on the NMR time scale, only an average relaxation rate is observed as follows:[106]

$$\frac{1}{T_1} = p_f \frac{1}{T_{1f}} + p_c \frac{1}{T_{1c}}, \tag{3}$$

where T_{1f} and T_{1c} are the intramolecular spin–lattice relaxation times for a spin in the free and complexed states, and p_f and p_c $(=1-p_f)$ are the fractional probabilities that CD (or guest) is found in the free and complexed states respectively. The values of p_f and p_c can be estimated from the association constant and the molar concentration of CD and guest.

For molecules of medium size whose motion is rapid enough on the ^{13}C NMR time scale, it is reasonably assumed that the ^{13}C T_1 value of the carbon nucleus directly linked to at least one proton is governed by ^{13}C–^{1}H dipole–dipole relaxation brought about by rotational motion.[107] In this case the ^{13}C T_1 of a nucleus undergoing isotropic reorientational motion is given by

$$\frac{1}{NT_1} = \hbar^2 \gamma_C^2 \gamma_H^2 r_{CH}^{-6} \tau_{eff}, \tag{4}$$

where τ_{eff} is the effective correlation time for overall molecular reorientation, r_{CH} is the carbon–hydrogen bond length, γ_H and γ_C are the gyromagnetic ratios of the ^{1}H and ^{13}C nuclei, and N is the number of protons directly bonded to the ^{13}C nucleus of interest. According to the Brownian diffusion mode,[108–110] τ_{eff} is related to the rotational diffusion constant D as follows:

$$\tau_{eff} = \frac{1}{6D} = \frac{8\pi\eta f_r r_0^3}{6kT} = \frac{V_m \eta f_r}{kT}, \tag{5}$$

where k is Boltzmann's constant, T is the absolute temperature, η is the viscosity of the solution, f_r is a microviscosity factor, r_0 is the radius of a

spherical molecule and $V_m = \frac{4}{3}\pi r_0^3$ is the molecular volume. Thus the relationship between T_1 and molecular volume is

$$\frac{1}{NT_1} = \frac{\hbar^2 \gamma_C^2 \gamma_H^2 \gamma_{CH}^{-6} \eta f_r V_m}{kT} \tag{6}$$

From these equations, the dynamic aspects of CD–guest complexation can be explained. In the limit of strong dynamic coupling both the CD and the guest molecules behave as if they belong to the same molecule, with a volume that is, however, not the simple sum of those of CD and guest. As a result, the protonated ^{13}Cs of both the CD and the guest have the same NT_1 value, if there is no local motion other than the overall molecular motion. If the dynamic coupling is weak, CD and guest molecules should have different NT_1 values. In general, the molecular volume or mass of the guest compound is somewhat smaller than that of the host CD. Therefore, upon formation of an inclusion complex, the ^{13}C NT_1 values of the former should show a greater decrease than those of the latter.

On the basis of ^{13}C T_1 measurements, molecular dynamics have been studied for the inclusion complexes of CDs[63,103,111,112] and permethylated CDs[104] with some aromatic amino acids and phenylalanine-containing dipeptides in aqueous solution. The observed NT_1 values of the ring carbons of CD in the free state are reproduced well by (6) and by assuming that α-CD is spherical.[63] Further, the observed T_1 values of some carbon atoms of the guests in the free state agree well with those calculated using (6) with the van der Waals volume.[63] Thus (4) and (6), derived for a molecule undergoing isotropic motion, are a good approximation for the analysis of the dynamics of CD complexation systems. In general, the viscosity of an aqueous solution of the guest changes significantly on the addition of a CD, and the T_1 value corrected for the viscosity change, i.e. ηNT_1, must be used when the T_1 value in the free state is compared with that in the complexed state.[111] For all CD–guest systems studied the ^{13}C NT_1 values of 100% complexed CDs are markedly less than those of 100% complexed guests, indicating the CD–guest dynamic coupling in these systems is rather weak and that motion of the guest molecule in the CD cavity is possible.

In the CD–Phe systems the ηNT_1 values decrease greatly on complexation with CDs, while those for the CDs decrease slightly or remain unchanged. The complexation-induced decrease in NT_1 can be explained in terms of a complexation-induced increase in apparent molecular volume, as expected from (6). Since the molecular volumes of α-, β- and γ-CD are more than six times larger than that of Phe, the change in molecular dimension induced by complexation is relatively small for CDs and relatively large for Phe.

The extent of complexation-induced reduction of ηNT_1 is not the same for all protonated carbons of Phe, but is noticeably larger in the phenyl-ring

carbons,[63,111] indicating the greater slowing down of the internal rotation of the phenyl ring than that of the overall reorientation. This result indicates the formation of the CD–Phe inclusion complex by insertion of the Phe phenyl ring into the CD cavity. Among the three CDs, β-CD gives the largest complexation-induced reduction of NT_1 of Phe phenyl carbons. On the other hand, α- and γ-CD induce only modest decreases. These results can be explained in terms of cavity-size effects on the dynamic coupling by using space-filling molecular models. The Phe phenyl ring is deeply and tightly included into the β-CD cavity, and the strongest dynamic coupling is observed for this system. The inclusion of the phenyl ring is shallower and looser in the case of α-CD, while it is deep but loose in the case of γ-CD.[111]

In the cases of CD complexes with Phe-containing dipeptides, the dynamic coupling depends on the types of amino acid residue adjoining the Phe residue and on their sequence,[63,103] and permethylation reduces the dynamic coupling owing to widening of the hydrophobic region of the CD cavity.[104] The difference in the binding strength of *R* and *S* enantiomers of tryptophan to α-CD has been studied by measurement of $^{13}C\ T_1$.[81]

Molecular motions in the α-CD inclusion complexes formed with *p*- and *m*-methylcinnamate and with *p*-(t-butyl)phenolate anions have been investigated by observing ^2H quadrupolar relaxation times and $^{13}C\ T_1$.[113] Upon inclusion, the reorientation times of these guests increase, and the overall tumbling motion of α-CD shows a guest-dependent increase. None of the guests investigated was tightly bound to α-CD from the dynamic point of view. The dynamic coupling between the sodium salts of *p*-nitrophenolate and 2,6-methyl-4-nitrophenolate as guests and the host α-CD has also been estimated based on the $^{13}C\ T_1$.[69] The $^{13}C\ T_1$ data combined with the geometry of the respective complexes determined by ^1H intermolecular NOE suggest that the α-CD-catalysed hydrolyses of *m*- and *p*-nitrophenyl acetate proceed by different mechanisms.

Based on ^{13}C NMR spin–lattice relaxation as well as on ^{13}C NMR chemical shifts, the CD inclusion mode and strength of dynamic coupling have been studied for a variety of drug molecules, which are known to be stabilized or endowed with enhanced water solubility on complexation with CDs. Only some examples are given here. Since sulphur-containing drugs such as phenothiazine and thiobarbiturate show large binding constants to β-CD,[114,115] $^{13}C\ T_1$ has been measured for the inclusion complex of β-CD with sulphathiazole in aqueous solution.[116] Data on $^{13}C\ T_1$ as well as ^{13}C shifts indicate that the driving force leading sulphathiazole–β-CD complexation is mainly a hydrophobic interaction. Prostaglandins (PGs) are a series of polyunsaturated fatty acids containing one five-membered ring and two side chains. Some PGs are solubilized by forming inclusion complexes with α- and β-CD,[117] but the binding mode is different for α- and β-CD. According to $^{13}C\ T_1$ data, the alkyl portion of the PGF_2 side chain is predominantly included in the α-CD cavity, in contrast to the β-CD case, where the

five-membered ring system is included. The substituted five-membered ring of PGF_2 may be too large to be fully inserted into the cavity.

These results indicate that descriptions by not only thermodynamic stability and association–dissociation kinetics but also by dynamic coupling are indispensable for the characterization of the CD inclusion phenomena.

2.5. Solid-state inclusion complexes of cyclodextrins

2.5.1. Solid-state structure of cyclodextrin complexes

As cyclodextrins are often utilized in many fields such as drugs, foods and so on in the form of solids, the characterization of solid-state CDs and their inclusion complexes is very important. High-resolution cross-polarization magic-angle sample spinning (CP/MAS) ^{13}C NMR[119–123] is an especially useful method for this. Detailed information on the solid-state structure of CD inclusion complexes can be obtained by X-ray analysis of single crystals. However, for cases where there is difficulty in obtaining single crystals of a CD complex, and X-ray analysis is therefore not applicable, CP/MAS ^{13}C NMR is indispensable for the characterization of the solid-state complex.

When X-ray data are available for the crystals of a CD inclusion complex, it is possible to establish more definite relationships between NMR chemical shifts and structure, in a particular conformation, than those obtainable for solution states. In the latter only information on average conformations are obtained from NMR data because of rapid interconversion among different conformers, as shown in Section 2.2. In contrast, in the solid state the conformational states are fixed, or at least the rate of interconversion among different conformers is effectively slowed down, allowing observations of NMR spectra of the respective conformational states.

As discussed in Section 2.3.3, the conformation of the CD macrocyclic ring, namely that about the glycosidic linkage in the solid state, may also be reflected in the ^{13}C chemical shifts of the C-1 and C-4 carbons.[56,124–127] This expectation is supported, for example, by the following observations. In a crystal of the α-CD–*m*-nitrophenol complex the dihedral angles defining the rotational state about the glycosidic linkage are distributed in a very narrow range;[55] for example, the six values of ϕ_1 (the torsion angle O5–C1–O4–C4) are 107.2° (two residues), 111.5° (two residues) and 113.1° (two residues), and the C-1 and C-4 ^{13}C resonances appear as sharp singlets.[56] In contrast, those angles are very widely distributed in the α-CD·H_2O crystal;[128] for example, the six values of the angle ϕ_1 are 88.2°, 90.4°, 100.7°, 104.8°, 107.5° and 112.8°, and the corresponding ^{13}C shifts of the C-1 and C-4 resonances are widely dispersed.[56] In spite of these experimental observations,

^{13}C NMR chemical shifts of the C-1 and C-4 resonances of CDs cannot be simply related to the dihedral angles at the glycosidic linkages, although rather simple correlations between the dihedral angles ϕ and ψ about the glycosidic linkage and the ^{13}C shifts of the C-1 and C-4 resonances have been proposed for cellulose and related carbohydrates[129] and for several oligosaccharides having an α-D-glucopyranosyl or α-D-galactopyranosyl unit at the nonreducing end of the molecule.[130]

It is well known that ^{13}C NMR chemical shifts are strongly affected by through-space steric perturbations.[131–134] The magnitude of the ^{13}C shift dispersions of the C-1 and C-4 resonances observed for some α-CD complexes can be qualitatively reproduced by an approximate calculation on the basis of a steric hindrance model of ^{13}C shifts[131–133] and by using X-ray crystallographic data, where only the glycosidic-linkage conformation-dependent, nearby nonbonded hydrogen–hydrogen steric repulsion is taken into account.[56] To explain the observed ^{13}C dispersion more quantitatively, all possible intra- and inter-molecular shielding effects must be taken into account. For a range of polymeric and oligomeric α-(1→4)-glucans, including α- and β-CD, rather good correlations are found between C-1 chemical shifts and the sum of the moduli of the two torsion angles (ϕ, ψ).[127] The sum of the moduli of torsion angles represents the extent of noncoplanarity of H-1, C-1, O-1, C-4′ and H-4′.

The C-6 resonance of CDs also shows almost the same magnitude of ^{13}C shift dispersion as found for the C-1 and C-4 resonances. The correlations between the ^{13}C chemical shifts of the C-6 resonance and the orientations of the hydroxymethyl groups with respect to the C-5—O-5 and C-5—C-4 bonds have also been investigated for CDs and related carbohydrates,[56,124–126] and qualitative correlations have been proposed.

It is very interesting to note that in several instances of α-CD[56,127] and β-CD[127] complexes the weight-averaged ^{13}C shifts for the multiplets of C-1, C-4 and C-6 resonances observed in the solid state are in good agreement with the ^{13}C shifts of the corresponding carbons observed in aqueous solution, within a reasonable experimental error of ±0.5 ppm. These similarities suggest that the time-averaged conformations of the glycosidic linkage as well as those of the C-5-hydroxymethyl linkage in solution are quite similar to the corresponding conformations obtained by weight-averaging the conformations of respective linkages in the solid state. In aqueous solution a linear relationship is found between the ^{13}C shifts induced in the C-1 resonance of α-CD by complexation and the thermodynamic parameters for the formation of α-CD inclusion complexes.[53] Thus those thermodynamic parameters can be correlated with the change in average conformation of glycosidic linkages upon complexation, which is reflected as a ^{13}C shift change of the C-1 resonance. No correlation was found between the observed complexation-induced ^{13}C shifts of the C-4 resonance and the thermodynamic parameters,[53] although C-4 and C-1 are

both involved in the glycosidic linkage, and the ^{13}C shifts of both are sensitive to its conformational change.

On the basis of ^{13}C chemical-shift changes induced for guest compounds by complexation with CDs, the geometrical structure has been investigated for some CD–guest complexes in the solid state for which no X-ray crystallographic data are available; examples include β-CD–tolubutamide,[135] γ-CD–prostaglandin F_2[136] and β-CD–*p*-nitrophenol.[137]

Benzaldehyde is used as an anticancer agent[138] in the form of inclusion complexes with α-, β- and γ-CD.[139] The stability of benzaldehyde to reaction with oxygen is improved by complexation with β-CD.[140] The ^{13}C chemical shifts for benzaldehyde resonances in the solid-state α-CD–benzaldehyde complex[141] agree well with the corresponding shifts for that in chloroform solution,[142] indicating that the benzaldehyde molecule in the α-CD complex is subjected to a low-polarity environmental effect similar to that in chloroform solution, and the steric perturbation of the included guest benzaldehyde molecule by the host CD cavity may be small. According to the X-ray crystallographic analysis, in the α-CD complex the benzene ring of benzaldehyde is located at the centre of the α-CD cavity, and its carbonyl group protrudes from the O-2,3 side of the latter and is in van der Waals contact with the primary hydroxyl side of the next α-CD molecule.[143] In the hexakis(2,3,6-tri-*O*-methyl)-α-CD (α-TMCD) complex the benzaldehyde molecule is included in the reverse fashion, and its carbonyl group is located at the centre of the cavity.[144] The trends of ^{13}C shift changes induced for some carbons of benzaldehyde by complexation with α-CD are quite different from those induced by α-TMCD,[141] reflecting the difference in binding mode. No crystallographic data have been reported for the β-CD–benzaldehyde complex. In this complex the ^{13}C shifts of the same carbon resonances are quite similar to those in the α-CD complex, but not to those in the α-TMCD complex,[141] suggesting that in the solid state benzaldehyde is included in the β-CD cavity in the same fashion as for α-CD. Thus the isotropic ^{13}C shifts of the guests observed by high-resolution NMR can provide information on the guest–host geometry of solid-state CD inclusion complexes.

2.5.2. *Molecular dynamics of cyclodextrin inclusion complexes in the solid state*

Similarly to the case of the solution state, the strength of the host–guest dynamic coupling in the solid state is directly related to the stability of the solid-state host–guest complexes. The rigidity of a guest molecule in a crystalline CD complex is not always reflected to the binding equilibrium constant between the host CD and the guest observed in aqueous solution.[145] The strength of the host–guest dynamic coupling in the solid state is also related to chiral molecular recognition as well as to the host

CD-mediated stereospecific reaction of the included guest molecules.[24] A variety of highly enantioselective reactions can be achieved when the reactants are rigidly held as guests in the chiral environments produced by the cavities of crystalline CDs.[145–150] The enantioselectivity is decreased if the reactant molecule is allowed to rotate in the CD cavity, even when the reaction is carried out in the crystalline CD complexes. Hence information on molecular dynamics is important when considering inclusion phenomena of CDs in the solid state.

In many cases ^{13}C NMR signals of guest molecules in the solid-state CD inclusion complexes observed by the high-resolution CP/MAS mode are partly or fully lost or show marked line-broadening, while CD molecules in solid-state complexes as well as the crystalline guest molecules alone show clear, well-resolved ^{13}C CP/MAS resonances.[125,135–137,151] In general, the peak intensity of a guest molecule is weak compared with that of the CD, because of the lower number of guest molecules relative to the number of CD glucopyranosyl residues (e. g., for a 1:1 α-CD–guest complex there are six glucopyranosyl residues per guest molecule). However, this cannot fully explain the intensity loss selectively observed for the resonance of guests. The resonances of all protonated carbons of *p*-nitrophenol (*p*NP) and *p*-hydroxybenzoic acid are broadened and virtually disappear from the ^{13}C CP/MAS NMR spectra of solid-state 1:1 α-CD–guest complexes observed at 50 MHz.[137,151,152] Similar selective line-broadening is observed for the resonances of protonated carbons of *m*NP,[56] benzoic acid[56] and *p*-iodoaniline[153] included in solid-state complexes with α-CD. In the case of the solid α-CD–*m*NP complex there are two types of *m*NP molecules per α-CD, as described in Section 2.2: one is included in the α-CD cavity and shows a set of broader ^{13}C resonances, while the other is outside the cavity and shows narrower resonances.[56]

There are many possible mechanisms inducing line-broadening of solid-state ^{13}C NMR resonances, such as inappropriate setting of CP/MAS experimental conditions,[154] chemical-shift dispersion[154] and molecular motion.[154–157] The most plausible reason is the unfavourable effect of molecular motion of the guest on the efficiency of the high-power proton dipolar-decoupling process usually used to observe ^{13}C CP/MAS NMR spectra.[157] According to the theory of spin–spin relaxation time (the inverse of the linewidth) for a ^{13}C spin dipolar-coupled to a proton spin under conditions of random rotational motion and ^{1}H-spin radiofrequency decoupling,[157] when the correlation time of the molecular motion, τ_c, is equal or nearly equal to the reciprocal of the frequency of the ^{1}H decoupling field, $1/\omega$, the maximum line-broadening is induced for a resonance of this ^{13}C spin. In the long-correlation limit, where $\omega\tau_c \gg 1$, the linewidth is narrowed with increasing τ_c by the efficient ^{13}C–^{1}H dipolar decoupling. Also, in the short-correlation limit, i.e. $\omega\tau_c \ll 1$, the linewidth is narrowed by the rapid motional averaging. Owing to the dependence of linewidth on r^{-6},

where r is the internuclear ^{13}C–^{1}H distance, the motional modulation is more significant for the resonance of a carbon directly bonded to a proton (or protons). Thus a selective reduction in peak intensity of the protonated carbons of guest-substituted benzene compounds upon complexation with α-CD should arise from their restricted motion with a rate close or equal to the nutation rate of the proton-decoupling field, i.e. corresponding to the correlation time for the motion $\tau_c \sim 10^{-5}$ s.[153]

The *p*NP molecule included in the cavity of solid-state β-CD and permethylated α-CD (α-TMCD) also undergoes molecular motion,[153] the rate of which depends on the cavity size. For these systems the following observations indicate the presence of rapid molecular motion: the peak splittings due to the nonequivalence of the two carbons *meta* to the NO_2-substituted carbon and due to the ^{14}N–^{13}C dipolar coupling (which cannot be completely suppressed by MAS[158,159]) and the spinning side bands appear in the ^{13}C CP/MAS spectrum of free *p*NP in the crystalline state, but they disappear and the *p*NP peaks become sharp with higher signal-to-noise ratio upon complexation with CDs.

The most direct evidence for the presence of molecular motion of the guests included in the CD cavity is obtained by observing ^{13}C CP/MAS NMR dipolar dephasing spectra using a delay-without-decoupling pulse sequence.[160] In this experiment a delay time as a dipolar-dephasing period, during which the ^{1}H decoupling field is removed and ^{13}C resonances are attenuated, is inserted just before detection of the ^{13}C free-induction decay. The attenuation rate depends on the strength of the ^{13}C–^{1}H dipolar interaction, and the presence of faster molecular motion usually weakens the ^{13}C–^{1}H interaction more significantly and results in a slower attenuation rate. According to dipolar dephasing experiments for solid-state β-CD and α-TMCD complexes with *p*NP,[153] all resonances of protonated carbons of β-CD and α-TMCD, except for the methyl resonances of α-TMCD, practically disappear from the spectra after a relatively short delay time, which is a typical dephasing period for almost total elimination of the methine and methylene resonances from the ^{13}C spectra of ordinary, rigid solid-state compounds,[160] while the resonances of the protonated carbons of *p*NP as well as those of the methyl carbons of α-TMCD remain even after longer dephasing periods. These results indicate that the CD macrocyclic rings and the side-chain methylene groups of β-CD and α-TMCD are almost rigid, while the *p*NP molecules undergo molecular motion in these CD cavities. The methyl groups of α-TMCD also undergo rapid internal rotation, even in the solid state. From the linewidth and the rate of dipolar dephasing, the *p*NP molecule in the β-CD cavity is found to undergo motion more rapidly than in that of α-TMCD.

The linewidths in the solid-state ^{13}C CP/MAS spectra of the crystal inclusion complex of the dipeptide sweetener aspartame (*N*-L-aspartyl-L-phenylalanine methyl ester) with β-CD indicate that the guest phenyl ring, which is included in the cavity of β-CD, rotates rapidly.[161]

Molecular dynamics and the host–guest molecular interactions were studied for the β-CD inclusion complexes of *m*- and *p*-aminobenzonitrile and adamantane-1-carbonitrile by solid-state ^{13}C CP/MAS NMR spectroscopy.[162] All the complexes have a molecular ratio of 1:1. The results of lineshape analysis suggest that the included guest *m*-aminobenzonitrile molecule is almost static in the host β-CD, the shape of which deviates considerably from sevenfold symmetry, while the other two guests rotate anisotropically in the β-CD cavity. The results for the three complex systems suggest that the smaller the deviation from the C_7 symmetry of the β-CD cavity, the greater is the mobility of the guest molecule.

The mobility of guest benzaldehyde included in the solid-state complexes with α-CD,[141,163,164] β-CD[141,163,164] and γ-CD[164] has been studied by ^{13}C CP/MAS NMR. The effects of complexation with CDs of different cavity size on the mobility of the guest have been analysed in terms of lineshape,[141] temperature effect and dipolar dephasing,[163] ^{13}C spin–lattice relaxation, ^{1}H spin–lattice relaxation in the rotating frame, and cross-polarization transfer.[164] The relaxation values suggest that correlation times for the guest motion should be in the 0.1–5 ms region, depending on the CD cavity size.[164]

Using ^{2}H quadrupolar solid echo NMR as well as ^{13}C CP/MAS NMR methods, molecular motion has been studied for a variety of organic molecules, such as benzene, toluene, biphenyl, dimethylsulphoxide, and some of their partially or fully deuterated derivatives, encaged in the cavities of α- and β-CD, heptakis(2,6-di-*O*-methyl)-β-CD and β-CD peracetate.[165,166] Both ^{2}H and ^{13}C data, particularly the former, can give the detailed information on the mode of molecular motion of the guest molecule within the cavity of the host. For example, the magnitude of ^{2}H quadrupole splitting clearly indicates that the benzene-d_6 molecule rotates rapidly about the sixfold axis and that the axis itself undergoes additional angular fluctuations in the cavity of heptakis(2,6-di-*O*-methyl)-β-CD.[165] It is shown that the motion of the smaller guests in the host CD cavity is least affected by the cavity size.[166] The temperature dependence of the molecular mobility of the guest molecule in the CD cavity has been also investigated, based on ^{2}H quadrupolar echo spectra.[165,166]

The degree and time scales of dynamic disorder processes of the hydrate and included molecules have been also studied based on ^{2}H NMR for powder and single-crystal samples of β- and γ-CD,[167] and the results have been compared with the structures obtained by X-ray and neutron diffraction.[168–170] At and above room temperature, the hydrate, sugar hydroxyl groups and included molecules (benzyl or ethyl alcohol) are found to be dynamically disordered to varying degrees, with reorientational rates that are fast on the ^{2}H NMR time scale, i.e. more than $10^6\ s^{-1}$.[167] The ^{2}H NMR data also indicate that the lattice water moves freely among the hydration sites of β- and γ-CD in a time less than 10^{-6} s.

By measuring the ^{13}C chemical-shift powder patterns using one-dimen-

sional SASS (switching-angle sample spinning[171,172]) NMR, location and molecular dynamics have been studied for the ferrocene molecule included in the β-CD cavity in the solid state.[173] The SASS spectrum indicates that in the unit cell of the inclusion complex the ferrocene molecule can be located at three inequivalent sites, with population ratios 0.42:0.32:0.26, and at each site the ferrocene molecule undergoes precessional motion with different amplitudes. The ^{13}C CP/MAS NMR spectrum cannot provide such information because of severe overlapping of the ferrocene resonances.

3. THEORETICAL STUDY OF CYCLODEXTRIN INCLUSION COMPLEXES ON THE BASIS OF NMR CHEMICAL SHIFTS

3.1. Geometry of cyclodextrin inclusion complexes determined by the quantum chemical analysis of complexation-induced ^{13}C chemical-shift changes in guest compounds

It is well known that NMR chemical shifts of organic molecules are sensitive not only to their chemical and stereochemical structure but also to the environment surrounding them. In the case of NMR chemical shifts such environmental effects can be treated as shielding effects of solvents, and are simply known as solvent effects.[174–176] The solvent effects on solute molecules may be classified into specific and nonspecific ones;[177] the former include hydrogen bonding, protonation, molecular association and ionic interactions, and the latter can arise from van der Waals effects, neighbour anisotropic susceptibility and electric field effects. Essentially, the non-specific effects are produced by electronic interactions between the dipole moments of the solute and solvent molecules.[176,177] The chemical-shift variations observed for the solute in different solvents reflect the physical nature of the latter. Thus NMR chemical shifts are sensitive indicators of the nature of molecular surroundings. Several theoretical explanations of the solvent effects on the NMR chemical shifts of solute molecules have been proposed.[174–177] Theoretical analysis of the solvent-induced chemical-shift changes observed for the solute (here the guest molecule) should provide insight into the nature of the solvent (here the cavity of the cyclodextrin).

^{13}C NMR studies of α-CD inclusion complexes with benzoic acid (BA), *p*-nitrophenol (*p*NP) and *p*-nitrophenolate in aqueous solution have shown that the included lead (or head—Fig. 9A) carbons are largely shielded (corresponding to a high-field shift) compared with the deshielding (low-field shift) of the corresponding *para* (or tail—Fig. 9A) carbons.[68,178] The directions of the BA carboxyl and *p*NP nitro groups in the α-CD cavity have been clearly demonstrated by ^{1}H NOE experiments,[68,72,73,76,178] as shown in Section 2.3.2. Similar contrasting ^{13}C shift changes have been also observed for the head and tail carbons of *p*-hydroxybenzoic acid (*p*HBA), and it has

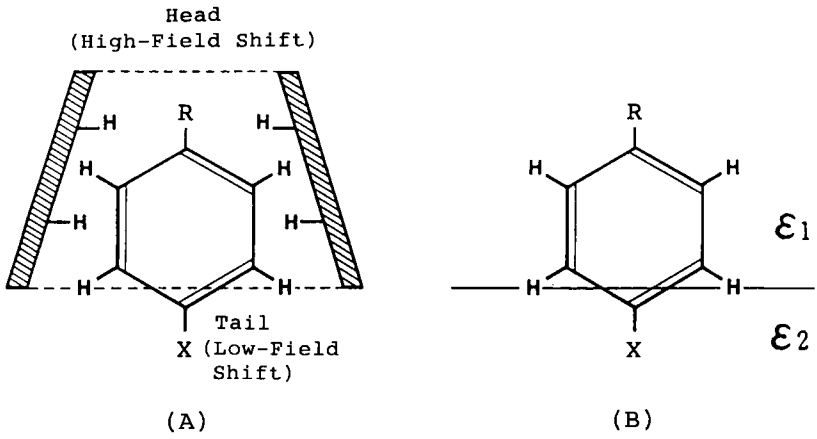

Fig. 9. (A) Geometry of α-CD (shaded) inclusion complexes with guest benzene derivatives. (B) Double-layer model used for explaining guest ^{13}C NMR chemical-shift changes induced by complexation with α-CD.

been concluded that the *p*HBA carboxyl group is directed into the α-CD cavity.[53] Many kinds of substituted benzenes are known to show quite similar ^{13}C high-field (head) and low-field (tail) shifts upon inclusion into the α-CD cavity.[53,60] These peculiar shifts are induced by transfer of the guest molecule from the free state, surrounded by water molecules, to the α-CD cavity. Hence, among several kinds of nonbonded interactions that could influence the ^{13}C chemical shifts, the electrical environmental effects should be the main contributor to the α-CD complexation-induced ^{13}C displacements of leading head and tail carbons of the guest molecules. Different trends have been observed for ^{13}C displacements of the guest molecules in high-resolution solid-state ^{13}C NMR spectra of the corresponding α-CD inclusion complexes.[137] In the solid state the α-CD complexation-induced shifts are caused by transfer of the guest from the free state, surrounded by the same molecules, to the CD cavity.

The fact that upon forming inclusion complexes in aqueous solution with α-CD some aromatic compounds such as *p*-(t-butyl)phenol[179] show UV spectral changes almost identical with that observed when the compounds are moved from aqueous to dioxane solution strongly suggests that the aforementioned peculiar ^{13}C shift changes of the substituted benzene guests induced by complexation with α-CD should arise from the change in environment from a highly polar one (water, with dielectric constant $\varepsilon = 80$) to a more apolar one (dioxane, with $\varepsilon = 2$).

By using the CNDO/2 quantum chemical method for the calculation of ^{13}C chemical shifts[180,181] combined with a model of the solvent effect on ^{13}C

chemical shifts[176,177] based on solvation theory,[182] the chemical-shift difference $\Delta\delta = \delta_2 - \delta_{80}$, was calculated for BA, *p*NP and *p*HBA,[183] where δ_2 and δ_{80} are the chemical shifts in media with $\varepsilon = 2$ and 80 respectively. The surroundings are assumed to be homogeneous continuum dielectrics. This combined CNDO/2–solvation method has been applied successfully to interpret the dielectric solvent effect on ^{13}C chemical shifts of many kinds of organic compounds,[176,177] including conjugated polyenes.[184] While this continuum solvent-effect model can reproduce well the gross trends of the solvent-dependent ^{13}C shifts of free BA, *p*NP and *p*HBA in a variety of solvents with ε values from about 2 to 50, it can only partly reproduce the peculiar ^{13}C shift changes of the head and tail carbons of guests. This may be due to the disregard of the actual geometry of the inclusion complexes. As shown in Section 2.3.1, part of a *para*-substituted phenol molecule complexed with α-CD is exposed to the aqueous medium. That is, the guest molecule is not surrounded by a homogeneous dielectric. By taking this into account, a more realistic model has been constructed in which the included part of the guest molecule is subjected to the more apolar environmental effect of $\varepsilon_1 = 2$ while its other part is exposed to the aqueous phase with $\varepsilon_2 = 80$. The observed peculiar ^{13}C shift changes of the head and tail carbons of three guests in α-CD complex systems have been reproduced satisfactorily by this heterogeneous model when the surroundings are divided into two regions with $\varepsilon_1 = 2$ and $\varepsilon_2 = 80$, as shown in Fig. 9(b). This position of the borderline should correspond to the wider rims of α-CD consisting of secondary hydroxyl groups. Thus theoretical calculations of environment-induced ^{13}C shifts provide the geometries of α-CD inclusion complexes in aqueous solution consistent with those found by NMR, as shown in Section 2.3. The peculiar ^{13}C shift changes observed for BA and *p*HBA induced by complexation with α-CD are quantitatively well reproduced by a more general and more exact theory of the medium effect,[185] which is applicable in estimating the electronic structure of a solute molecule surrounded by a multidielectric system with arbitrarily shaped boundaries.[186,187]

The geometry of the α-CD-*m*-nitrophenol (*m*NP) complex in aqueous solution has been investigated by comparing the α-CD complexation-induced ^{13}C chemical shifts with those predicted by the combined CNDO/2–solvation model.[54] As described in Section 2.3.2, two types of host–guest geometry have been proposed for the α-CD–*m*NP system. The first assumes that the nitrophenyl group is located in the α-CD cavity and the hydroxyl group is exposed to the aqueous medium,[53] while the second assumes the insertion of the hydroxyphenyl group.[80] The theoretical results indicate that the first geometry is more realistic, being consistent with the geometry determined by NOESY in aqueous solution[73] and with that by the X-ray method in the crystalline state.[55]

The theoretical results not only support the empirical expectation that the

α-CD cavity exerts a weaker dielectric environmental influence on the included guest molecule, but also give details of the geometry of α-CD inclusion complexes.

3.2. Formation mechanism of cyclodextrin inclusion complexes and NMR parameters

The driving force leading to the formation of CD inclusion complexes remains a controversial problem, although several mechanisms have been proposed.[23,24] The most important of these are

(a) van der Waals interactions between guest and host CD;[44,188–191]

(b) hydrophobic interactions;[191–193]

(c) release of water molecules with high energy from the CD cavity on complexation;[67,189]

(d) release of strain energy in the CD macrocyclic ring;[194–196]

(e) hydrogen bonding between the guest and the hydroxyl groups of CD;[197–200]

(f) effects of solvent surface tension.[201,202]

It is not possible on the basis of just one of these mechanisms to explain all aspects, especially the thermodynamic properties,[189,201,203,204] of CD inclusion phenomena. Two or more interactions are expected to operate simultaneously,[200,205,206] and the relative contribution of each to the driving force of CD complexation will depend on the combination of host and guest molecules.[200,205–208] Several attempts based on empirical theory have been made to elucidate the magnitudes of the contributions of interaction energies for the formation of CD inclusion complexes.[190,191] The main difficulty in identifying the dominant driving force lies in the intrinsic properties of CDs; that is, CDs have affinities for a variety of guest molecules, ranging from fully apolar molecule to organic anions.[23,24]

Elucidation of the physical nature of the CD cavity is essential for the study of the driving force for the formation of CD inclusion complexes. From analysis of ^{13}C NMR chemical-shift changes induced in guest compounds upon complexation with α-CD, as described in Section 3.1, the α-CD cavity provides the lower-dielectric (hydrophobic) environment on the included guest. Hence the hydrophobic interaction is expected to contribute more or less to inducing the formation of an inclusion complex for some guest compounds. However, the mutual molecular orientation of α-CD and the guest in the complexed state cannot be accounted for solely by the hydrophobic interaction. For example, as found by NMR spectroscopy as

described in the preceding sections, benzoic acid can only bind in the α-CD cavity with the carboxyl end first,[53,68] although it is possible for it to penetrate into the cavity with the phenyl group first without severe steric obstruction if the hydrophobic interaction is the only driving force. Further, both *p*-nitrophenol and *p*-nitrophenolate anion bind in the α-CD cavity only with the nitro end first,[72,73,76,178] the latter more tightly than the former. Hydration of the hydroxyl anion may lead to preferential inclusion of the nitrophenyl end, because the hydroxyl group is exposed to the aqueous medium. However, in the case of the neutral form the insertion of phenol group first may also be possible—but it does not occur. Many experimental results, including those obtained from NMR parameters,[53,68,72,73,76,178] suggest the importance of dipole–dipole interactions in the CD–guest inclusion phenomena.

Theoretical calculation of electrostatic potential maps of CDs indicates that there is a potential gradient along the cavity axis inside the CD cavity.[209] As a result, CD molecules have dipole moments, where magnitudes depend sensitively on the conformation of the CD molecules and hence on the type of guest compounds.[210–212] The dipole moment of each CD, including α-, β- and γ-CD and methylated CDs, is directed from the secondary to the primary hydroxyl side. In α-CD inclusion complexes with some aromatic guest molecules, such as *p*-nitrophenol and *p*-hydroxybenzoic acid, as a whole the side of the narrower rim of α-CD has a positive potential while the other has a negative potential, and the resulted dipole moment of the host α-CD is antiparallel to that of the guest. Thus the electrostatic interaction between the host α-CD and the guest is considered to contribute not only to stabilization of the inclusion complex but also to determining the mutual molecular orientation of the host and guest. As the positive and the negative centres are well separated from each other, the resulting dipole moment may become too large to influence the binding of some polar guest compounds. On the other hand, owing to the separation of the positive and negative centres, the middle part of the α-CD cavity is nearly electrically neutral, leading to an apolar character that might be reflected in the observed spectroscopic properties, such as UV absorption and NMR chemical shifts, as shown in Section 3.1, of the included guest compounds. Further discussion on the binding mechanisms of CDs is outside the scope of this review.

4. CONCLUDING REMARKS

As is clear from this chapter, high-resolution NMR in solution as well as in solid state is an indispensable tool for the study of cyclodextrin inclusion phenomena. It provides information not only on the structure and geometry of cyclodextrin inclusion complexes but also on their dynamic properties.

Furthermore, through the NMR information, the chemical and physical nature of cyclodextrins, especially their cavities, is brought to light, allowing investigation of the formation mechanisms of inclusion complexes. As described above, a number of NMR experimental data have been accumulated on cyclodextrins and their inclusion complexes. NMR has indeed played an important role in the developments of cyclodextrin chemistry, although CD complexation-induced changes of several NMR parameters are still not well understood.

A variety of new cyclodextrin derivatives with special functions are appearing. Cyclodextrins are very important chemical compounds, but they are not the only cyclic oligosaccharides that can form supramolecular structures. Several other kinds of cyclic oligosaccharides are also known to have such an ability. For example, cyclic (1→2)-α-D-glucans (called cyclosophoraoses or cyclosophorans), which have larger cavity diameters and depths than common CDs and can form inclusion complexes with several organic compounds,[213,214] are produced by many strains of *Agrobacterium* and *Rhizobium*.[215–217] Cyclic (2→1)-linked α-D-fructofuranoses, called cyclofructans, are also oligosaccharides produced from inulin by *Bacillus* strains.[218] One of them, cycloinulohexaose, has a macrocycle like that of 18-crown-6,[219] and can form inclusion complexes selectively with some metal cations in aqueous solution, as confirmed by ^{1}H and ^{13}C NMR spectroscopy.[220] Molecular recognition via inclusion phenomena of cyclic oligosaccharides is a rapidly growing field of host–guest and supramolecular chemistry. NMR spectroscopy should contribute to the future development of this field as an indispensable means of research.

REFERENCES

1. J.-M. Lehn, *Angew. Chem. Int. Ed. Engl.*, 1988, **27**, 89.
2. D. J. Cram and J. M. Cram, *Science*, 1974, **183**, 803.
3. E. L. Boschke (ed.), *Topics in Current Chemistry. Host–Guest Complexes*, Vols 1–3. Springer-Verlag, Berlin, 1982–83.
4. T. Osa (ed.), *Host–Guest Chemistry*. Kyoritsu Shuppan, Tokyo, 1979.
5. M. Hiraoka, H. Yanagida, M. Ohara and K. Koga, *Host–Guest Chemistry*. Kodansha Scientific, Tokyo, 1984.
6. B. C. Pressman and C. Moore, *Biochem. Biophys. Res. Commun.*, 1964, **15**, 562.
7. Y. A. Ovchinikov, V. T. Ivanov and A. M. Shkrob, *Membrane-Active Complexones*. Elsevier, Amsterdam, 1974.
8. J.-M. Lehn, *Struct. Bonding*, 1973, **16**, 1.
9. R. M. Izatt and J. J. Christensen (eds), *Synthetic Multidentate Macrocyclic Compounds*. Academic Press, New York, 1978.
10. D. J. Cram and J. M. Cram, *Acc. Chem. Res.*, 1978, **11**, 8.
11. J.-M. Lehn, *Acc. Chem. Res.*, 1978, **11**, 49.
12. F. Vögtle and E. Weber, *Angew. Chem. Int. Ed. Engl.*, 1979, **18**, 753.
13. G. W. Gokel and S. H. Korzeniowski, *Macrocyclic Polyether Synthesis*. Springer-Verlag, Berlin, 1982.

14. C. J. Pedersen, *J. Am. Chem. Soc.*, 1967, **89**, 2495.
15. B. Dietrich, J.-M. Lehn and J. P. Sauvage, *Tetrahedron Lett.*, 1969, 2889.
16. H. Stetter and E.-E. Roos, *Chem. Ber.*, 1955, **88**, 1390.
17. D. J. Cram, T. Kaneda, R. C. Helgeson and G. M. Lein, *J. Am. Chem. Soc.*, 1979, **101**, 6752.
18. P. R. Sundarajan, and V. S. Rao, *Carbohydr. Res.*, 1970, **13**, 351.
19. A. Villiers, *Compt. Rend.*, 1891, **112**, 536.
20. P. V. Demarco and A. L. Thakkar, *J. Chem. Soc. Chem. Commun.*, 1970, 2.
21. Y. Inoue, *JEOL News*, 1987, **23A**(2), 8.
22. Y. Yamamoto and Y. Inoue, *J. Carbohydr. Chem.*, 1989, **8**, 29.
23. (a) G. V. Caesar, *Starch and Its Derivatives* (ed. J. A. Radley), Chap. X. Chapman & Hall, London, 1968.
    (b) M. L. Bender and M. Komiyama, *Cyclodextrin Chemistry*. Springer-Verlag, Berlin, 1978.
    (c) J. Szejtli, *Cyclodextrins and Their Inclusion Complexes*. Akademiai Kiado, Budapest, 1982.
24. (a) R. J. Bergeron, *J. Chem. Educ.*, 1977, **54**, 204.
    (b) T. Kuge, *Biophysics (Jpn)*, 1977, **17**, 29.
    (c) T. Yoneda, *Chem. Chem. Ind. (Jpn)*, 1979, **32**, 253.
    (d) W. Saenger, *Angew. Chem. Int. Ed. Engl.*, 1980, **19**, 344.
    (e) W. L. Hinze, *Separ. Purif. Meth.*, 1981, **10**, 159.
    (f) K. Uekama, *Yakugaku Zasshi (Jpn)*, 1981, **101**, 857.
    (g) I. Tabushi, *Acc. Chem. Res.*, 1982, **15**, 66.
    (h) Y. Inoue, *Kagaku (Jpn)*, 1985, **55**, 710.
    (i) Y. Inoue, *Cell Technol.*, 1986, **5**, 360.
    (j) Y. Inoue, *Chem. Chem. Ind. (Jpn)*, 1990, **43**, 907.
    (k) A. Ueno, *Chem. Chem. Ind. (Jpn)*, 1990, **43**, 1226.
    (l) M. Sakurai, *Chem. Chem. Ind. (Jpn)*, 1991, **44**, 188.
    (m) K. Takahashi, *Chem. Chem. Ind. (Jpn)*, 1991, **44**, 254.
25. (a) L. D. Hall, *Adv. Carbohydr. Chem.*, 1964, **19**, 51.
    (b) T. D. Inch, *Ann. Rep. NMR Spectrosc.*, 1969, **2**, 35.
    (c) A. F. Casy, *PMR Spectroscopy in Medicinal and Biological Chemistry*, pp. 330, 361. Academic Press, New York, 1971.
26. (a) R. Freeman and G. A. Morris, *Bull. Magn. Reson.*, 1979, **1**, 5.
    (b) A. Bax, *Two-Dimensional NMR in Liquids*. Delft University Press, 1982.
    (c) G. Bodenhausen, *Prog. NMR Spectrosc.*, 1981, **14**, 137.
    (d) D. L. Turner, *Prog. NMR Spectrosc.*, 1985, **17**, 281.
    (e) R. R. Ernst, G. Bodenhausen and A. Wokaun, *Principles of Nuclear Magnetic Resonance in One and Two Dimensions*. Clarendon Press, Oxford, 1987.
27. Y. Yamamoto, Y. Inoue, R. Chujo and S. Kobayashi, *Carbohydr. Res.*, 1987, **166**, 156.
28. Y. Yamamoto, M. Onda, Y. Takahashi, Y. Inoue and R. Chujo, *Carbohydr. Res.*, 1987, **170**, 229.
29. I. Tabushi, T. Nabeshima, K. Yamamura and H. Fujita, *Bull. Chem. Soc. Jpn*, 1987, **60**, 3705.
30. W. Saka, Y. Yamamoto, Y. Inoue, R. Chujo, K. Takahashi and K. Hattori, *Bull. Chem. Soc. Jpn*, 1990, **63**, 3175.
31. S. R. Hartmann and E. L. Hahn, *Phys. Rev.*, 1962, **128**, 2042.
32. D. G. Davis and A. Bax, *J. Am. Chem. Soc.*, 1985, **107**, 2820.
33. A. Bax and D. G. Davis, *J. Magn. Reson.*, 1985, **63**, 355.
34. A. A. Bothner-By, R. L. Stephens, J. Lee, C. D. Warven and R. W. Jeanloz, *J. Am. Chem. Soc.*, 1984, **106**, 811.
35. A. Bax and D. G. Davis, *J. Magn. Reson.*, 1985, **63**, 207.

36. D. G. Davis and A. Bax, *J. Magn. Reson.*, 1985, **64**, 533.
37. H. Kessler, C. Griesinger, R. Kerssebaum, K. Wagner and R. R. Ernst, *J. Am. Chem. Soc.*, 1987, **109**, 607.
38. D. G. Davis and A. Bax, *J. Am. Chem. Soc.*, 1985, **107**, 7197.
39. C. M. Spencer, J. F. Stoddart and R. Zarzycki, *J. Chem. Soc. Perkin Trans. 2*, 1987, 1323.
40. M. Ikura and K. Hikichi, *Carbohydr. Res.*, 1987, **163**, 1.
41. G. Strecker, J. M. Wieruszeski, C. Martel and J. F. G. Vliegenthart, *Carbohydr. Res.*, 1989, **185**, 1.
42. Y. Yamamoto, M. Onda, Y. Takahashi, Y. Inoue and R. Chujo, *Carbohydr. Res.*, 1988, **182**, 41.
43. F. A. Bovey, *Nuclear Magnetic Resonance Spectroscopy*, 2nd edn, Chap. 5. Academic Press, San Diego, 1988.
44. R. J. Bergeron, M. A. Channing, G. J. Gibeily and D. M. Pillor, *J. Am. Chem. Soc.*, 1977, **99**, 5146.
45. R. L. Gelb, L. M. Schwartz and D. A. Laufer, *J. Am. Chem. Soc.*, 1978, **100**, 5875.
46. R. L. Gelb, L. M. Schwartz, C. T. Murray and D. A. Laufer, *J. Am. Chem. Soc.*, 1978, **100**, 3553.
47. R. L. Gelb, L. M. Schwartz, J. E. Markinac and D. A. Laufer, *J. Am. Chem. Soc.*, 1979, **101**, 1864.
48. J. Li, A. Harata, and M. Kamachi, *Polymer Preprints (Jpn)*, 1991, **40**, 893.
49. M. Watanabe, H. Nakamura and T. Matsuo, *Bull. Chem. Soc. Jpn*, 1992, **65**, 164.
50. M. Suzuki and Y. Sasaki, *Chem. Pharm. Bull.*, 1979, **27**, 609.
51. K. Harata, *Bull. Chem. Soc. Jpn*, 1976, **49**, 1493.
52. Y. Yamamoto, M. Onda, M. Kitagawa, Y. Inoue and R. Chujo, *Carbohydr. Res.*, 1987, **167**, C11.
53. R. L. Gelb, L. M. Schwartz, B. Cardelino, H. S. Fuhrman, R. F. Johnson and D. A. Laufer, *J. Am. Chem. Soc.*, 1981, **103**, 1750.
54. M. Sakurai, M. Kitagawa, H. Hoshi, Y. Inoue and R. Chujo, *Bull. Chem. Soc. Jpn*, 1989, **62**, 2067.
55. K. Harata, H. Uedaira and J. Tanaka, *Bull. Chem. Soc. Jpn*, 1978, **51**, 1627.
56. Y. Inoue, T. Okuda and R. Chujo, *Carbohydr. Res.*, 1985, **141**, 179.
57. D. J. Wood, F. E. Hruska, and W. Saenger, *J. Am. Chem. Soc.*, 1977, **99**, 1735.
58. M. Komiyama and H. Hirai, *Polymer J.*, 1981, **13**, 171.
59. M. Komiyama and H. Hirai, *Chem. Lett.*, 1981, 1467.
60. Y. Inoue, T. Okuda, Y. Miyata and R. Chujo, *Carbohydr. Res.*, 1984, **125**, 65.
61. Y. Yamamoto, M. Onda, Y. Takahashi, Y. Inoue and R. Chujo, *Carbohydr. Res.*, 1988, **182**, 41.
62. C. E. Johnson and F. A. Bovey, *J. Phys. Chem.*, 1958, **29**, 1012.
63. Y. Inoue, Y. Katono and R. Chujo, *Bull. Chem. Soc. Jpn*, 1979, **52**, 1692.
64. K. B. Lipkowitz, *J. Org. Chem.*, 1991, **56**, 6357.
65. K. Harata, *Bull. Chem. Soc. Jpn*, 1977, **50**, 1416.
66. P. E. Hansen, H. D. Dettman and B. D. Sykes, *J. Magn. Reson.*, 1985, **62**, 487.
67. R. Bergeron and R. Rowan, *Bioorg. Chem.*, 1976, **5**, 425.
68. R. J. Bergeron, M. A. Channing and K. A. McGovern, *J. Am. Chem. Soc.*, 1978, **100**, 2878.
69. R. J. Bergeron and M. A. Channing, *J. Am. Chem. Soc.*, 1979, **101**, 2511.
70. R. J. Bergeron, M. A. Channing, K. A. McGovern and W. P. Roberts, *Bioorg. Chem.*, 1979, **8**, 263.
71. J. H. Noggle and R. E. Schirmer, *The Nuclear Overhauser Effect. Chemical Applications*. Academic Press, New York, 1971.
72. Y. Inoue, Y. Takahashi and R. Chujo, *Carbohydr. Res.*, 1985, **144**, C9.

73. Y. Yamamoto, M. Onda, M. Kitagawa, Y. Inoue and R. Chujo, *Carbohydr. Res.*, 1987, **167**, C11.
74. S. Kobayashi, K. Kainuma, and S. Suzuki, *Agric. Biol. Chem.*, 1977, **51**, 691.
75. S. Kobayashi, N. Shibuya, B. M. Young and D. French, *Carbohydr. Res.*, 1984, **26**, 215.
76. Y. Inoue, Y. Kanda, Y. Yamamoto, R. Chujo and S. Kobayashi, *Carbohydr. Res.*, 1989, **194**, C8.
77. Y. Yamamoto, Y. Inoue, R. Chujo and S. Kobayashi, *Carbohydr. Res.*, 1987, **166**, 156.
78. Y. Yamamoto, Y. Kanda, Y. Inoue, R. Chujo and S. Kobayashi, *Chem. Lett.*, 1988, 495.
79. Y. Kanda, Y. Yamamoto, Y. Inoue, R. Chujo and S. Kobayashi, *Bull. Chem. Soc. Jpn*, 1989, **62**, 2002.
80. M. Komiyama and H. Hirai, *Bull. Chem. Soc. Jpn*, 1981, **54**, 828.
81. K. N. Lipkowitz, S. Raghothama, and J. Yang, *J. Am. Chem. Soc.*, 1992, **114**, 1554.
82. L. Stryer, *Biochemistry*, 3rd edn. Freeman, New York, 1988.
83. V. S. R. Rao and F. Foster, *J. Phys. Chem.*, 1963, **67**, 951.
84. B. Casu, M. Reggiani, G. G. Gallo and A. Vigevani, *Tetrahedron*, 1968, **24**, 803.
85. F. Cramer, G. MacKensen and K. Sensse, *Chem. Ber.*, 1969, **102**, 494.
86. B. Casu, M. Reggiani, G. G. Gallo and A. Vigevani, *Carbohydr. Res.*, 1970, **12**, 157.
87. Y. Inoue, Y. Takahashi, and R. Chujo, *Carbohydr. Res.*, 1986, **148**, 109.
88. Y. Yamamoto, M. Onda, Y. Takahashi, Y. Inoue and R. Chujo, *Carbohydr. Res.*, 1987, **170**, 229.
89. (a) P. C. Manor and W. Saenger, *J. Am. Chem. Soc.*, 1974, **96**, 3630.
    (b) K. K. Chacko and W. Saenger, *J. Am. Chem. Soc.*, 1981, **103**, 1708.
    (c) K. Lindner and W. Saenger, *Carbohydr. Res.*, 1982, **99**, 103.
    (d) K. Harata, *Bull. Chem. Soc. Jpn*, 1982, **55**, 2315.
    (e) K. Harata, *Bull. Chem. Soc. Jpn*, 1987, **60**, 2763.
    (f) K. Harata, *J. Chem. Soc. Chem. Commun.*, 1988, 928.
90. B. Casu, G. G. Gallo, M. Reggiani and A. Vigevani, *Die Stärke*, 1968, **20**, 387.
91. P. Colson, H. J. Jennings and I. C. P. Smith, *J. Am. Chem. Soc.*, 1974, **96**, 8081.
92. K. Takeo, K. Hirose and T. Kuge, *Chem. Lett.*, 1973, 1233.
93. K. Takeo and T. Kuge, *Agric. Biol. Chem.*, 1970, **34**, 1416.
94. M. St-Jacques, P. R. Sundarajan, K. J. Taylor and R. H. Marchessault, *J. Am. Chem. Soc.*, 1976, **98**, 4386.
95. M. Onda, Y. Yamamoto, Y. Inoue and R. Chujo, *Bull. Chem. Soc. Jpn*, 1988, **61**, 4015.
96. J. C. Christofides and D. B. Davies, *J. Chem. Soc. Chem. Commun.*, 1982, 560.
97. J. C. Christofides, D. B. Davies and E. B. Rathbone, *J. Am. Chem. Soc.*, 1986, **108**, 5738.
98. D. G. Streefkerk, M. J. A. de Bie and J. F. G. Vliegenthart, *Tetrahedron*, 1973, **29**, 833.
99. K. Takahashi, S. Nakata, H. Suzuki, K. Hata and K. Hattori, 6th Cyclodextrin Symposium, Chiba, Japan, November 1987.
100. Y. Inoue, Y. Kanda, Y. Yamamoto and S. Kobayashi, *Carbohydr. Res.*, 1992, **226**, 197.
101. T. Fujiwara, N. Tanaka, K. Hamada and S. Kobayashi, *Chem. Lett.*, 1989, 1131.
102. Y. Inoue, T. Okuda and Y. Miyata, *J. Am. Chem. Soc.*, 1981, **103**, 7393.
103. Y. Inoue, Y. Yamamoto and R. Chujo, *Carbohydr. Res.*, 1983, **118**, 37.
104. Y. Inoue, F.-H. Kuan and R. Chujo, *Bull. Chem. Soc. Jpn*, 1987, **60**, 2539.
105. S. Takahashi, E. Suzuki and N. Nagashima, *Bull. Chem. Soc. Jpn*, 1986, **59**, 1129.
106. J. R. Zimmerman and W. E. Brittin, *J. Phys Chem.*, 1957, **61**, 1328.
107. A. Allerhand, D. Doddrell and R. Komoroski, *J. Chem. Phys.*, 1971, **55**, 189.
108. J. H. Noggle and R. E. Schirmer, *The Nuclear Overhauser Effect*. Academic Press, New York, 1971.
109. R. D. Deslauries, A. C. M. Paiva, K. Schaumburg and I. C. P. Smith, *Biochemistry*, 1975, **14**, 878.
110. R. D. Deslauries, Z. Grzonka, K. Schaumburg, T. Shiba and R. Walter, *J. Am. Chem. Soc.*, 1975, **97**, 5093.

111. Y. Inoue and Y. Miyata, *Bull. Chem. Soc. Jpn*, 1981, **54**, 809.
112. Y. Inoue, T. Okuda and R. Chujo, *Carbohydr. Res.*, 1982, **101**, 187.
113. J. P. Behr and J. M. Lehn, *J. Am. Chem. Soc.*, 1976, **98**, 1743.
114. M. Otagiri, K. Uekama and K. Ikeda, *Chem. Pharm. Bull.*, 1975, **23**, 118.
115. M. Otagiri, T. Miyaji, K. Uekama and K., Ikeda, *Chem. Pharm. Bull.*, 1976, **24**, 1146.
116. K. Uekama, F. Hirayama and H. Koinuma, *Chem. Lett.*, 1977, 1393.
117. K. Uekama and F. Hirayama, *Chem. Pharm. Bull.*, 1978, **26**, 1195.
118. F. Hirayama, K. Uekama and H. Koinuma, *Chem. Pharm. Bull.*, 1980, **28**, 1975.
119. M. Mehring, *High Resolution NMR Spectroscopy in Solids*. Springer-Verlag, Berlin, 1976.
120. D. L. VanderHart, W. L. Earl and A. N. Garroway, *J. Magn. Reson.*, 1981, **44**, 361.
121. C. S. Yannoni, *Acc. Chem. Res.*, 1982, **15**, 201.
122. C. A. Fyfe, R. L. Dudley, P. J. Stephenson, Y. Deslandes, G. K. Hamer and R. H. Marchessault, *J. Macromol. Sci. Rev., Macromol. Chem. Phys.*, 1983, **C23**, 187.
123. P. E. Pfeffer, *J. Carbohydr. Chem.*, 1984, **3**, 613.
124. H. Saito and R. Tabeta, *Chem. Lett.*, 1981, 713.
125. H. Saito, G. Izumi, T. Mamizuka, S. Suzuki and R. Tabeta, *J. Chem. Soc. Chem. Commun.*, 1982, 1386.
126. J. M. Hewitt, M. Linder and S. Perez, *Carbohydr. Res.*, 1986, **154**, 1.
127. M. J. Gidley and S. M. Bociek, *J. Am. Chem. Soc.*, 1988, **110**, 3820.
128. P. C. Manor and W. Saenger, *J. Am. Chem. Soc.*, 1974, **96**, 3630.
129. F. Horii, A. Hirai and R. Kitamaru, *Polymers for Fibers and Elastomers* (ed. J. C. Arthur), *ACS Symp. Ser.*, 1984, **260**, 22.
130. K. Bock, A. Brignole and B. W. Sigurskjold, *J. Chem. Soc. Perkin Trans. 2*, 1986, 1711.
131. D. M. Grant and E. G. Paul, *J. Am. Chem. Soc.*, 1964, **86**, 2984.
132. D. M. Grant and B. V. Cheney, *J. Am. Chem. Soc.*, 1967, **89**, 5315.
133. B. V. Cheney and D. M. Grant, *J. Am. Chem. Soc.*, 1967, **89**, 5319.
134. H. N. Cheng and M. A. Bennett, *Makromol. Chem.*, 1987, **188**, 135.
135. H. Ueda and T. Nagai, *Chem. Pharm. Bull.*, 1981, **29**, 2710.
136. K. Uekama, F. Hirayama, A. Fujise, M. Otagiri, K. Inaba and H. Saito, *J. Pharm. Sci.*, 1984, **73**, 382.
137. Y. Inoue, T. Okuda, F.-H. Kuan and R. Chujo, *Carbohydr. Res.*, 1984, **129**, 9.
138. R. Sakaguchi, T. Miyakawa, S. Takeuchi, K. Nakagawa and E. Hayase, *Agric. Biol. Chem.*, 1979, **43**, 1775.
139. S. Takeuchi and M. Kochi, *Japanese Patent* 1 157 737, 1979.
140. J. Szejtli, *Cyclodextrins and Their Inclusion Complexes*, Chap. 6. Akademiai Kiado, Budapest, 1982.
141. F.-K. Kuan, Y. Inoue and R. Chujo, *J. Inclusion Phenom.*, 1986, **4**, 281.
142. E. Breitmaier and W. Voelter, *^{13}C NMR Spectroscopy*, 2nd edn, Chap. 4. Verlag Chemie, New York, 1978.
143. K. Harata, K. Uekama, M. Otagiri, F. Hirayama and H. Ogino, *Bull. Chem. Soc. Jpn*, 1981, **54**, 1954.
144. K. Harata, K. Uekama, M. Otagiri, F. Hirayama and Y. Sugiyama, *Bull. Chem. Soc. Jpn*, 1982, **55**, 3386.
145. H. Sakuraba, K. Natori and Y. Tanaka, *J. Org. Chem.*, 1991, **56**, 4124.
146. Y. Tanaka, H. Sakuraba and H. Nakanishi, *J. Chem. Soc. Chem. Commun.*, 1983, 947.
147. H. Sakuraba, T. Nakai and Y. Tanaka, *J. Inclusion Phenom.*, 1984, **2**, 829.
148. H. Sakuraba, H. Ishizaki, Y. Tanaka and T. Shimizu, *J. Inclusion Phenom.*, 1987, **5**, 449.
149. H. Sakuraba, N. Inomata and Y. Tanaka, *J. Org. Chem.*, 1989, **54**, 3482.
150. Y. Tanaka, H. Sakuraba and H. Nakanishi, *J. Org. Chem.*, 1990, **55**, 564.
151. Y. Inoue, T. Okuda and R. Chujo, *Carbohydr. Res.*, 1983, **116**, C5.
152. Y. Inoue, F.-H. Kuan, Y. Takahashi and R. Chujo, *Carbohydr. Res.*, 1985, **135**, C12.
153. Y. Inoue, F.-H. Kuan and R. Chujo, *Carbohydr. Res.*, 1987, **159**, 1.

154. D. L. VanderHart, W. L. Earl and A. N. Garroway, *J. Magn. Reson.*, 1981, **44**, 362.
155. D. Suwelack, W. P. Rothwell and J. S. Waugh, *J. Chem. Phys.*, 1980, **73**, 2559.
156. L. M. Gierash, M. H. Frey, J. G. Hexem and S. J. Opella, *ACS Symp. Ser.*, 1982, **191**, 233.
157. W. P. Rothwell and J. S. Waugh, *J. Chem. Phys.*, 1981, **74**, 2721.
158. J. G. Hexem, M. H. Frey and S. J. Opella, *J. Chem. Phys.*, 1982, **77**, 3847.
159. A. Naito, S. Ganapathy and C. A. McDowell, *J. Magn. Reson.*, 1982, **48**, 367.
160. S. J. Opella and M. H Frey, *J. Am. Chem. Soc.*, 1979, **101**, 5854.
161. S. Takahashi, E. Suzuki, Y. Amino, N. Nagashima, Y. Nishimura and M. Tsuboi, *Bull. Chem. Soc. Jpn*, 1986, **59**, 93.
162. M. Okazaki and C. A. McDowell, *Chem. Phys. Lett.*, 1983, **102**, 20.
163. J. Ripmeester, *J. Inclusion Phenom.*, 1986, **6**, 31.
164. F. O. Garces, V. P. Rao, M. A. Garcia-Garibay and N. J. Turro, *Supramol. Chem.*, 1992, **1**, 65.
165. L. D. Hall and T. K. Lim, *J. Am. Chem. Soc.*, 1984, **106**, 1858.
166. L. D. Hall and T. K. Lim, *J. Am. Chem. Soc.*, 1986, **108**, 2503.
167. M. G. Usha and R. J. Wittebort, *J. Am. Chem. Soc.*, 1992, **114**, 1541.
168. C. Betzel, W. Saenger, B. E. Hingerty and G. M. Brown, *J. Am. Chem. Soc.*, 1984, **106**, 7545.
169. V. Zabel, W. Saenger and S. A. Mason, *J. Am. Chem. Soc.*, 1986, **108**, 3664.
170. Th. Steiner, W. A. Saenger and R. E. Lechner, *Mol. Phys.*, 1991, **72**, 1211.
171. A. Bax, N. M. Szeverenyi and G. E. Maciel, *J. Magn. Reson.*, 1983, **55**, 494.
172. T. Terao, T. Fujii, T. Onodera and A. Saika, *Chem. Phys. Lett.*, 1984, **107**, 145.
173. J. Ashida, D. Kuwabara, F. Imashiro and T. Terao, *Proceedings of the 30th NMR Symposium, Tokyo, 1991*, p. 1.
174. J. B. Stothers, *Carbon-13 NMR Spectroscopy*. Academic Press, New York, 1972.
175. C. Reichardt, *Solvent Effects in Organic Chemistry*. Verlag Chemie, New York, 1976.
176. I. Ando and G. A. Webb, *Org. Magn. Reson.*, 1981, **15**, 111.
177. I. Ando and G. A. Webb, *Theory of NMR Parameters*. Academic Press, London, 1983.
178. R. J. Bergeron, M. A. Channing, G. J. Gibeily and D. M. Pillor, *J. Am. Chem. Soc.*, 1977, **99**, 5146.
179. R. L. VanEtten, J. F. Sebastian, G. A. Clowes and M. L. Bender, *J. Am. Chem. Soc.*, 1967, **89**, 3242.
180. M. Karplus and J. A. Pople, *J. Chem. Phys.*, 1963, **38**, 2803.
181. J. A. Pople and D. L. Beveridge, *Approximate Molecular Orbital Theory*. McGraw-Hill, New York, 1970.
182. G. Klopman, *Chem. Phys. Lett.*, 1967, **1**, 200.
183. Y. Inoue, H. Hoshi, M. Sakurai and R. Chujo, *J. Am. Chem. Soc.*, 1985, **107**, 2319.
184. M. Sakurai, I. Ando, Y. Inoue and R. Chujo, *Photochem. Photobiol.*, 1981, **34**, 367.
185. M. Sakurai, H. Hoshi, Y. Inoue and R. Chujo, *Chem. Phys. Lett.*, 1989, **163**, 217.
186. H. Hoshi, M. Sakurai, Y. Inoue and R. Chujo, *J. Chem. Phys.*, 1987, **87**, 1107.
187. H. Hoshi, M. Sakurai, Y. Inoue and R. Chujo, *J. Mol. Struct. (Theochem.)*, 1988, **180**, 267.
188. F. Cramer, *Angew. Chem.*, 1956, **68**, 115.
189. R. L. VanEtten, J. F. Sebastian, G. A. Clowes and M. L. Bender, *J. Am. Chem. Soc.*, 1967, **89**, 3242.
190. K. Harata, *Bull. Chem. Soc. Jpn*, 1976, **49**, 2066.
191. I. Tabushi, Y. Kiyosuke, T. Sugimoto and K. Yamamura, *J. Am. Chem. Soc.*, 1978, **100**, 916.
192. Y. Matsui, *Bull. Chem. Soc. Jpn*, 1982, **55**, 1246.
193. D. E. Tutt and M. A. Schwartz, *J. Chem. Soc. Chem. Commun.*, 1970, 113.
194. P. C. Manor and W. Saenger, *Nature*, 1972, **237**, 392.

195. P. C. Manor and W. Saenger, *J. Am. Chem. Soc.*, 1974, **96**, 3630.
196. B. Hingerty and W. Saenger, *J. Am. Chem. Soc.*, 1976, **98**, 3357.
197. F. Cramer, *Pure Appl. Chem.*, 1955, **5**, 143.
198. F. Cramer and W. Dietsche, *Chem. Ber.*, 1959, **92**, 1739.
199. F. Cramer and W. Kampe, *J. Am. Chem. Soc.*, 1965, **87**, 1115.
200. E. S. Hall and H. J. Ache, *J. Phys. Chem.*, 1979, **83**, 1805.
201. F. Cramer, W. Saenger and H.-Ch. Spatz, *J. Am. Chem. Soc.*, 1967, **89**, 14.
202. A. Orstan and J. B. A. Ross, *J. Phys. Chem.*, 1987, **91**, 2739.
203. T. S. Straub and M. L. Bender, *J. Am. Chem. Soc.*, 1972, **94**, 8881.
204. E. A. Lewis and L. D. Hansen, *J. Chem. Soc. Perkin Trans. 2*, 1973, 2081.
205. K. A. Connors and D. D. Pendergast, *J. Am. Chem. Soc.*, 1984, **106**, 7607.
206. I. Sanemasa and Y. Akamine, *Bull. Chem. Soc. Jpn*, 1987, **60**, 2059.
207. T. Okubo and M. Kuroda, *Macromolecules*, 1989, **22**, 3936.
208. W. C. Cromwell, K. Bystrom and M. R. Eftink, *J. Phys. Chem.*, 1985, **89**, 326.
209. M. Sakurai, M. Kitagawa, H. Hoshi, Y. Inoue and R. Chujo, *Chem. Lett.*, 1988, 895.
210. M. Kitagawa, H. Hoshi, M. Sakurai, Y. Inoue and R. Chujo, *Carbohydr. Res.*, 1987, **163**, C1.
211. M. Kitagawa, H. Hoshi, M. Sakurai, Y. Inoue and R. Chujo, *Bull Chem. Soc. Jpn*, 1988, **61**, 4225.
212. M. Sakurai, M. Kitagawa, H. Hoshi, Y. Inoue and R. Chujo, *Carbohydr. Res.*, 1990, **198**, 181.
213. K. Koizumi, Y. Okada, S. Horiyama, T. Utamura, T. Higashiura and M. Ikeda, *J. Inclusion Phenom.*, 1984, **2**, 891.
214. Y. Okada, S. Horiyama and K. Koizumi, *Yakugaku Zasshi*, 1986, **106**, 240.
215. M. Hisamatsu, A. Amemura, T. Matsuo, H. Matsuda and T. Harada, *J. Gen. Microbiol.*, 1982, **128**, 1873.
216. A. Dell, K. W. S. York, M. McNeil, A. G. Darvill and P. Albersheim, *Carbohydr. Res.*, 1983, **117**, 185.
217. J. E. Harris, F. A. Mellon, V. J. Morris, K. R. Parsley, B. J. H. Stevens and K. R. Austin, *Carbohydr. Polym.*, 1991, **16**, 321.
218. M. Sawada, T. Tanaka, Y. Takai, T. Hanafusa, K. Hirotsu, T. Higuchi, M. Kawamura and T. Uchiyama, *Chem. Lett.*, 1990, 2011.
219. M. Sawada, T. Tanaka, Y. Takai, T. Hanafusa, T. Taniguchi, M. Kawamura and T. Uchiyama, *Carbohydr. Res.*, 1991, **217**, 7.
220. N. Yoshie, H. Hamada and Y. Inoue, *Chem. Lett.*, 1993, 353.

This Page Intentionally Left Blank

Dynamic NMR Spectroscopy in Inorganic and Organometallic Chemistry

K. G. ORRELL and V. ŠIK

Department of Chemistry, The University, Exeter, UK

1. INTRODUCTION

The study of chemical exchange phenomena through the use of NMR techniques rests on the measurements of the four basic NMR parameters, namely relative signal intensities, internal chemical shifts, nuclear spin–spin couplings and nuclear spin relaxation times. These parameters and their temperature dependences can be measured with great precision these days by one- and two-dimensional techniques, thus providing chemists with almost a plethora of methods for precise measurement of molecular dynamics.

This review focuses on recent developments in measurements of intramolecular rearrangements of molecules in chemical equilibrium, but also includes some mention of intermolecular processes and time-dependent studies of non-equilibrium systems. The main advances in the theory and

ANNUAL REPORTS ON NMR SPECTROCOPY
VOLUME 27 ISBN 0-12-505327-4

methodology of dynamic NMR (DNMR) from 1986 onwards are described, thus providing an update to the authors' previous review in Volume 19 of this Series.[1] The literature coverage is for a 6½ year period up to and including Issue 13 of the *Chemical Abstracts Selects, Proton Magnetic Resonance and Carbon & Heteroatom NMR*. During such a time span many hundreds of papers have appeared in which NMR has been exploited for studying dynamical features of chemical structure. In order to keep the review within reasonable bounds, literature coverage has therefore been restricted to significant advances in one- and two-dimensional DNMR theory and methodology, and applications of these developments to new and novel dynamic systems, papers being selected only where emphasis was placed on the quantitative accuracy of the rate and activation energy data being extracted from the spectra. Inorganic coordination complexes and organometallic compounds provide the widest variety of internal dynamic or fluxional rearrangements, and thus, as in the earlier review,[1] applications have been taken from these areas of chemistry.

During the review period numerous books, monographs, and reviews containing aspects of DNMR have appeared. Of specific mention are those by Oki,[2] Chandrakumar and Subramanian,[3] Derome,[4] Sanders and Hunter[5] (where Chapter 7 is concerned solely with magnetization connections through chemical exchange), Friebolin[6] (where Chapter 11 is devoted to DNMR), and the authoritative monograph by Ernst, Bodenhausen and Wokaun.[7] Chapters 4 and 9 of this latter text cover the theory and methodology of 1D and 2D NMR of exchanging systems. Mention should also be made of two reviews dealing with applications of NMR to reaction kinetics and exchange,[8] and internal dynamics.[9]

1.1. NMR time scales

There is no single precisely defined NMR time scale, since its magnitude varies markedly according to the NMR experiment employed and the particular spectral parameter being modulated by the rate process under study.[5,10] Such processes may be followed either as a function of time for samples in a non-equilibrium state or as a function of physical parameters such as temperature and pressure for systems at chemical equilibrium. In time-dependent NMR signal intensities are usually monitored as the system approaches chemical equilibrium, and slow rate constants in the range 10^{-2}–10^{-4} s^{-1} can be measured with accuracy. For equilibrium samples the NMR parameters measured depend on whether the spectra relate to the slow or fast exchange regimes or whether they embrace both. Typical time scales and first-order rate constants that are measured by different NMR experiments are contained in Table 1.

Standard bandshape analysis (BSA) methods based on chemical shift

Table 1. NMR time scales and exchange rates.

NMR parameter/technique	τ (s)	k (s^{-1})
(1) Molecular correlation times[a]	10^{-10}–10^{-8}	10^{10}–10^{8}
(2) $T_{1\rho}$ measurements	10^{-6}–10^{-3}	10^{6}–10^{3}
(3) Chemical shift modulation[b]		
(i) $\Delta\nu_i$ = 1000 Hz (e.g. ^{195}Pt)	4.5×10^{-4}	2.2×10^{3}
(ii) $\Delta\nu_i$ = 100 Hz (e.g. ^{1}H)	4.5×10^{-3}	2.2×10^{2}
(4) Scalar coupling modulation[c]		
(i) J_{ij} = 50 Hz (e.g. ^{13}C–^{1}H)	9×10^{-3}	1.1×10^{2}
(ii) J_{ij} = 5 Hz (e.g. ^{1}H–^{1}H)	9×10^{-2}	1.1×10
(5) Dipole–dipole relaxation times/cross-relaxation times[d] (e.g. ^{1}H)	1	1
(6) Magnetization transfer experiments[e]		
2D-EXSY experiments	10^{-2}–10^{2}	10^{2}–10^{-2}
(7) Time-dependent studies[f]	10^{2}–10^{4}	10^{-2}–10^{-4}
Total ranges	10^{-10}–10^{4}	10^{10}–10^{-4}

[a] τ_c values, measured from relaxation or cross-relaxation times. For paramagnetic systems τ_c values may be in the picosecond range.
[b] Basis of bandshape analysis. Values calculated according to $k = \tau^{-1} = \pi|\Delta\nu_{ij}|/\sqrt{2}$.
[c] Basis of bandshape analysis. Values calculated according to $k = \tau^{-1} = \pi|J_{ij}|/\sqrt{2}$.
[d] Measured from 1D-NOE or 2D-NOESY experiments.
[e] Experiments require the dynamic process to be slow on time scales (3) and (4) and fast on time scale (5).
[f] Non-equilibrium studies.

and/or scalar coupling modulation by the rate process typically fall in the range 1–10^4 s^{-1}. The more recent introduction of one-dimensional magnetization transfer or two-dimensional exchange spectroscopy (2D-EXSY) has enabled the time scale to be extended by a factor of at least 10^2 over chemical-shift-based values, so that rate constants in the range 10^2–10^{-2} s^{-1} can be accurately obtained. The total range of lifetimes (10^{-10}–10^4 s) or exchanges rates (10^{10}–10^{-4} s^{-1}) is therefore very wide, making NMR the most versatile spectroscopic technique for chemists wishing to explore dynamic aspects of molecular structure.

Temperature dependences of rate constants provide activation energy data for dynamic processes. From typical temperature dependences of the range of rates given in Table 1, activation energies in the approximate range 15–100 kJ mol^{-1} can be evaluated. These lower and upper limits are determined more usually by experimental factors such as temperature variation of the NMR probe, physical properties of suitable solvents and thermal stabilities of the compounds being studied, rather than limitations of the technique itself. Activation energies are best expressed in terms of the

thermodynamic parameters, $\Delta G^{\ddagger}$, $\Delta H^{\ddagger}$ and $\Delta S^{\ddagger}$ arising from the Eyring rate theory. The Gibbs function changes $\Delta G^{\ddagger}$ are least prone to systematic errors,[11] and so this parameter, normally calculated at the standard temperature of 298.15 K, is usually chosen for comparing energy barriers of different dynamic processes. The entropy change $\Delta S^{\ddagger}$ is notoriously difficult to measure with high precision. Nevertheless, it provides a useful rule of thumb for distinguishing between purely intramolecular rearrangements, where its value should be around zero, and processes proceeding via a dissociative transition state, where its value is expected to be sizeably positive.

1.2. Exchange and molecular symmetry

Until quite recently DNMR theory took no account of the symmetries of rearranging molecules, with the exception of the case of intramolecular mutual exchange.[12] Consequently many DNMR bandshape calculations could not be attempted because of the size of the spin matrices involved. Szymanski[12] has now derived a new master DNMR bandshape equation, initially for intramolecular exchange, that contains the symmetries of the rearranging species. The equation is formulated in composite Liouville space (c space) of dimension d_c,

$$d_c = n_s d_p, \tag{1}$$

where n_s is the number of chemically distinct species in the system and d_p is the dimension of each primitive Liouville space corresponding to permutamers of each of the species. Each species is represented by only one of its permutamers, and so this approach differs from the earlier one of Kleier and Binsch,[13] where the dimension of the composite Liouville space was

$$d_c = (i + \ldots + n)\, d_p. \tag{2}$$

The initial dimensions of the spectral matrices in Szymanski's approach are significantly smaller than those in the more conventional approach, even before factorization. The group theoretical formulism developed by Szymanski enabled him to give precise definitions to concepts of macroscopic and microscopic exchange invariance of symmetry. These two invariances lead to corresponding factorizations of the spectral matrices, thus aiding the computation. The method has been applied to octahedral molybdenum and tungsten complexes of the type H_4ML_4, where L is a tertiary phosphine ligand. The most energetically favoured geometries for these complexes should be the trigonal dodecahedron (D)[**1**] and square antiprism (A)[**2**,**3**], with the latter occurring in two enantiomeric forms. Conventional DNMR bandshape calculations for a process that interconverts the four ^{1}H and four ^{31}P nuclei of the D and A isomers would involve

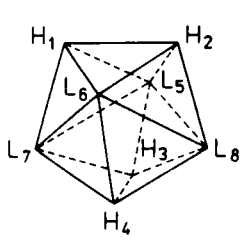

[1]

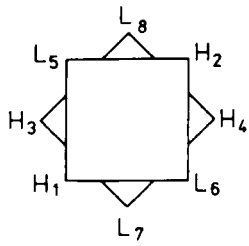

[2]

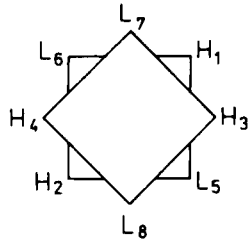

[3]

a block dimension of 1728×1728, an impossible task. The macroscopic symmetry factoring reduces the maximum block size to 328×328 for non-mutual processes and to 112×112 and 216×216 for mutual processes in the isomers D and A respectively.

This rigorous theoretical treatment was further extended to intermolecular exchange processes,[14] where the essential difference is that molecules do not retain their integrity during the exchange and the concept of microscopic symmetry invariance is no longer valid. Again major reductions in size of the spectral matrices result from this method. The same author has produced a Fortran program EXSYM that simulates DNMR bandshapes according to the new master equation and allows examination of the effect of magnetic equivalence breaking.[15] This effect arises when a set of magnetically equivalent nuclei does not preserve its integrity during exchange. A simple example is an AB_2 system where the static spectrum is independent of the scalar coupling J_{BB}. If, however, the A and B nuclei are exchanged by some dynamic process, the DNMR bandshapes become sensitive to the coupling between the equivalent nuclei, particularly near the slow-exchange limit. The effect is small in general, but may generate errors in bandshape analyses if it is neglected. For spin-½ nuclei the effect may sometimes be totally absent—it depends on which J couplings are involved.

Levitt and Beshah[16] have warned of the dangers of over-simplification in the treatment of symmetrical exchanging systems, and chose the heptamethylbenzenonium ion as an illustration. Its ^1H spectrum consists of just four lines, and therefore, despite the fact that each methyl spin is transported over seven sites, there is a temptation to treat the system as a four-site rather than a seven-site exchange problem. The authors have derived criteria for deciding when such reductions are possible. The problem reduces to the diagonalization of the appropriate Liouville superoperator $\hat{\hat{L}}$. This can be expressed in block-diagonal form if a symmetry-adapted basis can be chosen. One such symmetry element is the interchange of sites A_1 and A_2, corresponding to reflection in the horizontal plane. The exchange of the pair B_1/C_1 with the pair B_2/C_2 represents another symmetry operation, namely reflection in the vertical plane. It follows that the group of $\hat{\hat{L}}$ is

isomorphic with the point groups D_2 and C_{2v}, and the seven-dimensional representation can be reduced by standard methods to the dimension of four. In other cases, where no symmetry elements of $\hat{L}$ can be found, no reduction in the dimension of the problem is possible, even though the number of sites may exceed the number of different resonance frequencies. In general, reduction in dimension is possible if the sites not only have the same frequency, but also possess the same exchange rates with all other sites or, at least, the exchange superoperator has a symmetry element involving interchange of the equivalent sites.

2. DEVELOPMENTS IN DNMR THEORY, METHODS AND APPLICATIONS

2.1. One-dimensional methods

2.1.1. Bandshape analysis theory

The well-established computer programs of Binsch continue to be widely employed as the basis for total bandshape analysis (BSA), where the fittings of experimental and computer synthesized spectra are performed either visually (DNMR3)[13,17] or by an iterative procedure.[18] No major developments in either theory or methodology have occurred in recent years, but certain special cases of BSA have been investigated further. Kaplan[19] has examined the situation when an absorption lineshape is modified by another constituent the absorption signal of which cannot be observed experimentally either because of its low concentration or large linewidth. The exchanging system

$$A \rightleftharpoons B \rightleftharpoons C$$

was considered, where B is in very low concentration and the spectra appear to show exchange only between A and C. The question posed is whether the experimental lineshape can be expressed as a pseudo-exchange between A and C. Using density matrix arguments, the conclusion was that a direct two-site exchange model for A and C is appropriate when $i\Delta\omega_B - T_{2B}^{-1}$ can be neglected compared with $k_{BA} + k_{BC}$, where $\Delta\omega_B = \omega_{0B} - \omega$, and T_{2B}, k_{BA} and k_{BC} are respectively transverse relaxation times and rate constants involving B. If the above term cannot be neglected, there will be a distortion of the lineshape due to an imaginary component, i.e. an admixture of dispersion into the absorption lineshape.

The standard theory of NMR bandshapes in the presence of chemical exchange assumes exponential relaxation of nuclei. Kaplan[20] has now proposed a new model for non-exponential chemical exchange that depends explicitly on the overlap of vibrational normal modes in the two exchange

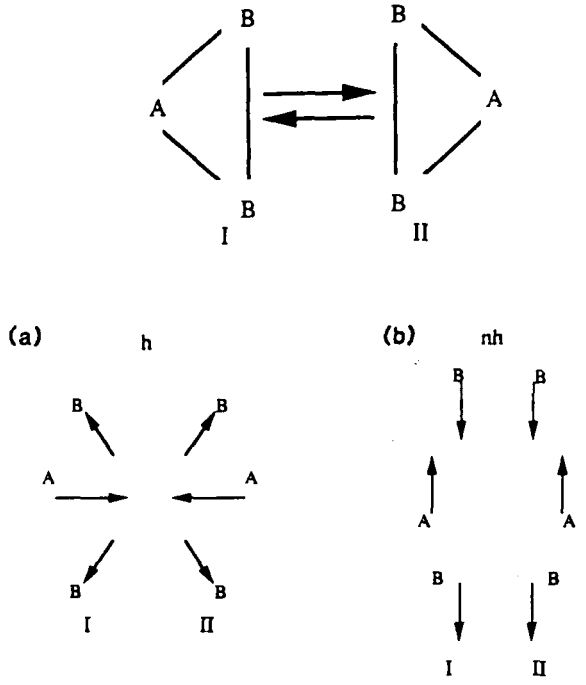

Fig. 1. Molecules (A, B, B) in configurations I and II. Representation of (a) hopping (allows for a I to II transition) and (b) non-hopping (no transitions allowed) vibrational modes.

configurations. A molecule (A, B, B) moving between configurations I and II was used to illustrate the theory (Fig. 1). The hopping mode, h, allows transitions between these configurations whereas the non-hopping mode, nh, will not, because of the small overlap of the wavefunction for I and II. Additionally, there will be internal transitions within I and II between the hopping and non-hopping modes. Density matrix equations for the exchange process were derived and lineshapes presented for a choice of determining parameters.

In some earlier work Vasavada and Kaplan[21] described a theoretical investigation of the effects of cross-relaxation in a two-spin system relaxed only by an intramolecular dipole–dipole mechanism. They calculated lineshapes for a two-spin system undergoing slow molecular tumbling, i.e. for $\omega\tau \gg 1$, but with $1/\tau \ll$ dipolar linewidth. When the lines strongly overlap, i.e. when the spins I and S are nearly like, a curious sharp dip was predicted to occur in the centre of the calculated spectrum. This has now been confirmed experimentally by Anet and O'Leary,[22] who have also defined the conditions for maximum peak separation and for coalescence. The rela-

tionships between lineshapes for transverse cross-relaxation and for chemical exchange are also discussed.

The general absorption mode lineshape $V(\omega)$, valid for like, nearly like and unlike spins, is given by

$$V(\omega) = -\mathrm{Re}\{[1\,,1]\boldsymbol{A}^{-1}[{}^{1}_{1}]\}, \tag{3}$$

where

$$\boldsymbol{A} = \begin{bmatrix} \mathrm{i}(\omega - \Delta) - 1/T_2^I & -1/T_2^{IS} \\ -1/T_2^{IS} & \mathrm{i}(\omega + \Delta) - 1/T_2^S \end{bmatrix}.$$

This equation can be solved to give numerical or explicit values of $V(\omega)$. For the case of interest the slow-tumbling limit holds and $V(\omega)$ can be expressed in terms of a relaxation rate $R = 1/T_2^I = 1/T_2^S = \frac{5}{4}T_2^{IS}$, where T_2^{IS} is the transverse cross-relaxation time, by

$$V(\omega) = \frac{2250R\omega^2 + 250R\Delta^2 + 90R^3}{625\omega^4 + 2050R^2\omega^2 - 1250\Delta^2\omega^2 + 81R^4 + 450R^2\Delta^2 + 625\Delta^4}. \tag{4}$$

This function exhibits two maxima for $R/\Delta < 5\sqrt{11}$. Under these conditions the peak frequencies are

$$\pm\tfrac{1}{15}[50\Delta(25\Delta^2 + 9R^2)^{1/2} - 9R^2 - 25\Delta^2]^{1/2}, \tag{5}$$

and the largest separation of these peaks, which occurs for $R/\Delta = 10\sqrt{\tfrac{2}{3}} \approx 8.165$, is 3.33Δ. This is 67% larger than the chemical shift difference 2Δ between spins I and S, and is quite unlike the usual exchange situation, where coalescence occurs at

$$k = \Delta/\sqrt{2} \tag{6}$$

and where the separation of the peaks is always less than the chemical shift difference in the absence of exchange. Signal shapes for a mutually exchanging AX system with $J_{AX} = 0$ were calculated for different values of k/Δ. The net shapes result from absorption (Lorentzian) and dispersion lines (Fig. 2).

Experimental support for this theory was achieved by obtaining the ^{1}H NMR spectra of the aromatic hydrogens of the *p*-chlorobenzenesulphonate ion present in rod-like micelles in a viscoelastic solution. Rotation about the 1,4-positions of the aromatic ring will be fast, whereas rotation perpendicular to this direction will be very slow, and thus pairs of hydrogens *ortho* to one another on each side of the ring, which are unaffected by the fast rotation along the 1,4-axis, give rise to very broad lines by virtue of

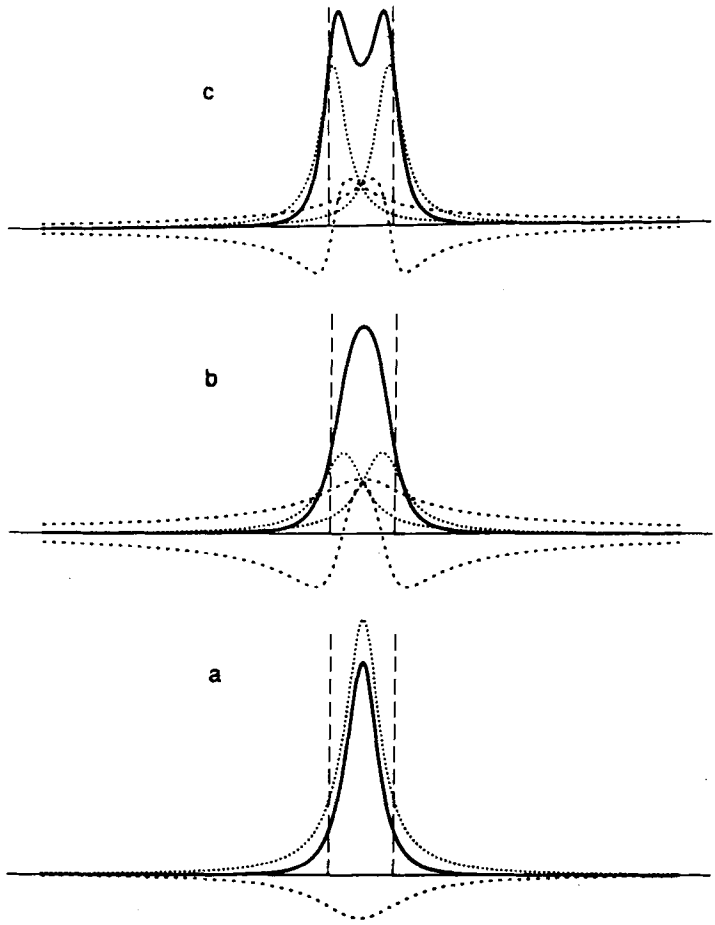

Fig. 2. Calculated lineshapes (——) for exchange ($k > \Delta$ or $k < \Delta$) in an equally populated uncoupled two-spin system with $1/T_2 = 0$ for (a) $k/\Delta = 1.1$, showing a dissection into positive (·····) and negative (------) Lorentzian lines, and for (b) $k/\Delta = 0.8$ and (c) $\Delta = 0.5$, showing a dissection into two positive Lorentzian lines (·····) and two dispersion components of opposite signs (------). The chemical shift difference 2Δ is shown by the vertical dashed lines.

intramolecular dipole–dipole relaxation. The 500 MHz experimental spectrum is shown above the theoretical spectrum, which was simulated for a cross-relaxation rate of $390\,s^{-1}$ (Fig. 3).

A theoretical study has been made[23] of the NMR lineshape function of a two-site exchange model of biological importance. The bound site was allowed to be in the slow-motion regime characterized by the inverse

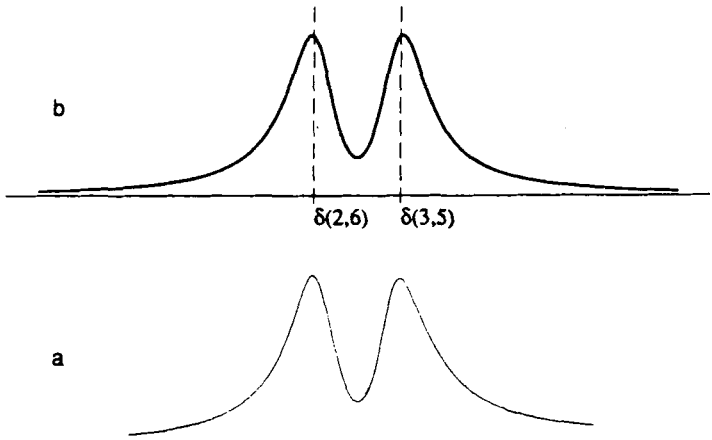

Fig. 3. Experimental (a) and calculated (b) 500 MHz ^{1}H NMR spectra of the aromatic protons of *p*-chlorobenzenesulphonate ion present in rod-like micelles in a viscoelastic solution. The parameters used in the calculations are $\delta(2,6) - \delta(3,5) = 0.42$ ($\Delta = 660\,\text{rad}\,\text{s}^{-1}$), $1/T_2^I = 1/T_2^S = 487\,\text{s}^{-1}$, $1/T_2^{IS} = 390\,\text{s}^{-1}$, $1/T_2^{\text{other}} = 40\,\text{s}^{-1}$. The experimental spectrum was obtained with a line broadening of 5 Hz, which gives a contribution of $1/T_2^{\text{other}}$ of $15.7\,\text{s}^{-1}$.

quadrupole interaction of one bound site being in the same range as the reorientational correlation time. Various chemical exchange models were compared and several different physical situations investigated.

Multisite exchange in conventional small molecule systems was the subject of a BASIC computer program, which provided a least-squares estimation of parameters influencing lineshapes. Up to five exchanging sites could be treated.[24] The relationship between such NMR-observed rate constants and intramolecular exchange rates has been examined in some detail by Green, Wong and Sella.[25] The authors argue that rate constants based on DNMR methods differ from those of the chemical process(es) giving rise to the exchange and that the derived chemical rate constants depend on the mechanism under consideration. They examine a number of particular systems starting with an AB case. The observed magnetization transfer rate constants are $k_{\text{obs}}(\text{A} \rightarrow \text{B})$ and $k_{\text{obs}}(\text{B} \rightarrow \text{A})$, and it is necessary to relate them to the rate constant for the "elementary process" or "chemical event" that gives rise to the transfer. For a general degenerate chemical exchange the species at the midpoint of the symmetrical reaction profile can decay back to the ground state structure along a number of pathways, as well as proceeding to the new ground state species. Only those pathways that result in magnetization transfer will be detectable by NMR techniques. For the AB case it takes on average two chemical events to give rise to an

observable magnetization transfer, which is equivalent to saying that half of the chemical processes are in a sense invisible by NMR techniques. The same argument applies to coalescence temperature studies, where one can write

$$k_A = k_{obs}(A \rightarrow B) = \frac{\pi \Delta \nu}{\sqrt{2}} \quad \text{or} \quad k_{chem} = \frac{2\pi \Delta \nu}{\sqrt{2}}. \tag{7}$$

These alternative descriptions relate back to the early formative days of DNMR. The present authors have formalized the difference between k_{obs} and k_{chem} values in the equation

$$k_{chem}(A \rightarrow B) = \frac{N_A}{\alpha} k_{obs}(A \rightarrow B) \tag{8}$$

where $\alpha = n_A n_B / n_{tot}$. Here n_A and n_B are the numbers of nuclei in sites A and B, and n_{tot} is the total number of nuclei involved in the exchange process. N_A is a normalization constant ensuring that the rate constant refers only to the concentration of the chemical compound and is independent of site population. It preserves the mass balance and is equal to the number of nuclei in the site from which magnetization is transferred.

An alternative approach is the use of the transmission coefficient κ in the Eyring equation (9) to relate the two types of rate constant:

$$\ln k = \ln\left(\frac{\kappa k_B T}{h}\right) - \frac{\Delta G^{\ddagger}}{RT}. \tag{9}$$

When k_{chem} is used in this equation, κ should always be unity. When k_{obs} is used, κ should be set as α/N. In the final analysis, however, researchers have a choice as to which rate constant to use in practice. Those who consider themselves first and foremost spectroscopists may opt for the NMR-based parameter k_{obs}, whereas chemists concerned primarily with mechanisms may prefer a rate constant relating to the elementary stage of a kinetic scheme. The important point, however, is that it should always be made clear which rate constant is being employed in any particular study.

Finally, a paper of somewhat more peripheral interest to the main thrust of this review should be mentioned. The theory of saturation factors, due to over-rapid pulsing, has been developed for the case of exchange between two species.[26] It was found that the saturation factors were not independent of the concentration of the chemical species. Errors of up to 10% in the measurement of the factors can occur if exchange effects are not accounted for.

2.1.2. *Applications to liquids and solutions*

(a) Pyramidal inversion. This structural phenomenon has been extensively investigated by DNMR techniques for decades. Earlier work was concerned primarily with nitrogen inversion, whereas recent studies have been directed more towards inversions of chalcogen atoms S, Se and Te coordinated to transition metals.

Studies in this area since 1986 have been particularly concerned with sulphur inversion. The fully iterative DNMR5 program[18] has been used to measure the kinetics of S inversion in bis(π-cyclopentadienyl) complexes of molybdenum and tungsten with thio ligands.[27] Accurate BSA using the DNMR3 program[17] has been applied to Group VI metal tetracarbonyl complexes. For example, the complexes *cis*-$[M(CO)_4(RSCH_2CH_2SR)]$ (M = Cr, Mo, W; R = Me, Et, ^{i}Pr and ^{t}Bu) exist as separate DL and *meso* isomers (invertomers) in low-temperature solutions, whereas room-temperature solutions exhibit exchange between the two species by S inversion as shown [**4**].[28,29] Rates of inversion were based on total BSA of ^{13}C–$\{^1H\}$ spectra over a wide temperature range, typically −80–10°C. Energy barriers represented by $\Delta G^{\ddagger}$ (298 K) were in the range 40–54 kJ mol^{-1}, following the trend W > Cr > Mo. In the Mo complexes ^{95}Mo chemical shifts at ambient

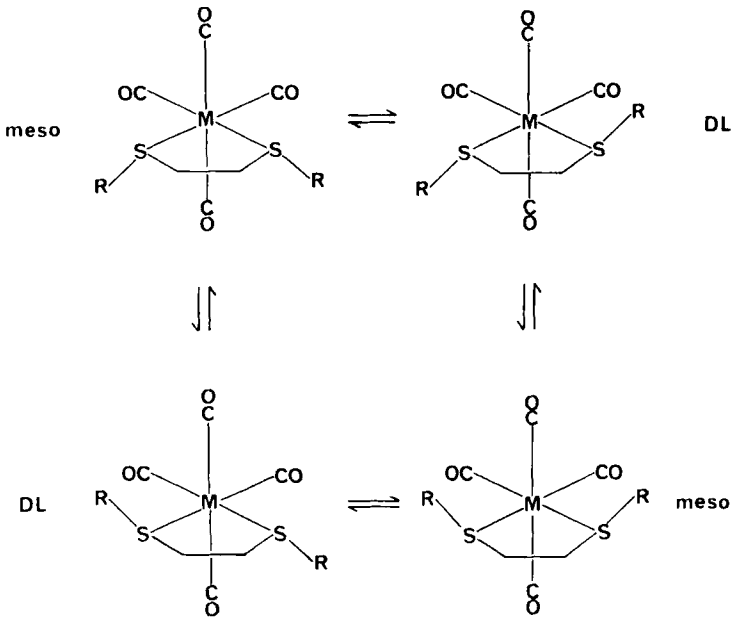

[4]

temperatures were reported,[29] but attempts to measure such shifts at low temperatures when S inversion was slow failed as a result of excessive line broadening of the quadrupolar nucleus.

A number of studies have involved platinum(II) complexes of sulphur ligands. Variable-temperature ^{1}H spectra were the basis of a study[30] of *cis*- and *trans*-$[Pt\{S(CH_2CHMe_2)_2\}Cl_2]$ and $[Pt(PPh_3)_2L]ClO_4$ (HL = isopropylthioacetic acid), whereas ^{195}Pt spectra were used for examining platinum(II)–methionine complexes.[31] The nuclide ^{195}Pt is rarely employed for BSA studies on account of its very wide chemical shift spread, which normally leads to such excessive line broadening in the coalescence region that signals are barely detectable. However, if chemical shift differences are very small, as in subtly different diastereoisomeric pairs, rate processes may be measured that might remain undetected by magnetically less sensitive nuclei. In the present study[31] moderately reliable exchange rate data were obtained despite the typically large temperature coefficients of the ^{195}Pt signals of these complexes. Energy values were in the range 64–70 kJ mol^{-1} for coalescence temperatures in the range 338–370 K. Exchange between pairs of DL isomers due to sulphur or selenium inversion was detectable in the complexes $[PtCl_2(L\text{-}L)]$ (L-L = $[(C_5H_4SCH_3)_2Fe]$, $[(C_5H_4SeCH_3)_2Fe]$ and $[(C_5H_4SCH_3)_2Ru]$) [**5**].[32] The ^{1}H signals of the cyclopentadienyl rings

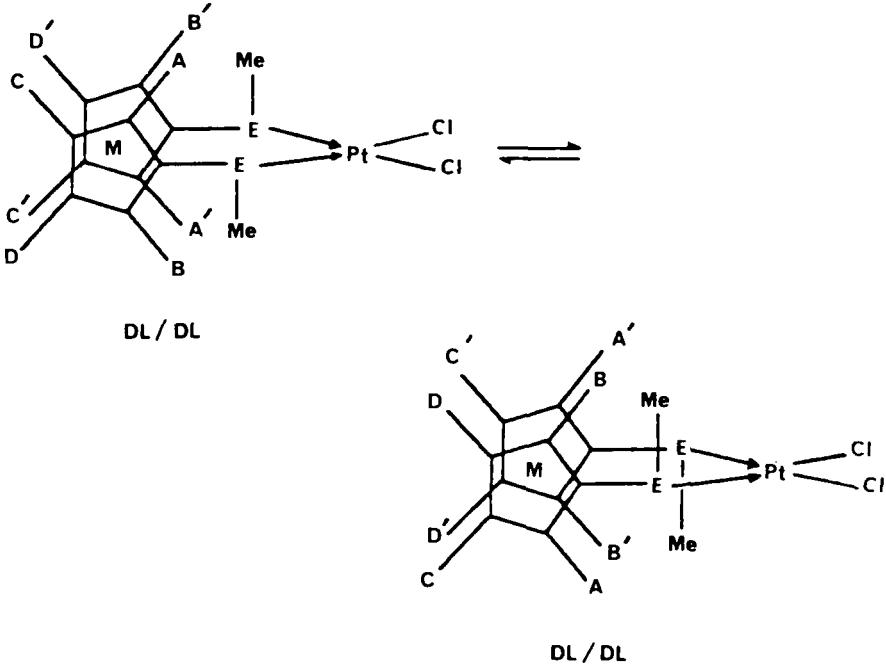

[5]

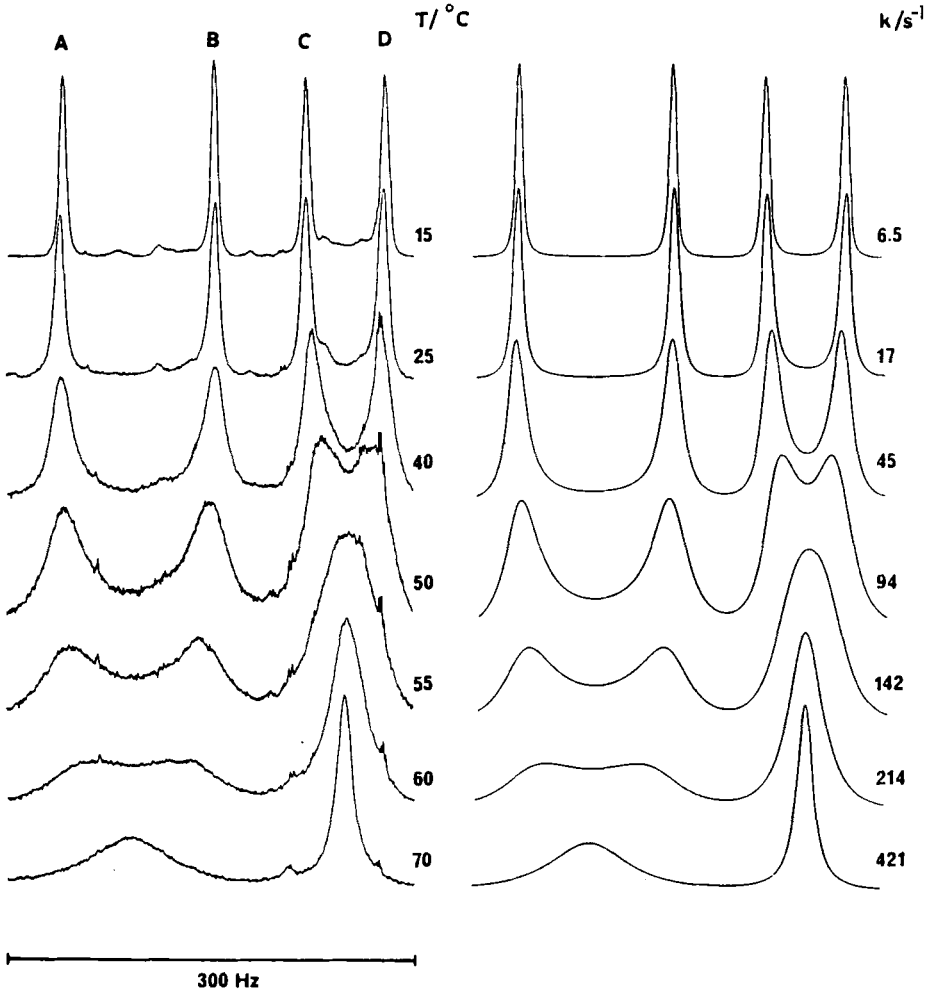

Fig. 4. Experimental (left) and computer-synthesized ^{1}H NMR spectra (methine region) of $[PtCl_2(C_5H_4SMe)_2Ru]$, showing the best-fit rate constants for each temperature.

were permuted by this double pyramidal inversion process, so that the ring proton spectra followed the dynamic scheme ABCD⇌BADC. This analysis was possible since the *meso* isomer was present in only very low abundance, and its signals could be omitted from the BSA without loss of accuracy. The matchings of experimental and computer synthesized spectra are shown in Fig. 4. Sulphur inversion energies were calculated to be 64.2 and 66.3 kJ mol^{-1} for the ferrocene and ruthenocene complexes respectively. Selenium inversion in the ferrocene complex occurred with an energy of 78.8 kJ mol^{-1}.

Sulphur inversion in new $ReX(CO)_3$ complexes with hybrid sulphur–phosphine ligands have been reported.[33] The ligands were mono- and bis(*o*-methylthio) derivatives of triphenylphosphine, and both act as S/P monochelates towards $ReX(CO)_3$. The coordinated S atom in these complexes undergoes pyramidal inversion, which was monitored by the effects on the coordinated SMe signals and, in the case of the bis[(*o*-methylthio)phenyl]phenylphosphine, on the uncoordinated SMe signals.

(*b*) *Cyclopentadiene ring rotations.* The barrier to rotation of η^5-cyclopentadienyl (Cp) groups about the ring–transition-metal axis is known to be particularly low and not directly measurable by solution NMR spectra. However, the cationic complexes $[(\eta^5\text{-Cp})(R_3P)_2\ (\eta^2\text{-olefin})M]^+$ (M = Ru or Os) do exhibit a splitting of the Cp signals in their ^{13}C and ^1H solution spectra at temperatures below −80°C, from which an approximate energy barrier of 34 kJ mol^{-1} was calculated.[34] Sterically demanding substituents on Cp rings cause considerable restriction to rotation of such rings in metal sandwich compounds. Recent studies of this type have involved 1,1′,3,3′-tetrakis(trimethyl)ferrocene,[35] 1,1′,3,3′-tetrakis- and 1,1′,2,2′,4,4′-hexakis-(trimethylsilyl)cobaltocenium ions,[36] 1,1′3,3′-tetra-*t*-butylcobaltocenium ion[37] and 1,1′3,3′-tetraalkyl-ferrocenes and -ruthenocenes.[38] Detailed analyses of these problems[35,38] identified five rotamers with eclipsed Cp rings (labelled "e") and five with fully staggered rings (labelled "s") as shown in [**6**]. The ground state structures comprise the enantiomeric e_0 pair with eclipsed Cp rings and the four R substituents in a fully staggered arrangement and eclipsed only by ring hydrogens. Rotation of the substituted Cp rings causes exchange between the pair of e_0 rotamers, and this can be measured by the coalescence of methine ^1H and ^{13}C NMR signals. These coalescences were noted to be somewhat asymmetric in the case of 1,1′3,3′-tetra(*t*-phenyl)ferrocene and this was attributed to some contribution (*ca.* 18% at −30°C) from the $s_{1/2}$ rotamer [**6**]. Energy barriers based on ^1H and ^{13}C BSA were in the range 45–57 kJ mol^{-1}.

(*c*) *Metal–arene rotations.* NMR BSA techniques have contributed notably to the understanding of the stereodynamics of metal carbonyl complexes with η^6-hexaalkylbenzenes. In the case of $[Mo(CO)_2LL']$ (L = η^6-hexaethylbenzene, L′ = PEt_3), detailed bandshape changes were interpreted in terms of uncoordinated rapid rotation of the ethyl groups about the aromatic ring and stereoisomerization of ligand L.[39] Energies of ethyl site exchanges were associated with $\Delta G^{\ddagger}$ values in the range 33–48 kJ mol^{-1}. In contrast, the ^{13}C NMR bandshape changes of $[Cr(CO)_2L]\ (\mu\text{-}N_2)]$ (L = η^6-hexaethylbenzene) at low temperatures were attributed to slowed ethyl group rotation.[40] The hexapropylbenzene ligand adopts a D_{3d} symmetry, with alkyl substituents alternately up and down, and this is retained in the $Cr(CO)_3$ complex, where a decoalescence phenomenon in its ^{13}C spectrum

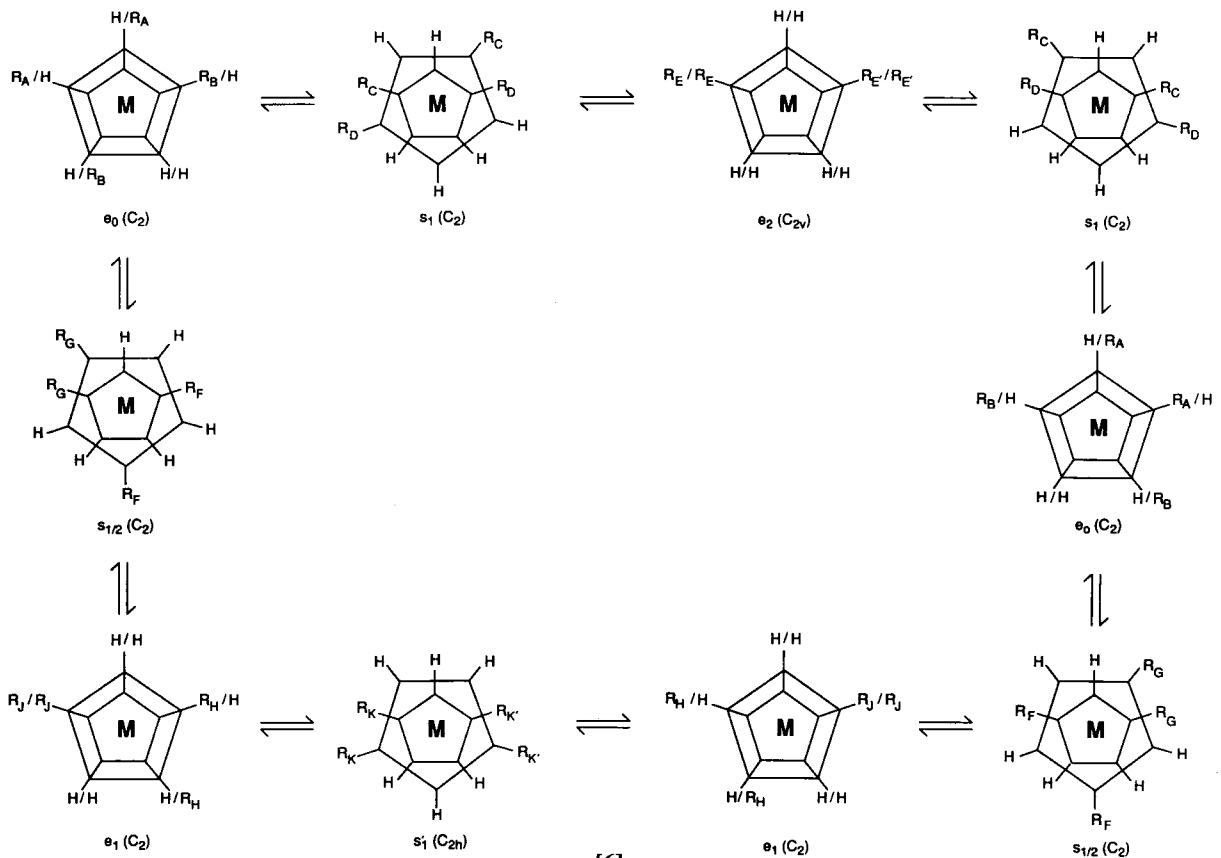
H/R_A
R_A/H
R_B/H
M
H/R_B
H/H
e_0 (C_2)
s_1 (C_2)
H/H
R_E/R_E
R_E'/R_E'
e_2 (C_2v)
s_1 (C_2)
R_G
R_F
s_1/2 (C_2)
e_0 (C_2)
H/H
R_J/R_J
R_H/H
H/R_H
e_1 (C_2)
R_K
R_K'
s'_1 (C_2h)
R_H/H
R_J/R_J
e_1 (C_2)
s_1/2 (C_2)

[6]

is attributed to slowed propyl rotation.[41] A somewhat higher rotation barrier was calculated for rotation of the dimethylsilyl group in the analogous complex $[Cr(CO)_3\{C_6(SiMe_2H)_6\}]$.[42]

The ^{13}C NMR spectrum of $[Cr(CO)_3(C_6Ph_6)]$ indicated that Cr is π-bonded to a peripheral phenyl ring. This ring exhibits slowed rotation on the NMR time scale with an activation barrier of *ca.* 51 kJ mol^{-1}, a value much lower than those associated with non-coordinated hexaaryl benzenes bearing *ortho* or *meta* methyl or methoxy substituents.[43] Metal π-hexaethylbenzene complexes and their protonated derivatives have been studied in some detail.[44,45] Low-temperature NMR studies of solutions of $[(C_6Et_6)Cr(CO)_2NO]^+$ and $[(C_6Et_6)Cr(CO)(CS)NO]^+$ revealed that each molecule exists as a single conformer.[45] At higher temperatures the latter complex undergoes two fluxional processes, namely tripodal rotation and uncorrelated rotation of ethyl groups. The related complex $[Mo(CO)_2(PPh_3)(\eta^6$-1, 3, 5-triethyl-2, 4, 6-tris(trimethylsilylmethyl)benzene] exhibits three fluxional processes, namely slowed ethyl group rotation, slowed rotation of the Ph_3P ligand about the Mo–P bond, and slowed rotation about the arene–Mo tripodal moiety bond.[46] This complex is an example of gated stereodynamics, a further example of which occurs in the complex [1,4-bis(4,4-dimethyl-3-oxopentyl)-2,3,5,6-tetraethylbenzene]chromium tricarbonyl.[47]

A variety of chromium complexes involving mesityl ligands have been isolated.[48] Bis(η^6-bimesityl)chromium exhibits restricted rotation that exchanges two rotamers with the bimesityl ligands twisted through 90° (or 270°) with respect to the sandwich axis [7]. In contrast, slowed rotation about the metal–arene bond was *not* observed in complexes of types (η^6-arene)dicarbonyl(triphenylphosphine)-chromium(0) and -molybdenum(0).[49] Instead, restricted rotation of the PPh_3 ligand about the M–P bond occurs with $\Delta G^{\ddagger}$(473 K) of *ca.* 36.6 kJ mol^{-1} if the arenes are heavily methyl-substituted.

More recent studies[50,51] in this area have invoked empirical force-field

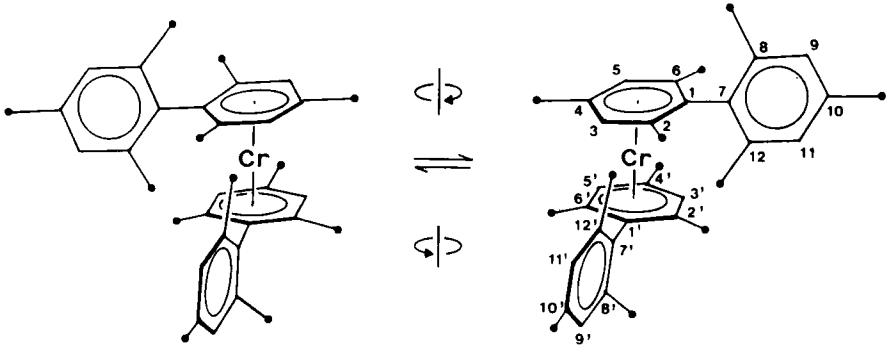

[7]

calculations to aid the interpretation of the NMR bandshape studies. The authors conclude that the steric effects of the ethyl groups of a hexahapto-coordinated arene can lead to slowed rotation about the η^6-arene–metal bond. The rotation barriers, however, are at the lower limit of the NMR chemical shift time scale ($\Delta G^{\ddagger}$ = 33–34 kJ mol^{-1}), and may be of a similar magnitude to the ethyl group rotational barrier. A recent ^{13}C NMR study[52] of a related $Mo(CO)_3$ complex **[8]** yielded free energies of activation for three dynamic processes as follows: free arene ethyl group rotation 47.3 ± 2.1 kJ mol^{-1}, complexed arene ethyl group rotation 47.7 ± 2.1 kJ mol^{-1} and $Mo(CO)_3$ tripod rotation 28.0 ± 2.1 kJ mol^{-1}. The last-mentioned process required cooling to −140°C in $CDCl_2F$ in order to "freeze" the rotation effectively.

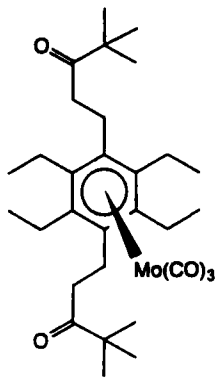

[8]

(*d*) *Metallotropic shifts*. NMR can often distinguish unambiguously between different metal–ligand shift mechanisms. A typical example is the study of the rearrangement mechanisms in the slipped triple-decker complexes $[Cp_2Rh_2(cot)]$[24] and $[Cp^*_2Co_2(cot)]^{2+}$ ($Cp^* = C_5Me_5$, cot = cyclooctatetraene).[53] Rigorous bandshape analysis of their ^{1}H spectra over a wide temperature range (245–358 K) showed that out of five possible exchange mechanisms, the one involving a 1,3-shift of one Rh atom at a time along the cot ring periphery gave the best agreement between experimental and computed spectra for the dirhodium complex, whereas for the dicobalt complex a 1,2-shift of both Co atoms was the mechanism indicated by DNMR.

Metallotropic shifts involving metal chelate complexes are rather less common. In general two mechanisms are possible. One involves the breaking of both metal–ligand bonds followed by an appropriate movement

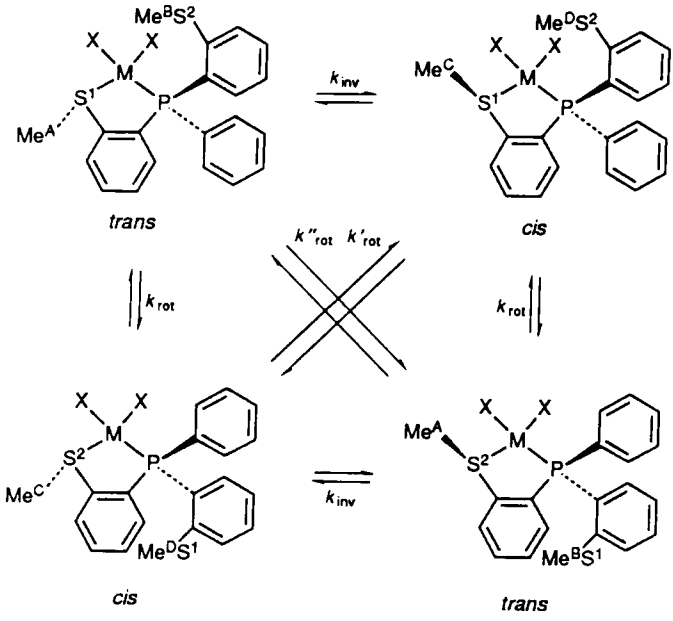

[9]

of the metal moiety relative to the ligand to form two new bonds. The second involves the retention of one metal–ligand bond and the breaking/remaking the second bond via some type of rotation mechanism. The latter mechanism was favoured in a study of the complexes [M{PPh(C_6H_4SMe-*o*)}X_2] (M = Pd, Pt; X = Cl, Br, I).[54] The presence of pyramidal inversion of the coordinated S atom leads to observable NMR exchange of four species [**9**]. Exchange of uncoordinated and coordinated SMe groups occurred at rates comparable to those of S inversion. The mechanism of SMe exchange was thought to involve weakening of the M–S bond followed by rotation about the intact M–P bond to form an equivalent structure. This mechanism, however, is brought into question somewhat by more recent studies involving N/N and N/S chelate ligand complexes. 2,2′:6′,2″-Terpyridine has been shown to act as a fluxional bidentate ligand in the octahedral complexes *fac*-[ReX(CO)$_3$(terpy)], *fac*-[PtXMe$_3$(terpy)] and *cis*-[M(CO)$_4$(terpy)] (M = Cr, Mo, W).[55–57] The ligand switches between equivalent N/N bonding modes by a mechanism that involves *both* M–N bonds breaking and the metal moiety rotating through an angle equal to the N–M–N angle of the octahedral centre [**10**]. Confirmation of this mechanism comes from the averaging effects experienced by the equatorial Pt–methyl signals in the Pt^{IV} complexes.[56] Rigorous BSA studies of the total ^{1}H spectrum of these complexes (Fig. 5)[57] gave very reliable energy data for

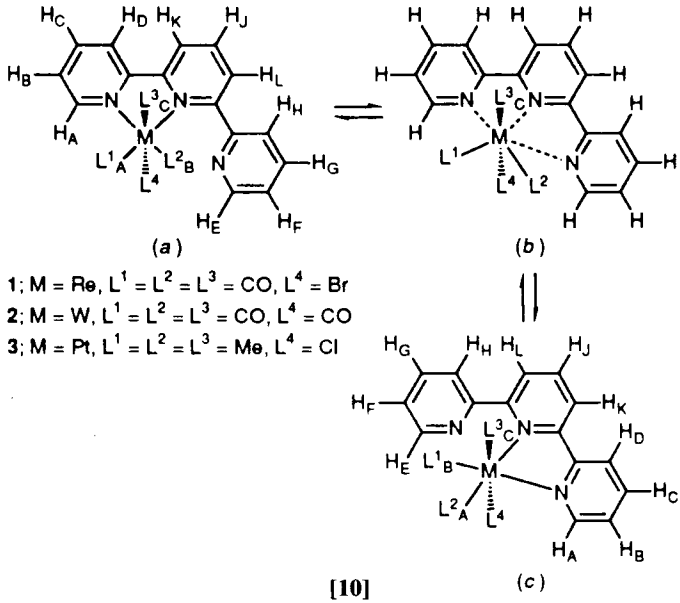

1; M = Re, $L^1 = L^2 = L^3 = CO$, $L^4 = Br$
2; M = W, $L^1 = L^2 = L^3 = CO$, $L^4 = CO$
3; M = Pt, $L^1 = L^2 = L^3 = Me$, $L^4 = Cl$

[10]

this novel M–ligand fluxion. BSA studies well below room temperature provided data on the restricted rotation of the uncoordinated pyridine ring in these complexes.

Analogous studies of Re(I)[58] and Pt(IV)[59] complexes of 2,6-bis(thioalkyl)- and 2,6-bis(thioaryl)-pyridines [11] showed that the same fluxional mechanism was operating with both M–L ligand bonds breaking and re-forming.

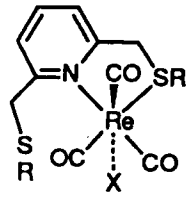

	R	X
1	C_6H_4Me-*p*	Cl
2	C_6H_4Me-*p*	Br
3	C_6H_4Me-*p*	I
4	Me	Cl
5	Me	Br
6	Me	I

[11]

Fig. 5. 250 MHz ^{1}H NMR spectra of $[ReBr(CO)_3(terpy)]$ in $(CDCl_2)_2$ in the temperature range from −10 to 130°C. Computer-simulated spectra are shown on the right, with "best-fit" rate constants for the fluxional process given.

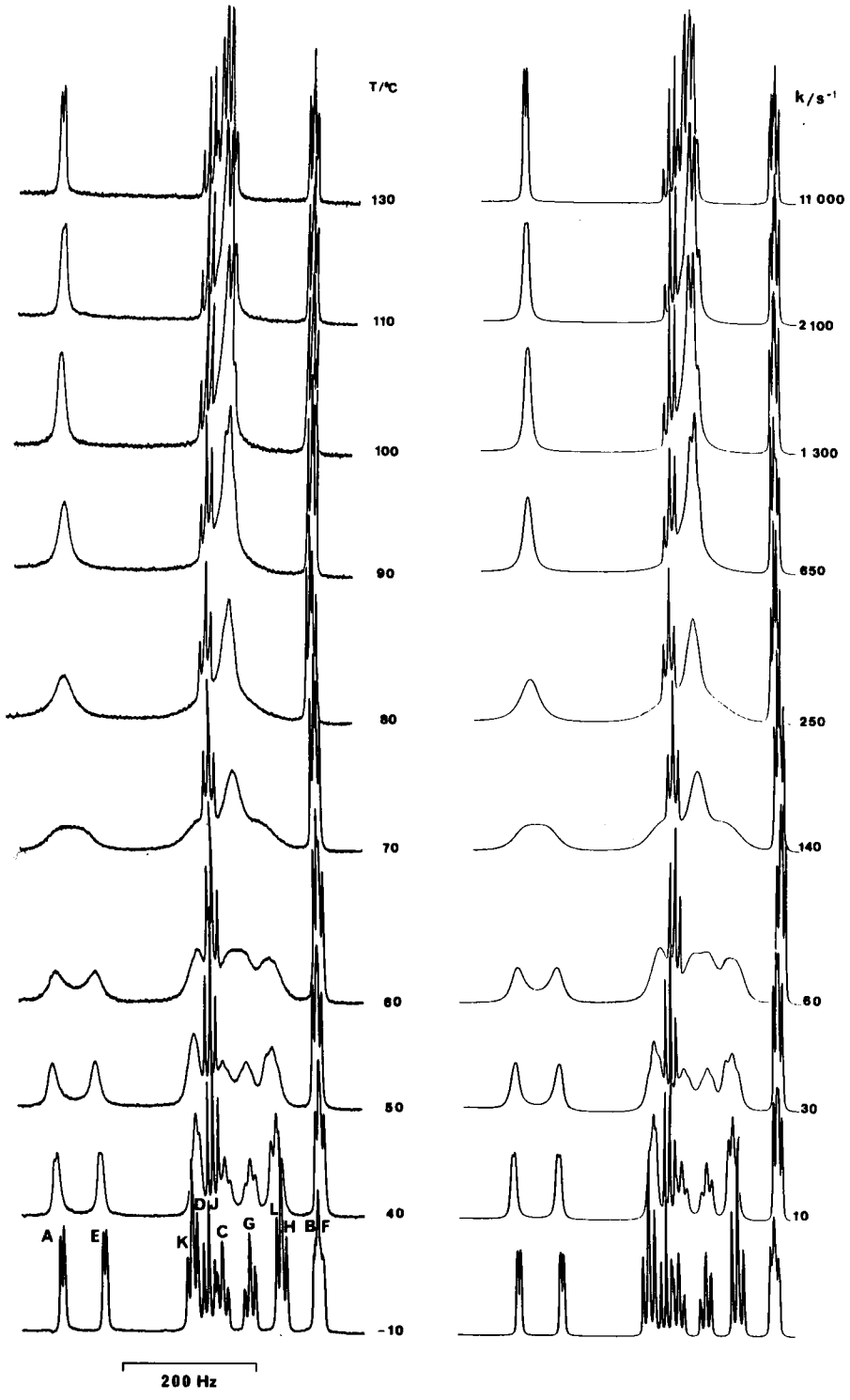
T/°C
130
110
100
90
80
70
60
50
40
-10
k/s⁻¹
11 000
2 100
1 300
650
250
140
60
30
10
A
E
K
D
J
C
G
L
H
B
F
200 Hz

(*e*) *Ring conformational changes*. Chair–chair conformational interconversions of six-membered rings are of classic importance in stereochemistry. In 1,2,3-trichalcogena[3]ferrocenophanes the trichalcogen bridge linking the two Cp rings can flip in a manner akin to that of cyclohexane. This is a relatively high-energy process,[60] in contrast to cases when the central bridging atom is a transition metal.[61–63] The [3]ferrocenophane compounds containing Te_2S, Te_2Se and Te_3 bridges have recently been studied by ^1H BSA, and $\Delta G^{\ddagger}(298\,K)$ values of 56.3, 55.4 and 51.8 kJ mol^{-1} were calculated for these respective compounds. The bandshape fittings for the Te_3 compound are illustrated in Fig. 6.[60] In transition metal complexes of these [3]ferrocenophanes the bridge reversal (BR) process was shown to be always fast on the NMR time scale. Thus, of the eight possible solution species **[12]** four weighted-averaged species are expected.[63] In fact, the spectra of the $ReX(CO)_3$ complexes indicate only two, these being essentially *meso*-1 and the DL-1 pair **[13]**. Exchange occurs between them as a result of inversion of the chalcogen atom pairs. Such a system should lead to 12 methine proton signals (A–M), 8 from DL-1 and 4 from *meso*-1. The total nuclear spin problem was

since all scalar couplings were negligibly small. For BSA, these four sets of exchanging signals required identification. This was accomplished by 2D-EXSY experiments (see Section 2.2.1) at temperatures just below those at which exchange broadening occurred. Knowledge of the assignments of these sets of signals enabled BSA to be accomplished, and good fittings based on independent values of the rate constants k_1(*meso*-1 → DL-1) and k_2(DL-1 → DL-1) were achieved.[63] This work illustrates the complementary virtues of 2D-EXSY and BSA experiments in providing reliable rate data, over a wide temperature range.

(*f*) *Miscellaneous fluxions*. Papers mentioned in this section contain certain special features relating to DNMR methodology. The analysis of exchanging AB_2 or AX_2 spin systems is quite commonplace when the scalar coupling J_{AB} or J_{AX} is treated as essentially temperature-independent. However, two recent studies have involved cases where the observable coupling constant is highly temperature-dependent as a result of a small contribution of quantum mechanical exchange coupling between hydrogen nuclei. Such couplings are well known for electrons but much less so for hydrogen nuclei in fluid solution. This type of coupling has now been detected in metallocene trihydride compounds of the type $[\eta\text{-}C_5H_5)_2MH_3]^{n+}$ (M = Mo, W, n = 1;

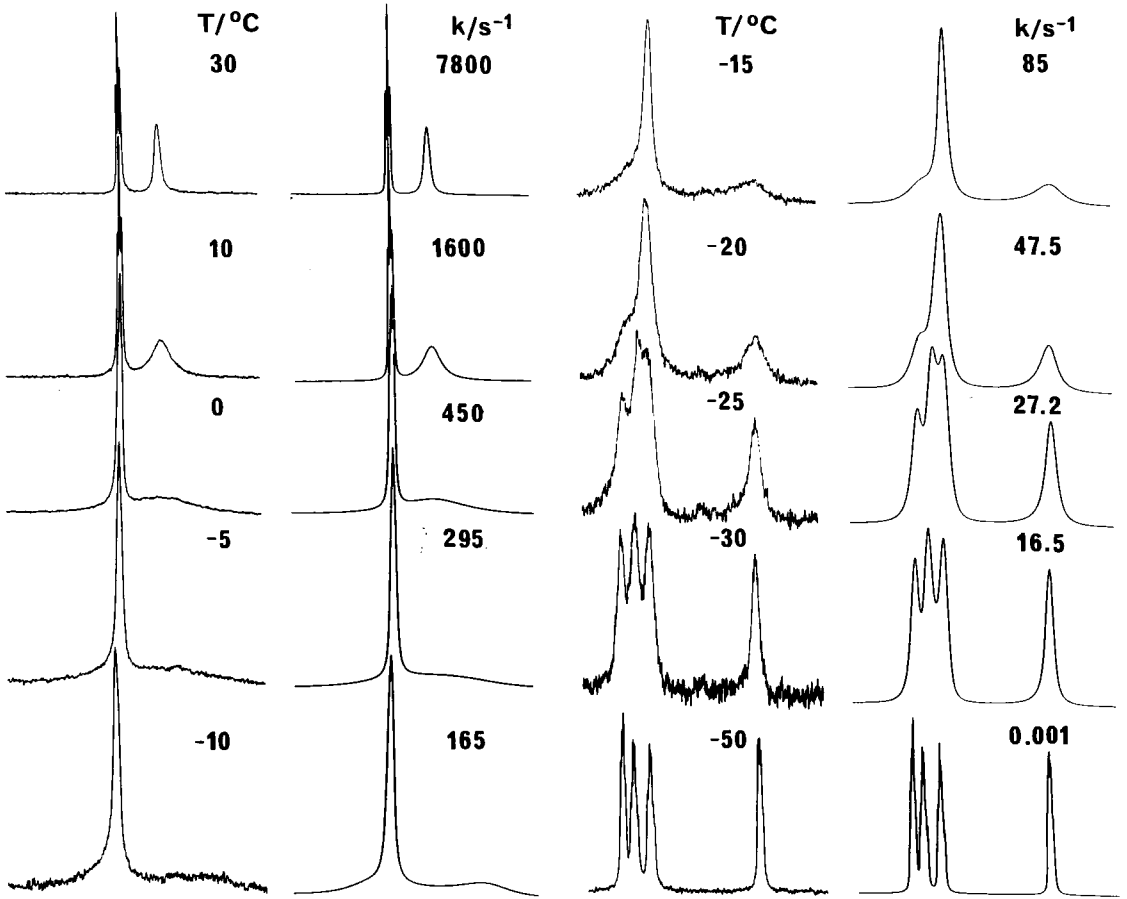

Fig. 6. Variable-temperature ^{1}H NMR spectra of $[Fe(C_5H_4Te)_2Te]$. Best-fit computer-synthesized spectra are shown alongside experimental spectra.

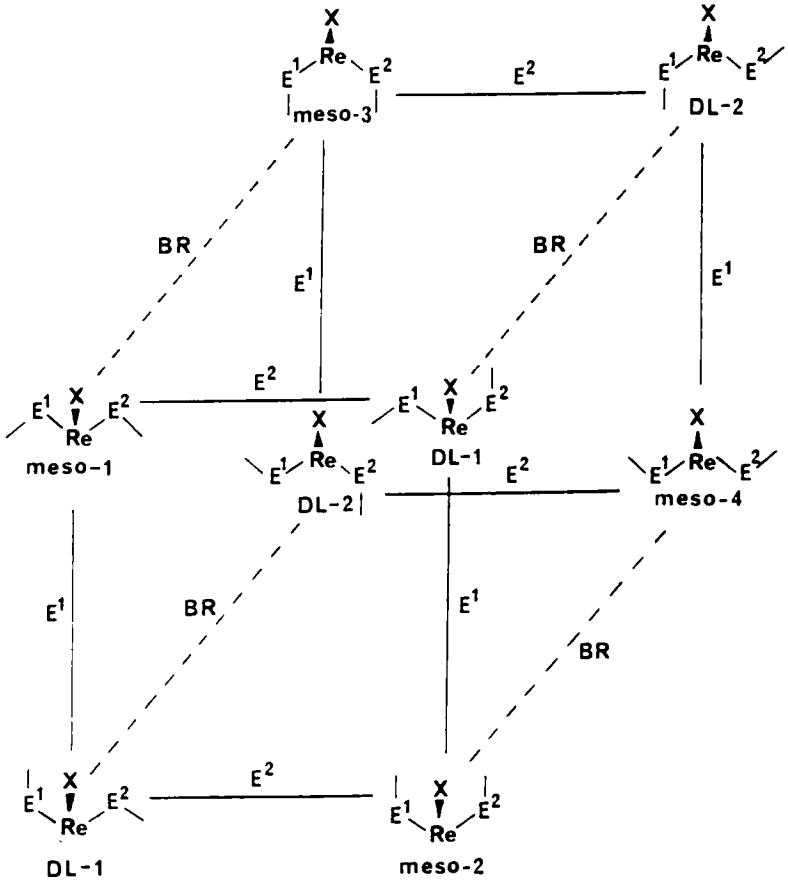

[12]

M = Nb, Ta, $n = 0$)[64] and in $[(\eta\text{-}C_6H_6)OsLH_3]^+$ (L = various phosphines).[65] Observable couplings are a combination of exchange (ex) and magnetic (mag) contributions given by

$$J_{obs} = -2J_{ex} + J_{mag} \tag{10}$$

Under certain circumstances these couplings terms can cancel, and no coupling is detected. This was found to be the case for the Nb complex, where the observed coupling decreased with decreasing temperature, became unresolvable at 243 K and then reappeared at 173 K.[64] The osmium complexes were fluxional at room temperature, giving a single signal for the hydridic protons, but low-temperature $^1H\text{-}\{^{31}P\}$ spectra consisted of well-resolved AB_2 spectra with large, temperature-dependent values of J_{AB} in the range 70–370 Hz.[65]

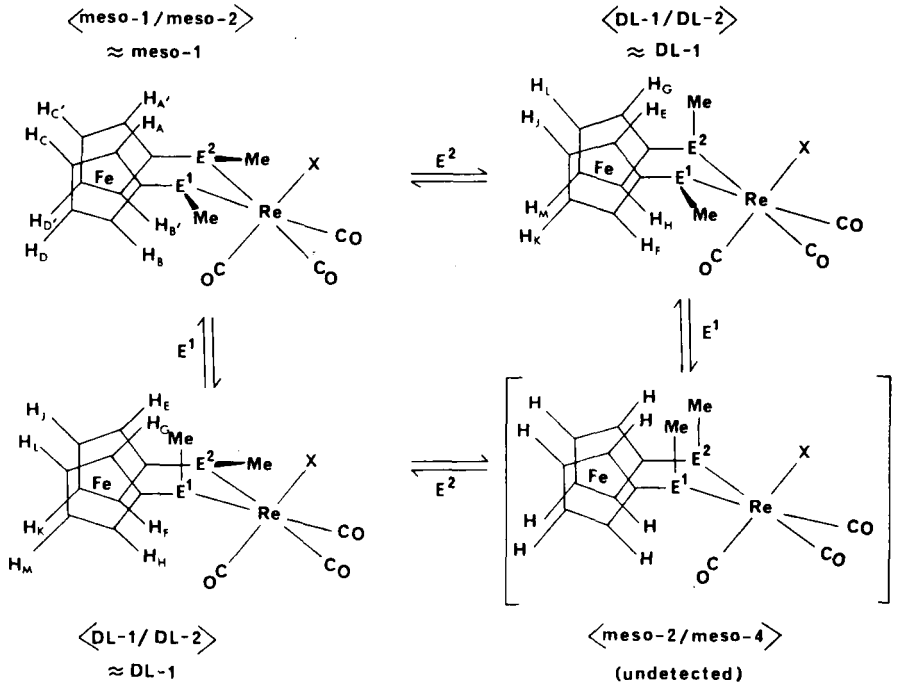

[13]

Complementary ESR and NMR investigations have been reported on the dichromium complex $[(CpCr)_2(\mu\text{-cot})]$[66] and the $19e^-$ complex $[\eta^5\text{-}C_5Ph_4H)Mo(CO)_2L_2]$ (L_2 = 2,3-bis(diphenylphosphino)maleic anhydride).[67] The variable-temperature spectra of the dichromium species were analysed in terms of a singlet–triplet equilibrium for the complex. Variable-temperature ESR spectra were more informative than NMR spectra in measuring the fluxionality (namely $\eta^5\text{-}C_5Ph_4H$ ring rotation) of the Mo complex. The two P atoms associated with the four-legged piano stool structure of this complex were non-equivalent in a room-temperature solution on the ESR time scale, but became equivalent at 185°C. This motion was associated with a low activation energy $\Delta H^{\ddagger}$ of 9.2 ± 0.4 kJ mol^{-1}.

A few examples of multinuclear DNMR are now given. Carbon-13 and fluorine-19 BSA studies were carried out to explain the Fe–P bond rotation in $[(\eta^5\text{-}C_5H_5)Fe(CO)(PPh_3)COCH_3]$.[68] Detailed BSA gave activation energies for phosphine rotation about the Fe–P bond, whereas phenyl ring rotation was rapid at all NMR-accessible temperatures due to a concerted motion of all the phenyls in a cog-like fashion and an oscillation about the P–Fe bond.

Phosphorus-31 DNMR may be represented by the study of a novel pivot fluxion in the platinum(II) complexes [**14**] and [**15**].[69] At temperatures above *ca.* 50°C the complex [**14**] exhibits an intramolecular rearrangement in which the non-coordinated S atom exchanges with the coordinated S *trans* to trimethylphosphine. The Pt–S bond *trans* to Cl remains inert and serves as a pivot for the exchange process. The complex [**15**] exhibits a similar fluxion, except that both Pt–S bonds are labilized by *trans* phosphine ligands and all three P=S groups are involved in the exchange.

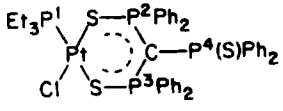

[**14**]

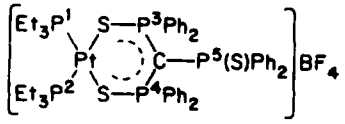

[**15**]

Two examples of the application of DNMR to tetranuclear platinum clusters have been reported.[70,71] The first involves mixed tetramers of the types $[(PtMe_3SMe)_2(PtMe_3X)_2]$ (X = Cl, Br, I) and $[(PtMe_3SMe)_3$ $(\{PtMe_3Cl\})]$ [**16**] derived from $[(PtXMe_3)_4]$.[70] The latter symmetrical tetramer was assumed to be stereochemically rigid, but this is now thought to be unlikely following the discovery of facile Pt–methyl scrambling in the above mixed tetramers. The compound [**16**] contains two $PtMe_3$ environments, namely Pt^2Me_3, with distinct methyls (Me_B and Me_D), and Pt^3Me_3, with all three methyls (Me_E) chemically equivalent and isochronous since they are all *trans* to SMe. Variable-temperature ^1H spectra (Fig. 7) showed averaging of the Me_B and Me_D environments, with the Me_E signal remaining sharp. Such changes were attributed to localized rotations of the

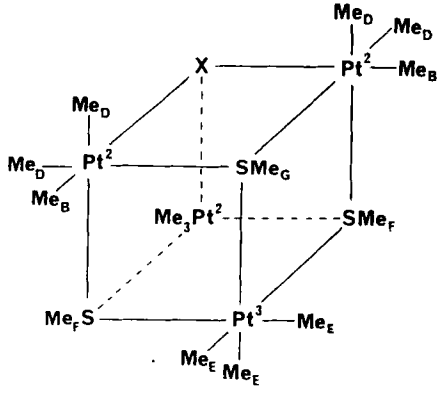

[**16**]

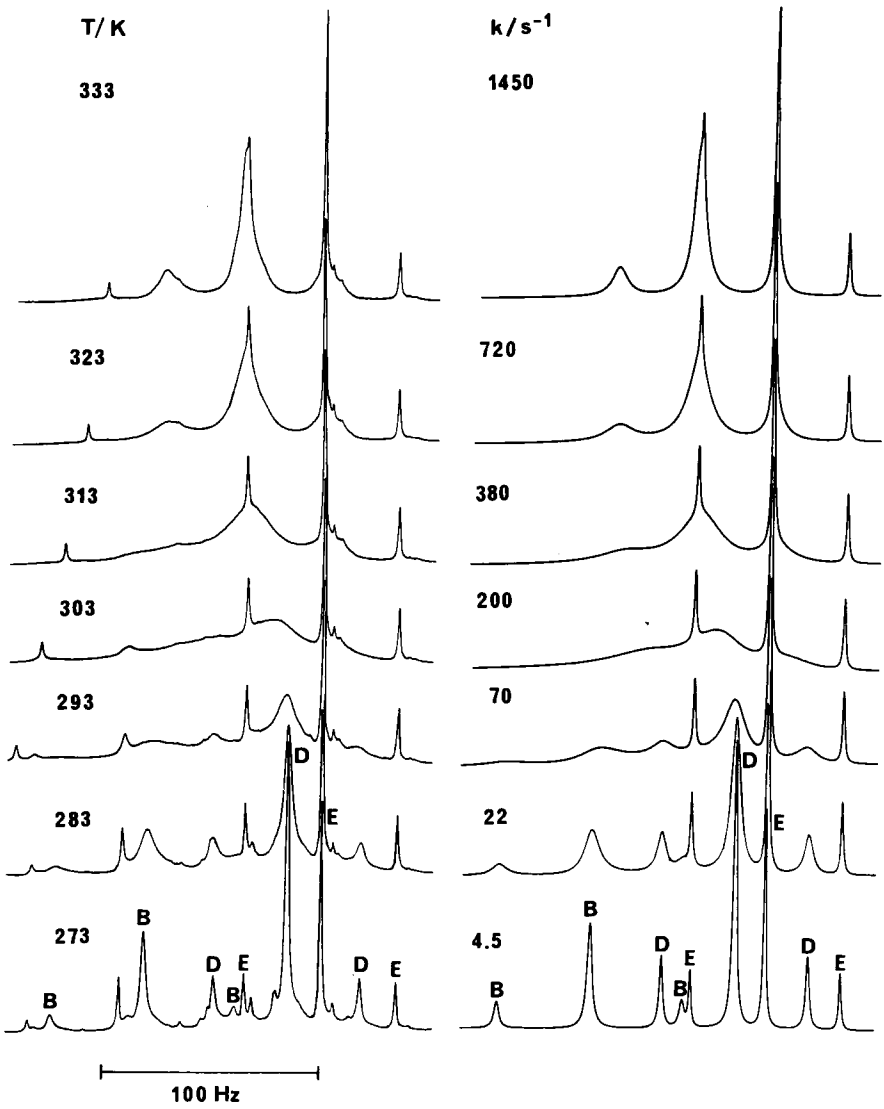

Fig. 7. Variable-temperature and computer-synthesized ^1H NMR spectra of $[PtMe_3SMe)_3(PtMe_3Cl)]$, showing the Pt-methyl scramling. Labelling refers to structure [**16**]. Rate constants refer to Me(b)→Me(D) in the Pt^2Me_3 moieties. Additional weak signals are attributed to traces of $[(PtMe_3SMe)_2(PtMe_3Cl)_2]$ and water.

$PtMe_3$ moieties about their cone axes without any breaking and remaking of the halogen bridge bonds, since the activation energies derived from total BSA were essentially halogen-independent. Variable-temperature ^1H, ^{13}C, ^{31}P and ^{195}Pt spectra were measured to provide insight into the fluxionality of the Pt_4 cluster cation $[Pt_4(\mu\text{-}H)(\mu\text{-}CO)_2(\mu\text{-}dppm)_3(dppm\text{-}P)]^+$ (dppm = $Ph_2PCH_2PPh_2$).[71] The NMR bandshape changes, and particularly the strong temperature dependence of the ^{195}Pt coupling constants, indicated that the fluxionality involved migration of the μ-H and $Pt^3(CO)_2$(dppm-P) groups from edge to edge of the Pt_3 triangle. One such edge-to-edge migration via a tetrahedral Pt_4 intermediate is shown in [**17**], where μ-dppm groups have been omitted for clarity.

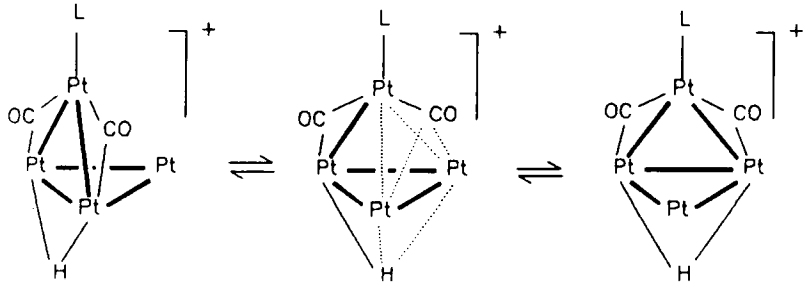

[17]

Lithium compounds may in principle be studied by ^6Li (I = 1) and/or ^7Li (I = 3/2) NMR spectroscopy. The latter nuclide is normally preferred on account of its much higher receptivity. A recent example of such a study concerned the lithium "ate" complexes [$(ArBMe_3)$Li.D] (Ar = $C_6H_4CH(X)NMe_2$-2, X = H, Me; D = OEt_2, THF).[72] Variable-temperature NMR measurements in the range 173–333 K involving ^1H, ^{13}C, ^{11}B as well as ^7Li enabled the intramolecular rearrangements to be analysed. Lithium-6 in organolithium compounds normally exhibits much longer relaxation times than those of ^7Li, and behaves very much like a spin-½ nucleus in such systems. This gives ^6Li particular advantages over ^7Li for BSA, and has been utilized by Thomas *et al.*[73] in a study of the fluxionality of *t*-butyllithium tetramers.

2.1.3. Applications to solids

Many internal motions that exist in liquid and solution phases of materials are, of course, absent in the more ordered and tightly packed solid phase. However, many molecular fluxions still persist in solids, and these may be amenable to NMR investigation, particularly by ^{13}C CP–MAS methods. A

recent issue of *Chemical Reviews* was devoted solely to magnetic resonance of solids, and a number of contributors referred to motional studies. In particular, Spiess[74] discussed dynamic studies with emphasis on 2D and 3D NMR methods (see later).

Typical examples of ^{13}C CP–MAS DNMR studies are those of the metal sandwich compounds (*s-cis*-η^4-butadiene)$(RCp)_2Zr$[75] and $(\eta^5\text{-CpR})_2ZrL_2$.[76] In the former case activation energy barriers were measured for hindered (RCp)–M rotation, with topomerization of the butadiene metallocene framework also occurring.[75] In the other complexes, where L_2 were various dienes, RCp rotation and diene topomerization occurred in the solid state.[76] Rotational energy barriers were very dependent on whether alkyl substituents were introduced to the η^5-bonded rings, whereas the diene fluxion was fairly unaffected, having an energy value of around 57 kJ mol^{-1}.

Variable-temperature ^{13}C CP–MAS studies of $Ti(\eta\text{-}C_5H_5)_2$ $(\sigma\text{-}C_5H_5)_2$ employed both magnetization transfer and BSA studies.[77] Typical spectra of the isotropic resonances are shown in Fig. 8. Simulations were performed using the DNMR4 program,[78] and matchings were based on 1,2-sigmatropic shifts or with random shifts. Results were consistent with 1,2-shifts being the main rearrangement pathway, but there was also evidence for 1,3-shifts as a minor pathway. Interchange of the $\eta\text{-}C_5H_5$ and $\sigma\text{-}C_5H_5$ rings occurs rapidly in solution above a temperature of 333 K but is substantially retarded in the solid state. In contrast, the $\sigma\text{-}C_5H_5$ sigmatropic rearrangement occurs with similar facility in the solid and solution phases ($E_a = 33.2 \pm 1.0$ kJ mol^{-1}, $A = 2.9 \times 10^{10}$ s^{-1}), suggesting that the activation energy is principally determined by electronic factors.

Both liquid state (^{13}C–{^1H} and ^{31}P–{^1H}) and solid state (CP–MAS ^{31}P and ^{13}C) techniques were applied to the η^2-naphthalene complexes $[(C_{10}H_8)(i\text{-}Pr_2P(CH_2)_n i\text{-}Pr_2P)Ni]$ (n = 2,3).[79] In both the liquid and solid states the P_2Ni moiety moves between the 1,2- and 3,4-positions within one naphthalene ring, without exchanging the P atoms. Energy barriers were greater than 96 kJ mol^{-1} in the solid and less than 25 kJ mol^{-1} in solution. Solution 2D-EXSY experiments revealed two further fluxions involving rotation and migration of the P_2Ni moiety around the 1,2-, 3,4-, 5,6- and 7,8-positions of both six-membered rings. The energy barrier for the migration process was approximately 60 kJ mol^{-1}.

The power of NMR techniques when applied to solids was exemplified by the variable-temperature ^{13}C CP–MAS experiments on the trisosmium μ_3-arene/alkene complex $Os_3(CO)_8(\eta^2\text{-}CH_2CH_2)(\mu_3\text{:}\eta^2\text{:}\eta^2\text{:}\eta^2\text{-}C_6H_6)$, where four out of the five intramolecular dynamic processes observed for this molecule in solution were also detected in the solid state.[80] The processes included alkene reorientation, jump-like benzene reorientation, turnstile rotation of the $Os(CO)_3$ moieties and exchange between different molecular conformers. The trigonal twist process that interchanges axial and equatorial carbonyls of the $Os(CO)_2(C_2H_4)$ group and transfers the ethene between

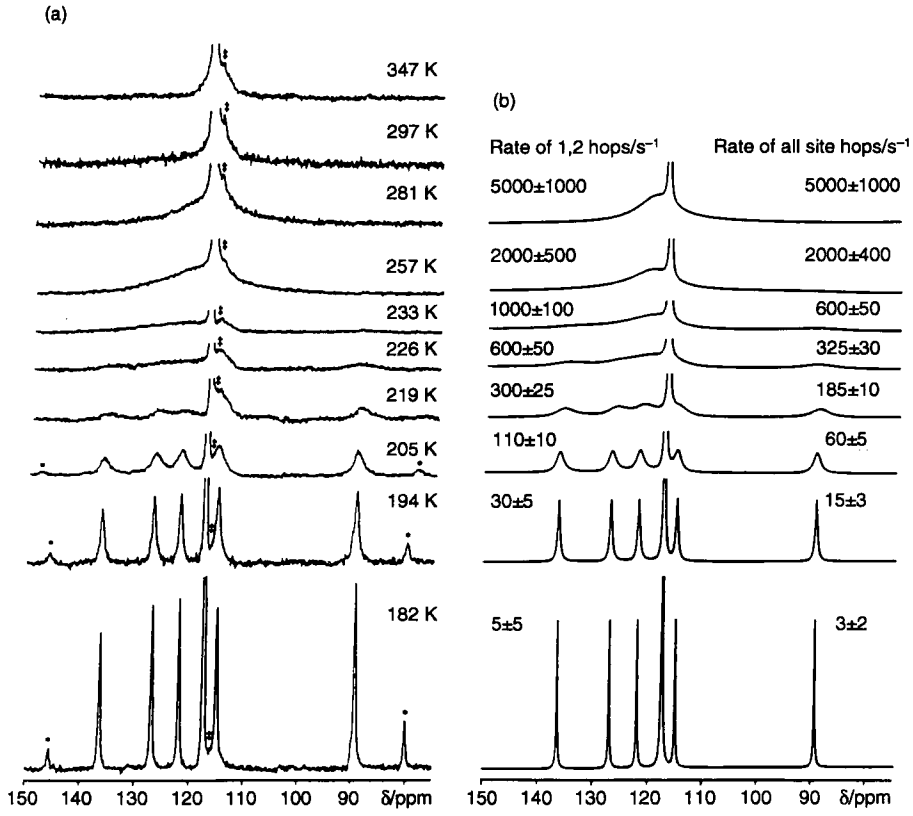

Fig. 8. (a) ^{13}C CP/MAS NMR spectra of $Ti(C_5H_5)_4$ at various temperatures, showing the isotropic resonances. Spectra are normalized with the intensity of the isotropic resonance of the η-C_5H_5 functionality being constant. Signals (•) are spinning sidebands. (b) Simulation of the centre band using the program DNMR4. A simple five-site exchange model was used and exchange was modelled with [1,2] or with random shifts.

equatorial sites was not observed in the solid state, presumably because of crystal packing effects. The four types of solution fluxionality are depicted in [**18**].

These same authors[80] offer some interesting generalizations on comparing dynamic processes in solution and in the solid state. First, some low-energy processes are detected in solids but not in solution because they are always fast on the solution NMR time scale. Exchanges between different molecular conformations in the solid state structure may be quite common, but often go undetected since they show up in crystallographic data only as minor disorder. Some dynamic processses have very similar energy barriers in both

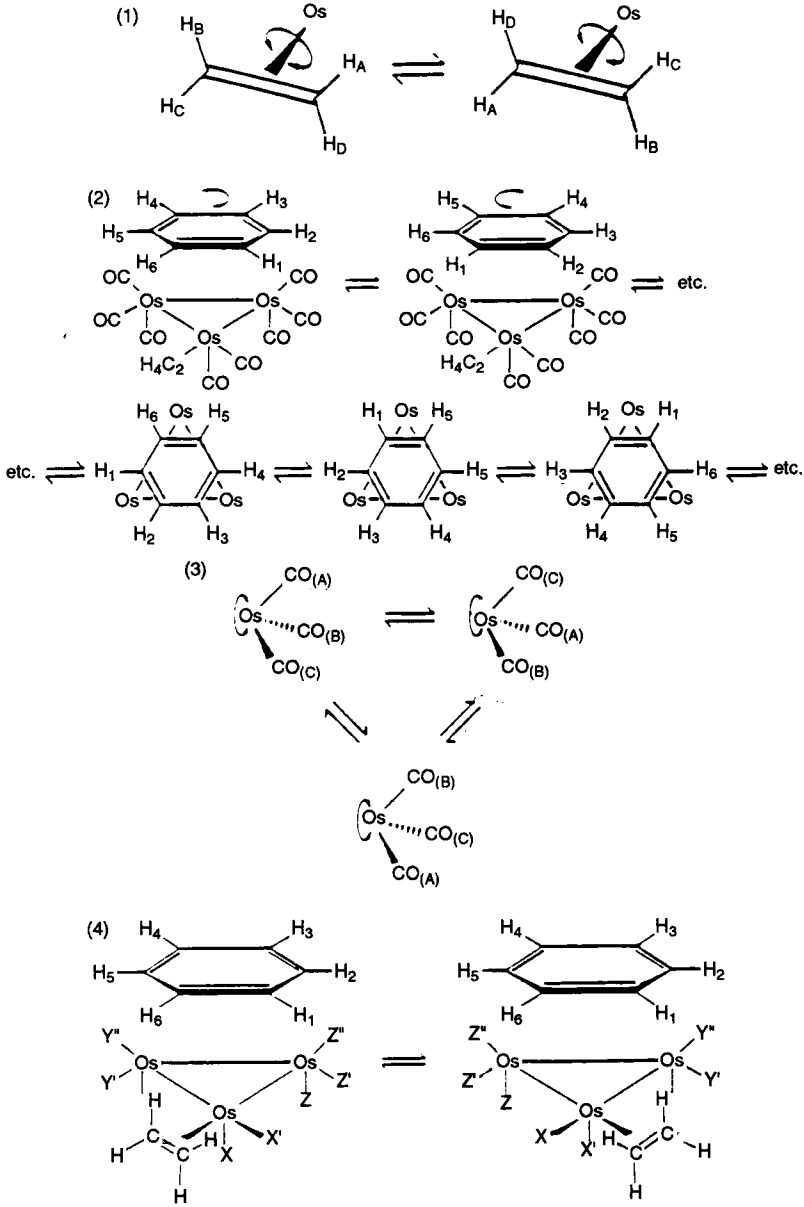

[18]

solution and solid states. This implies that such processes are controlled primarily by valence electronic factors with intra- and intermolecular steric factors being insignificant. However, sterically demanding processes such as the trigonal twist of the $Os(C_2H_4)(CO)_2$ group may be prevented from occurring by the molecular packing in the solid. For other processes for which the relative facility of motion in solution is mainly determined by intramolecular steric effects the intermolecular effects of the crystalline state may influence the situation in a variety of ways and affect the relative rates of a process in the solution and solid phases.

A specific example of the above is the rapid fluxionality of nine-coordinate transition metal complexes in solution between tricapped-trigonal-prismatic (TTP) geometries via a monocapped-square-antiprismatic (MSA) intermediate. In the solid state this fluxion, as exemplified by $W(PMe_3)_6H_6$, is considerably slower, and ^{13}C and ^{31}P CP–MAS studies at temperatures above *ca.* 340 K enabled its kinetics to be measured.[81] Analysis of lineshapes and magnetization transfer data gave activation parameters of $E_a = 148.8 \pm 15\ kJ\ mol^{-1}$ and $A = 6.6 \times 10^{23}\ s^{-1}$ for the ligand interchange process. The rate of the process reached *ca.* $2000\ s^{-1}$ by the decomposition temperature of the material, 381 K.

Variable-temperature ^1H MAS spectra were used to augment the more conventional ^{13}C CP–MAS spectra in a study of the fluxionality of $CH(SiMe_3)_2$ groups in organolanthanide complexes.[82] The solid state ^1H spectra were measured at MAS speeds of 10–11 kHz between −100°C and ambient. In all cases this fast spinning substantially eliminated broadening from ^1H–^1H dipolar couplings and anisotropic contributions to the chemical shift tensor, giving spectra containing essentially isotropic chemical shifts.

2.1.4. Magnetization transfer experiments

Chemical exchange rates that are of comparable magnitude to nuclear spin–lattice relaxation rates are most suitably measured by selective saturation or selective inversion techniques. Measurements are straightforward for two-site exchange. When multisite exchanges occur, the method requires solutions to several rate equations plus the knowledge of several relaxation rates and signal intensities during excitation of the exchange partner. Such a problem may be handled more efficiently by 2D-EXSY (see Section 2.2.1) but the general theory of 1D magnetization transfer for a spin system of n exchanging sites has been developed. In such a case there are $\frac{1}{2}n(n-1)$ exchange rates and n longitudinal relaxation rates to be evaluated. There is no general analytical solution to the mathematical model involved, but computational methods have been developed[83,84] to provide all rate constants and T_1 values from the n magnetization time dependences following a selective inversion of one magnetization. It can be shown that

chemically exchanging magnetizations M_z in a selective inversion recovery experiment follow the equation

$$\frac{\mathrm{d}[\boldsymbol{M}-\boldsymbol{M}(\infty)]}{\mathrm{d}t} = \boldsymbol{L}[\boldsymbol{M}-\boldsymbol{M}(\infty)], \tag{11}$$

where M_i is the z magnetization of the ith site at time t, $M_i(\infty)$ is the equilibrium magnetization at the ith site and the matrix $\boldsymbol{L}$ has elements

$$L_{ij} = \begin{cases} k_{ji} & (i \neq j), \\ -\sum_{l \neq i} \left(k_{il} - \dfrac{1}{T_{1i}} \right) & (i = j). \end{cases}$$

Solution of (11) involves diagonalization of $\boldsymbol{L}$ either after a preliminary symmetrization[83,84] or without it.[85] This yields eigenvalues λ and eigenvectors $\boldsymbol{X}$, the final solution being

$$M_l(t) = M_l(\infty) + \sum_{i,j} \exp(\lambda_i t) X_{li} X_{ij}^{-1} [M_j(0) - M_j(\infty)]. \tag{12}$$

It then requires fitting a series of experimentally measured magnetizations $M_l(t)$ using rate constants k_{ij} and relaxation times T_{1i} by a nonlinear least squares procedure. Problems arise when the pulse is not completely selective, because if more than one signal is perturbed then there will be too many unknown parameters. In such a case Gesmar and Led[83] recommend n different experiments corresponding to the individual inversion of each signal and a simultaneous analysis of all n^2 time dependences. This is likely to be a time-consuming matter, and Muhandiram and McClung[85] have suggested a different least squares procedure with $M_i(0)$ and $M_i(\infty)$ as additional variable parameters. This method works even with imperfect selectivity of inversion.

A simplified approach involving the measurement of magnetizations at only three time points has been proposed.[86] For the case of two slowly exchanging spins A and B the integrated solutions of the differential z Bloch equations are

$$(A_t - A_0) = \exp(\boldsymbol{L}t_m)_{ii} (A_{t=0} - A_0) + \exp(\boldsymbol{L}t_m)_{ij} (B_{t=0} - B_0), \tag{13}$$

$$(B_t - B_0) = \exp(\boldsymbol{L}t_m)_{ji} (A_{t=0} - A_0) + \exp(\boldsymbol{L}t_m)_{jj} (B_{t=0} - B_0). \tag{14}$$

Selective inversion of spin A and measurement of A_t and B_t with a non-selective 90° observe pulse at times $t = 0$, t_m and $5T_1$ affords values of

$A_t = 0$, A_t and B_t, and A_0 respectively, from which the *ii* and *ji* elements of $\exp(\boldsymbol{L}t_m)$ can be calculated. Analogous treatment of spin B affords the *ij* and *jj* elements of $\exp(\boldsymbol{L}t_m)$. Diagonalization of the latter yields the rate matrix $\boldsymbol{L}$ without the need for iterative least squares analysis. The authors found that this method gave rates within 15% of those calculated by the 2D-EXSY method.

A distinctly different approach to 1D chemical exchange NMR experiments has been suggested.[87] It is based on measurement of ^{13}C intensities from a ^{1}H–^{13}C DEPT magnetization transfer experiment. The state of an exchanging spin system is described by the density operator ρ, and the equation of motion is

$$\frac{d\rho}{dt} = i[\rho,\mathscr{H}] - k(\rho - \boldsymbol{P}\rho\boldsymbol{P}) \tag{15}$$

where $\mathscr{H}$ is the spin Hamiltonian in the absence of radiofrequency fields, k is the rate constant and $\boldsymbol{P}$ is a permutation operator describing nuclear exchanges. Using the product operator description it can be shown that the ^{13}C signal intensities in the DEPT experiment depend periodically on the delay τ of the pulse sequence and the rate constant k. The most precise determination of exchange rate is obtained near the coalescence temperature, as in the BSA method. In the limits of very slow and very fast exchange the τ dependence of the DEPT intensities is rather insensitive to the exchange rate, in common with the BSA method.

Applications of magnetization transfer experiments to dynamic chemical problems are many and varied. The DANTE pulse sequence is the commonly used method for measuring the transfer process. This has been applied in ^{31}P spectra to studying ^{31}P site exchanges in rhodium biphosphine[88] and triphosphine[89] complexes where the interest lay in the catalytic properties of these complexes in hydrogenation processes. Selective irradiation by DANTE was not possible in an ^{17}O study for the heptamolybdate anion $[Mo_7O_{24}]^{6-}$, since T_1 and T_2 values are very short.[90] Fortunately in these strongly ionic solutions the 180° pulse is sufficiently long (*ca.* 100 μs) to be quite selective, and it was possible to show by two interlayed experiments with sequences $(\pi\text{–}t\text{–}\frac{1}{8}\pi\text{–}0.1\text{ s})_n$ (t = 3 ms and 100 ms) that transfer occurred solely between the terminal and bridging oxygens without involving the solvent.

Spin magnetization transfer techniques have been employed to investigate isomerization of the cyclohexadienyl ligand in the complex [Re(η-C_6H_7)H_2(PPh_3)],[91] and ethene rotation in bis(η^2-ethene)(2′-acetylphenoxy-*o*,*o*′)rhodium(I).[92] In the case of the rhodium complex activation parameters based on both magnetization transfer and BSA were in good agreement. Magnetization transfer experiments appear to be superior in clarifying the mechanisms of fluxionality in the complexes [Ru(η^6-C_8H_8)(η^4-C_7H_8)] (C_8H_8 = cyclooctatetraene, C_7H_8 = 2,5-norbornadiene) and [Os(η^6-

$C_8H_8)(\eta^4\text{-}C_8H_{12})]$ (C_8H_{12} = 1,5-cyclooctadiene).[93] Using DANTE-based selective ^{13}C irradiation, magnetization transfer experiments showed that the dominant mechanism in both complexes was a 1,5-shift, with 1,3-shifts occurring at a slower rate. The osmium complex in addition exhibits two lower-energy processes, one being an oscillation of the two ligands producing an apparent plane of symmetry and the other a complete rotation of the two ligands.

The mechanisms of fluxionality in $[Fe_3(CO)_{12}]$ and its substituted derivatives $[Fe_3(CO)_{12-n}\{P(OR)_3\}_n]$ have been a long-standing source of controversy. The problem has recently been reinvestigated by Mann *et al.*[95] The solution structures of the major isomers of $[Fe_3(CO)_{10}\{P(OMe)_3\}_2]$ and $[Fe_3(CO)_9\{P(OMe)_3\}_3]$ were unambiguously established, and probable structures proposed for $[Fe_3(CO)_{11}\{P(OMe)_3\}]$ and the minor isomers of $[Fe_3(CO)_{10}\{P(OMe)_3\}_2]$ and $[Fe_3(CO)_9\{P(OMe)_3\}_3]$. The relevance of these findings to the solution structures of $[Fe_3(CO)_{12}]$ and $[Fe_3(CO)_{11}\{P(OMe)_3\}]$ was discussed. It was concluded that there is an exceptionally low-energy carbonyl exchange process involving concerted bridge opening and closing [**19**]. This is outside the NMR time scale of detection, but there is some evidence of it from X-ray data. In addition, there are at least three higher-energy processes, which were established from ^{13}C and ^{31}P measurements. These may be described as (i) the "merry-go-round" mechanism, (ii) edge-bridging carbonyl exchange and (iii) metal-centred ligand exchange. The mechanism of fluxionality in $[Ir_4(CO)_{11}(PEt_3)]$ has recently been reappraised by the same group.[95] Detailed experiments indicate a mechanism involving an intermediate retaining bridging carbonyls rather than species containing only terminal carbonyls.

Magnetization transfer experiments have been applied to hydride fluxionality in the case of $[W(\eta\text{-}C_5H_5)_2(CH{=}CHCH_3)H]^+$, where transfer from the hydride to the propene methine occurs in the *endo* structure and from the hydride to the methylene in the *exo* form. Interconversion of *endo* and *exo* forms was monitored from both directions, and was thought to involve alkene rotation.[96]

A recent example of a haptotropic rearrangement studied by magnetization transfer is that among the nickel anthracene complexes [**20**].[97] The $(R_3P)_2Ni$ moiety migrates between the two terminal rings, rates being independent of concentration of free ligand and $(R_3P)_2Ni$. Both BSA and magnetization transfer experiments were performed, and activation parameters of $\Delta H^{\ddagger} = 56.9\ \text{kJ mol}^{-1}$ and $\Delta S^{\ddagger} = 18\ \text{J K}^{-1}\ \text{mol}^{-1}$ calculated.

2.1.5. Relaxation time studies

Spin–lattice relaxation times of nuclei measured as a function of temperature are often sensitive to rate processes that are far faster than those able to be

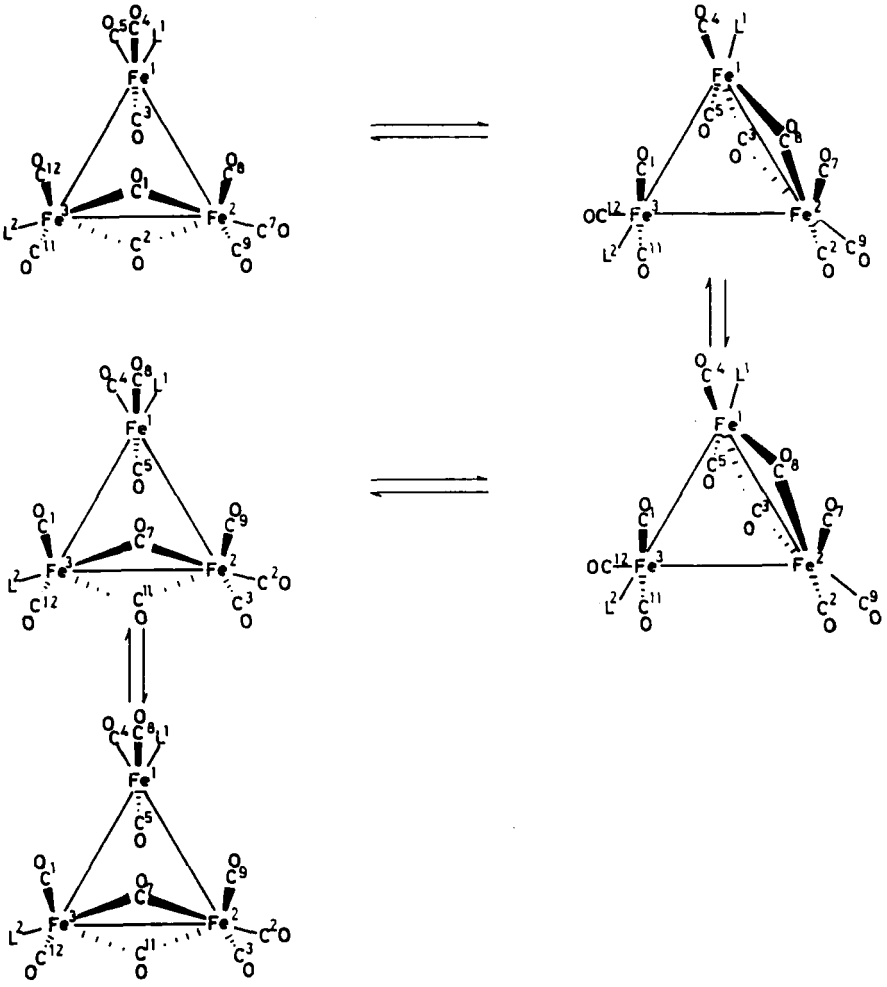

[19]

measured by BSA (see Table 1). The method is most commonly applied to ^{13}C nuclei, since these are normally relaxed predominantly by intramolecular effects. In contrast, ^{1}H nuclei, since they tend to occupy more peripheral sites in molecules than ^{13}C nuclei, are influenced by both intra- and intermolecular relaxation processes.

^{103}Rh T_1 values were used in addition to ^{13}C values to investigate the rates of cyclopentadienyl rotation and molecular tumbling in $[M(\eta^5\text{-}C_5H_5)(\eta^4\text{-}COD)]$ (M = Rh, Ir; COD = cycloocta-1,5-diene).[98] Dipole–dipole interaction was the main contributor to ^{13}C T_1 values, but made no significant contribution to the ^{103}Rh T_1 values, which were primarily the result of

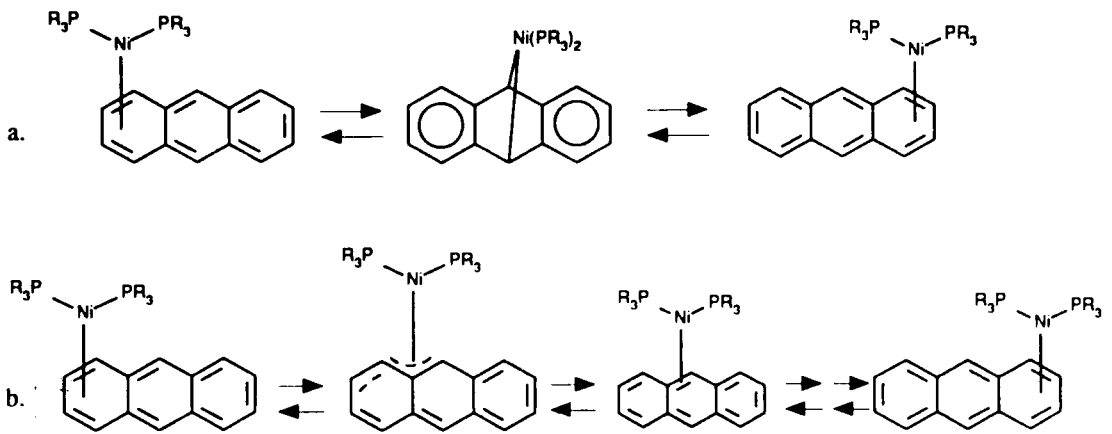

[20]

chemical shielding anisotropy. For the Rh complexes $\Delta H^{\ddagger}$ values were 5.69 ± 0.50 kJ mol^{-1} for C_5H_5 rotation and 9.46 ± 0.75 kJ mol^{-1} for molecular tumbling. Cyclopentadienyl rotation was also the subject of solid state deuterium NMR studies of μ-$(CO)_2[FeCp^d(CO)]_2$ (Cp^d = *ca.* 70% deuterated η^5-C_5H_5).[99] Deuterium T_1 values show that the orientation of the Cp ligand is averaged over the five ring sites, with nearest neighbour jump rates in the range $(1.2\text{–}2.4) \times 10^{11}$ s^{-1} and an activation energy of 12.5 kJ mol^{-1}. Another research group[100] showed that in the *cis* isomer of this compound the two non-equivalent Cp ligands rotate at different rates and have different associated activation energies (E_a = 7.2 and 15.8 kJ mol^{-1}). These values were based on wide-line proton T_1 values, with ^{13}C $T_{1\rho}$ values supporting the findings. The virtue of $T_{1\rho}$ measurements of nuclei is that they are sensitive to chemical exchange rates in the range 10^3–10^6 s^{-1} (Table 1), which are somewhat beyond the normal upper limit of the BSA technique. The accuracy of the rate data using both techniques has recently been rigorously assessed and found to be very comparable.[101] The $T_{1\rho}$ technique has recently been performed under high-pressure conditions. By combining the rotating frame technique with BSA methods, it was shown that the barrier height to conformational isomerization of cyclohexane was independent of pressure.[102]

Finally, mention should be made of measurements of reorientational dynamics and internal rotations of two tricobalt clusters by ^{13}C T_1 relaxation data. In $Cp_2Co_3(\mu_3\text{-}CO)(CO)_3(\mu_3\text{-}CPh)$ internal rotation rates of the phenyl and Cp were calculated. The much slower rate of Ph ring rotations was attributed to an electronic interaction of the π^* molecular orbital of the bridging carbonyl with the phenyl π system.[103] Similar studies were performed on the benzylidyne-capped cluster $Co_3(CO)_9(\mu_3\text{-}CPh)$, but in this case extremely facile internal rotation of the Ph ring was calculated.[104] The rotation barrier was appreciably greater in the trinuclear cluster $FeCo_2(CO)_9(\mu_3\text{-}PPh)$.[105]

2.2. Multidimensional methods

The extension of NMR methodology from one- to two-frequency regimes has been of very great benefit to investigations of molecular stereodynamics. During this review period the 2D-exchange spectroscopy (2D-EXSY) technique based on the 2D-NOESY pulse sequence has become well established as a very powerful structural method.

2.2.1. 2D-EXSY

(a) Theoretical developments. One-dimensional NMR bandshape analysis remains one of the most powerful methods for determining exchange rates.

However, the method suffers from two serious limitations. Firstly, in the region of slow exchange it is difficult to distinguish between broadening caused by exchange and by numerous other factors contributing to natural linewidths. As a rule of thumb, a rate constant of $1\ s^{-1}$ will cause exchange broadening of 1 Hz independent of magnitude of chemical shift difference. This broadening is comparable with typical linewidths of NMR signals in the absence of exchange. Secondly, in complex multisite exchanging systems, where the bandshape is a function of several independent rate constants, it is often impossible to find a unique solution to the problem. Both these difficulties can be largely overcome by the use of multidimensional methods, particularly 2D-EXSY. The theory and methodology of this technique have been the subject of several reviews.[106–109] Only a short and simplified description of this important experiment will be given here. The pulse sequence is shown in Fig. 9. Let us consider a two-spin system of spins A and B mutually interacting through exchange or cross-relaxation. After the first 90°_x pulse the magnetization vectors will evolve in the $x'y'$ plane in the usual manner of free induction decay (FID) for a period t_1 (evolution time). At this point a second 90°_x pulse, the mixing pulse, is applied, tipping the magnetization vectors into the $-z$ direction. During the mixing period t_m, exchange (or cross-relaxation) takes place between nuclei A and B, which changes the longitudinal magnetization of B, $M_{BZ}(t_1)$, by an amount $C_k M_{AZ}(t_1)$, where C_k is a constant depending on the exchange rate. A third 90°_x pulse, the detection pulse, converts this term into transverse magnetization of B, where it is detected as a part of the familiar FID during the detection period t_2. The amplitude of the detected magnetization of B is thus modulated with frequency ν_A as a function of t_1. A two-dimensional Fourier transformation will then result in a spectrum with cross-peaks at (ν_A, ν_B), provided that exchange took place during the mixing time t_m. Correlations arising from any other cause, e.g. through scalar coupling, may be eliminated by phase cycling and a random variation of the mixing period t_m.

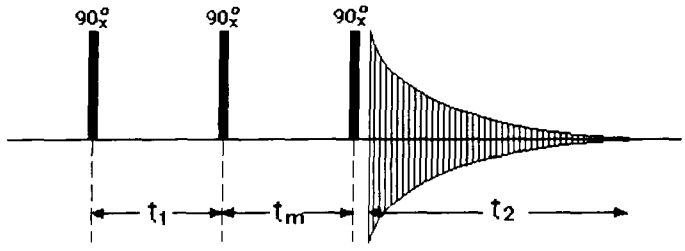

Fig. 9. Pulse sequence for two-dimensional NOESY or EXSY experiments.

To obtain quantitative exchange rates from this experiment, some care has to be taken in the choice of lengths of the mixing time. If this is too short then the resulting cross-peaks are weak and subject to large experimental errors. If t_m is too long then the intensities of cross-peaks may approach those of the diagonal peaks and become rather insensitive to the exchange rates. It should also be remembered that spins relax during the mixing period with a time constant of T_1, and if $t_m > 1/T_1$, then no magnetization may be left to be detected. In practice, one has to optimize t_m to minimize the error in the rate constant. Perrin and Dwyer[109] give the following approximate expression for optimum mixing time:

$$t_m(\text{opt}) \approx \frac{1}{T_1^{-1} + k_{AB} + k_{BA}}. \tag{16}$$

For multisite systems the situation is more complex. In general there can be no optimum t_m for all magnitudes of rate constants, and so it may be necessary to repeat the experiment for several magnitudes of mixing times. To extract accurate rate information, it is necessary to perform reliable measurements of peak intensities, usually by volume integration. Since absolute-value-mode spectra may lead to intensity distortions and peak broadening, it is desirable to obtain pure absorption mode spectra in two dimensions, usually by the method of time-proportional phase incrementation (TPPI).[110] The method involves incrementing the phase of the first excitation pulse in 90° intervals in concert with the incrementation of the evolution time t_1. The eight-cycle phase-cycling routine used in this method[110] achieves quadrature detection and also eliminates the undesirable axial peaks. These arise from spin–lattice relaxation during t_m, which creates additional z magnetization that is converted to a signal by the final 90° pulse. Scalar coupling tends to interfere with 2D-EXSY spectroscopy by creating so called J cross-peaks, but this contribution can also be reduced by the above-mentioned phase cycling or by random variation δt_m of the mixing time t_m.

It should also be stressed that the effects of cross-relaxation (nuclear Overhauser effects) and chemical exchange on the final 2D spectrum are analogous. This leads to cross-peaks between nuclei that are spatially close in the molecule, and it is necessary to separate these NOESY contributions from chemical exchange effects. Fortunately, this is usually easily achieved, because exchange rates are strongly temperature-dependent whereas cross-relaxation rates are not. Also, in phase-sensitive 2D-EXSY chemical exchange and cross-relaxation cross-peaks may be distinguished by their opposite phases. Another undesirable feature in 2D-EXSY spectra are so called t_1 ridges, i.e. signals appearing as ridges parallel to the F_1 frequency axis. These can contribute to false cross-peak intensities after symmetrization. Once again, proper phase cycling minimizes this artefact.

For a simple spin system involving chemical exchange between two sites, explicit expressions have been derived[111] for the intensities of diagonal peaks I_{ii} and cross-peaks I_{ij} in the 2D EXSY spectrum:

$$I_{ii} = \tfrac{1}{2}\exp(-Rt_m)[1 + \exp(-2kt_m)], \tag{17}$$

$$I_{ij} = \tfrac{1}{2}\exp(-Rt_m)[1 - \exp(-2kt_m)], \tag{18}$$

where R is the spin–lattice relaxation rate of the nuclei at either site and k is the rate constant to be determined from the experiment. It is clear that k can be determined from the experimental ratio I_{ij}/I_{ii} for any given value of t_m. Equations (17) and (18) also show that the accuracy of measurement of k is poor for very small or very large values of the mixing time t_m. Cross-peak I_{ij} values vanish for very small t_m, whereas for a large t_m, $I_{ij} \approx I_{ii}$ and is insensitive to k. Careful analysis of the problem has shown[112] that the optimum choice of the mixing time can be expressed as

$$t_m(\text{opt}) = \frac{\alpha(t_m)}{R + k}, \tag{19}$$

where $\alpha(t_m)$ is a factor taking account of the errors in measuring signal intensities.

Extraction of rate constants from 2D-EXSY spectra of multisite exchanging systems is more complex, and in general, there are no explicit solutions for rates as functions of signal intensities. Three strategies have been employed to tackle the problem:

(*i*) *Measurement of rate of change of cross-peak intensities as a function of small values of* t_m. This initial slope directly represents the value of the rate constant, and can be measured by repeating the experiment for several values of t_m and extrapolating to zero mixing time. This, however, is an extremely time-consuming procedure.

(*ii*) *Iterative computer analysis*. Hawkes *et al.*[113] formulated the problem in matrix form. One chooses initial trial values of k_{ij} and R_{ij}, and constructs a magnetization transfer matrix. Diagonalization of the latter yields the intensity matrix, i.e. the 2D spectrum corresponding to these initial values for rates and given t_m. The computed spectrum is then compared with experimental intensities. Finally, an iterative procedure varies both the exchange rates and relaxation rates until the "best-fit" spectrum is obtained together with "best-fit" values of rates. Errors in k_{ij} and R_{ij} are also obtained. The disadvantage of this method is that it involves fairly complex computation and requires initial "guessed" values for the rate constants.

(*iii*) *Method of direct matrix transformations.* An N-site 2D-EXSY spectrum can be expressed as an intensity matrix $\boldsymbol{I}$ with elements

$$I_{ij} = p_i \sum_{k=1}^{N} A_{ijk} \exp(\lambda_k t_m) \tag{20}$$

where p_i is the relative population of the ith site, and A_{ijk} and λ_k are constants. In matrix form

$$\boldsymbol{I} = \boldsymbol{JP}, \tag{21}$$

where $\boldsymbol{P}$ is the population matrix (array) consisting of relative populations p_i, and $\boldsymbol{J}$ is a matrix with elements $\exp(\lambda_k t_m)$. On the other hand, the kinetic matrix $\boldsymbol{K}$, consisting of rate constants k_{ij}, is related to the 2D spectral intensity matrix $\boldsymbol{I}$ by

$$\boldsymbol{I} = \boldsymbol{P} \exp(\boldsymbol{K} t_m). \tag{22}$$

Now, $\boldsymbol{J}$ can be obtained from $\boldsymbol{I}$ as

$$\boldsymbol{J} = \boldsymbol{I}\boldsymbol{P}^{-1}. \tag{23}$$

It can be seen[114] that diagonalization of $\boldsymbol{J}$ will regenerate the array $\exp(\boldsymbol{\Lambda} t_m)$

$$\boldsymbol{J} = \boldsymbol{X} \exp(\boldsymbol{\Lambda} t_m) \boldsymbol{X}^{-1}. \tag{24}$$

Taking the natural logarithm of the eigenvalues and dividing by t_m,

$$\frac{\ln \boldsymbol{J}}{t_m} = \boldsymbol{X} \frac{\ln \exp(\boldsymbol{\Lambda} t_m)}{t_m} \boldsymbol{X}^{-1} \tag{25}$$

one obtains the matrix $\boldsymbol{\Lambda}$.

Finally, simple matrix multiplication

$$\boldsymbol{X}\boldsymbol{\Lambda}\boldsymbol{X}^{-1} = \boldsymbol{K} \tag{26}$$

yields the kinetic matrix, i.e. all rate constants for a general N-site exchange.

It is also necessary to take into account the relaxation matrix $\boldsymbol{R}$, which is then added to the kinetic matrix $\boldsymbol{K}$ to give the total magnetization transfer matrix

$$\boldsymbol{L} = \boldsymbol{K} + \boldsymbol{R}, \tag{27}$$

where the diagonal elements of $\boldsymbol{R}$ are $-R_{1j} = -T_{1j}^{-1}$, and the off-diagonal elements $-\sigma_{ij} = -R_{ij}$ represent cross-relaxation. The matrix $\boldsymbol{L}$ thus takes into account all exchange rates, all NOEs and all spin–lattice relaxation rates.

The above procedure has been incorporated into a computer program

D2DNMR.[114] The program input consists of the number of exchanging sites, N, the relative populations of each site, spin–lattice relaxation rates and experimental 2D signal intensities. It does not take into account cross-relaxation effects, but these are totally absent in studies of low-abundance nuclei, e.g. ^{13}C, and are often negligible for ^{1}H 2D-EXSY experiments on small molecules. This is not the case, however, for large, slowly tumbling molecules, where it is necessary to separate rate constants k_{ij} from cross-relaxation rates σ_{ij}.[115]

An ingenious method has been proposed[116] for eliminating cross-relaxation and for suppressing coherence-transfer effects from 2D exchange spectra of macromolecules. For such molecules $\omega_0\tau_c \gg 1$ and the ratio of the longitudinal to transverse cross-relaxation rates is equal to $-½$. The direct cross-relaxation peaks can be made to cancel each other if the mixing period of an exchange experiment is designed so that the magnetization components alternately cross-relax along the longitudinal axis for twice as long a time as they cross-relax along the transverse axis. This is achieved by employing a mixing pulse sequence consisting of interlayed NOESY and ROESY (rotating frame NOESY) mixing periods. Thus longitudinal and transverse relaxation are forced to compensate each other by time averaging. The technique is particularly useful for studies of proteins.

In special cases it is possible to separate exchange and cross-relaxation information by gradient-enhanced exchange spectroscopy (GEXSY).[117] Pulse sequences incorporating field gradients have been designed that employ differences in diffusional properties of exchanging molecules so that exchange information can be obtained without changing the mixing time. Expressions have been given for fast and intermediate exchange.

Attention should be drawn to the treatment of errors in determination of k values. The iterative approach[113] yields the error analysis explicitly, while in the non-iterative method[114] the variances of the rate constants are estimated by performing a "reverse" calculation starting from errors in peak intensities caused by finite signal-to-noise ratios, instrumental drifts and errors in volume integration. Both methods have been compared,[118] and found to give similar results. More rigorous analysis of standard deviations of rate constants derived from 2D EXSY has to include measurements of r.m.s. noise.[119] The question of precision of volume integrals in 2D NMR has been investigated[120] by proper treatment of correlation functions of noise and the signal-to-noise ratio for peak volumes. Having determined the variance of the peak volume σ_k^2, use is made of the classical error propagation formula

$$\sigma_{R_{kl}}^2 \propto \sigma_k^2/t_m^2, \tag{28}$$

where $\sigma_{R_{kl}}^2$ is the standard deviation of an element R_{kl} of the kinetic matrix.

It must be borne in mind, however, that absolute signal intensities are meaningless in NMR. Volume ratios are used for calculations, and the precision of R_{kl} is therefore only about one-half of that predicted by (28). Important sources of integration errors are baseline (or base-surface) distortions. These can be reduced either by optimal phase cycling and oversampling during acquisition, or by various corrections applied to the time-domain frequency-domain data. A computer program FLATT[121] has been developed that improves each individual row or column separately in two steps. First, the regions of the row representing "pure baseline" are identified. Secondly, a function that represents a correction of the first few time-domain data points is "best-fitted" to the pure baseline regions and then subtracted from the complete row. The procedure is normally performed in both dimensions.

^{1}H 2D EXSY can be difficult to apply to studies of peptides because of the presence of a large number of cross-relaxation peaks. Nitrogen-15 would be the nucleus of natural choice here were it not for its low inherent sensitivity. However, a modified EXSY pulse sequence has been proposed[122] in which the first 90° pulse is replaced by a DEPT polarization sequence. Thus ^{1}H polarization is transferred to the low-γ, low-natural-abundance ^{15}N nuclei via the creation of multiple-quantum coherence involving J coupling with the sensitivity improvement of $\gamma_H/\gamma_N \approx 10$.

The experimental time required to obtain kinetic data from 2D-EXSY can be quite considerable, especially if long relaxation delays, long mixing times and high digital resolution in both dimensions are required. Much time is spent scanning through the whole range of incremental evolution periods t_1, yet many rows of the final spectrum do not contain any useful information, and it is tempting to omit some of the t_1 values. However, this would be equivalent to omitting some of the points of the FID, which clearly is not possible in such a direct manner, because each value of t_1 in the time domain contributes to every frequency in the frequency domain. One method of collecting only the informative rows of the 2D matrix is using selective excitation or 2D spectroscopy without an evolution period. The feasibility of this approach has been demonstrated by a so-called "pseudo-COSY" experiment[123] where the F_1 dimension may be investigated only in those regions where signals are known to lie. A similar technique has been proposed for exchange spectroscopy and called multiplet-selective excitation or 2D-MUSEX.[124] This is based on selective excitation of only one nucleus of the coupled spin system using typically a DANTE pulse sequence. It can be shown that under such conditions the multiplet structure of the excited nucleus behaves as an uncoupled system, resulting in the suppression of coherence-transfer magnetization as well as in reduction of the size of the data table. Another simplified variant of 2D-EXSY is based on the usual non-selective pulse sequence and difference spectroscopy.[125] First, a spectrum is measured without mixing ($t_m = 0$) and then with non-zero mixing,

both for a particular evolution time t_1. Difference spectra obtained by subtracting the equilibrium spectrum from spectra recorded both without and with mixing yield exchange information. Although the process has to be repeated for several evolution times, depending on the number of exchanging sites, there is a large time saving by avoiding full 2D data acquisition. The method should also be more accurate, since it avoids line distortions due to limited digital resolution, magnetic field inhomogeneity, truncation effects and improper weighting of the data points. Even greater accuracy is achieved if the experiment is performed for more different t_1 values than are strictly necessary.[126] In general, to analyse an N-site exchange system, $2N+1$ spectra are required for N different t_1 values. If a larger series of experiments is performed for m values of t_1, where $m > N$, then the system is over-determined, and an analytical procedure has been described[126] for obtaining both the data and the errors.

Another effective way of improving accuracy is to use multiple mixing times. This is not always feasible in 2D-EXSY because of experimental time considerations, but is advisable for all 1D selective inversion experiments as well as 1D analogues of 2D-EXSY.[127] The method has been demonstrated on multiple 1D experiments, where the experiment was performed a total of N times, each with a different initial perturbation, in this case selective inversion of each successive site. This can be summarized by the equation[127]

$$\boldsymbol{M}\boldsymbol{M}_0^{-1} = \exp(-t_m \boldsymbol{L}) \tag{29}$$

where $\boldsymbol{M}$ and $\boldsymbol{M}_0$ are square matrices, each row of which corresponds to one site and each column corresponds to one experiment, and $\boldsymbol{L}$ is the kinetic matrix. To obtain all N^2 elements of $\boldsymbol{L}$ (and all the rate constants), the experimental data can be fitted to (29), which is a sum of exponentials. By converting this equation into the linear form

$$\ln(\boldsymbol{M}\boldsymbol{M}_0^{-1}) = \boldsymbol{X}(\ln \boldsymbol{\Lambda})\boldsymbol{X}^{-1} = -t_m \boldsymbol{L}, \tag{30}$$

the exponentials are eliminated and a plot of each element $(\ln \boldsymbol{M}\boldsymbol{M}_0^{-1})_{ij}$ versus t_m is a straight line of slope $-L_{ij}$ or k_{ji}. Here $\boldsymbol{X}$ is the square matrix of eigenvectors that diagonalizes $\boldsymbol{M}\boldsymbol{M}_0^{-1}$ to $\boldsymbol{\Lambda}$.

Weighted linear least squares fitting then yields the rate constants with higher accuracy compared with single-time-point 2D measurements. In the given example of the three-site NH proton exchange in acrylamide the calculated errors were less than 10% for 12 values of t_m. This is compared with errors of 20–25% obtained for 2D measurements at a single time point.

All the above-mentioned simplified methods are extremely useful if there are only two or three exchanging sites. For multisite exchange kinetics, however, 2D-EXSY remains the most powerful means of both qualitative identification of mutually exchanging sites and quantitative studies of a wide

range of chemical systems. Recently, essentially the same technique was applied to 2D FT-EPR studies of slow intramolecular processes such as ring inversion in cyclic free-radical systems.[128] Here "slow" rates on the EPR time scale are anything up to $10^5\,s^{-1}$ and mixing times are of the order 1 μs. Analogous experiments to NMR 2D-EXSY have recently been reported using pure nuclear quadrupole resonance (NQR),[129] and the differing experimental requirements of the two techniques discussed. The NQR method was applied to the ^{35}Cl nuclei of polycrystalline samples of $CHCl_3$ and *p*-chlorobenzotrichloride.

Ever since the development of pulse NMR spectrometers, Fourier transformation (FT) has been the method of converting the time-domain free induction decay data into the familiar frequency-domain spectrum. This approach is being increasingly challenged on the grounds that FT is not necessarily the ideal method of conversion, especially when, for various reasons, one has to acquire distorted or incomplete signals. For example, if the FID is truncated then narrow signals cannot be obtained, because either they are distorted by sinc function "wiggles" or by a window function broadening. Other distortions arise because of field inhomogeneity or receiver dead-time effects on the first few points of the FID. Two new data processing methods have been developed that deal both with the problem of instrumental distortions and missing parts of the signal.

(*i*) *Linear prediction* (*LP*). This retrieves frequencies, amplitudes and phases from time-domain signals using a linear least-squares procedure.[130] Each point of an FID is assumed to be a linear combination of all previous points resulting in the improved signal-to-noise ratio and the possibility to reconstruct accurately missing parts of the time-domain signal. The method has been extended to 2D NMR,[131] where it offers several additional advantages: the F_2 frequency determination is more accurate than in the 1D case, because the entire 2D FID can be included in the calculation; it has the ability to distinguish between signal and noise, and the processing produces a set of spectral parameters (frequencies, intensities) which make further automated analysis easier. The method has been successfully applied to a 2D-EXSY study of the solid state cadmium–thiolate complex involving a three-site ^{113}Cd NMR exchange system.[132]

(*ii*) *The maximum entropy method* (*MEM*). This originated as a method for enhancing images from radio telescopes,[133] and has since been applied to enhancement of the Hubble Space Telescope images, deconvolution of blurred photographs, X-ray crystallography and other areas dealing with incomplete and/or corrupted data. Essentially, it selects from a large family of possible solutions the one solution having greatest entropy. In the NMR context,[134] one starts from a family of possible trial spectra that, after inverse FT, produce time-domain functions compatible with the ex-

perimental FID. The aim is to select one, usually unique, solution that has the largest value of entropy S, which is the quantity defined as

$$S = -\sum_{k=1}^{N} p_k \ln p_k, \tag{31}$$

where p_k are intensity ordinates defining the trial spectrum and N is the total number of ordinates. Any particular algorithm[135] choosing the maximum entropy spectrum has to try to ensure that the spectrum contains only features for which there is sufficient evidence in the data. MEM can take into account known instrumental distortions, and it can restore missing parts of a signal as well as producing resolution- or sensitivity-enhanced spectra. Whether it can simultaneously suppress noise and enhance resolution is debatable, and this claim has recently been examined[136] using a Monte Carlo method. A critical comparison of MEM with FT[137] shows that some of the examples in the literature may be idealized. However, the latest advertised Cambridge algorithm, called MemSys 5,[138] appears to show the ability to extract NMR spectra with high resolution and high signal-to-noise ratio together with quantitative error bars.

There appears to be only one study of the application of MEM to 2D NMR data,[139] which may be due to the fact that the entropy function is non-linear. Application of any non-linear data processing method in areas of NMR which rely on linearity (e.g. difference spectroscopy) must be pursued with caution. Also, computational time required by MEM is substantially larger than for conventional FT, which is disadvantageous for 2D NMR

(*b*) *Chemical applications*. The examples chosen in this section have been grouped according to the nuclide being detected. ^{1}H is a favoured nucleus for 2D-EXSY experiments on account of its very high receptivity, but care must always be taken to ensure that cross-peak intensities contain negligible contributions from ^{1}H–^{1}H cross-relaxation of neighbouring hydrogens. This was shown to be the case in a study of $[M(CO)_3(\eta^6\text{-COT})]$ (M = Cr, W) complexes,[140] where data from both ^{1}H and ^{13}C 2D-EXSY were compared. The experiments indicated that for the W complex 1,2(α) and 1,3(β)-shifts **[21]** are almost equally favoured, whereas for the Cr complex the 1,3-shift mechanism was slightly preferred.

Platinum(IV) complexes derived from $[(PtXMe_3)_4]$ have a rich fluxionality. The power of the 2D-EXSY method was illustrated in the case of $[PtXMe_3\{(MeS)_2CHCH(SMe)_2\}]$.[141,142] The ligand acts in a bidentate mode, thus leaving two uncoordinated S atoms, which can be brought into coordination by a novel 1,3-metal pivot. The process involved individual Pt—S bonds breaking, followed by 109.5° pivots of the pendant $-CH(SMe)_2$ group about its attached C—C bond. Such a process brings a previously uncoordinated *gem* S-methyl into coordination with Pt, and simultaneously

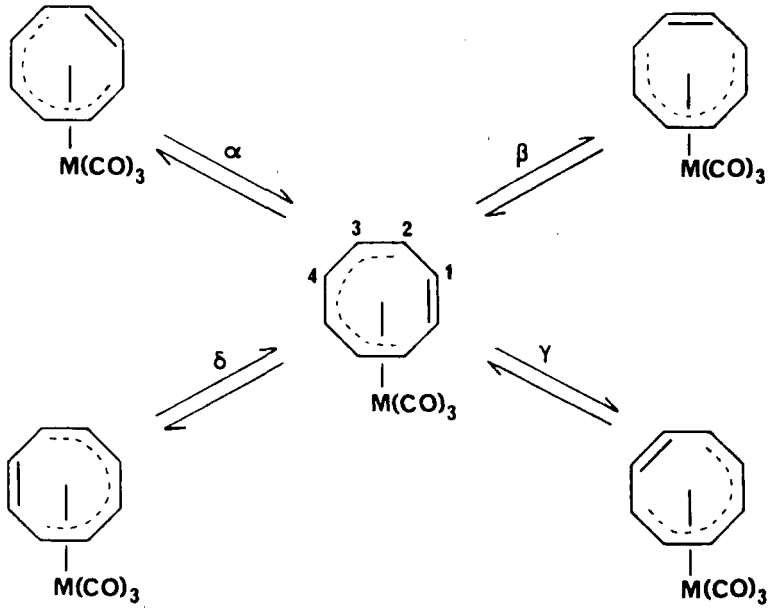

[21]

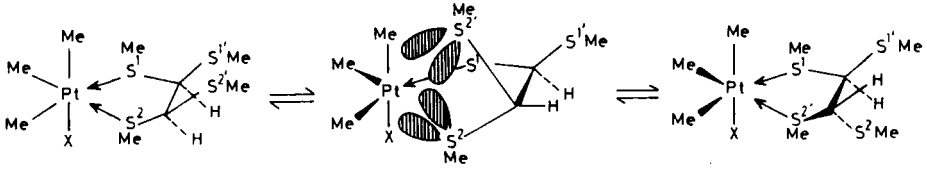

cis [22] *trans*

interconverts *cis* and *trans* isomers. This is shown schematically in [22]. Conclusive evidence for this change was provided by ^{1}H 2D-EXSY studies of the S-methyl region (Fig. 10).[142] All signals undergo exchange, so there are 30 cross-peaks in the exchange matrix. However, the total 6×6 matrix can be simplified by dividing the total spectral map into four quadrants, each containing nine signals. The top-left and bottom-right quadrants contain only cross-peaks (CP), whereas the other quadrants contain both diagonal signals and cross-peaks, D1 and D2 corresponding to coordinated and uncoordinated S-methyl signals respectively. Thus the exchange problem is reduced to a 2×2 matrix with the populations of the signal sets D1 and D2 being equal, since signals due to *cis* and *trans* isomers were now combined. The matrices required as input for the D2DNMR program[114] are

$$\boldsymbol{I} = \begin{bmatrix} \text{D1} & \text{CP} \\ \text{CP} & \text{D2} \end{bmatrix}, \quad \boldsymbol{P} = \begin{bmatrix} 0.5 \\ 0.5 \end{bmatrix}.$$

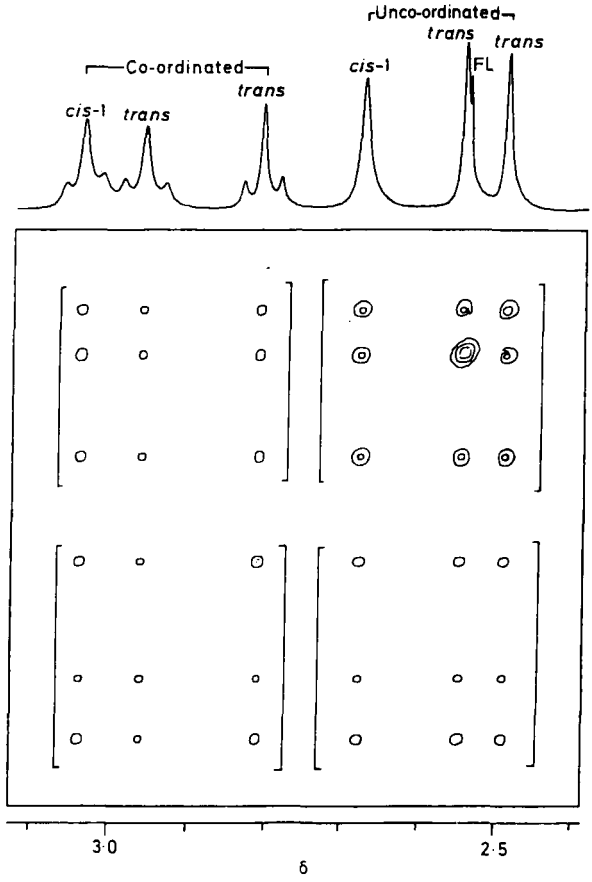

Fig. 10. ^{1}H 2D-EXSY spectrum of the S-methyl signals of $[PtClMe_3\{(MeS)_2CHCH(SMe)_2\}]$ at 363 K, showing how the total contour plot was divided into four quadrants. FL is free ligand.

This method led to activation energies for the pivot process in the range 88.7–91.2 kJ mol^{-1} for the three halide complexes. A similar simplification procedure was applied to the Pt-methyl region of the 2D spectrum, which displayed the effects of a Pt-methyl scrambling process accompanying the ligand pivot fluxion.

^{1}H 2D-EXSY has also been used to study the bridge reversal process that occurs in chalcogen-bridged [3]metallocenophanes [**23**].[143] This process can be monitored by its exchange effects on the ring methine hydrogen environments. It is a high-energy process, which occurs too slowly to be amenable to BSA but is well suited to 2D-EXSY experiments. These were performed in the temperature range 60–110°C for the Ru and Os com-

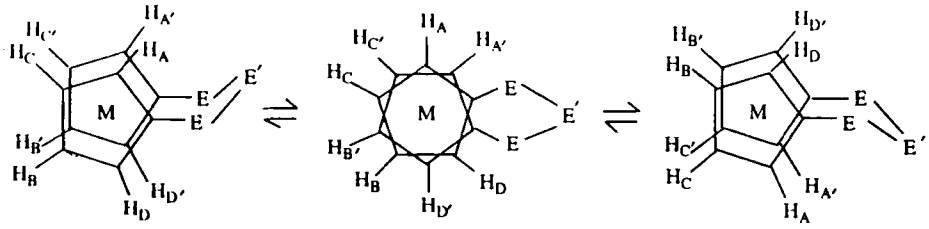

$$[ABCD]_2 \rightleftharpoons [BADC]_2$$

[23]

pounds with triple sulphur bridges. Energy barriers in the range 89–93 kJ mol^{-1} were reported. ^1H 2D-EXSY has also been employed to identify the pairwise exchanges associated with a fluxion, code-named the Bloomington Shuffle, in the tetratungsten compound $W_4(O\text{-}^iPr)_{12}$.[144] This fluxion is depicted in [24], and involves an oscillation of the cluster about a time-averaged symmetrical rhombus, i.e. through a D_{2h} $W_4(\mu\text{-}O)_4(O)_8$ transition state. This leads to an averaging of the μ-OR ligands and a correlated motion of the terminal wingtip W—OR groups such that pairwise methine exchange occurs.

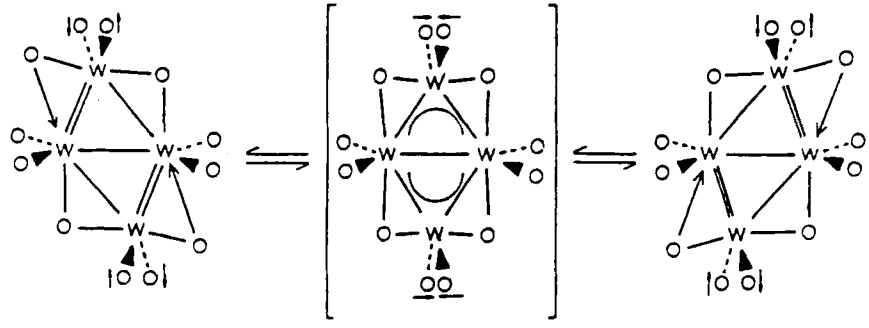

[24]

Hydrogen scrambling processes in the complex $[Ta(\eta\text{-}C_5Me_5)(\eta\text{-}C_5H_5)\{(\mu\text{-}H)_2BH_2\}]$ have been examined rigorously by quantitative 2D-EXSY experiments. The observed scrambling of terminal and bridging hydrogens of the $(\mu\text{-}H)_2BH_2$ ligand has been shown to proceed by a dominant mechanism in which surprisingly there is no direct exchange between the terminal hydrogens.[145] The proposed mechanism proceeds via a $Ta\{(\mu\text{-}H)_3BH\}$ intermediate accompanied by simultaneous $\eta 5 \leftrightarrow \eta^3$ shifts of the C_5 rings upon coordination of the terminal hydrogens to Ta [25]. Three

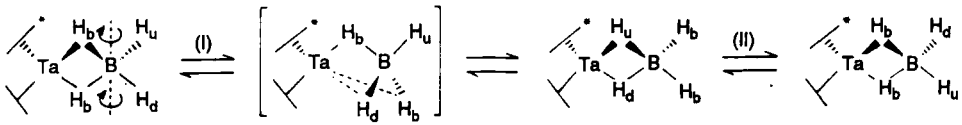

(a)

[25]

separate fluxional processes have been detected and quantitatively measured in the compounds $[M(\eta\text{-}C_5H_5)_2(\eta\text{-}CH_3CH{=}CH_2)H]$ (M = Nb, Ta).[146] The kinetics were accurately determined by combined ^1H 2D-EXSY and ^{13}C magnetization transfer experiments. A mechanism involving agostic η^2-alkyl ligands was most favoured. Another example of the utility of 2D-EXSY is the study of intramolecular exchange of R groups between metal and a three-coordinate B atom in alkenyl boranes of type $R_2BCR{=}CR^1MR^2_3$, where M is Sn or Ph and R^2 is Me, Et or Ph.[147]

The first applications of quantitative 2D-EXSY to paramagnetic systems have been reported.[148,149] They concerned the dynamics of lanthanide(III) complexes of diethylene triaminepentaacetate (DTPA). At low temperatures (0–25°C) the complexes $M(DTPA)^{2-}$ (M = Pr, Eu or Yb) undergo slow exchange on the ^1H NMR time scale, but on raising their temperatures exchange between pairs of enantiomers occurs. Rates of such exchanges were calculated from diagonal and cross-peak intensities, which were based on signal radii measured at different contour levels. Very short mixing times (e.g. 15 ms) could be used in these rapidly relaxing paramagnetic systems. More recent applications have concerned an Ni(II)–salicylideneiminato complex[150] and Co(II)–crown ether complexes.[151,152] In the case of $[Co([12]crown\text{-}4)_2]^{2+}$, 2D-EXSY revealed a novel fluxion involving the Co^{2+} ion jumping through the crown ether ring plane. This penetration process was assisted by the usually inert ClO_4^- or $CF_3SO_3^-$ anions. A detailed 2D-NMR study involving COSY, TOCSY and EXSY experiments has been carried out on the diiron complexes $[Fe_2(BPMP)(O_2P(OPh)_2)_2]^{n+}$ (BPMP = 2,6-bis[(bis(2-pyridylmethyl)amino)methyl]-4-methylphenol; n = 1,2) in both its diferrous and mixed valence states.[153] The electron transfer process was slow on the NMR time scale. By using a very short mixing time of 10 ms (less than the T_1 values of the ring protons), all exchange partners for the ring protons were revealed by their cross-peaks. This enabled correlations to be made of all proton resonances in the reduced complex with those in the mixed valence complex.

Two reports on vanadate complexes are very worthy of mention on account of their combined ^1H and ^{51}V NMR studies. Reactions between $H_2VO_4^-$ and nucleosides gave primarily dimeric binuclear bis(ligand) complexes. ^1H 2D-EXSY was used to demonstrate selective exchange pathways between anomeric protons of various riboside moieties of the vanadate complexes.[154] Oligomerization reactions of vanadate in aqueous solutions

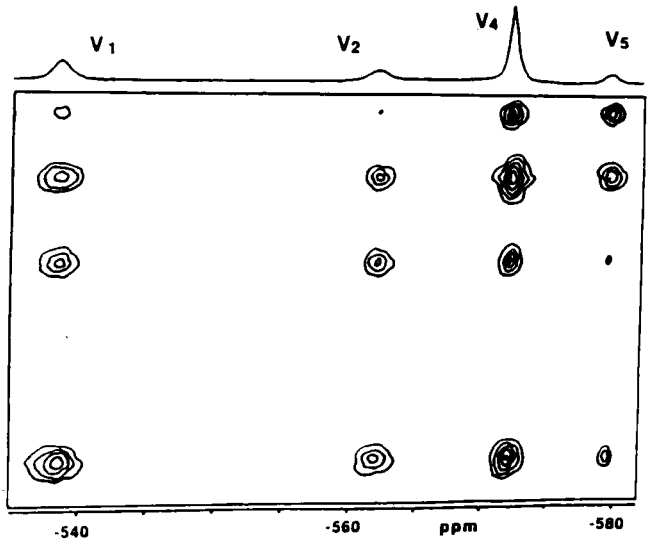

Fig. 11. ^{51}V 2D-EXSY spectrum (131.5 MHz) of a solution containing 10 mM vanadate, 1.0 M KCl and 20% D_2O at pH 8.6, recorded with a mixing time τ_m of 10 ms. TPPI phase cycling was used, and 1000 scans were acquired for each of 256 t_1 increments. Recycle time for each scan was *ca.* 8 ms. A $\frac{1}{2}\pi$-shifted sine bell and zero-filling were applied in both time domains prior to 2D Fourier transformation. Final resolutions were 30 and 60 Hz per point in F_2 and F_1 respectively.

have been studied by ^{51}V 2D-EXSY.[155] This is the first quantitative measurement of complex intermolecular chemical exchange rates using ^{51}V in a 2D-EXSY experiment. The 2D spectra (e.g. Fig. 11) show that all the major vanadate oligomers observed at pH 8.6 (namely monomer, dimer, tetramer and pentamer) exchange with each other. Kinetic analysis combined with exchange rates derived from the 2D-EXSY experiments allowed quantification of several exchange paths. 2D-EXSY spectra were obtained using TPPI phase cycling. Optimal mixing times τ_m were in the range $\frac{1}{2}T_1 < \tau_m < \frac{3}{2}T_1$, and spectra used for calculations were based on values in the range 8–10 ms. The method clearly has great potential for studying multipath exchange reactions, particularly in biological systems.

Platinum(IV) complexes with chalcogen ligands are highly fluxional. For example, complexes of the type $[PtXMe_3(RECH_2CH_2ER')]$ (E = S, Se, Te; R = Me; R′ = Me, Et, ^{t}Bu) undergo pyramidal inversion of the chalcogen atoms, 180° rotations of the ligand with respect to the $PtXMe_3$ moiety and 120° rotations of the latter group. These fluxions have been studied quantitatively by ^{1}H BSA when the ligands are symmetrical thioethers (R = R′). For unsymmetrical ligands (R ≠ R′) the stereodynamics are

intractable by ^{1}H studies, and ^{195}Pt[156,157] and/or ^{125}Te[158] have been used as the nuclide probes. When chalcogen inversion is slow on the NMR time scale, the complexes exist as four distinct invertomers: DL-1, DL-2, DL-3 and DL-4. This means that there are six independent rate constants characterizing the exchange pathways arising from single- and double-site inversions. ^{195}Pt 2D-EXSY is highly suited for this type of study on account of its large chemical shift range and absence of cross-relaxation effects. Reliable rate data for the single-site inversion processes were obtained, values for the synchronous double inversion process being zero within experimental accuracy.[156,157] In the case of ditelluroether complexes $[PtIMe_3(RTe(CH_2)_3TeR)]$ (R = Me, Ph), ^{125}Te 2D-EXSY was shown to be a very suitable monitor of the Te inversion process that interconverts the *meso*-1, DL and *meso*-2 species **[26]**.[158] A typical spectrum is shown in Fig. 12. The authors have compared the relative merits of ^{195}Pt and ^{125}Te 2D-EXSY, and have shown ^{195}Pt to be the marginally preferred nucleus in these complexes. Tellurium pyramidal inversion energies were in the range 70–84 kJ mol^{-1}, and established the trend of chalcogen inversion energies, namely Te > Se > S, with consecutive reductions being *ca.* 12 and *ca.* 10 kJ mol^{-1}.

Chemical applications using ^{13}C 2D-EXSY will now be considered. First, in the binuclear tungsten complex $[W_2(CO)_6(\eta^5\text{-}C_5H_5)_2]$ the method confirmed that simple rotation about the W—W bond was responsible for its isomerization in solution.[159] In the related complexes $[WRh(\mu\text{-}CO)_2(CO)(PPh_3)_2(\eta^5\text{-}C_5H_5)]$ variable-temperature $^{31}P\text{-}\{^{1}H\}$ and $^{13}C\text{-}\{^{1}H\}$ spectra identified a pseudorotational process that interchanges the non-equivalent PPh_3 groups and all the carbonyl ligands. Carbonyl fluxionality is the subject of investigation in the triply bridged tricobalt compound

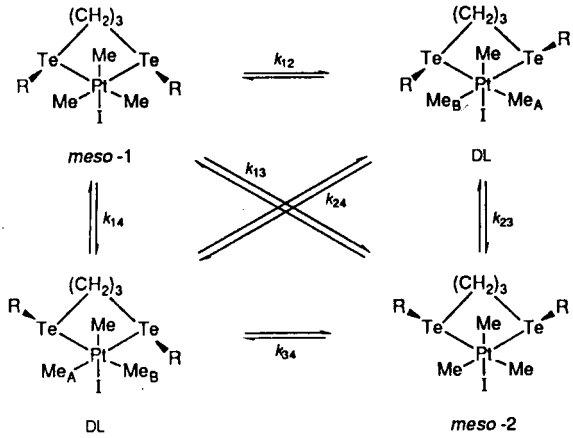

[26]

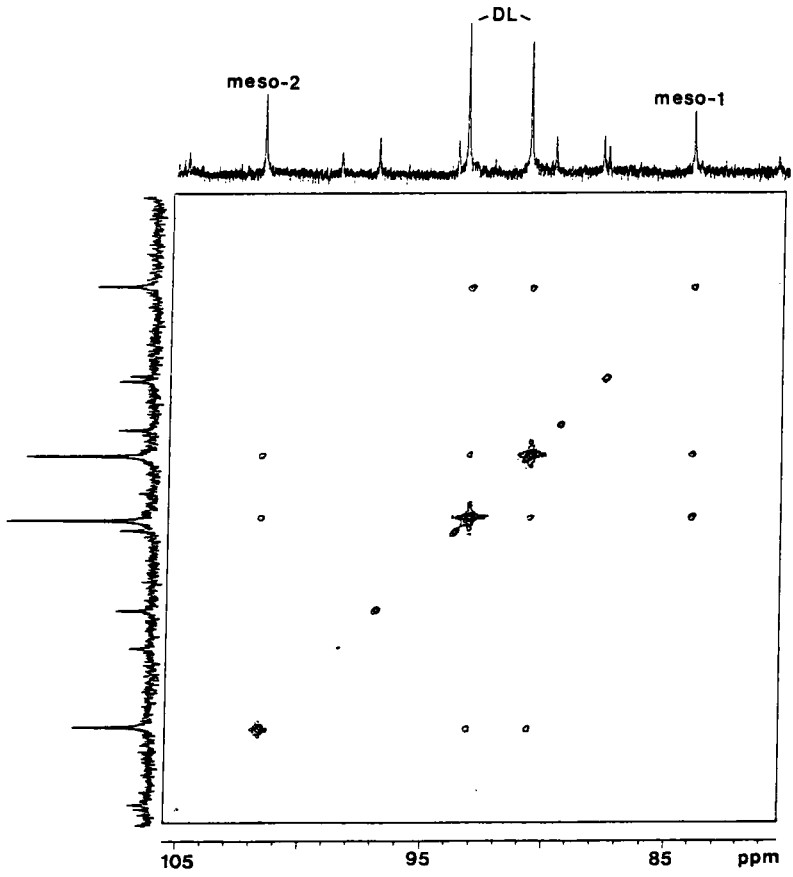

Fig. 12. ^{125}Te 2D-EXSY spectrum of $[PtIMe_3\{MeTe(CH_2)_3TeMe\}]$ in $CDCl_3$ at 313 K. The mixing time was 0.4 s and the number of transients per experiment was 112.

$CH_3CCo_3(CO)_8P(c\text{-}C_6H_{11})_3$.[160] The coalescence effects of the ^{13}CO signals in the 1D spectra can be explained in terms of a mechanism involving a completely bridge-opened structure in which local rotation of the $Co(CO)_3$ vertices is rapid. This mechanism [27] requires that there be more than one carbonyl exchange rate. This was confirmed independently by 2D-EXSY, although quantitative accuracy was limited by the narrow temperature range in which useful spectra could be measured.

There have been a number of reports of ^{13}C 2D-EXSY applied to triosmium and triosmium–platinum clusters. The clusters $[Os_3(\mu\text{-}H)_2(CO)_9(L)]$ (L = phosphines) exhibit a range of solution structures that

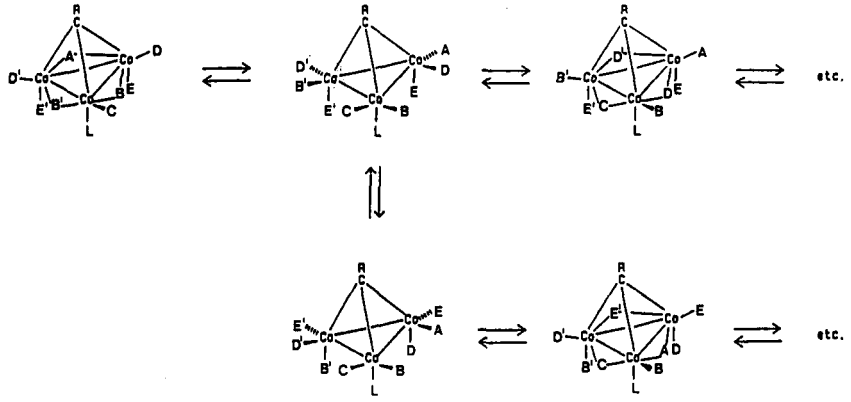

Rapid local rotation can occur at the bridge-opened stage.

[27]

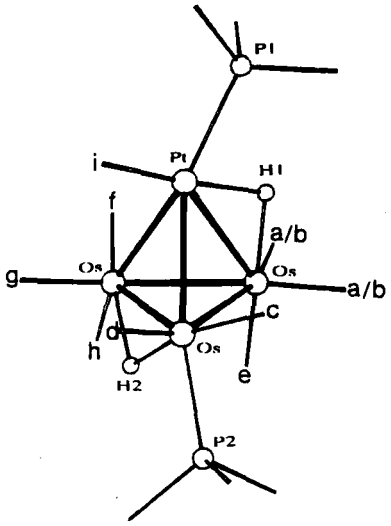

[28]

depend on whether the phosphine occupies an equatorial or an axial site.[161] Exchange between these conformational isomers has been measured by 2D-EXSY. Tripodal rotation of the $Os_3(CO)_3$ group was found in all derivatives, and in the complexes L = P(*o*-tolyl)$_3$ and PPh(1-naphthyl)$_2$ there was evidence of slowed rotation about the Os—P bond or slowed inversion of chirality of the propeller configuration of the aryl groups. Tetrahedro-triosmium platinum clusters have a rich fluxionality.[162,163] One such complex is illustrated in [**28**]. Its ^{13}C 2D-EXSY spectrum (Fig. 13)

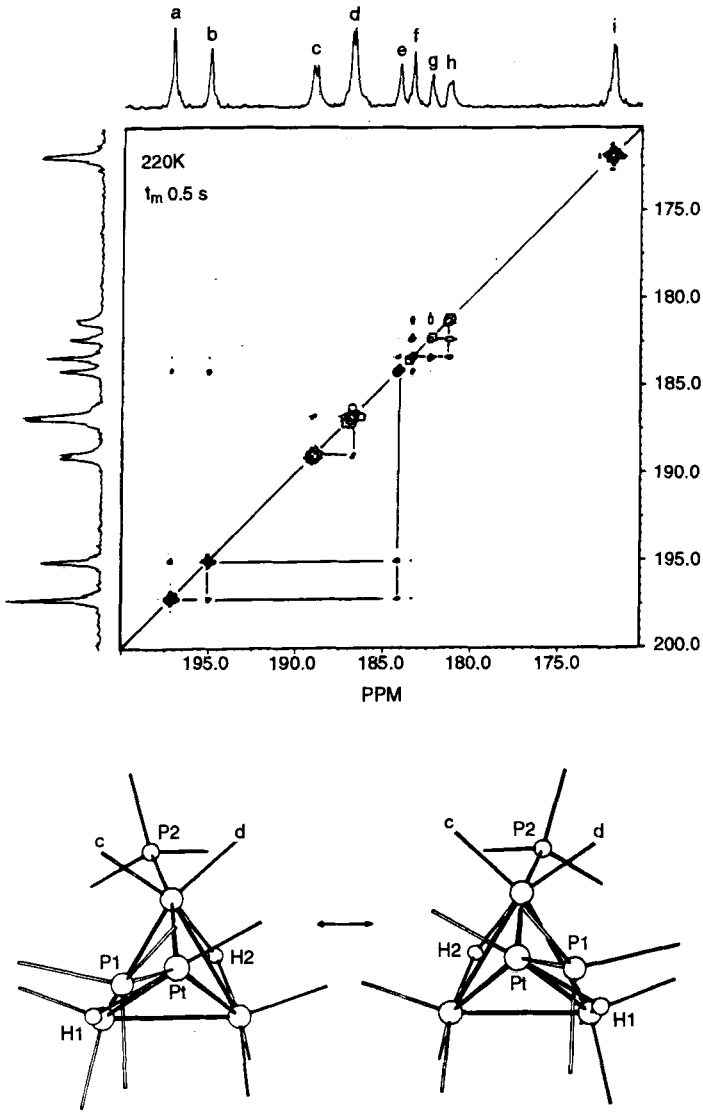

Fig. 13. ^{13}C-{^1H}2D-EXSY spectrum (carbonyl region) of [$Os_3Pt(\mu$-$H)_2(CO)_9(PtPCy_3)Os$—PMe_2Ph)], and proposed mechanism for the enantiomerization process. Labelling refers to structure **[28]**.

shows several independent CO exchange pathways. There are strong cross-peaks between signals a, b and e, and also between f, g and h, indicating tripodal rotations in the $Os(CO)_3$ groups. Weak cross-peaks between these two groups of signals are also observed. This has been explained in terms of a 120° "windshield-wiper" rotation of the $Pt(H)(CO)(PCy_3)$ group, coupled with a migration of H2 to the adjacent Os—Os edge. This motion also accounts for the exchange of signals c and d. The same authors have made a reappraisal of the fluxional behaviour of $[Ru_3(\mu\text{-}H)(\mu_3\text{-}\eta^2\text{-}C{\equiv}C^tBu)(CO)_9]$ using variable-temperature ^{13}C NMR, 2D-EXSY and 1D magnetization transfer experiments.[164] In the 2D-EXSY experiments no single mixing time value t_m provided an accurate evaluation of all rate constants, and so 1D magnetization transfer experiments were also used for providing rate data. A careful analysis of the results led to the conclusion that three fluxional processes are occurring, as shown in [29].

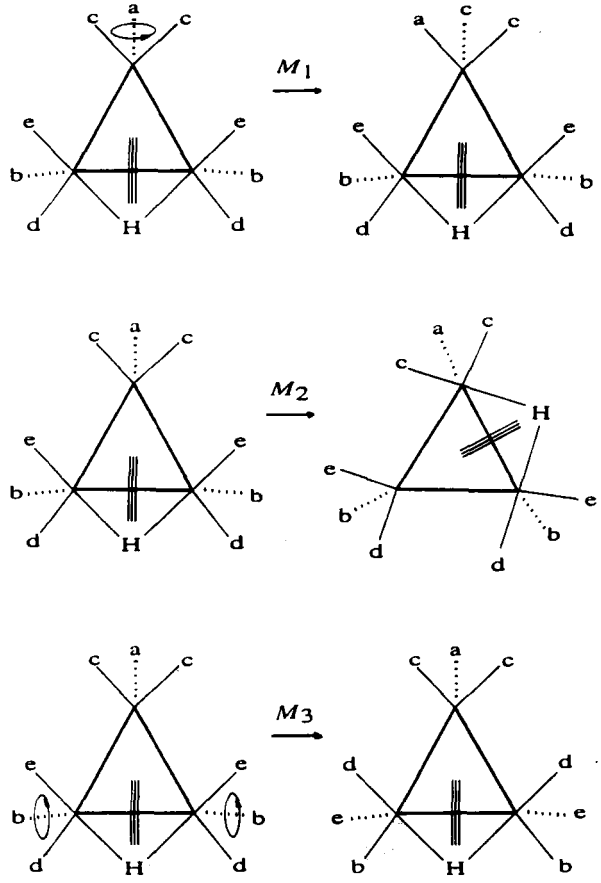

[29]

Mode M_1 is a tripodal rotation of the unique $Ru(CO)_3$ group that exchanges carbonyls a and c with an activation energy $\Delta G^{\ddagger} = 59.1\,kJ\,mol^{-1}$, mode M_2 is the rotation of the alkynyl ligand in concert with hydride migration with $\Delta G^{\ddagger} = 67.0\,kJ\,mol^{-1}$, and mode M_3 is a tripodal rotation of the two equivalent $Ru(CO)_3$ groups with $\Delta G^{\ddagger} = 72.0\,kJ\,mol^{-1}$.

The dynamics of carbonyl fluxionality have been measured by ^{13}C 2D-EXSY in the tetranuclear iridium clusters $[Ir_4(CO)_{11}Br]^-$,[165] $[Ir_4(CO)_{10}(diarsine)]$ and $[Ir_4(CO)_{10}(1,5\text{-cyclooctadiene})]$.[166] In the bromo complex the bridging and Br-site-sharing carbonyls do not exchange with other carbonyls. In the diarsine and cyclooctadiene complexes different fluxional mechanisms exist, which are thought to be a consequence of the different ground state geometries; in the former complex two carbonyls are semibridging, while in the latter the basal carbonyls are symmetrical bridging ligands. Similarly complex fluxionality exists in the μ_3-arene/olefin complexes $[Os_3(CO)_8(\eta^2\text{-}CH_2CHR)(\mu_3\text{:}\eta^2\text{:}\eta^2\text{:}\eta^2\text{-}C_6H_6)]$.[167] Five independent fluxional processes were detected. ^{13}C 2D-EXSY defined a 1,2-ring hopping motion that permutes nuclei in the face-capping benzene ligands, plus two types of π-bonded olefin fluxionality—one involving rotation about metal ligand axes and the other by a trigonal twist mechanism that interchanges ligands in the $Os(CO)_2$(olefin) polytopes. In addition to these helicopter-like rearrangements, there are localized turnstile rotations among the two tricarbonyl ligand sets.

The fluxionality of alkyllithium compounds has been investigated by ^1H, ^{13}C and ^6Li NMR studies. The ^{13}C and ^6Li bandshape analysis of *t*-butyl lithium has already been referred to.[73] The reaction of *n*-butyllithium with diphenylacetylene yields mono- and dilithium products.[168] The latter in THF-d_8 solvent exist as a temperature- and concentration-dependent monomer–dimer equilibrium, which has been studied by ^6Li BSA and 2D-EXSY. The dimeric structure comprised a central C_4Li_4 cube, the ^6Li signals of which were assigned by ^1H–^6Li heteronuclear Overhauser spectroscopy (HOESY). ^7Li 2D-EXSY has been applied for the first time to a kinetic study of the complex [(lithium–monobenzo-15-crown-5]$^+$ in nitromethane.[169] Mixing times varied from 5 to 100 ms, and the number of pulses was 16. Nine experiments were performed, each requiring 1 h of spectrometer time. The rates extracted for the sum of the two pseudo-first-order rate constants were in very close agreement with those measured by BSA, confirming that the technique can be applied with confidence to systems such as certain cryptands where the exchange is too slow to be sensitive to the standard BSA method.

^{11}B 2D-EXSY has recently been applied to the well-known redistribution reactions that occur in mixtures of boron trihalides. The particular mixture studied was a 1:1 M mixture of BCl_3 and BBr_3 at 400 K.[170] The spectrum for a mixing time of 50 ms is shown in Fig. 14. Pseudo-first-order rate constants were calculated by three different methods (Section 2.2.1) proposed for

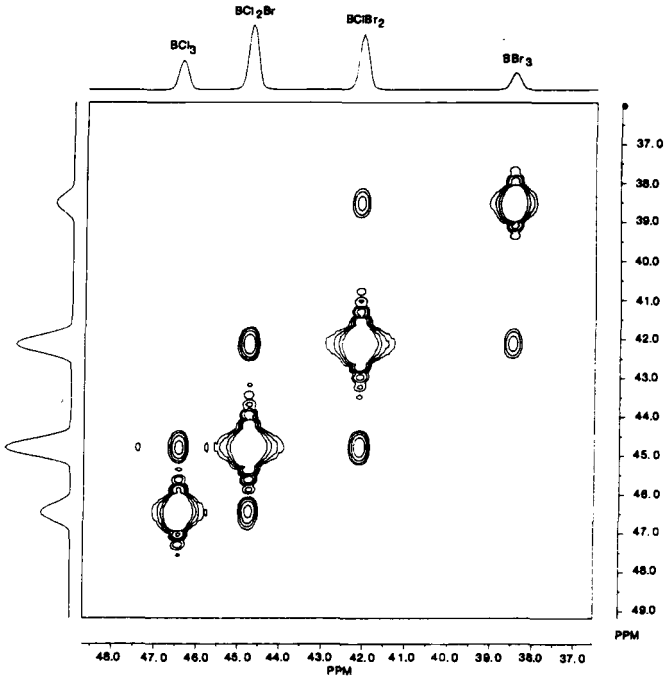

Fig. 14. ^{11}B 2D-EXSY spectrum (128.37 MHz) of a 1.05:1.0 M mixture of BCl_3 and BBr_3 at 400 K, using a mixing time of 50 ms.

$I = ½$ nuclei. The matrix diagonalization procedure of Abel *et al.*[114] involving linear least squares fitting of the intensity data to the linear form of the equation relating the 2D intensity matrix to the rate matrix, proved to be the most reliable method and provided the most straightforward estimate of errors in the rate constants.

^{29}Si 2D-EXSY has proved to be a valuable method for exploring silicate anion exchange pathways in ^{29}Si-enriched potassium silicate solutions.[171] Four intermolecular exchanges were detected involving the monomeric anion, dimer, linear trimer, linear tetramer and substituted cyclic trimer. Two intramolecular exchanges were also found, involving ring opening/closing of a cyclic trimer and an internal rearrangement of a bicyclic pentamer. Although this study utilized 2D-EXSY only in a qualitative manner, it illustrates the greater power of the method over its 1D counterpart. ^{29}Si NMR spectroscopy was also employed very effectively in studying a 1,2-diaryl rearrangement in tetraaryldisilenes that led to the exchange $A_2Si{=}SiB_2 \rightleftharpoons ABSi{=}SiAB$, where A, B represent different aryl moieties.[172] Rates of exchange were obtained from 1D ^{29}Si spectra based on spectral assignments from 2D ^{1}H–^{29}Si spectra. When A = mesityl and

B = 2,6-xylyl, the rearrangement was found to be first-order, with $\Delta H^{\ddagger} = 63 \pm 8\ \text{kJ mol}^{-1}$.

An example of the use of ^{119}Sn 2D-EXSY is a study of the compounds $[RSn(CH_2CH_2CH_2)_2NCH_3]_2$ (R = Cl or CH_3).[173] When R = Cl, restricted rotation about the Sn—Sn bond occurs, in contrast to the compound R = Me, where there was no evidence of any restriction. Instead, solution isomerization occurred, with exchange being detected between three isomers [**30**]. A second example of ^{119}Sn 2D-EXSY is the study of hydrolysis exchange kinetics of $SnCl_6^{2-}$. Mao *et al.*[174] employed the D2DNMR program,[114] but used a Taylor expansion

$$\ln \boldsymbol{a} = (\boldsymbol{a} - 1) - \tfrac{1}{2}(\boldsymbol{a} - 1)^2 + \tfrac{1}{3}(\boldsymbol{a} - 1)^3 \ldots \qquad (32)$$

for evaluating the equation $\boldsymbol{K}t_m = \ln \boldsymbol{a}$ (cf. (22)) rather than the subroutines ALLMAT and BLLMATT in the D2DNMR program.

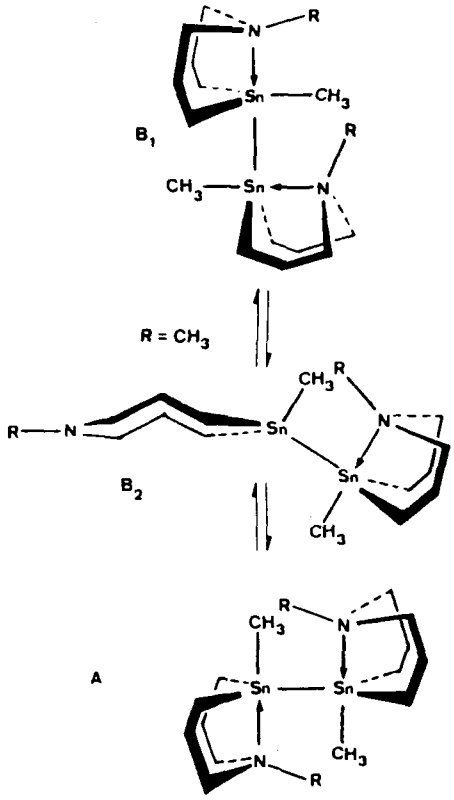

[30]

Phosphorus 2D-EXSY is a particularly powerful technique by virtue of the high receptivity and large chemical shift dispersion of the ^{31}P nuclide. It has been used to investigate some octahedral organochromium(0) complexes of the general type $[Cr(CO)_2(CX)\{(MeO)_3P\}_3]$ (X = O, S, Se).[175] These are stereochemically non-rigid octahedral complexes that, in the cases of X = S and Se, undergo rearrangement via trigonal-prismatic (Bailar) intermediates rather than bicapped-tetrahedral structures. The 2D-EXSY experiments were of the "accordion" type, with the parameter κ having a magnitude of 30. Rate constants for *fac*→*mer* and *mer*→*fac* isomerizations were calculated, and activation enthalpies in the range 64.9–75.3 kJ mol^{-1} were reported.

^{31}P NMR is one of the obvious techniques for identifying fluxionalities of metal phosphine complexes. This is exemplified in the studies of bis- and tris(ether phosphine)ruthenium(II) chloro and acetato complexes.[176] These exhibit exchange between the bidentate (P- and O-bonded) and monodentate (P-bonded) coordination modes of the ether phosphine ligands as the labile metal–oxygen bonds are broken and reformed, causing the exchange (I)–(III) [**31**].[176] A second type of fluxional process was observed in the six-coordinate tris(ether phosphine) complexes. This is attributed to a Berry-type exchange mechanism involving a trigonal-bipyramidal intermediate via the pathways (I)⇄(VII) and (I)⇄(VIII) [**31**]. For the dichloride complex $[RuCl_2(P{-}O)(PO)_2\}$ the activation energies of the two processes were 49.1 and 56.9 kJ mol^{-1} respectively. ^{31}P 2D-EXSY was able to define the mode of interconversion of diastereomeric π-aldehyde complexes of rhenium, namely $[\eta^5\text{-}C_5H_5Re(NO)(PPh_3)(\eta^5\text{-}O{=}CHAr)]BF_4$.[177] Activation energies were in the range 41–64 kJ mol^{-1}, depending on the nature of the Ar group.

Cyclopalladated tertiary phosphite complexes of the type $[Pd(\mu\text{-}Cl)(P(OR^1)_2(OC_6H_3R^2))]_2$ exhibit *sym-cis*/*sym-trans* interconversions, as seen in their ^{31}P 2D-EXSY spectra.[178] The platinum analogue behaves similarly. However, its 2D-EXSY spectrum revealed no exchange of the ^{195}Pt isotopomer with that of the magnetically inactive Pt isotopomers, thereby showing the exchange to be purely intramolecular. Another example of 2D-EXSY applied to dinuclear metal complexes is in the case of the mixed Ni/Pd complexes $[NiPd(CNMe)_3(dppm)][PF_6]_2$.[179] These exchange between covalent and dative metal–metal bonded isomers. Isomer populations were strongly solvent-dependent, with equilibrium constants $K^{\ominus}$ varying between 3.5 (CH_2Cl_2) and 0.28 (DMSO). This work represented the first quantitative study by ^{31}P 2D-EXSY. Mixing times varied from 5 ms to 0.1 s. Rate constants for this two-site problem were evaluated using the explicit expressions for the diagonal and cross-peak intensities. The free energies of activation for the forward and reverse exchange processes were 67.5 and 67.2 kJ mol^{-1}.

Finally, an example of ^{31}P 2D-EXSY applied to a metal cluster compound

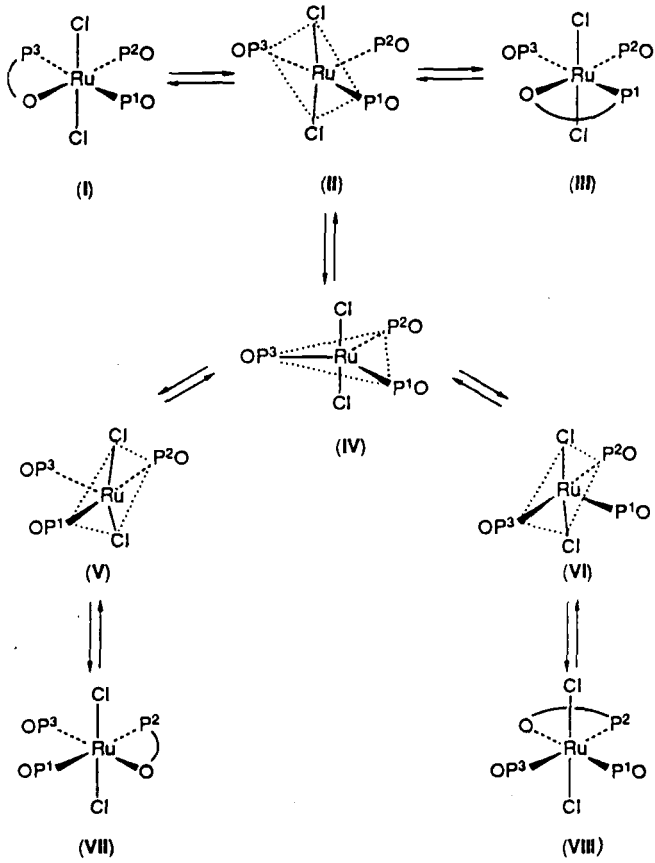

[31]

is provided by the study of mutual exchange and isomerization in the three isomers of the triangular cluster $[Re_2Pt(\mu\text{-}H)_2(CO)_8(PPh_3)_2]$.[180] The three isomers are depicted in [32]. Isomer 1a rearranges irreversibly at temperatures above 273 K to give an equilibrium mixture of isomers 1b and 1c, which differ in the location of the phosphine bound to Re. This slow first-order reaction was followed in a standard kinetic experiment. The 1b⇄1c isomer exchange was followed by ^{31}P 2D-EXSY in the temperature range 295–316 K and by ^{1}H–$\{^{31}P\}$ BSA in the range 333–363 K. 1D- and 2D-derived rate data fell on the same Arrhenius and Eyring straight lines, and led to activation parameters $E_a = 74.0 \pm 1.7\ kJ\ mol^{-1}$, $\Delta H^{\ddagger} = 71.4 \pm 1.7\ kJ\ mol^{-1}$ and $\Delta S^{\ddagger} = -17.4 \pm 5.2\ J\ K^{-1}\ mol^{-1}$.

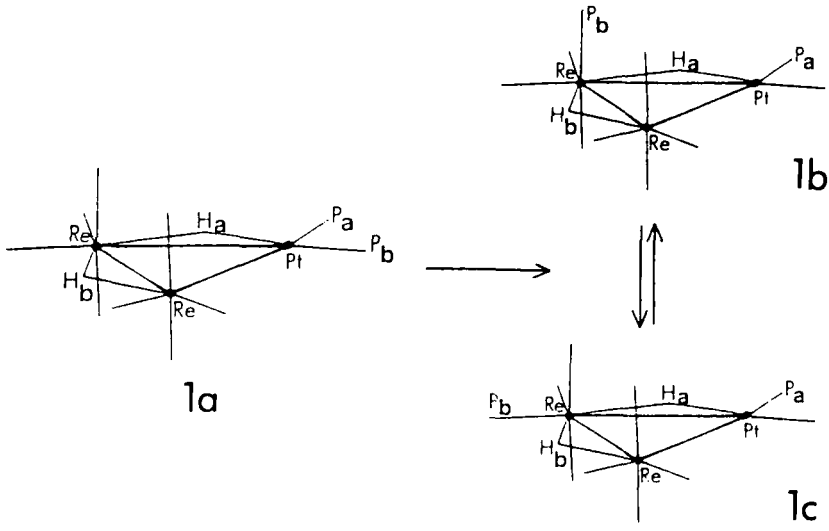

[32]

2.2.2. 3D exchange experiments

Three-dimensional NMR experiments have gradually been emerging over the last five years. There are numerous types of such experiments, since two processes are involved that pairwise-relate three frequency coordinates. In 3D exchange spectra two successive exchange processes are mapped.[181] These may be chemical exchange (EXSY) or cross-relaxation either in the laboratory frame (NOESY) or in the rotating frame (ROESY), resulting in 3D experiments such as EXSY–EXSY (Fig. 15), NOESY–ROESY and so on. Experiments can also be devised that combine coherent and incoherent transfers, e.g. NOESY–COSY or NOESY–TOCSY. In 3D time-domain spectroscopy two 2D pulse sequences are merged, and the 3D signals are a function of two evolution times t_1 and t_2 and a detection time t_3. The computation involved in such experiments is usually very considerable, but may be justified if the additional information content over corresponding 2D experiments is sufficiently high. This may be the case for example in the structural elucidation of proteins. For small molecules the advantages of 3D experiments are less obvious. There has been a single report of a 3D-EXSY–EXSY experiment to date.[182] This concerned heptamethylbenzenonium sulphate in sulphuric acid, where the 1,2-methyl group commutations round the ring were monitored qualitatively. The method can clearly be applied to chemically exchanging systems, but in this particular case no advantages over the analogous 2D-EXSY experiments were apparent. The present authors are not aware of any 3D-EXSY-type experiments applied to

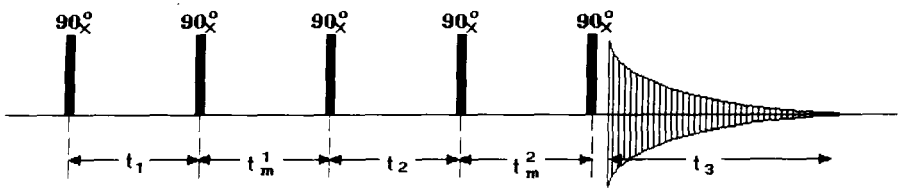

Fig. 15. 3D-EXSY–EXSY pulse sequence for studies of multisite exchange processes. The same pulse sequence is employed for NOESY–NOESY, EXSY–NOESY and NOESY–EXSY experiments.

inorganic or organometallic systems to date, but practitioners of 2D exchange methods should follow future developments carefully.

3. FUTURE TRENDS

Recently, Sorensen[183] has speculated about the potential feasibility and practical importance of 4D NMR methods and beyond. He has argued that two is a natural number of dimensions in time-domain spectroscopy because 2D spectra represent a direct mapping of various coherence transfer processes between pairs of eigenmodes, and this pairwise nature of coherence transfer is not altered in any way in higher-dimensional experiments. Thus an *N*-dimensional spectrum, in principle, does not contain any information that is not extractable from a set of individual 2D spectra. *N*-dimensional spectra do, however, possess a superior resolution power, and where this is of fundamental importance, as in solution studies of biomolecules, higher-dimensional spectra may well have much to offer.

For studies of lower-molecular-weight species, particularly with regard to their dynamic solution structures, 2D-EXSY methods are not likely to be superseded in the immediate future. Such methods, particularly when combined with 1D bandshape or magnetization transfer techniques, provide chemists with highly sensitive and discriminating probes of molecular stereodynamics.

REFERENCES

1. K. G. Orrell and V. Šik, *Ann. Rep. NMR Spectrosc.*, 1987, **19**, 79.
2. M. Oki, *Applications of Dynamic Nuclear Magnetic Resonance Spectroscopy to Organic Chemistry*, VCH, Deerfield Beach, 1985.
3. N. Chandrakumar and S. Subramanian, *Modern Techniques in High Resolution FT NMR*. Springer-Verlag, Berlin, 1987.
4. A. E. Derome, *Modern NMR Techniques for Chemistry Research*. Pergamon Press, Oxford, 1987.

5. J. K. M. Sanders and B. K. Hunter, *Modern NMR Spectroscopy. A Guide to Chemists*, Chap. 7. Oxford University Press, 1987.
6. H. Friebolin, *Basic One- and Two-Dimensional NMR Spectroscopy*, Chap. 11. VCH, Weinheim, Germany, 1991.
7. R. R. Ernst, G. Bodenhausen and A. Wokaun, *Principles of NMR in One and Two Dimensions*, Chaps 4 and 9. Clarendon Press, Oxford, 1987.
8. C. Detellier, *Pract. Spectrosc.*, 1991, **11**, 521.
9. A. Gryff-Keller, *Wiad. Chem.*, 1989, **43**, 799.
10. R. G. Bryant, *J. Chem. Educ.*, 1983, **60**, 933.
11. G. Binsch and H. Kessler, *Angew. Chem. Int. Ed. Engl.*, 1980, **19**, 411.
12. S. Szymanski, *Mol. Phys.*, 1985, **55**, 763.
13. D. A. Kleier and G. Binsch, *J. Magn. Reson.*, 1970, **3**, 146.
14. S. Szymanski, *Mol. Phys.*, 1987, **60**, 897.
15. S. Szymanski, *J. Magn. Reson.*, 1988, **77**, 320.
16. M. H. Levitt and K. Beshah, *J. Magn. Reson.*, 1987, **75**, 222.
17. G. Binsch, *J. Am. Chem. Soc.*, 1969, **91**, 1304.
18. G. Binsch and D. Stephenson, *J. Magn. Reson.*, 1978, **32**, 145.
19. J. I. Kaplan, *J. Magn. Reson.*, 1988, **80**, 340.
20. J. I. Kaplan, *J. Magn. Reson.*, 1991, **91**, 39.
21. K. V. Vasavada and J. I. Kaplan, *J. Magn. Reson.*, 1985, **62**, 37.
22. F. A. L. Anet and D. J. O'Leary, *J. Magn. Reson.*, 1990, **86**, 358.
23. E. Berggren and P. O. Westlund, *Biophys. J.*, 1990, **58**, 167.
24. V. Nurchi, G. Crisponi and M. L. Ganadu, *Anal. Chim. Acta*, 1990, **239**, 157.
25. M. L. H. Green, L.-L. Wong and A. Sella, *Organometallics*, 1992, **11**, 2660.
26. R. G. S. Spencer, J. A. Ferretti and G. H. Weiss, *J. Magn. Reson.*, 1989, **84**, 223.
27. M. de Deus Corceiro de Carvalho, Report 1990, Order PB91-209320 [*Government Report Announcements Index (US)*, 1991, **91(19)**, Abstr. 151 802].
28. E. W. Abel, I. Moss, K. G. Orrell and V. Šik, *J. Organomet. Chem.*, 1987, **326**, 187.
29. E. W. Abel, D. E. Budgen, I. Moss, K. G. Orrell and V. Sik, *J. Organomet. Chem.*, 1989, **362**, 105.
30. S. Toyota, Y. Yamada, M. Kaneyoshi and M. Oki, *Bull. Chem. Soc. Jpn*, 1989, **62**, 1509.
31. D. D. Gummin, E. M. A. Ratilla and N. M. Kostic, *Inorg. Chem.*, 1986, **25**, 2429.
32. E. W. Abel, N. J. Long, K. G. Orrell, A. G. Osborne and V. Šik, *J. Organomet. Chem.*, 1991, **405**, 375.
33. E. W. Abel, D. Ellis, K. G. Orrell and V. Šik, *Polyhedron*, 1991, **10**, 1603.
34. R. Mynott, H. Lehmkuhl, E. M. Kreuzer and E. Joussen, *Angew. Chem. Int. Ed. Engl.*, 1990, **29**, 289.
35. J. Okuda and E. Herdtweck, *J. Organomet. Chem.*, 1989, **373**, 99.
36. J. Okuda, *J. Organomet. Chem.*, 1989, **367**, C1.
37. J. Okuda, *J. Organomet. Chem.*, 1990, **385**, C39.
38. E. W. Abel, N. J. Long, K. G. Orrell, A. G. Osborne and V. Šik, *J. Organomet. Chem.*, 1991, **403**, 195.
39. G. Hunter, T. J. R. Weakley, K. Mislow and M. G. Wong, *J. Chem. Soc. Dalton Trans.*, 1986, 577.
40. S. Denholm, G. Hunter and T. J. R. Weakley, *J. Chem. Soc. Dalton Trans.*, 1987, 2789.
41. G. Hunter, T. J. R. Weakley and W. Weissensteiner, *J. Chem. Soc. Perkin Trans. 2*, 1987, 1633.
42. I. I. Schuster, W. Weissensteiner and K. Mislow, *J. Am. Chem. Soc.*, 1986, **108**, 6661.
43. B. Mailvaganam, B. G. Sayer and M. J. McGlinchey, *J. Organomet. Chem.*, 1990, **395**, 177.
44. B. Mailvaganam, B. G. Sayer and M. J. McGlinchey, *Organometallics*, 1990, **9**, 1089.
45. B. Mailvaganam, C. S. Frampton, S. Top, B. G. Sayer and M. J. McGlinchey, *J. Am. Chem. Soc.*, 1991, **113**, 1177.

46. J. A. Chudek, G. Hunter, R. L. MacKay, G. Faerber and W. Weissensteiner, *J. Organomet. Chem.*, 1989, **377**, C69.
47. K. V. Kilway and J. S. Siegel, *J. Am. Chem. Soc.*, 1991, **113**, 2332.
48. C. Elschenbroich, J. Schneider and H. Burdorf, *J. Organomet. Chem.*, 1990, **391**, 195.
49. J. A. Chudek, G. Hunter, R. L. MacKay, P. Kremminger, K. Schloegl and W. Weissensteiner, *J. Chem. Soc. Dalton Trans.*, 1990, 2001.
50. J. A. Chudek, G. Hunter, R. L. MacKay, P. Kremminger and W. Weissensteiner, *J. Chem. Soc. Dalton Trans.*, 1991, 3337.
51. G. Hunter, R. L. MacKay, P. Kremminger and W. Weissensteiner, *J. Chem. Soc. Dalton Trans.*, 1991, 3349.
52. K. V. Kilway and J. S. Siegel, *Organometallics*, 1992, **11**, 1426.
53. J. Edwin, W. E. Geiger and C. H. Bushweller, *Organometallics*, 1988, **7**, 1486.
54. E. W. Abel, J. C. Dormer, D. Ellis, K. G. Orrell, V. Šik, M. B. Hursthouse and M. A. Mazid, *J. Chem. Soc. Dalton Trans.*, 1992, 1073.
55. E. W. Abel, N. J. Long, K. G. Orrell, A. G. Osborne, H. M. Pain and V. Šik, *J. Chem. Soc. Chem. Commun.*, 1992, 303.
56. E. W. Abel, V. S. Dimitrov, N. J. Long, K. G. Orrell, A. G. Osborne, V. Šik, M. B. Hursthouse and M. A. Mazid, *J. Chem. Soc. Dalton Trans.*, 1993, 291.
57. E. W. Abel, V. S. Dimitrov, N. J. Long, K. G. Orrell, A. G. Osborne, H. M. Pain, V. Šik, M. B. Hursthouse and M. A. Mazid, *J. Chem. Soc. Dalton Trans.*, 1993, 597.
58. E. W. Abel, D. Ellis and K. G. Orrell, *J. Chem. Soc. Dalton Trans.*, 1992, 2243.
59. E. W. Abel, P. Heard and K. G. Orrell, Unpublished work.
60. E. W. Abel, K. G. Orrell, A. G. Osborne, V. Šik and W. Guoxiong, *J. Organomet. Chem.*, 1991, **411**, 239.
61. E. W. Abel, N. J. Long, K. G. Orrell, A. G. Osborne, V. Šik, P. A. Bates and M. B. Hursthouse, *J. Organomet. Chem.*, 1989, **367**, 275.
62. E. W. Abel, N. J. Long, K. G. Orrell, A. G. Osborne and V. Sik, *J. Organomet. Chem.*, 1989, **378**, 473.
63. E. W. Abel, N. J. Long, K. G. Orrell, A. G. Osborne, V. Šik, P. A. Bates and M. B. Hursthouse, *J. Organomet. Chem.*, 1990, **38**, 253.
64. D. M. Heinekey, *J. Am. Chem. Soc.*, 1991, **113**, 6074.
65. D. M. Heinekey and T. G. P. Harper, *Organometallics*, 1991, **10**, 2891.
66. J. Heck and G. Rist, *J. Organomet. Chem.*, 1988, **342**, 45.
67. F. Mao, C. E. Philbin, T. J. R. Weakley and D. R. Tyler, *Organometallics*, 1990, **9**, 1510.
68. S. G. Davies, A. E. Derome and J. P. McNally, *J. Am. Chem. Soc.*, 1991, **113**, 2854.
69. J. Browning, K. A. Beveridge, G. W. Bushnell and K. R. Dixon, *Inorg. Chem.*, 1986, **25**, 1987.
70. E. W. Abel, K. G. Orrell and D. Stephenson, *J. Organomet. Chem.*, 1989, **373**, 401.
71. G. Douglas, L. Manojlovic-Muir, K. W. Muir, M. C. Jennings, B. R. Lloyd, M. Rashidi, G. Schoettel and R. J. Puddephatt, *Organometallics*, 1991, **10**, 3927.
72. E. Kalbarczyk-Bidelska and S. Pasynkiewicz, *J. Organomet. Chem.*, 1991, **407**, 143.
73. R. D. Thomas, M. T. Clarke, R. M. Jensen and T. C. Young, *Organometallics*, 1986, **5**, 1851.
74. H. W. Spiess, *Chem. Rev.*, 1991, **91**, 1321.
75. G. Erker, R. Nolte, C. Krueger, R. Schlund, R. Benn, H. Grondey and R. Mynott, *J. Organomet. Chem.*, 1989, **364**, 119.
76. R. Benn, H. Grondey, G. Erker, R. Aul and R. Nolte, *Organometallics*, 1990, **9**, 2493.
77. S. J. Heyes and C. M. Dobson, *J. Am. Chem. Soc.*, 1991, **113**, 463.
78. C. H. Bushweller, L. J. Letendre, J. A. Brunelle, H. S. Bilofsky, M. R. Whalon and S. H. Fleischman, DNMR 4, Program 466, QCPE, Indiana University.
79. R. Benn, R. Mynott, I. Topalovic and F. Scott, *Organometallics*, 1989, **8**, 2299.
80. S. J. Heyes, C. M. Dobson, M. A. Gallop, B. F. G. Johnson and J. Lewis, *Inorg. Chem.*, 1991, **30**, 3850.

81. S. J. Heyes, M. L. H. Green and C. M. Dobson, *Inorg. Chem.*, 1991, **30**, 1930.
82. C. J. Schaverien and G. J. Nesbitt, *J. Chem. Soc. Dalton Trans.*, 1992, 157.
83. H. Gesmar and J. J. Led, *J. Magn. Reson.*, 1986, **68**, 95.
84. M. Grassi, B. E. Mann, B. T. Pickup and C. M. Spencer, *J. Magn. Reson.* 1986, **69**, 92.
85. D. R. Muhandiram and R. E. D. McClung, *J. Magn. Reson.*, 1987, **71**, 187.
86. S. F. Bellon, D. Chen and E. R. Johnston, *J. Magn. Reson.*, 1987, **73**, 168.
87. D. R. Muhandiram and R. E. D. McClung, *J. Magn. Reson.*, 1988, **76**, 121.
88. J. M. Brown, P. A. Chaloner and G. A. Morris, *J. Chem. Soc. Perkin Trans 2*, 1987, 1583.
89. J. M. Brown, P. L. Evans and A. R. Lucy, *J. Chem. Soc. Perkin Trans. 2*, 1987, 1589.
90. O. W. Howarth and P. Kelly, *J. Chem. Soc. Chem. Commun.*, 1988, 1236.
91. D. Baudry, P. Boydell and M. Ephritikhine, *J. Chem. Soc. Dalton Trans.*, 1986, 525.
92. E. B. Wickenheiser and W. R. Cullen, *Inorg. Chem.*, 1990, **29**, 4671.
93. M. Grassi, B. E. Mann, B. T. Pickup and C. M. Spencer, *J. Chem. Soc. Dalton Trans.*, 1987, 2649.
94. H. Adams, N. A. Bailey, G. W. Bentley and B. E. Mann, *J. Chem. Soc. Dalton Trans.*, 1989, 1831.
95. B. E. Mann, B. T. Pickup and A. K. Smith, *J. Chem. Soc. Dalton Trans.*, 1989, 889.
96. J. P. McNally and N. J. Cooper, *Organometallics*, 1988, **7**, 1704.
97. A. Stanger and K. P. C. Vollhardt, *Organometallics*, 1992, **11**, 317.
98. H. Adams, N. A. Bailey, B. E. Mann, B. F. Taylor, C. White and P. Yavari, *J. Chem. Soc. Dalton Trans.*, 1987, 1947.
99. M. I. Altbach, Y. Hiyama, R. J. Wittebort and L. G. Butler, *Inorg. Chem.*, 1990, **29**, 741.
100. S. Aime, M. Botta, R. Gobetto and A. Orlandi, *Magn. Reson. Chem.*, 1990, **28** (Spec. Issue), S52.
101. Y. S. Wang and S. Ikuta, *Magn. Reson. Chem.*, 1989, **27**, 1134.
102. D. M. Campbell, M. Mackowiak and J. Jonas, *J. Chem. Phys.*, 1992, **96**, 2717.
103. P. Yuan, M. G. Richmond and M. Schwartz, *Inorg. Chem.*, 1991, **30**, 679.
104. S. P. Wang, A. F. T. Chen, M. G. Richmond and M. Schwartz, *J. Organomet. Chem.*, 1989, **371**, 81.
105. P. Yuan, M. G. Richmond and M. Schwartz, *Inorg. Chem.*, 1991, **30**, 588.
106. H. Kessler, M. Gehrke and C. Griesinger, *Angew. Chem. Int. Ed. Engl.*, 1988, **27**, 490.
107. R. Willem, *Prog. Nucl. Magn. Reson. Spectrosc.*, 1987, **20**, 1.
108. K. G. Orrell, V. Šik and D. Stephenson, *Prog. Nucl. Magn. Reson. Spectrosc.*, 1990, **22**, 141.
109. C. L. Perrin and T. J. Dwyer, *Chem. Rev.*, 1990, **90**, 935.
110. E. R. Johnston, M. J. Dellwo and J. Hendrix, *J. Magn. Reson.*, 1986, **66**, 399.
111. G. Bodenhausen and R. R. Ernst, *J. Am. Chem. Soc.*, 1982, **104**, 1304.
112. C. L. Perrin, *J. Magn. Reson.*, 1989, **82**, 619.
113. G. E. Hawkes, L. Y. Lian, E. W. Randall, K. D. Sales and S. Aime, *J. Magn. Reson.*, 1985, **65**, 173.
114. E. W. Abel, T. P. J. Coston, K. G. Orrell, V. Šik and D. Stephenson, *J. Magn. Reson.*, 1986, **70**, 34.
115. G. Wagner, G. Bodenhausen, N. Muller, M. Rance, O. W. Sorensen, R. R. Ernst and K. Wüthrich, *J. Am. Chem. Soc.*, 1985, **107**, 6440.
116. J. Fejzo, W. M. Westler, S. Macura and J. L. Markley, *J. Magn. Reson.*, 1991, **92**, 20.
117. C. T. W. Moonen, P. Van Gelderen, G. W. Vuister and P. C. M. Van Zijl, *J. Magn. Reson.*, 1992, **97**, 419.
118. T. Beringhelli, G. D'Alfonso, H. Molinari, G. E. Hawkes and K. D. Sales, *J. Magn. Reson.*, 1988, **80**, 45.
119. P. W. Kuchel, B. T. Bulliman, B. E. Chapman and G. L. Mendz, *J. Magn. Reson.*, 1988, **76**, 136.
120. R. Nadjari and J.-Ph. Grivet, *J. Magn. Reson.*, 1992, **98**, 259.

121. P. Güntert and K. Wüthrich, *J. Magn. Reson.*, 1992, **96**, 403.
122. R. A. Schiksnis, A. L. Rockwell, L. M. Gierasch and S. J. Opella, *J. Magn. Reson.*, 1988, **79**, 318.
123. S. Davies, J. Friedrich and R. Freeman, *J. Magn. Reson.*, 1987, **75**, 540.
124. Yu. E. Chernysh, G. S. Borodkin, E. V. Sukhołenko and L. E. Nivorozhkin, *J. Magn. Reson.*, 1992, **96**, 131.
125. R. E. Engler, E. R. Johnston and C. G. Wade, *J. Magn. Reson.*, 1988, **77**, 377.
126. B. T. Bulliman, P. W. Kuchel and B. E. Chapman, *J. Magn. Reson.*, 1989, **82**, 131.
127. C. L. Perrin and R. E. Engler, *J. Magn. Reson.*, 1990, **90**, 363.
128. J.-M. Fauth, S. Kababya and D. Goldfarb, *J. Magn. Reson.*, 1991, **92**, 203.
129. E. Rommel, P. Nickel, F. Rohmer, R. Kimmich, C. Gonzales and D. Pusiol, *Z. Naturforsch.*, 1992, **A47**, 382.
130. H. Barkhuizsen, R. De Beer, W. M. M. J. Bovée and D. Van Ormondt, *J. Magn. Reson.*, 1985, **61**, 465.
131. H. Gesmar and J. J. Led, *J. Magn. Reson.*, 1988, **76**, 575.
132. B. A. Johnson, J. A. Malikayil and I. M. Armitage, *J. Magn. Reson.*, 1988, **76**, 352.
133. S. F. Gull and G. J. Daniell, *Nature*, 1978, **272**, 686.
134. S. Sibisi, J. Skilling, R. G. Brereton, E. D. Laue and J. Staunton, *Nature*, 1984, **311**, 446.
135. G. L. Daniell and P. J. Hore, *J. Magn. Reson.*, 1989, **84**, 515.
136. J. A. Jones and P. J. Hore, *J. Magn. Reson.*, 1991, **92**, 363.
137. J. A. Jones and P. J. Hore, *J. Magn. Reson.*, 1991, **92**, 276.
138. MaxEnt Solutions Ltd, Isleham, Ely, Cambridge. Publicity Information, Nov. 1992.
139. J. C. Hoch, *J. Magn. Reson.*, 1985, **64**, 436.
140. E. W. Abel, K. G. Orrell, K. B. Qureshi, V. Šik and D. Stephenson, *J. Organomet. Chem.*, 1988, **353**, 337.
141. E. W. Abel, T. P. J. Coston, K. M. Higgins, K. G. Orrell, V. Sik and T. S. Cameron, *J. Chem. Soc. Dalton Trans.*, 1989, 701.
142. E. W. Abel, T. P. J. Coston, K. G. Orrell and V. Šik, *J. Chem. Soc. Dalton Trans.*, 1989, 711.
143. E. W. Abel, N. J. Long, K. G. Orrell, A. G. Osborne and V. Sik, *J. Organomet. Chem.*, 1991, **419**, 375.
144. M. H. Chisholm, D. L. Clark and M. J. Hampden-Smith, *J. Am. Chem. Soc.*, 1989, **111**, 574.
145. M. L. H. Green and L.-L. Wong, *J. Chem. Soc. Chem. Commun.*, 1989, 571; *J. Chem. Soc. Dalton Trans.*, 1989, 2133.
146. M. L. H. Green, A. Sella and L.-L. Wong, *Organometallics*, 1992, **11**, 2650.
147. B. Wrackmeyer and K. Horchler, *Organometallics*, 1990, **9**, 1881.
148. B. G. Jenkins and R. B. Lauffer, *J. Magn. Reson.*, 1988, **80**, 328.
149. B. G. Jenkins and R. B. Lauffer, *Inorg. Chem.*, 1988, **27**, 4730.
150. C. Luchinat, S. Steuernagel and P. Turano, *Inorg. Chem.*, 1990, **29**, 4351.
151. F. L. Dickert and H. U. Meissner, *Ber. Bunsen-Ges. Phys. Chem.*, 1989, **93**, 1450.
152. F. L. Dickert, M. Feigl, W. Gumbrecht, H. U. Meissner and P. P. Otto, *Z. Phys. Chem. (Munich)*, 1991, **170**, 185.
153. L. J. Ming, H. G. Jang and L. Que, Jr, *Inorg. Chem.*, 1992, **31**, 359.
154. A. S. Tracey and C. H. Leon-Lai, *Inorg. Chem.*, 1991, **30**, 3200.
155. D. C. Crans, C. D. Rithner and L. A. Theisen, *J. Am. Chem. Soc.*, 1990, **112**, 2901.
156. E. W. Abel, I. Moss, K. G. Orrell, V. Šik and D. Stephenson, *J. Chem. Soc. Dalton Trans.*, 1987, 2695.
157. E. W. Abel, I. Moss, K. G. Orrell, V. Šik, D. Stephenson, P. A. Bates and M. B. Hursthouse, *J. Chem. Soc. Dalton Trans.*, 1988, 521.
158. E. W. Abel, K. G. Orrell, S. P. Scanlon, D. Stephenson, T. Kemmitt and W. Levason, *J. Chem. Soc. Dalton Trans.*, 1991, 591.

159. W. E. Lindsell and P. J. Tomb, *J. Organomet. Chem.*, 1989, **378**, 245.
160. L. Li, M. F. D'Agostino, B. G. Sayer and M. J. McGlinchey, *Organometallics*, 1992, **11**, 477.
161. L. J. Farrugia, *J. Organomet. Chem.*, 1990, **394**, 515.
162. L. J. Farrugia, *Organometallics*, 1989, **8**, 2410.
163. L. J. Farrugia and S. E. Rae, *Organometallics*, 1991, **10**, 3919.
164. L. J. Farrugia and S. E. Rae, *Organometallics*, 1992, **11**, 196.
165. A. Strawczynski, R. Ros and R. Roulet, *Helv. Chim. Acta*, 1988, **71**, 867.
166. A. Strawczynski, R. Ros, R. Roulet, F. Grepioni and D. Braga, *Helv. Chim. Acta*, 1988, **71**, 1885.
167. M. A. Gallop, B. F. G. Johnson, J. Keeler, J. Lewis, S. J. Heyes and C. M. Dobson, *J. Am. Chem. Soc.*, 1992, **114**, 2510.
168. W. Bauer, M. Feigel, G. Mueller and P. v. R. Schleyer, *J. Am. Chem. Soc.*, 1988, **110**, 6033.
169. K. M. Briere, H. D. Dettman and C. Detellier, *J. Magn. Reson.*, 1991, **94**, 600.
170. E. F. Derose, J. Castillo, D. Saulys and J. Morrison, *J. Magn. Reson.*, 1991, **93**, 347.
171. C. T. G. Knight, R. J. Kirkpatrick and E. Oldfield, *J. Magn. Reson.*, 1988, **78**, 31.
172. H. B. Yokelson, D. A. Siegel, A. J. Millevolte, J. Maxka and R. West, *Organometallics*, 1990, **9**, 1005.
173. K. Jurkschat, Z. Tzschach, C. Muegge, J. Piret-Meunier, M. Van Meerssche, G. Van Binst, C. Wynants, M. Gielen and R. Willem, *Organometallics*, 1988, **7**, 593.
174. X. Mao, X. You and A. Dai, *Magn. Reson Chem.*, 1989, **27**, 836.
175. A. A. Ismail, F. Sauriol and I. S. Butler, *Inorg. Chem.*, 1989, **28**, 1007.
176. G. M. McCann, A. Carvill, E. Lindner, B. Karle and H. A. Mayer, *J. Chem. Soc. Dalton Trans.*, 1990, 3107.
177. N. Quiros Mendez, C. L. Mayne and J. A. Gladysz, *Angew. Chem. Int. Ed. Engl.*, 1990, **29**, 1475.
178. A. Albinati, S. Affolter and P. S. Pregosin, *Organometallics*, 1990, **9**, 379.
179. J. Ni and C. P. Kubiak, *Inorg. Chem.*, 1990, **29**, 4345.
180. T. Beringhelli, G. D'Alfonso and A. P. Minoja, *Organometallics*, 1991, **10**, 394.
181. C. Griesinger, O. W. Sorensen and R. R. Ernst, *J. Magn. Reson.*, 1987, **73**, 574.
182. C. Griesinger, O. W. Sorensen and R. R. Ernst, *J. Magn. Reson.*, 1989, **84**, 14.
183. O. W. Sorensen, *J. Magn. Reson.*, 1990, **89**, 210.

This Page Intentionally Left Blank

The Use of Proton MR in Cancer Pathology

CAROLYN E. MOUNTFORD, CYNTHIA L. LEAN, WANDA B. MACKINNON

Membrane-NMR Unit, Department of Cancer Medicine, University of Sydney, Australia

PETER RUSSELL

Department of Anatomical Pathology, Royal Prince Alfred Hospital, Camperdown, Australia

ANNUAL REPORTS ON NMR SPECTROSCOPY
VOLUME 27 ISBN 0-12-505327-4

1. INTRODUCTION

Cancer is arguably the most feared disease in the western world this century.[1] This is not surprising, since it is the second most common cause of death (the first being diseases of the cardiovascular systems).[2] Despite public awareness programmes designed to alleviate disproportionate fear, cancer is still perceived as a disease affecting all sections of society and accompanied by long and painful illness exacerbated by the side effects of adjuvant therapy. In the last three decades significant advances have been made in the areas of prevention, detection and treatment of malignant disease, with the most significant shift in public perception of cancer being the acceptance that early detection increases the likelihood of successful intervention in the disease process. Histopathological techniques employed to diagnose cancer have, however, changed little during this time.

1.1. Pathological assessment of cancer

Cancer is not one but a myriad of disease entities with various causes, appearances and clinical courses. Predicting the clinical course in the individual patient is the basis for rational treatment, and traditionally the gold standards for such assessments are histopathological typing and grading of the malignancy and clinicopathological staging. Both these procedures are subjective and fraught with difficulties.

1.1.1. Histopathology

The final or definitive diagnosis of invasive or preinvasive malignancy in tissue is currently undertaken by a histopathologist. The skill, experience and thoroughness of both surgeon and pathologist all play a part in ensuring the suitability of a given biopsy for the necessary assessment of a neoplastic

lesion. Further sampling errors are possible during the processing of each biopsy. From any one tissue biopsy, usually less than 1% of the sample is routinely assessed. As noted above, tumour typing and grading are subjective techniques, dependent on sampling and open to observer error. A method that examined the entire specimen and provided an objective assessment, independent of the morphological manifestations, would be a significant advance.

1.1.2. Clinical staging and grading

Clinical staging of cancer determines the extent and spread of the disease, i.e. the extent of penetration of the tumour through local tissues, the involvement of local and distant lymph nodes and the presence of other secondary growths. It does not distinguish between young and aggressive primary tumours and older but more slowly growing ones that have progressed to the same stage. This has traditionally been the role of histological grading. Grading of a cancer correlates the degree of differentiation of tumour cells and number of mitoses present with the aggressiveness of the tumour. Such a distinction, made objectively, would facilitate a more precise diagnosis and aid in the choice of adjuvant therapy.

Problems inherent in the classical histopathological approach are predominantly the accuracy of the initial biopsy procedure and the variable skills applied to its histological assessment.[3] An even greater problem is faced when attempting to provide adequate histopathological assessments of lymph nodes for staging purposes owing to the large volumes of tissue often to be assessed and the logistical difficulties in thorough and complete examination.

In 1990 a retrospective study undertaken by Bettelheim *et al.*[4] revealed that: "Serial sectioning of lymph nodes judged to be disease-free after routine examination revealed micrometastases in an additional 83 (9%) of 921 breast cancer subjects." It has subsequently been suggested that histopathological examination of single haematoxylin and eosin (H&E) stained node sections is probably no longer acceptable. In our laboratory step-serial sectioning of all embedded lymphoid tissue (as opposed to a single section from each node) from radical pelvic node dissection in patients with Stage Ib–IIa cervical cancer has (since its introduction in 1979) increased the proportion of "node-positive" women by about 50%, with implications for more soundly based use of post-operative adjuvant therapy (P. Russell, unpublished data).

Thus there exists a body of opinion that current histopathological procedures are subjective, imprecise and open to observer error. Development of a new modality to remove sampling errors, improve specificity and produce a grading of tissues that relates to established biological criteria would be welcomed.

1.2. The potential of proton magnetic resonance for the detection and diagnosis of cancer

Proton magnetic resonance spectroscopy (^{1}H MRS) is approximately 16 times more sensitive than ^{31}P MRS, and has the advantage of providing information on a large number of cellular metabolites. Hence detailed information may be obtained about cellular biochemistry and energy and lipid metabolism. A disadvantage of ^{1}H MRS is the large natural water signal obtained from cells and tissue (see Fig. 1a). However, new probe technology and water suppression procedures (Fig. 1b) have made ^{1}H MRS a practical proposition for assessing the pathology of tissue. In addition, by using multipulse sequences, molecules with different T_2 relaxation values may also be discerned (Fig. 1c). As a consequence of these technical developments, we consider here the possibility that ^{1}H MRS could aid, or in some instances ultimately replace, histopathology for the detection and grading of cancers in certain organs. In so doing, it would remove sampling errors and subjective assessment procedures inherent in histopathology.

The ^{1}H MRS method has been developed successfully for human cervical and thyroid biopsies, and rat lymph nodes, based on the different chemical make-up of normal, diseased, precancerous and cancerous states. The histopathological categories are distinguished on the basis of characteristic chemical profiles, and it is therefore necessary to document the ^{1}H MR-visible chemistry from intact viable tissues and then devise the most efficient means of obtaining the diagnostic information. Central to this working philosophy is an understanding of the chemical changes that accompany tumour development and progression.

1.3. Tumour development and progression

Tumour development refers to the transition of a population of abnormal or initiated cells to a biologically malignant neoplasm.[2] It should be remembered that 90% of human tumours are epithelial. Premalignant and early malignant changes occur first within normally sited cells of the epithelium, and result in the formation of a localized malignancy referred to as a carcinoma *in situ* (CIS).

At any point in development, a neoplasm may change from a benign or low-grade malignant tumour to a rapidly growing, virulent neoplasm. Invasion begins when tumour cells penetrate through the basement membrane of the epithelium and into the underlying stroma, and thence into subjacent tissues (e.g. muscle or fat). Once invasion has occurred, the possibility exists for tumour cells to enter the lymphatics or blood vessels and be transported to distant sites in the body. This event is termed metastasis. The biological and genetic characteristics of a neoplasm, which

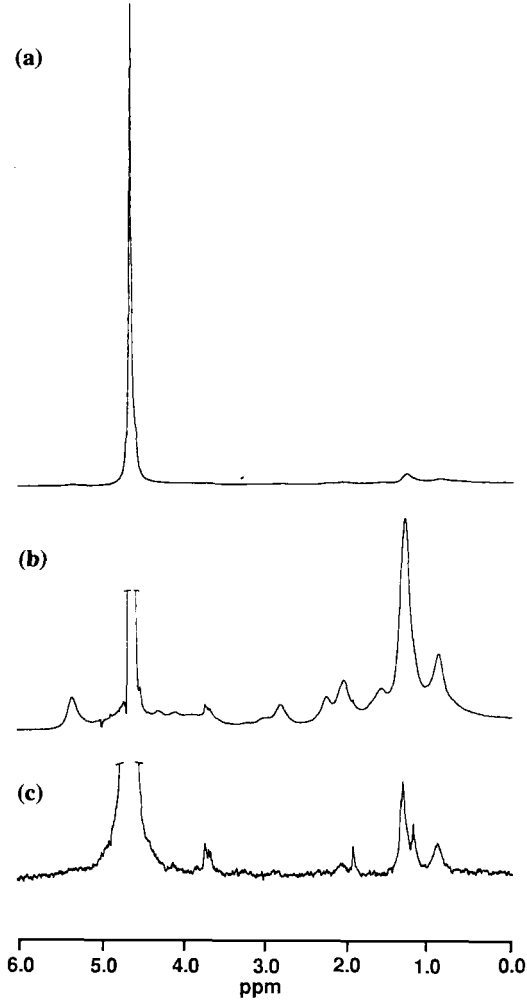

Fig. 1. Ovarian adenocarcinoma. 1D ^{1}H MR spectra (at 360 MHz) of ovarian adenocarcinoma acquired (a) without water suppression, (b) with water suppression[13] and (c) using a Carr–Purcell–Meiboom–Gill (CPMG) T_2-filter ($n2\tau$ = 720 ms, where n is the the number of π pulses and τ = 1 ms) to reduce dominant lipid resonances (courtesy of Dr W. B. Mackinnon, Cancer Medicine, University of Sydney, Australia). All MR data were obtained at 37°C on a Bruker wide-bore AM-360 spectrometer equipped with an Aspect 3000 computer. A standard 5 mm probe head was used with the sample spinning at 20 Hz. Residual water signals were suppressed by selective gated irradiation and all chemical shifts were referenced to aqueous sodium 3-(trimethylsilyl)propanesulphonate (TSPS) at 0.00 ppm. T_2-filtered and unfiltered 1D spectra were acquired over a sweep width of 3597 Hz (10.0 ppm) using 8192 data points, 100 accumulations (unless otherwise specified), a 90° pulse angle, an acquisition time of 1.14 s and a relaxation delay of 2 s. Prior to Fourier transformation, a line broadening of 3.0 Hz was applied. In preparation for the MR experiment, tissue specimens (approximately 3 mm^3) were trimmed of visible fat, washed thoroughly in PBS/D_2O and positioned on glass wool in a 5 mm MR tube in 400 μl PBS/D_2O.

often change with time (tumour progression),[5] include alterations in growth rate, invasiveness, metastatic frequency, hormonal responsiveness and morphology.

Metastatic spread of malignant cells from the primary tumour to distant and separate sites in the body is one of the last stages in the progression of a neoplasm, and the usual reason for the failure of treatment in many forms of cancer.[1] Metastasis, which in general primarily occurs via the lymphatics for carcinomas and through the bloodstream for sarcomas,[2] includes several major steps collectively known as the metastatic cascade. Tumour cells must first detach from the primary tumour, invade local tissue and gain access to the route of spread, survive movement to a new location and, finally, establish growth at a new site.[6]

1.4. Magnetic resonance and cancer management

Research concerning the use of magnetic resonance in cancer management has developed over the last decade because of the potential to utilize this information for magnetic resonance imaging (MRI) and localized *in vivo* magnetic resonance spectroscopy (MRS).[7,8] In recent reviews Daly and Cohen[9] and Czuba and Smith[10] concluded that a combination of MRS and MRI should provide complementary information not available by either modality alone. This potential has yet to be realized.

1.4.1. In vivo

The use of MRI to discriminate between normal and malignant tissue on the basis of the relaxation rates of water signals was proposed by Damadian[11] over 20 years ago. Although MRI technology has dramatically improved since then, and is an important clinical tool in cancer management, its usefulness in cancer detection has been disappointing. While MRI can define a lesion or oedema relatively well, it was found to be unable to diagnose the pathology (for reviews see refs 7 and 8). Another factor with major implications in the disappointing ^{1}H MRS results for tumour pathology is the presence of the changes in cellular chemistry now known to occur during tumour development and progression.[12]

1.4.2. In vitro

During the 1960s and 1970s, ^{1}H MRS was rarely used to study cells, since the water signal eclipsed much of the spectrum (Fig. 1a). Nor was the wealth of information available from resonances obscured by the broad intense water signal fully appreciated. Furthermore, the remaining overlapping resonances were, in some tissues, obscured by the presence of large concentrations of fat.

Another perception that restricted the use of ^{1}H MRS was that cell suspensions and tissue should be perfused in order to maintain metabolism. Perfusing cells during a ^{1}H MRS experiment was not advantageous, since perfusate introduced more molecules and removed others of diagnostic importance, further complicating the spectrum.

Several major advances made in the 1970s and 1980s facilitated the use of ^{1}H MRS in the diagnosis of cancer pathology. First, the design of MR probes was much improved, as were water suppression techniques.[13] The second advance was the development of two-dimensional spectroscopy[14,15] and the realization that such MR methods, previously confined to the chemists, could be applied to cells[16,17] and tissues.[18] The use of two-dimensional spectroscopy was a major advancement in the ^{1}H MRS analysis of complex biological spectra. COrrelated SpectroscopY (COSY) allowed the assignment of resonances from cells and biopsies by allowing those molecules, which were eclipsed in the 1D spectrum, to be observed in the second frequency.[17]

It was also to become obvious that the detection of many diagnostic markers on the surface of these cells did not depend upon the cells being allowed to metabolize. Furthermore, the viability of the cells suspended in phosphate-buffered saline remained close to 100% for the duration of a COSY MR experiment. As a consequence, many molecules present in small quantities, but important in the biological characterization of cells, were now available for inspection.

During the 1980s, cultured cell lines of known differentiation and tumorigenicity became available for study. These cell lines, derived from various organs and different types of tumours, provided a model for tumour development and progression, and allowed the chemical and MR properties of these processes to be studied using reproducible samples in the laboratory. The availability of biologically reproducible cell lines also allowed optimal MR acquisition and processing parameters to be developed for both tissues and cells alike.

The thrust of our present research programme is to ascertain if ^{1}H MRS can provide an independent modality to assess human cancers that can then be validated by histological correlation. Where this correlation is established, the ^{1}H MR experiment will be extended to its technical limits, testing its ability to support, surpass or perhaps replace routine histopathology. Our objectives here are to

(1) consider the potential of ^{1}H MRS as an independent modality to provide an adjunct to, or replace conventional pathological procedures for the recognition and grading of primary cancers and lymph node metastases;

(2) ascertain if ^{1}H MRS can or has the potential to provide a prognostic index for any of these cancers;

(3) determine if, with prior knowledge of the chemical changes associated with malignant transformation, chemical shift imaging may be utilized (*ex vivo*) to determine the spatial location and pathology of human cancers.

The scope of this report has been restricted to the use of ^{1}H MRS to assess cancer pathology.

2. EXPERIMENTAL CONSIDERATIONS

2.1. Viable tissue, intact cells, cellular fractions or perchloric acid extracts?

It was originally believed that chemical differences in tissue, relating to specific pathologies, could be recorded from cellular fractions or perchloric acid extracts. The literature[19–22] and our own work[17,23,24] has, however, shown that for a tight correlation to be obtained between the pathology and the chemistry, tissues and cells must be examined intact and viable. The majority of ^{1}H MR-visible diagnostic molecules are present in small concentrations as part of the plasma membrane (see Section 3.1), on the surface of cancer cells or shed from the cells as complex material.[25–27] These diagnostic molecules are only observable because most of the remaining cellular chemicals are not MR-visible. Once cells are lysed, intracellular chemicals present in much larger quantities than those on the cell surface mask chemical information of diagnostic relevance. This phenomenon was demonstrated in our laboratory by comparison of the chemical composition of whole leukaemic lymphocytes and Chinese hamster ovary cells with their highly purified plasma membrane.[23,24] The subtle differences in membrane chemistry that occurred with malignant transformation, and which correlated with the whole-cell ^{1}H MR spectra, were not observed in whole-cell chemical analyses. Studies by others, comparing perchloric acid extracts from cells and tissues, support this concept.[19,22,28–32]

2.2. Sample handling

To date, all successful studies of viable tissues have relied heavily on careful sample handling prior to ^{1}H MR experiments. Tissues are placed into sterile tubes immediately after excision. Cervix,[33] thyroid,[34] breast,[35] prostate,[36] ovary and uterine (W. B. Mackinnon, G. L. May, P. Russell and C. E. Mountford, unpublished data) tissues are immersed immediately in liquid nitrogen and stored in a −70°C freezer. Colon and lymph node tissues, which have been found to produce increased levels of metabolites when frozen and thawed, have to date been analysed fresh, but the possibility of

using protease inhibitors to reduce metabolic breakdown is currently being investigated (D. Ende, P. Chapuis, L. Bokey, C. L. Lean and C. E. Mountford, unpublished data).

2.3. MR data acquisition and processing

The viability of cell and tissue specimens assessed by MR methods is limited. Time constraints imposed by this limited viability require careful selection of acquisition parameters for 2D spectroscopy.[37] As it is often necessary to terminate the experiment before a complete 2D data set can be collected, there is a trade-off between signal-to-noise, spectral resolution and sample viability, which must be addressed for each tissue type.

The adjustment of acquisition parameters is based on obtaining the maximum amount of spectroscopic information within a time such that the biopsy is still amenable to correlative histopathological assessment. Ideally, a minimum of three hours is necessary for good-quality 2D spectra of small (3 mm^3)-size specimens. At 360 MHz the three-hour time constraint allows approximately 8000 transients (e.g. 250 FIDs of 32 transients) to be acquired before viability drops below an acceptable level.[37].

Data processing also requires consideration. Cells and tissues contain a variety of molecules present in a range of concentrations with T_2 relaxation values ranging from below 100 ms to more than 1 s. The choice of window functions during processing has dramatic effects on the resolution, sensitivity and appearance of the 2D spectra. In particular, shortening time domains by using Lorentzian–Gaussian window functions or by processing fewer experiments leads to an overall loss of J coupling, but can also often lead to the appearance of numerous short T_2 relaxation crosspeaks not observable using more conventional processing methods. To obtain all available information from one data set on a cell line or biopsy specimen, the 2D data file needs to be processed using a number of different window functions.[37]

Equally important, with prior knowledge of the pertinent diagnostic molecules (see Table 1), the processing parameters can be used effectively to remove or reduce the contribution from molecules present in significant amounts, so that they no longer mask others of diagnostic importance.[37]

Manipulation of biological MR data in the processing stage, as opposed to filtering of data during acquisition, is a major conceptual advance in the use of MRS for the detection and diagnosis of cancer. The philosophy allows all available data to be collected and then processed using several different weighting functions to extract pertinent diagnostic information. This statement is borne out in the results described below for MRS diagnosis of malignancy in cervical and colorectal tissue, and the detection of metastases in lymph nodes.

3. ASSIGNMENT OF DIAGNOSTIC RESONANCES

It should be stated clearly that some molecules are diagnostic for malignancy in some tissues, but not others. In addition, where there is disagreement in the literature, particularly relating to excised biopsies or *in vivo* studies, there are mixtures of cell types being measured and the biochemical behaviour differs according to the cellular populations.

While 1D spectroscopy is preferred for rapid diagnosis, 2D spectroscopy is the means for unambiguously identifying resonances in the spectra. There are in excess of 50 crosspeaks in the COSY spectra of some invasive biopsies and malignant cell lines. Many of these crosspeaks have been assigned[16,17,27,38–43] (E. J. Delikatny, W. E. Hull, K. T. Holmes, B. Kunnecke, W. B. Mackinnon, C. L. Lean and C. E. Mountford, unpublished data) and are summarized in Tables 1 and 2. Those molecular species often used as diagnostic markers for tumour development and progression are discussed below.

3.1. Lipid

The presence of a lipid spectrum from cervical,[18,33,44] thyroid,[34] ovarian[45,46] (W. B. Mackinnon, G. L. May, P. Russell and C. E. Mountford, unpublished data) and uterine (W. B. Mackinnon, P. Russell, G. L. May and C. E. Mountford, unpublished data) tissue is adequate to diagnose the presence of invasive cells. Determining the origin of this lipid signal was given a high priority in our laboratory.

Most normal cells and tissues do not produce a high-resolution MR spectrum, but a narrow line lipid signal is observed from malignant cells,[18,47,48] fibroblasts,[49,50] stimulated lymphocytes[50–52] and neutrophils.[39] It was shown that the intensity of the MR lipid signal did not correlate with the number or size of intracellular lipid droplets.[53] Paramagnetic broadening experiments and spectra of isolated ghosts indicated that these lipid signals arose instead from plasma membrane lipid.[50] The suggestion that membrane lipid was sufficiently mobile to generate a high-resolution signal was contentious, since it was believed that all membrane lipid was in bilayer form and hence moving too slowly to be observed by high-resolution MRS.

Over the last decade, it has been confirmed that ^{1}H MR-visible lipid can originate from the plasma membrane of malignant cells, because, in addition to normal bilayer lipid, these membranes contain triglyceride and cholesteryl esters.[17,23,24] These neutral lipids have the ability to tumble isotropically and hence generate a high-resolution MR spectrum.[48,54] Assignments were made using a combination of 2D ^{1}H MRS and chemical analysis of highly purified plasma membranes. In order to accommodate this physico-chemical data, a new model was proposed where the neutral lipid

Table 1. Chemical species identified in ^{1}H MR COSY spectra of cells and tissue.

Molecule	Abbreviation	Coupling (H)	Chemical shift (ppm) $F_2 - F_1$
Triglyceride[a]	A	$(CH_2)_2-CH_2-CH_3$	0.90–1.33
	B	$CH_2-(CH_2)_3-CH_3$	1.33–2.08
	C	$CH=CH-CH_2$	2.02–5.38
	D	$CH_2-CH=CH$	2.84–5.38
	E	CH_2-CH_2	1.33–1.62
	F	$O=C-CH_2-CH_2$	1.60–2.30
	G	$O-CH_2-CH-O$	4.12–5.26
			4.26–5.26
	G′	$O-CH_2$	4.09–4.29
Ether-linked triglyceride	K	$O-CH_2-CH-O$	3.52–5.19
	L	$O-CH_2-CH_2$	1.53–3.42
Cholesterol	Z	CH_3-CH-ring α	0.85–1.52
Choline	Chol	$N-CH_2-CH_2$	3.50–4.07
Phosphorylcholine	PC	$N-CH_2-CH_2-OP$	3.61–4.25
Glycerol PC	GPC	$N-CH_2-CH_2-OPO$	3.69–4.38
Phosphoethanolamine	PE	$N-CH_2-CH_2-OP$	3.30–4.14
Inositol	Inos	HOCH–HCOH (ring)	3.28–3.64
Alanine	Ala	$CH-CH_3$	1.49–3.79
Aspartic acid	Asp	$CH-CH_2-COOH$	2.89–4.03
Glutamic acid/ glutathione	Glu/ Glut	CH_2-CH_2-COOH CH_2-CHNH_2-COOH	2.21–2.62 2.21–3.81
Histidine	His	$CH-CH_2-$ring	3.22–3.95
Isoleucine	Ile	CH_2-CH_3	0.97–2.12
Leucine	Leu	$CH-CH_3$	0.97–1.78
Lysine[b]	Lys	CH_2-CH_2	1.72–3.05
Proline	Pro	$\alpha CH-\beta CH_2$	2.39–4.14
		$\gamma CH_2-\beta CH_2$	2.11–2.38
		$\gamma CH_2-\delta CH_2$	1.99–3.38
Threonine	Thr	$HOCH-CH_3$	1.33–4.27
Valine	Val	$CH-CH_3$	1.03–2.34
Taurine	Tau	$H_2N-CH_2-CH_2-OS$	3.28–3.50
Lactate anion	Lac	$CH-CH_3$	1.33–4.12
Fucose	Fuc I	$CH-CH_3$	1.33–4.27
	Fuc II	$CH-CH_3$	1.25–4.28
	Fuc III	$CH-CH_3$	1.41–4.30
	Fuc IV	$CH-CH_3$	1.31–4.38
UDP–GlcNAc	Ribose	H1′, H2′	5.99–4.38
	Glucose	H1, H2	5.52–3.99
		H2, H3	3.99–3.82
		H3, H4	3.82–3.55
		H4, H5	3.55–3.94

[a]Crosspeaks A–F are from the fatty acid chain and G and G′ from the glycerol backbone.[42]
[b]And polyamines.

Table 2. Methyl–methine couplings from bound fucose present in COSY spectra of cells and tissue.

Abbreviation	Chemical shift (ppm) $F_2 - F_1$	LIM1215 (highly tumorigenic human colorectal cell line)	LIM1863 (lowly tumorigenic human colorectal cell line)
Thr/Fuc I	1.33–4.27	Yes	Yes
Fuc II	1.25–4.28	Yes	No
Fuc III	1.41–4.30	Yes	No
Fuc IV	1.31–4.38	No	Yes

exists in domains, resembling serum lipoproteins, intercalated with the bilayer lipid.[24,55] Accumulation of neutral lipids in the plasma membranes of malignant cells has been confirmed by others.[56,57]

Although the signal from neutral lipid in the plasma membrane of malignant cells is smaller than that from water, it makes a significant, albeit varying, contribution to the total ^{1}H MR spectrum. The intensity of the lipid signal shows little correlation with whole-cell neutral lipid content,[23,24,54] but is representative of the plasma membrane lipid content.[24,55]

A recent study of plasma membranes isolated and purified from a series of malignant Chinese hamster ovarian cell lines has indicated that the chemical association and fatty acyl chain composition of cholesteryl esters and triglycerides in the plasma membrane are akin to, if not the same as, those reported for serum lipoproteins.[24]

3.2. Choline metabolites

The choline resonance at 3.2 ppm represents a multicomponent signal from phosphocholine (PC), glyceroylphosphocholine and choline plasmalogen, with contributions from cytidinediphosphocholine, acetylcholine and choline. The increase in choline resonances is often linked to proliferation.[58,59] Both choline and phosphocholine have been found to be increased in tumours,[60] and these species are integral to phospholipid synthesis necessary for membrane turnover.[58,61] A higher level of phospholipid synthesis in tumour cells has also been reported for various cell and tumour types, using ^{31}P MRS, by Daly and colleagues.[10,62]

The increased ^{1}H MR-visible choline metabolite content of carcinomatous colorectal tissue compared with normal mucosa has been reported by Smith *et al.*[63] and Lean *et al.*,[64] and is supported by *in vitro* studies, where highly compared with lowly tumorigenic human colorectal cells are found to contain 10 times the level of choline metabolites.[43]

3.3. Lactate

Lactate, a product of anaerobic respiration, was one of the first molecular species to be linked to malignant disease. In the brain, metastatic cancers and gliomas often contain lactate, distinguishing them from meningiomas, neurinomas and lymphomas.[65–69] Lactate was observed in paediatric gliomas irrespective of grade,[70,71] making it a useful diagnostic marker.

Care is, however, advised when considering using lactate as a marker of malignancy. For example, lactate is observed in both normal colorectal mucosa and human colorectal adenoma cell lines.[64,72,73]

3.4. *N*-Acetylaspartate (NAA)

Modulation to MR-visible *N*-acetylaspartate (NAA) (2.0 ppm) levels has been often recorded by ^{1}H MRS, with the ratio of NAA/choline or NAA/creatine reported to be a potential diagnostic indicator for damage or loss of neuroaxonal integrity (for a review see ref. 59).

3.5. Cell surface fucose

Cell surface fucosylation is a new ^{1}H MR marker of tumour development and progression. There is now a large body of evidence, summarized in recent reviews,[74–79] indicating that many glycoconjugates are altered in primary cancerous and metastatic tissues and that these alterations are the major factors responsible for the cell surface composition characteristic of the malignant phenotype.

The cell surface, being at the interface of all cell–cell and cell–matrix interactions, is concerned with many normal physiological properties related to neoplastic development and metastatic spread: cell shape, growth, division and differentiation; cellular recognition, communication, adhesiveness and migration; contact inhibition of growth and immunological competence.[80] The composition of the surface of a cell reflects the content of the plasma membrane, which is equipped with a variety of complex molecules, many of which are glycoconjugates (glycolipids, glycoproteins and glycosaminoglycans). These molecular species consist of a lipid or protein backbone, integrated (glycolipids and glycoproteins) or loosely attached (glycosaminoglycans) to the plasma membrane, and carbohydrate chains of varying complexity. The sugar moieties are hydrophilic by nature, and thus orient themselves away from the membrane and extend into the surroundings of the cell.[76]

Malignancy-associated alterations to glycoconjugates most often involve structural changes in the carbohydrate portions of the molecules, and result

in an increase in the content of both fucose and sialic acid on the surface of the neoplastic cell. The involvement of cell surface fucosylation in tumour development and progression has been documented for colorectal cancer (for a review see ref. 79). Much of this information was derived from the isolation and purification of glycosylated antigens from colorectal tumours, and the subsequent production of monoclonal antibodies. The studies concluded that specific fucosylated antigens, such as extended and poly-fucosylated Le^y, were prevalent on the surface of cells in colorectal tumours. Monoclonal antibodies raised against these fucosylated antigens strongly suggested the existence of a preinvasive state denoted transitional mucosa.[81]

Using two-dimensional ^1H MRS, it was found that a crosspeak (1.3–4.3 ppm) in the COSY spectrum of malignant rat mammary adenocarcinoma cells, consistent with the H_5–H_6 coupling of bound fucose, was removed by treatment of the cells with fucosidase. Most importantly, the metastatic capacity of the cells was severely retarded *in vivo* after treatment of the cells with this enzyme.[82] The unequivocal assignment of this crosspeak (1.3–4.3 ppm) to the methyl–methine coupling of bound fucose was made in a subsequent study using plasma membrane material shed from a human malignant colorectal cell line.[27]

The methyl–methine coupling region of the COSY spectrum from human cancers is more complex, with many crosspeaks being observed. The assignment of crosspeaks to bound fucose was the subject of a study using a series of human colorectal cell lines with known tumorigenicity and differentiation.[27,43,73,83] The objective was to observe alterations to cell surface fucosylation on intact viable cells, and so ascertain if any sites of cell surface fucosylation correlated with specific biological functions. It is important to note that the information obtained had not been compromised by isolation and purification of the antigen.

The implementation of specific data-processing parameters was important in this project. In contrast to cervical epithelium, ovarian and thyroid tissue, healthy colonic tissue has an intense lipid spectrum. It was necessary to reduce the lipid signal by using appropriate window functions in order to observe crosspeaks from bound fucose present at much lower concentrations. Using two human malignant colorectal cell lines, LIM1863 and LIM1215,[84,85] four crosspeaks from the H_5–H_6 coupling of covalently linked fucose moieties (Table 2) were assigned following addition of free fucose to the cells and observation of significant increases in the volumes of methyl–methine coupling crosspeaks.[27,43] Other crosspeaks were not perturbed by addition of exogenous fucose substrate.

Assignment of ^1H MR resonances to cell surface fucose offered the possibility of identifying a biological role for this phenomenon and/or determining if such fucosylation was an indicator of tumour development and/or progression.

3.6. Ribose

Protons of ribose and glucosamine moieties of UDP–GlcNAc have been assigned in human colorectal cell lines.[73,86] This was an important assignment by the Hull group, since released cellular levels of UDP–GlcNAc have been linked with loss of cellular differentiation[87] and promised to provide unique information not previously available.

3.7. Citrate

Citrate, which produces a peak at 2.53 ppm from the CH_2 protons, is a secretory product of the prostate. Biochemical data have suggested that the metabolism of citrate may be interrupted in prostate cancer.[88] Use of citrate as a diagnostic species for determining the pathology of prostate cancer is contentious,[30] but the discrepancies may be due to comparisons being made between different grades of prostate tumour.

4. COLORECTAL CANCER

Carcinoma of the colon is the second most common visceral malignancy in the United States in both men and women, and is considered a disease of modern western society. While there is still doubt as to the genesis of most colonic cancers, many arise in pre-existing benign adenomas. A histopathological progression from benign polyp to carcinoma can be expected in up to 5% of all resected colonic adenomas, and this progression is a size- and type-related phenomenon.[89] Such a biological progression may be observed in many resected colonic lesions and polyps, thus providing substantial study material for the documentation of ^{1}H MRS changes paralleling malignant transformation.

Use of ^{1}H MRS to assess the pathological state of colorectal cancers was first reported by Mountford and colleagues in 1986,[45] where it was found that the presence of a narrow-lined resonance at 1.3 ppm with a long T_2 relaxation value correlated with the presence of invasive cells in the primary tumour. In subsequent studies[63,72] several resonances in the 1D ^{1}H MR spectra were used to distinguish normal and benign colorectal tissues from early malignant (Dukes A or B1) tumours. Two-dimensional ^{1}H COSY identified diagnostic resonances associated with triglyceride, choline metabolites, lactate and cell surface fucose.

Primary tumours from patients with advanced disease (Dukes B2, C and D, Canadian modification of the Astler–Coller staging system) could not be distinguished from normal tissue by 1D ^{1}H MRS owing to alterations in MR

lipid profiles that occurred with tumour progression. In these cases two-dimensional COSY was necessary for a correct diagnosis, but even then the spectral signal-to-noise was less than optimal owing to high levels of lipid present in colorectal tissue.

In order to develop a means of overcoming technical difficulties associated with analysis of human colorectal biopsies, cell lines grown *in vitro* were studied. A number of human colorectal cultured cell lines with known growth characteristics, degree of differentiation, tumorigenicity and metastatic potential had been established.[84,90–96] It was therefore possible to simulate the biological events characteristic of tumour development and progression *in vitro*, and thus to study defined, reproducible samples in the laboratory. Once the *in vitro* cell model was analysed comprehensively, it would be possible to return to analyse the biopsies with prior knowledge of the pertinent diagnostic molecules and their clinical and biological relevance.

4.1. Colorectal cell model

Six human colorectal cell lines, including two derived from adenomas and four from carcinomas, have been characterized by ^{1}H MRS.[73,83] These cell lines constituted a model of development and progression of human colorectal cancer, and could be ranked according to loss of cellular differentiation and increased tumorigenicity (Table 3).

In order directly to compare the spectra of the six cell lines, the same cell numbers, sample preparation and experimental conditions were used for each cell line, and the FIDs were scaled prior to Fourier transformation. The 1D MR spectra of the six cell lines are presented in Fig. 2 in the same order as they are described in Table 3, i.e. the highly tumorigenic carcinoma line SW620 uppermost and the non-tumorigenic adenoma line PC/AA last. There is an obvious increase of ^{1}H MR-visible molecules ascending through the series, which clearly ranks the cell lines in the same order as determined by their biological features. The methylene (1.3 ppm) resonance is four times more intense in the SW620 as compared with the PC/AA spectrum, and peaks midway through the series in the spectrum of the SW1222 cell line. The intensity of the choline $^{+}N(CH_3)_3$ resonance (3.2 ppm) gradually increases on ascending through the series, and is 20 times more intense in the SW620 as compared with the PC/AA cell spectrum.

Thus, on the basis of the 1D MR spectra alone, a clear ranking was observed from the premalignant adenoma to the highly malignant carcinoma lines (Fig. 2). In particular, the gradation in ^{1}H MR-visible lipid and metabolites correlated with altered biological characteristics, such as loss of differentiation, within the series (Table 3). The proton from the ribose of UDP–GlcNAc (5.99 ppm) was observed to increase in intensity with

Table 3. Biological characteristics of human colorectal cell lines.

Cell line (origin)	Tumorigenicity[a]	Differentiation	Culture appearance[b]	Cell morphology[c]	Functional maturity[d]	CEA[e]	Modal chromosome no.	Split ratio per week	Growth factors[f,g]	Ref.
SW620 Dukes' C lymph 2°	High (s.c. 10^7; 5/5; 21 days)	Poor	M PE ≈ 50%	E, −m	MAbs1 −ve MAbs2 +ve	11	56	1:32	DMEM	91
SW480 Dukes' B 1°	High (s.c. 10^7; 5/5; 30 days)	Poor	M, C PE ≈ 40%	E, +m		21	55	1:8	DMEM	91
SW1222 Dukes' C_2 1°	High (s.c. 5×10^6; 6/6; 21 days)	Moderate	C	E, +m	MAbs1 +ve MAbs2 +ve collagen binding,[145] mu		44	1:8	DMEM + T	142
PC/JW FPC[h] 1°	Moderate (s.c. 5×10^6; 5/6; 48 days)	Moderate good	C CFE 0.001% 0.21%[i]	E			46	1:4	DMEM + T, I	94 143
PC/AAC1 from PC/AA at $p = 50$	None (s.c. 10^7; 0/6; >180 days)	Good	M, D CFE 1.05%	E			*ca.* 70	1:4	DMEM +FBS, H, I	144 143
PC/AA premalignant adenoma, FPC	None (s.c. 10^7; 0/26; >180 days)	Good	M, G non-clonogenic	E, g, +m	mu	↑ with p	$p < 50$: 46 $p > 50$: *ca.* 48	<1:2	DMEM +FBS, H, I, 3T3 feeder	144 94 143

The two cell lines shaded grey are of adenoma origin. The others are derived from carcinomas. p is the passage number.

[a]Tumorigenicity assessed by subcutaneous (s.c.) injection of indicated number of cells into athymic nu/nu mice. The proportion of tumour-bearing mice after a specified time period (days) is given.

[b]M, monolayer of mainly individual cells; C, monolayer with clusters of tightly packed cells; D, dome formation; G, spheroids showing glandular organization (note that SW1222 displays glandular organization only in 3D collagen gel); PE, plating efficiency; CFE, colony-forming efficiency on plastic.

[c]E, epithelial-like; m, evidence of microvilli; g, goblet cells.

[d]MAbs1, a panel of monoclonal antibodies (PR, Group 1) that react with mucus constituents of human colorectal epithelium;[145] MAbs2, a panel of monoclonal antibodies (PR, Group 2) that react only with non-mucus components of human epithelial cells;[145] mu, mucin production.

[e]Carcinoembryonic antigen (ng/10^6 cells).

[f]Absolute growth factor requirement at 1–4 cells cm^{-2}. Note that the AA and AAC1 lines have not been tested.[146] For purposes of comparison by MRS, all cell lines have been grown in DMEM (with 3T3 feeder or added insulin and hydrocortisone where required) plus 10–20% v/v FBS (Cytosystems, Australia, Lot no. 00511074).

[g]T, transferrin; I, insulin; H, hydrocortisone.

[h]Familial (adenomatous) polyposis coli.

[i]In the presence of 3T3 feeder.

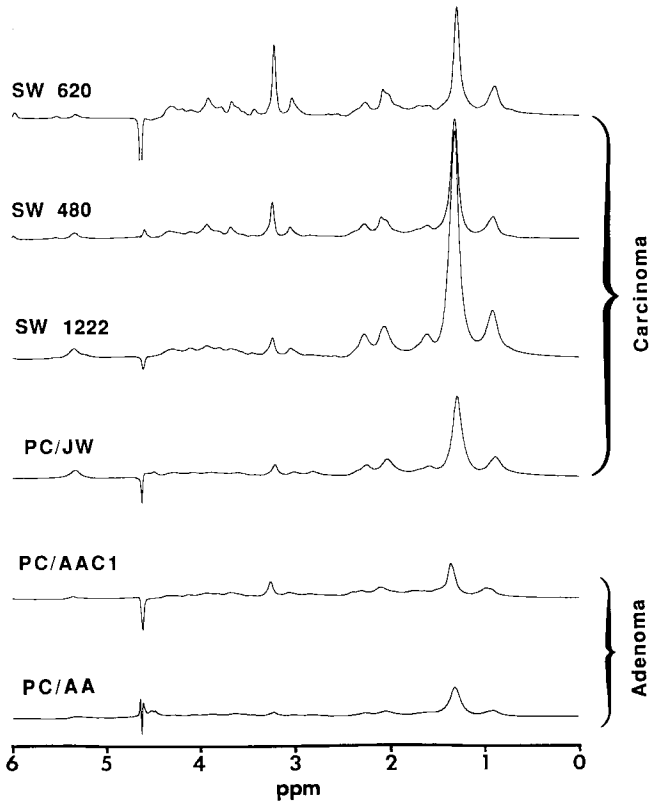

Fig. 2. Colorectal cells grown *in vitro*. 1D ^{1}H MR spectra of the six colorectal cell lines as presented in Table 3.[73,83] Spectra were acquired and processed as described in the legend to Fig. 1. Culture conditions for each cell line are described in the references given in Table 3. For MR experiments 10^8 cells (just confluent) were harvested, washed three times in PBS/D_2O and transferred to a 5 mm MR tube in a volume of 400 μl. Cell numbers, sample preparation and experimental conditions were maintained constant for all cell lines.

reduced cellular differentiation in spectra from carcinoma cell lines, but was not observed in spectra of adenoma cell lines. This result suggested that UDP–GlcNAc could be a unique marker for colorectal carcinomatous tissue.

Selected processing parameters were applied to the 360 MHz COSY data files (SW = 1497 Hz) to reduce the intensity of the lipid signal (Lorentzian–Gaussian, LB = −40 and GB = 0.15) in t_2, and all data files were scaled to the SW1222 line. A clear increase in the number and intensity of crosspeaks from the most to the least differentiated cell line was apparent.[73]

The expanded COSY methyl–methine coupling regions (F_1, 3.9–4.5 ppm and F_2, 1.0–1.6 ppm) of the six colorectal cell lines are shown in Fig. 3. A coupling from the methyl–methine group of lactate anion (1.33–4.12 ppm) is present in each spectrum (including the preinvasive adenoma cells), and is denoted Lac. Other crosspeaks present have been assigned to the methyl–methine couplings of threonine and covalently linked fucose,[27,43] and are indicated as Thr/Fuc I, Fuc II and Fuc III. These three crosspeaks are all observed in spectra of the highly tumorigenic cell lines, SW1222, SW480 and SW620, and increase in volume by a factor of two with decreasing cellular differentiation. The crosspeak Fuc III is observed in the spectra from all carcinoma lines. The spectra from the two adenoma lines do not have crosspeaks Fuc II or III, but do have a weak crosspeak at the same chemical shift as Thr/Fuc I.

Thus, by comparing the methyl–methine coupling region from the COSY spectra of a series of human colorectal cell lines, the *cell surface fucosylation is seen to reflect reduced cellular differentiation*. If these diagnostic markers can be observed in colorectal biopsy specimens then ^{1}H MRS could well provide a prognostic indicator for colorectal polyps and early malignancy.

4.2. Colorectal tissues

The initial clinical study of colorectal tissues was undertaken by Smith and colleagues in the late 1980s.[63,72] These studies were carried out *prior* to the development of data acquisition and processing techniques necessary to reduce the intense lipid signals from healthy colorectal tissue.[37] As a consequence, while there were diagnostic molecules apparent in the colorectal biopsy spectra, the changing lipid content that accompanied tumour development prevented a definitive diagnosis for patients staged Dukes B and C. A new study has now commenced where the histopathological criteria recorded for polyps and carcinomatous tissue are compared with ^{1}H MR profiles in which the lipid signal has been reduced. With prior knowledge of appropriate data acquisition and processing procedures, the resultant spectra allow a distinction to be made between normal mucosa and colorectal invasive carcinoma[64] and between polyps of varying but defined levels of dysplasia (D. Ende, P. Chapuis, C. L. Lean, R. Newland and C. E. Mountford, unpublished data).

Colorectal tissue samples were obtained from the primary carcinoma (n = 15) and resection margin (n = 15) of patients staged A, B, C and D according to the Australian Clinicopathological Staging System (ACPS).[97] The 15 specimens of carcinoma used for ^{1}H MRS assessment were confirmed to be invasive. All resection margin specimens were classified histopathologically as normal colonic mucosa. It was important to observe that MR spectral information obtained from these tissues was directly

comparable to that recorded for cultured human colorectal cell lines, with resonances from triglyceride, choline and non-choline-based metabolites and bound fucose clearly visible in the COSY spectra.[73]

The increased choline metabolite content recorded for malignant tissue was represented by the ratio of the intensities of the 1D *N*-trimethyl and methyl resonances, with malignant tissue having a ratio (0.86 ± 0.35) twice that for normal mucosa (0.40 ± 0.27). The large standard deviations inherent in this ratio were reduced by calculating a second ratio, that of *N*-trimethyl/methyl obtained from T_2-filtered spectra using delays of $n2\tau = 720$ and 8 ms (Fig. 4). In this case the carcinomatous tissue was most readily distinguished from normal mucosa.

Interestingly, three of the eight histopathologically normal tissue specimens were diagnosed to be abnormal using ^{1}H MRS criteria, since the linewidth at half-height, $\Delta\nu_{1/2}$, of the CH_2 resonance was found to be similar to that of malignant tissues. In the two-directional plot of $(N\text{-trimethyl/methyl})_{720\,ms}/(N\text{-trimethyl/methyl})_{8\,ms}$ versus $\Delta\nu_{1/2}CH_2$ (Fig. 5) these biopsies were positioned as a distinct population intermediate between the malignant and ^{1}H MRS-normal tissues. This observation is not unexpected, since Kim and colleagues,[81] using monoclonal antibodies raised against the Le^y antigen, reported the existence of a premalignant state in human colorectal disease. It is acknowledged that for 90% of colorectal adenocarcinomas transitional mucosa exists adjacent to the cancer.[98] These MRS results support this concept.

Two-dimensional ^{1}H MRS was able to detect cell surface fucosylation of malignant colorectal tissue. Three crosspeaks (Fuc I, Fuc II and Fuc III) from the methyl–methine couplings of bound fucose, previously assigned in the COSY spectra of human colorectal cell lines,[27,43,73,83] were present in the spectra from colorectal carcinoma (Fig. 6c). In contrast, normal mucosa COSY showed only the methyl–methine coupling from lactate anion (Fig. 6a). Interestingly, ^{1}H MR spectra of histopathologically normal but ^{1}H

Fig. 3. Colorectal cells grown *in vitro*. Expanded methyl–methine coupling region (F_2: 1.00–1.60 ppm; F_1: 3.90–4.50 ppm) of ^{1}H MR symmetrized COSY data (32 scans, 200 experiments) from colorectal cells described in Table 3.[73,83] Crosspeaks are labelled as assigned in ref. 43. Magnitude mode COSY experiments were performed using standard Bruker software. A total of 2048 data points were collected in the t_2 time domain over a sweep width (SW2) of 2994 Hz (8.32 ppm). Data sampling was carried out with an initial delay between the two 90° pulses of $t_1^{min} = 1$ ms, an increment time of 334 μs (=2DW2) and a relaxation delay of 1 s. Data matrices underwent zero-filling to 1 K in t_1, Fourier transformation and then magnitude calculation, $\sqrt{(\text{real}^2 + \text{imaginary}^2)}$, to give 1024×1024 real data points for each 2D spectrum. Sine-bell window functions were applied in the t_1 domain and Lorentzian–Gaussian (LB = −40.0 and GB = 0.15) window functions in the t_2

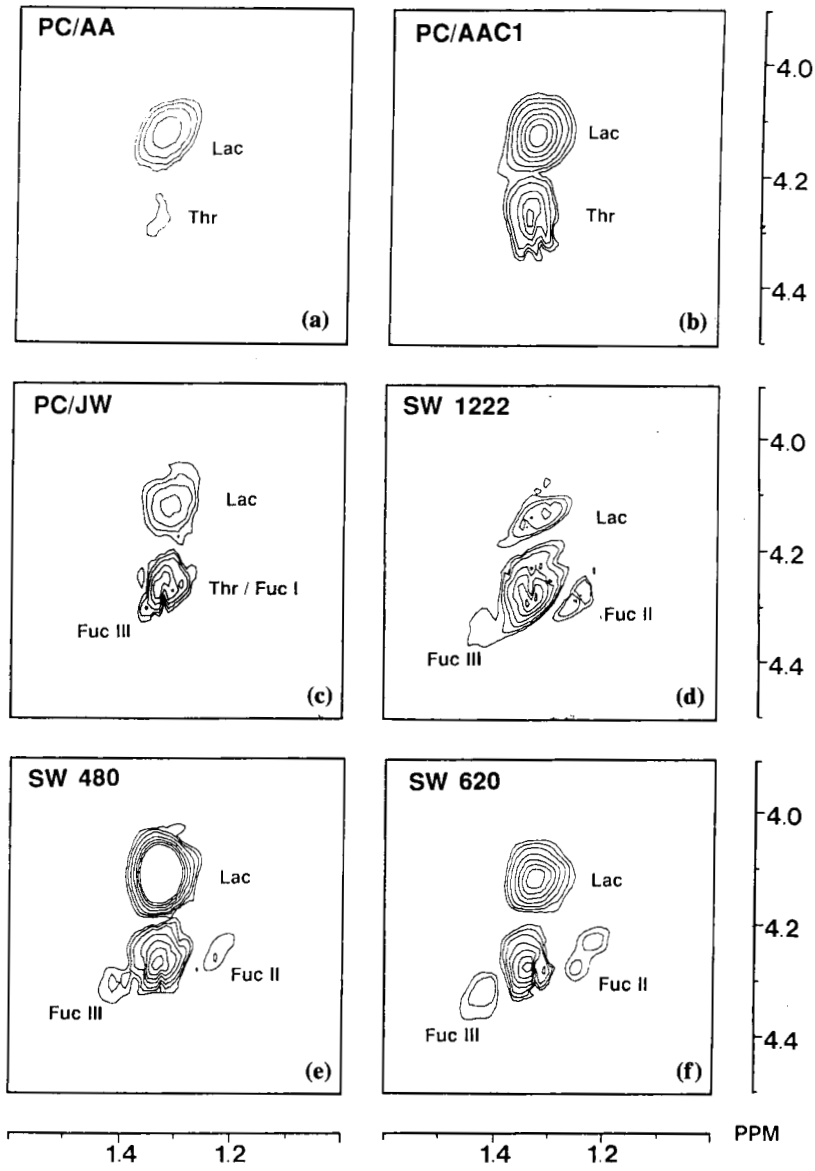

domain prior to Fourier transformation as previously described by Delikatny *et al.*[37] All spectra are scaled to SW1222. Contour plots were generated with the lowest level set close to the noise level, and with subsequent levels increasing in the first two instances by an increment of 250 and thereafter by increments of 500. (a) PC/AA adenoma; (b) PC/AAC1 adenoma; (c) PC/JW carcinoma; (d) SW1222 carcinoma; (e) SW480 carcinoma; (f) SW620 carcinoma.

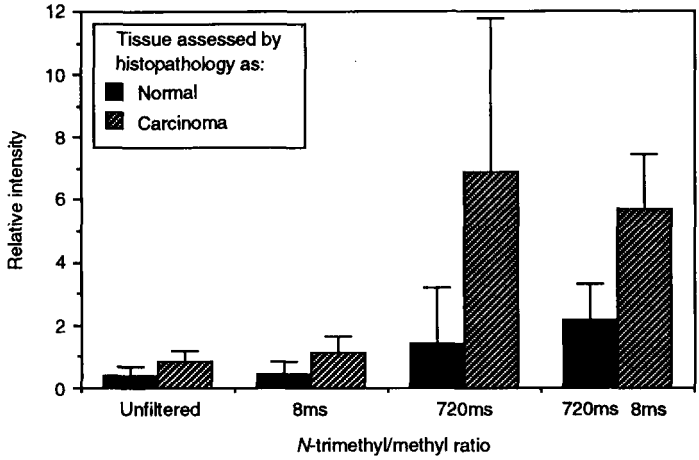

Fig. 4. Colorectal biopsies. The ratios of the intensities of the *N*-trimethyl and methyl resonances (*N*-trimethyl/methyl) for normal mucosa and colorectal carcinoma calculated from unfiltered and T_2-filtered ($n2\tau$ = 8 and 720 ms) 1D ^{1}H MR spectra together with the ratio of *N*-trimethyl/methyl calculated from T_2-filtered spectra ($n2\tau$ = 720 ms) to that calculated from filtered spectra using $n2\tau$ = 8 ms.[64] Samples of tissue were obtained from surgical specimens resulting from the treatment of carcinoma of the colon. Fresh specimens were transported immediately from the operating theatre to the pathology laboratory, where 2–5 mm^3 samples of tumour and normal mucosa were allocated for MR study and transported directly to the MR laboratory. Tissues were prepared for MRS analysis, and spectra acquired and processed as described in the legend to Fig. 1. The material used for ^{1}H MR analysis was subsequently placed in formalin and processed for histopathological assessment.

MRS-abnormal mucosa (Fig. 6b) showed aberrant MR-visible cell surface fucosylation. Increases of such glycosylation in preinvasive tissue, which are not morphologically manifest, remains to be confirmed by both ^{1}H MRS and monoclonal antibody studies. While these results suggest a future role for ^{1}H MRS as a prognostic indicator for colorectal tissues, the concept of a preinvasive state that is chemically but not morphologically manifest offers an interesting challenge to MR technology.

5. CERVICAL CANCER

A substantial increase in preinvasive and invasive carcinoma of the cervix has been reported in women under 35 years of age in the past 20 years.[99–106] There is a strong correlation between the presence of HPV infection and

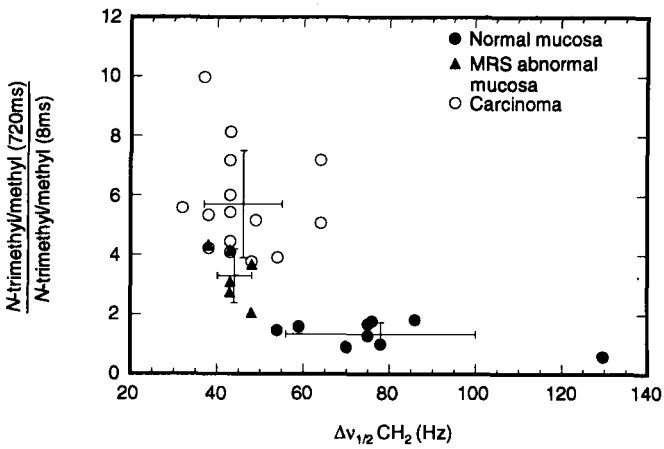

Fig. 5. Colorectal biopsies. A two-directional plot of the 1D ^{1}H MR (N-trimethyl/methyl)$_{720\,ms}$ to (N-trimethyl/methyl))$_{8\,ms}$ ratio versus $\Delta\nu_{1/2}CH_2$ (Hz) for normal mucosa (n = 15) and colorectal carcinoma (n =15).[64] The data identify two categories of normal mucosa, described as MRS-normal mucosa ($\Delta\nu_{1/2}CH_2 > 50$ Hz) and MRS-abnormal mucosa ($\Delta\nu_{1/2}CH_2 < 50$ Hz). Tissue specimens were obtained as described in the legend to Fig. 4 and prepared for ^{1}H MR analysis, and spectra were acquired and processed as described in the legend to Fig. 1.

cervical dysplasia, an association having been made between the presence of HPV types 16, 18, 31, and 33 and the development of high-grade intraepithelial and invasive malignant lesions of the cervix.[107] Although some cervical intraepithelial neoplastic lesions or dysplasias regress, current diagnostic techniques cannot distinguish them from those that progress ultimately to become invasive. Ablative therapy is therefore generally recommended for all lesions showing moderate to severe dysplasia or carcinoma *in situ*.

5.1. Human cervical biopsies

Studies completed on cervical biopsy specimens have shown that ^{1}H MRS can distinguish between preinvasive lesions (including cervical intraepithelial neoplasia, CIN, and carcinoma *in situ*, CIS) and frankly invasive carcinomas of the uterine cervix with $p < 0.0001$.[33,108]

The ^{1}H MRS acquisition was completed in 12 min on fresh or frozen tissue, required little preparation,[44] and was not subject to vagaries of sampling, since the entire specimen was examined. The distinction made between invasive and preinvasive tissue was based on altered cellular chemistry, i.e. the presence or absence of lipid resonances, and could often

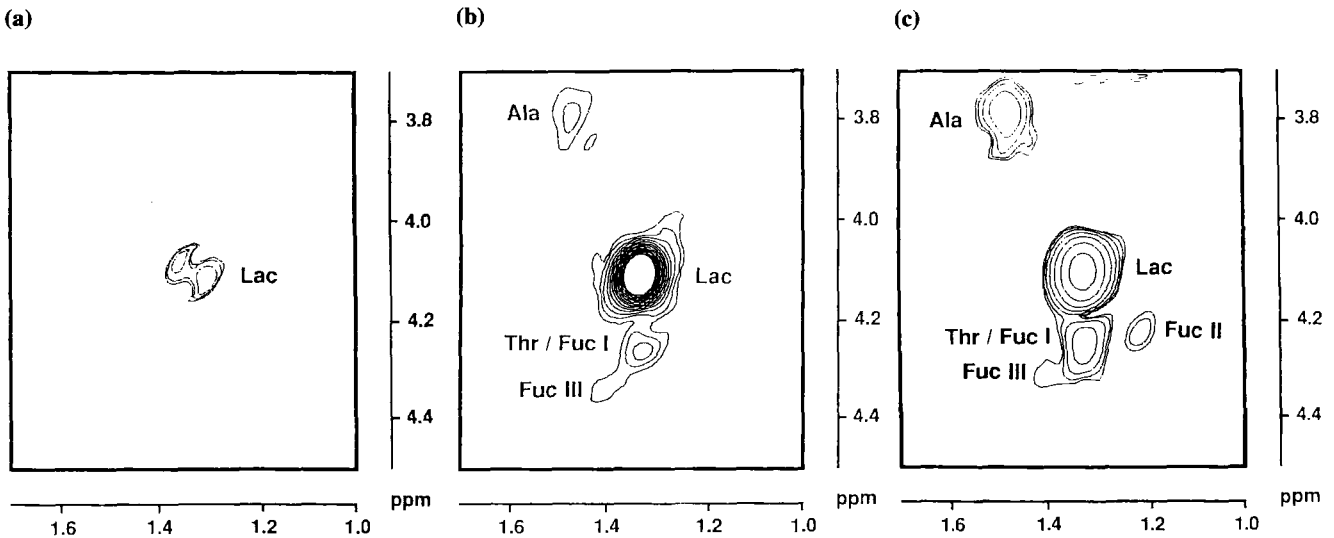

Fig. 6. Colorectal biopsies. Expanded methyl–methine coupling region (F_2: 1.00–1.70 ppm; F_1: 3.70–4.50 ppm) of symmetrized COSY spectra (40 scans, 180 experiments) of normal colonic mucosa (MRS-normal and MRS-abnormal), and colorectal carcinoma in PBS/D_2O.[64] Tissue specimens were obtained as described in the legend to Fig. 4 and prepared for ^1H MR analysis as described in the legend to Fig. 1. COSY data were acquired at 37°C with the sample spinning as described in the legend to Fig. 3, and were processed using sine-bell and Lorentzian–Gaussian (LB = −50.0, GB = 0.125) window functions in the t_1 and t_2 domains respectively. Contour plots were generated with the lowest level close to the noise level and subsequent levels increasing linearly by increments of 1000. (a) MRS-normal mucosa; (b) MRS-abnormal mucosa; (c) colorectal carcinoma.

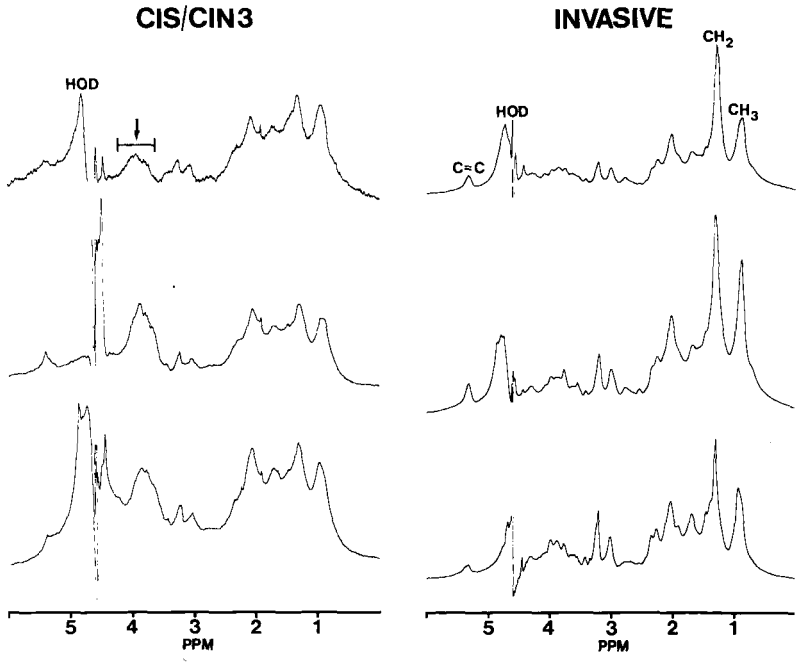

Fig. 7. Cervical biopsies. Typical 1D ^1H MR spectra of CIS/CIN III and invasive cervical punch biopsy specimens.[18,33,44] Uterine cervical biopsy specimens were obtained from patients during colposcopic examination following atypical Papanicolaou smears. Specimens were placed in PBS/D_2O immediately after excision, and MRS measurements were made either the same day or after storage at −70°C for less than six weeks. Tissue specimens were prepared for ^1H MR analysis and spectra acquired and processed as described in the legend to Fig. 1.

be done by inspection of the 1D spectrum alone.[18,33,108] Typical spectra of preinvasive and invasive cervical epithelium are shown in Fig. 7.

Spectra of invasive tumours are characterized by intense lipid resonances at 0.9, 1.3 and 5.2 ppm. In contrast, spectra of preinvasive lesions are free of high-resolution lipid. A second resonance that provides diagnostic information is a broad and featureless resonance between 3.4 and 4.2 ppm (denoted CH), which is more prevalent in spectra from preinvasive than invasive specimens. In Fig. 8 the ratio of the most intense resonance between 3.4 and 4.2 ppm and the methylene resonance at 1.3 ppm is plotted against the ratio of the methylene to methyl resonances at 1.3 and 0.9 ppm respectively. It can be seen that the separation between CIS and invasive cancer is quite remarkable. The p values obtained when comparing invasive cancer with CIN I, CIN II or CIN III are all less than 0.0001, with a specificity of 0.94 and sensitivity of 0.98.[33] A similar study has also been completed by Smith

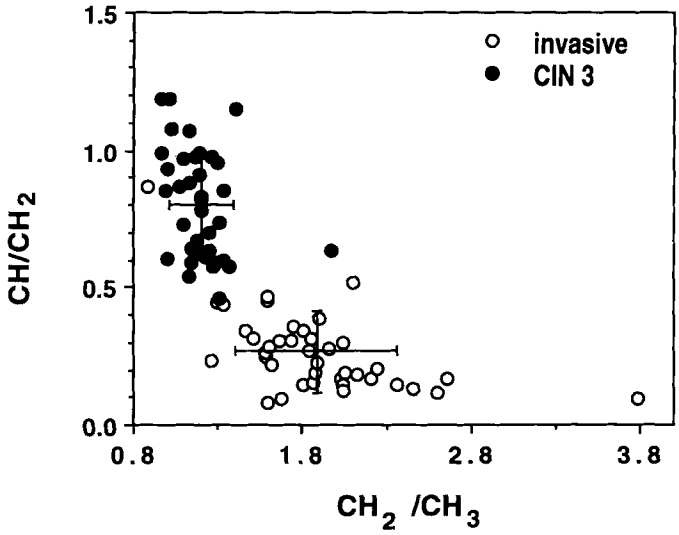

Fig. 8. Cervical biopsies. Peak height ratios from the 1D ^{1}H MR spectra of cervical punch biopsy specimens obtained and prepared for MR analysis as described in the legend to Fig. 7.[33] Two ratios are plotted on the same graph: the ratio of the most intense resonance from the 3.4–4.2 ppm region/1.3 ppm (CH/CH_2) versus the ratio of the resonances at 1.3/0.9 ppm (CH_2/CH_3). The crosshairs show the mean ± standard deviation for each category. A Student's t test gives $p < 0.0001$ for CH/CH_2 and CH_2/CH_3 for both CIN II and CIN III when compared with invasive.

and colleagues at the National Research Council of Canada, confirming these results.[44,109]

6. LYMPH NODE METASTASES

Many cancers metastasize first to draining lymph nodes, and the presence of lymph node metastases is significant in deciding if postoperative adjuvant therapy is advisable.[110,111] Despite evidence that traditional histopathological methods of identifying metastatic disease are subject to error, due to time and resource constraints on the volume of tissue that can be examined, there are few, if any, alternative methods that are as sensitive or cost-effective.[5,112,113]

Preliminary *in vivo* ^{1}H MRS studies have detected differences in the chemical composition of metastases, including high levels of lactate.[59] We considered the possibility that ^{1}H MRS (*ex vivo*) may provide a more sensitive method of identifying the presence of metastatic disease in lymph nodes based on different chemical make-up of the tissue when malignant cells are present.

6.1. Rat lymph nodes

A study using a rat mammary adenocarcinoma cell line (R13762)[114] that spontaneously metastasizes to the lymph nodes and lungs has been completed.[115] Thirty rats were injected with 5×10^6 R13762 cells in the fat pad of the mammary line on day zero. Lymph nodes were excised from six rats on days 8, 9, 10 and 11 and two rats on days 12, 13, 15 and 17. Lymph nodes from age-matched healthy rats and rats immunochallenged with *B. pertussis* were also examined.

Axillary lymph nodes were combined for ^{1}H MRS, and after 1D and 2D spectroscopy (4 h later) were placed in fixative for standard histopathological assessment, i.e. examination at 40-fold magnification of a total of six 7 μm slices taken at 350 μm intervals, with intermediate tissue blocks discarded.

Lymph nodes from control animals were found to contain significant amounts of fat. As a consequence, 1D MRS showed all lymph node tissue to contain significant quantities of ^{1}H MR-visible lipid, irrespective of the pathology. When carefully devised data acquisition and processing parameters were employed, COSY spectra showed that nodes with metastatic deposits contained significantly higher quantities of ^{1}H MR-visible molecules (including membrane precursors, amino acids, peptide molecules, taurine, lactate anion and cell surface fucose) than control specimens. Importantly, nodes from immunochallenged rats gave COSY spectra similar to the control lymph nodes from healthy rats.

These spectral differences were quantified by measuring the volumes of four crosspeaks (lactate 1.33–4.12, fucose/threonine 1.33–4.27, choline 3.50–4.07 and unassigned 3.25–4.00 ppm) and plotting the ratio of the lactate to threonine/fucose against that of the choline to an unassigned peak (Fig. 9). The relative increase in both lactate and choline reflected the extent of metastatic disease observed by the histopathologist. Increase in lactate content was consistent with anaerobic respiration by malignant cells, while increased choline level was indicative of a high rate of cellular replication, specifically with increased phospholipid synthesis and membrane turnover.[58]

Of particular interest were nodes from seven of the nine tumour-bearing rats (black dots in Fig. 9) which, histopathologically, were initially regarded as normal but which contained quantities of MR-visible species associated with the presence of metastatic cells. Step-serial 7 μm sections prepared from the nodes of each of these animals were re-examined by the pathologist using higher (×200) magnification. Two of the nodes previously diagnosed as normal had microfoci of malignant cells present directly under the capsule of the lymph node. Tissue discarded in preparing for initial histopathological examination may have included additional microfoci of tumour.

In a second experiment—this time looking only at animals 8, 9, and 10

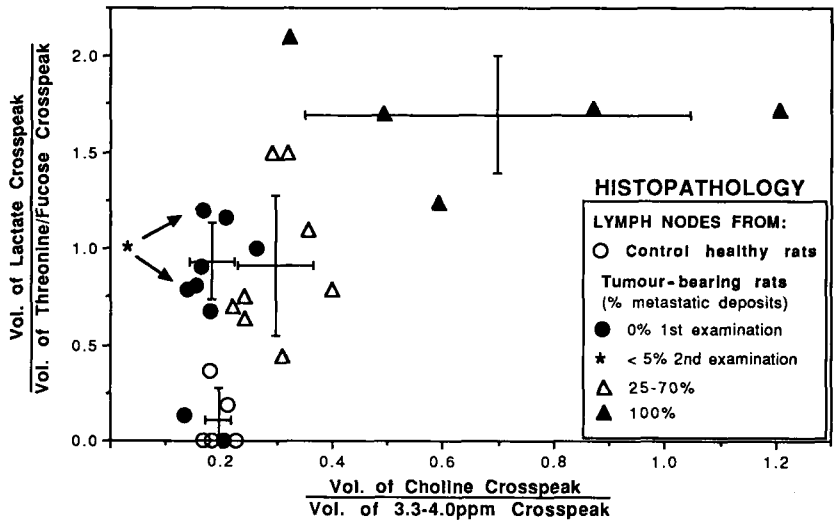

Fig. 9. Rat lymph nodes. Comparison of the pathology of rat axillary lymph nodes determined by ^{1}H MRS and step-section histopathological examination at routine (×40) magnification.[115] The ratio of the volumes of MR COSY crosspeaks from lactate and threonine/fucose is plotted against the ratio of those from choline and an unassigned resonance (3.3–4.0 ppm) for nodes from healthy control (○) and tumour-bearing rats. The six 7 μm sections from these nine lymph node specimens that on first examination were determined to be tumour-free (●) were re-examined by the histopathologist at higher (×200) magnification. For those specimens indicated by * re-examination revealed microfoci of metastatic cells directly beneath the capsule of the node. At least six axillary nodes from each Fischer rat (female, 12–13 weeks old) were combined as a single sample, trimmed of visible fat, washed in PBS/D_2O and positioned on glass wool in a 5 mm NMR tube and covered with 400 μl PBS/D_2O. The origin and properties of the R13762 cell lines used to produce metastatic tumours *in vivo* are reported elsewhere,[114] as are the methods used for cell culture and induction of primary and secondary tumours.[147] COSY spectra (48 scans, 200 experiments) were obtained as described in the legend to Fig. 3. Sine-bell window functions were applied in the t_1 domain and Lorentzian–Gaussian (LB = −30.0, GB = 0.2) window functions in the t_2 domain prior to Fourier transformation.[37] Expansion and integration of crosspeaks using standard Bruker software gave measurement of peak volume.[27]

days after injection, where the pathology had previously failed to identify the microfoci in five of the seven nodes—MRS identified all eight rats as containing malignant cells in the axillary lymph nodes (Fig. 10). Nodes were fully serial-sectioned at 5 μm, and each section was examined by the pathologist using ×200 magnification. Micrometastases were identified in three out of the eight nodes. While aggregates of tumour cells are usually correctly identified by histopathology, it is very difficult to discern individual cancer cells, and verification of the sensitivity of the MRS method relied on

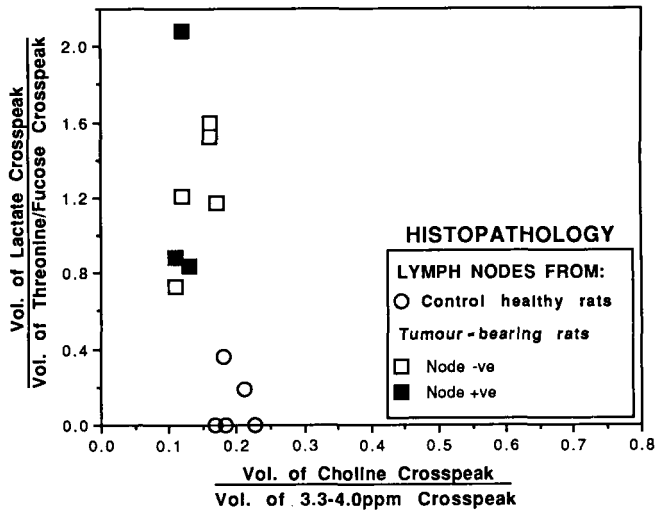

Fig. 10. Rat lymph nodes. Comparison of the pathology of rat axillary lymph nodes determined by ^{1}H MRS and histopathological examination of the entire node tissue at ×200 magnification.[115] The ratio of the volumes of MR COSY crosspeaks from lactate and threonine/fucose is plotted against the ratio of those from choline and an unassigned resonance (3.3–4.0 ppm) for nodes from healthy control and tumour-bearing rats. Lymph nodes were obtained, prepared for MR analysis, and spectra were acquired and processed as described in the legend to Fig. 9.

xenografting nodes into nude mice. Palpable tumours (1 cm^2) grew from nodes excised from animals days 9, 10 and 11 after inoculation, supporting the ^{1}H MRS diagnosis.

Lymph nodes from healthy rats and those stimulated with *B. pertussis* (cellular proliferation was confirmed by [^{3}H]-thymidine incorporation) were analysed by MRS as controls, but did not constitute false positives for the detection of micrometastases by ^{1}H MRS.

6.2. Human lymph nodes

Preliminary studies on human lymph nodes from both healthy controls and tumour-bearing patients have indicated that similar ^{1}H MR information is available. However, in contrast to the rat model, where the rats are of comparable age, in humans the fat content of the nodes appears to vary with age. The effect of age, sex and hormonal influences on the ^{1}H MR properties of human lymph nodes must now be established (C. L. Lean, P. Russell and C. E. Mountford, unpublished data).

7. THYROID CANCER

Thyroid nodules are common, and are estimated as being clinically evident in up to 10% of the population.[116] While the vast majority (95–98%) of these lesions are benign—either simple colloid nodules or benign follicular adenomas—the exclusion of thyroid malignancy remains a significant problem.[117] In particular, follicular adenomas and carcinomas are indistinguishable on the basis of clinical, radiological and gross pathological features. In such tumours the criteria for malignancy are the finding of capsular or vascular invasion at the tumour perimeter. This requires surgical removal of the entire tumour and extensive laboratory examination, which is rarely complete (10 blocks will sample only 30% of the capsule of a tumour 6 cm in diameter). As such, the diagnosis of malignancy is a function of sampling and sometimes pure serendipity. Indeed a significant number of "atypical" follicular neoplasms cannot be definitely categorized as benign on histological grounds, and may present many years later with metastatic malignancy, a potentially preventable situation had the diagnosis of follicular cancer been made initially.

It is currently not possible to diagnose or exclude malignancy on a biopsy sample of a follicular thyroid tumour (either open biopsy or fine needle aspirate), because the entire capsule of the tumour is not included.[116] Ultrastructural, flow cytometric or morphometric analyses cannot distinguish between benign and malignant follicular lesions of the thyroid.[118–120] Similar difficulties are encountered during "frozen section" examination. Therefore, since the vast majority of follicular thyroidal tumours removed surgically are benign, it can be said that major surgery is carried out principally for diagnostic purposes only. This is a highly unsatisfactory state of affairs. A yawning chasm exists between this practice and that of firm pre-operative diagnosis and surgery based on clinical need.

The results of an ^{1}H MR pilot study on human thyroid neoplasms evoked much excitement in the local endocrine surgery community. Normal tissue was compared with papillary carcinomas and follicular neoplasms by ^{1}H MRS.[34] One-dimensional spectroscopy clearly distinguished normal thyroid tissue from papillary carcinoma (Fig. 11). While these two tumour categories are readily distinguishable by conventional histopathology, the potential existed for distinguishing genuinely benign follicular adenomas from follicular carcinomas. The MR parameters clearly separated follicular neoplasms into one of two categories, each of which was directly comparable with either normal thyroid (Category A) or papillary carcinoma (Category B) (Fig. 12). The patients with clinically proven or histologically invasive follicular carcinoma were categorized by ^{1}H MR together with papillary cancers, as were a number of patients with clinically or morphologically atypical neoplasms. The spectral assessments in this study took only 12–15 min, and the examination was independent of diagnostic changes,

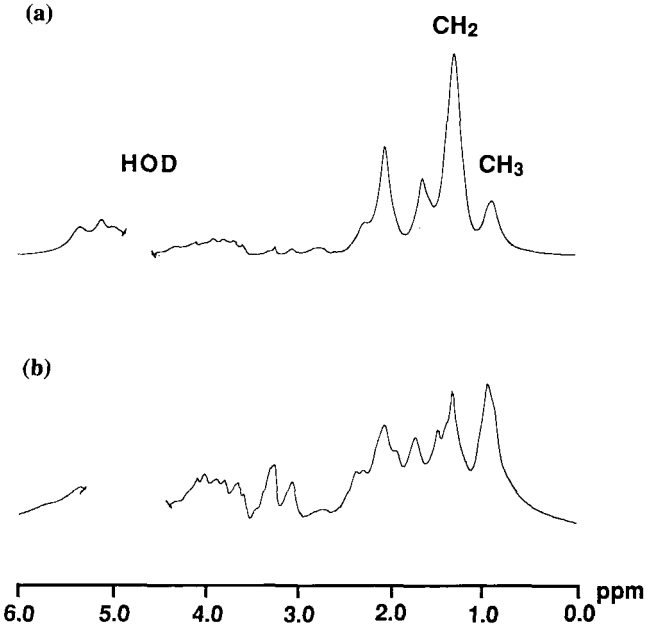

Fig. 11. Thyroid biopsies. Typical 1D ^{1}H MR spectra (128 scans) of thyroid tissue specimens: (a) normal and (b) papillary carcinoma.[34] Tissues were obtained at the time of surgery from patients undergoing partial or total thyroidectomy for solitary thyroid lesions. Specimens (3 mm^3) were placed in 1 ml PBS/D_2O in polypropylene vials, immediately immersed in liquid nitrogen and subsequently stored at −70°C for less than six weeks. Samples were prepared for MR analysis, and 1D ^{1}H MR spectra were acquired and processed as described in the legend to Fig. 1. After the MR experiment tissues were placed into FAA fixative (formalin : acetic acid : alcohol) and processed for histopathological assessment.

which are focal and therefore prone to sampling errors. *This study indicates that ^{1}H MRS may provide a method for unambiguously diagnosing potentially metastatic follicular thyroid cancer.* The extension of this technology to fine needle aspirate biopsy or *in vivo* spectroscopy could remove the need for much unnecessary surgery.

8. OTHER CANCERS

As the potential for using ^{1}H MRS as an adjunct to histopathology has become apparent, neoplasias from other organs are being examined.

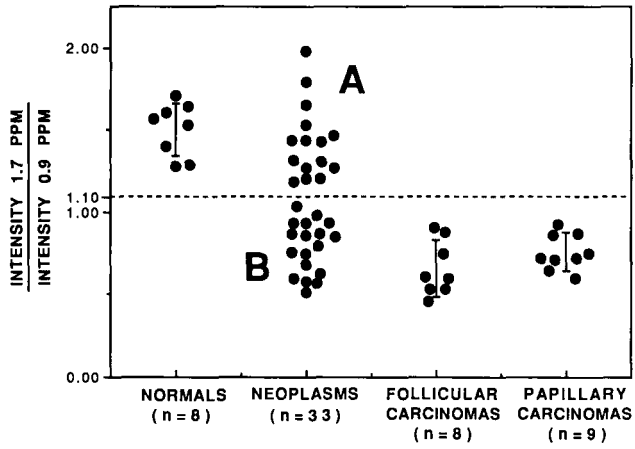

Fig. 12. Thyroid biopsies. Proton MRS assessment of normal thyroid, papillary and follicular carcinoma and neoplastic follicular thyroid.[34] The ratio of the intensity of resonances at 0.9 and 1.7 ppm is plotted against the pathology state of the specimen. Thyroid tissues were obtained and prepared for MR analysis as described in the legend to Fig. 11. 1D ^{1}H MR spectra were acquired and processed as described for tissues in the legend to Fig. 1.

8.1. Breast

Current understanding of premalignant lesions of the female breast and a trend towards more conservative surgical management necessitate greater precision of diagnosis by pathologists. Attempts to define subtle qualitative histological variations may be compromised by (a) limited sampling, (b) variable quality of sample preparation, (c) a plethora of similar but overlapping taxonomies and (d) histological criteria based solely on "crude" increases in the risk of cancer to the patient.[121] There is no clear definition of the point at which breast epithelial cells undergo malignant transformation and/or are committed to producing a clinical cancer. Proceeding with or withholding major surgery for individual patients is based on a statistical likelihood of increased risk of developing a clinical cancer in the same or opposite breast (about 30% for so-called "atypical hyperplasias" and 70% for ductal or lobular carcinoma *in situ*). This uncertainty leads to over-treatment for many patients and under-treatment for others.

Grading of common types of invasive carcinomas is also an important correlate of prognosis, and is useful in stratification of patients for post-operative adjuvant therapy, but again is based on subjective assessment of microscopic appearances with inherent limitations in consistency and reproducibility.[122]

Breast tissue is lipid-rich, and has proved to be the most difficult from which to acquire useful ^{1}H MR data. A previous study by Bradamante and

colleagues[123] indicated that specific T_1 and T_2 relaxation values of ^{1}H MR resonances from water and lipid correlated with malignancy. It was further suggested that diagnostic ^{1}H MR resonances were present under the strong lipid signals. A pilot study comparing normal tissue with neoplasms using two-dimensional spectroscopy with carefully selected acquisition and processing parameters has now commenced.[35] A combination of COSY and T_2-filtered COSY[124] procedures applied to breast tissues of varying pathology are producing promising results, with the fucosylation state in invasive breast tumours proving to be more complex than carcinomatous colonic tumours.

It is apparent from the spectra of breast biopsies containing invasive cells that the diagnostic molecular species observed in cervix and colon are present. However, the relative intensity of these diagnostic species is difficult to quantify owing to the intense fat signal that still remains after modification of acquisition and processing parameters. Since it will be difficult to quantify such resonances from breast tissue, the T_2 relaxation values of such crosspeaks could provide the pertinent diagnostic information (E. J. Delikatny, C. L. Lean, S. Roman and C. E. Mountford, unpublished data). However, for this to be a practical application a method must be developed to remove the time constraints of a series of T_2-filtered COSY experiments. Should such methods be devised, it is conceivable, but not yet established, that ^{1}H MRS may be able to provide information on both preinvasive lesions and grade carcinomas of the breast.

8.2. Prostate

Prostatic adenocarcinoma is the third most common malignancy in western males. Its incidence is age-dependent and therefore likely to increase. Screening for prostatic carcinoma is in its infancy, and the vast majority of cases are diagnosed in the course of investigation or treatment of urethral obstruction. Histopathology of tissue removed by needle biopsy or transurethral resection is currently the mainstay of diagnostic confirmation.

Magnetic resonance imaging (MRI) is used in the detection of prostate cancer, and effectively identifies 96% of malignant tumours more than 4 mm in size.[36] ^{1}H MR *in vivo* has been used effectively to identify both prostate cancer and benign prostate hyperplasia (BPA) from normal tissue on the basis of a marked decrease in citrate concentration in malignant prostate when compared to both normal tissue and benign lesions.[125] A wide range of citrate concentrations were recorded for BPA; however, the variable cellular composition of BPA may account for these differences.

A recent study[36] has established that, with careful preparation, human prostatic tissues give rise to reproducible 1D and 2D COSY ^{1}H MR spectra. A study aimed at correlating the histology of prostate tissues with ^{1}H MRS,

chemistry and diagnostic implications is now underway by Ross and colleagues. Should this be successful and with consideration to the varied cell composition of prostate tissues, the use of ^{1}H MRS in combination with chemical shift imaging (CSI) may well bridge these two technologies by providing chemical information necessary to confirm diagnosis and both stage and grade the malignancy *in vivo*.[126]

8.3. Brain

Radiological and pathological information used to evaluate brain tumours is frequently ambiguous, but this may be due to the large number of pathologies investigated and a variation in the number of MR techniques used. It should be remembered that brain was the first major organ where ^{1}H MR was applied to tumour pathology. In 1989 Bruhn *et al.*[28] published water-suppressed ^{1}H MR spectra of human brain, and subsequently MRS characterization of over 200 brain tumours has been completed.[59] Indeed, *in vivo* ^{1}H MRS studies of brain tumours have revealed significant spectral differences compared with normal brain tissue.[127–129] Metabolic alterations observed in malignant brain include decreased *N*-acetylaspartate (NAA) and phosphocreatine (PCr) and creatine (Cr), and increased levels of choline-containing compounds, lactate and lipids. Depletion of NAA is thought to represent damage or loss of neuroaxonal integrity, while increased choline and lactate may reflect a high level of proliferation and enhanced glycolytic activity.[29] A preliminary study aimed at comparing ^{1}H MR profiles with the type and stage of brain tumours reports an increased concentration of inositol in gliomas compared with normal brain tissue, and increased saturated fatty acid concentrations present in all metastatic compared with non-metastatic lesions.[130]

Attempts have been made to use ^{1}H MRS analysis of perchloric acid extracts of brain tissue to determine markers of malignancies. While extracts overcome limited spectral resolution and restricted measuring times inherent in *in vivo* studies, the usefulness of extract MRS data for diagnostic and/or staging purposes has so far been limited.[20,21,29] It is also now known that many chemicals are ^{1}H MR-invisible in intact cells and tissues; hence perchloric acid extracts often confuse the overall outcome by identifying all chemical species present.

An alternative *ex vivo* approach has been undertaken involving characterization of viable brain biopsies.[131] Preliminary data suggest that, using this approach, ^{1}H and ^{31}P MR may indeed complement the histopathological procedures currently used to distinguish between various types of brain tumours. As has been described for other organs, this will ultimately provide the data bank needed to complement *in vivo* brain spectroscopy to determine the correct pathology.

9. CHEMICAL SHIFT IMAGING

Spectroscopic imaging (SI), sometimes known as chemical shift imaging (CSI), has the combined advantages of both MRI and MRS. It provides spatial information like MRI, but the image is constructed on the basis of chemical information. Although in its infancy clinically,[132] CSI has the potential to revolutionize the detection of cancers, since it will, in principle, provide information on the chemical make-up and hence biological potential of the neoplasm, as well as the spatial location of the lesion. To know the spatial location and the pathology of a neoplasm prior to surgery would be a significant clinical advance. As with other localized spectroscopic techniques, the low concentration of metabolites present in most tissues increases the acquisition time of the SI data.

Several groups have studied human brain cancers using both ^{1}H SI[128,133] and ^{31}P SI.[134,135] As the patient is conscious at the time of the experiment, the precision with which the SI experiment can be performed has defined the limits of the lesion, and pathology of the tumour cannot be verified. As a consequence, these reports can only state that SI implies malignancy.[136] ^{1}H SI of the prostate looks equally promising,[137] but until chemical and MR profiles of possible pathologies of the prostate are documented, the method cannot be used effectively in the clinical context.

Our group has taken a different approach. We have used CSI as was first described by Dixon,[138] but employing the pulse sequence developed by Hall *et al.*,[139] where the image is constituted from a single specific frequency other than water. We have previously compared the chemical and ^{1}H MRS profiles for over 200 human cervical biopsies, and have established a correlation with the gold standard—histopathology.[33] As described in Section 5, the presence of a lipid spectrum signifies the presence of malignant cells in cervical tissue. Thus we considered that by constructing a CS image based on the intense methylene signal at 1.2 ppm, invasive cancer of the cervix should be distinguished from both normal tissue and preinvasive lesions.[140]

The normal water-based image, as would be produced in a routine MR image, and the lipid-based image (excited at 1.2 ppm) of two human cervical punch biopsies are shown in Fig. 13. The water-based image (a) and lipid-based image (b) (lipid excitation at 1.2 ppm, 450 Hz at half-height) were collected simultaneously over 2 h at 8 T. The histomorphology of the specimens is shown in Fig. 13(c). Magnifications (×10) of the areas denoted by arrows are shown in Fig. 13(d), to confirm the histology of the samples imaged. The lower biopsy is an invasive adenocarcinoma, while the upper is a low-grade squamous dysplasia (CIN I).

In the water-based image (a) both biopsies are observed as distinct components with equal intensities. In contrast, in the lipid-based CS images only the lower malignant biopsy shows substantial accumulation of MR-

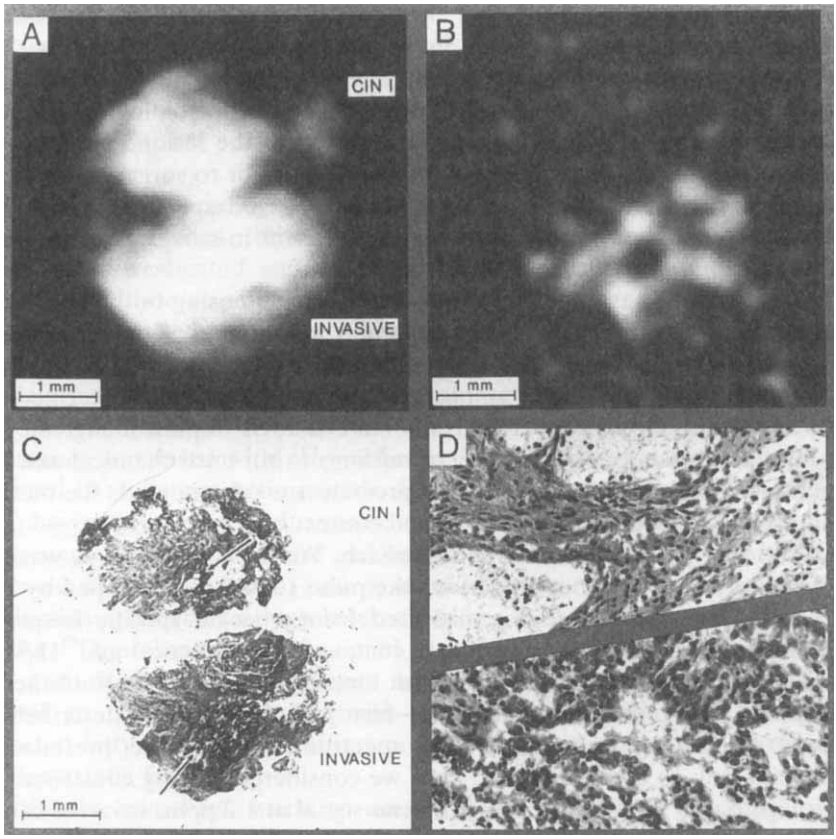

Fig. 13. Imaging of cervical biopsies. Water-based (a) (excitation at 4.8 ppm) and lipid-based (b) (excitation at 1.2 ppm) chemical shift images of two human cervical punch biopsies. Upper: low-grade interepithelial neoplasia (CIN I). Lower: invasive adenocarcinoma.[140] The images were simultaneously accumulated over two hours. A 500 μm slice through the biopsy with an in-plane resolution of 40 μm by 40 μm was acquired with TR/TE of 340 ms/11 ms. A Gaussian filter ((a) 1 ms, (b) 0.5 ms at half-height) was applied in both imaging directions prior to Fourier transformation. (c) Histological sections taken through each biopsy at the point corresponding to the centre of the imaged area. (d) Magnification ($\times$10) of the tissue area indicated by the arrows in (c): CIN I (upper) and invasive carcinoma (lower).

visible lipids. No such hyperintense lipid regions are seen in the preinvasive biopsy above. Histological assessment revealed that the lipid-rich areas detected by CSI correspond to foci of malignant cells, while the lipid-deficient areas correspond to normal cervical stroma.[140] Thus we have shown that, with prior knowledge of the chemical changes associated with specific pathologies of the human uterine cervix proton, CSI can diagnose the pathology and provide a spatial map of the diseased areas.

These data were collected at 8 T on an excised biopsy, whereas most whole-body MRI instruments are at 2 T. Although 3 and 4 T human whole-body magnets are now in use, the minimum frequency at which this cervical pathology can be determined *in vivo* remains to be ascertained, and many other technical problems, such as motion artefacts, need to be overcome.

10. WILL HISTOPATHOLOGY REMAIN THE GOLD STANDARD FOR THE ASSESSMENT OF MALIGNANT DISEASE?

Legg[141] summarized the situation in the following way: "Biopsies will supply the best answers when clinicians know what question they are asking, when they know the limitations of the technique used to obtain the biopsy, when they explain the diagnostic problem to the pathologist, when the pathologist knows the limitations of the morphology, when the pathologist uses whatever accessory techniques are required and when the pathologist and clinician use whatever communication is necessary to secure understanding." Thus, while histopathology is justly recognized as a mature discipline with a cumulative experience dating back well into the last century, it is nevertheless very much an art, subject to all the subtle nuances of individual variation in observer skill and experience, technical procedures and infinite variability of nature. The pathologist is not a technican in morphology but a physician with skills honed by constant exposure to clinical and morphological problems. While some morphological features are fully definitive and specific (pathognomonic) for a particular disease entity or diagnosis, others are prey to subjective assessment.

Errors of judgement carry a high cost when the question to be answered is one of human malignancy. The search for reproducibility and objectivity has led pathologists to computer-based histomorphometry and image analysis, both of which test their accuracy against an inherently imperfect discipline—histopathology. While these may add a measure of objectivity and reproducibility to histological assessment, they are very labour-intensive and often at greater cost to the community than the surgery they are intended to obviate. In this present report we have assessed the current usage of ^{1}H MRS, testing its ability to support, surpass and perhaps replace a flawed gold standard. For some organs ^{1}H MR in the future will offer an alternative modality for the assessment of malignant disease with increased sensitivity.

11. CONCLUSIONS

It is clear that water-based MRI is, at present, independently unable to identify the pathology of human tumours. However, the literature and our own work indicate that by studying carefully controlled model systems and excised human tissues, ^{1}H MRS can extract chemical information relating directly to the pathology. Furthermore, by tailoring data acquisition and processing parameters to report specifically on those molecules of known diagnostic relevance, ^{1}H MRS should, in the future, be able to diagnose invasive cancer in many organs *ex vivo* and some *in vivo*. Specifically, ^{1}H MRS has the potential to provide an independent modality that can

(1) report on the presence of invasive or preinvasive neoplastic cells in biopsy specimens;

(2) detect microfoci of metastatic cells missed by routine histopathology;

(3) grade malignancies by reporting on molecular species that correlate with reduced cellular differentiation;

(4) provide a prognostic index to aid in selection of patients for surgery and therapy;

(5) provide a precise diagnosis to aid in the decision on treatment and subsequent patient management.

Chemical and ^{1}H MRS databases for neoplasms of thyroid, colon and cervix are now well underway, and should, with advances in MR technology, allow chemical shift imaging experiments to be tailored to measure specific markers of tumour pathology. Databases for ovary, prostate, uterus, breast and brain are currently being compiled in our laboratory and in those of Ross and Smith in the USA and Canada respectively.

We therefore conclude that cancer can be diagnosed by ^{1}H MRS if the pathological criteria are linked to specific chemical changes ascertained from intact cells and tissues. This concept was clearly demonstrated by the cervix program, where CSI (*ex vivo*) not only defined the pathology of the tissue but also provided a spatial map of the diseased areas.

ACKNOWLEDGEMENTS

We are indebted to Drs E. J. Delikatny, Lily Huschtscha, W. Hull, A. Kuesel, B. Kunnecke, Wanda B. Mackinnon and Susan Dowd and to our many other scientific and clinical collaborators and the nurses and patient record personnel who have made this interdisciplinary programme possible. The clinical personnel include, at the Royal North Shore Hospital, Drs L. Delbridge, A. Ferrier, J. Freyer, J. C. Hunter, J. Philips and I. P. Truskett; at

the Concord Repatriation Hospital, Drs L. Bokey, P. Chapuis, C. Fung and R. Newland; at the Royal Prince Alfred Hospital, K. Atkinson; and at the Royal Women's Hospital, N. Hacker, C. van Haaften-Day and G. Watson. We should particularly like to thank Professors Ian Smith and Martin Tattersall for their long-standing support and many useful discussions through the difficult times, Allison Rutter for helpful comments regarding this report, Rebecca Hancock for preparing the diagrams and Judy Hood for typing the manuscript.

This work was supported in part by the following organizations: the Australian National Health and Medical Research Council (Public Health), the Australian National Health and Medical Research Council (Project Grant), the Leo and Jenny Foundation of Australia, NIH (USA) CA51054-03 and the University of Sydney Cancer Research Fund.

REFERENCES

1. H. C. Pitot, *Fundamentals of Oncology*, 3rd edn. Marcel Decker, New York, 1986.
2. C. J. Williams, *Cancer Biology and Management: An Introduction*. Wiley, Chichester, 1990.
3. A. Ferenezy and B. Winkler, *Blaustein's Pathology of the Female Genital Tract* (ed. R. J. Kuman), p. 218. Springer-Verlag, New York, 1987.
4. R. Bettelheim, K. N. Price, R. D. Gelber, B. W. Davis, M. Castiglione, A. Goldhirsch, A. M. Neville and the International (Ludwig) Breast Cancer Study Group, *Lancet*, 1990, **335**, 1565.
5. L. Foulds, *Cellular Control Mechanisms and Cancer* (ed. P. Emmelot and O. Muhlbock), p. 242. Elsevier, Amsterdam, 1964.
6. R. P. Hill, *The Basic Science of Oncology* (ed. I. F. Tannock and R. P. Hill), p. 160. Pergamon, New York, 1987.
7. P. A. Bottomley, C. J. Hardy, R. E. Argersinger and G. Allen-Moore, *Med. Phys.*, 1987, **14**, 1.
8. P. A. Bottomley, *Radiology*, 1989, **170**, 1.
9. P. F. Daly and J. S. Cohen, *Cancer Res.*, 1989, **49**, 770.
10. M. Czuba and I. C. P. Smith, *Pharmac. Ther.*, 1991, **50**, 147.
11. R. Damadian, *Science*, 1971, **171**, 1151.
12. I. J. Fidler, and M. L. Kripke, *Science*, 1977, **197**, 893.
13. J. P. Jesson, P. Meakin and G. Kneissel, *J. Am. Chem. Soc.*, 1973, **95**, 618.
14. J. Jeener, Ampère International Summer School, Basko Polje, Yugoslavia, 1971 (unpublished).
15. W. P. Aue, E. Bartholdi and R. R. Ernst, *J. Chem. Phys.*, 1976, **64**, 2229.
16. K. Cross, K. T. Holmes, C. E. Mountford and P. E. Wright, *Biochemistry*, 1984, **23**, 5895.
17. G. L. May, L. C. Wright, K. T. Holmes, P. G. Williams, I. C. P. Smith, P. E. Wright, R. M. Fox and C. E. Mountford, *J. Biol. Chem.*, 1986, **261**, 3048.
18. C. E. Mountford, E. J. Delikatny, M. Dyne, K. T. Holmes, W. B. Mackinnon, R. Ford, J. C. Hunter and I. D. Truskett, *Magn. Reson. Med.*, 1990, **13**, 324.
19. Y. H. Kim, E. K. Orenberg, K. F. Faull, N. G. Wade-Jardetzky and O. Jardetzky, *J. Invest. Dermat.*, 1989, **92**, 210.
20. J. Peeling and G. Sutherland, *Magn. Reson. Med.*, 1992, **24**, 123.

21. G. S. Gill, *J. Comp. Ass. Tomogr.*, 1990, **14**, 886.
22. H. L. Tang, R. J. Buist, R. H. Rixon, J. F. Whitfield and I. C. P. Smith, *NMR in Biomed.*, 1992, **5**, 69.
23. G. L. May, L. C. Wright, M. Dyne, W. B. Mackinnon, R. M. Fox and C. E. Mountford, *Int. J. Cancer*, 1988, **42**, 728.
24. W. B. Mackinnon, G. L. May and C. E. Mountford, *Eur. J. Biochem.*, 1992, **205**, 827.
25. A. Rosi, L. Guidoni, A. M. Luciani, G. Mariutti and V. Viti, *Cancer Lett.*, 1988, **39**, 153.
26. W. B. Mackinnon, PhD thesis, University of Sydney, 1990.
27. C. L. Lean, W. B. Mackinnon and C. E. Mountford, *Magn. Reson. Med.*, 1991, **20**, 306.
28. H. Bruhn, J. Frahm, M. L. Gyngell, K. D. Merboldt, W. Hänicke, R. Sauter and C. Hamburger, *Radiology*, 1989, **172**, 541.
29. H. Bruhn, T. Michaelis, K. D. Merboldt, W. Hänicke, M. L. Gyngell, C. Hamburger and J. Frahm, *NMR in Biomed.*, 1992, **5**, 253.
30. M. E. Yacoe, G. Sommer and D. Peehl, *Magn. Reson. Med.*, 1991, **19**, 429.
31. T. A. D. Smith, J. Glaholm, M. O. Leach, L. Machin, D. J. Collins, G. S. Payne and V. R. McCready, *Br. J. Cancer*, 1991, **63**, 514.
32. K. L. Behar and T. Ogino, *Magn. Reson. Med.*, 1991, **17**, 285.
33. E. J. Delikatny, P. Russell, J. C. Hunter, R. Hancock, K. Atkinson, C. van Haaften-Day and C. E. Mountford, 1993, *Radiology*, in press.
34. P. Russell, C. L. Lean, L. Delbridge, G. L. May, S. Dowd and C. E. Mountford, 1993, *Am. J. Med.*, revised and resubmitted.
35. S. Roman, BSc Med. thesis, University of Sydney, 1992.
36. R. Moats, L. Jones, L. Gravely, J. Gmelich and B. D. Ross, *Proc. Soc. Magn. Reson. Med.*, 1992, **2**, 3619.
37. E. J. Delikatny, W. E. Hull and C. E. Mountford, *J. Magn. Res.*, 1991, **94**, 563.
38. R. U. Lemieux, K. Bock, T. J. Delbaere, S. Koto and V. S. Rao, *Can. J. Chem.*, 1980, **58**, 631.
39. G. L. May, K. Sztelma, T. C. Sorrell and C. E. Mountford, *Magn. Reson. Med.*, 1991, **19**, 191.
40. G. L. May, L. C. Wright, C. L. Lean and C. E. Mountford, *J. Magn. Reson.*, 1992, **98**, 622.
41. D. Y. Sze and O. Jardetzky, *Biochim. Biophys. Acta*, 1990, **1054**, 181.
42. K. T. Holmes and C. E. Mountford, *J. Magn. Reson.*, 1991, **93**, 407.
43. C. L. Lean, W. B. Mackinnon, E. J. Delikatny, R. H. Whitehead and C. E. Mountford, *Biochemistry*, 1992, **31**, 11095.
44. A. C. Kuesel, T. Kroft, J. K. Saunders, M. Prefontaine, M. Mikhael and I. C. P. Smith, *Magn. Reson. Med.*, 1992, **27**, 349.
45. C. E. Mountford, J. K. S. Saunders, G. L. May, K. T. Holmes, P. G. Williams, R. M. Fox, M. H. N. Tattersall, J. R. Barr, P. Russell and I. C. P. Smith, *Lancet*, 1986, **i** 651.
46. C. E. Mountford and M. H. N. Tattersall, *Cancer Surv.*, 1987, **6**, 285.
47. R. E. Block, *The Nuclear Resonance Effect in Cancer* (ed. R. Damadian), Chap 10. Pacific Publishing Company, Portland, Oregon, 1976.
48. C. E. Mountford, W. B. Mackinnon, M. Bloom, E. E. Burnell and I. C. P. Smith, *J. Biochem. Biophys. Meth.*, 1984, **9**, 323.
49. C. Nicolau, W. Dietrich, M. R. Steiner, S. Steiner and J. L. Melnick, *Biochim. Biophys Acta*, 1975, **382**, 311.
50. C. E. Mountford, G. Grossman, G. Reid and R. M. Fox, *Cancer Res.*, 1982, **42**, 2270.
51. K. T. Holmes, C. L. Lean, N. H. Hunt and N. J. C. King, *Magn. Reson. Med.*, 1990, **16**, 1.
52. A. J. Dingley, N. J. C. King and G. F. King, *Biochemistry*, 1992, **31**, 9098.
53. W. B. Mackinnon, M Dyne, K. T. Holmes, R. S. Gupta and C. E. Mountford, *NMR in Biomed.*, 1989, **2**, 161.

54. M. Bloom, K. T. Holmes, C. E. Mountford and P. G. Williams, *J. Magn. Reson.*, 1986, **69**, 73.
55. C. E. Mountford and L. C. Wright, *Trends Biochem. Sci.*, 1988, **13**, 172.
56. I. Frietas, P. Pontiggia, S. Barni, Y. Bertone, M. Parente, A. Novariva, G. Poveta, G. Gerzeli and P. Stoward, *Anticancer Res.*, 1990, **10**, 613.
57. T. Hirakawa, K. Maruyama, N. E. Kohl, T. Kodama and H. E. Ruley, *Oncogene*, 1991, **6**, 289.
58. J. Ruiz-Cabello and J. S. Cohen, *NMR in Biomed.*, 1992, **5**, 226.
59. W. Negendank, *NMR in Biomed.*, 1992, **5**, 303.
60. C. Remy, M. Von Kienlin, S. Lotito, A. Francois, A. L. Benabid and M. Decorps, *Magn. Reson. Med.*, 1989, **9**, 395.
61. A. C. Kuesel, G. Graschew, W. E. Hull, W. Lorenz and H. W. Thielmann, *NMR in Biomed.*, 1990, **3**, 78.
62. P. F. Daly, R. C. Lyon, P. J. Faustino and J. S. Cohen, *J. Biol. Chem.*, 1987, **262**, 14875.
63. I. C. P. Smith, E. J. Princz and J. K. S. Saunders, *J. Can. Assoc. Radiol.*, 1990, **41**, 32.
64. C. L. Lean, R. N. Newland, D. Ende, E. L. Bokey, I. C. P. Smith and C. E. Mountford, 1993, *Magn. Reson. Med.*, in press.
65. J. R. Alger, J. A. Frank, A. Bizzi, M. J. Fulham, B. X. DeSouza, M. O. Duhaney, S. W. Inscoe, J. L. Black, P. C. M. van Zijl, C. T. W. Moonen and G. Di Chiro, *Radiology*, 1990, **177**, 633.
66. S. Furuya, S. Naruse, M. Ide, K. Murakami, T. Miyazaki and T. Yamamoto, *Nippon Acta Radiol.*, 1991, **51**, 836.
67. K. Herholz, W. Heindel, P. R. Luyten, J. A. den Hollander, U. Pietrzyk, J. Voges, H. Kugel, G. Friedmann and W.-D. Heiss, *Ann. Neurol.*, 1992, **31**, 319.
68. H. Kugel, W. Heindel, R.-I. Ernestus, J. Bunke, R. du Mesnil and G. Friedmann, *Radiology*, 1992, **183**, 701.
69. D. Ott, T. Ernst and J. Henning, *Radiology*, 1993, in press.
70. G. E. Sheline, *Cancer*, 1977, **39**, 873.
71. E. R. Laws, *J. Neurosurg.*, 1984, **61**, 665.
72. E. Princz, PhD thesis, University of Ottawa, 1988.
73. W. B. Mackinnon, C. L. Lean, R. Hancock, L. Huschtscha and C. E. Mountford, *Proc. Soc. Magn. Reson. Med.*, 1992, 3531.
74. G. L. Nicolson, *Biochim. Biophys. Acta*, 1976, **458**, 1.
75. R. H. Kennett, Z. L. Jonak and R. Byrd, *Meth. Cancer Res.*, 1982, **20**, 355.
76. V. Schirrmacher, P. Altevogt, M. Fogel, J. Dennis, C. A. Waller, D. Barz, R. Schwartz, R. Cheingsong-Popov, G. Springer, P. J. Robinson, T. Nebe, W. Brossmer, I. Vlodavsky, N. Paweletz, H. P. Zimmermann and G. Uhlenbruck, *Invasion and Metastasis*, 1982, **2**, 313.
77. G. Yogeeswaran, A. Granberg, R. M. Welsh and R. Kiessling, *Int. J. Cancer*, 1983, **31**, 501.
78. R. V. Iozzo, *Cancer Metastasis Rev.*, 1988, **7**, 39.
79. S. Hakomori, *Adv. Cancer Res.*, 1989, **52**, 257.
80. J. A. Alhadeff, *Crit. Rev. Oncol. Hematol.*, 1989, **9**, 37.
81. Y. S. Kim, M. Yuan, S. H. Itzkowitz, Q. Sun, T. Kaizu, A. Palekar, B. F. Trump and S. Hakomori, *Cancer Res.*, 1986, **46**, 5985.
82. L. C. Wright, G. L. May, P. Gregory, M. Dyne, K. T. Holmes, P. G. Williams and C. E. Mountford, *J. Cellular Biochem.*, 1988, **37**, 49.
83. W. B. Mackinnon, C. L. Lean, R. Hancock, L. Huschtscha and C. E. Mountford, *Proc. Soc. Magn. Reson. Med.*, 1992, **2**, 3531.
84. R. H. Whitehead, F. A. Macrae, D. J. B. St. John and J. Ma, *J. Nat Cancer Inst.*, 1985, **74**, 759.
85. R. H. Whitehead, J. K. Jones, A. Gabriel and R. E. Lukies, *Cancer Res.*, 1987, **47**, 2683.

86. S. F. Shedd, N. W. Lutz and W. E. Hull, *Proc. Soc. Magn. Reson. Med.*, 1992, **2**, 3510.
87. B. M. Wice, G. Trugnan, M. Pinto, M. Rousset, G. Chevalier, E. Dussaulx, B. Lacroix and A. Zweibaum, *J. Biol. Chem.*, 1985, **260**, 139.
88. J. F. Cooper and I. Farid, *J. Urol.*, 1964, **92**, 533.
89. H. S. Cooper, *Diagnostic Surgical Pathology* (ed. S. S. Sternberg), p. 1015. Raven Press, New York, 1989.
90. S. Carrel, B. Sordat and C. Merenda, *Cancer Res.*, 1976, **36**, 3978.
91. A Leibovitz, J. C. Stinson, W. B. McCombs, C. E. McCoy, K. C. Mazur and N. D. Mabry, *Cancer Res.*, 1976, **36**, 4562.
92. M. G. Brattain, M. E. Marks, J. McCombs, W. Finely and D. E. Brattain, *Br. J. Cancer*, 1983, **47**, 373.
93. J. A. McBain, J. L. Weese, L. F. Meisner, W. H. Wolberg and K. V. Willson, *Cancer Res.*, 1984, **44**, 5813.
94. C. Paraskeva, B. G. Buckle, D. Sheer and C. B. Wigley, *Int. J. Cancer*, 1984, **34**, 49.
95. S. C. Kirkland and I. G. Bailey, *Br. J. Cancer*, 1986, **53**, 779.
96. J. Park, H. K. Oie, P. H. Sugarbaker, J. G. Henslee, J. G. Chen, B. E. Johnson and A. Gazdar, *Cancer Res.*, 1987, **47**, 6710.
97. N. C. Davies and R. C. Newland, *Aust. NZ J. Surg.*, 1983, **53**, 211.
98. M. Mori, R. Shimono, Y. Adachi, M. D. Matsuda, H. Kuwano, K. Sugimachi, M. Ikeda and M. Saku, *Dis. Colon Rectum*, 1990, **33**, 498.
99. B. K. Armstrong and D. Holman, *Med. J. Aust.*, 1981, **1**, 460.
100. C. D'Aray, J. Holman and B. J. Armstrong, *Med. J. Aust.*, 1987, **146**, 410.
101. K. E. Kjörstad, *Obstet. Gynaecol.*, 1977, **50**, 28.
102. I. Gynning, J. E. Johnston, P. Alm and C. Tropé, *Gynecol. Oncol.*, 1983, **15**, 18.
103. T. Prempree, V. Patnaphan, W. Sewchand and R. M. Scott, *Cancer*, 1983, **51**, 1764.
104. M. Coppleson, P. Elliott and B. L. Reid, *Med. J. Aust.*, 1987, **146**, 405.
105. P. M. Elliott, M. H. N. Tattersall, M. Coppleson, P. Russell, F. Wong, A. S. Coates, H. J. Solomon, P. M. Bannatyne, K. H. Atkinson and J. C. Murray, *Br. Med. J.*, 1989, **298**, 288.
106. D. M. Fedorkow, D. I. Robertson, M. A. Duggan, J. G. Nation, S. E. McGregor and C. E. Stuart, *Am. J. Obstet. Gynecol.*, 1988, **158**, 307.
107. W.-H. Zhang, M. Coppleson, B. R. Rose, E. A. Sorich, B. N. Nightingale, C. H. Thompson, Y. E. Cossart, P. M. Bannatyne, P. M. Elliott and K. H. Atkinson, *J. Med. Virol.*, 1988, **26**, 163.
108. E. J. Delikatny, P. Russell, J. C. Hunter and C. E. Mountford, *Proc. Soc. Magn. Reson. Med.*, 1992, **1**, 55.
109. R. L. Somerjai, A. E. Nikulin, A. C. Kuesel, M. Prefontaine, N. Mikhael and I. C. P. Smith, *Proc. Soc. Magn. Reson. Med.*, 1992, **1**, 56.
110. M. Peckham, *Metastasis, Ciba Foundation Symposium* (ed. G. Bock, J. Whelan), p. 224. Wiley, Chichester, 1988.
111. S. A. Brooks and A. J. C. Leathem, *Lancet*, 1991, **338**, 71.
112. S. Ciatto, S. Cecchini, G. Grazzini, A. Iossa, D. Bartoli and A. Rasponi, *Neoplasma*, 1990, **37**, 179.
113. A. M. Neville, K. N. Price, R. D. Gelber, A. Goldhirsch and the International (Ludwig) Breast Cancer Study Group, *Lancet*, 1991, **337**, 1110.
114. I. A. Ramshaw, S. T. Carlsen, D. Hoon and R. C. Warrington, *Int. J. Cancer*, 1982, **30**, 601.
115. C. E. Mountford, C. L. Lean, R. Hancock, S. Dowd, W. B. Mackinnon, M. H. N. Tattersall and P. Russell, 1993, *Invasion and Metastasis*, in press.
116. V. A. Li Volsi, *Surgical Pathology of the Thyroid*, p. 173. Saunders, Philadelphia, 1990.
117. E. L. Mazzaferri, *Am. J. Med.*, 1992, **93**, 359.
118. J. B. Luck, V. C. Mumaw and W. J. Frable, *Acta Cytologica*, 1981, **25**, 718.

119. J. V. Johannessen and M. Sobrinho-Simoes, *Am. J. Clin. Path.*, 1982, **78**, 299.
120. H. Joensuu, P. Klemi, E. Eerola, *J. Path.*, 1987, **124**, 373.
121. C. D. Haagensen, N. Lane, R. Lattes and C. Bodian, *Cancer*, 1978, **42**, 737.
122. C. W. Elston, *Diagnostic Histopathology of the Breast* (ed. D. L. Page and T. J. Anderson), p. 300. Churchill Livingstone, Edinburgh, 1987.
123. S. Bradamante, E. Barchiesi, S. Pilotti and G. Borasi, *Magn. Reson. Med.*, 1988, **8**, 440.
124. P. G. Williams, J. K. S. Saunders, M. Dyne, C. E. Mountford and K. T. Holmes, *Magn. Reson. Med.*, 1988, **7**, 463.
125. J. Kurthanewicz, W. Chew, D. Vigneron, S. J. Nelson, B. Konety, J. M. Macdonald, T. L. James and P. Narayan, *Proc. Soc. Magn. Reson. Med.*, 1992, **2**, 3306.
126. D. B. Vigneron, S. J. Nelson, M. D. Prados, P. K. Sneed, R. R. Lee and D. Norman, *Proc. Soc. Magn. Reson. Med.*, 1992, **1**, 52.
127. J. H. Langkowski, J. Wieland, D. Bomsdorf, D. Leibfritz, M. Westphal, W. Offermann and R. Maas, *Magn. Reson. Imag.*, 1989, **7**, 547.
128. C. M. Segebarth, D. F. Balériaux, P. R. Luyten and J. A. den Hollander, *Magn. Reson. Med.*, 1990, **13**, 62.
129. J. Frahm, H. Bruhn, W. Hänicke, K. D. Merboldt, K. Mursch and E. Markakis, *J. Comput. Assist. Tomogr.*, 1991, **15**, 915.
130. T. Vogl, A. Jassoy, C. Becker, A. Dadashi, C. Hamburger, R. Sauter and J. Lissner, *Proc. Soc. Magn. Reson. Med.*, 1992, **2**, 3607.
131. A. Rutter, I. C. P. Smith, J. K. Saunders and H. Hugenholtz, *Proc. Soc. Magn. Reson. Med.*, 1991, **1**, 1065.
132. T. R. Brown, *NMR in Biomed.*, 1992, **5**, 238.
133. S. Furuya, S. Naruse, M. Ide, N. Kakoi, M. Ikejiri, K. Takaya, T. Yamamoto and T. Miyazaki, *Proc. Soc Magn. Reson. Med.*, 1992, **2**, 641.
134. J. S. Taylor, D. B. Vigneron, J. Murphy-Boesch, S. J. Nelson, H. B. Kessler, L. Coia, W. Curran and T. R. Brown, *Proc. Nat. Acad. Sci. USA*, 1991, **88**, 6810.
135. D. B. Vigneron, S. J. Nelson, J. Murphy-Boesch, D. A. C. Kelley, H. B. Kessler and T. R. Brown, *Radiology*, 1990, **177**, 643.
136. W. Heindel, K. Herholz, H. Kugel, P. R. Luyten, J. Bunke, W.-D. Heiss and K. Lackner, *Proc. Soc. Magn. Reson. Med.*, 1992, **1**, 51.
137. J. A. Sanders, D. M. Thomasson and L. O. Sillerud, *Proc. Soc. Magn. Reson. Med.*, 1992, **2**, 3305.
138. W. T. Dixon, *Radiology*, 1984, **153**, 189.
139. L. D. Hall, S. Sukumar and S. L. Talagala, *J. Magn. Reson.*, 1984, **56**, 275.
140. B. Künnecke and C. E. Mountford, *Proc. Soc. Magn. Reson. Med.*, 1993, in press.
141. M. A. Legg, *N. Engl. J. Med.*, 1981, **305**, 950.
142. A. Leibovitz *per* L. P. Rutzky, *Adv. Cell Culture*, 1984, **4**, 47.
143. C. Paraskeva, S. Finerty and S. Powell, *Int. J. Cancer*, 1988, **41**, 908.
144. A. C. Williams, S. J. Harper and C. Paraskeva, *Cancer Res.*, 1990, **50**, 4724.
145. M. Pignatelli and W. F. Bodmer, *Proc. Nat. Acad. Sci. USA*, 1988, **85**, 5561.
146. L. Huschtscha, E. Rozengurt and W. Bodmer, *Eur. J. Cancer*, 1991, **27**, 1680.
147. L. C. Wright, G. L. May, W. B. Mackinnon, P. Gregory, K. T. Holmes, M. Dyne, D. Sullivan and C. E. Mountford, *Invasion and Metastasis*, 1991, **11**, 332.

This Page Intentionally Left Blank

Pulsed-Field-Gradient NMR Studies of the Diffusion of Chain Molecules in Polymer Matrices

TAKUHEI NOSE

Department of Polymer Chemistry, Tokyo Institute of Technology, Ookayama, Japan

ANNUAL REPORTS ON NMR SPECTROSCOPY
VOLUME 27 ISBN 0-12-505327-4

1. INTRODUCTION

The diffusion behaviour of polymer chains depends strongly upon the structure and mobility of the surroundings. Chain diffusion in ordinary polymer matrices, such as low-molecular-weight solvents, semidilute solutions and polymer melts, has been extensively studied both experimentally and theoretically.[1,2] In these studies entanglement and hydrodynamic interaction have been the main issues.

The diffusion mechanism of a single chain in a polymer melt depends on the absolute and relative chain lengths of diffusant and matrix. This is illustrated as a plot of N_N versus N_p space in Fig. 1, where N_N and N_p are the degrees of polymerization of the diffusant and the matrix respectively.[3] A similar plot can be drawn from a semidilute solution. In this case N should be replaced by the number of units ("blobs") in the polymer chain, with the unit size depending on concentration.[4]

In contrast to such relatively homogeneous matrices, one can consider more heterogeneous matrices such as porous glasses, porous membranes, branched polymers and microstructured block copolymers in the presence or absence of solvent. In the macroscopic diffusion and permeability of the tracer chain through a heterogeneous matrix, the spatial distribution of the

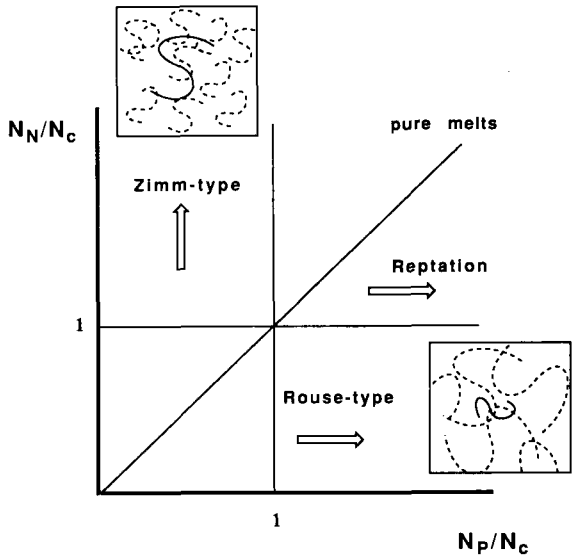

Fig. 1. Diffusion mechanism of single chains (N_N) in polymer matrices (N_p) in a space of N_N versus N_p. N_c is the critical degree of polymerization for entanglements.

tracer chain in the latter can play an important role, together with hydrodynamics and chain motion in the confined space.[5–17]

To measure the tracer diffusion coefficient in a polymeric system, several techniques are available: dynamic light scattering, forced Rayleigh scattering, elastic recoil detection, forward recoil spectrometry and pulsed-field-gradient NMR (PFG-NMR). Of these, PFG-NMR has great merits for the study of tracer diffusion in complex systems, such as chain diffusion in polymer matrices.

This chapter will deal with three topics concerning chain diffusion in polymeric matrices.

The first is connected with homogeneous polymer matrices, namely *tracer diffusion of a single polymer chain in polymer melts of different molecular weights*. Crossover behaviour from Rouse- to Zimm-type diffusion in unentangled systems (see Fig. 1) will be discussed.

The second topic is an example of chain diffusion in heterogeneous matrices, namely *diffusion of short chains dissolved in microstructured block copolymers*. Particular attention is paid to the dependence of the diffusion coefficient on the molecular weight of the tracer chain, which shows a particular behaviour.[18]

The third topic involves tracer diffusion under large concentration fluctuations, namely *chain diffusion in polymer/polymer/solvent systems near the critical point*. Near the critical point, concentration fluctuations with mutual diffusion become infinitely large. Combination of dynamic light scattering and PFG-NMR measurements reveals the effects of concentration fluctuations on the tracer diffusion, if any.

Through this chapter we shall show how the matrix affects the tracer diffusion of polymer chains and also demonstrate the applicability of PFG-NMR to complex systems of polymers.

In Section 2 the technique of PFG-NMR as applied to polymeric systems will be described. In the following sections the three topics mentioned above will be discussed, and we shall present experimental results from PFG-NMR and their analysis.

2. APPLICATION OF THE PFG-NMR METHOD TO CHAIN DIFFUSION IN POLYMERIC SYSTEMS

2.1. A brief description of the PFG-NMR method

The NMR method of diffusion measurement is based on the fact that if the magnitude of a magnetic field varies with spatial position then on applying it to a spin attached to a molecule it will change with time as the molecule is displaced by Brownian motion. If a magnetic field with time-dependent field

gradient $G(t)$ is applied to a system then the time-variation of the magnetic moment $\Phi(t)$ of the system is given by[18]

$$\frac{\Phi(t)}{\Phi(0)} = \exp\left[-D\gamma^2 \int_0^t \left(\int_0^{t'} G(t'')\,dt''\right)^2 dt'\right], \tag{1}$$

where D is the diffusion coefficient and γ is the gyromagnetic ratio. Here the spins move randomly, following Gaussian statistics as in case of simple Brownian motion, with the mean-square displacement $\langle z^2\rangle$ of the spins in the z direction of the field gradient during the diffusion time T_D obeying the equation

$$\langle z^2\rangle = 2DT_D \tag{2}$$

The PFG-NMR method was proposed by Hahn[19] and established by Carr and Purcell.[20] The idea is to use the spin-echo technique, with a pulsed field gradient $G(t)$ instead of a stationary gradient. A typical pulse sequence is illustrated in Fig. 2. If there were no displacement of the spins, the effects of the two gradient pulses (1 and 2 in Fig. 2) on the echo signal would cancel each other because the second field gradient pulse is applied after the 180° pulse, so the direction of the spins is opposite to that at the time of the first pulse. Quantitatively, the attenuation $A(2\tau)/A^*(2\tau)$ of the echo signal due to the displacement of the spins in the system is evaluated from (1) with the explicit expression for $G(t)$. That is, for the present case,

$$\frac{A(2\tau)}{A^*(2\tau)} = \exp(-\gamma^2 g^2 \delta^2 D(\Delta - \tfrac{1}{3}\delta)], \tag{3}$$

here $A^*(2\tau)$ is the amplitude of the echo signal in the absence of the gradient ($g = 0$). When $\Delta \gg \delta$, the time interval Δ is regarded as the diffusion time T_D, i.e. $\Delta = T_D$, and then, from (2) and (3),

$$\frac{A(t)}{A^*(t)} = \exp(-\tfrac{1}{2}\gamma^2 g^2 \delta^2 \langle z^2\rangle). \tag{4}$$

This equation holds even in more general cases where $\langle z^2\rangle$ does not necessarily obey (2).

The echo signal may decay owing to spin–spin interactions with relaxation time T_2. $A^*(t)$ is then given by

$$A^*(t) = A^*(0)\exp(-t/T_2) \tag{5}$$

Therefore Δ should be taken to be not much longer than T_2. Otherwise, i.e. if $\Delta \gg T_2$ and accordingly $t \gg T_2$, the echo signal decays not by diffusion but

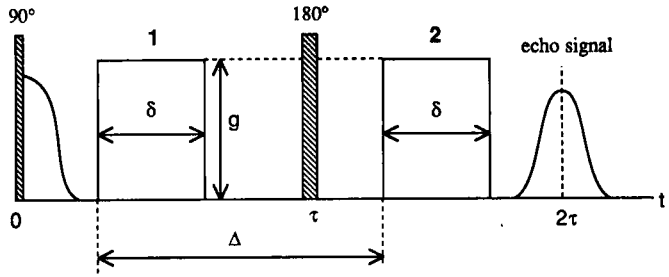

Fig. 2. A pulse sequence of the PFG-NMR method. ▨, radio frequency; □, pulsed field gradient.

by T_2 relaxation—in other words, the labelling by the pulsed field gradient has been erased by T_2 relaxation before the displacement of the molecules can be measured.

2.2. Applicability to polymeric systems

Study of the diffusion of polymeric systems using the PFG-NMR method started with measurements of the self-diffusion of low-molecular-weight polyethylenes in melts by McCall *et al.*[21] and the tracer diffusion of polymer chains in solution by Tanner *et al.*[22] Since then, PFG-NMR has been applied to a wide variety of polymeric systems, such as dilute solutions, semidilute solutions, concentrated solutions, melts, network polymers and more complex polymer systems. These studies have been summarized in the excellent review articles by von Meerwall.[23]

It is self-diffusion or tracer diffusion that is observed by the PFG-NMR method (ordinary diffusion driven by a concentration gradient is mutual diffusion). The advantages of the PFG-NMR method are in general as follows:

(i) no artificial labelling is needed for tracers;

(ii) the tracer-diffusion coefficient of each component in the system can be clearly measured by utilizing differences in resonance frequency;

(iii) the method is applicable to systems having complex morphological structures.

A serious disadvantage, especially in applications to polymeric systems, is that the distance over which the diffusant moves during the time T_2 must be greater than the minimum distance detectable by differences in the magnetic field. Therefore this method cannot be used for slow diffusion, which is generally the case in bulk polymers. At present, the maximum gradient g of an ordinary apparatus is about $500\,\mathrm{G\,cm^{-1}}$. In this case the distance

resolution is evaluated from (4) as $\langle z^2\rangle^{1/2} = 2^{1/2}(\gamma g\delta)^{-1} = 2^{1/2}(2.675\times10^4\,\mathrm{G^{-1}\,s^{-1}}\times 500\,\mathrm{G\,cm^{-1}}\times\delta)^{-1} = 1.06/\delta\,\mathrm{nm}$ (δ in s), so that, supposing δ to be 5 ms, the minimum distance that can be measured is about 210 nm. Here the value of γ is put equal to $2.675\times10^4\,\mathrm{G^{-1}\,s^{-1}}$ for proton nuclei, which are the most frequently used. This corresponds to a diffusion coefficient $D = \langle z^2\rangle/2\Delta = 4.5\times10^{-9}\,\mathrm{cm^2\,s^{-1}}$ if $\Delta = 10\delta = 50$ ms. If the labelling lifetime, i.e. T_2, is longer, say 100 ms, then δ can be taken to be about 10 ms, and consequently the minimum distance $\langle z^2\rangle^{1/2}$ becomes 105 nm, and one can reach a smaller D of $10^{-9}\,\mathrm{cm^2\,s^{-1}}$.

For the translational diffusion of the centre of mass of a polymer chain, the diffusion coefficient that can be observed is limited by the lifetime T_2 of the labelling and the chain size, irrespective of g, since the minimum $\langle z^2\rangle^{1/2}$ has to be larger than the radius of gyration R_g of the chain. For a typical value of $R_g = 20$ nm the minimum D that can be reached is $2\times10^{-11}\,\mathrm{cm^2\,s^{-1}}$ (estimated by (2)), supposing T_2 to be 100 nm, which is the maximum lifetime of an ordinary polymer with mobile protons in the liquid state.

This limitation, arising from the large size of polymers, presents a challenge to the measurement of the molecular motions of polymers, i.e. their rotational and/or internal motions. In the time domain where the diffusion time is less than or comparable to the relaxation time of rotational diffusion, the mean square displacement $\langle z^2\rangle$ does not follow the ordinary diffusion process (2), but reflects the internal modes of motion having a different time dependence. At present, to the author's knowledge, no measurements of such internal motions have been reported.

Many possible studies taking advantage of the PFG-NMR method in polymeric systems are yet to be carried out in detail, including tracer diffusion in multicomponent systems. Brown *et al.*[24,25] and Pinder *et al.*[26,27] measured tracer-diffusion coefficients in ternary polymer solutions, while the case of polymer mixtures in bulk will be presented in this chapter. Combination of PFG-NMR and dynamic light scattering (DLS) is also an interesting approach to the study of polymer dynamics,[24,25,27–29] as presented in Section 5, since PFG-NMR and DLS can pick up different features of diffusion, tracer diffusion and mutual diffusion. Other trends of recent studies with the PFG-NMR technique are time-resolved measurements[30] and applications to NMR imaging,[31] relying on rapid measurements of diffusion coefficients. PFG-NMR has been applied to more complex polymer systems,[32–35] including a polymer solution in shear flow.[35]

2.3. The experimental method

Here the experimental method used in the present studies will be described briefly.

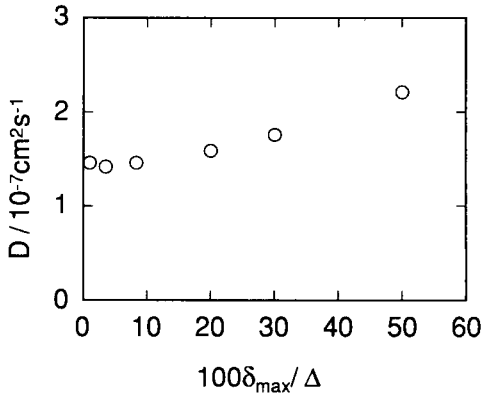

Fig. 3. Effects of the residual magnetic field at $G = 162.5\,\mathrm{G\,cm^{-1}}$ for PEG ($M_w = 400$) at 30°C.

The NMR apparatus was a JEOL GSX/GX270 with a pulsed-field-gradient generator unit NM-502. Two probes were used, which could generate a field gradient g of up to 70 and 600 $\mathrm{G\,cm^{-1}}$, respectively. The probe with 70 $\mathrm{G\,cm^{-1}}$ was a commercial one, while that with 600 $\mathrm{G\,cm^{-1}}$ was especially designed for slow-diffusion measurements. The diameter of the sample tube was 5 mm, and in the case of the 600 $\mathrm{G\,cm^{-1}}$ probe the height of a sample in an NMR tube was limited to be less than 8 mm in order to maintain a uniform magnetic field gradient in the sample.

The magnetic field gradient was calibrated using H_2O, n-$C_{18}H_{38}$ and poly(ethylene glycol)s ($M_w = 200$ and 400). The pulse sequence applied was of the Hahn type[19,20] for the spin-echo technique, which is illustrated in Fig. 2. The time interval Δ and the width δ of the pulsed field gradient ranged from 30 to 200 ms and from 0.6 to 37 ms respectively, depending on the field gradient g and the nature of the tracers, i.e. Δ and T_2.

The effects of the residual magnetic field were examined according to the method of von Meerwall and Kamat.[36] An example of the dependence of the calculated D on the ratio δ_{max}/Δ is shown in Fig. 3, where δ_{max} is the maximum δ used in measuring the diffusion coefficient. At large values of this ratio, i.e. when the pulse width δ is not small compared with the pulse interval Δ, the apparent D increases with increasing δ_{max}/Δ, indicating the presence of effects of the residual magnetic field. To avoid these, the value of δ was always kept less than one-tenth of the value of Δ.

In the usual cases the attenuation A/A^* of the echo signal was analysed using the second-order cumulant expansion

$$\ln(A/A^*) = -\bar{D}X + \tfrac{1}{2}\mu_2 X^2, \tag{6}$$

with

$$X = \gamma^2 g^2 \delta^2 (\Delta - \tfrac{1}{3}\delta),$$

where $\bar{D}$ is an average diffusion coefficient, μ_2 is the second moment of polydispersity of $\bar{D}$, i.e. $\mu_2 = \overline{(D - \bar{D})^2}$. In the case of polymer liquids with narrow molecular-weight distributions, the polydispersity index $\mu_2/\bar{D}^2$ was very small (<0.05), so the single-exponential fitting was substantially valid. The analytical method for the attenuation A/A^* of bimodal mixtures with different molecular weights will be described in Section 3.

3. CHAIN DIFFUSION IN MATRICES OF UNENTANGLED POLYMER MELTS WITH DIFFERENT CHAIN LENGTHS: CROSSOVER FROM ZIMM- TO ROUSE-TYPE DIFFUSION[3]

Chain diffusion in polymer melts has been extensively investigated both experimentally and theoretically.[1,2] The entanglement effect is of great importance in the chain dynamics of polymer melts. As can be seen from Fig. 1, however, hydrodynamic interaction must play an important role in the diffusion of short chains in pure melts and of long chains in polymer matrices of short chains. In the limit $N_N \gg N_p$, such as in a dilute solution, a polymer chain behaves like a rigid sphere in translational diffusion owing to hydrodynamic interaction,[2] whereas in the limit $N_N \ll N_p$ chain diffusion is described by the Rouse model if the tracer chain has no entanglements with the matrix.[37–39] In this limit hydrodynamic interaction is suppressed, since, with increasing chain length of the matrix polymer, the viscosity of the matrix increases while the segmental diffusion remains unchanged. The Rouse-type regime for $N_N < N_p$ has been observed in polymer melts[40] and polymer solutions.[41] This unique effect of hydrodynamic interaction in polymeric systems can be revealed by observing the crossover behaviour on changing the relative chain length of the matrix. Nemoto *et al.*[42] studied the molecular-weight (M_N) dependence of tracer diffusion in an unentangled polymer solution matrix of fixed molecular weight (M_p) for polystyrene/dibutyl phthalate solutions, and observed crossover behaviour from Rouse-type diffusion to diffusion with hydrodynamic interaction.

In order to see the crossover, we must measure the tracer-diffusion coefficient of polymer chains dissolved in polymer melts with the same chemical species but different molecular weights. In this section it will be demonstrated that the PFG-NMR method can be a powerful technique for this purpose. We selected poly(dimethylsiloxane)s (PDMS) with no entanglements in melts, where $M_p < M_c$ (M_c is the critical molecular weight for entanglement), and measured the tracer-diffusion coefficient of PDMS with M_N in polymer matrices of PDMS with M_p.

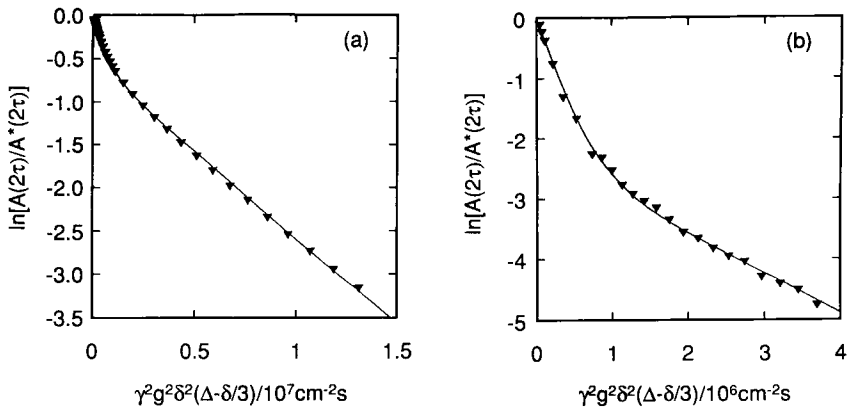

Fig. 4. Attenuation of the echo-signal intensity for the mixtures PDMS5/PDMS55 at 30°C: (a) wt% of PDMS55, $W_{55} = 10\%$ ($\Delta = 100$ ms; $\delta = 0.6$–4.3 ms, $g = 40.0\,\mathrm{G\,cm^{-1}}$); (b) $W_{55} = 6.0\%$ ($\Delta = 100$ ms; $\delta = 0.6$–14 ms, $g = 40.0\,\mathrm{G\,cm^{-1}}$).

3.1. Data analysis for bimodal polymer mixtures

The attenuation A/A^* for bimodal mixtures with different diffusion coefficients can be described by

$$\frac{A}{A^*} = f\exp(-D_1X) + (1-f)\exp(-D_2X), \tag{7}$$

which allows us to determine the tracer-diffusion coefficients D_1 and D_2 of the two components separately, with f being the fractional proton numbers of component 1. The present data for bimodal polymer mixtures with different molecular weights could be analysed using (7). An example of the bimodal fitting is shown in Fig. 4. D_1 and D_2 were determined by least squares fitting to (7) as a function of composition. The extrapolation of D_1 and D_2 to the dilute limits of the respective components gave the tracer-diffusion coefficient of single chains of one component in the matrix of the other, as shown in Fig. 5.

3.2. Theoretical background of chain diffusion in unentangled polymer melts

In the Rouse model, where the polymer is a Gaussian chain with no hydrodynamic interaction, the diffusion coefficient D_R and the shear

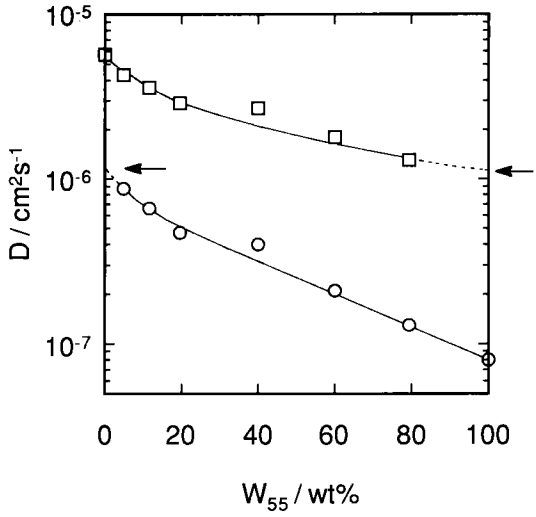

Fig. 5. Tracer-diffusion coefficient of each component in PDMS5/PDMS55 mixtures as a function of PDMS55 wt% W_{55} at 30°C: □, PDMS5; ○, PDMS55. Arrows indicate the dilute limit.

viscosity η_R for a polymer with molecular weight M are given respectively by[43–45]

$$D_R = \frac{k_B T}{\zeta M/M_0}, \tag{8}$$

$$\eta_R = \frac{A\zeta M}{M_0}, \tag{9}$$

where ζ is the friction coefficient of the monomer, k_B is Boltzmann's constant, T is the absolute temperature, M_0 is the molecular weight of a monomer unit and $A = \frac{1}{6}N_A a^2 \rho/M_0$ is independent of ζ and M, with N_A being Avogadro's number, a the statistical length of the monomer and ρ the polymer density.

On the other hand, the diffusion coefficient D_Z of a Gaussian chain with strong hydrodynamic interactions is given in the framework of the Kirkwood–Reiseman theory by[46,47]

$$D_Z = \frac{Ck_B T}{\eta M^{1/2}}, \tag{10}$$

where η is the solvent (or matrix) viscosity, and $C = 0.196/(a/M_0{}^{1/2})$. Hereinafter, we refer to this as the Zimm-type diffusion model.

Consider the diffusion of a chain with molecular weight M_N in a matrix of polymers with molecular weight M_p, where M_N and M_p are small enough to have no entanglements. If η of the matrix is given by η_R of (9) then

$$D_Z = \frac{C}{A} \frac{k_B T}{(\zeta_p/M_0) M_p M_N^{1/2}}, \tag{11}$$

while

$$D_R = \frac{k_B T}{(\zeta_p/M_0) M_N} \tag{12}$$

where ζ_p is ζ of the matrix, assumed to be the same as ζ of a single chain in the matrix. Comparing (11) and (12), one can see that Rouse-type diffusion is dominant ($D_R > D_Z$) if $M_p > (C/A) M_N^{1/2}$; otherwise Zimm-type diffusion is dominant.

Hence, in general, we have the following scaling expression:

$$D = \frac{k_B T}{\zeta_p M_N / M_0} f_D \left(\frac{M_N^{1/2}}{M_p} \right), \tag{13}$$

with

$$f_D = \begin{cases} 1 & (M_p \gg M_N^{1/2}), \qquad (14a) \\ \dfrac{C}{A} \dfrac{M_N^{1/2}}{M_p} & (M_p \ll M_N^{1/2}). \qquad (14b) \end{cases}$$

3.3. Experimental results and scaling description

The weight-average molecular weight of the PDMS used ranged from 460 to 19 300, with the polydispersity index M_w/M_n ranging from 1.0 to 1.29. The samples are coded as PDMS (number), where the number indicates $1/100 M_w$, corresponding approximately to the degree of polymerization.

Figure 6 represents the molecular weight dependence of the self-diffusion coefficient D_s and the shear viscosity η for pure melts. Here the shear viscosity was measured by a Ubbelohde viscometer for PDMS5 and PDMS13 and by the rolling-ball method for the other samples. Both D_s and η have stronger dependences on the molecular weight M_w than those predicted by the Rouse model, (8) and (9) respectively, as is usually observed. This discrepancy has been attributed to an M_w dependence of the monomer friction coefficient ζ.[37,48]

The tracer-diffusion coefficient D for various molecular weights M_N at the

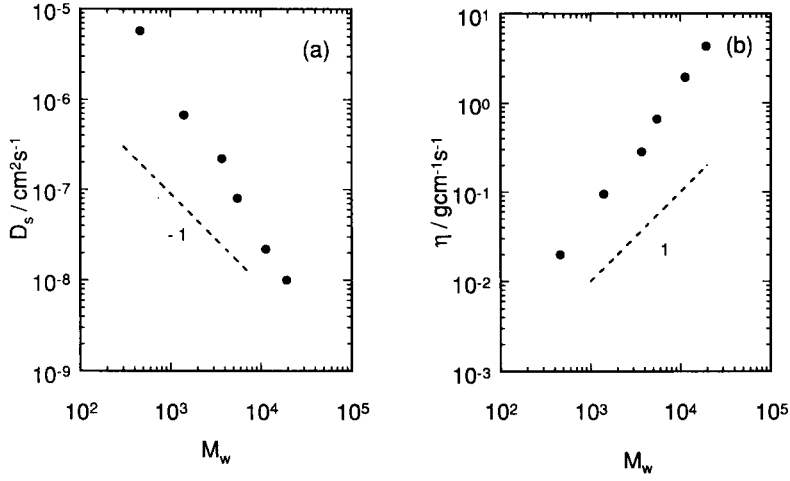

Fig. 6. Self-diffusion coefficient D_s and viscosity η of PDMS at 30°C as functions of molecular weight: (a) D_s; (b) η.

limit of dilution was obtained as a function of the molecular weight M_p of the matrix polymer. The numerical data are listed in Table 1. It should be noted here that the excluded-volume effect on chain dimension can be substantially ignored in the present range of molecular weights.

3.3.1. Self-diffusion of pure melts

The polymer chain in pure melts has been supposed to behave like a Rouse chain following (8) and (9). To test these equations, we have to know the molecular-weight dependence of ζ. However, a general test, independent of the ζ evaluation, can be made by checking the constancy of $D\eta$: according to (8) and (9),

$$D\eta/Ak_BT = 1.$$

Figure 7 shows a plot of $D_s\eta/Ak_BT$ versus M_w. Here the value of the constant Ak_BT was estimated to be 2.9×10^{-8} g cm s^{-2}, using $a^2/M_0 = R^2/M = 4.36 \times 10^{-3}$ nm^2,[49,50] and $\rho = 0.965$ g cm^{-3},[51] where R^2 is the mean square end-to-end distance. The product $D\eta$ is not always constant over the whole experimental molecular-weight range, but only in an intermediate range where it levels off. The departure from $D \propto M_w^{-1}$ and $\eta \propto M_w$ at lower M_w is not due to a failure in the evaluation of ζ, but rather to the breakdown of the Rouse model in this M_w region. At higher M_w, the value of $D\eta$ still

Table 1. Tracer-diffusion coefficient D at the limit of dilution in polymer matrices.

Tracer[a]	Matrix[a]	D (10^{-7} cm^2 s^{-1})
PDMS5	PDMS13	18
	PDMS30	13
	PDMS55	11
	PDMS193	10
PDMS14	PDMS5	24
	PDMS55	4.2
	PDMS193	3.4
PDMS37	PDMS5	17
	PDMS193	1.6
PDMS55	PDMS5	11
	PDMS13	2.5
	PDMS193	0.65
PDMS193	PDMS5	5.5
	PDMS13	1.5
	PDMS30	0.70
	PDMS55	0.35
	PDMS113	0.15

[a]The samples are coded as PDMS (number), where the number indicates $\frac{1}{100}M_w$, corresponding approximately to the degree of polymerization.

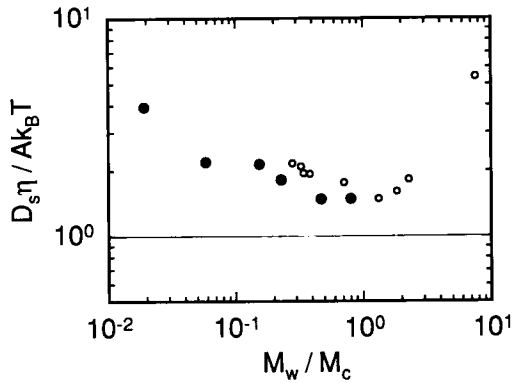

Fig. 7. Test of the Rouse model for pure PDMS by plots of $D_s\eta/Ak_BT$ versus M_w/M_c: ●, PDMS; ○, polyethylene.[52].

decreases with increasing M_w, which at first appears to be inconsistent with the entanglement effects because it is expected that

$$D\eta \propto M_w^{(1-1.5)}$$

for $M_w > M_c$. However, the present finding is understandable if we recall the experimental observation that the molecular weight at the onset of the entanglement effect on D is smaller than that for η. The experimental value of $D_s\eta/Ak_BT$ is larger than the theoretical value (unity), being about two at intermediate M_w values. Similar behaviour of the $D\eta$–M_w relation has been observed in polyethylene,[52] as illustrated in Fig. 7.

3.3.2. *Tracer diffusion in polymer matrices*

To show the asymptotic behaviour of Zimm-type diffusion (10), $D\eta_pM_N^{1/2}/Ck_BT$ is logarithmically plotted against M_p for various M_N in Fig. 8 on a log–log scale. The constant value of Ck_BT was calculated to be 1.24×10^{-6} g cm s^{-2} by putting $a^2/M_0 = 4.36 \times 10^{-3}$ nm^2 as before. The theoretical prediction from (13) and (14) is depicted schematically in the inset. At lower M_p values the data points tend to merge to a certain constant

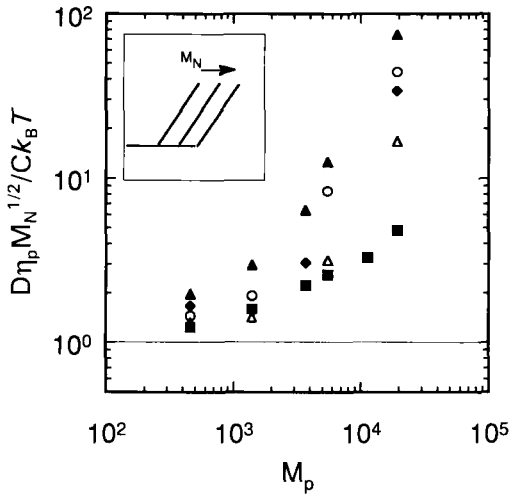

Fig. 8. Plots of $D\eta_pM_N^{1/2}$ versus M_p for testing Zimm-type diffusion at the limit of longer chains in shorter-chain matrices. Tracer polymers are PDMS5 (▲), PDMS14 (○), PDMS37 (◆), PDMS55 (△) and PDMS193 (■). The inset shows the theoretical prediction from (13) and (14) schematically.

value irrespective of M_N, while at higher M_p the value of $D\eta_p M_N^{1/2}$ increases with increasing M_p, departing from the constant value at smaller values of M_p for lower M_N. This is in agreement with the predicted crossover behaviour from Zimm-type to Rouse-type diffusion. The experimental values change slightly with M_p even at lower M_p, but seem to merge and reach the theoretical value of unity. It is well known that the theoretical value in the Kirkwood–Reiseman approach is about 15% lower than the experimental value for polymer chains in low-molecular-weight Θ solvents.[53] However, the difference is too small to be detected in this study.

To examine the asymptotic behaviour on approaching Rouse-type diffusion (8), we have to confront the problem of ζ_p evaluation, and here we adopt the approximation $\zeta_p \propto D_5^{-1}(M_p)$ because the diffusion at the lowest M_w may be of Rouse type, (8), where $D_5(M_p)$ is the diffusion coefficient of PDMS5 in a PDMS matrix of M_p. Log–log plots of $DM_N/D_5(M_p)M_5$ versus M_p are shown in Fig. 9, where M_5 is the molecular weight of PDMS5, and the inset shows the theoretical prediction from (13) and (14). One can see the Rouse region, where DM_N/D_5M_5 is constant, at lower M_N and higher M_p, with increased DM_N/D_5M_5 at lower M_p and higher M_N, in accordance with the theoretical prediction. Obvious discrepancies were found for the tracers of PDMS113 and PDMS193 in the highest-molecular-weight PDMS193, which may be ascribed to entanglement effects, as in the pure melts (data for these have been omitted from Fig. 9).

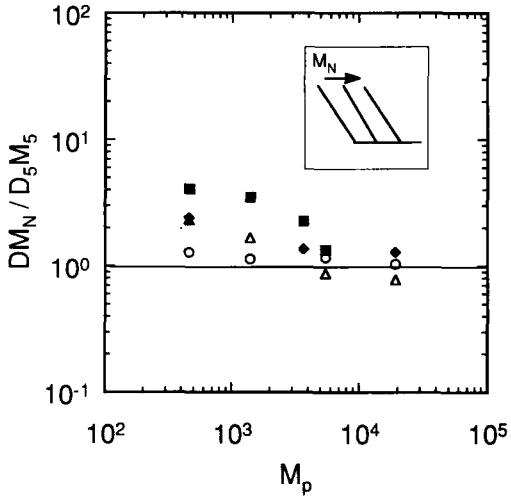

Fig. 9. Plot of DM_N/D_5M_5 versus M_p for testing Rouse-type diffusion at the limit of shorter chains in longer-chain matrices. Symbols are the same as in Fig. 8. The inset shows the theoretical prediction from (13) and (14) schematically.

3.3.3. Crossover behaviour from Zimm- to Rouse-type diffusion

A simple expression for the scaled function f_D of (13) is given by the sum of the two asymptotic equations (14a,b) in the form of the semiempirical equation

$$f_D = \frac{C}{A}\frac{M_N^{1/2}}{M_p} + 1. \tag{15}$$

This is equivalent to the equation

$$D = D_Z + D_R. \tag{16}$$

If we leave η_p as it is without using (9) then (16) can be written as

$$D = \frac{Ck_BT}{\eta_p M_N^{1/2}} + \frac{k_BT}{(\zeta_p/M_0)M_N}. \tag{17}$$

In order to test the scaled relation, the value of ζ as a function of M_p is again needed. Strictly speaking, the assumption that $\zeta_p \propto D_5^{-1}(M_p)$, which was used in Section 3.3.2, is not consistent with the fact that the diffusion of PDMS5 is not always of Rouse type and, for instance, pure PDMS5 ($M_p = M_5$) shows a breakdown of the Rouse model, as seen in Fig. 7. To avoid this inconsistency, the monomer friction coefficient was evaluated from $D_5(M_p)$ using (17) instead of using (8):

$$\zeta_p = \frac{k_BT}{D_5'(M_p)M_5/M_0},$$

with

$$D_5'(M_p) = D_5(M_p) - \frac{Ck_BT}{\eta_p(M_p)M_5^{1/2}}.$$

The scaling plots for (13) can now be made using the values of ζ_p obtained above.

Figure 10 shows a plot of $\log[D(\zeta_p/M_0)M_N/k_BT]$ versus $\log(M_p/M_N^{1/2})$, along with the curves calculated from (13) and (15), where the experimental value $D_s\eta = Ak_BT = 4.6 \times 10^{-8}\,\mathrm{g\,cm\,s^{-1}}$ has been used. The result indicates the applicability of the scaling expression (13) and of the approximation (15) for f_D. Most of the data points are located in the crossover region from Zimm- to Rouse-type diffusion, where the chain diffusion is not of pure Rouse-type but hydrodynamic interaction should be taken into account.

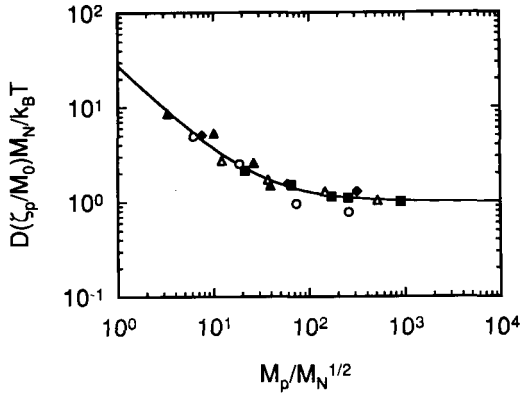

Fig. 10. Log–log plots of $D\zeta_p M_N$ versus $M_p/M_N^{1/2}$: symbols indicate tracer polymers (see Fig. 8); —, (9) and (11).

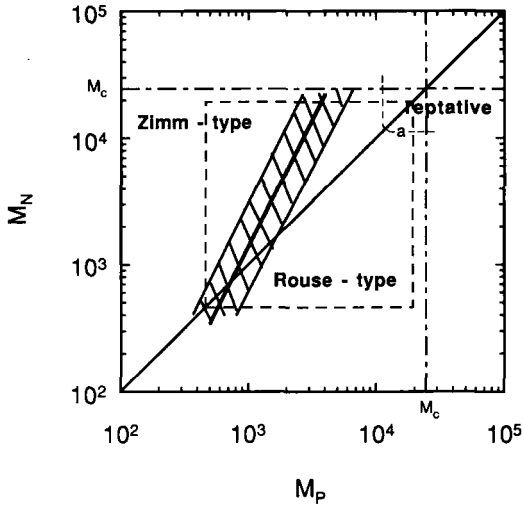

Fig. 11. Boundary separating hydrodynamic and non-hydrodynamic regions for PDMS. ⬚, *region covered by the present experiments;* ▨, *boundary where deviations from asymptotic* behaviour are from about 50% to 100%. M_c was evaluated from the relation between η and M.[48] "a" indicates the region where the entanglement effect appears.

The value of $M_p M_N^{-1/2}$ at the centre of the crossover region was evaluated as the intersection of the asymptotic straight lines, that is, $M_p M_N^{-1/2} \approx 27$. This gives the boundary separating the hydrodynamic and non-hydrodynamic diffusion regions for PDMS, which is shown in Fig. 11. In pure melts the pure-Rouse region is very narrow, and the onset of entanglement effects

shows up immediately after the appearance of the Rouse region as the molecular weight is increased.

4. TRACER DIFFUSION OF SHORT CHAINS IN THE BLOCK COPOLYMER MESOPHASE

Recently, much attention has been paid to tracer diffusion of polymer chains in heterogeneous matrices. Chain diffusion in porous media has been investigated by means of dynamic light scattering[3–6] and forced Rayleigh scattering,[7] and discussed on the basis of various theoretical treatments.[8–11] The permeability of polymer chains through porous membranes has also been studied experimentally and theoretically in terms of inhomogeneity of the channel size in the membrane.[12–15] In such heterogeneous matrices the partition (spatial distribution) of the chain in the matrices can play an important role (as can hydrodynamics and confined chain motion in a limited space) in the macroscopic tracer diffusion and the permeability of the chain through the matrices.

Another interesting example of diffusion in heterogeneous matrices is the diffusion of chains dissolved in the microphase of a block copolymer. This is interesting and important both practically and theoretically. Very recently, Balsara *et al.*[16] measured the diffusion coefficient of tracer chains in microstructured block copolymer solutions by forced Rayleigh scattering, and found slowing-down of the diffusion in the microstructure compared with that in homogeneous solution. A theoretical treatment of chain diffusion in microstructured block copolymers has been proposed by Fredrickson and Milner.[17] In this case the spatial distribution may be an important factor in determining the diffusion coefficient.

In the study reported here the tracer-diffusion coefficient of linear homopolymer chains dissolved in the microphase domains of block copolymers were measured by the PFG-NMR method. The tracer chains were confined in the fringe of matrix chains attached to the other layer at their ends. Two types of block copolymers were chosen: a diblock copolymer, and a triblock copolymer having many grafted branches on the middle block. The tracer chain dissolved in the microphase had the same monomer structure as one of the blocks for the diblock copolymer, and as the grafted chains for the triblock copolymer. Here particular attention is focused on the dependence on the molecular weight of the tracer chain, because the characteristic behaviour, being unique to the system, must reflect on the molecular-weight dependence of the tracer diffusion. In fact, we shall report a particular molecular-weight dependence of tracer diffusion in the microstructured block copolymer. We shall also demonstrate that PFG-NMR can be a powerful technique for measuring the tracer-diffusion coefficient in complex systems with no artificial labelling.

4.1. Description of the systems and PFG-NMR experiments

System 1 was a blend of the diblock copolymer and the homopolymer in the presence of benzene-d^6 (dBZ). The diblock copolymer was a polystyrene–*block*-poly(dimethylsiloxane) (PS–b–PDMS). The molecular weights M_n of the polystyrene (PS) and poly(dimethylsiloxane) (PDMS) blocks were 8100 and 6900 respectively, and the polydispersity index M_w/M_n of the diblock copolymer was 1.39. The molecular weight M_n of the tracer polymer PDMS ranged from 460 to 6500, and the polydispersity indices M_w/M_n were less than 1.1. Two sets (1B and 1S) of samples were prepared. The samples of 1B were blended ones, with various molecular weights of PDMS tracers and with the ratio [PDMS]/[PS–b-PDMS] fixed at 10/90 in wt%, and the content of dBZ in a total blended sample was fixed at about 20 wt%. The addition of the solvent dBZ was to increase the miscibility and mobility of the blended polymers. The other set, 1S, comprised references, which were PDMS with various molecular weights in the presence of dBZ of about 20 wt%, i.e. the same content as in the blended samples.

System 2 was a blend of the grafted triblock copolymer and the homopolymer. The triblock copolymer was a polystyrene–*block*-poly[hydroxystyrene–*graft*-poly(ethylene glycol)]–*block*-polystyrene [(PS–b-P(S–g-PEG)–PS]. The molecular weights M_w of the two PS blocks were respectively 47 000 and 50 000, that of the PS backbone in the P(S–g-PEG) blocks was 31 000, and the M_w and the number of the grafted poly(ethylene glycol) (PEG) were 290 and 130 respectively. The molecular-weight distribution of the sample was reasonably narrow.[54] The nominal molecular weight of linear PEG for the tracer ranged from 200 to 8500. The molecular-weight distribution was considered to be narrow, M_w/M_n being around 1.1–1.2. Ethylene glycol (M_w = 62) was used as the lowest-molecular-weight tracer. Set 2S was for reference, consisting of pure PEG with different molecular weights. In the blended samples (Set 2B), [PEG]/[block copolymer] was fixed at 30/70 in wt%.

To prepare the NMR samples of System 1, the polymer sample with a desired composition was dissolved in dBZ in an NMR tube, and the solvent was then removed by evaporation. The sample tube was subsequently flame-sealed under mild vacuum to avoid further evaporation of solvent. For Set 2B a polymer sample of desired composition was dissolved homogeneously in benzene in an NMR tube, and the solvent was completely removed by evaporation.

The formation of the mesophase was confirmed by small angle X-ray scattering (SAXS) and electron micrography. From the block composition and tracer concentration, the structure was most likely lamellar in these two blended systems.[54] No detectable orientation of the structure to the sample tube was observed by SAXS, and this was confirmed by measuring the tracer diffusion coefficient with the magnetic field gradient applied in

different directions to the sample piece, i.e. no dependence of the diffusion coefficient on direction was observed.

The field gradient g ranged from 60 to 600 G cm^{-1} in the present PFG-NMR experiments. The attenuation of the echo signal was analysed by a second-order cumulant expansion. In the cases of PDMS in the presence of dBZ (Set 1S), PEG in the copolymer (Set 2B), and pure PEG (Set 2S) the polydispersity index $\mu_2/\bar{D}^2$ was so small that the single-exponential fitting ($\mu_2 = 0$) was applied. The signal from the grafted PEG in the blend of PEG/graft-block-copolymer was negligible compared with that of the tracer PEG because of slow molecular motions. In the case of PDMS in the PS–b-PDMS/dBZ, the attenuation A/A^* did not follow a single-exponential decay, but required a μ_2 term, probably owing to the presence of the signal from PDMS in the block of PS–b-PDMS. The signal intensity from the block copolymer was very low compared with that of the tracer polymer PDMS, which was confirmed by observing a very short spin–spin relaxation time of the protons in the methyl group of the block copolymer. The tracer-diffusion coefficients of PDMS of the block copolymer were extremely small compared with those of the tracer polymer PDMS. Considering these facts and recalling that the $\bar{D}$ evaluated by the cumulant method was more heavily weighted by the faster diffusant, $\bar{D}$ obtained from (6) was regarded as the diffusion coefficient of the tracer PDMS.

The displacement $\langle z^2 \rangle^{1/2}$ of the tracer in the block copolymer matrix during the diffusion measurement was of the order of 10 μm, estimated from the relation $\langle z^2 \rangle = 2Dt$. $\langle z^2 \rangle^{1/2}$ was much larger than the interdomain distance of the microstructure, which was 30–45 nm, and probably even much larger than the microstructure domain size where a regular structure is maintained. If the microstructure domain size had been larger than $\langle z^2 \rangle^{1/2}$, the attenuation of echo signal would have shown non-single-exponential decay, because the orientational distribution of the microstructure must directly reflect the distribution of the diffusion coefficient. However, there was no distribution of the diffusion coefficient—at least in the case of the PEG blends. This is consistent with the fact that the morphological structure was isotropic, i.e. the diffusion coefficient was isotropic as mentioned before. In the sense that $\langle z^2 \rangle^{1/2}$ is much greater than both the interdomain distance and the microstructure domain size, the diffusion coefficient obtained here was the macroscopic one.

4.2. Diffusion of the homopolymer PDMS dissolved in the PDMS microphase domain of the block copolymer PS–b-PDMS

Figure 12 shows the tracer-diffusion coefficients D of the PDMS tracers in the microstructured block copolymer (Set 2B) as 30°C as a function of the molecular weight of the tracers PDMS, along with those of the pure PDMS,

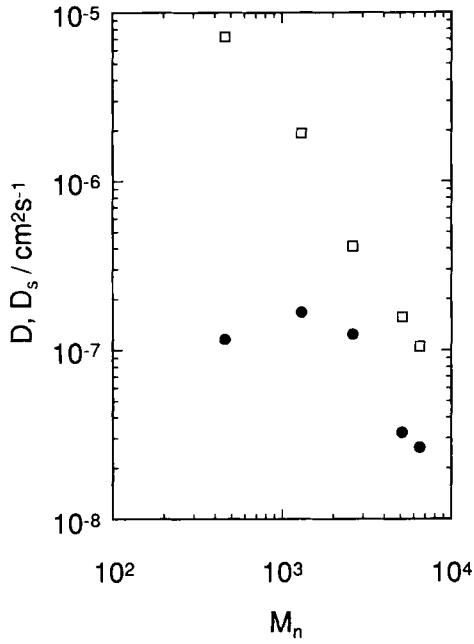

Fig. 12. Dependence of the tracer-diffusion coefficients of PDMS on the molecular weight M_n of the tracer in the microphase domain and in free space at 30°C: ●, in the microdomain (Set 1B); □, in the melt in the presence of 20 wt% dBZ (Set 1S).

D_s, in the presence of dBZ (Set 2S). With increasing molecular weight, the tracer-diffusion coefficient first slightly increase, and then decreases in parallel to D_s, while D_s decreases monotonically with increasing molecular weight.

To illustrate the effects of confinement, the ratios D/D_s are shown in Fig. 13. In the higher-molecular-weight range (M_n>2600), which is here referred to as Regime II, the ratio D/D_s was almost constant, being about 0.15. In contrast, in the lower-molecular-weight range (M_n<2600), referred to as Regime I, D/D_s decreased sharply with decreasing molecular weight, going down to 1/100.

This characteristic molecular-weight dependence can be explained by the molecular-weight dependence of the spatial distribution of the tracer chains in the microdomain of the block copolymer. Figure 14 illustrates the spatial distribution of blended homopolymers in the microphase domain proposed by Hashimoto *et al.*[55] In Regime I, where the M_n of the homo-PDMS is smaller than the M_w (6900) of the PDMS block of the copolymer, the homopolymer may be gradually squeezed out of the brushes of PDMS chains of the block copolymers as shown in Figs 14(a,b). As a result, the

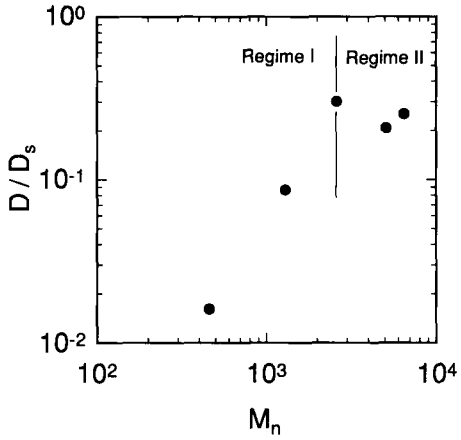

Fig. 13. Dependence of the ratio D/D_s on the molecular weight M_n of the tracer PDMS at 30°C.

diffusion of the tracer chain becomes faster because of the fewer obstacles with increasing molecular weight of the tracer. On the other hand, in Regime II, where the M_n of the tracer is comparable to the M_w of the PDMS brush, the PDMS homopolymer may be localized between the brushes, as illustrated in Fig. 14(c). Therefore the decrease in the mobility of the segmental motion can be expected owing to interposition between the microphase layers, and this restriction of the segmental motion must be independent of molecular weight. This is considered to be responsible for the constancy of D/D_s at a value less than unity.

4.3. Diffusion of the homopolymer PEG dissolved in the PEG microphase domain of the block copolymer PS–b-P(S–g-PEG)–b-PS

The diffusion coefficient of the tracer PEG in the microstructured triblock copolymer and in the pure melt is shown as a function of the molecular weight of the tracer PEG in Fig. 15, while their ratio D/D_s is shown in Fig. 16. These molecular-weight dependences of D and D/D_s were quite similar to those in the PDMS system, System 1. In this case of System 2 one can see Regime III ($M_n \geq 2000$), in addition to Regimes I and II, where the tracer-diffusion coefficients in the blended samples were the same as those in the pure melts. At higher molecular weights the tracer PEG could not be dissolved in the microphase domain, and separated macroscopically from the block copolymer. This leads to the appearance of Regime III. At the crossover from Regime II to Regime III, D changed rather abruptly. The value of D/D_s in Regime II was about 0.12, which was almost the same as

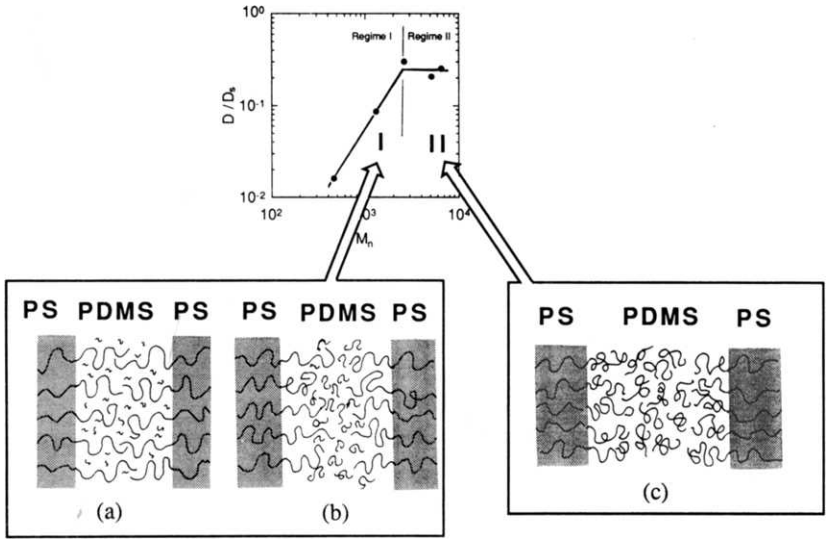

Fig. 14. Schematic representations of the spatial distributions of homopolymer chains (PDMS) in a microdomain formed by PS–b-PDMS.

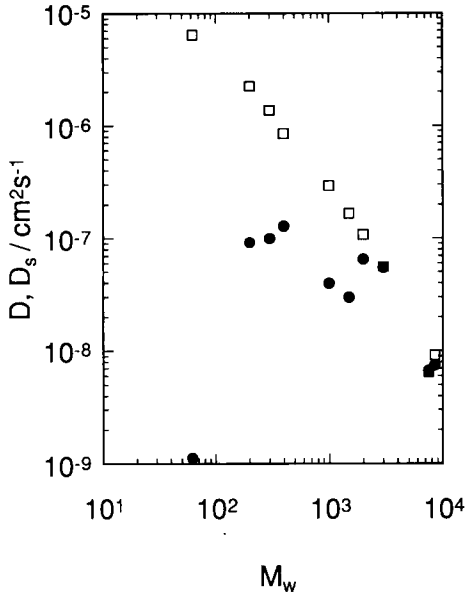

Fig. 15. Dependence of the tracer-diffusion coefficient of PEG on the molecular weight M_w of the tracer in the microphase domain and in free space at 80°C: ●, in the microdomain (Set 2B); □, in the pure melt (Set 2S).

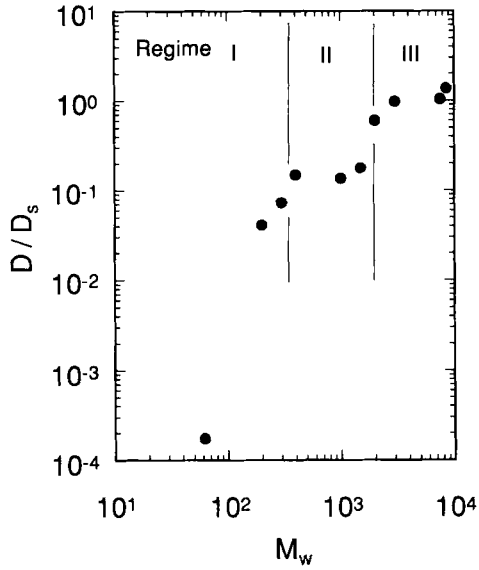

Fig. 16. Dependence of the ratio D/D_s on the molecular weight M_w of the tracer PEG at 80°C.

that in the PDMS system. The molecular weight around which the crossover from Regime I to Regime II occurred was almost identical with the molecular weight of the grafted PEG (290). The tracer-diffusion coefficient of the shortest tracer (ethylene glycol) decreased by four orders of magnitude on solution in the microdomain.

The above-mentioned behaviour of the tracer diffusion can again be interpreted in terms of the spatial distribution of the tracer in the microphase structure. A schematic picture of the spatial distribution of PEG homopolymer in microstructured PS–b-P(S–g-PEG)–b-PS is shown in Fig. 17. In contrast to the case of System 1, the diblock-copolymer/homopolymer, the brush chains of the grafted PFG are attached to the backbone chains across neighbouring PS layers. Consequently, solution of the lower-molecular-weight PEG results in expansion of the backbone chains on which the PEG are grafted, while the higher-molecular-weight PEG should be squeezed out between the backbone chains in the direction parallel to the layer. On the other hand, in the case of the diblock-copolymer/homopolymer the homopolymer of higher molecular weight is squeezed out in the direction perpendicular to the layers. Irrespective of this difference in the spatial distribution of the homopolymers, the spatial distribution of the tracer on the brushes of the microstructured copolymer is essentially the same in both cases. Therefore, the diffusion behaviour is also very similar.

Figure 18 shows the temperature dependence of the diffusion coefficient for a PEG tracer (M_w = 400) in Regime II. The apparent activation energy

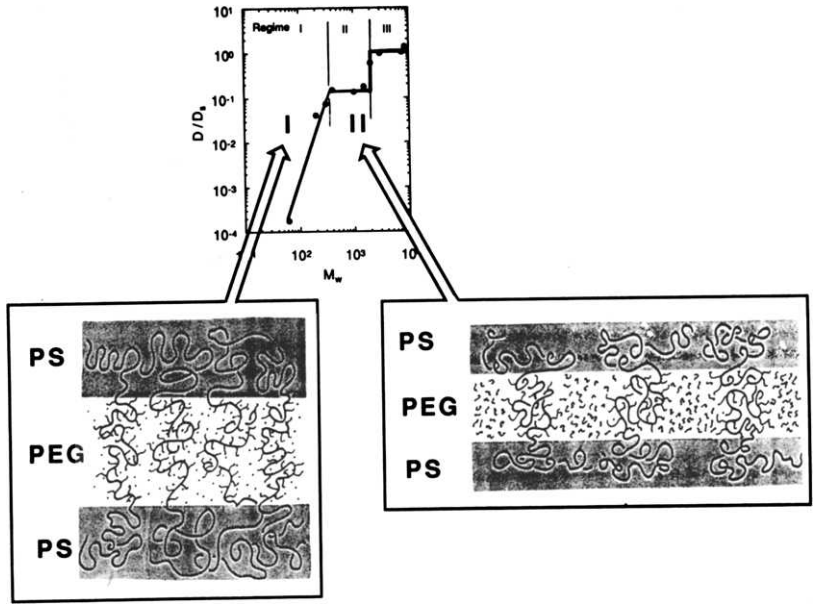

Fig. 17. Schematic representations of the spatial distributions of homopolymer chains (PEG) in a microdomain formed by PS–b-P(S–g-PEG)–b-PS.

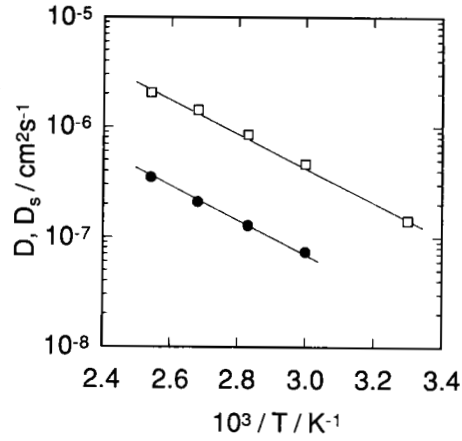

Fig. 18. Semilogarithmic plots of D (or D_s) against $1/T$ for PEG (M_w = 400 g mol^{-1}) in PS–b-P(S–g-PEG)–b-PS/PEG (●) and in pure melts (□).

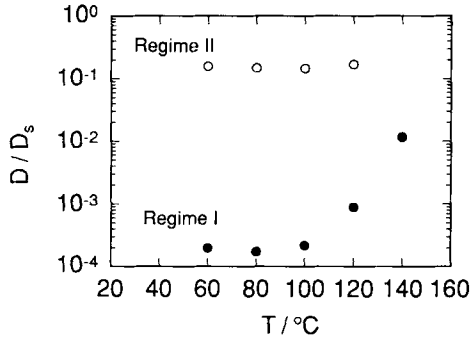

Fig. 19. Temperature dependence of D/D_s for PEG tracers in PS–b-P(S–g-PEG)–b-PS/PEG: •, M_w = 62 (Regime I); ○, M_w = 400 (Regime II).

for the diffusion is 28.2 kJ mol^{-1} in the microstructured matrix and 29.7 kJ mol^{-1} in the pure melt. No large difference between D and D_s was found in the temperature dependence. In Regime II the effect of the matrix on the diffusion of the homopolymer is indirect because of the localization of spatial distribution of the tracer, and, as a result, D and D_s have similar temperature dependences. In contrast, the tracer diffusion in the microphase in Regime I has a different temperature dependence from that in the pure melt, as shown in Fig. 19, where the ratios D/D_s for Regimes I and II are plotted against temperature. D/D_s in Regime I starts to increase sharply with increasing temperature around 100°C, while D/D_s in Regime II remains constant. Recalling that the glass transition temperature of PS is about 100°C, the tracer diffusion in Regime I is more directly affected by molecular motions of the matrix. This is expected from the spatial distribution of the tracer illustrated in Fig. 17: above this temperature, the PS backbones with the grafted PEG chains acquire a higher mobility of molecular motions owing to softening of the PS layers, and this leads directly to an increase in the diffusion coefficient of the tracer PEG.

It should be noted here that the change in D with temperature shown in Fig. 19 was reversible on increasing and decreasing temperature, so that no irreversible change in the microphase structure and no phase separation could be supposed in Regimes I and II.

4.4. Change of segmental motions of the tracer dissolved in the microdomain as measured by the spin–spin relaxation time

In the case of PEG, since the protons are directly attached to the backbone chain, the proton spin–spin relaxation time T_2 should directly reflect the segmental motions of the polymer chain. So, in order to see the change of

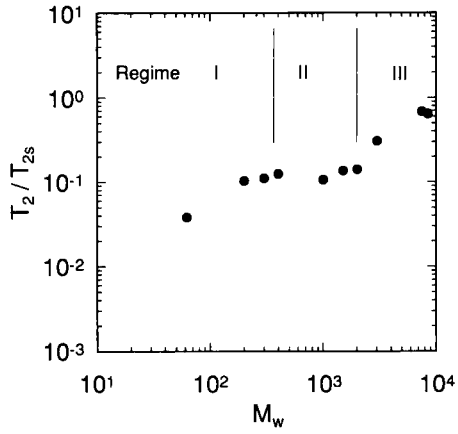

Fig. 20. Ratio of spin–spin relaxation times T_2/T_{2s} versus molecular weight M_w of the tracer for PS–b-P(S–g-PEG)–b-PS/PEG at 80°C.

the segmental motions with confinement, the proton relaxation time T_2 for the PEG of System 2 was measured using the Carr–Purcell–Meiboom–Gill method.[56] Attenuation of the echo signal M_y for pure PEG could be fitted to the single-exponential decay function $M_y/M_{y0} = \exp(-t/T_2)$ to determine the value of T_2, where M_{y0} is the signal intensity after the 90° pulse. To evaluate the value of T_2 for the blended system (Set S2B), the attenuation was fitted to the following bimodal decay function by non-linear least squares fitting:

$$\frac{M_y}{M_{y0}} = f\exp\left(\frac{-t}{T_{2a}}\right) + (1-f)\exp\left(\frac{-t}{T_{2b}}\right),$$

where f is the proton fraction of component a, and T_{2a} and T_{2b} are the values of T_2 for components a and b respectively. T_{2a} of the faster component a ($T_{2a} > T_{2b}$) is the T_2 of the tracer PEG. T_{2b} is that for the grafted PEG of the block copolymer. No signal from the PS part could be detected, since the PS was in the solid state.

To represent the change in the segmental motion of the tracer on solution in the microdomain, the ratio T_2/T_{2s} is plotted against the molecular weight of the tracer in Fig. 20. Here T_2 and T_{2s} are the relaxation times of proton nuclei of the tracer PEG in the microstructured block copolymer and in the pure melt respectively. Corresponding to Fig. 16, one can see the three regimes. In Regime I the ratio T_2/T_{2s} increases with increasing molecular weight of the tracer, but the increase is very small compared with that of D/D_s. This implies that in Regime I it is not the change of segmental

mobility but rather the disturbance of the translational diffusion caused by the grafted chains that is responsible for the slowing-down of tracer diffusion in the microstructured matrix. In contrast with Regime I, T_2/T_{2s} in Regime II is constant at 0.12, exhibiting the same behaviour as D/D_s i.e. $T_2/T_{2s} = D/D_s$. Therefore the reduction of the diffusion coefficient in the microdomain comes totally from depression of segmental mobility. This also allows us to suppose that the slowing down arising from the tortuosity of the microphase structure is negligible. In Regime III, where the homopolymer and the copolymer are immiscible, T_2/T_{2s} approaches unity as expected, similarly to D/D_s.

The behaviour of T_2 is consistent with our explanation of the diffusion behaviour described in the previous sections.

As seen above, the unique molecular-weight dependence observed in the tracer diffusion of the chain molecules dissolved in the block copolymer is considered to be commonly observed in any microstructured block-copolymer/tracer-homopolymer systems. In the lower-M_w regime (Regime I), the ratio D/D_s increased remarkably with increasing M_w, whereas in the higher-M_w regime (Regime II), the ratio was independent of M_w, being about 0.15. This behaviour can be explained as follows. In Regime I the tracers penetrate deeply into the brushes of the PDMS or grafted PEG of the copolymers, where the depth of penetration may depend upon M_w. On the other hand, in Regime II the tracer chains do not penetrate well into the PDMS or the PEG brushes, but rather are interposed between these layers. The spatial distribution of the tracer is the dominant factor controlling tracer diffusion in the heterogeneous matrix.

5. TRACER DIFFUSION AND CONCENTRATION FLUCTUATIONS NEAR THE CRITICAL POINT OF A POLYMER/POLYMER/GOOD-SOLVENT SYSTEM

As a fluid mixture approaches its critical point, the wavelength and decay time of concentration fluctuations become infinite, and the mutual-diffusion coefficient D_m vanishes at the critical point. In contrast, the tracer-diffusion coefficient D of constituting molecules remains finite, being independent of the critical fluctuations, since Brownian motion is not affected by concentration fluctuations.[57–59] In the case of polymeric systems the critical dynamics are not necessarily similar to those of ordinary fluid mixtures. The nature of the chain molecules and entanglement effects may play important roles in the relation between tracer and the mutual diffusion. In the static critical properties a crossover from Ising to mean-field behaviour has been observed.[60,61] In the critical dynamics of some polymeric systems it has been pointed out theoretically that hydrodynamic interactions, i.e. the mode–mode coupling, may become less important.[62] To our knowledge, the

tracer-diffusion coefficient near the critical point has not been studied extensively to verify its independence of critical fluctuations—partly because of experimental difficulties. PFG-NMR may be a suitable experimental technique for this purpose. Temperature control must be the most difficult part of the experiment in ordinary fluid mixtures, where the temperature must usually be controlled to within to a few millikelvin because the critical anomalies appear in a very narrow temperature region. However, in the case of polymeric systems the critical region is relatively wide, sometimes over more than 10 K, so that temperature control is no longer a serious problem in the NMR measurements. In this respect polymeric systems are attractive for studying tracer diffusion in the critical region.

In this section, in order to elucidate the effects of concentration fluctuations on tracer diffusion, we study the critical dynamics of a polystyrene (PS)/poly(methylmethacrylate) (PMMA) blend in benzene-d^6 (dBZ) solution, observed by a combination of dynamic light scattering (DLS) and PFG-NMR. The DLS gives the decay rate of concentration fluctuations. First, we shall show that this ternary polymer solution exhibits Ising-type critical phenomena, and that the hydrodynamic interactions dominate the critical dynamics of concentration fluctuations. Then the results on the tracer-diffusion coefficient near the critical point will be presented in terms of mobility, and compared with those on the mutual-diffusion coefficient representing the decay rate of concentration fluctuations.

The molecular weight M_w and the polydispersity index of PS were 3.55×10^5 and 1.02 respectively, and those of PMMA were 3.27×10^5 and <1.10, so that the system was approximately symmetrical in molecular weight. The total polymer concentration was fixed at 8.2 vol%, which corresponded to a degree of overlap $C/C^* = 12.9$. The sample codes PSXX/PMMAYY indicate the volume % of PS(XX) and PMMA(YY) in the total polymer in the solution. The system has a lower critical solution temperature around room temperature, with the phase diagram shown in Fig. 21. The critical concentration is located at around 40–50 vol% of PS.

5.1. Critical exponents of static properties: osmotic compressibility and correlation length

Static critical behaviour is usually characterized by critical exponents, which are unique to the universality class of the system. In fluid mixtures the osmotic susceptibility χ and the correlation length ξ diverge on approaching the critical point, with critical exponents γ and ν as follows:[63]

$$\chi \propto \varepsilon^{-\gamma}, \quad \xi \propto \varepsilon^{-\nu}, \tag{18}$$

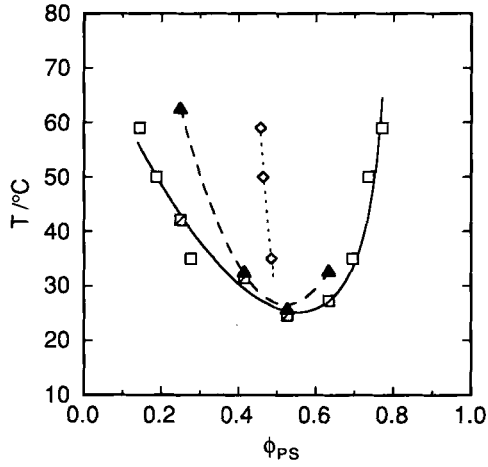

Fig. 21. Phase diagram of a PS/PMMA/dBZ solution at a fixed total polymer concentration of 8.2 vol%: ϕ_{ps}, the volume fraction of PS in the total polymer; □, binodal points; ⊠, cloud points; ▲, spinodal points; ◇, diameter ($=\frac{1}{2}(\phi' + \phi'')$) ($\phi'$, ϕ'': the ϕ_{ps} values of the coexisting phases).

where ε is the temperature difference from the critical temperature T_c, defined as $\varepsilon = |T - T_c|/T_c$. Ordinary fluid mixtures exhibit Ising-type critical phenomena, where the large concentration fluctuations result in breakdown of the mean-field theory. For the Ising-type phenomena $\gamma = 1.26$ and $\nu = 0.63$, whereas mean-field theory predicts that $\gamma = 1$ and $\nu = 0.5$. In polymer blends mean-field theory is applicable up to very near the critical point, and the crossover from mean-field to Ising-type behaviour has been observed,[60,61] as originally suggested by de Gennes[64] on the basis of the Ginzburg criterion. de Gennes also suggested that the polymer/solvent system and the polymer/polymer/good-solvent system should show Ising-type critical behaviour. In reality, experiments show that the polymer/solvent system is of Ising type.[65,66] For a polymer blend in the presence of solvent, i.e. a polymer/polymer/good-solvent system, the effects of composition fluctuations between the solvent and the polymer are manifested by whether or not the critical exponent is renormalized.[67,68] The possible crossovers of critical behaviour for the ternary system are illustrated in Fig. 22, along with predicted critical exponents. Recently, Broseta, Liebler and Joanny[68] examined this point theoretically, together with the crossover from Ising to mean-field behaviour, and concluded that the non-renormalized Ising regime will be realized in a real ternary solution of polymer/polymer/good-solvent. No experimental observation has been reported as yet, to our knowledge. We try to confirm the theoretical prediction using the PS/PMMA/dBZ solution. The angular dependence of the integrated intensity $I(q)$ of scattered light from the solution was analysed using the Ornstein–

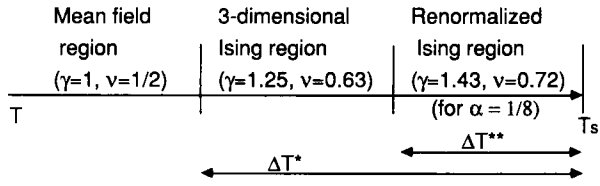

Fig. 22. Critical behaviour in the temperature region near the critical (or spinodal) temperature T_s of a polymer/polymer/solvent system. α is the critical exponent for heat capacity.

Zernike-type equation $I(q) \propto \chi/(1 + \xi^2 q^2)$ to evaluate the osmotic susceptibility and the correlation length ξ, with q being the wavenumber of the scattering vector.

Figures 23 and 24 are log–log plots of χ and ξ versus ε for solutions near the critical concentration, with ε defined as $\varepsilon = |1/T - 1/T_s|$ (T_s is the spinodal temperature). In polymeric systems, the temperature difference ε is usually defined as $\varepsilon = |1/T - 1/T_c|$ instead of $\varepsilon = |T - T_c|/T_c$ since the temperature dependence of the interaction parameter is described as $A/T + B$. Here we have followed this definition, using the spinodal temperature T_s instead of T_c because the concentration of the sample could not exactly be identified with the critical concentration. The slopes of these plots give the critical exponents as 1.23 for γ and 0.63 for ν, which are in good agreement with those of the Ising region. Consequently, the critical behaviour of the present ternary polymer solution can be classified in the universality class of the non-renormalized three-dimensional Ising type, in accordance with the theoretical prediction.

5.2. Dynamical behaviour

5.2.1. The decay rate of concentration fluctuations

In fluid mixtures the decay of concentration fluctuations near the critical point is not a simple result of mutual diffusion, but rather is due to hydrodynamic flow induced by large concentration fluctuations, i.e. so-called mode–mode coupling between diffusion and convective flow. Ordinary concentration fluctuations far from the critical point decay, with the mutual diffusion being driven by the gradient in the chemical potential, so that the decay rate Γ is described by

$$\Gamma = q^2 D_m = \frac{q^2 m_m}{\chi}, \tag{19}$$

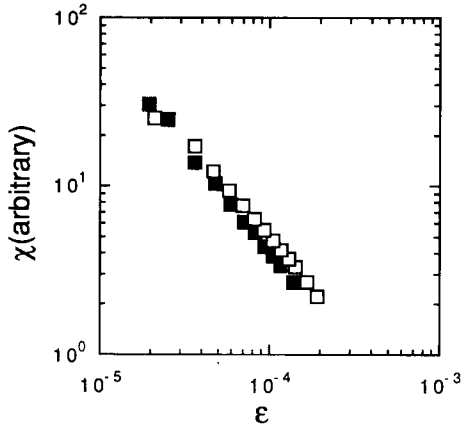

Fig. 23. Log–log plots of the osmotic susceptibility χ versus ε $(=1/T - 1/T_s)$ for PS/PMMA/dBz solutions with a fixed total polymer concentration of 8.2 vol%: ■, PS41/PMMA59; □, PS53/PMMA47.

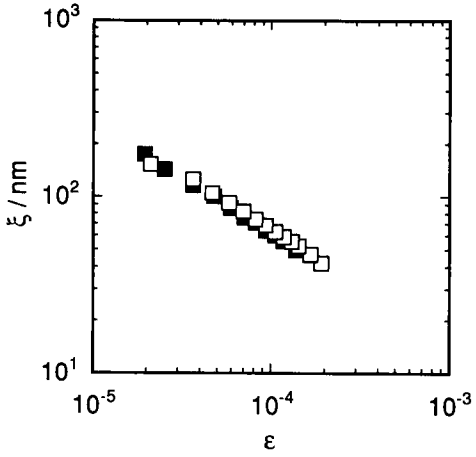

Fig. 24. Log–log plots of the correlation length ξ versus ε $(=1/T - 1/T_s)$ for PS/PMMA/dBz solutions with a fixed total polymer concentration of 8.2 vol%: ■, PS41/PMMA59; □, PS53/PMMA47.

where m_m is the mobility of mutual diffusion. On the other hand, near the critical point the decay rate can be written as the sum of the critical part Γ_c and the background Γ_b:

$$\Gamma = \Gamma_c + \Gamma_b. \tag{20}$$

Γ_b is essentially described by (19), while Γ_c is described by the Kawasaki function $K(q\xi)$ derived from the mode–mode coupling theory for fluid mixtures:[69]

$$\Gamma_c = \frac{kT}{6\pi\eta}\xi^{-3}K(q\xi), \tag{21}$$

with

$$K(x) = \tfrac{3}{4}[1 + x^2 + (x^3 - x^{-1})\tan^{-1}x]. \tag{22}$$

Equations (21) and (22) give the following asymptotic q dependences:

$$\Gamma_c \propto \begin{cases} q^2 & (q\xi < 1), \quad (23) \\ q^3 & (q\xi > 1), \quad (24) \end{cases}$$

depending upon the relation between the experimental length scale q^{-1} and the wavelength ξ of the fluctuation. Recently, Fredrickson[62] suggested theoretically that in highly entangled systems there exists a non-mode-coupled region where the concentration fluctuations decay primarily with the pure diffusion described by the classical diffusion equation (19).

The present polymer blend solution exhibits a typical mode-coupled critical dynamics, illustrated by the Kawasaki plot in Fig. 25. Here the decay rate Γ was obtained from DLS measurements using the self-beat method. The effect of Γ_b on the plot was so small that the critical Γ_c was approximated by the total Γ. It can be seen that the decay rates of different

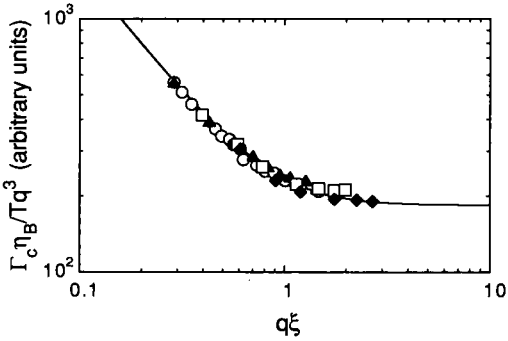

Fig. 25. Log–log plots of $\Gamma_c\eta_B/T_q{}^3$ versus $q\xi$ for the critical solution PS53/PMMA47/dBZ (η_B is the viscosity of benzene): ○, at scattering angle 20° for different T; ▲, □, ◆, at 10°C, 16°C, 21°C respectively for different q. The Kawasaki function (22) was shifted along the vertical axis in order to fit to the experiments.

ε and q are well described by the scaling form of (21) with (22). Therefore hydrodynamic flow coupled with concentration fluctuations is the dominant relaxation process of concentration fluctuations in this system. As the result, the apparent mobility of the mutual diffusion, defined by $m_m = D_m\chi = \Gamma\chi/q^2$ (19), showed a divergence near the critical point, as shown in Fig. 26.

5.2.2. *Tracer diffusion under large concentration fluctuations*

The proton NMR spectra of PS and PMMA have peaks at different positions, so that the tracer-diffusion coefficients of PS and PMMA in the blend solution can be evaluated separately by PFG-NMR. An example of the attenuation of the echo signal for PS and PMMA in a blend solution is shown in Fig. 27. The PS signal was from the benzene ring, while that of PMMA was from the methyl group of the ester. The attenuation of each signal obeyed a single-exponential decay with a respective decay rate, providing the tracer-diffusion coefficient of each component.

Figure 26 shows the temperature dependence of the mobility m of the tracer diffusion of PS and PMMA in the blend solution PS45/PMMA55/dBZ near the spinodal temperature. Here the mobility m_t was defined by $m_t = k_B T/D_t$, with D_t being the tracer-diffusion coefficient. While the apparent mobility m_m of the mutual diffusion diverges near the spinodal point, the mobility m_t shows no anomalous behaviour near the spinodal temperature. Therefore tracer diffusion, directly reflecting Brownian motion, is basically independent of concentration fluctuations, even in the critical region where hydrodynamic flow occurs. This has already been

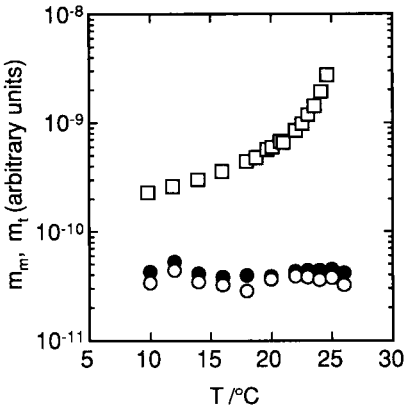

Fig. 26. Temperature dependence of the mobility m_m of mutual diffusion for PS53/PMMA47/dBZ (□) and the mobility m_t of tracer diffusion for PS (○) and PMMA (●) in PS45/PMMA55/dBZ near the spinodal temperature.

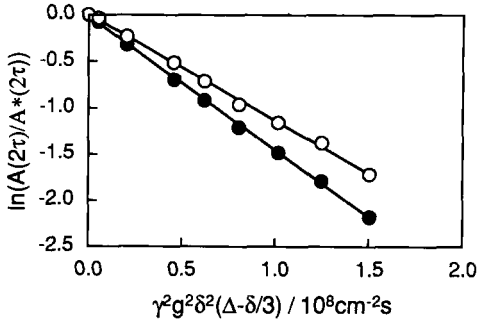

Fig. 27. Attenuation of echo signals for PS (○) and PMMA (●) in their blend solution.

observed in simple fluid mixtures.[57–59] Here we see that it is also the case in the polymer blend solution.

It is noteworthy that the length scale of the diffusion measurement is much greater than the correlation length of the concentration fluctuations in the present study. The diffusion of tracer within the length scale of the correlation might be affected by concentration fluctuations. This situation can be realized at temperatures closer to the critical point, which may be achieved more easily in polymeric systems than in simple fluid mixtures.

REFERENCES

1. T. P. Lodge, N. A. Rotstein and S. Prager, *Adv. Chem. Phys.*, 1990, **89**, 1.
2. M. Doi and S. F. Edwards, *The Theory of Polymer Dynamics*. Clarendon Press, Oxford, 1986.
3. T. Kubo and T. Nose, *Polym J.*, 1992, **24**, 1350.
4. N. Numasawa, K. Kuwamoto and T. Nose, *Macromolecules*, 1986, **19**, 2593.
5. M. T. Bishop, K. H. Langley and F. E. Karasz, *Phys. Rev. Lett.*, 1986, **57**, 1741; see also *Macromolecules*, 1989, **22**, 1220.
6. Y. Guo, K. H. Langley and F. E. Karasz, *Macromolecules*, 1990, **23**, 2022.
7. N. Easwar, K. H. Langley and F. E. Karasz, *Macromolecules*, 1990, **23**, 738.
8. W. D. Dozier, J. M. Drake and J. Klafter, *Phys. Rev. Lett.*, 1986, **56**, 197.
9. F. Brochard, *J. Phys. (Paris)*, 1977, **38**, 1285.
10. F. Brochard and P. G. de Gennes, *J. Chem. Phys.*, 1977, **67**, 52.
11. M. G. Davidson and W. M. Deen, *J. Membrane Sci.*, 1988, **35**, 167.
12. M. Muthukumar and A. Baumgartner, *Macromolecules*, 1989, **22**, 1937, 1941.
13. G. Guillot, L. Leger and F. Rondlez, *Macromolecules*, 1985, **18**, 2531.
14. G. Guillot, *Macromolecules*, 1987, **20**, 2600, 2606.
15. N. P. Balsara, C. E. Eastman, M. D. Foster, T. P. Lodge and M. Tirrell, *Makromol. Chem. Macromol. Symp.*, 1991, **45**, 213.
16. G. H. Fredrickson and S. T. Milner, *Mater. Res. Soc. Symp. Proc.*, 1990, **177**, 169.
17. J. Kärger, H. Pfeifer and W. Heink, *Adv. Magn. Reson.*, 1988, **12**, 1.

18. J. Baba, T. Kubo, A. Takano and T. Nose, *Rep. Prog. Polym. Phys. Jpn*, 1991, **34**, 153.
19. E. L. Hahn, *Phys. Rev.*, 1950, **80**, 580.
20. H. E. Carr and E. M. Purcell, *Phys. Rev.*, 1954, **94**, 630.
21. W. D. McCall, D. C. Douglass and E. W. Anderson, *J. Chem. Phys.*, 1959, **30**, 771.
22. J. E. Tanner, K.-J. Liu and J. E. Anderson, *Macromolecules*, 1971, **4**, 586.
23. E. D. von Meerwall, *Adv. Polym. Sci.*, 1983, **42**, 288; see also *Rubber Chem. Magn. Reson.*, 1985, **12**, 1; *J. Non-Cryst. Solids*, 1991, **131–133**, 735.
24. W. Brown and P. Zhou, *Macromolecules*, 1989, **22**, 4031.
25. W. Brown, C. Konak, R. M. Johnsen and P. Zhou, *Macromolecules*, 1990, **23**, 882.
26. D. N. Pinder, *Macromolecules*, 1990, **23**, 1724.
27. P. J. Daivis, D. Pinder and P. T. Callagham, *Macromolecules*, 1992, **25**, 170.
28. P. Zhou and W. Brown, *Macromolecules*, 1990, **23**, 1131.
29. W. Brown and P. Zhou, *Macromolecules*, 1991, **24**, 5151.
30. W. Yu and E. D. von Meerwall, *Macromolecules*, 1990, **23**, 882.
31. L. S. Weisenberger and J. L. Koenig, *Macromolecules*, 1990, **23**, 2445.
32. I. R. Gafurov, V. D. Skirda, A. I. Maklakov and I. I. Ryskina, *Polym. Sci. USSR*, 1988, **30**, 1639.
33. E. von Meerwall and T. Stone, *J. Polym. Sci. Polym. Phys. Ed.*, 1989, **27**, 503.
34. G. Iannacchione and E. von Meerwall, *J. Polym. Sci. Polym. Phys. Ed.*, 1991, **29**, 659.
35. Y. Xia and P. T. Callagham, *Macromolecules*, 1991, **24**, 4777.
36. E. von Meerwall and M. Kamat, *J. Magn. Reson.*, 1989, **83**, 309.
37. E. von Meerwall, J. Grigsby, D. Tomich and R. van Antwerp, *J. Polym. Sci. Polym. Phys. Ed.*, 1982, **20**, 1037.
38. R. Bachus and R. Kimmich, *Polymer*, 1983, **24**, 964.
39. G. Fleisher, *Polym. Bull.*, 1984, **11**, 75.
40. P. F. Green and E. J. Kramer, *Macromolecules*, 1986, **19**, 1108.
41. N. Nemoto, M. Kishine, T. Inoue and K. Osaki, *Macromolecules*, 1990, **23**, 659.
42. N. Nemoto, T. Kojima, T. Inoue, M. Kishine, T. Hirayama and M. Kurata, *Macromolecules*, 1989, **22**, 3793.
43. P. E. Rouse, *J. Chem. Phys.*, 1953, **21**, 1272.
44. M. Doi and S. F. Edwards, *The Theory of Polymer Dynamics*, p. 91. Clarendon Press, Oxford, 1986.
45. M. Doi and S. F. Edwards, *The Theory of Polymer Dynamics*, p. 225. Clarendon Press, Oxford, 1986.
46. B. H. Zimm, *J. Chem. Phys.*, 1956, **24**, 269.
47. M. Doi and S. F. Edwards, *The Theory of Polymer Dynamics*, p. 97. Clarendon Press, Oxford, 1986.
48. G. C. Berry and T. G. Fox, *Adv. Polym. Sci.*, 1968, **5**, 261.
49. P. J. Flory, L. Mandelkern, J. B. Kinsinger and W. B. Schulz, *J. Am. Chem. Soc.*, 1952, **74**, 3364.
50. G. V. Schulz and A. Haug, *Z. Phys. Chem. (Frankfurt)*, 1962, **34**, 328.
51. H. Shih and P. J. Flory, *Macromolecules*, 1972, **5**, 758.
52. D. S. Pearson, G. Ver Strate, E. von Meerwall and F. C. Schilling, *Macromolecules*, 1987, **20**, 1133.
53. M. Schmidt, W. Burchard, *Macromolecules*, 1981, **14**, 210.
54. Y. Isono, T. Fujimoto and O. Watanabe, *Polym. Prepr. Jpn*, 1989, **38**, 1681.
55. T. Hashimoto, H. Tanaka and H. Hasegawa, *Macromolecules*, 1990, **23**, 4378.
56. S. Meiboom and D. Gill, *Rev. Sci. Instrum.*, 1958, **29**, 688.
57. H. M. Leister, J. C. Allegra and G. F. Allen, *J. Chem. Phys.*, 1969, **51**, 3701.
58. J. E. Anderson and W. H. Gerritz, *J. Chem. Phys.*, 1970, **53**, 2584.
59. J. C. Allegra, A. Stein and G. F. Allen, *J. Chem. Phys.*, 1971, **55**, 1716.
60. F. S. Bates, J. H. Rosedale, P. Stepanek, T. P. Lodge, P. Wiltzius, G. H. Frederickson and R. P. Hjelm, *Phys. Rev. Lett.*, 1990, **65**, 1893.

61. B. Chu, Q. Ying, K. Linliu, P. Xie, T. Gao, Y. Li, T. Nose and M. Okada, *Macromolecules*, 1992, **25**, 7382, and references therein.
62. G. H. Frederickson, *J. Chem. Phys.*, 1986, **85**, 3556.
63. H. E. Stanley, *Introduction to Phase Transitions and Critical Phenomena*, Oxford University Press, 1971.
64. P. G. de Gennes, *J. Phys. (Paris) Lett.*, 1977, **38**, L-411.
65. K. Hamano, N. Kuwahara and M. Kaneko, *Phys. Rev.*, 1980, **A21**, 1312.
66. K. Hamano, T. Nomura, T. Kawazura and N. Kuwahara, *Phys. Rev.*, 1982, **A26**, 1153.
67. M. E. Fisher, *Phys. Rev.*, 1988, **A38**, 885.
68. D. Broseta, L. Leibler and J. F. Joanny, *Macromolecules*, 1987, **20**, 1935.
69. K. Kawasaki, *Ann. Phys. (NY)*, 1970, **61**, 1.

Advances in Theoretical and Physical Aspects of Spin–Spin Coupling Constants

R. H. CONTRERAS

Deparamento de Física, Facultad de Ciencias Exactas y Naturales, Universidad de Buenos Aires, Argentina

J. C. FACELLI

Utah Supercomputing Institute and Department of Chemistry, University of Utah, Salt Lake City, Utah 84112, USA

ANNUAL REPORTS ON NMR SPECTROSCOPY
VOLUME 27 ISBN 0-12-505327-4

NOTATION

CCSD	coupled-cluster singlets and doublets
CI	configuration interaction
CLOPPA	contributions from localized molecular orbitals within the polarization propagator approach
DSO	diamagnetic spin orbital
EHT	extended Hückel theory
EOM	equation of motion
FC	Fermi contact
FFPT	finite-field perturbation theory
FOPPA	first-order polarization propagator approach
FPT	finite perturbation theory
HF	Hartree–Fock
HOMO	highest occupied molecular orbital
IPPP	inner projections of the polarization propagator
LCAO	linear combination of atomic orbitals
LMO	localized molecular orbitals
LP	lone pair
MBPT	many-body perturbation theory
MCSCF	multiconfiguration self-consistent field
MECI	monoexcited configuration interaction
MNDO	modified neglect of diatomic overlap
NMR	nuclear magnetic resonance
NNBI	neglect of non-bonded interactions
PP	polarization propagator
PRMO	partially restricted molecular orbitals
PSO	paramagnetic spin orbital
REX	relativistic extended Hückel
RPA	random phase approximation
SCPT	self-consistent perturbation theory
SD	spin dipolar
SOPPA	second-order polarization propagator approach
SOS	sum over states
TB	through-bond
TS	through-space

UHF	Unrestricted Hartree–Fock
UV	ultraviolet
VB	valence bond

1. INTRODUCTION

From both theoretical and experimental points of view, the analysis of high-resolution NMR parameters is a very important problem, and its significance for the understanding of molecular electronic structure can hardly be stressed enough. When both approaches are taken together, an excellent example of the Born–Opperheimer approximation is obtained, since experimentalists measure transitions between nuclear states, which are modified by the interaction between magnetic nuclei and the external magnetic field and the electrons, while theoreticians study how the electronic wave function is modified owing to those interactions.

The empirical Hamiltonian[1]

$$H = -\frac{1}{2\pi}\sum_{N} \gamma_N \boldsymbol{I}\cdot(\boldsymbol{1}-\boldsymbol{\sigma})\cdot\boldsymbol{B}_0 + \sum_{N\neq N'} \boldsymbol{I}_N\cdot(\boldsymbol{J}_{NN'}+\boldsymbol{D}_{NN'})\cdot\boldsymbol{I}_{N'} \qquad (1)$$

describes how the nuclear spin energy levels are modified both by the static magnetic field $\boldsymbol{B}_0$ provided by the spectrometer and by the interactions between magnetic nuclei and electrons belonging to a given molecule. NMR spectra are obtained as induced transitions between those nuclear levels. $\boldsymbol{\sigma}_N$ is the magnetic shielding tensor and is defined by the electronic environment surrounding the nucleus N. $\boldsymbol{D}_{NN'}$ is the direct dipolar spin–spin coupling tensor between the magnetic nuclei N and N'. This is a traceless tensor, and therefore does not show up in spectra taken in isotropic phase. $\boldsymbol{J}_{NN'}$ is the indirect spin–spin coupling tensor. Although some care should be taken, since during the last few years several papers have been published reporting couplings originating from a quantum mechanical exchange phenomenon (see below), $\boldsymbol{J}_{NN'}$ can be taken to correspond to the coupling between magnetic nuclei mediated by the electrons of the molecule under study. Theoreticians analyse both $\boldsymbol{\sigma}$ and $\boldsymbol{J}$ tensors, considering how the molecular electronic wave function and its energy levels are modified by the interactions between magnetic nuclei and electrons in the presence of an external magnetic field. Theoretical analyses of magnetic shieldings have been reviewed a number of times,[2] as well as on an annual basis in the *Specialist Periodical Reports* series.[3]

The calculation of spin–spin coupling constants poses a real challenge, since accurate results are very difficult to obtain for molecules of chemical interest. They depend on subtle aspects of the electronic structure, and for

this reason a deeper understanding of the relationships between coupling constants and molecular structure could greatly broaden the application of high-resolution NMR spectroscopy to the elucidation of molecular electronic structures. Nevertheless, there are reasons to believe that, at least from a qualitative point of view, the description of spin–spin coupling constants does not require the most sophisticated methods of quantum chemistry. Because of this, many experimental trends have been described adequately without resort to accurate and expensive calculations.

All in all, the theoretical analysis of spin–spin coupling constants is presently progressing along two different lines, namely accurate calculations where better and better techniques are applied, taking advantage of modern computational methods, and simple approximate calculations where the relationships between physical phenomena and experimental data are sought. In spite of the prodigious increase in computational facilities that has taken place during the last decade, *ab initio* calculations are still restricted, with few exceptions, to small molecules containing only light atoms, i.e. up to the second row (Na to Cl).

The present work aims at updating Kowalewski's second review[4] which in turn was a follow-up to the same author's earlier review.[5] It is a very difficult challenge to undertake such a task, since those already classic reviews are so complete and carefully written that it can be expected that they will be basic references for most theoretical work on J couplings for many years to come. Moreover, monographs dealing in some detail with the theory of NMR parameters have been published during this review period.[6] During the last decade, several good reviews have also appeared, covering special topics, as quoted in Section 3 below. And last, but not least, in the *Specialist Periodical Reports on Nuclear Magnetic Resonance*, both theoretical aspects[7] and applications[8] of spin–spin coupling constants are reviewed on an annual basis. These considerations, *a fortiori*, mean that this review must have a structure different from those of Kowalewski. To keep the length of this work within reasonable limits, the following criteria have been adopted. Concepts already described in either of Kowalewski's reviews[4,5] will not be repeated here. Detailed descriptions of topics covered in reviews that have appeared during the period of this work will also not be repeated here. Instead, appropriate references will be given.

Instead of dividing this review into sections on the basis of the nature of coupled nuclei, physical phenomena affecting different types of couplings have been used. However, not all physical phenomena affecting couplings will be dealt with. Emphasis is put on factors studied during the review period from a theoretical point of view that has yielded a better understanding of them. As in most instances it is not possible to make a clear separation between these phenomena, and, besides, only total couplings are amenable to measurement, the divisions adopted here have a certain degree of arbitrariness. For this reason some work could be described in more than

one section. This is, for instance, the case for through-space transmission by overlap of proximate lone pairs. This point could well be taken into account when discussing the lone pair effect on couplings (Section 3.2) or as a special topic in Section 3.3, where through-space transmission is discussed.

The large number of papers relevant to the present work that have been published during the 10-year period of this review means that it has been impossible to quote all of them. For this reason, instead of an exhaustive listing of references, in many instances only a few papers that are relevant for the point dealt with are cited. This practical criterion may lead to the omission of some important papers. The authors wish to apologize to anyone who feels that their work has been thus overlooked.

The following structure has therefore been adopted for this review. Computational methods used during its period are discussed in Section 2. Emphasis is put on details less frequently discussed, with particular comments on both advantages and shortcomings of the methods.

The discussion of computational methods is preceded by a brief account of the interaction mechanisms from which spin–spin coupling constants originate. Section 2.2.3 is devoted to a description of theoretical methods for analysing transmission mechanisms of couplings. Most of the relevant results are given in Section 3, where both theoretical and experimental data are discussed in order to analyse some physical factors that are important for the actual values of coupling constants and that have been discussed using theoretical approaches.

In order to simplify notation, it is assumed, unless otherwise indicated, that coupled nuclei correspond to spin-½ isotopes with the largest natural abundances.

2. CALCULATION OF SPIN–SPIN COUPLING CONSTANTS

2.1. Interaction mechanisms

The electron–nucleus interaction mechanisms in which J couplings originate have been described in Ramsey's pioneering work.[9] Over the years, researchers have studied different properties as well as alternative ways to derive the perturbative Hamiltonians from which the J couplings arise. In this section new developments along these lines that have been published during the last 10 years are reviewed.

2.1.1. Symmetry of the coupling tensor

The symmetry of the spin–spin coupling tensor has been revisited by Buckingham *et al.*,[10] who extended the previous formulation by Buckingham

and Love.[11] The new rules take into account nuclear exchange under a symmetry operation, and the authors have listed all the non-vanishing elements of both the symmetric and antisymmetric parts of the coupling tensor for the most common molecular point groups. Non-zero antisymmetric components can be found for the following point groups: C_1, C_s, C_2, D_2, C_{2v}, C_n ($n>2$) and D_n ($n>2$). For point groups of higher symmetry all components of the antisymmetric part vanish owing to symmetry. Calculations show that the antisymmetric components are significant, but so far no measurements have been reported.

2.1.2. Units for reduced couplings

Coupling constants are frequently reported in hertz or, more correctly, in cycles per second or (in SI units) in s^{-1}. However, when couplings for different isotopic species are compared in a series of molecules, it is more convenient to consider a parameter that does not depend on the magnetogyric ratio of the coupled nuclei. For this reason, the reduced coupling constant $K(AB)$ is defined as

$$K(AB) = 4\pi^2 \frac{J(AB)}{h\gamma_A \gamma_B}, \tag{2}$$

while for making comparisons independent of the electronic density at the site of the coupled nuclei it is convenient to define the reduced absolute coupling constant $K'(AB)$, which is related to $K(AB)$ through[12,13]

$$K'(AB) = \frac{K(AB)}{S_A^2(0) S_B^2(0)}. \tag{3}$$

This constant $K'(AB)$ seems to be particularly appropriate for comparing one-bond couplings in homologous series of compounds, since such a comparison yields insight on the electronic structure of the A–B bond. An interesting use of $K'(AB)$ was discussed by Schröbilgen *et al.*[14] when analysing a series of Group 5 hexfluoride anions. While $^1K(BiF)$ in BiF_6^- shows an anomalously high value, when comparing $^1K'(BiF)$ a smaller value than for any of its congeners is obtained.

In general, $K(AB)$ is reported in SI units ($N A^{-2} m^{-3}$), although c.g.s. units are sometimes also used. As these SI units are rather cumbersome, Raynes[15] has recently proposed the adoption of a simpler SI unit, $T^2 J^{-1}$. This unit will be used here.

2.1.3. Magnetic field dependence of couplings

So far it has been observed experimentally that coupling constants are independent of the spectrometer magnetic field strength. However, ex-

perimental techniques are progressing very rapidly, and spectrometers with higher and higher magnetic fields are becoming available. This poses the question as to how sensitive the couplings to the external magnetic field are. Recently, Raynes and Stevens[16] tried to answer this question using third- and fourth-order perturbation theory. In this way, they derived appropriate expressions for the magnetic-field-dependent parts of couplings. Estimates predict that they vary as $5 \times 10^{-6} B^2$ Hz (B in T). This implies that for a spectrometer with a magnetic field of 14 T (600 MHz) a change of *ca.* 0.001 Hz would be expected in couplings.

2.1.4. The Fermi contact (FC) term

To overcome the difficulties associated with the calculation of the FC term, many attempts have been made to obtain less singular representations of the operator describing this interaction. These representations were also aimed at obtaining a better physical understanding of its origin. During this review period, Kutzelnigg[17] has published an extensive discussion on the origin of the FC interaction, analysing traditional methods of derivation and showing that the FC interaction can be derived from first-order perturbation theory applied to the non-relativistic wave function equation for Lévy-Leblond spin-½ particles.[18,19] Blinder[20] proposed a new exactly solvable model for the FC operator in which the nucleus is represented by a magnetized spherical shell of radius r_0 and the FC interaction is calculated by solving the Schrödinger equation exactly using the Coulomb Green function. Bréchamet[21] derived the hyperfine integration operators involved in NMR spin-coupling effects using standard Racah algebra methods.[22] Using this methodology, it is also possible to avoid the use of integration around the origin to find the FC term. Geertsen[23] used the global representation of the Dirac delta function $\delta(r)$ to avoid the high sensitivity of the FC term to small local inaccuracies of the wave function, which are typical when using Gaussian-type functions in the basis set[24] (the "cusp problem"[4]). Geertsen's results for the HD molecule are shown in Table 1. It is observed that, using the global representation, a much faster convergence with basis set is obtained as compared with those using the Dirac delta function $\delta(r)$.

2.1.5. The diamagnetic spin–orbital (DSO) contribution

Before this review period, very few studies were reported on calculations of the DSO term of couplings. This term was usually disregarded in most calculations, as was pointed out in the pioneering numerical work of Lee and Schulman.[25]

Matsuoka and Aoyama's analytical work[26] made feasible systematic studies of the DSO term for large numbers of molecules and basis sets. Galasso *et al.*[27–30] and Overill *et al.*[31,32] included the DSO contribution in

Table 1. Comparison of convergence properties on basis set for the FC calculation using the $\delta(r)$ and the global representations in the HD molecule.[a]

Basis set	SCF energy (a.u.)	$J^{FC}[\delta(r)]$ (Hz)	J^{FC}[global] (Hz)
(2s/2s)	−1.093 426	12.926	33.488
(6s1p/3s1p)	−1.131 643	35.188	39.111
(8s2p/4s2p)	−1.133 477	40.489	42.835
(10s2p/6s2p)	−1.133 497	42.089	44.060
(10s5p1d/6s3p1d)	−1.133 571	40.688	41.726
(10s5p2d/6s4p2d)	−1.133 604	40.643	41.520

[a]Second-order polarization propagator results taken from ref. 23.

their calculation of couplings in small molecules including first- and second-row atoms. These authors concluded that the DSO contribution is not always negligible and that in many cases it accounts for a large fraction of the total coupling. In particular, it has been determined that the DSO term is considerable for geminal H–H couplings, where in most cases the inclusion of this term worsens the agreement between calculated and experimental results.

A comprehensive study of the DSO dependence in a large number of molecules and couplings using a variety of basis sets has been presented by Scuseria.[33] This study confirmed the important role played by the DSO contributions and demonstrated the rapid convergence of its calculation with the enlargement of the basis set. In fact, basis sets larger than the DZ P level or the inclusion of correlation effects do not dramatically affect the DSO contribution.

Oddershede[34] has demonstrated that the DSO contribution is independent of the gauge origin of the vector potential describing the external magnetic field.

Pérez *et al.*[35] presented a general numerical method for calculating the DSO term. The singularities in the integrals are overcome by calculating them in a cylindrical coordinate system. These integrals are split into six spatial regions in which the function has a definite sign. Such a partition allows one to obtain an intuitive idea of the importance of this term. In the same paper it is shown how the DSO term can be decomposed into contributions originating from occupied LMOs representing bonds or lone pairs.

2.1.6. Proton–proton exchange couplings

During the period of this review, a number of J(HH) couplings of a magnitude in some cases larger than 1000 Hz were reported in some transition-metal hydrides.[36–41] Such couplings exhibit very anomalous

Table 2. ^1J(HH) coupling constants (in Hz) in some iridium trihydride complexes, showing anomalous temperature and isotope substitution dependence.[a]

	Temperature (K)				
Ligand	176	181	186	191	196
PCy_3	61	64	68	73	77
PMe_3	96	106	114	122	135
$SbPh_3$	147	158	171	180	196
PPh_3	260	291	320	355	397
$P(OPh)_3$	358	397	432	469	526
MPTB[b]	972	1119	1274	1425	1565

[a]Values taken from ref. 40.
[b]MPTB is 1-methyl-4-phospha-3,6,8-trioxabicyclo[2.2.2]octane.

temperature and isotope substitution behaviour. Several attempts have been made to explain them using existing theories of electron transmitted or indirect couplings, but none of these could explain their isotope substitution effects. In Table 2 some examples of these couplings are shown for iridium trihydride complexes. To explain these large couplings with such anomalous behaviour the quantum mechanical exchange of ^1H nuclei has been invoked. As protons in those hydrides lie in shallow overlapping potential wells, they can tunnel from one to the other, introducing an additional splitting between the symmetric and antisymmetric ground states of the Hamiltonian. In this model the tunnelling frequency is strongly dependent on temperature, because the corresponding potential wells are very sensitive to temperature-induced conformational changes. Therefore small changes in the potential energy can dramatically change the tunnelling frequency. On the other hand, replacement of ^1H by ^2H or ^3H quenches the quantum mechanical exchange mechanism, leaving only the traditional electron-mediated interactions defining the corresponding couplings. In this way, the anomalous isotope effect shown by such couplings can be explained. Using the two-coupled three-dimensional oscillators model Zilm and co-workers[41] found the following expression for the quantum exchange term J^{ex}:

$$J^{ex}(\text{Hz}) = \frac{-3\hbar a}{8\pi m\delta^3}\left(\frac{3}{\pi}\right)^{1/2}\exp\left(-\frac{3}{4}\frac{a^2+\lambda^2}{\delta^2}\right), \tag{4}$$

where m is the mass of the particle undergoing quantum exchange, a is the internuclear distance, $\delta^2 = \langle x^2 + y^2 + z^2\rangle$ is the average delocalization of each particle in the three-dimensional oscillator, and λ is the characteristic diameter of the circle of closest approach of the nuclei in the hard sphere model.

2.1.7. Relativistic effects on couplings

Relativistic electronic effects and their importance in formulating theoretical models of couplings have attracted a great deal of attention in the past.[4,5]

The relativistic formulation of coupling constants given previously by Pyykkö[42] and later applied in a series of papers[43–47] to the calculation of couplings involving heavy nuclei in a variety of compounds was reviewed by Pyykkö.[48]

The ideas of Pitzer *et al.*[49,50] on relativistic effects in molecules were applied to carry out calculations at the RPA MNDO level of approximation.[51] Although valence electrons can be directly or indirectly affected by relativistic effects, when they are in the valence region they behave non-relativistically. However, in the region where the interaction with magnetic nuclei essentially takes place, relativistic effects can be quite important. The perturbative polarization propagator formulation of couplings allows one to factorize each second-order contribution into factors corresponding to the interaction with magnetic nuclei, the perturbations, and a factor corresponding to the transmission of that interaction through the electronic system. Using the polarization propagator approach (see below), Pitzer's ideas can be implemented easily by taking explicit account of relativistic effects only in the calculation of the perturbations and not in the polarization propagator. The MNDO method is parametrized to best fit experimental data;[52,53] therefore the semiempirical parameters take into account the indirect relativistic effects.[48]

Burns *et al.*[54] estimated relativistic effects on one-bond couplings in a series of Zintl anions, assuming that they are strongly dominated by the FC term, taking the relativistic contribution for each element as

$$[|\Psi_{ns}(0)|^2]_{\text{rel}}/[|\Psi_{ns}(0)|^2]_{\text{non-rel}} \tag{5}$$

The corresponding values of $\Psi_{ns}(0)$ were taken from Pyykkö and Wiesenfeld's tabulation.[45] In Table 3 the Burns *et al.*[54] relativistically corrected reduced coupling constants in the series of anions $SnCh_4^{4-}$, $SnCh_3^{2-}$, $TlCh_3^{3-}$, $CdTe_2^{2-}$ and $HgCh_2^{2-}$ (Ch = Se, Te) are displayed and compared with the experimental values. The same approach was used to estimate relativistic effects on other couplings.[55,56]

Gillespie *et al.*[57] measured a very large $^1J(\text{HgHg}) = 139\,600$ Hz in Hg_3^{2+}, i.e. $^1K(\text{HgHg}) = 3.66 \times 10^{24}\,\text{T}^2\,\text{J}^{-1}$. In order to study the origin of such a large coupling, the largest known so far, they analysed it using Pople and Santry's model.[58] According to this scheme, the FC term of the reduced coupling constant $K^{\text{FC}}(\text{AB})$ can be written as

$$K^{\text{FC}}(\text{AB}) = \tfrac{4}{9}\mu_0\mu_{\text{B}}[S_{\text{A}}^2(0)][S_{\text{B}}^2(0)]\Pi_{\text{AB}} \quad (\text{in T}^2\,\text{J}^{-1}), \tag{6}$$

Table 3. Reduced coupling constants, ^1K and relativistically corrected reduced coupling constants, $^1K^{RC}$ for the anions $SnCh_4^{4-}$, $SnCh_3^{2-}$, $TlCh_3^{3-}$, $CdTe_2^{2-}$ and $HgCh_2^{2-}$.[a]

Anion	K(MSe)[b] (10^{19} T^2 J^{-1})		K(MTe)[b] (10^{19} T^2 J^{-1})	
	^1K	$^1K^{RC}$	^1K	$^1K^{RC}$
$SnTe_4^{4-}$			2016	982
$SnTe_3Se^{4-}$	1481	899	2205	1075
$SnTe_2Se_2^{4-}$	1571	954	2361	1151
$SnTeSe_3^{4-}$	1642	997	2525	1230
$SnSe_4^{4-}$	1714	1041		
$SnTe_3^{2-}$			3206	1562
$SnTe_2Se^{2-}$	2245	1363	3388	1651
$SnSe_3^{2-}$	2403	1459		
$TlTe_3^{3-}$			7403	1682
$TlTe_2Se^{3-}$	5171	1464	7756	1762
$TlTeSe_2^{3-}$	5327	1508	8103	1841
$TlSe_3^{3-}$	5486	1553		
$CdTe_2^{2-}$			2552	1215
$HgSe_2^{2-}$	5531	1525		
$HgSeTe^{2-}$	5560	1533	9563	2116
$HgTe_2^{2-}$			9608	2126

[a]From ref. 54.
[b]M = Sn, Tl, Cd or Hg.

where Π_{AB} is the mutual polarizability of the orbitals in A and B:

$$\Pi_{AB} = 4 \sum_{i}^{occ} \sum_{j}^{unocc} (\varepsilon_i - \varepsilon_j)^{-1} C_{iA} C_{iB} C_{jA} C_{jB}. \tag{7}$$

In order to obtain an estimate of $^1K^{FC}$(HgHg), Gillespie *et al.* considered that in Hg_3^{2+} the HOMO is mainly of s character and used UV experimental data to estimate $\varepsilon_i - \varepsilon_j$. The $S^2(0)$ values were obtained from the work of Pyykkö *et al.*,[59] using the hyperfine integral ν_{-1} through

$$S^2(0) = \frac{-137}{2\pi} \nu_{-1} a_0^{-3}. \tag{8}$$

They took the average of the ν_{-1} hyperfine integrals for Hg and Hg^+. The result thus obtained is compared in Table 4 with unpublished REX results of Pyykkö.[60] Although Gillespie *et al.*[57] were not able to measure ^1J(HgHg) in Hg_2^{2+}, they estimated, by comparing the leading terms of (6), that it should be substantially larger than in Hg_3^{2+}. The REX value is also shown in Table

Table 4. Comparison between calculated ^1K(HgHg) reduced couplings (in 10^{19} T^2 J^{-1}), in Hg_3^{2+} and Hg_2^{2+}.

	Hg_2^{2+}	Hg_3^{2+}
REX (6s basis)[a]	800 093	295 517
REX (6s + 6p)[a]	705 204	260 974
Gillespie *et al.*[b]	[c]	210 000
Experimental[b]	—	366 000

[a]From ref. 60.
[b]From ref. 57.
[c]Estimated to be substantially larger than in Hg_3^{2+}.

4, where it can be seen that it is at least twice as large as that in Hg_3^{2+}, supporting the estimate by Gillespie *et al.*

In analogous cyclic bis(amino)stannylene, Sn(II), and bis(amino)plumbylene, Pb(II), compounds Wrackmeyer *et al.*[61] found the quotient ^1K(PbN)/^1K(SnN) $\approx$ 3.1, which is close to the calculated ratio of the valence s-electron densities, 3.37, given by Pyykkö[42,43] when relativistic contributions are taken into account.

Deviations from the linear correlation between ^nK(EX) and the atomic number of atom X in ferrocenes of the type $(Me_3E_{cp})_2Fe$ (E = C, Si, Ge, Sn, Pb) for ^1J(PbC) couplings were ascribed also to relativistic effects.[62]

2.2. Computational approaches for calculating couplings

2.2.1. Ab initio *methods*

Most papers dealing with *ab initio* methods to calculate coupling constants published during the review period explore problems associated with extending calculations beyond the coupled Hartree–Fock (CHF) approach (or, equivalently, the random phase approximation (RPA), the finite perturbation theory (FPT) for a Hartree–Fock (HF) state, etc.). Such an effort was motivated by two points discussed in previous accounts[4,5] of theoretical approaches for calculating coupling constants, namely (i) the generally poor results obtained at the Hartree–Fock level, and (ii) the lack of physical meaning in the calculation of the Fermi contact (FC) and spin dipolar (SD) interactions in systems showing a non-singlet instability for the ground state wave function.[63–65]

In this section some relevant theoretical work corresponding to this period is reviewed. Papers are grouped according to the perturbation scheme used in the calculations.

(i) Finite perturbation theory (FPT). FPT or finite-field perturbation theory (FFPT) is a convenient, but perhaps expensive, way for calculating coupling constants at any level of accuracy of the electronic ground state wave function. In this approach couplings are calculated explicitly by finite differences using

$$J(\mathrm{AB}) = \frac{1}{h}\frac{\partial^2 E(I_\mathrm{A}, I_\mathrm{B})}{\partial I_{\mathrm{A}z}\partial I_{\mathrm{B}z}}\bigg|_{I_{\mathrm{A}z}, I_{\mathrm{B}z}} \tag{9}$$

where $E(I_\mathrm{A},I_\mathrm{B})$ is the total energy of the system in the presence of the interaction Hamiltonians, which are added explicitly to the molecular one in the SCF procedure. Calculation of the energy is straightforward at any level of accuracy, since H_{int} is a one-electron operator for any of the three second-order terms contributing to J couplings, namely the Fermi contact (FC), the paramagnetic spin–orbital (PSO) and the spin dipolar (SD). By calculating the energy for different states of I_A and I_B, it is possible to calculate J(AB) using finite differences. In general, two such values are sufficient; unfortunately the FPT process can be extremely inefficient, since it is necessary to evaluate the energy of the system at least twice for each component of each coupling tensor. Certainly, the situation is not so complicated for the isotropic FC term, in which only two calculations of the energy are required, although when all couplings belonging to a molecule are sought, it also becomes quite inefficient.

Iwai and Saika[66,67] used the FFPT to calculate the FC contribution to J(HD) in the HD molecule, employing a ground state wave function calculated including diagrams up to third order in many-body perturbation theory (MBPT). They presented a comprehensive study of the MBPT calculation of coupling constants, and calculated the diagrammatic contributions by explicitly including the FC interaction. Their results are summarized in Table 5.

Kowalewski *et al.*[63] used the FPT approach to calculate the FC contribution to couplings in unsaturated compounds using the MCSCF method to

Table 5. Diagrammatic MBPT contributions to the FC term of J(HD) in the HD molecule.[a]

Contribution	J^{FC}(HD) (Hz)
Zeroth-order[b]	54.3
Second-order	−15.4
Third-order	−1.7
Total	37.2

[a]From ref. 66. Obtained using a (12s5p1d) basis set.
[b]Equivalent to CHF.

overcome the non-singlet instability problems mentioned above. Calculations were presented for the following molecules: $H_2C{=}CH_2$, $H_2{=}NH$, $H_2C{=}O$, $HC{\equiv}CH$ and $HC{\equiv}N$. They showed that it is sufficient to include two configurations (or Slater determinants) to overcome the non-singlet instabilities in double-bonded compounds [(σ core)$(\pi)^2$ and (σ core)$(\pi^*)^2$] and three determinants for the configurations [(σ core)$(\pi)^4$ and (σ core)$(\pi)^2$ $(\pi^*)^2$] in triple-bonded compounds. Their results are in overall agreement with the experimental values. However, in view of more recent results,[33,68] where the importance of non-contact contributions is shown, such an agreement may be considered somewhat fortuitous.

Fukui *et al.*[69] applied the FP–MBPT method to calculate the FC term in the first-row hydrides HF, H_2O, NH_3 and CH_4. Their results for ^1J(XH) (X = F, O, N, C) are in good agreement with the experimental values, suggesting that these couplings are dominated by the FC term. The corresponding geminal J(HH) couplings are largely overestimated, in agreement with other studies where the importance of non-contact contributions to these couplings has been shown.[33] In a subsequent paper Fukui *et al.*[70] calculated all interaction terms using finite-field many-body perturbation theory (FF–MBPT) for the same compounds as well as for some second-row hydrides.

(ii) Coupled-cluster methods. Bartlett and co-workers[71,72] presented an extensive discussion of the use of the coupled-cluster singlets and doublets (CCSD) method to calculate coupling constants. The effects of the "orbital relaxation" introduced by the perturbation and the "correlation" effects calculated using unrelaxed orbitals were compared for the FC calculation in several molecules. Their numerical results show that both approaches yield extremely close results, as can be expected from analytical derivations. Besides, CCSD calculations in ethylene show that this method overcomes the non-singlet instability problem that appears in *ab initio* calculations of couplings for molecules of unsaturated compounds.

The J(HF) coupling was calculated in the FH molecule using a coupled-cluster polarization propagator method including all single and double excitations. This coupling, although dominated by the FC term, presents a significant PSO contribution of about 25–30%. Smaller contributions from the SD and DSO interactions were found.

The second-order polarization propagator approach (SOPPA) has been applied to a CCSD reference state to calculate the FC term in the C_2H_2 and CH^+ systems.[73] The same approach was also applied to perform a detailed analysis of the J(HD) coupling in the HD molecule.[74] The total value that Oddershede *et al.*[74] obtained after vibrational averaging, and including all four interaction terms, is 42.79 Hz, which compares favourably with the best experimental value recently reported[75] of 42.94 ± 0.04 Hz.

Table 6. Selected Galasso SOS–CI coupling constants.

Molecule	J	J^{DSO} (Hz)	J^{PSO} (Hz)	J^{SD} (Hz)	J^{FC} (Hz)	J^{tot} (Hz)	J^{exp} (Hz)
B_2H_4[a]	^1J(BB)	0.04	−1.43	0.39	90.29	89.29	
	^1J(BH)	0.25	−1.97	0.01	156.19	154.48	
B_2H_6[a]	^1J(BB)	0.08	−1.95	−0.07	−1.71	−3.65	
	$^1J(BH_t)$	0.37	−0.62	0.06	181.83	181.64	137
	$^1J(BH_b)$	0.72	0.07	−0.10	68.94	69.63	48
BH_3PH_3[a]	^1J(BP)	0.10	−3.16	0.79	56.64	54.37	
	^1J(BH)	0.68	−0.23	−0.01	158.40	158.84	
	^1J(PH)	0.41	3.84	−2.25	401.75	403.75	372
LiF[b]	^1J(LiF)	0.06	−4.08	−0.02	141.38	137.35	
CO[b]	^1J(CO)	0.01	13.99	−8.40	−13.25	−7.65	
CH_4[b]	^1J(CH)	0.38	1.38	−0.08	166.40	168.07	125.0
	^2J(HH)	−3.27	1.17	0.69	−35.44	−36.85	−12.4
NH_3[b]	^1J(NH)	−0.19	−2.51	0.08	−72.28	−74.91	−61.1
	^2J(HH)	−5.12	1.98	1.39	−28.92	−30.33	−10.4
HN=NH[c] (*cis*)	^1J(NN)	0.01	−11.41	0.16	−10.47	−21.71	
	^1J(NH)	−0.18	1.41	1.27	−38.60	−36.10	
HN=NH[c] (*trans*)	^1J(NN)	0.01	−15.05	0.25	−1.99	−16.78	
	^1J(NH)	−0.17	2.27	1.23	−47.91	−44.58	
HP=PH[c] (*cis*)	^1J(PP)	0.03	−426.00	17.74	−149.52	−557.81	
	^1J(PH)	0.29	−6.76	−2.60	118.00	108.93	
HP=PH[c] (*trans*)	^1J(PP)	0.03	−497.71	22.31	−76.44	−551.87	
	^1J(PH)	0.30	−6.95	−2.54	144.85	135.66	
MgH_2[d]	^2J(HH)	−2.69	0.14	−0.01	250.51	250.64	
AlH_3[d]	^2J(HH)	−2.22	0.08	0.07	104.17	102.10	
SiH_4[d]	^2J(HH)	−2.16	0.21	0.10	−17.70	−19.55	−2.8
PH_3[d]	^2J(HH)	−1.08	0.28	0.26	−46.82	−47.37	−13.2
H_2S[d]	^2J(HH)	−0.71	0.68	0.28	−48.77	−48.51	

[a]From ref. 77.
[b]From ref. 29.
[c]From ref. 30.
[d]From ref. 27.

(iii) Configuration interaction methods. The SOS–CI method was originally introduced by Nakatsuji,[76] and its results are equivalent to those obtained with the FPT, CHF and RPA approaches, provided the same ground state wave function is employed. Couplings are calculated as explicit summation over perturbed excited states of the Hamiltonian.

Galasso reported many calculations using the SOS–CI method with modest basis sets[27,29,30,77,78] to evaluate the PSO, SD and FC terms. Those calculations were complemented with the calculation of the DSO term as the expectation value over the HF ground state wave function. In Table 6 some representative values of Galasso's SOS–CI calculations are shown.

Table 7. MCSCF-calculated contributions with different basis sets to coupling constants in HCN.[a]

Coupling	Basis set[b]	FC (Hz)			PSO (Hz)	J^{tot} (Hz)	J^{exp} (Hz)
		MC SCF	Corr.[c]	FC^{tot}			
^1J(CN)	I	−14.0	7.5	−6.5			
	II	−25.2	12.5	−12.7			
	III	−27.5	13.4	−14.1	−5.2	−19.3	−18.6
^1J(CH)	I	299.0	−60.8	238.2			
	II	312.2	−62.1	250.1			
	III	292.2	−50.7	241.5	−3.6	237.9	275
^2J(NH)	I	−2.3	3.2	0.9			
	II	−1.4	−1.5	−2.9			
	III	−4.8	−0.1	−4.9	−4.6	−9.5	±8.7

[a]From ref. 79.
[b]I, (4,2/2); II, (6,3/3); III, (6,3,1/3,1).
[c]Electronic correlation contribution.

(iv) Multiconfiguration self-consistent-field (MCSCF) methods. During this period two papers reported calculations of couplings using MCSCF methods. Laaksonen and Saunders[79] used the UHF MCSCF method to calculate the FC contribution of the HCN molecule, whose HF ground state wave function presents a non-singlet instability. The minimum amount of configurations necessary to overcome this instability was used, namely $|K\pi_x\bar{\pi}_x\pi_y\bar{\pi}_y|$, $|K\pi_x^*\bar{\pi}_x^*\pi_y\bar{\pi}_y|$ and $|K\pi_x\bar{\pi}_x\pi_y^*\bar{\pi}_y^*|$. To be able to compare the results thus obtained with experimental values, the PSO term was calculated using the standard CHF theory, and both the DSO and SD terms were neglected. Laaksonen and Saunders's results for some basis sets are displayed in Table 7.

MCSCF calculations for couplings in the HD and CH_4 molecules were reported by Vahtras *et al.*[80] All four terms—DSO, PSO, SD and FC—were included in their calculation. This is one of the most comprehensive studies of the electronic correlation effects on couplings. The total J(HD) value in HD, without vibrational corrections, is $J(HD)(T = 40\,K) = 43.18$, which compares very favourably with the most recent measured values in the gas phase, namely 42.94 ± 0.04 Hz[75] and 43.11 ± 0.02 Hz.[81] In methane the MCSCF-calculated couplings are $^1J(CH) = 123.87$ Hz and $^2J(HH) = -14.3$ Hz, which are also in good agreement with the experimental values 120.78 ± 0.05 Hz[82] and -12.564 ± 0.004 Hz[83] respectively. It is important to note that ^1J(CH) is overwhelmingly dominated by the FC term, which is the only one that depends strongly on electronic correlation effects. ^2J(HH) is also dominated by the FC term, but its DSO and PSO terms are by no means negligible. In this last coupling the FC term is also the most affected by electron correlation effects.

Table 8. Selected set of calculated coupling constants with the EOM method.

Compound	Coupling	FC (Hz)	DSO (Hz)	PSO (Hz)	SD (Hz)	J^{tot} (Hz)	J^{exp} (Hz)
CH_4[a]	^1J(CH)	113.84	0.28	1.30	−0.06	115.36	125.0
$H_2C{=}CH_2$[a]	^1J(CC)	80.04	0.07	−6.94	1.83	75.00	67.6
	^1J(CH)	141.96	0.47	0.38	0.06	142.87	156.4
	^2J(CH)	−3.54	−0.69	−0.78	−0.06	−5.07	−2.4
	^2J(HH)	−3.39	−3.83	2.92	0.26	−4.04	2.5
	^3J(HH) (*cis*)	9.79	−1.09	0.45	−0.05	9.10	11.6
	^3J(HH) (*trans*)	14.14	−3.56	3.48	0.21	14.22	19.1
H_2O[b]	^1J(OH)	−64.99	−0.11	−10.13	0.07	−75.16	−79
NH_3[b]	^1J(NH)	−54.10	0.10	−2.47	−0.02	−56.68	−61.1
$H_3Si{-}SiH_3$[c]	^1J(SiSi)	92.92	0.02	−0.44	2.53	95.03	88.3
	^1J(SiH)	−171.24	−0.14	0.63	−0.05	−170.80	−197.71
$HSi{\equiv}SiH$[c]	^1J(SiSi)	461.50	0.01	14.23	14.36	490.10	
	^1J(SiH)	−377.35	−0.08	1.12	−0.01	−376.32	
B_2H_6[d]	^1J(BB)	−0.90	0.07	−1.43	−0.03	−2.29	±3.8
	$^1J(BH_b)$	42.61	0.61	0.06	−0.09	43.19	±46.3
	$^1J(BH_t)$	121.26	0.29	−0.34	0.10	121.31	133.5

[a]From ref. 64.
[b]From ref. 86.
[c]From ref. 87.
[d]From ref. 88; for definitions of H_b and H_t see ref. 88.

(v) The equation-of-motion (EOM) approach. The EOM approach was originally proposed by Rowe[84] and Shibuya and McKoy[85] to calculate excitation energies and transition moments. During this period, Galasso[64] applied this approach to calculate coupling constants. As the EOM approach allows one to obtain expressions for coupling constants using correlated ground state wave functions, it can be used to overcome the non-singlet instability problem in unsaturated compounds and to investigate the importance of electron correlation effects on coupling constants. In Galasso and Fronzoni's papers extensive calculations were presented using correlated ground state wave functions including all the (1p–1h) excitations for the second-order terms PSO, SD and FC. The DSO term was calculated with an HF wave function.[86–90] Some selected values are displayed in Table 8.

A comprehensive theoretical study of the sign of ^1J(NN) couplings in hydrazine, isodiazene, the azide anion and N_2 was undertaken by Galasso[91] using a 6-31G** basis set and the EOM approach. It was found that, irrespective of the nature of the bond, the EOM always predicts a negative ^1J(NN) coupling, the only exception being that of hydrazine for a transoid arrangement. In all cases studied the FC term is the dominant one for singly bonded N atoms. For multiply bonded N atoms the PSO term yields a sizeable negative contribution to the total coupling.

Galasso and Fronzoni[92] reported a limited study of the effect of the inclusion of (2p–2h) interactions in the description of the ground state wave function used for the EOM calculations using a 6-31G** basis set. That inclusion improves the agreement with experimental values, affecting mainly the FC term. Owing to the limited flexibility of the basis set that Galasso and Fronzoni used in those calculations, it is difficult to assess unambiguously the importance of the correlation effects introduced by the (2p–2h) excitations.

(vi) First- and second-order polarization propagator approach (FOPPA and SOPPA). As non-singlet instabilities in the ground state wave function render the FC and SD calculations devoid of physical meaning, calculations of couplings with the FOPPA method employing *ab initio* wave functions are limited to saturated compounds. For instance, Lazzeretti *et al.*[93] reported FOPPA calculations for SiH_4 and AlH_4^-.

The SOPPA approach includes sufficient electronic correlation effects to overcome the non-singlet instability problems for the FC and SD calculations. A detailed account of the polarization propagator (PP) equations to calculate couplings within the SOPPA approach was given by Geertsen and Oddershede.[68] The same authors also presented higher-order equations.[94]

SOPPA results so far published suggest that this method yields good results for couplings. Unfortunately, its high computational requirements precludes its use in systems of chemical interest within current computational resources. So far, results have been presented for the following systems: H_2O,[68] C_2H_2,[94] C_2H_2, H_2CO, CH_4 and HCN,[95] CO and N_2,[96] and BH and AlH.[97] In Fig. 1 a correlation between the best calculated values of selected coupling constants obtained with the SOPPA method with extended basis sets and their experimental values is shown, and good agreement is observed. In fact, its correlation coefficient is 0.9975, with a standard deviation of 7 Hz, a slope of 1.02 and an intercept of 0.59 Hz.

(vii) Other perturbation techniques. The FC contributions in HF and CN^- have been studied[98,99] using the perturbation–variational method, where the FC operator is replaced by the perturbation operator

$$W_N = -2C_N \sum_i \frac{1}{r_{iN}^2} \frac{\partial S_{iZ}}{\partial r_{iN}} \tag{10}$$

2.2.2. *Semiempirical methods*

Owing to the limited success of *ab initio* methods for describing couplings along the Periodic Table without resorting to the most expensive methods, semiempirical approaches have been the most commonly used to calculate

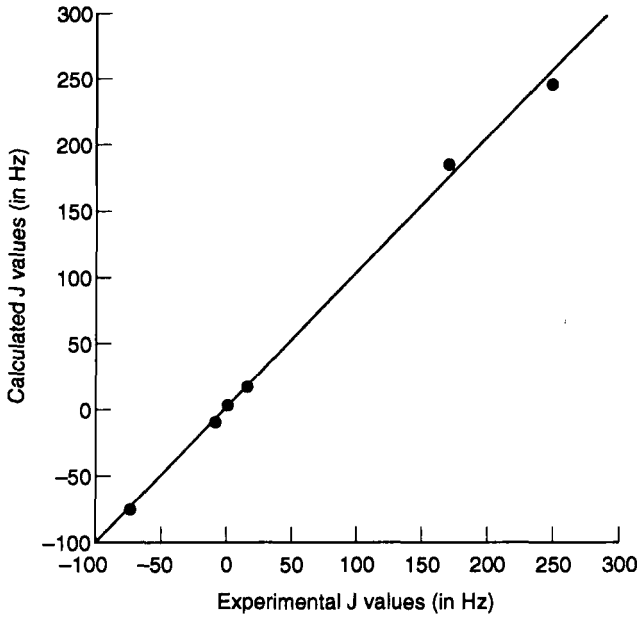

Fig. 1. Correlation between theoretical and experimental values of coupling constants calculated with the SOPPA approach and extended basis sets. The correlation coefficient is 0.9975 and the standard deviation is 7 Hz.

couplings in compounds of chemical interest during the period of this review. Perturbative approaches are, in general, similar to those used with *ab initio* ground state wave functions, although some exceptions are worthy of note. Most calculations are based on the INDO approximation originally introduced by Pople *et al.*[100] using the FPT for the FC term, and later extended by Blizzard and Santry[101] to include all second-order terms FC, PSO and SD within the SCPT formalism. Although in some instances it fails badly, many experimental trends are nicely accounted for, yielding insight into different chemical problems. In the current literature quite often experimental measurements are complemented with calculations based on it. The following are relevant works reported during the review period that attempted to improve the performance of the current semiempirical methods.

The FPT– and SCPT–INDO approaches employ the one-centre approximation in the perturbative calculation, and this gives for the second-order non-contact terms identically zero values when at least one of the coupled nuclei is a proton. Two different approaches were introduced by Facelli *et al.* to overcome this problem, namely to extend the INDO basis set to include 2p orbitals for H (the INDO/p approach[102,103]) and the inclusion of

multicentre integrals in the perturbative calculation (the INDO/MCI approach[104,105]). In Table 9 both approaches are compared for a selected set of molecules.

The better performance of the CNDO/S and INDO/S[106] approximations in describing photoelectron spectra than the standard INDO parametrization[107] prompted an attempt to use them for calculating couplings.[108] Their success in describing several trends in chemical shifts was already known.[109] However, it was found that in unsaturated compounds the ground state wave function either presents an unrestricted HF instability of the non-singlet type or is close to it. A similar problem was met[110] with an MNDO wave function.[111] The instability problem was already known for *ab initio* wave functions in unsaturated systems.[65] With INDO/S and MNDO

Table 9. Comparison of CHF–INDO/p and CHF–INDO/MCI calculations of the FC, PSO and SD terms in a selected set of coupling constants.[a]

Compound	^nJ(XH).		FC (Hz)	PSO (Hz)	SD (Hz)	Total (Hz)	Exp. (Hz)
CH_4	^1J(CH)	INDO/p	112.8	8.52	2.40	123.72	125.45
		INDO/MCI	132.9	−0.44	0.14	132.60	
	^2J(HH)	INDO/p	−6.95	−4.21	−1.66	−12.82	−12.4
		INDO/MCI	−3.09	0.90	0.38	−1.81	
C_2H_2	^1J(CH)	INDO/p	159.26	1.12	0.51	160.89	156.4
		INDO/MCI	163.47	−0.38	0.0	163.09	
	^3J(HH) (*cis*)	INDO/p	10.83	−1.87	−0.45	8.51	11.7
		INDO/MCI	7.81	−0.56	0.05	7.30	
	^3J(HH) (*trans*)	INDO/p	24.00	−1.55	−0.34	22.11	19.1
		INDO/MCI	23.48	0.06	0.40	23.94	
CH_3F	^2J(HF)	INDO/p	21.85	−6.74	3.52	18.63	46.4
		INDO/MCI	40.71	21.34	−3.61	58.44	
CF_3H	^2J(HF)	INDO/p	30.54	−1.36	0.02	29.20	79.23
		INDO/MCI	14.16	10.88	−4.19	20.85	
1,1-Difluoroethene							
	J^3(HF) (*trans*)	INDO/p	60.26	−1.16	0.22	59.32	33.90
		INDO/MCI	43.57	−0.22	0.49	42.86	
	^3J(HF) (*cis*)	INDO/p	16.33	−0.16	0.29	16.46	0.64
		INDO/MCI	2.35	−1.46	−1.15	−0.26	

[a]From refs 102–105.

Table 10. Calculated J^{π}_{FC} in ethylene for unstable (INDO/S) and quasi-unstable (MNDO) ground state wave functions; they are compared with the INDO results, which are free from the instability problem, and with calculated values using the SPPA–INDO/S method, which overcomes the instability problem.

Coupling	INDO/S[a] (Hz)	MNDO (Hz)	INDO (Hz)	SPPA INDO/S[b] (Hz)
^2J(HH)	4.20	−54.28	−1.27	−1.06
^3J(HH)(*cis*)	−4.20	54.28	1.27	1.06
^3J(HH)(*trans*)	−4.20	54.28	1.27	1.06
^1J(CH)	−17.41	155.94	4.36	4.36
^2J(CH)	17.41	−155.94	−4.36	−4.36

[a]From ref. 108; coupling constants are calculated at the RPA level.
[b]Taken from ref. 112; coupling constants are calculated at the SPPA level.[113]

wave functions instability and quasi-instability problems also arise in unsaturated compounds. While in the former they were traced to the "screening constant" of the INDO/S Hamiltonian, in the latter they arise from the large difference between the MNDO bonding parameters for carbon p and s orbitals, namely $\beta^0_s(C) = -18.985\,044$ eV and $\beta^0_p(C) = -7.934\,122$ eV. The ethylene molecule is a suitable case to illustrate some consequences of instability and quasi-instability problems. The PRMO calculated J^{π} components for its J(HH) and J(CH) couplings using the MNDO, INDO and INDO/S wave functions are displayed in Table 10. It is important to note that, while the INDO wave function is far from non-singlet instability, the MNDO one is quasi-unstable and the INDO/S one is unstable. In all three cases the following two features of the J^{π}_{FC} component are retained: (a) path invariance and (b) the alternating sign rule. However, the latter shows an inversion in sign for the INDO/S case. Although, with the MNDO wave function, the alternating sign rule is the correct one, the magnitudes of J^{π}_{FC} are dramatically exaggerated. These two features are typical of the instability and quasi-instability problems respectively, originating from the π-electron system.

The quasi-unstable character of a wave function may help in understanding the origin of some failures of semiempirical methods. Lambert and Klessinger[114] used the PRMO technique to investigate the failure of the FPT–INDO method in describing the geminal J(CC) couplings involving an sp-hybridized C atom. They concluded that no quasi-instability originating in the π-electron system leads to that failure. However, some caution should be taken in generalizing this result, since quasi-instabilities may originate in molecular orbitals that are not of the π type. This is the case, for example, with some silanes, where the quasi-instability arises in a σ-type Si–H orbital.[115]

The above results also call for some caution when considering electronic correlation effects on couplings. Obviously, when the HF ground state wave function presents a non-singlet or a quasi-non-singlet instability, the inclusion of electronic correlation beyond CHF (or equivalently RPA) overcomes that problem for calculating couplings. With semiempirical wave functions the instability problem was overcome[112,115] using the SPPA approach.[113] Another possibility is to resort to a simpler approximation, either in the ground state wave function or in the perturbative procedure. For instance, in benzaldehyde, where the INDO wave function is close to an unrestricted HF non-singlet instability, the CNDO/2 wave function performs better, since it is free from the instability problem owing to the neglect of σ–π exchange integrals in CNDO/2, and therefore the π-electron system cannot be spin-polarized. Obviously, such calculations do not include the π-transmitted component. The second case is met, for instance, with the perturbative SOS scheme of Towl and Schaumburg,[116] which does not include electronic excitations corresponding to transmission through the π system.[117] Similar reasons hold for the use of Geertsen's[68] MECI scheme.

When considering quasi-unstable wave functions, two important questions arise. First, what is the precise meaning of "near a non-singlet HF instability"? Secondly, which orbital(s) define(s) such a condition? First of all, it should be noted that a non-singlet quasi-instability manifests itself in the FPT or SCPT calculations of the FC term as slow convergence in the iterative procedure.[110] When the polarization propagator formalism is used in the perturbative procedure, a non-singlet quasi-instability manifests itself in the triplet propagator as an eigenvalue close to zero. It remains to be defined quantitatively what "close to zero" means.

It is important to point out that the calculations of both spin–orbital terms, PSO and DSO, are unaffected when a non-singlet HF instability is present. However, the former can be affected by the less common non-real instabilities of the wave function.[118]

Galasso's[119] *ad hoc* INDO parametrization for calculating couplings involving Se and/or Te, or other couplings in molecules containing any of these chalcogen atoms, has been used to study several problems, some of them mentioned in Section 3. When using the INDO approximation for couplings involving such heavy nuclei, the question of relativistic effects arises.[120] A close look at the way in which the parametrization was done shows that Pitzer's[49,50] ideas were used. In fact, to include Se and Te, a reparametrization of first-row atoms was required to fit experimental data. In this way, indirect relativistic effects were taken into account. Direct relativistic effects were also taken into account, since the parameters $S_x^2(0)$ and $\langle r^{-3} \rangle$ for both atoms were empirically determined to fit the experimental data.

The extended Hückel theory (EHT) was used by the Leiden group to calculate coupling constants.[121] All three second-order terms, FC, PSO and

SD, were included in their calculations. Multicentre integrals were calculated using the Ruedenberg expansion.[122] This method provides a computationally simple and rapid procedure to calculate certain types of coupling constants with reasonable success. The EHMO parameters were optimized for calculating J(CH) and J(HH) couplings using a data set of 76 experimental ^1J(CH) and ^3J(HH) couplings. After that refinement, a final r.m.s. of 3.9 Hz was obtained, but better agreement can be obtained for each type of coupling if these parameters are independently refined for ^1J(CH) and ^3J(HH) couplings.

Pyykkö and co-workers continued using the semiempirical REX formulation[123,124] to study couplings involving heavy atoms. Reference 46 describes the reformulation of the REX approach to use time-reversal symmetry to halve the computational effort for calculating couplings. This new version of REX also includes the iterative version of the relativistic extended Hückel method (ITREX). This approach has been applied with modest success to a series of heavy element fluorides. ^1J(MTe) couplings (M = Cd, Hg, Pb) were calculated for cluster models of CdTe, HgTe and PbTe. In Table 11 several ^1K couplings calculated using the REX method are compared with experimental values.

The PP at the RPA level was employed[51] to calculate couplings, including for heavy atom compounds, using an MNDO wave function.[52,53] Although very few results have been published, trends for couplings involving some heavy nuclei are correctly reproduced. Results for ^1J(XH) (X = C, Si, Ge, Sn, Pb) in the Group IV hydrides are compared with experimental values

Table 11. Comparison between REX-calculated one-bond couplings and experimental values.[a]

Compound	REX (10^{19} T^2 J^{-1})	Exp.[b] (10^{19} T^2 J^{-1})
CdTe	3.9	7.7
HgTe	8.1	74
PbTe	22.2	27
CO	144	40
CO_2	188	39
CSe_2	−96	−392
XeF_2	708	1820
XeF_4	160	1236
XeF_6	−62	104
SF_6	25	289
SeF_6	−119	649
TeF_6	−49	1033
UF_6	−531	*ca.* 0

[a]From refs 46, 47 and 125.
[b]Sign unknown unless explicitly stated.

Table 12. RPA–MNDO $^1J^{FC}$(XH) couplings in Group IV XH_4 hydrides.

X	RPA–MNDO[a] (Hz)	REX[b] (Hz)	Exp.[b]
C	143.2	70.1	124.8
Si	−206.9	−126.7	−202.5
Ge	−1707.5	−537.4	−875.5
Sn	−2455.8	−1301.8	−1937.0
Pb	2313.0	2099.5	2333.3

[a]From ref. 51.
[b]From ref. 126.

and with those reported by Pyykkö[126] in Table 12. It is important to recall that in unsaturated compounds this version of the MNDO method presents the same instability problems[110] as the former one,[111] and therefore its applicability is restricted to saturated compounds unless the IPPP technique is applied to project the PP internally onto MOs not involved in the instability problem (see Section 2.2.3).

2.2.3. *Decomposition of coupling constants according to the mechanisms involved in their transmission*

The theoretical analysis of different electronic transmission mechanisms of nuclear spin–spin coupling constants has received a great deal of attention during the review period. On the one hand, new approaches have been presented, while, on the other, techniques that appeared shortly before this period have been applied to a number of different problems. In this section a brief account of methods used to analyse transmission mechanisms is given, emphasizing the following points: the basic ideas, the types of problems that can be studied, the range of applicability and possible shortcomings. Most applications are reviewed in Section 3.

(i) The NNBI method. In order to study the influence of non-bonded intramolecular interactions on couplings, Barfield introduced modifications into the FPT–INDO method. The off-diagonal elements of the Fock matrix for electrons of α spin within the UHF–INDO method can be written as

$$F^{\alpha}_{\mu\nu} = \tfrac{1}{2}(\beta^0_A + \beta^0_B) S_{\mu\nu} - P^{\alpha}_{\mu\nu} \gamma_{AB}, \tag{11}$$

with a similar expression for electrons of β spin.

In its first version[127] the NNBI approach consisted in setting equal to zero in each SCF cycle the overlap integrals $S_{\mu\nu}$ associated with the sets of atomic orbitals whose non-bonded interactions are under study. It was assumed that the

elements of the charge-density bond order matrix $P_{\mu\nu}$ between non-bonded atoms are too small to make any significant contribution to $F^{\alpha}_{\mu\nu}$ in (11). In a later version[128] the full off-diagonal element $F^{\alpha}_{\mu\nu}$ is set equal to zero in each SCF cycle for atomic orbitals centred on non-bonded atoms and whose direct interaction is intended to be eliminated from the MO calculation.

The NNBI approach has only been implemented using the FPT to calculate the FC term of couplings. Laatikainen[129,130] combined the NNBI and PRMO methods to study different transmission mechanisms of the FC interaction. Several of those applications are described in Section 3. The combined use of the IPPP and NNBI methods[131] allows one to obtain insight into the difference between proximity effects affecting the ground state wave function and those arising from the transmission of spin polarization through a proximate moiety.

(ii) The partially restricted molecular orbitals (PRMO) method. This approach was intended to separate σ- and π-electron transmitted components of coupling constants.[132] Shortly afterwards, it was extended to study the through-space transmission of couplings.[133] However, some caution should be taken in the latter studies, since the partially restricted condition is imposed on AOs and, since canonical MOs are extended over the whole molecule, AOs in the wave function do not accurately represent the molecular fragment.

The main idea of the PRMO method for calculating the σ-transmitted component consists in performing an unrestricted LCAO–SCF on σ-type molecular orbitals and a restricted one on π-type orbitals. This calculation provides J^{σ}, while J^{π} is obtained as

$$J^{\pi}(NN') = J^{\text{total}}(NN') - J^{\sigma}(NN'). \tag{12}$$

It should be kept in mind that such a classification is strictly applicable only for planar unsaturated compounds. However, in planar unsaturated compounds with side-chain groups containing out-of-plane σ-type bonds an approximately similar description holds. The mixing of those bonds with the unsaturated π-electron system can be described as a hyperconjugative interaction.

Two different versions of the PRMO method have been presented. They use respectively the FPT[100] and SCPT[101] perturbational approaches for calculating total coupling constants.

(a) The FPT-PRMO approach. This has been implemented only to study the FC term.[132] It is based mainly on the following ideas. To evaluate the total FC terms with the FPT approach, an unrestricted LCAO–SCF

calculation is required. The corresponding Fock Hamiltonian for α orbitals can be written as

$$F^{\alpha}_{\mu\nu} = H^{\text{core}}_{\mu\nu} + \sum_{\lambda\sigma} [P_{\lambda\sigma}(\mu\nu|\lambda\sigma) - P^{\alpha}_{\lambda\sigma}(\mu\sigma|\lambda\nu)]. \tag{13}$$

A similar expression holds for β orbitals. In order to perform an unrestricted calculation on σ MOs and a restricted one on π MOs, the density matrix elements $P^{\alpha}_{\mu\nu}$ and $P^{\beta}_{\mu\nu}$ obtained in each SCF cycle are dealt with differently, depending on whether or not μ and ν AOs contribute to a π-type MO. If they do then $\frac{1}{2}(P^{\alpha}_{\mu\nu} + P^{\beta}_{\mu\nu})$ is taken to form the α and β Fock matrices for the next SCF cycle. If they do not then the unmodified $P^{\alpha}_{\mu\nu}$ and $P^{\beta}_{\mu\nu}$ elements are employed in the next SCF cycle. This procedure is followed until SCF convergence is achieved. This scheme is similar to that used a few years earlier by Yoshida.[134] The π-transmitted component is obtained as in (12). Computational programs that implement FPT–PRMO calculations are available from QCPE.[135,136]

(b) The SCPT PRMO approach. In ref. 103 the PRMO scheme, formerly presented for the FPT perturbational approach, was extended to Blizzard and Santry's SCPT scheme.[101] In this scheme the perturbation equations can be written as

$$C^{(1)}_{\mu i} = -\sum_{m}^{\text{unocc}} \sum_{\nu\lambda} \frac{C_{\mu m} C_{\nu m}}{\varepsilon_m - \varepsilon_i} F^{(1)}_{\nu\lambda} C_{\lambda i}, \tag{14}$$

where $C^{(1)}_{\mu i}$ are the first-order corrections to the MO coefficients, $C_{\lambda i}$, $F^{(1)}_{\nu\lambda}$ is the first-order correction to the Fock operator matrix, and ε_i are the orbital energies. While the first summation is carried over all vacant MOs, the sum over ν and λ is carried out over all AOs used in the basis set. In order to adapt the idea of a PRMO calculation to this formalism, the ν and λ summations are restricted to those AOs that can be spin-polarized. For instance, in order to apply the restricted condition to the π orbitals, all ν and λ values corresponding to AOs contributing to the π-electron system are excluded from the summation.

With the present approach, the PRMO technique can be applied to decompose into different contributions both the FC term and the second-order non-contact contributions, PSO and SD terms.[137]

(iii) The SOS2 method. Fukui *et al.*[117] introduced into the SOS scheme for calculating the FC term doubly excited states in a restricted way, rendering it equivalent to the FPT one.[138] The resulting scheme was called SOS2. In order to carry out calculations at the INDO level, Fukui *et al.*[117] adapted

Nakatsuji's expressions[76] to take into account the monocentric approximation:

$$J(NN') = -\frac{4}{h}\left(\frac{4}{3}\beta\hbar\right)^2 \gamma_N \gamma_{N'} S_N(0)^2 S_{N'}(0)^2$$

$$\times \sum_n \sum_{i,j}^{\text{occ}} \sum_{a,b}^{\text{unocc}} T_n^{-1} V(i \rightarrow a, n) V(j \rightarrow b, n) C_{Ni} C_{Na} C_{N'b} C_{N'j}, \qquad (15)$$

where T_n^{-1} is the nth eigenvalue of the matrix **H** whose elements are given by

$$H_{ia,jb} = \delta_{ij}\delta_{ab}(\varepsilon_a - \varepsilon_i) - [ij|ab] - [ib|ja] \qquad (16)$$

and $V_{ia,n}$ is the coefficient of the triplet excitation $i \rightarrow a$ in the nth eigenvector of **H**.

As the π transmission of the FC term originates from the elements $H_{*_{\sigma\pi},*_{\pi\pi}}$, the σ-transmitted contribution $J^{\sigma}(NN')$ can be calculated neglecting these elements. The π-transmitted component is obtained as in (12).

π-Transmitted components obtained using the SOS2–INDO approach in planar unsaturated compounds are exactly the same as those obtained using PRMO–FPT–INDO.[139] Recently, the SOS2 scheme was extended by Fukui *et al.*[140] to be used with the SOS–CI scheme with *ab initio* ground state wave functions.

(iv) The IPPP–CLOPPA method. The IPPP method (inner projections of the polarization propagator)[141] was first applied to decompose the calculated FC term into contributions originating in some molecular fragments of the compound under study. Molecular fragments are defined through a localization procedure based on Verwoerd's technique.[142] Local contributions are obtained by means of Löwdin's inner projection technique;[143] if the molecular fragment considered is the whole molecule then the calculation yields the RPA value of the FC term. The IPPP method was later extended to include the PSO and SD terms.[144] A program that implements IPPP calculations at the RPA level using an INDO wave function is available,[145] and a brief description, including some examples showing its versatility, is found in ref. 146. The following type of problems have so far been analysed using this approach: (a) the decomposition of couplings transmitted through the σ- and π-electron systems; (b) the through-space transmission of couplings between nuclei proximate in space to each other; (c) the transmission through each pathway of couplings in multicyclic compounds where there is more than one path connecting the coupled nuclei; and (d) the proximity effect of a moiety close to the coupled nuclei.

The IPPP technique has also been employed using *ab initio* ground state

wave functions to study the through-space transmission of J(FH) couplings between proximate F and H atoms.[147]

The CLOPPA method (contributions from localized orbitals within the polarization propagator approach)[148] is closely related to the IPPP one. The localization procedure is applied repeatedly in order to obtain localized orbitals, both occupied and vacant, corresponding to chemical moieties like bonds or lone pairs (occupied) and antibonding orbitals (vacant). Detailed descriptions of the CLOPPA method can be found in refs 149–151, where some examples are also given.

A brief description of the resulting CLOPPA equations is now given. The coupling tensor $\boldsymbol{J}_{\mathrm{NN}'}$ can be written as

$$\boldsymbol{J}_{NN'} = \boldsymbol{J}_{NN'}^{\mathrm{DSO}} + \boldsymbol{J}_{NN'}^{\mathrm{PSO}} + \boldsymbol{J}_{NN'}^{\mathrm{SD}} + \boldsymbol{J}_{NN'}^{\mathrm{FC}} + \boldsymbol{J}_{NN'}^{\mathrm{FC,SD}}. \tag{17}$$

Since the DSO term is a first-order quantity, it is trivial to decompose it into contributions from LMOs.[35] The second-order quantities expressed at the RPA level using LMOs are

$$J_{NN'}^{\mathrm{FC}} = -\frac{4}{h}\left(\frac{4}{3}\pi\beta\hbar\right)^2 \gamma_N \gamma_{N'} \sum_{ia,jb} U_{ia,N}^{\mathrm{FC}} ({}^3\mathbf{A} - {}^3\mathbf{B})_{ia,jb}^{-1} U_{jb,N'}^{\mathrm{FC}}, \tag{18}$$

$$J_{NN'}^{\mathrm{PSO},\alpha} = -\frac{4}{h}(4\beta\hbar)^2 \gamma_N \gamma_{N'} \sum_{ia,jb} U_{ia,N}^{\mathrm{PSO},\alpha} ({}^1\mathbf{A} + {}^1\mathbf{B})_{ia,jb}^{-1} U_{jb,N'}^{\mathrm{PSO},\alpha}, \tag{19}$$

$$J_{NN'}^{\mathrm{SD},\alpha\beta} = -\frac{4}{h}(\beta\hbar)^2 \gamma_N \gamma_{N'} \sum_{ia,jb} U_{ia,N}^{\mathrm{SD},\alpha\beta} ({}^3\mathbf{A} - {}^3\mathbf{B})_{ia,jb}^{-1} U_{jb,N'}^{\mathrm{SD},\alpha\beta}, \tag{20}$$

$$J^{\mathrm{FC,SD},\alpha\beta} = -\frac{16\pi}{3h}(\beta\hbar)^2 \gamma_N \gamma_{N'} \sum_{ia,jb} (U_{ia,N}^{\mathrm{FC}} U_{jb,N'}^{\mathrm{SD},\alpha\beta} + U_{ia,N}^{\mathrm{SD},\alpha\beta} U_{jb,N'}^{\mathrm{FC}}) ({}^3\mathbf{A} - {}^3\mathbf{B})_{ia,jb}^{-1}, \tag{21}$$

It should be recalled that the FC term is isotropic, and the FC,SD cross-term is purely anisotropic, i.e. it is a traceless tensor. In all summations in (18)–(21) each term is factorized into two different types of terms, one originating from the polarization propagator, and the other from the perturbations.

In (18)–(21) α and β label the Cartesian components, i (a), j (b) are occupied (vacant) LMOs representing bonds or lone pairs (antibonding orbitals), and ${}^3\mathbf{A} - {}^3\mathbf{B}$ and ${}^1\mathbf{A} - {}^1\mathbf{B}$ are the triplet and singlet polarization propagators respectively. The sums run over all occupied and vacant LMOs

given by the molecular orbital calculation. $U^x_{ia,N}$ are the perturbations for each interaction, given explicitly by

$$U^{FC}_{ia,N} = \langle i|\delta(\mathbf{r})|a\rangle, \tag{22}$$

$$U^{PSO,\alpha}_{ia,N} = \langle i|L^{\alpha}_{N}|a\rangle, \tag{23}$$

$$U^{SD,\alpha\beta}_{ia,N} = \langle i|[3r_{N\alpha}r_{N\beta} - r^2_N\delta_{\alpha\beta}]r^{-5}_N|a\rangle. \tag{24}$$

These expressions indicate that each second-order term of a given coupling $J(NN')$ can be written as

$$J^x(NN') = \sum_{ia,jb} J^x_{ia,jb}(NN'), \tag{25}$$

where each term of the sum depends explicitly on at most two occupied LMOs, i and j, and two vacant LMOs, a and b. Each $J^x_{ia,jb}(NN')$ term can be factorized into two different types of factors, i.e. the PP and the perturbations. If the SCF calculation yields n occupied and m vacant MOs then the total number of terms of (25) amounts to $\frac{1}{2}nm(nm+1)$.

If the localization procedure is applied repeatedly in the IPPP method, local contributions can also be expressed as the sums of contributions originating in LMOs. An expression similar to (25) can be obtained (see (26) below), with, however, the following differences. The triplet and singlet polarization propagator terms should be replaced by their internal projections onto the set of LMOs defining the molecular fragment of interest. The sum should also be truncated to include only LMOs belonging to the chosen molecular fragment. If the molecular fragment is built up from n' occupied and m' vacant MOs then the total amount of terms is now $\frac{1}{2}n'm'(n'm'+1)$. The final expression is thus

$$J^{x\langle local\rangle}(NN') = \sum_{ia,jb} J'^x_{ia,jb}(NN'), \tag{26}$$

where $J'^x_{ia,jb}$ differs from $J^x_{ia,jb}$ of (25) in that the former is obtained by internally projecting the polarization propagator term onto the subspace of local LMOs, while in the latter the whole polarization propagator is employed. A detailed comparison between them can yield further insight into factors defining experimental trends.

3. ANALYSIS OF PHYSICAL ASPECTS OF COUPLING CONSTANTS

Excellent reviews dealing with specific types of couplings or specific problems related to couplings have been published during the last decade.

Overlap with these reviews will be kept as low as possible. In general they have been organized according to the types of nuclei involved in the couplings. Comprehensive reviews covering much experimental data, and describing trends and physical aspects of J(CC) couplings have recently been published by Krivdin and Kalabin[152,153] for one-bond couplings and by Krivdin and Della[154] for longer-range couplings. An excellent description of J(CC) and J(CH) couplings has been given by Marshall.[155] Trends and physical aspects affecting J(CH) couplings have been reviewed by Hansen.[156] Couplings between an alkynyl carbon atom and a variety of other nuclei have been reviewed by Wrackmeyer and Horschler.[157] Hansen[158] has presented a detailed discussion of couplings involving at least one of the nuclei belonging to the double bond in compounds containing C=C, C=O, C=N and N=N moieties. Experimental data on couplings involving quadrupolar nuclei have been reviewed by Mlynárik.[159] Couplings involving H, C and N nuclei in 1,4-diazines have been presented in the review by Chupakhin *et al.*[160] Trends and physical aspects of couplings involving at least one P nucleus have been discussed in several reviews. For instance, Gorenstein has reviewed non-biological aspects of P NMR spectroscopy[161] and given a discussion of coupling constants.[162] Many aspects of P couplings are also discussed in ref. 163. Couplings involving Si have been discussed by Marsmann,[164] those involving Ge by Mackay and Thomson,[165] and those involving Sn by Wrackmeyer,[166] who have also reviewed those involving Pb.[167] Couplings of the types J(MoX) and J(WX) have been reviewed by Minelli *et al.*[168] J(PtX) couplings have been reviewed by Pregosin.[169,170] Those involving Tl have been reviewed by Hinton *et al.*[171] A brief description of features of J(TlC) couplings has been given by Anderegg *et al.*[172] who concluded that such couplings vary markedly for no apparent reason. Those involving N have been reviewed and discussed by Philipsborn and Müller[173] and by Witanowski, Stefaniak and Webb.[174a,b] The latter reviews are updates of a previous one by the same authors.[175]

Effects of lone pairs on couplings have been systematically classified and discussed in detail by Gil and Philipsborn.[13] The influence of substituents and of the positive charge on ^1J(CF) and ^4J(FF) couplings in polyfluorinated allyl cations have been discussed by Bakhmutov and Galakhov.[176] Isotope effects on couplings have been critically reviewed by Sergeyev.[177] Several aspects of the through-space transmission of couplings have been dealt with in ref. 178 A brief and clear account of several factors affecting coupling constants has been given by Jameson,[179] including discussions of important structural factors on ^1K, ^2K and ^3K along the Periodic Table. For the first type of couplings questions such as coordination number, oxidation state, formal hybridization, electronegativity of substituents and stereospecific aspects are dealt with. A section of ref. 179 is devoted to an analysis of the effects of intermolecular interactions and intramolecular dynamics. A brief theoretical description of couplings is also included. Most other chapters of

the same monograph,[12] dealing with particular elements or groups of elements, include a section where couplings involving them are discussed. Several chapters of Volume 2 of *NMR of Newly Accessible Nuclei*[180] also include a section on coupling constants.

The sign inversion that takes place for some ^1K(NE) couplings (E = Si, Sn, Pb) in *N*–arylamino derivatives has been reviewed by Wrackmeyer and Zhou.[181] Relationships between *J*(PP) couplings and structural parameters in derivatives of phosphazene have been discussed by Shaw.[182] The anisotropy of coupling constants has been covered in a detailed review by Lounila and Jokisaari.[183]

3.1. Transmission through the σ and π electronic systems

The existence of long-range H–H coupling constants in unsaturated compounds aroused the curiosity of NMR spectroscopists at an early stage of the development of this technique. The first attempt to explain the origin of those couplings was made by McConnell,[184] who proposed that the spin information associated with the FC interaction is transmitted through the π-electron system in planar unsaturated compounds. As the FC interaction cannot originate in π-type orbitals (since they have a node at the molecular plane) a σ–π exchange interaction was invoked by McConnell to justify such a model. Since those early days, much work, both theoretical and experimental, has been devoted to deepening the understanding of such transmission mechanisms.

A survey of different theoretical approaches intended to decompose coupling constants in their σ- and π-transmitted components has been published.[178] Earlier comprehensive reviews in which this mechanism is discussed at length are those of Murrel,[185] Barfield and Chakrabarti[186] and Günther and G. Jikeli.[187] This point is also discussed in some detail in both of Kowalewski's reviews.[4,5]

This section is divided into three parts. In the first part papers dealing with the σ–π decomposition of couplings in planar unsaturated compounds are reviewed, together with those papers showing relevant data that may help in understanding the physical aspects of these coupling pathways along the Periodic Table. In the second part papers dealing with couplings transmitted through a hyperconjugative mechanism are reviewed. Other couplings affected by a hyperconjugative interaction are also discussed. The third part is devoted to a discussion of some stereospecific aspects of the σ-transmitted components.

3.1.1. π-Transmitted component in planar unsaturated compounds

The π-transmitted component of the FC term shows some definite trends. The most conspicuous of these are the alternating sign rule on the number

of bonds that separate both coupled nuclei, and the low sensitivity to the coupling pathway. These trends are exemplified for J(HH), J(CH) and J(CC) couplings in different unsaturated compounds using the PRMO–FPT–INDO method[132] and the SOS2–INDO one.[117,139] Both methods yield exactly the same results.[139] Fukui *et al.*[140] repeated the same type of calculations for acetylene and ethylene using the *ab initio* SOS–CI approach with two different levels of approximation and several basis sets. They found that J^{π} INDO values are larger than the *ab initio* ones. However, both approaches yield similar trends.[140]

Decompositions of calculated J(NH) couplings within the PRMO SCPT INDO approach were discussed in ref. 188. The effect of the dielectric constant of the solvent on J^{σ} and J^{π} was discussed in ref. 189.

For couplings between nuclei other than protons the three second-order interaction terms were decomposed in σ- and π-transmitted components using the PRMO–SCPT–INDO approach.[137,190] In ref. 190, J(SeC) and J(TeC) couplings were also considered.

Pachter *et al.*[191] applied the PRMO–INDO method[132] to calculate the π-transmitted component of $^1J(C_2H_2)$ and $^1J(C_3H_3)$ couplings in *N*-substituted indoles and discussed the substituent effects on this component. They compared the PRMO values with those obtained using the method proposed by Steiger, Gey and Radeglia.[192]

Holak *et al.*[193] correlated the vicinal $^3J(C_1–C_2–C_3–H)$ couplings in biphenylene and dihydroanthracene with the $C_1–C_2$ bond length R_{12} and MNDO bond orders P_{12}. They found

$$^3J(C_1H_3) = -315.5R_{12} + 51.25 \quad \text{(in Hz)}$$

$$^3J(C_1H_3) = 13.73P_{12} - 1.66 \quad \text{(in Hz)}$$

Vicinal J(HCCH) couplings also depend on the C–C bond order. Good examples are fused aromatic rings, where the C–C bond order is not the same for all positions with respect to the central bond.[194] For instance, while in quinoline $^3J(H_2H_3) = 4.2$ Hz, in isoquinoline $^3J(H_3H_4) = 5.8$ Hz.[195]

Cassidei and Sciacovelli[196] continued their study of inter-ring couplings in fluoro derivatives of naphthalene. Although there are notorious exceptions, most of these couplings are considered to be mainly transmitted through the aromatic π system. Exceptions are either cases in which the coupled nuclei are connected by a W or an extended zig-zag path such as *epi* ^5J(FF) coupling, or the well-known *peri* ^4J(FF) coupling, which is dominated by a through-space mechanism. An inversion of the alternating sign rule for inter-ring J(FH) couplings with respect to those of J(HH) and J(FF) has been reported,[196] i.e. inter-ring J(FH) couplings are positive when an even number of bonds separate both coupled nuclei and negative when that number is odd—this is also the case for long-range J(FH) couplings between an H side-chain atom and an F atom attached to the aromatic ring. It is

interesting to note that the SOS INDO-calculated J(FH) couplings in 2-fluoro-naphthalene do not reproduce the alternating sign rule, while the FPT INDO scheme follows the experimental trend.[196] This difference can be easily traced out to the fact that the SOS approach does not take into account the π-transmitted component.[139]

Long-range J(HH) and J(CH) couplings in serotonin, tryptamine and L-tryptophan have been studied both experimentally and at the INDO level.[197] J(HH) couplings in butyrolactone have been studied with the FPT INDO method.[198a]

As pointed out by Krivdin and Kalabin,[152,153] ^1J(CC) couplings provide unique structural information on organic molecules. For this reason, interaction and transmission mechanisms of such couplings are of particular theoretical interest. As Krivdin and Kalabin's reviews[152,153] are detailed accounts and discussions of the bibliography dealing with trends and physical aspects of such couplings, only a few comments are added here.

Recently, new experimental values of ^1J(CC) couplings in benzene (55.8 Hz) and cyclohexane (33.10 Hz) have been reported.[198b] Such a large difference originates not only from the π-transmitted component of the FC term, since the σ component also seems to be affected by the greater bond order.[137] Non-contact terms in unsaturated compounds can also play an important role in defining the total ^1J(CC) couplings. Several attempts at correlating the C–C bond order with the corresponding ^1J(CC) have been reported. For instance, ^1J(CC) couplings in 1- and 2-methylnaphthalene were found by Berger[199] to correlate linearly with the corresponding HMO bond orders. However, a similar attempt in azulene completely failed,[199] although the small value found for ^1J(CC) across the central bond in azulene (45.5 Hz) is in line with theoretical predictions, which indicate that this is a rather weak bond.[200] The linear relationship between ^1J(CC) and the π-bond order was employed by Fox and Schultz[201b] to study the twisting angle in the tetraphenylethylene dianion. ^1J(CC) and ^3J(CC) couplings have been measured in monosubstituted anilines and compared with SCPT–INDO-calculated values for the FC, PSO and SD terms. Non-additivities of ^1J(CC) couplings in p-substituted compounds were ascribed to mesomeric interactions of substituents.[201b] In nitrosamines ^1J(NN) couplings have been linearly correlated with the N–N π-bond order.[202]

For 2-fluorobiphenylene [1] the following two J(CF) long-range couplings, which are expected to be mainly transmitted through the π-electron system,

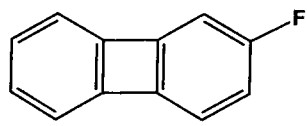

[1]

have been published: $^{6}J(C_7F) = 1.9$ Hz and $^{7}J(C_6F) = 1.2$ Hz (signs were not determined).[203] Similar long-range J(CF) couplings were reported by Sardella and Boger[204] in fluorinated benzo[a]pyrenes. In *trans*-4-fluorostilbene a ^{10}J(CF) coupling has been observed,[205] and the possibility discussed of using long-range couplings dominated by a π-transmitted component in binuclear fluorinated aromatic compounds to estimate conformations through their $\cos^2$ dependence. A similar dependence has been discussed by Fox and Scultz.[201]

Interligand J(CH) and J(CF) couplings in systems in which one of the bonds linking the coupled spins is formed mainly by π electrons have been reported in ref. 206.

3.1.2. The effect of hyperconjugation on spin–spin coupling constants

(i) Transmission of couplings through a hyperconjugative interaction. For planar unsaturated compounds with non-planar side-chain groups similar σ- and π-transmission mechanisms are expected for couplings involving side-chain atoms and an atom belonging to the unsaturated fragment. The most conspicuous case is toluene, and the corresponding long-range couplings are those of the methyl protons with those attached to the benzene ring, i.e. benzylic couplings.[186] The transmission of the spin information associated with the FC term takes place as a result of the hyperconjugative interaction between a side-chain σ bond and the π-electron system.[207] The hyperconjugative interaction depends on the dihedral angle θ between the bond and the planar unsaturated compound. The π-transmitted component follows the same trend:[186]

$$J^{\pi} = a + b \sin^2 \theta \tag{29}$$

Different approaches to determine the coefficients a and b in (29) have been proposed during the review period. One is to use any method to decompose calculated coupling constants in σ- and π-transmitted components, such as the PRMO[132] or IPPP[141] methods. Another approach is to use the NNBI method[128] to determine which is the component transmitted through the π-electron system. However, by far the most common is that of Schaefer *et al.*[208] Total FPT–INDO couplings are calculated for different θ values, and the resulting plot is fitted, including terms of $\cos^2 \theta$, $\sin^2 \theta$, and $\sin^2 \frac{1}{2}\theta$. As INDO-calculated coupling constants in some instances overestimate and in others underestimate some components, coefficients obtained in the fitting procedure are in general scaled to reproduce experimental values. However, some caution should be taken when applying this approach, since, although the π-transmitted component follows a $\sin^2 \theta$ dependence, not all terms with this behaviour correspond to a coupling transmitted through the

hyperconjugative interaction. This is, for instance, the case with some terms of the Karplus-like curve in $^4J^{\sigma}$(FH) couplings in fluoroderivatives of toluene.

Schaefer's group neglect systematically the coefficient a in (29), even when the FPT–INDO method yields a non-zero value. Such a result is considered to be an artifact of the computational approach. However, the possibility of a non-negligible a has been discussed in several papers.[209] For instance, such a term, apparently negative and about 0.1 Hz in magnitude, is thought to exist for $^6J^{\pi}$(HH) in styrene.[130] A more accurate value of -120 mHz for a has recently been reported.[210] For benzaldehyde a value of $+10$ mHz for a in $^6J^{\pi}$(HH) has been reported,[211] i.e. in this last case the coefficients a and b in (29) are of opposite signs, although in other cases both a and b follow the alternating sign rule. PRMO results[132] at the INDO level of approximation for J(HH) benzylic couplings in toluene closely follow (29) for $^4J^{\pi}$(HH), $^5J^{\pi}$(HH) and $^6J^{\pi}$(HH) components. While a and b for $^4J^{\pi}$(HH) are positive, those for $^3J^{\pi}$(HH) and $^5J^{\pi}$(HH) are negative, as expected from the alternating sign rule.

The coefficients a and b for benzylic couplings in derivatives of toluene show very low sensitivity to ring substitution. This supports the use of the J method[208] for studying side-chain conformation by accurately measuring benzylic couplings largely dominated by the J^{π} component. For instance, the coefficient b was estimated by Schaefer *et al.* to vary from -1.20 Hz in toluene[212] to -1.176 Hz in 3,5-difluorotoluene. Low sensitivity was also observed by Collins *et al.*[213] for $^4J(CH_3,H)$ interproton couplings in several substituted toluenes with different ring substituent patterns. However, they noted that ring substitution with methyl groups leads to a small decrease in the magnitude of $^4J(CH_3,H)$ couplings that is linearly related to the number of methyl groups attached to the benzene ring. This suggests that a kind of saturation of the hyperconjugative interaction takes place on increasing the number of methyl groups attached to the benzene ring.

The $^nJ^{\pi}$(HH) component of benzylic couplings is of approximately the same absolute value but opposite sign to the $^{n-1}J^{\pi}$(HH) coupling in the benzene derivative where the methyl group is replaced by an H atom. This is the well-known "methyl group replacement rule".[5] Unpublished PRMO–INDO results indicate that this approximate rule also holds for long-range J(HH) couplings in other unsaturated compounds.

Factors affecting the hyperconjugative interaction are expected to alter J^{π}. The following effects are worthy of comment. The π-bond order of the unsaturated fragment defines the magnitude of $^4J(CH_3,H)$ couplings. For instance, in *ortho*-benzylic couplings that component is smaller than in allylic couplings. This effect has been discussed from a theoretical point of view using the PRMO–INDO method.[214] Barfield *et al.*[215] used the magnitudes of *ortho*-benzylic couplings as a probe for determining the degree of bond fixation in aromatic systems. In a later paper from the same

laboratories[216] experimental $^4J(CH_3,H)$ values in a series of methyl-substituted aromatic hydrocarbons were related to the π-bond order of the corresponding C–C fragment. Experimental couplings correlate best with the square of the SCF MO bond orders and with the Pauling (VB) bond orders, as expected from theoretical considerations.[216] The correlation between $^4J(CH_3,H)$ couplings and the C–C π-bond orders was used by Karuso and Taylor[217] to determine the bond fixation in a series of 4-methylbenzo(*h*)quinolines and 4-methylbenzo(*h*)quinolin-2-ones. For *m*-methylbenzaldehyde Schaefer *et al.*[218] measured $^4J(CH_3,H_2) = -0.741$ Hz and $^4J(CH_3,H_4) = -0.697$ Hz. They also obtained the 6-31G optimized geometry for the O-*cis* and O-*trans* conformers, and found that the C_2-C_3 bond length is slightly shorter than the C_3-C_4 one, implying that the former presents a slightly larger bond order than the latter.

For cisoid allylic couplings an important sensitivity to substitution at the α carbon atom has been reported.[213] This apparently correlates with substituent electronegativity.[219] The total range of variation for this type of coupling is approximately a factor of 2. This sensitivity is much larger than that of substitution at the β carbon.[213] This trend is assumed to explain the differences in magnitude of $^4J(CH_3,H)$ couplings across the same bond observed in 2-methylfurans and α-picolines.[213] It is not yet clear how this substituent effect operates, and how much the σ and π components are affected. In furan a similar asymmetry for $^2J(CH)$ across the same bond was also observed for $^2J(C_3H_2) = 13.7$ Hz and $^2J(C_2H_3) = 11.03$ Hz.[220] This trend is reversed in thiophene, $^2J(C_3H_2) = 4.66$ Hz and $^2J(C_2H_3) = 7.61$ Hz[220] and in dithieno[*b*,*d*]pyridines.[221]

When a lone pair is proximate in space to a C–H bond, its electronic structure is modified, yielding a slight shortening in the bond length. This seems to decrease the hyperconjugative interaction of a methyl group proximate to a lone pair[222] such as in α-picoline. The smaller absolute value of $^6J(HH)$ couplings measured in derivatives of α-picoline compared with those in β-picolines[223] is in line with the reduction of the hyperconjugation owing to the proximity to the N lone pair. Such an effect should also operate in the $^4J(CH_3,H)$ coupling in 2-methylfuran and 2-methylthiophene.

A change in the hybridization of the C–H bond also affects the $J^\pi(HH)$ transmitted through the hyperconjugative interaction. The replacement of a methyl H proton by a more electronegative group yields a small reduction in the coefficient *b*. For $^6J^\pi(HH)$ couplings in toluene, $b = -1.20$ Hz,[212] while in ethylbenzene it is -1.16 Hz,[224] and in isopropylbenzene[225] and phenyl cyclohexane[226] it is -1.12 Hz. For other types of α substituents the following values have been reported: CH_2SiH_3, $b = -1.34$ Hz;[227] $CH_2Si(CH_3)_3$, $b = -1.26$ Hz;[228] CH_2OR, $b = -1.02$ Hz;[229–231] CH_2Cl, $b = -1.06$ Hz;[232] $CHCl_2$, $b = -0.98$ Hz;[233] $CH(OCOCH_3)_2$, $b = -0.93$ Hz;[209] and CH_2F, $b = -0.95$ Hz.[234] For fluorene the coefficient *b* for $^6J^\pi(HH)$ was estimated as -1.04 Hz,[235] and in indene as -0.88 Hz.[236] If these results are rationalized

in terms of Bent's rule,[237] it can be concluded that the greater the s character of a C–H bond, the lower is its ability to hyperconjugate with the aromatic ring. However, it is important to note that this is a rather small effect. A comparison of coefficients b for sp^3- and sp^2-hybridized C–H bonds can also shed some light on this effect, although the difference in the H–C_α–C(1) angle and the C_α–C(1) bond length should also affect b. For styrene Schaefer *et al.* estimated the b coefficient for $^6J^\pi$(HH) as -1.0 Hz[238,239] and for benzaldehyde as less than -0.4 Hz.[210,240] ^5J(HH) couplings with important J^π contributions originating in the hyperconjugation of C(sp^2)–H bonds have been reported by Neuenschwander *et al.*[241] in 10-dimethylaminononafulvene and in some heptafulvenes.[242]

Equation (29) also holds for J^π(CH)[243] and J^π(FH),[244] where in both cases H is a methyl proton, C corresponds to a ring carbon atom and F is a fluorine atom attached to the benzene ring. The main difference is that an inversion of the sign rule is observed in these two cases. The coefficients a and b are positive for an even number of bonds separating the coupled nuclei and negative for an odd number. This is in agreement with the fact that these coefficients are proportional to the corresponding hyperfine interaction coefficients.[186] The FPT–PRMO–INDO method correctly describes this trend,[245] and the calculated value of the total ^6J(FH) coupling in *p*-fluorotoluene is not far from the experimental one, although it is somewhat underestimated (the averaged FPT–INDO value is $+0.94$ Hz,[245] while the experimental value is 1.12 Hz[246]).

Experimental and FPT–INDO studies of ^4J(FH) and ^5J(FH) couplings in fluoroolefins have been reported by Barfield *et al.*[247]

For thiophenol the coefficient b in $^6J^\pi$(HH) was estimated as -0.97 Hz.[248]

The deuterium isotope effect on the hyperconjugation of a C–^{2}H/^{1}H bond has been discussed by Schaefer *et al.*[249]

σ-Type X–Y bonds where X and Y are other than hydrogen can also undergo a hyperconjugative interaction that defines a pathway for transmitting the FC spin information between the out-of-plane Y nucleus to a Z one belonging to the unsaturated fragment. The following cases are worthy of mention: the C–F bond in derivatives of benzotrifluoride;[250,251] the O–C(sp^3) bond in anisole derivatives;[252–256] the S–C(sp^3) bond in methyl phenyl sulphides[257] and thioanisoles;[258] the O–C(sp^2) bond in diphenyl ethers[259] and phenyl esters;[260] the C(sp^3)–C(sp^3) bond in α-alkyl derivatives of toluene;[261,224] the C(sp^3)–C(sp^2) bond in phenylacetaldehyde[262] and α-methylstyrene;[263] the C(sp^2)–C(sp^2) bond in biphenyls;[264] the S–Sn(sp^3) and C(sp^3)–Sn(sp^3) bonds in benzyltin compounds of the types $(CH_3)_3SnSPh_2$ and $(PhCH_2)_3SnCl$;[265] and the C(sp^3)–P^{III} bond in bis(diethoxyphosphinomethyl)naphthalenes.[266] Schaefer *et al.*,[253] using the methyl group replacement rule, verified experimentally that $^6J(CH_3,H)$ in anisole is mainly transmitted through the aromatic π system. Therefore in these compounds long-range ^6J(CX) (X = H, F attached to the ring) and

Table 13. Coefficients b in (29) for $^5J(C(sp^3)C_4)$ couplings originating from a hyperconjugative interaction of an X–C(sp^3) bond (X = O, S, Se, Te) with X attached to an aromatic ring.

X	b (Hz)
O	0.98[a]
S	0.91[b]
Se	0.62[c]
Te	0.50[c]

[a]From ref. 268.
[b]From ref. 258a.
[c]From ref. 269.

$^5J(CC_4)$ couplings can be used as probes to detect the side-chain conformation. Another example is 2-methoxypyridine, where the lack of that type of coupling was used by Wildman *et al.*[267] to assess the planarity of the OMe conformation. In Table 13 the coefficients b for $^5J(C(sp^3)C_4)$ couplings originating from a hyperconjugative interaction of an X–C(sp^3) bond (X = O, S, Se, Te) and an aromatic ring are compared for different members of this series.

An electronegative substituent attached to the $^{13}C_\beta$ coupled nucleus of the side chain yields an increase in the coefficient b. Such an increase is simply interpreted in terms of the CLOPPA approach.[148] Although the hyperconjugative effect appears through the polarization propagator term,[149] the perturbations at the site of the coupled nuclei also influence the total coupling. The perturbation at the C_β carbon should increase when an electronegative group is attached to it, since, according to Bent's rule,[237] such a substituent increases the $C_\beta(s)$ character of the $X_\alpha-C_\beta$ bond.

In the case of a C(sp^2)–C(sp^2) bond undergoing a hyperconjugative interaction, there can also be a conjugative effect between both π-electron systems. In that case couplings involving the $C_\beta(sp^2)$ carbon can have an important π component transmitted through that conjugative effect. This is, for instance, the case in 4-fluorostyrene,[261] where the magnitude of $^6J(CF)$ decreases as the vinyl group twists out of the benzene plane.

Long-range $J(FH)$ couplings originating from the hyperconjugation of a C–F bond have been studied using the PRMO–INDO method[245] in α-fluorotoluenes. The $J^\pi(FH)$ component closely follows (29) with the same alternating sign rule as for $J^\pi(HH)$ couplings. The corresponding coefficients a and b depend on the substitution in the fluoromethyl group. For instance, while in α-fluorotoluene (benzyl fluoride) $a = 0.043$ Hz and $b = -3.089$ Hz, in α,α,α-trifluorotoluene (benzotrifluoride) $a = -0.001$ Hz and $b = -2.472$ Hz. As pointed out above for C–H bonds, α substitution with an electronegative group reduces the coefficient b corresponding to the C–F bond that undergoes hyperconjugation. Again, resorting to Bent's rule,[237] it

seems that the hyperconjugative interaction of a C–F bond is stronger the greater its C(p) character. However, these values should be taken only as indicative of the sensitivity to side-chain substitution, since the FPT–INDO method overestimates this component.[251] These latter J^{π}(FH) coefficients *b* also seem to be more sensitive to the presence of ring substituents than those of $^{6}J^{\pi}$(HH) in toluene derivatives.[251]

A point that is not yet fully understood is the extent to which the hyperconjugative interaction undergone by an X–Y bond of a side-chain group affects the transmission of spin information of long-range couplings involving an X atom attached to an unsaturated fragment. For instance, it is not known how much the hyperconjugative interaction affects the five-bond $J(C_{\alpha}H)$ coupling in toluene. In 2-methylnaphthalene $^{3}J(CH_3,H_{(1)}) = 5.1$ Hz and $^{3}J(CH_3,H_{(3)}) = 4.1$ Hz,[155] i.e. the vicinal coupling involving in its pathway the C–C bond with higher π-bond order is larger than that involving the C–C bond with lower π-bond order. The large long-range couplings observed for other types of groups that also undergo a hyperconjugative interaction suggest that the side chain X–Y bond hyperconjugation constitutes a pathway for transmitting the spin information from the in-plane X atom to, for instance, the aromatic ring protons. A few examples are as follows: in 1-$SnCl_3$-toluene, $^{3}J(SnH) = -120.81$ Hz, $^{4}J(SnH) = -51.68$ Hz and $^{5}J(SnH) = -17.73$ Hz.[270] In 1-$TlCl_2$-naphthalene $^{3}J(TlH_{(2)}) = +948$ Hz; $^{4}J(TlH_{(3)}) = +287$ Hz and $^{5}J(TlH_{(4)}) = +118$ Hz.[171] If this last coupling is compared with $^{6}J(TlH_{Me}) = +58$ Hz in 1-$TlCl_2$-4,7-dimethylnaphthalene,[171] the methyl group replacement rule suggests that $^{5}J^{\pi}(Tl,H_{(4)}) \approx -58$ Hz in 1-$TlCl_2$-naphthalene, which indicates that the alternating sign rule yields a negative π component when the number of bonds separating the coupled nuclei is odd.

Apparently, the hyperconjugative interaction of an X–Y (σ-type bond may also constitute a pathway for transmitting spin information between an H atom attached to Y and atoms belonging to the unsaturated fragment. This is the case, for instance, for phenyl formate, where Schaefer *et al.*[271] reported $^{7}J(H_4,CHO) = +0.051$ Hz. They investigated the pathway by means of detailed FPT–INDO calculations for different angles θ and ψ, which yield an adequate dependence on θ, agreeing fairly well with the experimental value. This pathway was also experimentally verified by the methyl group replacement rule, since in *p*-tolyl formate they reported $^{8}J(CH_3,CHO) = -0.031$ Hz.[271]

Allylic ^{4}J(CH) couplings have been calculated at the SCPT–INDO level and compared with experimental values in monoterpene derivatives.[272]

(ii) Effect of the hyperconjugative interaction on coupling constants

(a) One-bond couplings. The way in which the hyperconjugative interaction of a σ-type bond affects its electronic structure has been studied

extensively for C–H bonds. It is known[273,274] that lengthening of a C–H bond takes place when the hyperconjugative interaction is increased. As one-bond couplings are dominated by the FC term, which reflects the electronic structure of the corresponding bond, it can be expected that when a hyperconjugative interaction takes place, its coupling must also be affected. Although during the review period no detailed study has been published, several reported experimental values indicate that this effect may be important enough to constitute an interesting probe to study conformations. Large differences were observed for C–H methylene protons placed α to a carbonyl group. However, it is important to recall that for configurations of this type the orientation of a C–H bond with respect to the carbonyl oxygen lone pairs should also be important in defining the actual value of the corresponding ^1J(CH) coupling. A few examples are as follows. In the compound [2] two different ^1J(CH) couplings involving the methylene protons have been reported:[275] $^1J(CH_{8(1)}) = 125.0 \pm 0.07$ Hz and $^1J(CH_{8(2)}) = 120.2 \pm 0.07$ Hz. In prazepam [3] a very large difference between $^1J(C_3H_A)$ and $^1J(C_3H_B)$ has been reported, 131.5 and 152.2 Hz respectively.[276] In this compound not only the orientation of the C–H bond with respect to the carbonyl O lone pairs but the orientation with respect to the N lone pair could also play an important role in defining such a large

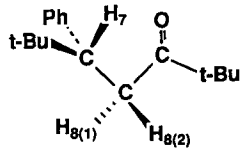

[2]

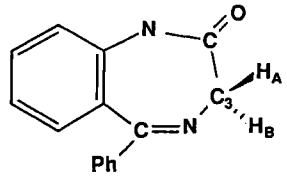

[3]

difference. In cyclobutanone [4] the methylene ^1J(CH) couplings for the α and β positions are also different, namely $^1J(C_\alpha H_\alpha) = 132$ Hz and $^1J(C_\beta H_\beta) = 138$ Hz.[277] In 3,5-dimethyl-4-methoxybenzaldehyde ^1J(C=O, H) = 155.98 Hz for a planar conformation and 151.21 Hz for a perpendicular CHO conformation.[278]

The extent to which the one-bond coupling in other types of σ bonds

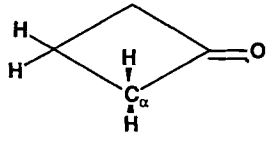

[4]

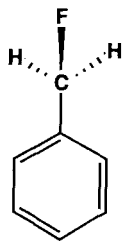

[5]

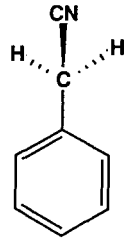

[6]

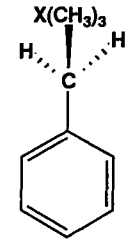

[7]

attached in the α position to a π-electron system is affected by the hyperconjugative interaction has not yet been studied systematically. Several experimental values indicate that such an effect can be very important. This is, for instance, the case for the ^1J(CF) coupling in benzyl fluoride [**5**], which ranges from −170.52 Hz in CS_2 to −161.92 Hz in DMSO.[234] The greater polarity of the latter solvent stabilizes the conformation [**5**], increasing the hyperconjugative interaction between the C−F bond and the aromatic π-electron system. The FPT–INDO-calculated FC term of this ^1J(CF) shows the opposite trend, i.e. its absolute value increases when increasing θ,[234] suggesting that the experimental trend should be defined by the dependence on θ of non-contact contributions. According to the CLOPPA description, ^1J(CF) couplings are negative, since their "lone pair contributions" are greater than their "bond contribution". The latter is always positive (provided that both magnetogyric ratios are of the same sign). Therefore the Schaefer *et al.*[234] FPT–INDO calculations suggest that the bond contribution is reduced on increasing the hyperconjugative interaction, in agreement with the trend followed by ^1J(CH) couplings.

Hyperconjugative interactions are larger for a C−C bond than for a C−H one.[279] Therefore that interaction should also affect ^1J(CC) couplings. In benzyl cyanide [**6**] Schaefer and Penner[280] found that the experimental value of $^1J(C_\alpha,C{\equiv}N)$ decreases on increasing the polarity of the solvent. Polar solutions stabilize a conformation like that depicted in [**6**]. Therefore the increase in the hyperconjugative interaction reduces that coupling. FPT–INDO calculations of its FC term reproduce this trend, giving a smaller $^1J(C_\alpha,C{\equiv}N)$ coupling on increasing θ.[281]

The hyperconjugative interaction between C_α−X bonds (X = Si, Ge, Sn, Pb) with a π-electron system is so important that it determines the preferential conformation about the $C_\alpha-C_{ipso}$ bond in compounds of the type [**7**] with X = Si, Ge, Sn, Pb.[282] This was verified by Schaefer *et al.*[227] using the *J* method for $^6J(CH_2,H_6)$ couplings in benzylsilane. In derivatives of [**7**] (X = Sn) (benzyltin compounds), as well as in allyltin compounds, $|^1J(C_\alpha Sn)|$ is generally lower that those of most organotin(IV) compounds.[283–285] This trend is ascribed to the hyperconjugative interaction

between the $C_\alpha-Sn$ bond and the π-electron system.[286] A quantitative estimation of the hyperconjugative interaction effect on this type of coupling was made by comparing the effects of polar substituents or of a ligand on tribenzyltin and analogous n-butyltin compounds. Such a comparison leads to a correlation (J in Hz) given by $^1J(SnC)[Bz_3Sn)] = (1.12 \pm 0.01)^1J(SnC)[n\text{-}Bu_3Sn] - (91.91) \pm 4.61$, (in Hz) with a correlation coefficient $r = 0.999$.[283] The intercept shows, on one hand, that the hyperconjugative interaction of an Sn–C bond reduces the absolute value of the corresponding $^1J(SnC)$ couplings. On the other hand, since the slope is larger than one, $^1J(SnC)$ couplings increase more rapidly in benzyltin than in n-butyltin compounds. The hyperconjugative effect can explain, at least in part, the difference between $|^1J(Sn,CH_3)| = 326$ Hz and $|^1J(Sn,C_\alpha)| = 294$ Hz in **[7]** with X = Sn, reported by Schaefer *et al.*[228] A very small coupling constant, $^1J(SnC) = 125$ Hz, has been reported in *C*-stannylmethyleneborane, corresponding to the $Sn-C(sp^2)$ bond, which is assumed to undergo a strong hyperconjugative interaction.[287] A comparison between $^1J(SnC_{(sp^2)})$ in alkene and allene tin derivatives shows that in the latter the absolute value of the coupling is notably smaller than in the former. For allene derivatives values of -222.6 Hz[288] and -296.0 Hz[289] have been reported. For alkene derivatives a value of -478.4 Hz has been reported.[290]

(b) Geminal couplings. Geminal couplings are notably affected by hyperconjugative interactions acting on the respective C–H bonds. This is the case when both H atoms are attached to a carbon atom placed α to a π-electron system. $^2J(HH)$ depends on $\cos^2\phi$, where ϕ is the rotation angle of these C–H bonds around the C_1-C_α bond.[291] This dependence makes these geminal couplings interesting probes for analysing that structural feature.[292,293] For glycyl residues in peptides Barfield *et al.*,[294,295] using the FPT–INDO method, studied the dependence on the backbone torsional angles ϕ and φ. Wong and Clark[296] established the following empirical relation between $^2J(HH)$ and the C(1)–C(2)–C(3)–C(4) torsion angle ϕ for protons placed α to the carbonyl group:

$$^2J(HH)\,(\text{in Hz}) = -12.6 - 6.0\cos^2\phi. \qquad (30)$$

At this point it is important to recall that for a carbonyl group the C–H orientation with respect to the carbonyl oxygen lone pairs can also important role in defining (30). This latter effect is expected to be mainly a proximity effect, while the hyperconjugative effect is expected to be both a proximity effect and a transmission through the π-electron system.[189] Wong *et al.*[296] found that, although the SOS–INDO-calculated couplings are far smaller than the experimental values, they follow the same trend as the measured values. As the SOS–INDO method[117] does not take into account the π-transmitted component, this could, on the one hand, explain the small

calculated values, and, on the other, it suggests that the proximity effects on ^2J(HH) follow the same trend as the hyperconjugative effect.

For methylene protons placed α to a C=C double bond, values as large (in absolute value) as -24 Hz have been reported[297] for cyclohexenes annellated to bicyclo(2.2.1)hept-2-enes, which are notably larger (in absolute value) than, for instance, those reported by Hunter *et al.*[298] in various 4-chlorocyclopentenes, *ca.* -16 Hz.

Mohanakrishnan and Easwaran[299] used the Dirac vector model and the Penny–Dirac bond order formulation for studying the dependence upon hyperconjugation of geminal J(C=O,H) couplings. Contributions transmitted through the π-electron system and the σ framework were calculated separately. The σ contribution shows a very small angular variation. The angular dependence of the total ^2J(CH) coupling can be expressed as

$$^2J(\mathrm{CH}) = A + B\cos^2(\phi + 90°), \tag{31}$$

where ϕ is the torsional angle between the C–H and C=O bonds.

3.1.3. Stereospecific aspects of the σ-transmitted component in unsaturated and saturated compounds

Perhaps the most quoted paper using coupling constants to elucidate conformational problems is that of Karplus,[300a] describing ^3J(HH) couplings as a function of the dihedral angle. Since this pioneering paper, a great deal of work has been reported on the angular dependence of coupling constants involving different nuclei. A comprehensive review of these topics has been published by Bystrov,[300b] and theoretical developments have been reported by Kowalewski[4,5] when describing calculations of couplings. The general use of J couplings in conformational problems is reviewed annually in the chapters on applications of spin–spin coupling constants and on conformational analysis in the *Specialist Periodical Reports, Nuclear Magnetic Resonance* series, edited by G. A. Webb and published by The Royal Society of Chemistry.

In this section some relevant contributions to the understanding of the conformational dependence of couplings transmitted through a pathway defined by an arrangement of σ bonds published during the last 10 years are reviewed. However, this is not a comprehensive listing of works published in this field, since the length of this work has to be kept within reasonable limits. Reviews dealing with specific types of coupled nuclei in general describe this problem in some detail. This is the case, for instance, for Marshall's work on J(CC) and J(CH) couplings,[155] Hansen's review of J(CH) couplings[156] and Krivdin and Della's review of J(CC) couplings.[154]

The σ-transmitted component of the FC interaction is known[186] to have strong stereospecific characteristics. The best known of these are the

cis–trans difference, the "W" rule, and the extended zig-zag path. The last two cases are very efficient pathways for transmitting FC spin information in long-range couplings, and in many instances they are used to determine conformations and configurations. When extending these ideas to couplings involving nuclei other than protons, some caution should be taken. Several couplings for a *cis* conformation have been reported as being larger than for a *trans* one. A significant through-space contribution may contribute to the former, as discussed in Section 3.3. The "anti-Karplus" behaviour of Schaefer *et al.* should also be quoted; in 2-*X*-thioanisoles, where the SCH_3 group preferentially adopts a *cis* conformation with respect to the ring position 6, $^3J(CH_3,C_2) < {}^3J(CH_3,C_6)$, i.e. the *cis–trans* relationship is altered by the substituent attached to the coupled nucleus.[258a] Although not on a quantitative basis, FPT–INDO calculations correctly reproduce this trend. The "anti-Karplus" denomination is somewhat misleading, since it refers to a case where the *cis* and *trans* pathways are not equivalent because for the *trans* arrangement a substituent is attached to one of the coupled nuclei. Exceptions to the *cis–trans* relationship can also be observed when there is more than one pathway connecting both coupled nuclei.

One of the points that is not yet settled is how much non-contact contributions participate in defining the *cis–trans* difference. A few calculations published during the review period indicate that the PSO and SD terms lead to important stereospecific properties. For instance, ^3J(SeSe) couplings calculated at the RPA–INDO level for the *trans* and *cis* isomers of 1,2-bis(methylseleno)ethylene are PSO = −21.03 and −86.89 Hz respectively, and SD = 1.38 and 14.46 Hz respectively.[120] As only total couplings can be measured experimentally it is important to assess whether non-contact contributions can alter the *cis–trans* relationship, especially in heavy nuclei. Recently, Kupče *et al.*[301] reported $|^3J_{trans}| > |^3J_{cis}|$ for ^3J(SnC), ^3J(SnN) and ^3J(SiN).

The dependence of the *trans* ^3J(CXCH) couplings on the CXC angle has been studied in benzene, pyridine and 2-pyridone using the IPPP–INDO method.[302] Such a dependence allows one to consider $^3J(C_2H_6)$ couplings as probes to differentiate -ine and -one structures.[303]

In olefins of type $CH_2{=}C(CH_3)R$ it was found[304] that $|^4J^{transoid}(HH)| < |^4J^{cisoid}(HH)|$. Apparently, a negative J^{TS}(HH) component arises in the latter. A similar relationship holds for ^4J(FF) couplings in $F_3CN{=}CF_2$.[305]

Barfield *et al.*[306] have studied the molecular association effect on the structural dependence of five-bond couplings in $H{-}C_\alpha{-}C(O){-}N{-}C_\alpha{-}H$ peptide moieties, calculating the J surface, $J(\theta,\rho)$, for *cis-* and *trans-N*-methylacetamide and in the cyclic dipeptides cyclo-(Gly–Gly) and cyclo-(Gly–Tyr) using the FPT–INDO method. Additional calculations in hydrated systems have also been performed, showing that the conformational dependence of $^5J(H{-}C_\alpha{-}C(O){-}N{-}C_\alpha{-}H)$ is more complicated than previous-

ly proposed,[307] since both the value and the sign of those couplings depend strongly on the electronic characteristics of the amine group, which are affected by environmental changes, rendering them solvent-dependent.

A detailed theoretical study of the dihedral-angle dependence of ^3J(CC) couplings in saturated and unsaturated fragments was undertaken by Severson and Maciel.[308] They found that for conjugated systems the SD term strongly depends on the dihedral angle. In order to study different transmission pathways, they set equal to zero some selected exchange integrals in the SCPT–INDO calculations.

The importance of the α-substituent effect on ^3J(CC) couplings in a series of 2,2-dimethylcyclopropanes has been studied[309] with the FPT–INDO method and compared with experimental data obtained in $^{13}C_1$-labelled compounds. Calculations of the FC term are in good agreement with the experimental values. When they are compared with NNBI–FPT–INDO calculations, it is concluded that the most important contributions to ^3J(CC)(0°) arise from non-bonded interactions. Consequently, the largest ^3J(CC)(0°) values are observed for primary alcohols and the smallest ones for tertiary alcohols, which have no hydrogen bonded directly to the coupled carbons.

The conformational and substituent dependence of ^4J(CC) couplings was studied by measuring those couplings in ^{13}C-enriched 1- and 2-substituted adamantanes and 2-bornanes, and by FPT–INDO calculations in pentane, 1-pentanol and pentanoic acid.[310] Depending on the orientation of bonds connecting the coupled nuclei, values ranging from 0.1 to 0.73 Hz were measured, and the largest values were observed for conformations for which the coupled nuclei are in close proximity to each other. The FPT–INDO-calculated ^4J(CC) surface for pentane is displayed in Fig. 2.

A similar study of ^2J(CC) couplings was reported in ref. 311. Although the FPT–INDO method reproduces some qualitative trends observed on those couplings, it fails to reproduce their magnitude quantitatively, since they are calculated as 5–6 Hz too negative, perhaps owing to neglect of non-contact contributions.

A comprehensive study of ^3J(C(O)–N–C_α–C) and ^3J(C(O)–N–C_α–H) couplings was presented by Kao and Barfield[312] using ^{13}C-labelled lactams and amines as model compounds for peptides. The experimental values can be fitted by a three-term expansion in terms of the dihedral C(O)−N−C−C angle θ as

$$^3J(\mathrm{CC}')(\theta) = 1.84\cos^2\theta - 0.23\cos\theta + 0.51 \quad \text{(in Hz)}, \tag{32}$$

while

$$^3J(\mathrm{CH})(\theta') = 3.96\cos^2\theta' - 1.83\cos\theta' + 0.81 \quad \text{(in Hz)}, \tag{33}$$

where θ' is the dihedral angle C(O)−N−C_α−H.

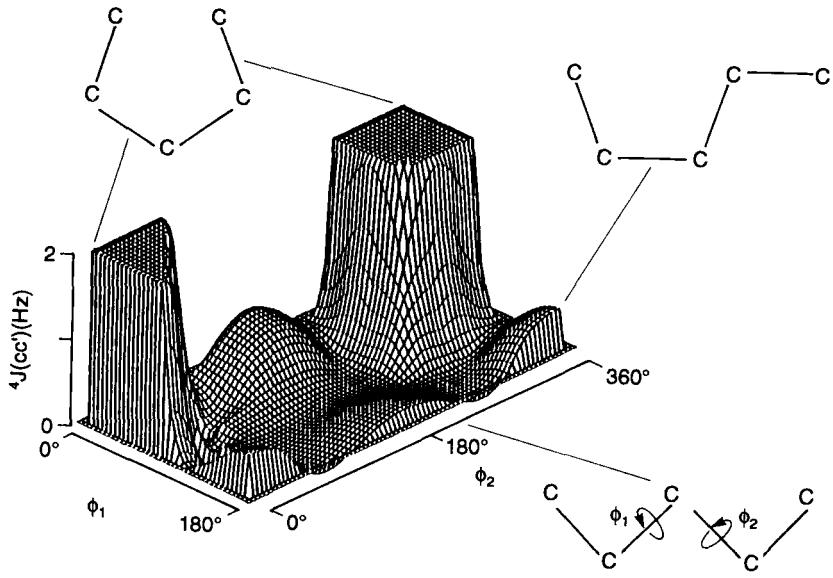

Fig. 2. Plot of calculated FPT–INDO values of the FC term of $^4J(CC')$ in pentane as a function of the dihedral angles ϕ_1 and ϕ_2. Reproduced, with permission, from ref. 310.

FPT–INDO calculations for *cis*- and *trans*-acetamide reproduce quite well the experimental trend of $^3J(CH)$ couplings, but fail to reproduce the experimental trend of $^3J(CC)$ couplings.

A new analytical derivation, using a simple molecular orbital model, for the dependence of $^3J(HH')$ couplings on the torsional angle ϕ, including the effects of the H–C–C and C–C–H′ angles θ_1 and θ_2 respectively, was given by Barfield and Smith:[313]

$$^3J(HH')(\theta_1, \theta_2, \phi) = C_a a(\theta_1, \theta_2) \cos^2 \phi + \sum_i C_{bi} b_i(\theta_1, \theta_2) \cos \phi + C, \quad (34)$$

where

$$a(\theta_1, \theta_2) = (1 + \cos \theta_1)(1 + \cos \theta_2),$$

$$b_1(\theta_1, \theta_2) = \cot \tfrac{1}{2}\theta_1 \cot \tfrac{1}{2}\theta_2 \cos \theta_1 \cos \theta_2,$$

$$b_2(\theta_1, \theta_2) = \cot \tfrac{1}{2}\theta_1 \cot \tfrac{1}{2}\theta_2 (\cos \theta_1 \cos \theta_2)^{1/2},$$

$$b_3(\theta_1, \theta_2) = \cot \tfrac{1}{2}\theta_1 \cot \tfrac{1}{2}\theta_2 [\cos \theta_2 (-\cos \theta_1)^{1/2} + \cos \theta_1 (-\cos \theta_2)^{1/2}].$$

Table 14. Coefficients in (32) obtained for ethanic, ethylenic, allylic and diene moieties.[a]

	CHCH	CH=CH	C=CHCH	C=CHCH=C
a (Hz)	33.8	41.1	23.8	17.5
C_{b1} (Hz)	−1258.4	−752.8	−183.0	−1949
C_{b2} (Hz)	−650.5	−406.06	−21.7	−883.3
C_{b3} (Hz)	−905.3	−541.6	−67.9	−1302
C (Hz)	−0.3	1.9	1.2	3.7
r^b	0.974	0.982	0.9998	0.989
σ^c (Hz)	0.5	0.6	0.1	0.4

[a]From ref. 313.
[b]Correlation coefficient.
[c]Standard deviation.

The coefficients in (34) were evaluated using empirical data and angular data from *ab initio* MO and molecular-mechanics optimized structures for couplings in ethanic, ethylenic, allylic and diene moieties. The parameters thus obtained are displayed in Table 14.

The effect of substituents and of the interactions between them on the Karplus curve was studied in several papers during the review period. Diez *et al.*[314] expressed ^3J(HH) couplings as a truncated Fourier series in the torsional angle, where independent terms are used to describe the angular dependence in ethane, and linear and quadratic terms for substituent and substituent interaction effects respectively. The empirical parameters were estimated using 3132 vicinal couplings calculated with the FPT–INDO method.[315]

Revised versions of the Karplus equation have also been presented in refs 316, 317. In the first the shortcomings of several Karplus relations were reviewed and new formulae proposed to take into account the electronegativity effect of a substituent. Both Fourier and electronegativity parameters were optimized using a large set of 1404 ^3J(HH) couplings, calculated using the EHT method. In ref. 317 the same issues were addressed by studying new experimental ^3J(HH) values measured at 300 MHz for a series of mono- and 1,1′-disubstituted ethanes. The results thus obtained show that it is possible to use modified Karplus relationships to describe the electronegativity dependence of ^3J(HH) couplings, but it is necessary to use a scale of substituent or electronegativity parameters λ derived for this purpose. λ values for 50 different chemical groups are presented in ref. 317.

Another empirical extension of the Karplus equation was presented by Imai and Ōsawa[318] using 198 ^3J(HH) couplings measured in non-polar solvents for compounds with rigid structures. $^3J(HNC_\alpha H)$ and $^3J(C'NC_\alpha H)$ were measured and fitted to a Karplus-like relationship for *N*-acetyl-*N*′-

methylamides of aliphatic aminoacids Gly, Ale, Leu, Ile and t-Leu. The effect of the torsion angles ϕ and χ_1 on the J(HH) couplings of hen lysozyme in solution were reported by Smith *et al.*[319]

FPT–INDO and EHMO/VB calculations carried out by Barfield *et al.*[127] for ^4J(HH) couplings for different HCCCH dihedral angles were fitted by Abraham and Fisher[320] with the equation

$$^4J(\mathrm{HH}) = a\exp[-2(2+\cos\phi_1+\cos\phi_2)] - b\cos\phi_1\cos\phi_2 - C, \qquad (35)$$

with different coefficients for FPT–INDO and EHMO/VB couplings. They compared couplings thus obtained with those measured in norbornene. Only moderate agreement was found. Apparently, contributions from more than one pathway affected the overall agreement.

^3J(CH) couplings in substituted norbornanes have been used to reinvestigate the corresponding Karplus-like relationship.[321] Geometries were obtained from molecular mechanics calculations, and the α-substituent effect on those couplings was estimated with the FPT–INDO method. Deviations of the Karplus-type curve for ^3J(CH) couplings through the cyclopropane framework in 3-carene have been quoted by Denisov *et al.*[272]

A Karplus-type relationship for ^3J(FH) couplings has been discussed and applied in several papers,[322–325] as has also been done for ^3J(SiH).[326,327]

Karplus-like relationships for couplings involving a P nucleus have also been studied.[328,329] Considering 10 oligoribonucleoside phosphates, the following relationships were obtained:[328]

$$^3J(\mathrm{CCOP}) = 6.9\cos^2\phi - 3.4\cos\phi + 0.7 \quad (\text{in Hz}), \qquad (36)$$

$$^3J(\mathrm{HCOP}) = 15.3\cos^2\phi - 6.1\cos\phi + 1.6 \quad (\text{in Hz}). \qquad (37)$$

α,β-Diphosphonates with either norbornane or cyclohexane skeletons[329] yielded a series of Karplus-like equations of the form

$$^3J(\mathrm{PP}) = A + B\cos\phi + C\cos 2\phi + D\cos 3\phi, \qquad (38)$$

where the empirical parameters are different for esters, acids and anions. The respective parameters are given in Table 15.

^3J(PCCC) couplings in phosphonic acid esters[329] are reproduced by the equation

$$^3J(\mathrm{PCCC}) = 7.23 - 5.41\cos\phi + 6.29\cos 2\phi \quad (\text{in Hz}). \qquad (39)$$

For the ^3J(PNCC) couplings the Karplus-like curve is affected by both the pyramidality at the N atom and the P–N bond length.[330]

The Leiden conformational group has reported extensive use of Karplus-

Table 15. Empirical parameters for the Karplus-like relationship (38) determined in esters, acids and anions for ^3J(PP) couplings.[a]

Parameter	Esters	Acids	Anions
A (Hz)	32.06	31.85	23.40
B (Hz)	−28.49	−25.12	−19.22
C (Hz)	29.41	30.05	22.25
D (Hz)	−3.53	−1.79	−2.07

[a]From ref. 329.

like equations to elucidate oligonucleotide structures in solution. This work has recently been reviewed by Altona.[331] Readers are referred to that review and to the references cited therein for further details.

Only a few additional papers in which Karplus-like relationships were applied to determine structures in biological compounds will be quoted as examples.

Tvaroška *et al.*[332–334] studied conformations in oligosaccharides.

Some examples of Karplus-like relationships involving heavy nuclei are for ^3J(SnC),[335–337] ^3J(PtNCC),[338] ^3J(HgC)[339] and ^3J(TlH).[340]

The stereospecific properties of longer-range couplings mainly transmitted by the σ-electron framework were used rather extensively during the review period to study conformations. A few examples are quoted here. The ^5J(HH) coupling involving the formyl proton in compounds with a CHO group side chain is one of the "classical" examples. It has been applied by Salman[341] to study the relative populations of the SO-*cis* and SO-*trans* conformers in thiophene-2-carbaldehyde. Theoretical values were calculated by Salman[341] using the FPT–CNDO/2 method. Salman[342] applied a similar approach for determining the preferential conformation of the OH group in 1- and 2-naphthols. In both compounds he found that the OH group prefers a conformation *cis* to the C−C bond, with a larger mobile bond order. ^5J(OH,H) couplings were also considered by Laatikainen *et al.*[230] when studying conformations in salicyl alcohol and by Schaefer *et al.*[343] in 2-t-butylphenol derivatives. In substituted benzaldehydes this type of coupling was studied by Kolehmainen *et al.*[344] and Schaefer *et al.*[345,346] ^5J(HH) couplings with a similar pathway were analysed by Dandárova *et al.*[347] in a study of conformations in 2-furyl- and 2-thienylethylene derivatives and by Benasi *et al.* in formyl derivatives of furan and thiophene[348] and of benzo[*b*]thiophene.[349] Extensive studies of the conformational dependence of ^4J(CHO,CHO) and ^3J(CHO,CHO) couplings in methylenemalonaldehyde were carried out by Laatikainen and Král[350] with the FPT–INDO method. The nature of the factors contributing to the maximum value was analysed with both the NNBI and PRMO approaches and with a combina-

tion. When applying the FPT–INDO method in that particular carbonyl compound, Laatikainen and Král[350] met convergence problems.

3.2. The lone pair effect on coupling constants

A systematic and careful review of the effect of lone pairs on nuclear spin–spin coupling constants has been given by Gil and von Philipsborn.[13] This description includes different configurations between the coupled nuclei and the lone pair, as well as different types of couplings. Jameson[179] has given a brief and clear account of how lone pairs in configurations A.1 **[8]** and A.2 **[9]** (cf. ref. 13) affect the reduced coupling constant $^1K(AB)$.

[8] **[9]**

From a theoretical point of view, two different approaches have been followed to study the effect of the orientation of lone pairs on couplings. In the first, couplings were calculated for different configurations between the lone pairs and the coupled nuclei. This is the case with the calculations reported by Schulman and Lee[351] and Duangthai and Webb.[352] The second approach consisted in decomposing couplings in different electronic transmission mechanisms, analysing how the orientation of the lone pair affects each of them. A short overview of the application of the CLOPPA method to the study of several types of lone pair contributions is given in ref. 353.

Although the lone pair effect has been studied extensively, there are many questions that remain unanswered. For instance, it is not very clear to what extent non-contact terms contribute to the observed orientational effects, and how the lone pair effect varies for different types of atoms. A comparison of this type is not easy to make, since it is difficult to isolate these effects from others. For instance, when comparing the lone pair effect in similar compounds containing different heteroatoms from the same group of the Periodic Table, the orientation as well as the geometrical distance to the coupled nuclei may also play an important role. A few CLOPPA studies of the lone pair effect are exemplified in the following subsections. For simplicity the convention followed in ref. 13 will be used.

The proximity to a lone pair may affect a given coupling by (a) affecting the ground state wave function, and (b) participating in the virtual excitations that define a second-order property according to the perturbation theory. While the former will be discussed in Section 3.4, the latter is

considered here. However, it is important to note that both phenomena may play a role simultaneously in defining the total trend.

3.2.1. *Directly bonded nuclei*

(i) The A.1 configuration. Perhaps the best examples where the lone pair effect can be studied using the CLOPPA scheme are those cases with an A.1 configuration [**8**]. Moreover the analysis of the A.1 case may shed some light on more complicated cases such as an A.2 configuration [**9**] or one where atom B bears more than one lone pair. Jameson[179] described qualitatively the A.1 case [**8**]. The lone pair makes a negative contribution to ^1K(AB), which increases in magnitude for heavier atoms. The simplest example is ^1K(XH) in the hydrides along the Periodic Table. A comparison of ^1K(XH) and $^1K'$(XH) for the following hydrides is given by Gil and von Philipsborn:[13] BH_4^-, CH_4, NH_3, NH_4^+, H_2O, H_3O^+, HF, SiH_4, PH_4^+, PH_3, PH_2^-, SH_2, ClH, SnH_4, SnH_3^-, AsH_3 and AsH_4^+. In all cases ^1K(XH) has been considered to be positive, but, owing to the increase in the negative lone pair contribution on increasing atomic number, a sign reversal is possible in ^1K(XH). According to the RPA–MNDO method, the sign reversal for the FC contribution takes place for SnH_3^-.[51] A preliminary account of the CLOPPA analysis of such effect has also been given.[51] A more detailed description of the main contributions to ^1K(XH) in the Group IV hydrides and their anions is given in ref. 354. The results can be summarized as follows. In this type of compounds the CLOPPA description of ^1K(XH), (25), corresponding to its FC analysis, is overwhelmingly dominated by two different types of $K_{ia,jb}$ terms, namely that corresponding to $i = j$ = LMO, representing the X–H bond containing the coupled nuclei, and $a = b$ = LMO, representing the corresponding antibonding orbital. Hereinafter this is called the "bond" contribution $^1K^{\mathrm{b}}$(XH); it is always positive. The other important type of $^1K_{ia,jb}$ term in (25) is that in which i = LMO, corresponding to the bond containing the coupled nuclei, j is another LMO-attached atom X, and $a = b$ = LMO, representing the antibonding orbital of i. In the Group IV hydrides XH_4 j corresponds to an X–H bond other than that containing the coupled nuclei. The corresponding contribution to the FC term is hereinafter called the "other-bond contribution" $^1K^{\mathrm{ob}}$(XH); it is always negative. In the Group IV anions XH_3^- the LMO j can be either the "other bond" or the "lone pair", with contributions $^1K^{\mathrm{ob}}$(XH) and $^1K^{\mathrm{LP}}$(XH) respectively. Both of these are always negative, and their magnitudes depend strongly on the s character of the LMO j, i.e. $|^1K^{\mathrm{LP}}(\mathrm{XH})| > |^1K^{\mathrm{ob}}(\mathrm{XH})|$, since the s character of the lone pair is notably larger than that of an X–H bond.

The sign of ^1K(XH) depends on the ratio $|^1K^{\mathrm{b}}/^1K^{\mathrm{LP}}|$, which decreases with increasing s character of the lone pair. According to Bent's rule,[237] the greater the lone pair s character, the smaller the s character of bond b. For

atoms belonging to the same group, the s character of its lone pair increases when going down the Periodic Table. This trend is the origin of the negative ^1K(SnH) coupling in SnH_3^-. The increase in the lone pair effect with increasing s character is nicely exemplified by Gil and von Philipsborn[13] by comparing the values of $|^1J(NH)|$ couplings for formally hybridized sp^3 and sp^2 nitrogen atoms. For instance, $|^1J(NH)|$ values are smaller in imines than in amines. In the latter the s character of the N lone pair increases with increasing pyramidality at the N atom. This leads, for instance, in *p*-X-anilines to an increase in $|^1J(NH)|$ with increasing electron donor capability of the X substituent,[355] which results in a more planar amino group. It is also known that $|^1J(NH)|$ has a large value in pyrrol, 96.5 Hz.[356] In indazole the pyrrolic $|^1J(NH)| = 106.4$ Hz is the largest known for an uncharged protonated nitrogen.[357] Apparently, in this case the effect of planarity at the pyrrolic N atom is reinforced by the proximity to the N_2 lone pair. The change of the pyramidality at the N atom also affects $^1J(NC_1)$ couplings in aniline and *N*,*N*-dimethylaniline. Those couplings are respectively -12.1 and -13.2 Hz; an NO_2 group at ring position 4 changes those couplings to -14.7 and -15.6 Hz respectively.[358] Another interesting example of the dependence of the N lone pair effect on its s character is the change in sign of ^1J(CN) couplings in pyrimidines upon chloro substitution at carbons adjacent to the coupled N atom.[359] In fact, it is known that a pyridinic N atom behaves electronically like an NO_2 group in a benzene ring.[360] Therefore the mesomeric interaction between the Cl atom and the coupled N atom somewhat inhibits the lone pair effect, rendering ^1J(CN) more negative, i.e. ^1K(CN) more positive. For α- and γ-aminopyridines the mesomeric interaction between the side chain and the N ring atom diminishes the pyramidality at the NH_2 group, increasing the respective $|^1J(NH)|$ couplings, which for β-aminopyridine is $|^1J(NH)| = 80.5$ Hz, while for α- and γ-aminopyridines $|^1J(NH)| = 85.2$ and 87.6 Hz respectively.[361]

A similar effect of the s character of the N lone pair on ^1J(SiN) couplings has been observed in Si derivatives of cyclic amines. In fact, ^1J(SiN) decreases with diminishing ring size,[362,363] and this effect has been ascribed to an enhancement of the N pyramidality in the smaller rings. In silazanes an increase in $|^1J(SiN)|$ with the electronegativity of substituents on the Si atom was taken[364] as indicative of $^1K(SiN) > 0$. The CLOPPA description given above together with Bent's rule[237] allows one to make an easy rationalization of such behaviour. The electronegative group attached to the Si atom increases the Si s character of the Si–N bond, increasing the "bond contribution" without introducing substantial changes in the N "lone pair contribution". On the other hand, when an electronegative group is attached to the N atom, the s character of the N lone pair is increased, leading to an increase in the "lone pair contribution". For this reason, very small ^1J(SiN) and $|^1J(NH)|$ couplings, 6.5 and 64.8 Hz respectively, have been observed in $Me_3SiNHOSiMe_3$,[364] while in $(Me_3Si)_2NH$ the following

couplings have been reported: $^1J(SiN) = 13.5$ Hz and $|^1J(NH)| = 69.6$ Hz.[364]

When atom X bears more than one lone pair, a similar description can be expected from a qualitative point of view, although exact additivity of each individual lone pair effect cannot be expected. For instance, $^1K(FH) = +4.69 \times 10^{20}\,T^2\,J^{-1}$ in FH while $^1K(IH) = -3.3 \times 10^{20}\,T^2\,J^{-1}$ in IH,[179] i.e. the heavy atom increase of the lone pair effect is still observed.

For other types of compounds and other types of $^1K(XY)$ couplings the CLOPPA analysis shows similar trends, although the number of terms that are important in (25) may increase in comparison with the hydrides.[354] For such couplings the following trends are worthy of comment. The ratio $|^1K^b/^1K^{LP}|$ depends on the nature of atom Y (atom X bears the lone pair). For instance, the replacement of the three H atoms in SnH_3^- by methyl groups yields a reduction in that ratio from 0.74 to 0.64. The experimental $^1K(SnC)$ in $Sn(CH_3)_3^-$ is $-1.37 \times 10^{21}\,T^2\,J^{-1}$.[365] If Y belongs to Group IV, the importance of $^1K^{LP}$ increases going down the Periodic Table. For instance, in $Sn(CH_3)_3^-$ $|^1K^b/^1K^{LP}| = 0.64$, while in $Sn(SnH_3)_3^-$ $|^1K^b/^1K^{LP}| = 0.16$.[354] There are many experimental values, some of them published recently, that support this "heavy Y atom effect". A few examples are shown in Table 16; others can be found in ref. 373. These values suggest that the hybridization at the Y atom may also be important in defining the role played by the X lone pair, although other factors can also be operating, such as the electronegativity effect. A few examples are as follows. $^1J(PC) = +8.8$ Hz in $P(C{\equiv}CCH_3)_3$; $^1J(PC) = -39.1$ Hz in $(OEt)_2P(C{\equiv}CCH_3)$ and $^1J(PC) = -50$ Hz in $(OEt)_2P(C{\equiv}CH)$;[374] $^1J(PC) = -60.2$ Hz in $P(C{\equiv}N)_3$; $^1J(PC) = -102.5$ Hz in $P(C{\equiv}N)_2Cl$ and $^1J(PC) = -152.4$ Hz in $P(C{\equiv}N)Cl_2$, although these last three values depend on solvent (signs assumed).[375]

Table 16. Experimental values illustrating the "heavy Y atoms effect" on the X lone pair contribution to $^1K(XY)$ couplings.

Compound	$^1(K(X,Y)$	Experimental value ($10^{19}\,T^2\,J^{-1}$)	Ref.
NH_2CH_3	$^1K(NC)$	+14.7	366
$NH(SiCH_3)_2$	$^1K(NSi)$	+55.7	364
$N(Si(CH_3)_3)_3$	$^1K(NSi)$	+3.14	367
$N(SiH_3)$	$^1K(NSi)$	+25	363, 368
$N(Sn(CH_3)_3)_3$	$^1K(NSn)$	−17.3	367
$NHPhPb(CH_3)_3$	$^1K(NPb)$	−1019	369
$N(Pb(CH_3)_3)_3$	$^1K(NPb)$	−131.1	367
$N(SiCH_3)_2[Pb(CH_3)_3]$	$^1K(NPb)$	−945	370
PH_3	$^1K(PH)$	+77.8	179
$P(CH_3)_3$	$^1K(PC)$	−11	179
PPh_3	$^1K(PC)$	−10.22	370
$PH_2(Si(CH_3)_3)$	$^1K(PSi)$	−16.7	371
$P(Sn(CH_3)_3)_3$	$^1K(PSn)$	−456	372

Apparently, in compounds similar to triphenylphosphine the lone pair contribution depends on the orientation between the P lone pair and the phenyl ring.[376] It is also important to note that some ^1K(NSn) values have been reported as positive and others as negative.[166,377] The negative lone pair effect on the reduced coupling constant also seems to be important in Sn(II) and Pb(II) compounds. In fact, Wrackmeyer *et al.*[378] have recently reported $^1K(MC) < 0$ in $M[CH(SiMe_3)_2]_2$ (M = Sn, Pb).

A similar "heavy Y atom effect" seems to hold when atom X bears more than one lone pair. However, in such cases some caution should be taken, since non-contact contributions may be quite important. For instance, the PSO term is the dominant one in $^1J(Se,C(sp^2))$ couplings in selenophene derivatives[379,380] and selenoimidates,[381] and in $^1J(Te,C(sp^2))$ in tellurophene derivatives.[379] In these couplings the PSO and FC terms are of the same sign. However, it is important to recall that Duddeck *et al.*[382] consider that ^1J(SeN) and ^1J(SeC) couplings in selenadiazole derivatives are dominated by the FC interaction, since fair correlations between chemical shifts and these couplings have been found. Gombler[383] established the correlations

$$^1J(Se,CH_3) = -0.23\%s(Se)\%s(C), \quad \text{(in Hz)} \tag{40}$$

$$^1J(Se,CF_3) = -0.32\%s(Se)\%s(C) - 64, \quad \text{(in Hz)} \tag{41}$$

and concluded in the first case that the FC is by far the dominant term, while in the second case important non-contact terms are expected. A few examples where the H atom is replaced by a methyl group, giving $^1K(XC) < 0$, are shown in Table 17. For CH_3SeH, $|^1J(SeC)|$ is somewhat smaller than in CH_3SeCH_3.[385] Replacement of the CH_3 groups by CF_3 gives still more negative values: $^1K(SeC) = -2.33 \times 10^{21}\ T^2\ J^{-1}$ in CF_3SeCF_3 and $^1K(TeC) = -4.41 \times 10^{21}\ T^2\ J^{-1}$ in CF_3TeCF_3.[383] Assuming that the FC term is the dominant one, such a trend can be understood in terms of Bent's rule.[237] For heavier atoms coupled to Se and Te, $^1K(SeSn^{IV})$ and $^1K(TeSn^{IV})$ have also been reported to be negative.[386]

Wrackmeyer *et al.*[387] have recently determined that in azaphospholes $^1K(PN) < 0$ and its magnitude is similar for pyridine- and pyrrole-type

Table 17. Experimental values of ^1K(XH) and ^1K(XC) showing the methyl group effect on the direct reduced coupling constant for atom X bearing more than one lone pair (in each hydride all H atoms are replaced by CH_3 groups).

X	^1K(XH) ($10^{19}\ T^2\ J^{-1}$)	^1K(XC) ($10^{19}\ T^2\ J^{-1}$)	Ref.
Se	+28	−107	384
Te	+15.5	−170	383, 384
F	+46.9	−57	179

nitrogen atoms. This seems to indicate that the P lone pair is the main factor determining the magnitude of ^1K(PN). Such couplings refer to an sp^2-hybridized P atom, and therefore a large s character is expected for its lone pair. However, it should be noted that non-contact terms may also play an important role. It is interesting to note that negative $^1J(Pb,CH_3)$ couplings have also been reported for extremely distorted tetrahedral surrounding of the lead atom.[388]

(ii) The A.2 configuration [**9**]. When both coupled nuclei bear a lone pair, a configuration like A.2 [**9**] is obtained. In this case the relative orientation of both lone pairs is of crucial importance in defining the total couplings. Such a dependence indicates that there is an important interaction between both lone pairs, and therefore exact additivity of each lone pair effect cannot be expected. Examples of these types of couplings are ^1J(NN), ^1J(PN) and ^1J(PP), since each atom bears only one lone pair. Insight into these cases may help in understanding more complicated cases such as ^1J(SeSe) couplings. Schulman and Lee[351] reported *ab initio* calculations of the FC term of the ^1J(NN) in hydrazine for different values of the dihedral angle ϕ between the N lone pairs. They compared those results with similar calculations carried out previously at the CHF–INDO level.[389] In both cases the trends are quite similar, although the INDO values show a stronger dependence on ϕ. The corresponding values were fitted with the following functions (in Hz):

ab initio $$^1J^{FC}(NN') = -1.805 - 5.076\cos\phi + 0.768\cos^2\phi, \quad (42)$$

INDO $$^1J^{FC}(NN') = -3.8 - 11.5\cos\phi + 3.5\cos^2\phi. \quad (43)$$

Both of these predict negative values for a *cis* orientation of the N lone pairs and positive values for a *trans* one. Galasso,[91] using the EOM approach, also obtained a negative $^1J(NN')$ coupling in hydrazine for a *cis* arrangement of the N lone pairs and a positive coupling for a *trans* one. However, for sp^2-hybridized N atoms Galasso[91] found negative $^1J(NN')$ values for both *cis* and *trans* arrangements of the N lone pairs, in agreement with experimental values measured by Kuroda *et al.*[390,391]

^1J(PN) couplings have been calculated at the SCPT–INDO level for some tri- and pentavalent P atoms by Duangthai and Webb.[392] Although the PSO term was found to be non-negligible, the angular dependence of ^1J(PN) is dominated by the FC term, which is positive for trivalent P atoms (note that $\gamma[^{15}N] < 0$) and negative for the pentavalent species, indicating the large importance of the P lone pair.

Duangthai and Webb[352] have carried out SCPT–INDO calculations of the dependence of ^1J(PP) upon the relative orientation of the phosphorus lone pairs. They used an spd basis set for P and a K INDO factor of 1.00. They

studied the ^1J(PP) dependence on the angle ϕ, i.e. the dihedral angle defined by both P lone pairs and the P–P bond, for P_2H_4, $P_2H_2F_2$ and P_2F_4. Although Duangthai and Webb[352] found that for most angles ^1J(PP) is dominated by the FC term, non-contact contributions are by no means negligible. Both the FC and SD terms depend strongly on ϕ, although the larger absolute value of the former defines the general trend. When the FC term is negative, it can be expected that the lone pair contributions are larger, in absolute value, than the P–P bond contribution. While in H_2P-PH_2 there is a sign inversion of the FC term, which is negative for calculated values between 30° and 90°, in F_2P-PH_2 as well as in F_2P-PF_2, the FC term is negative for all calculated ϕ values. For the latter compound the absolute value of the negative FC term is notably larger than that for F_2P-PH_2. This trend can easily be explained in terms of the CLOPPA analysis discussed above for the A.1 configuration [**8**] if Bent's rule[237] is considered. According to this rule, each electronegative substituent, an F atom in this case, increases the s character of the lone pair of the P atom to which it is attached. This increases the lone pair s character, yielding a larger negative contribution. For this reason, the FC term is negative in the fluorinated compounds for all ϕ values. The increase in ^1J(PP) couplings towards positive values when the P lone pairs go to a *trans* conformation found by Duangthai and Webb[352] has experimental support.[393,394]

Negative $^1K(Sn^{(II)}N)$ and $^1K(Pb^{(II)}N)$ couplings have been reported by Stader and Wrackmeyer[395] in cyclic and non-cyclic amides.

(iii) Other configurations. When neither A nor B bear a lone pair, but are proximate to a heteroatom bearing one, an important stereospecific effect is observed. These cases have been extensively discussed by Gil and von Philipsborn.[13] For this reason, in this section only a brief account of the CLOPPA description of that effect for configuration B [**10**, **11**] for ^1J(CC) couplings is given. Experimental values, where such an effect is stressed, have been given by Krivdin *et al.*[396,397]

The CLOPPA method[148,398] has been applied[399] to determine the contribution of the N lone pair in defining the difference between $^1J^E$(CC) = 41.5 Hz and $^1J^Z$(CC) = 49.3 Hz in acetoxime [**12**]. Upon protonation of the N lone pair [**13**] this difference is practically cancelled out, $^1J^E$(CC) = 41.9 Hz and $^1J^Z$(CC) = 42.2 Hz.[399] Although the RPA–INDO method yields somewhat exaggerated ^1J(CC) couplings in [**12**] and [**13**], the experimental difference between $^1J^Z$(CC) and $^1J^E$(CC) is adequately reproduced. It originates mainly from the FC term. The sum of the CLOPPA terms involving the N lone pair in [**12**] and the $N-H^+$ bond in [**13**] are displayed in Table 18. It is interesting to note that both types of contribution are of the same sign for each coupling, i.e. positive when the LMO is placed *cis* to the C–C bond containing the coupled nuclei and negative when placed *trans*. However, the LP contributions are noticeably larger. This

Table 18. Sum of $J_{ia,jb}$ contributions from (25) to $^1J^Z$(CC) and $^1J^E$(CC) involving the lone pair in [12], Σ_{LP}, and the N–H$^+$ bond in [13], Σ_{NH^+}.[a]

	Σ_{LP} (in [12]) (Hz)	Σ_{NH^+} (in [13]) (Hz)
$^1J^Z$(CC)	+2.480	+0.781
$^1J^E$(CC)	−2.142	−0.366

[a]From ref. 399.

result seems to indicate that a similar conclusion holds for configuration B [**10**, **11**] than for $^1K^{ob}$ and $^1K^{LP}$ in configuration A.1 [**8**], i.e. the LP contribution is similar in character to that of a bond, but is larger owing to its greater s character. A similar CLOPPA analysis of the $^1J^E$(CC) and $^1J^Z$(CC) difference in monoprotonated acetone [**14**] supports this conclusion. As the first protonation in acetone takes place in the oxygen lone pair with larger s character, it is expected that the lone pair contribution in [**14**] is smaller than in [**12**]. In fact, while in [**12**] the difference between Σ_{LP} for $^1J^Z$(CC) and $^1J^E$(CC) amounts to 4.62 Hz, in [**14**] that difference amounts to only 2.53 Hz.[400]

This conclusion indicates that the "quenching" of the lone pair effect on couplings upon protonation proceeds via a reduction in the s character of the LMO representing the LP in the neutral compound and the X–H$^+$ bond in the protonated one. Similar conclusions seem to be valid for other

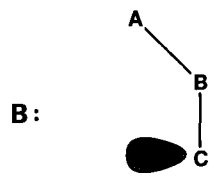

[10]

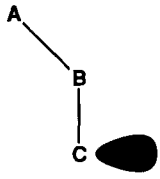

[11]

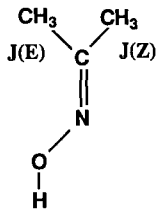

[12]

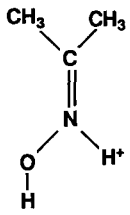

[13]

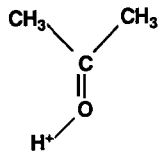

[14]

couplings in different configurations. A detailed study of the dependence of the ^2J(NH) coupling on solvent in 3,5-dimethylpyridine was undertaken by Holger and von Philipsborn.[401] A change from −11.04 Hz in hexane to −3.15 Hz in formic acid was found. A similar effect was used in 8-quinolinol to determine the existence of an intramolecular hydrogen bond,[402] and to study the chelation of the 8-quinolinato ligand in several complexes.[403]

^1J(CH) couplings in a configuration like B [**10**, **11**] with respect to a lone pair show also important differences for *E* and *Z* orientations.[13,404,405] The CLOPPA–INDO analysis of ^1J(CC) couplings mentioned above suggests that a similar contribution to ^1J(CH) couplings may exist besides the proximity effect described in Section 3.4.

The *cis* lone pair effect on ^2J(NH) couplings across a fragment N=C−H was found by von Philipsborn *et al.*[406] to decrease with increasing delocalization of the π-electron system in the formal double bond. This effect was studied with the CLOPPA INDO method, comparing the lone pair effect on ^2J(NH) in [**15**] and in pyridine.[353] The lone pair contribution was taken as the sum of $J_{ia,jb}$ involving the N lone pair, Σ_{LP}. While in [**15**] $\Sigma_{LP} = -28.99$ Hz, in pyridine $\Sigma_{LP} = -23.42$ Hz, paralleling the trend described by von Philipsborn *et al.*[406]

The N lone pair effect on ^2J(NC) couplings when both atoms belong to aromatic rings is nicely exemplified by Römer's measurements[407] in phenazine [**16**] $|^2J(N_{10},C_1)| = 8.3$ Hz and $|^2J(N_{10},C_{4\alpha})| = 1.9$ Hz.

The s character of the P lone pair also seems to increase its orientational effect on ^2J(PH) couplings. In fact, in phosphirane, $^2J^{cis}$(PH) = + 16.14 Hz and $^2J^{trans}$(PH) = − 2.64 Hz deviate somewhat from the plot of ^2J(PCH) versus dihedral angle.[408] In this strained small ring the C−P−C angle is 47.4°, and this leads to a substantial increase in the s character of the P lone pair, giving ^1J(PH) = + 158.34 Hz, which is the smallest value for any organic phosphirane, and a large and negative ^1J(PC) = − 33.0 Hz.[408]

The P lone pair orientational effect on geminal J(PC) couplings can be appreciated, for instance, in 3-methyl-1,3-oxaza-2-phospholane bearing an exocyclic dimethylamino substituent on the P(III) atom, since at low temperatures $^2J^{cis}$(PNC) = + 44.6 Hz and $^2J^{trans}$(PNC) = −9.2 Hz,[409] and in

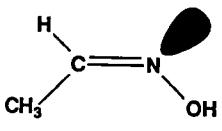

[15]

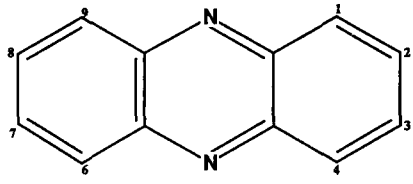

[16]

the diphosphacyclopropane, $(t\text{-BuP})_2CHMe$, with $^2J^{cis}(PCC) = +23.1$ Hz and $^2J^{trans}(PCC) = -2.6$ Hz.[410]

Large differences between $^2J^{cis}(PF)$ and $^2J^{trans}(PF)$ couplings have been reported in [17].[411] A CLOPPA–INDO analysis was carried out[353] for such couplings, replacing the CF_3 group by an F atom in [17] since the INDO ground state function with the CF_3 group presents a quasi-instability of the non-singlet type. The asymmetry between the *cis* and *trans* couplings is largely dominated by the PSO term, as shown in Table 19. This result suggests that there can be other instances where the orientational lone pair effect is defined by non-contact terms, as for instance in $^1J(NF)$ and $^2J(NF)$ couplings[412,413] or $^2J(SeC)$ couplings.[414]

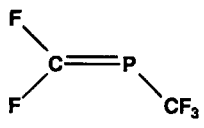

[17]

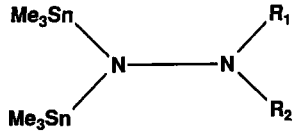

[18]

In stannylhydrazines of the type [18] $^2J(SnSn)$ couplings were found to be extremely sensitive to the nitrogen lone-pair–lone-pair interactions.[415–417]

The important P lone pair orientational effect on $^{2,3}J(PC)$ couplings reported by Quin *et al.*[418,419] in 7-phosphanorbornene derivatives was analysed by Aucar *et al.*[420] using the IPPP–CLOPPA–INDO approach. Contributions from different bonds were discussed in detail. The stereospecific behaviour is overwhelmingly dominated by the FC term, with the PSO and SD terms being much smaller than the FC one in all cases.

A relationship between the magnitude of $|^3J(SnN)|$ couplings and the orientation of the N lone pair has been proposed by Kupče *et al.*[301]

Table 19. The orientational lone pair effect on geminal $J(PF)$ couplings in $FP{=}CF_2$.[a]

	cis $^2J(PF)$ (Hz)	*trans* $^2J(PF)$ (Hz)	Δ(*cis–trans*) (Hz)
FC	157.02	145.02	12.00
PSO	−30.14	−99.20	69.06
SD	68.60	62.26	6.36
Total	195.48	108.06	87.42
Experimental[b]	191.4	103.9	87.5

[a]From ref. 353.
[b]Values in [17]; from ref. 411.

3.3. The through-space transmission of coupling constants

One of the transmission mechanisms that has attracted much attention since first postulated[421] is through-space (TS) transmission. Hilton and Sutcliffe[422] published a detailed review on early work, where many experimental trends as well as theoretical models were discussed. Barfield preferred to speak of non-bonded interactions instead of through-space transmission. His NNBI approach[128] has been applied to study several problems during the review period. The PRMO method,[132] although first intended to decompose σ- and π-transmitted components, was also applied[133] to study through-space transmission between proximate protons in anisole. Laatikainen's[129] criticisms of the application of this approach for studying through-space transmission were discussed in ref. 178. The IPPP approach[141] has been applied to study the through-space transmitted component of different types of couplings using different ground state wave functions, namely INDO,[107,141] MNDO[51–53] and *ab initio*[147] ones. The IPPP method has been improved[398] in such a way that the through-space component of a given coupling $J^{TS}(NN')$ is expressed as a sum of the terms involving LMOs representing bonds or lone pairs (occupied orbitals) and antibonding orbitals (vacant LMOs) belonging to molecular fragments that are proximate in space, (26).

As happens when decomposing total coupling constants into components transmitted through different electronic mechanisms, the definition of $J^{TS}(NN')$ has some degree of arbitrariness. In addition several effects that could also be termed TS are discussed in other sections of this work. For instance, the orientational lone pair effect on one- and two-bond couplings has been mainly discussed in Section 3.2. However, ^2J(PP) couplings in compounds where there is significant overlap of the lone pairs of both coupled nuclei will be discussed in this section. When part of a molecule is proximate to the bonds connecting two coupled nuclei, two different situations may arise; when the closeness of two molecular fragments affects the given coupling through the ground state wave function, this will be referred to as a proximity effect. The most conspicuous case so far studied is that of the difference between vicinal *endo–endo* and *exo–exo* J(HH) couplings in norbornane and related compounds.[423] This effect is discussed in Section 3.4. On the other hand, when LMOs belonging to the molecular fragment close to the bonds connecting the coupled nuclei appear in (26) with non-negligible contributions, this will be considered as through-space transmission. In this case the proximate molecular fragment contributes to the given coupling constant through a second-order effect.

In this section papers dealing with theoretical analysis of couplings transmitted through space that appeared during the review period will be considered. Experimental results relevant for these calculations are also described.

3.3.1. Through-space couplings involving at least one proton

The PRMO–INDO approach[132] has been applied to study J^{TS}(HH) couplings in anisole derivatives between the methyl protons and the *ortho* ring proton placed in a *cis* conformation with respect to the methoxy group.[133] For direct overlap of the electrons surrounding the proximate coupled protons, a negative contribution was thus calculated, in good agreement with the sign determined experimentally in similar compounds.[424] For methyl protons with other configurations with respect to the ring *ortho* proton, contributions of different sign were also calculated.[133]

Detailed computations with the FPT–INDO method were also carried out in anisole by Schaefer and Laatikainen.[425] They found a rapid decrease in the magnitude of $^5J(H_o,CH_3)$ as ψ increases. In order to determine the TS component, they also carried out NNBI[128] calculations for different angles ψ. Two different cases were considered, namely one in which all Fock matrix elements between the s orbitals of the CH_3 moiety as well as the ring H_o s orbital were set equal to zero, and another where only the methyl proton s orbitals as well as the ring H_o s orbital were set equal to zero. These results confirm that $^5J(H_o,CH_3)$ in anisole for a planar conformation is negative and is mainly transmitted through space. In spite of its small absolute value, its strong dependence on ψ, closely proportional to $\cos^4\psi$ for $0° \leqslant \psi \leqslant 60°$,[426] makes it an adequate probe to determine the OCH_3 group conformation, and, when it is very accurately determined, information can also be obtained on the torsion angle around the planar conformation.[426] Schaefer *et al.*[427] reported $^5J(H_o,CH_3) = -0.141$ Hz (sign assumed) in anisole. This is about one-half the value reported in *ortho*-substituted derivatives.[425] The same group reported afterwards more accurate values in acetone-d_6 (−0.155 Hz) and in CS_2 (−0.152 Hz).[428] Such results are consistent with a heavy atom planar conformation with a barrier to inner rotation around ψ much larger than kT at room temperature but not high enough to prevent rapid passage between both planar conformers.[427] This is further confirmed taking into account that for some *meta*-substituted anisole derivatives the sum of both $^5J(H_o,CH_3)$ couplings is close to −0.28 Hz.[427]

A few cases where such TS-dominated coupling was used to determine the preferential OMe group conformation for compounds without an *ortho* substituent are as follows. In 4-methoxy-2-nitroaniline the OMe group preferential conformation is *cis* to H(3).[429] In 4-methoxysalicylaldehyde $^5J(H(3),CH_3) = -0.197$ Hz while $^5J(H(5),CH_3) = -0.07$ Hz,[427] showing that the preferential conformation in this case is also *cis* to H(3). In 2,5-dimethoxybenzaldehyde the preferential conformation of the OMe(5) is *cis* to H(6).[430] In 3-fluoroanisole the conformation of the OMe group *cis* to H(2) is slightly preferred.[431] In 2-methoxyphenazine **[19]** only $^5J(H(1),CH_3)$ was observed,[432] and was interpreted[178] as showing that the OMe preferential conformation is *cis* to H(1). All these cases indicate that the methoxy

group prefers a *cis* arrangement with the *ortho* C–C bond with the largest mobile bond order.[427,433,434]

Schaefer's group has also detected a $^5J(H_o,CH_3)$ coupling in thioanisole. The experimental values are −0.141 Hz in benzene-d_6 and −0.137 Hz in acetone-d_6.[435] A similar dependence on the torsion angle ψ to that determined in anisole[426] was assumed to hold for $^5J(H_o,CH_3)$ in thioanisole and its derivatives,[436] i.e. one proportional to $\cos^4 \psi$. With this assumption, for $\psi = 0$ Schaefer *et al.*[436] found $^5J(H_o,CH_3) = -0.43$ Hz, which is, in absolute value, a bit larger than that in anisole, −0.292 Hz.[435] Since this is mainly a TS coupling, it is expected that its magnitude depends strongly on the H–H distance between the coupled nuclei. It should be noted that

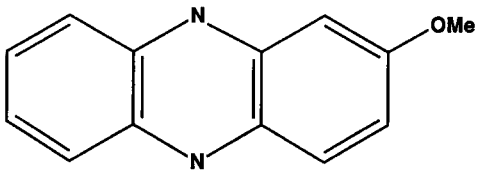

[19]

although the C(sp^2)–S bond is longer than the C(sp^2)–O bond, the C–S–C angle in thioanisole is only 102.6°,[436] while in anisole the C–O–C angle is 119.8°.[437] The strong dependence of that coupling on ψ makes it a useful probe to detect both the conformation[438] and the torsional mobility of the thiomethyl group in thioanisole derivatives.[436]

J(HH) couplings, mainly transmitted through space, have also been reported in other compounds, and have been used as probes to detect conformations.[439] This is, for instance, the case for *o*-hydroxyacetophenone and *o*-aminoacetophenone, where $^5J(H(6),CH_3)$ couplings of *ca.* ±0.18 Hz were observed and considered to be an indication of a *cis* conformation between the Me group and the ring proton H(6).[440] For acetophenone Schaefer and Peeling[441] reported $^5J(CH_3,H_o) = \pm 0.054$ Hz, which is very close to the corresponding value in *p*-fluoroacetophenone and *p*-amino acetophenone. Schaefer and Peeling[441] carried out an FPT–CNDO analysis of this coupling because of instability problems in the INDO wave function for this type of carbonyl-substituted benzenes.

In *o*-isopropylbenzaldehyde $^5J(CHO,CH(CH_3)_2) = -0.39$ Hz was reported,[434] and a relative population of 0.83 was estimated for the conformation with a close approach between both C–H bonds. Both FPT–CNDO/2 and FPT–INDO calculations using the STO-3G optimized geometry predicted $^5J(CHO,H(CH_3)_2) = -0.30$ Hz, in reasonable agreement with the experimental value.

Although the sign of J(HH) couplings transmitted mainly through space has been reported in only a few cases, the values quoted above seem to indicate that all J^{TS}(HH) are negative. Apparently, the positive contributions predicted by the PRMO–FPT INDO method[133] are so small that so far they cannot be detected. A different situation is found for J(FH) couplings. Both the PRMO[245] and IPPP[141] methods have been applied at the INDO level to study the through-space component of the ^4J(FH) coupling in α-fluorotoluene for different angles θ between the fluoromethyl C–F bond and the ring plane. It is noteworthy that, in spite of the important differences between the two methods, they predict similar trends. Such a trend is also similar for the IPPP–INDO $^4J^{TS}$(FH) coupling in 1-fluoropropene,[141] although in this case its magnitude is larger, reflecting the closer proximity between the coupled nuclei owing to the shorter C=C distance in the vinylic compound as compared with the corresponding aromatic one. Such trends predict a change in sign for J(FH) versus θ, corresponding to a negative value for $\theta = 0$, which becomes positive for an angle around $60° < \theta < 90°$. Although several works report only absolute values of J(FH) couplings transmitted mainly through space,[442–444] there are cases in which they are reported to be negative and in other cases positive. Negative values were reported for *o*-fluorophenol,[445] *o*-hydroxybenzotrifluoride,[446] *o*-fluorobenzyl alcohol,[447] 2,6-dimethylbenzoyl fluoride,[448] 1-fluorobenzo[*c*]phenanthrene, 4-fluorophenanthrene, 10-fluorobenzo[*a*]pyrene and 11-fluoro-5-methylcrysene.[449] Positive values were reported for 8-fluoro-1-methylnaphthalene,[450] *o*-trifluoromethylbenzaldehyde,[451] 1-alkyl-8-fluoroquinolinium halides,[452] *o*-fluoroacetophenone,[440] 5-fluoro-3,3-dimethyl-1,2,3,4-tetrahydrophenanthrene,[453] 2-fluorobiphenyl[454] and α,α,α-trifluoroanisole.[356] These results support the trend predicted by the PRMO[245] and IPPP[141] calculations at the INDO level, indicating that positive J^{TS}(FH) are possible for certain values of θ. However, there is evidence that the FPT–INDO method cannot describe quantitatively the behaviour of these positive contributions. The IPPP–INDO analysis of J^{TS}(FH) in *o*-fluoroacetophenone,[455] whose experimental value of the total coupling is +4.484 Hz,[440] predicts for a methyl group conformation with a C–H bond eclipsing the C=O bond the following values: $J^{TS}(\theta = 60°) = -1.48$ Hz and $J^{TS}(\mathrm{FH})(\theta = 180°) = +8.74$ Hz.[455] The average value is much too negative with respect to the experimental one. It should be recalled that the TS component in the IPPP approach is obtained from an inner projection of the polarization propagator on molecular orbitals belonging only to the side chains (in this case the $COCH_3$ and CF moieties); therefore the quasi-non-singlet HF instability in the INDO ground state wave function that frequently appears in carbonyl compounds is circumvented. Such an analysis, together with Yamamoto and Oki's measurements[456] of the $J(F_1,CH_3)$ coupling, in 8,13-dichloro-1,2,3,4-tetrafluoro-9-methyltriptycene, largely dominated by a

Table 20. RPA–IPPP *ab initio* through-space contributions to the FC, SD, PSO and DSO terms of $J(FH^t)$ and $J(FH^s)$ couplings in 1-fluoropropane, $H^tCH_2^s-CH_2-CH_2F$, where H^t and H^s correspond approximately to $\theta = 180°$ and $\theta = 60°$ conformations.[a]

Interaction	$J^{TS}(FH^t)$ (Hz)	$J^{TS}(FH^s)$ (Hz)
FC	14.86	4.24
SD	−0.18	0.05
PSO	0.29	−0.96
DSO	−1.21	0.61
Total	13.75	3.94

[a]From ref. 147.

through-space mechanism, suggests that the IPPP–INDO $J^{TS}(FH)$ component is not well reproduced for θ close to 60°. In fact, Yamamoto and Oki determined that the averaged value with the three methyl protons is 7.0 Hz. Measurements of those couplings at low temperature when the methyl moiety is frozen yielded $|J(FH)|_{180°} = 8.7$ Hz and $|J(FH)|_{60°} = 6.1$ Hz. Therefore both couplings are of the same sign. Those results seem to indicate that the FPT–INDO method correctly describes the positive contribution for $\theta = 180°$, while it fails to reproduce the positive contributions to $J^{TS}(FH)$ for $\theta = 60°$. In view of this, IPPP *ab initio* calculations[147] were carried out using 1-fluoropropane $H^tCH_2^s-CH_2-CH_2F$ as a model compound, employing a configuration where the C–F bond lies on the plane defined by the three C atoms, and the methyl group is in a staggered conformation, having the in-plane C–H bond pointing away from the F atom. Results for such a conformation using a double zeta basis set for the FC, SD, PSO and DSO terms of the TS component are displayed in Table 20. The following features of the data are worthy of note. $J^{TS}(FH^s)$ is positive, this result being an improvement compared with the IPPP–INDO value. However, the relationship between $J^{TS}(\theta = 180°)$ and $J^{TS}(\theta = 60°)$ is notably different from that measured by Yamamoto and Oki.[456]

The much too negative value that the FPT–INDO method yields for $J^{TS}(FH)(\theta = 60°)$ is apparently the origin of its failure reported for several compounds, e.g. 1-alkyl-8-fluoro quinolinium halides,[452] *o*-fluorotoluene derivatives,[250] and α,α,α-trifluoroanisole and its *p*-fluoro derivative.[256] This same problem has also been addressed by Schaefer *et al.*[457] who applied the NNBI approach[128] to study *o*-fluoroacetophenone in order to determine the origin of the discrepancy between theoretical and experimental values in that compound.

In spite of these shortcomings, Benassi *et al.*[257] used the FPT–INDO method to describe successfully the trend of $^5J(CH_3,F)$ in *o*-fluorophenyl methyl sulphoxide in terms of the torsional angle γ, round the $C(sp^2)-S$ bond, where the fitting parameters were scaled to better reproduce the

experimental values:

$$^5J(CH_3,F)\,(\text{in Hz}) = -\exp(12.537\cos\gamma - 6.189) + 0.883\sin^2\gamma + 0.268\sin^2(\gamma + 7.31) - 0.354\cos\gamma. \quad (44)$$

A systematic determination of J(FH) couplings mainly transmitted through space, together with their signs, was recently undertaken.[458] The experimental values indicate that the change in sign takes place somewhere in the range $30° < \theta < 40°$. This indicates that the sign determination for this type of coupling is an important probe to determine preferred conformations.

Trends described above for J^{TS}(FH) couplings suggest that other J(XH) couplings mainly transmitted through space could also undergo a similar change in sign for different angles, especially if X is an atom bearing a lone pair, such as J(NH), J(PH) and J(SeH) couplings. During the review period only a few J(PH) couplings dominated by a through-space mechanism were measured, but their signs were not determined.[459]

Important through-space J(PtH) couplings have been reported in several platinum(II) complexes.[460,461] Their signs were not determined. J(Tl,H) couplings mainly transmitted through space have been reported by Cheesman *et al.*[462] in *o*-alkylphenylthallium compounds.

3.3.2. Through-space transmission by overlap of lone pairs

In order to rationalize the large J^{peri}(FF) couplings in fluorinated derivatives of naphthalene, Mallory[463] formulated a theoretical picture to describe the through-space transmission of couplings between atoms proximate in space that bear lone pairs. According to this scheme, the overlap of lone pairs of certain p character belonging to each atom generates one σ-type bonding and one σ*-type antibonding orbital connecting the two coupled nuclei. However, such an overlap interaction would not lead to net chemical bonding, but would provide only an adequate coupling pathway for transmitting spin information between the coupled nuclei.[464] This scheme was employed by Mallory *et al.*[465] to describe the through-space transmission of ^4J(FF) = 65 Hz in 1-methyl-4,5-difluoronaphthalene. During the review period these ideas were used by Mallory *et al.*[464] to rationalize the large four-bond J(FN) coupling, 22.4 Hz, that they measured in 3,4-dihydro-8-fluoro-5-methyl-1(2*H*)-naphthalenone oxime [**20**]. According to this formulation, the large coupling should lead to the generation of a σ(FN) bonding and a σ*(FN) antibonding orbital owing to the overlap between the proximate F lone pair and that of the N atom. It is interesting to observe that Mallory *et al.*[464] have also compared the reduced coupling constant ^4K(FN) in [**20**] with the corresponding ^4K(FF) in 1-methyl-4,5-difluoronaphthalene, and found that the former is about three times as large as the latter.

This was explained by them as resulting from the formal sp^2 hybridization of the N lone pair, which provides a more efficient pathway for transmitting the FC interaction, since its s character is greater than in the F lone pair forming the coupling pathway for ^4J(FF). According to Mallory,[463] the high p character of this F lone pair requires an indirect spin polarization mechanism from the s electrons.

Most works dealing with J(FF) couplings dominated by a through-space mechanism report only absolute values.[266,444,464–467] However, Bakhmutov *et al.*[176,468] reported negative couplings transmitted mainly through space for arrangements similar to those in J^{peri}(FF) couplings in fluorinated derivatives of naphthalene, and they rationalized them as couplings mainly transmitted through space but dominated by the PSO interaction. The RPA–INDO value of the J^{peri}(FF) coupling is much too small in magnitude with the FC term being about +5 Hz and the non-contact terms negligible. Preliminary *ab initio* calculations[469] indicate that for a very small angle between the C–F bonds to which the F atoms are attached, the J^{TS}(FF) coupling is dominated by a negative PSO term, while the FC makes a small positive contribution, in qualitative agreement with the findings of Bakhmutov *et al.*[468,470]

For a different relative orientation of the C–F bonds a good performance of the RPA–INDO method has been reported.[398] The IPPP–INDO-calculated J^{TS}(FF) coupling in **[21]** which mimics **[22]**, shows that it is overwhelmingly dominated by the FC term, which is positive and decreases exponentially with increasing F. . .F distance.

An unpublished IPPP–CLOPPA analysis of the through-space transmission of J(FN) couplings in **[20]** and in 2-fluoropyridine shows that the F lone pair with the largest s character is involved in the coupling pathway. This result does not support the Mallory scheme, where it is assumed that the p-type lone pair participates in this transmission mechanism.

The experimental value in 2-fluoropyridine is ^2J(FN) = −52.64 Hz.[471] It is interesting to note that the RPA–INDO calculation predicts that this coupling has an important negative PSO contribution. The IPPP analysis shows that the through-space transmission is overwhelmingly dominated by the FC term. Similar experimental ^2J(FN) values have recently been reported in perfluoropyridine and several perfluorodiazines by Costa *et al.*,[472] ranging from −59.5 to −45.1 Hz.

There are other cases where the overlap of lone pairs gives an efficient pathway for directly transmitting the spin information associated with the FC interaction. However, in no such case is any support found for Mallory's scheme, since the role played in the transmission by the rear lobe of antibonding orbitals is quite evident. The most conspicuous cases studied with the IPPP method during the review period are those of the ^2J(PP) coupling in $HN(PF_2)_2$,[473] the ^3J(PP) coupling in **[23**, X = Y = Z = H**]**[474] and the ^3J(SeSe) coupling in **[24]**.[120] $HN(PF_2)_2$ belongs to the family of $XN(PF_2)_2$ compounds where very large ^2J(PP) couplings are known ex-

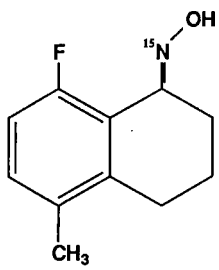

[20]

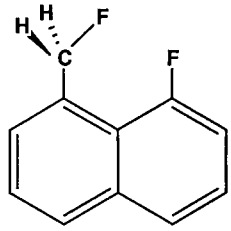

[21]

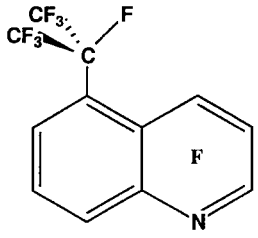

[22]

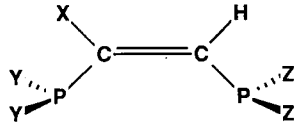

[23]

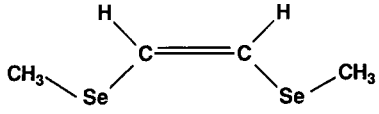

[24]

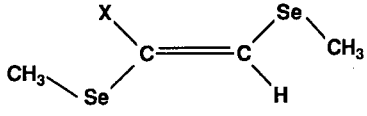

[25]

perimentally for a variety of X moieties. These experimental couplings depend strongly on temperature, and are notably reduced both upon cation formation and upon complexation with coordination metals and with BH_3 molecules. The IPPP–INDO analysis[120] indicates that these geminal couplings are largely dominated by the FC term, and the large positive $^2J^{TS}$(PP) contribution depends strongly on the P–N–P angle. The through-bond (TB) contribution to this geminal coupling is negative. This analysis, together with experimental data on compounds of the type $Y_1Y_2P–Z–PY_3Y_4$, allow one to obtain insight on factors defining the transmission. In Table 21 a few experimental ^2J(PP) couplings are collected. Comparing, for instance, entries 3 and 6, it is observed that the three electronegative groups attached to each P atom in the former lead to a notably larger ^2J(PP) coupling. According to Bent's rule,[237] the s character

Table 21. Experimental $^2J(PP)$ couplings in compounds of the type $Y_1Y_2P-Z-PY_{34}$.

	Z	Y	$^2J(PP)$ (Hz)	Ref.
(1)	$NGeH_3$	F_4	405	475
(2)	$NSiH_3$	F_4	367.6	476
(3)	NCH_3	F_4	442	477
(4)	NCH_2CH_3	F_4	446	478
(5)	NPh	F_4	382	477
(6)	CH_2	Ph_4	+125	479
(7)	$C=CH_2$	Ph_4	+98	479
(8)	$CHSiMe_3$	$(SiMe_3)_2N$; Cl; Ph_2	227	480
(9)	CF_2	$(cyclohexyl)_2$, H, CF_3	72.5	481

Table 22. Experimental values of $^3J(PP)$ couplings where important overlap of the P lone pairs can be expected.

Substituents in [23]			$^3J(PP)$ (Hz)	Ref.
X	Y	Z		
H	Ph	Ph	+105.5	479
			>100	483
PPh_2	Ph	Ph	+142.8	484
CF_3	Ph	Ph	131	485
Ph	Ph	Ph	146	485
t-Bu	Ph	Ph	37	485
o-Bis(diphenylphosphino)benzene			145	486

of the P lone pairs should be notably larger in the former than in the latter; therefore these experimental values support theoretical results indicating that a high s character of the overlapping lone pairs increases the efficiency of transmission of the FC interaction along this pathway. Other interesting examples are compounds of the type $(i\text{-}Pr_2N)_2P_A-P_B=P_C-R$, where $^2J(P_AP_C)$ couplings between 522 and 602 Hz have been reported.[482] It should be noted that P_C is an sp^2-hybridized P atom and two electronegative substituents are attached to P_A. In [**23**, X = Y = Z = H] the transmission of $^3J^{TS}(PP)$ is essentially similar to that of $^2J^{TS}(PP)$. In this case there are also several experimental values in analogous compounds that support the main conclusions of the IPPP–INDO analysis. A few examples are displayed in Table 22. These values are notably larger than $^3J^{trans}(PP)$ couplings in similar compounds, e.g. in *trans*-$Ph_2PCH=CHPPh_2$ $^3J(PP) = +13.4$ Hz.[479]

A peculiar case is the large $^2J(PP)$ coupling, 125.4 Hz, reported[487] between two proximate P atoms, neither bearing a lone pair and which are

very close in space, d(P. . .P) = 2.689 Å. Such a large coupling may be indicative of an attractive P. . .P interaction.[487]

Compounds [**24**] and [**25**] are intended to model the *cis* and *trans* isomers of 1,2-bis(methylseleno)-1-phenylethylene, for which Johannsen and Eggert[488] reported the following experimental data: $^3J^{trans}$(SeSe) = 12.0 Hz and $^3J^{cis}$(SeSe) = 96.5 Hz, which can be considered typical since in mono-, di- and triselenosubstituted alkenes $^3J^{cis}$(SeSe) couplings range from 77 to 177 Hz and $^3J^{trans}$(SeSe) range from 2 to 12 Hz.[489] According to the IPPP–INDO analysis, the positive component of the FC term transmitted through space in the *cis* coupling defines this trend. The main coupling pathway for the through-space component is determined by the in-plane Se lone pairs and the rear lobes of the Se−Me antibonding orbitals.[120]

The large magnitude of ^2J(SeSe) couplings reported by Laitinen and Pakkanen[490] in selenium sulphide ring molecules of the type S_nSe_{8-n} and by Eggert *et al.*[491] in dialkyl polyselenides of the type R−Se_m−R suggests that a through-space mechanism is also operating in such cases in much the same way as in ^2J(PP) couplings in compounds like $HN(PF_2)_2$.

3.3.3. Through-space couplings via an intermediate moiety

One of the first applications of the IPPP approach to study a through-space mechanism was the analysis of J^{TS}(FC) couplings transmitted via an intermediate C−H attached to the coupled C nucleus.[144] Considering derivatives of *cis*-1,3-difluoropropene with different numbers of fluorine atoms at the methyl group as model compounds, the $^3J^{TS}$(CF) component in each case was calculated for different values of the rotation angle θ of the fluoromethyl group. It was found that the proximity of a methyl C−H bond to the vinyl F atom constitutes an efficient pathway for transmitting a positive contribution to the FC term of the ^3J(CF) coupling. Further fluorine substitution at the methyl group gives a larger $^3J^{TS}$(CF) component, indicating that the efficiency of that pathway increases with increasing s character of the C−H bond. Experimental values supporting these theoretical results have been published.[443,452,453,455,492] An IPPP–CLOPPA analysis performed on ^4J(CHO,F) in 1-fluoro-8-naphthaldehyde indicates that there is an exponential decay of that coupling with F. . .H_{formyl} distance.[448] A dependence of this type was experimentally verified by Hsee and Sardella,[449] while a J^{TS}(CH) coupling transmitted via an intermediate C−H bond has also been reported[302] in *N*-methyl-2-pyridone.

J^{TS}(PC) and J^{TS}(SeC) transmitted via an intermediate C−H bond have also been reported in the *Z* isomer of $Ph_2PHC{=}CHCH_3$[493] and in the *Z* isomers of selenoimidates[381] respectively. In both types of compounds inversion of the $^3J^{cis}$(XC)/$^3J^{trans}$(XC) relationship with respect to the *E* isomers was known experimentally.[494–496] These analyses were also briefly reviewed in ref. 150. In these cases the main coupling pathway is defined by

the X lone pair and the C–H bond. Additional experimental support for this theoretical prediction comes from the work of Spassov *et al.*,[497] which shows that $^3J^{cis}$(PC) is smaller than $^3J^{trans}$(PC) for a C–C=C–P fragment with a pentavalent P atom. The greater efficiency observed for $^3J^{TS}$(SeC) than for $^3J^{TS}$(PC) in these compounds studied in refs 381 and 493 can easily be ascribed to the larger s character of the Se lone pair as compared with that of P. Radeglia *et al.*[498] studied with the INDO–SOS approach the angular dependence of ^2J(NC) and ^3J(NC) couplings. Their results suggest that J^{TS}(NC) is mediated by a C–H bond.

"Anti-Karplus" behaviour for vicinal $^3J(P^{III}C)$ couplings has also been reported in other types of compounds,[499,500] while for $^3J(P^{IV}C)$ couplings a Karplus-type relationship has been reported,[162,163,497] supporting the IPPP results concerning the role played by the P lone pair in the through-space transmission.

The IPPP analysis of J^{TS}(CF) in *cis*-1,3-difluoropropene[144] shows that for a transoid arrangement of the F atoms a positive contribution is calculated. This means that the rear lobe of the C–F bond is also efficient in transmitting the FC interaction contributing to $^3J^{TS}$(CF). However, when there are three fluorine atoms in the methyl group, this pathway is notably inhibited, since only a small and negative contribution to $^3J^{TS}$(FC) is predicted. This suggests that the lone pairs of the two fluorine atoms with a staggered conformation modify such pathway, leading to a sign inversion of $^3J^{TS}$(CF). Recently, experimental support for this sign inversion was reported by Rae *et al.*[458] for a similar arrangement of two 2-coordinated oxygen atoms bearing lone pairs placed in a staggered conformation with respect to the coupled carbon.

The IPPP analysis of $^3J^{TS}$(CF) in *cis*-1,3-difluoropropene also shows the following trend. When a C–F bond is placed proximate to the coupled F atom, only a small and negative J^{TS}(CF) coupling is predicted. The different behaviour of a C–F bond as compared with a C–H one originates in the lone pairs of the intermediate F atom.[144]

The existence of a through-space component in the J(FH) coupling in trifluoromethylated vinyl compounds gives $|^4J^{cis}(FH)| > |^4J^{trans}(FH)|$, which has been used as a criterion to distinguish between Z and E configurations. However, the angular dependence, both in sign and absolute value, of J^{TS}(FH) components mentioned above suggests that for compounds with a geminal substituent it is very likely that $^4J^{cis}$(FH) cannot be observed. Bégué *et al.*[501] found that in such cases the relationship $|^3J^{cis}(CF)| > |^3J^{trans}(CF)|$ still holds, and therefore it can be used to determine the Z and E configurations. Many other cases where the *cis/trans* relationship is inverted can be quoted. Only one further example is given here. In bisarylmercury compounds where a CH_3 group is placed *ortho* to Hg it is observed that $^3J(Hg,CH_3) > {}^3J(HgC_{3,5})$.[502]

In cage compounds the overlap of rear lobes is accepted as an efficient

pathway for transmitting through space the spin information associated with the FC term. This is called the "Barfield effect".[178] During the review period both the NNBI[309,503,504] and IPPP[505–507] methods were applied to study the through-space transmission via the bridgehead carbon atoms in bicycloalkanes. Comparisons obtained with both methods for the same couplings have also been presented in refs 154 and 178.

Other cases where such an effect has been assumed to make important contributions to the couplings are $^7J(FF) = \pm 2.8$ Hz in **[26]** measured by Olah *et al.*,[508] where the respective C–F bonds are coaxial, favouring the overlap of their rear lobes. In 1,3-difluoroadamantane Della *et al.*[509] assumed that $^3J(C_3F) = 9.9$ Hz has a rear lobe through-space contribution. This is a case where a *trans* coupling is increased owing to a through-space contribution.

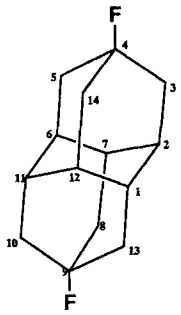

[26]

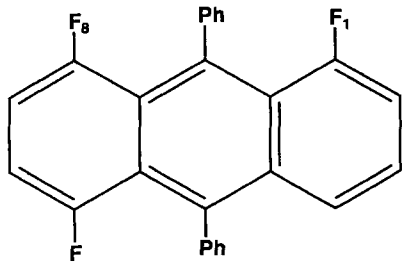

[27]

Some unusual pathways for through-space couplings have been reported recently. Long-range couplings with part of their pathway being through space are favoured by a zig-zag arrangement as in for 5-fluoro-3,3-dimethyl-1,2,3,4-tetrahydrophenanthrene, with $J^{TS}(F \ldots C_4{-}C_3{-}C_2) = \pm 1.0$ Hz and $J^{TS}(F \ldots C_4{-}C_3) = \pm 3.8$ Hz.[453] In 12*H*-dibenzo(*d*,*g*)(1,3,2)dioxaphosphocins a $J^{TS}(PH) \approx 2$ Hz was reported,[510] which is expected to be transmitted through space. A $J^{TS}(FF)$ coupling transmitted through an intervening phenyl group was reported by Mallory *et al.*[466] in **[27]**, with $J(F_8,F_1) = 6.4$ Hz. A $J^{TS}(PSn)$ coupling transmitted via a P . . . H–C–Sn pathway has recently been reported.[459]

3.3.4. Through-space couplings via hydrogen bonds

The existence of a two-bond NH. . .S(cys)–Cd coupling in ^{113}Cd-substituted rubredoxin is taken as indicative that this hydrogen bond has a significant covalent character.[511] However, the existence of through-space long-range couplings where there is no covalent bond between the proximate fragments and where through-space transmission occurs, such as those

reported by Gribble and Kelly[453] in 5-fluoro-3,3-dimethyl-1,2,3,4-tetrahydrophenanthrene, $J^{TS}(F\ldots C_4{-}C_3) = \pm 3.8$ Hz and $J^{TS}(F\ldots C_4{-}C_3{-}C_2) = \pm 1.0$ Hz, does not support such an assertion.

The transmission of a long-range J(HH) coupling where part of the pathway involves a hydrogen bond, H . . . N=C−H, has also been reported by Afonin *et al.*,[512] while Schaefer *et al.*[513] have reported positive J(HH) couplings transmitted through the pathway H−C=O . . . H−O between side chains in derivatives of salicylaldehyde. Such a pathway is enhanced either by substituents that sterically force a closer proximity between the O . . . H atoms, or by electronic interactions between substituents that place more negative charge on the carbonyl atom.

3.4. Proximity effects on spin–spin coupling constants

There is a certain overlap between this section and others presented above. However, it was decided to discuss separately several theoretical and experimental trends originating mainly from crowding around at least one of the two coupled nuclei. This crowding modifies the ground state wave function in the surroundings of any of the coupled nuclei, which leads to slight changes in the LMOs in the vicinity of both nuclei. These changes modify the corresponding $J_{ia,jb}$ terms in (26) but terms originating in virtual excitations involving LMOs of the proximate group are negligible.

Two conspicuous examples of proximate effects were analysed in the literature during the review period, namely the ^1J(CH) coupling when the C−H bond is proximate to a lone pair,[514] and the *exo-exo–endo-endo* difference in vicinal J(HH) couplings in norbornane and norbornene.[423]

3.4.1. Proximity effects on one-bond couplings

Departures from the linear correlation between $^1J(C_2H)$ couplings and the s character of the C_2−H bond in *N*-substituted indoles were ascribed by Pachter *et al.*[191] to proximity effects of the N side chain. An estimation of this effect was obtained using Barfield's NNBI method[128] in 1-methoxyindole for an OCH_3 conformation *cis* to the ring position 2. To that end, non-bonded interactions between H_2 and the Me hydrogen atoms were neglected. A contribution of 4.9 Hz to $^1J(C_2H)$ was estimated for that proximity effect.[191]

In formyl and acetyl derivatives of benzo[*b*]thiophene Benassi *et al.*[349] observed that the ring C−H bonds facing a carbonyl group present ^1J(CH) couplings increased by a few hertz. Such increases can be rationalized in terms of proximity effect of the carbonyl lone pairs.[514] Similar effects were also reported by Defay *et al.*[515] for C−H bonds in the bay region of benzo[*f*]quinoxaline derivatives that are proximate to the N_4 lone pair.

Gronowitz *et al.*[221] reported similar effects in dithieno[*b*,*d*]pyridines for C−H bonds of the bay region proximate to S lone pairs. Denisov *et al.*[516] used this proximity effect to identify tautomers in aromatic nitrogen heterocycles. The large formyl ^1J(CH) coupling reported in *o*-nitrobenzaldehyde[517] can be ascribed to a similar effect.

The CLOPPA method has been applied to study the proximity effect of 2-coordinated oxygen lone pairs on ^1J(CH) couplings in aromatic compounds.[514] Results were compared with experimental values in methylenedioxybenzene derivatives and substituted anisoles. It was found that the proximity effect affects mainly the "bond contribution", $^1J^b$ (see Section 3.2).

It is important to recall the different nature of these proximity effects on ^1J(CH) couplings and the orientational lone pair effect discussed in Section 3.2. In fact, in the present case the proximity to a lone pair modifies the electronic structure of the C−H bond, leading to a small degree of shortening for a *syn*-periplanar arrangement.[222,518] In addition, this proximity effect, unlike that described in Section 3.2, does not depend on the s character of the lone pair. For instance, a large variation in a ^1J(CH) coupling for different orientations with respect to a p-type N lone pair has been reported by Davies *et al.*[519] in pyrimidine nucleotides.

A detailed experimental and FPT–INDO study of the conformational dependence of ^1J(CH) couplings in oligosaccharides has been carried out by Hricovini and Tvaroška.[520] The variation of that coupling is expressed as a truncated series in the dihedral angle about the glycosidic C−O bond.

The increase in ^1J(CH) couplings due to the proximity of the corresponding C−H bond to a lone pair was taken by Afonin *et al.*[521,522] and Satonaka *et al.*[523,524] as an indication that a C−H . . . X hydrogen bond is formed. However, this assertion seems to be in contradiction with the following two facts. First, it was found in some instances that the proximity of a C−H bond to a lone pair yields a slight shortening of that bond,[222,518] which is incompatible with the existence of a hydrogen bond. Secondly, an increase in the coordination number yields, in general, a decrease in the one-bond couplings involving this atom.[179] Although there are exceptions to this trend, most of them are observed when the additional coordination takes place through a p-type orbital, which obviously cannot be the case for an H atom. A dramatically small ^1J(CH) coupling for a 2-coordinated H atom has been reported: ^1J(CH) = 47 Hz.[525]

The γ-compression effect corresponding to a repulsive interaction of the type C−H . . . H−N corresponds to a decrease in the corresponding ^1J(NH) coupling.[526] In the formyl and acetyl derivatives of benzo[*b*]thiophene studied by Benasi *et al.*[349] it is observed that the aromatic C−H bond facing the methyl moiety of the acetyl group shows a reduction in the corresponding ^1J(CH) coupling amounting to a few hertz. In norbornane the difference between $^1J^{exo}(C_2H)$ = 128.85 Hz and $^1J^{endo}(C_2H)$ = 131.00 Hz[527,528] can be

traced out to the repulsive interaction between the proximate *exo* C_2-H and C_7-H bonds.

Important differences between the two $^1J(CF)$ couplings have been measured[529] in [**28**], with $^1J(C_8F'_8) = 318.7$ Hz and $^1J(C_8F_8) = 274.5$ Hz. The proximity between F'_8 and H'_7 can be assessed owing to the large $^4J(C_7F'_8) = 14.5$ Hz, which indicates that this coupling is mainly transmitted through space via the $C_7-H'_7$ bond. In fact, although a dual pathway separates both coupled nuclei, both correspond to *anti* zig-zag arrangements. Besides, $^4J(C_7F_8)$ could not be observed. Several factors can be expected to lead to such a large difference of 44 Hz. One should be the proximity effect between F'_8 and H'_7.

In fluoroadamantanes the algebraic decrease in $^1J(CF)$ values upon successive introduction of a fluorine at γ_{anti} carbon atoms has been interpreted by Olah *et al.*[508] as originating from rear lobe interactions inside the cage compound.

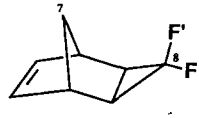

[**28**]

3.4.2. Proximity effects on other types of couplings

The marked difference between $^3J(H_{exo},H_{exo})$ and $^3J(H_{endo},H_{endo})$ in norbornane, which has been known for many years,[530,531] has been analysed during the review period by de Leeuw *et al.*[532] using the NNBI approach and by Cavasotto *et al.*[423] using the CLOPPA method. The earlier version of the NNBI method[127] had been used by Marshall *et al.*[533] to address the same problem. The origin of the difference was traced to the non-bonded interactions between the *exo* C−H bonds and the methylene C_7-H bond, which affect the electronic distribution around the coupled nuclei, modifying the local contributions in (26).

Proximity effects on $^5J_t(CHO,H_3)$ were reported by Schaefer *et al.* in salicylaldehyde [**29**][534] and *o*-isopropylbenzaldehyde [**30**].[535] As the sum $^5J_t(CHO,H_3) + {}^5J_c(CHO,H_5)$ in *o*-fluorobenzaldehyde does not deviate by more than 0.01 Hz[536] from that in benzaldehyde, which is 0.862 Hz (in CS_2/C_6D_{12}),[537] Schaefer *et al.* suggest that the small values observed in [**29**] and [**30**] are due not to a substituent effect but to a perturbation of the carbonyl group orbitals resulting from the proximate interaction with the OH and i-Pr groups respectively, since they conclude that the oxygen $2p_z$ orbital plays a significant role in the transmission of those couplings.[538] It is

interesting to recall that both the FPT–CNDO/2 and FPT–INDO calculations give $^5J_t(CHO,H_3)$ 0.1 Hz smaller than $^5J_t(CHO,H_5)$ ([**30**] and [**31**] respectively).

Proximity effects on $^2J(FH)$ couplings were observed by Salon *et al.*[539] The dependence of $^2J(CH)$ couplings on the orientation of an O atom attached to the coupled carbon was discussed by Prytulla *et al.*[540] The effect of the orientation of the carbonyl moiety on $J(CC)$ couplings involving the C=O carbon atom has been described in detail by Hansen.[158]

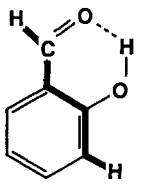

[29]

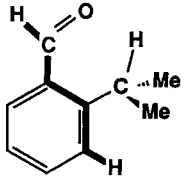

[30]

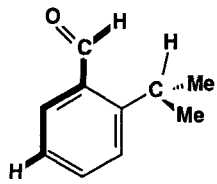

[31]

Large variations in $^1J(^{31}P^{17}O)$ couplings were measured by Quin *et al.*,[541] suggesting that proximity effects on this type of coupling may be quite important. However, no obvious relationship with the large effects observed on $\delta(^{17}O)$ chemical shifts in the same compounds was found.

Another proximity effect frequently quoted in the literature is the case in which the steric crowding around a given moiety alters bond lengths and bond angles within it. Such changes result in rehybridization of bonds, which in turn leads to changes in the corresponding coupling constants. The following example is worthy of mention: $^1J(Sn,CH_3)$ couplings in 9-trimethylstannyl triptycenes.[542] Although with much lower sensitivity, $^1J(CF)$ couplings are also known to be dependent on steric effects.[543] Steric effects on $^1J(CC)$ couplings have been discussed by Krishnamurthy *et al.*[544]

3.5. The anisotropy of coupling constants

In this section a few papers in which anisotropies of couplings have been analysed in some detail are reviewed. Anisotropies of many couplings have been reported in the context of theoretical papers describing calculations of couplings, and appropriate references were given in Section 2.2.

There is a scarcity of experimental measurements of the anisotropic part of the indirect coupling tensor, ***J***. Such measurements are difficult to carry out, since it is not easy to separate the contribution from the direct coupling tensor ***D*** from the anisotropic part of ***J***. Theoretical results seem to indicate that the anisotropic part of ***J*** is larger for heavy nuclei. A detailed account of work published prior to the review period has been given by Lounila and

Jokisaari.[183] Efforts experimentally to determine the anisotropy of coupling tensors have been periodically reviewed.[545]

A new approach to determining the anisotropy of $\boldsymbol{J}$ was applied by Hiltunen *et al.*[546] It takes into consideration the deformational contributions, both in the direct dipolar couplings and in the corresponding anisotropic couplings.

Several attempts to evaluate the anisotropy of coupling tensors using solid state NMR have been complicated by the difficulties met in attempting to separate the vibrational–librational corrections to the direct coupling constants from the genuine anistropy in the electron-mediated indirect couplings. These problems have been discussed in detail by Haiping and Harris[547] in the context of their experimental work on Sn NMR. They also pointed out how the experimental determination of Δ^1J(SnF) depends on precise knowledge of the Sn−F distance for Me_3SnF, $(i\text{-}Bu)_3SnF$ and Ph_3SnF.

Zilm and Grant[548] estimated the magnitude of the anisotropy of ^1J(CC) couplings in C_2H_2, C_2H_4 and of ^{1}J(CF) in CH_3F using low-temperature matrix-isolation dipolar spectroscopy. The corresponding ΔJ values were extracted from the observed D couplings using the librational model of Manz,[549] and appear to be much larger than the theoretical estimates. However, the large experimental errors precluded obtaining definite information on these parameters.

An extensive semiempirical study of the anisotropy of couplings has been presented by Facelli and Barfield,[105] who included all second-order terms. It is important to recall that the cross-term between the FC and SD interactions contributes to the anisotropy of $\boldsymbol{J}$ but not to the isotropic coupling since it is traceless. These semiempirical results are in fair agreement with the *ab initio* ones in the cases where they are available, and they support previous assumptions that the FC/SD cross-term is the dominant one in determining the anisotropy of the total tensor.[183] This assertion is also supported by the work of Lazzeretti *et al.*,[550–552] who have reported CHF anistropy calculations using high-quality basis sets for PH_2^-, PH_3, PH_4^+, H_2O, NH_4^+, NH_2^-, BH_4^- and CH_4. In all cases the FC/SD cross-term plays a dominant role in determining the anisotropy of the total coupling tensor. Unfortunately, the agreement between theoretical calculations and experimental estimates is only limited, in spite of the near-Hartree–Fock limit of the ground state wave function used in the calculations. Any of the following four reasons can be envisioned as the origin of the poor agreement: (i) further electronic correlation is necessary for obtaining good-quality anisotropy contributions; (ii) the DSO term, which is not isotropic, is neglected in those calculations; (iii) theoretical calculations are extremely sensitive to small changes in the geometry used to perform them; and, last but not least, (iv) experimental measurements are determined with large uncertainties.

Anisotropies of the ^1J(CC), ^1J(CN) and ^2J(CN) couplings in acetonitrile have been measured and experimental values compared with those obtained using the REX approach.[553] A positive relative anisotropy $R = \Delta J/J$ for ^1J(CH) in acetonitrile was calculated that is of the opposite sign to that calculated by Lazzeretti and Zanasi[552] in CH_4.

Experimental evidence has been found for an anistropic contribution to ^5J(FF) in *p*-difluorobenzene.[554] This result is in line with theoretical predictions indicating that some long-range J(FF) couplings in conjugated compounds have a large SD contribution.[555]

The dominant role predicted theoretically for the FC/SD cross-term means that caution must be taken in adopting the commonly made assumption that the presence of a large anisotropic component is evidence that non-contact contributions dominate or at least are important in the isotropic coupling.[556]

The important lone pair effect on the FC term of one-bond couplings described in Section 3.2 suggests that similar effects may be operating on the FC/SD cross-term. Such effects could be especially important when one of the coupled nuclei bears more than one lone pair. The following experimental values involving halogen nuclei are worthy of mention. The relative anisotropy of ^1J(CF) in methyl fluoride was reported as -2.5 ± 0.2.[557] Δ^1J(SnCl) values in the range of -400 to -800 Hz have been reported in several compounds.[558]

It is interesting to note that the papers of Lazzeretti *et al.* provide numerical examples for the symmetry rules of Buckingham *et al.*[10] In fact, these numerical values show the existence of antisymmetric components in the coupling tensor, which are also predicted by semiempirical calculations.[105] To the authors' knowledge, no experimental information on the asymmetric components of the tensor $\boldsymbol{J}$ has yet been reported.

3.6. Isotopic effects on coupling constants

During the last decade the isotopic effect on NMR parameters has received much attention, and many papers have appeared dealing with this topic. However, most works refer to the magnetic shielding tensor, with only a few dealing with the influence of isotopic substitution upon coupling constants. The most detailed surveys of this effect on these parameters are those of Jameson and Osten[559] and Sergeyev.[177] The former is an excellent attempt to systematize the classification and the origin of this effect. The latter has appeared more recently, and is a critical review of the current literature. The large precision required to measure couplings in order to obtain data on the isotopic effect is emphasized. Other reviews that have appeared during the last decade in which the isotope effects on couplings are at least briefly discussed are those of Specialist Periodical Reports[3] and Jameson.[179] In this

latter work a brief and clear description of the intramolecular dynamics leading to the isotopic effect is given.

It is important to note that there is a small difference in the definitions of both the primary and secondary isotope effects on couplings given by Jameson[179,559] and by Sergeyev.[177] In refs 179 and 559 the primary and secondary isotope effects are defined respectively as

$$\Delta_p J(XY) = \left| \frac{\gamma(^mY)}{\gamma(^nY)} J(X^nY) \right| - |J(X^mY)|, \tag{45}$$

$$\Delta_s J(XY)\{Z\} = |J(XY)_{heavy}| - |J(XY)_{light}|, \tag{46}$$

where $\Delta_p J(XY)$ is the primary isotope effect on $J(XY)$ due to the replacement of the lighter isotope ^mY by the heavier one ^nY, i.e. $n > m$. $\Delta_s J(XY)$ is the secondary isotope effect due to the isotopic substitution of a neighbouring nucleus Z. On the other hand, in ref. 177 the isotope effects are defined using the J values with their respective signs. Therefore if $J(XY) > 0$ and both magnetogyric ratios $\gamma(^mY)$ and $\gamma(^nY)$ are of the same sign then the two definitions coincide.

It is important to note that Sergeyev has made a clear distinction between primary and secondary isotope effects in data taken from the literature where such division was not taken properly into account. To fix ideas, Sergeyev[177] gives as an example the way in which the primary deuterium isotope effects on $^1J(CH)$ in methane should be determined. To obtain the primary isotope effect, the following two measurements should be carried out: $^1J(^{13}C^1H)$ in $^{13}CH_4$ and $^1J(^{13}C^2H)$ in $^{13}CH_3D$. $\Delta_p {}^1J$ is obtained as

$$\Delta_p {}^1J(CH) = \left| \frac{\gamma_H}{\gamma_D} {}^1J(^{13}C^2H)[CH_3D] \right| - |{}^1J(^{13}C^1H)[CH_4]|. \tag{47}$$

To obtain the secondary isotope effect, the following two measurements should be carried out: $^1J(^{13}C^1H)$ in $^{13}CH_4$ and $^1J(^{13}C^1H)$ in $^{13}CH_3D$. $\Delta_s {}^1J$ is obtained as

$$\Delta_s {}^1J(CH) = \left| \frac{\gamma_H}{\gamma_D} {}^1J(^{13}C^1H)[CH_3D] \right| - |{}^1J(^{13}C^1H)[CH_4]|. \tag{48}$$

The definitions (45) and (46) are employed here.

Sergeyev's analysis involved not only the $J(XY)$ coupling constants but the respective reduced values $K(X,Y)$. For this last type of couplings the same discrepancy appears between the definitions of Sergeyev[177] and of Jameson and Osten.[559]

By far the most studied isotope effect is that observed upon substituting one or more protons by deuterons, i.e. the deuterium isotope effect. On

increasing the deuterium substitution, the secondary deuterium isotope effect is approximately additive.[177,559] Jameson[179] defined the primary deuterium isotope effect on the reduced coupling constant as

$$\Delta_p K(X|^{2/1}H) = |K(XD)| - |K(XH)|. \tag{49}$$

Again this definition coincides with that of Sergeyev[177] when $K(XD) > O$. Hereinafter the definitions (45), (46) and (49) will be used, since they are more useful when the sign of $J(XY)$ is unknown.

Changes in conformation or arrangements and ordinary rotational and vibrational averaging upon isotope substitution are supposed to be the origin of the isotope effect on couplings.[559] This rationalization is similar to that of the isotope effect on magnetic shielding constants.[2a] From a theoretical point of view, the isotope effect is investigated by considering the sensitivity of a given coupling constant to changes in molecular geometry. This is the case, for instance, with the geminal $J(HH)$ coupling in methane,[560,561] where the coupling surface was calculated, choosing many geometries around equilibrium. These geminal couplings were found to be particularly sensitive to the angle between the C–H bonds containing the coupled protons. Such a dependence has also been studied by Klessinger and Bolte[562] for the FC term, keeping all other geometrical parameters constant. They found a strong sensitivity of the geminal coupling to the hybridization of the C–H bonds of the coupled nuclei. It is interesting to note that Lazzeretti[563] found the $^2J(HH)$ couplings in bicyclo(1.1.1)pentane to have only a weak dependence on the C–C*–C angle, where C* is the carbon atom to which the coupled protons are attached. The 6-31G** optimized geometry of that compound yields a C–C*–C angle of about 72°. The corresponding RPA–FC term is −14.65 Hz.

Similar studies aimed at determining the coupling surface have also been reported for other homonuclear geminal couplings,[564] and for the $^1J(CH)$ coupling in methane.[565] Recently, Raynes *et al.* have studied the sensitivity of these couplings to the C–H distance using the SOPPA and CCPPA approximations. They found that at these levels of approximation the couplings are much more sensitive than at the RPA one.

The primary deuterium isotope effect (45) and (49) can be of either sign. In most cases its magnitude is very small, and this is the main reason why it is so difficult to perform measurements sufficiently accurate to detect it. Since deuterium is a spin-1 nucleus, its electric quadrupole moment prevents $J(XD)$ from being obtained with adequate precision in many cases.

Jameson and Osten[559] have tabulated a series of primary and secondary isotope effects, and, among other conclusions, they observed that the primary deuterium isotope effect on $^1J(XH)$ is negative when the atom X does not contain a lone pair, and positive if X bears at least one lone pair. A few conspicuous cases are as follows. $\Delta_p {}^1J(CH) = -0.8 \pm 0.2$ Hz in CDH_3/

CH_4; $\Delta_p{}^1J(PH) = +12.19$ Hz in PH_2D/PH_3; $\Delta_p{}^1J(SiH) = -0.9 \pm 0.7$ Hz in SiH_2DI/SiH_3I; and $\Delta_p{}^1J(SeH) = +2.55 \pm 0.8$ Hz in $SeHD/SeH_2$. It should be especially noted that $\gamma(^{29}Si) < 0$. With the definition (45), $\Delta_p{}^1J(SiH) < 0$ in SiH_3I, i.e. it is of the same sign as $\Delta_p{}^1J(CH)$ in methane. Support for the assumption that the presence or not of a lone pair in the atom X determines the sign of $\Delta_p{}^1J(XH)$ has been given by Jameson and Osten,[559] who noted that in 4-coordinated phosphorus compounds $\Delta_p{}^1J(PH) < 0$.

Assuming that changes in conformation or arrangement do not take place, the deuterium isotope effect on $^1J(XH)$ can be approximated

$$\Delta_p{}^1J(X^{2/1}H) = \frac{\partial J}{\partial \Delta r_{XH}}\bigg|_e [\langle \Delta r_{XD}\rangle - \langle \Delta r_{XH}\rangle] \tag{50}$$

where it is assumed that the stretching mode of the bond X–H (X–D) makes by far the greatest contribution to the rovibrational averaging. The CLOPPA method is particularly suited for analysing factors that define the behaviour of the derivative $\partial^1J(XH)/\partial\Delta r_{XH}$, provided the MO approach employed in its calculation is adequate to describe the $^1J(XH)$ coupling. An analysis of this type at the INDO level for $^1J(CH)$ in methane has been presented in ref. 151. According to (25), the derivative can be written as

$$\frac{\partial^1J(CH)}{\partial \Delta r_{CH}} = \sum_{ia,jb} \frac{\partial^1J_{ia,jb}}{\partial \Delta r_{CH}}. \tag{51}$$

This sum is overwhelmingly dominated by the term corresponding to the "bond contribution" (see Section 3.2), $^1J^b$. In terms of the polarization propagator and perturbations, this term can be written as $^1J^b = U^b(C)P^bU^b(H)$. Table 23 shows the CLOPPA–INDO results for methane. It can be seen that the main contribution to the derivative comes from the polarization propagator term, i.e. from the electronic structure of the C–H bond. On the other hand, the electron density at the site of the H atom makes a negligible contribution.

In (50) $\langle \Delta r_{XD}\rangle$ is shorter than $\langle \Delta r_{XH}\rangle$. For instance, the difference $\Delta\langle \Delta r\rangle = \langle \Delta r_{XD}\rangle - \langle \Delta r_{XH}\rangle$ for C–H bonds is about 5×10^{-3} Å.[567] This indicates that for $^1J(XH)$ couplings where X is an atom bearing a lone pair, such as $^1J(PH)$ in PH_3 or $^1J(SeH)$ in SeH_2,[568]

$$\frac{\partial |^1J(XH)|}{\partial \Delta r_{XH}}\bigg|_e < 0 \tag{52}$$

while in cases where X does not bear a lone pair, such as $^1J(CH)$ in CH_4,[569] $^1J(PH)$ in PH_4^+,[570] $^1J(PH)$ in $H_2P(O)OH$,[559] etc.

$$\frac{^1\partial |J(XH)|}{\partial \Delta r_{XH}}\bigg|_e > 0. \tag{53}$$

Table 23. CLOPPA–INDO analysis of $\partial\,{}^1J(\mathrm{CH})/\partial\Delta r_{\mathrm{CH}}|_e$ in methane.[a]

$^1J(\mathrm{CH})$	123.2 Hz[b]
$\left.\dfrac{\partial\,{}^1J(\mathrm{CH})}{\partial\Delta r_{\mathrm{CH}}}\right\|_e$	193.6 Hz Å^{-1} [b]
$\dfrac{1}{P^b}\dfrac{\partial P^b}{\partial\Delta r_{\mathrm{CH}}}$	1.89
$\dfrac{1}{\|U^b(\mathrm{C})\|}\dfrac{\partial}{\partial\Delta r_{\mathrm{CH}}}\|U^b(\mathrm{C})\|$	−0.685
$\dfrac{1}{\|U^b(\mathrm{H})\|}\dfrac{\partial}{\partial\Delta r_{\mathrm{CH}}}\|U^b(\mathrm{H})\|$	<0.01

[a]From ref. 151.
[b]The values from ref. 559 are $^1J(\mathrm{CH}) = 125.3$ Hz and $\partial\,{}^1J(\mathrm{CH})/\partial\Delta r_{\mathrm{CH}}|_e = 189.8$ Hz Å^{-1}.

However, some caution should be taken in considering these rules as completely general. There are some instances where other phenomena could also be playing an important role. For instance, in cyclobutene **[32]** Hansen and Led[571] reported the following interesting two one-bond deuterium isotope effects on $^1J(\mathrm{CH})$:

$$\Delta_p\,{}^1J(\mathrm{C_1H_1}) = -0.38\ \mathrm{Hz}, \tag{54}$$

$$\Delta_p\,{}^1J(\mathrm{C_3H_3}) = +0.16\ \mathrm{Hz}. \tag{55}$$

Although these values are too small for a definite conclusion to be drawn, it is interesting to observe that $\Delta_p\,{}^1J(\mathrm{CH})$ for the sp^3-hybridized carbon atom is positive, while it is negative for the sp^2-hybridized one. Obviously, this different behaviour cannot be ascribed to the different carbon atom

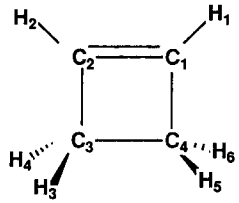

[32]

hybridizations, since for other ^1J(CH) couplings with the carbon atom either with sp or sp^3 hybridization, Δ_p ^1J(CH) was found to be negative.[559] A comparison of Δ_p ^1J(CH) for differently hybridized carbon atoms has recently been reported by Sergeyev *et al.*[569] Although the magnitude of these isotope effects depends on the hybridization at the carbon atom, all of them are negative. The positive sign of Δ_p $^1J(C_3H_3)$ can be rationalized in the following terms. The configuration for the C_3-H_3 bond in cyclobutene is such that an important hyperconjugative interaction with the C_1-C_2 π-electron system can take place. This interaction leads to a lengthening of the C_3-H_3 bond[279] and a reduction in the $^1J(C_3H_3)$ coupling (see Section 3.1). According to Wesener and Günther,[572] a C–D bond has less hyperconjugative interaction ability than a C–H one. The isotope effect on hyperconjugation has also been discussed by Berger[573] and Jameson and Osten.[2a] The lower hyperconjugative ability of a C–D bond compared with a C–H one is also exemplified by recently reported five-bond couplings in $C_6H_5CH_3$ and $C_6H_5CH_2D$:[569] while $^5J(C_4,CH_3) = 0.840 \pm 0.003$ Hz in the former, $(\gamma_H/\gamma_D)^5J(C_4,CH_2D) = 0.831 \pm 0.002$ Hz in the latter. Since the pathways of these couplings are overwhelmingly dominated by the hyperconjugative interaction, when it is reduced a decrease in the corresponding coupling is observed. Therefore, upon deuteration, the C_3-H_3 bond of cyclobutene undergoes a decrease in its hyperconjugative interaction with the π-electron system, and the isotope effect on $^1J(C_3H_3)$ is determined by competition between two opposing phenomena. Therefore in similar cases Δ_p ^1J(CH) can be of either sign, depending on the total hyperconjugative interaction affecting that C–H bond. Other experimental data can also be rationalized in similar terms. Apparently, Δ_p $^1J(C(sp^3)H)$ increases in magnitude when an electronegative group is attached to the C atom. For instance, while in CH_4 Δ_p ^1J(CH) = −0.2 Hz has been reported,[569] in $CHCl_3$ Δ_p ^1J(CH) = −0.96 Hz[574] was measured and in nitromethane Δ_p ^1J(CH) = −0.97 Hz.[575] It is noteworthy that, according to this trend, the magnitude of Δ_p $^1J(C(sp^3)H)$ in toluene should be greater than in methane. However, it amounts to only −0.002 Hz,[569] which again can be explained as being due to the reduction of the hyperconjugative interaction upon deuterium substitution. Further support for such a rationalization is obtained in the recently reported data on phenylsilanes of the type $(C_6H_5)_{4-n}SiH_n$ (n = 1–3).[576] Δ_p ^1J(SiH) can be calculated from these values using (47). They are displayed in Table 24. An increase in the hyperconjugative interaction undergone by a Si–H bond is expected along the series n = 3 to n = 1, since in the first case that interaction takes place with only one phenyl group, while in the last it takes place with three different phenyl groups. An algebraic increase of Δ_p ^1J(SiH) is observed along that series, becoming positive for n = 1. It is interesting to note that a decrease of $|^1J(SiH)|$ is also observed along that series, paralleling the increase in the hyperconjugative interaction.

Table 24. Primary deuterium isotope effect on ^1J(SiH) couplings in phenylsilanes $(C_6H_5)_{4-n}SiH_n$.[a]

Compound	^1J(SiH) (Hz)	$\Delta_p{}^1J$(SiH)[b] (Hz)
$C_6H_5SiH_3$	200.43	−0.37
$C_6H_5SiH_2D$	200.06[c]	
$(C_6H_5)_2SiH_2$	199.28	−0.19
$(C_6H_5)_2SiHD$	199.09[b]	
$(C_6H_5)_3SiH$	198.20	+0.55
$(C_6H_5)_3SiD$	198.75	

[a]Experimental ^1J(SiH) couplings are from ref. 576.
[b]Calculated using (47).
[c]Calculated as $^1J(SiH) = (\gamma_H/\gamma_D)\,{}^1J(SiD)$.

As mentioned in Section 3.2, the lone pair contribution to the FC term of the reduced ^1K(XY) coupling is negative. On the other hand, the bond contribution to that component is positive. According to Jameson and Osten,[559] the different trends of the derivatives in (52) and (53) originate in the different behaviour of those contributions. There are several recently reported measurements consistent with this rationalization. Negative primary deuterium isotope effects on ^1J(XH) couplings have been reported in different methane isotopomers at different temperatures,[82] in different stannane and stannonium cation isotopomers,[577] and in different PH_4^+ isotopomers.[578] Positive primary deuterium isotope effects on ^1J(XH) couplings have been reported in ammonia and water,[578] in PH_3 and PH_2^-,[570] and in the stannyl ion, which appears to be the largest, in magnitude, primary isotope effect so far known.[579] The case of ammonium ion isotopomers is somewhat singular, since the measured primary deuterium isotope effect on ^1J(NH) is positive, but the calculated one is negative.[578] Values reported previously by Wasylishen and Friederich[580] also point towards a positive primary isotope effect, although couplings have not been determined with sufficient precision to confirm this. The case of the stannyl ion deserves special comment. The sign of the ^1J(SnH) coupling in this compound has not been determined. However, the recently reported RPA–MNDO-calculated value[51] corresponds to $^1K(SnH) < 0$, i.e. the heavy atom effect on the lone pair contribution makes the FC term of the reduced coupling constant negative. Therefore, if Jameson and Osten's[559] rationalization for the positive primary deuterium isotope effect when the X atom bears a lone pair is applied straightforwardly to the stannyl ion then a negative sign should be obtained. However, it must be recalled that so far it has not been verified experimentally that ^1K(SnH) is negative in the stannyl ion. If it is then Jameson and Osten's rationalization should be somewhat modified for cases where the reduced coupling is negative.

Table 25. Secondary deuterium isotope effect on $^1J^{trans}$(PtP) and $^1J^{cis}$(PtP) in [**33**].[a]

	X = H	X = D
$^1J^{trans}$(PtP)[b] (Hz)	2055.6	2031.5
$^1J^{cis}$(PtP)[b] (Hz)	2516.3	2513.9

[a]From ref. 581.
[b]±1.5 Hz.

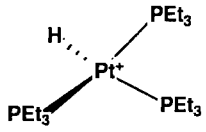

[**33**]

Secondary isotope effects have also been considered in detail by Sergeyev.[177] They will not be considered further here. A few examples not quoted in that review will be cited, however, since they may help in understanding other physical aspects of coupling constants. This is the case, for instance, with the much larger *trans* than *cis* deuterium isotope effect on ^1J(PtP) and ^1J(PtC) couplings reported by Crabtree and Habib.[581] An example is shown in Table 25 for [**33**]. This large effect is considered to be in line with the Pt–H distance being on average 0.005 Å greater than the Pt–D one.

Few further comments will be added here, since the recent and detailed review by Sergeyev[177] renders additional quotations redundant.

Very accurate measurements indicate that ^2J(HD) values in isotopomers of methane are almost independent of solvent, temperature and the number of deuterons present.[83]

The very large secondary deuterium isotope effect reported by Meić *et al.*[582] in *trans*-stilbene has been shown by Ernst[583] to originate in the interpretation of the proton-coupled ^{13}C spectra, which were wrongly taken to be first-order.

3.7. Intermolecular effects on coupling constants

During the review period a novel study of the intermolecular contributions to the relaxation times by intermolecular J couplings[584] using Monte Carlo simulations has been published. The coupling constants between F^- and the first hydration shell of water molecules (^{1}H and ^{17}O) have been calculated using *ab initio* wave functions and the CHF method. The calculated average of couplings is 20–40 Hz, depending upon the temperature, which results in

contributions to ^{19}F relaxation rates of order $10^{-6}\,s^{-1}$. Therefore these contributions appear to be negligible compared with dipolar contributions, which are of order $1\,s^{-1}$.

The solvation model proposed by Klopman[585] has been used extensively in the semiempirical study of solvent effects on coupling constants. In this model the solvent is represented by its dielectric constant; therefore it only describes non-specific solute–solvent interactions. When comparing with experimental results, it is important to keep this limitation in mind, since good agreement can be expected only for those cases in which non-specific interactions are present. The results are totally unsatisfactory, for instance, in cases in which hydrogen bonding is the main interaction between solute and solvent.

Shargi and Webb[586] studied, using the SOS and SCPT methods, the solvent effects on the ^1J(CH), ^1J(CF), ^2J(FH), ^3J(FF) and ^1J(CC) couplings in several fluorocarbons using the INDO approximation. In all cases, except for the *cis* ^3J(FH) in trifluoroethylene, they found that couplings increase as the polarity of the solvent increases. The results are in good agreement with the experimental values. The decrease in the *cis* ^3J(FH) in trifluoroethylene is also observed experimentally, and in most cases disagreements between theory and experiment can be traced to known specific intermolecular interactions. In couplings not involving hydrogen bond electrostatic solvent effects are much larger in the FC term than in the non-contact interactions. SCPT and SOS calculations follow the same qualitative trends.

A detailed FPT–INDO study of the solvent dependence of ^3J(FH) couplings in fluoroethylenes has been presented in ref. 587. The increase in couplings was correlated with the increase in bond orders between the coupled atoms when the dielectric constant of the medium increases.

Solvent effects on ^1J(NC) couplings were studied in ref. 588 using the FTP and SOS–INDO methods, including the solvation model. The largest variations were observed in the FC term, which does not show a definite trend with the dielectric constant ε, since it increases or decreases when increasing ε, depending on the molecule. Variations of about 0.6 Hz on increasing ε to about 80 were observed.

Solvent and rotational effects on ^3J(FH) and ^3J(HH) couplings in 1,2-difluoroethane have been studied by Watanabe and Ando.[589] They concluded that solvent effects on couplings originated from changes in the electronic structure of the molecule and not from conformational changes.

Calculations of solvent effects on couplings in acetaldehyde and methanol have been carried out to complement experimental measurements of medium effects on couplings in these compounds.[590,591]

Ruiz-López *et al.*[592] have modelled the solvent effect on couplings using a spherical cavity and expanding the electronic interaction between solvent and solute in multipoles. This approach had been discussed previously.[593] It was implemented using the INDO approximation to calculate couplings.

The inclusion of higher multipoles in this expansion constitutes an improvement of the dipolar expansion by Barfield and Johnston,[594] which allows the treatment of molecules without a permanent electric dipole moment, such as *trans* symmetrically substituted ethylenes. Unfortunately, multipole contributions are not monotonic, and large multipole expansions are necessary to obtain reliable results.

Facelli *et al.*[189] studied the solvent effect on different transmission mechanisms of the FC term in acetamide using the solvation method and the PRMO–FPT–INDO approach to calculate σ- and π-transmitted components of couplings. The results indicate that π-transmitted contributions are more sensitive to medium effects than the σ-transmitted components. In general, a highly polar medium increases the σ-transmitted contributions while quenching the π-transmitted contributions.

3.8. Multipath additivity of coupling constants

In cyclic and multicyclic compounds large values are known for couplings between nuclei connected by more than one pathway. It is now accepted that—at least in many cases—the experimental value is given by the algebraic sum of couplings transmitted via the different pathways.[595] Klessinger *et al.*[596–599] have discussed this pathway additivity in J(CC) couplings. Stöcker[600] has discussed the dual-path transmission of the ^1J(CC) coupling in cyclopropane, carrying out SCPT–INDO calculations in compounds with equivalent pathways.

Couplings between bridgehead atoms or between nuclei attached to different bridgehead atoms of bicycloalkanes are excellent examples of multipath transmission. Many values for different compounds and different substituents have been reported. A few examples will be quoted here: J(CC) couplings,[503,504,601] J(HH) and J(CH) couplings,[503] J(HF) and J(CF) couplings,[504,602] J(NH) couplings,[603] J(SiC) couplings,[604] and J(RhC) and J(PtC) couplings.[605]

The IPPP approach seems to be particularly suitable for analysing multipath additivity in multicyclic compounds.[606,607] Such results will not be discussed further here, since they have been critically analysed by Krivdin and Della.[154]

The IPPP–INDO method has also been applied to study the dual-path additivity of J(HH) and J(CH) couplings in chalcogen heterocyclopentadienes (with O, S, Se and Te).[608] Such analysis was carried out after separating the σ- and π-transmitted components of J(HH) and J(CH) couplings. The dual-path transmission of the σ component was considered.

In two-pathway J(SeSe) couplings largely dominated by the PSO interaction, an intrinsic non-additivity of the dual-path transmission has been discussed.[609] The CLOPPA analysis of the different contributions indicates

that this is a general behaviour of couplings dominated by non-contact interactions.

Dual-path additivity in J(SnSn) couplings has been discussed by Mitchell *et al.*[610]

ACKNOWLEDGEMENTS

This work has been partially supported by a grant (INT 90-24192) from the NSF–CONICET cooperative agreement. Support from UBACYT is gratefully acknowledged.

REFERENCES

1. R. K. Harris, *NMR Spectroscopy: A Physicochemical View*. Pitman, London, 1983.
2. (a) C. J. Jameson and H. J. Osten, *Ann. Rep. NMR Spectrosc.*, 1986, **17**, 1.
   (b) H. Fukui, *Magn. Reson. Rev.*, 1987, **11**, 205.
   (c) D. B. Chesnut, *Ann. Rep. NMR Spectrosc.*, 1989, **21**, 51.
   (d) J. A. Tossell (ed.), *Nuclear Magnetic Shielding and Molecular Structure*.
   (e) J. C. Facelli, D. M. Grant and J. Michl, *Acc. Chem. Res.*, 1987, **20**, 152.
   (f) J. C. Facelli and D. M. Grant, *Top. Stereochem.*, 1989, **19**, 1.
3. G. A. Webb (ed.), *Specialist Periodical Reports, Nuclear Magnetic Resonance*, Vols 12–21, Chapters on Theoretical and physical aspects of nuclear shielding, The Royal Society of Chemistry. 1983–1992.
4. J. Kowalewski, *Ann. Rep. NMR Spectrosc.*, 1982, **12**, 81.
5. J. Kowalewski, *Prog. NMR Spectrosc.*, 1977, **11**, 1.
6. (a) I. Ando and G. A. Webb, *Theory of NMR Parameters*. Academic Press, London, 1983.
   (b) G. A. Webb, *Nato ASI, Ser. C.*, 1986, **164**, 19.
   (c) G. A. Webb, *The Royal Society, Annual Reports C, NMR Spectrosc.*, 1983, p. 39.
7. G. A. Webb (ed.), *Specialist Periodical Reports, Nuclear Magnetic Resonance*, Vols 12–21, Chapters on theoretical aspects of spin–spin couplings. The Royal Society of Chemistry, 1983–1992.
8. G. A. Webb (ed.), *Specialist Periodical Reports, Nuclear Magnetic Resonance*, Vols 12–21, Chapters on applications of spin–spin couplings. The Royal Society of Chemistry, 1983–1992.
9. N. F. Ramsey, *Phys. Rev.*, 1953, **91**, 303.
10. A. D. Buckingham, P. Pyykkö, J. B. Robert and L. Wiesenfeld, *Mol. Phys.*, 1982, **46**, 177.
11. A. D. Buckingham and I. Love, *J. Magn. Reson.*, 1970, **2**, 338.
12. J. Mason (ed.), *Multinuclear NMR*, Plenum, New York, 1987.
13. V. M. S. Gil and W. von Philipsborn, *Magn. Reson. Chem.*, 1989, **27**, 409.
14. K. Morgan, B. G. Sayer and G. J. Schröbilgen, *J. Magn. Reson.*, 1983, **52**, 139.
15. W. T. Raynes, *Magn. Reson. Chem.*, 1992, **30**, 686.
16. W. T. Raynes and S. J. Stevens, *Magn. Reson. Chem.*, 1992, **30**, 124.
17. W. Kutzelnigg, *Theor. Chim. Acta*, 1988, **73**, 173.
18. J. M. Lévy-Leblond, *Commun. Math. Phys.*, 1967, **6**, 286.
19. J. M. Lévy-Leblond, *Riv. Nuov. Cim.*, 1967, **4**, 99.
20. S. M. Blinder, *Theor. Chim. Acta*, 1979, **53**, 159.

21. L. Bréchamet, *J. Math. Phys.* 1983, **24**, 1968.
22. U. Fano and G. Racah, *Irreducible Tensorial Sets*. Academic Press, New York, 1959.
23. J. Geertsen, *Chem. Phys. Lett.*, 1985, **116**, 89.
24. E. Yurtsever and J. Hinze, *J. Chem. Phys.*, 1978, **69**, 3431.
25. W. S. Lee and J. M. Schulman, *J. Chem. Phys.*, 1979, **70**, 1530.
26. O. Matsuoka and T. Aoyama, *J. Chem. Phys.*, 1980, **73**, 5718.
27. V. Galasso, *Theor. Chim. Acta*, 1983, **63**, 35.
28. V. Galasso, P. Lazzeretti, E. Rossi and R. Zanasi, *J. Chem. Phys.*, 1983, **79**, 1554.
29. V. Galasso, *J. Mol. Struct. THEOCHEM*, 1983, **93**, 201.
30. V. Galasso, *Chem. Phys.*, 1984, **83**, 407.
31. R. E. Overill and M. F. Guest, *Chem. Phys. Lett.*, 1983, **98**, 229.
32. R. E. Overill and V. R. Saunders, *Chem. Phys. Lett.*, 1984, **106**, 197.
33. G. E. Scuseria, *Chem. Phys.*, 1986, **107**, 417.
34. J. Oddershede, *Lecture Notes on Magnetic Properties of Molecules*, Department of Chemistry, The University of Utah, 1991.
35. J. E. Pérez, F. S. Ortiz, R. H. Contreras, C. G. Giribet and M. C. Ruiz de Azua, *J. Mol. Struct. THEOCHEM*, 1990, **210**, 193.
36. D. M. Heinekey, N. G. Payne and G. K. Schulte, *J. Am. Chem. Soc.*, 1988, **110**, 2303.
37. A. Antinolo, B. Chaudret, G. Commenges, M. Fajardo, F. Jalon, R. H. Morris, A. Otero and C. T. Schweltzer, *J. Chem. Soc. Chem. Commun.*, 1988, 1210.
38. D. H. Jones, J. A. Labinger and D. P. Weiterkamp, *J. Am. Chem. Soc.*, 1989, **111**, 3087.
39. K. W. Zilm, D. M. Heinekey, J. M. Millar, N. G. Payne and P. Demov, *J. Am. Chem. Soc.*, 1989, **111**, 3088.
40. D. M. Heinekey, J. M. Millar, T. F. Koetzle, N. G. Payne and K. W. Zilm, *J. Am. Chem. Soc.*, 1990, **112**, 909.
41. K. W. Zilm, D. M. Heinekey, J. M. Millar, N. G. Payne, S. P. Neshyba, J. C. Duchamp and J. Szczyrba, *J. Am. Chem. Soc.*, 1990, **112**, 920.
42. P. Pyykkö, *Chem. Phys.* 1977, **22**, 289.
43. P. Pyykkö, *J. Organomet. Chem.*, 1982, **232**, 21.
44. P. Pyykkö, A. Gorling and N. Rösch, *Mol. Phys.*, 1987, **61**, 195.
45. P. Pyykkö and L. Wiesenfeld, *Mol. Phys.*, 1981, **43**, 557.
46. N. Rösch and P. Pyykkö, *Mol. Phys.*, 1986, **57**, 193.
47. A. Viste, M. Hotokka, L. Laaksonen and P. Pyykkö, *Chem. Phys.*, 1982, **72**, 225.
48. P. Pyykkö, *Methods in Computational Chemistry*, Vol. 2 (ed. S. Wilson). Plenum, London, 1987.
49. Y. S. Lee, W. C. Ermler and K. S. Pitzer, *J. Chem. Phys.*, 1977, **67**, 5861.
50. K. Balasubramanian and K. S. Pitzer, *Ab Initio Methods in Quantum Chemistry* (ed. K. P. Lawley). Wiley, New York, 1987.
51. G. A. Aucar and R. H. Contreras, *J. Magn. Reson.*, 1991, **93**, 413.
52. M. J. S. Dewar, G. L. Grady, K. M. Merz and J. J. P. Stewart, *Organometallics*, 1985, **4**, 1964.
53. M. S. J. Dewar, M. K. Holloway, G. L. Grady and J. J. P. Stewart, *Organometallics*, 1985, **4**, 1973.
54. R. C. Burns, L. A. Devereux, P. Granger and G. J. Schröbilgen, *Inorg. Chem.*, 1985, **24**, 2615.
55. M. Björgvinsson, J. F. Sawyer and G. J. Schröbilgen, *Inorg. Chem.*, 1987, **26**, 741.
56. M. J. Collins and G. J. Schröbilgen, *Inorg. Chem.*, 1985, **24**, 2608.
57. R. J. Gillespie, P. Granger, K. R. Morgan and G. J. Schröbilgen, *Inorg. Chem.*, 1984, **23**, 887.
58. J. A. Pople and D. P. Santry, *Mol. Phys.*, 1963, **8**, 1.
59. J. Jokisaari, K. Raisanen, P. Pyykkö and L. Lajunen, *Mol. Phys.*, 1980, **39**, 715.
60. P. Pyykkö, Personal communication.
61. B. Wrackmeyer, C. Stader and K. Horchler, *J. Magn. Reson.*, 1989, **83**, 601.

62. F. H. Kohler, W. A. Geike and N. Hertkorn, *J. Organomet. Chem.*, 1987, **334**, 359.
63. A. Laaksonen, J. Kowalewski and V. R. Saunders, *Chem. Phys.*, 1983, **80**, 221.
64. V. Galasso, *J. Chem. Phys.*, 1985, **82**, 899.
65. M. F. Guest, V. R. Saunders and R. E. Overill, *Mol. Phys.*, 1978, **35**, 427.
66. M. Iwai and A. Saika, *Phys. Rev.*, 1983, **A28**, 1924.
67. A. Saika, *Bull. Magn. Reson.*, 1985, **7**, 100.
68. J. Geertsen and J. Oddershede, *Chem. Phys.*, 1984, **90**, 301.
69. H. Fukui, K. Miura and H. J. Matsuda, *Chem. Phys.*, 1991, **94**, 533.
70. H. Fukui, K. Miura, H. Matsuda and T. Baba, *J. Chem. Phys.*, 1992, **97**, 2299.
71. E. A. Salter, H. Sekino and R. J. Bartlett, *J. Chem. Phys.*, 1987, **87**, 502.
72. H. Sekino and R. J. Bartlett, *J. Chem. Phys.*, 1986, **85**, 3945.
73. J. Geertsen, *Chem. Phys. Lett.*, 1987, **134**, 400.
74. J. Oddershede, J. Geertsen and G. E. Scuseria, *J. Phys. Chem.*, 1988, **92**, 3056.
75. J. R. Becket, PhD thesis, Rutgers University, 1979.
76. H. Nakatsuji, *J. Chem. Phys.*, 1974, **61**, 3728.
77. V. Galasso, *J. Chem. Phys.*, 1984, **80**, 365.
78. V. Galasso, *Chem. Phys. Lett.*, 1984, **108**, 435.
79. A. I. Laaksonen and V. R. Saunders, *Chem. Phys. Lett.*, 1983, **95**, 375.
80. O. Vahtras, H. Agren, P. Jorgensen, Aa. Jensen, S. B. Padkjaer and T. Gelgaker, *J. Chem. Phys.*, 1992, **96**, 6120.
81. Yu. I. Neronov and A. E. Barsach, *Zh. Eksp. Teor. Fiz.*, 1975, **69**, 1872.
82. B. Bennet, W. T. Raynes and C. W. Anderson, *Spectrochim. Acta*, 1989, **45A**, 821.
83. F. A. L. Anet and D. J. O'Leary, *Tetrahedron Lett.*, 1989, **30**, 2755.
84. D. J. Rowe, *Rev. Mod. Phys.*, 1970, **40**, 153.
85. T. Shibuya and V. McKoy, *Phys. Rev.*, 1970, **A2**, 2208.
86. G. Fronzoni and V. Galasso, *J. Mol. Struct. THEOCHEM*. 1985, **122**, 327.
87. G. Fronzoni and V. Galasso, *Chem. Phys.*, 1986, **103**, 29.
88. V. Galasso and G. Fronzoni, *J. Chem. Phys.*, 1986, **85**, 5200.
89. G. Fronzoni and V. Galasso, *J. Magn. Reson.*, 1987, **71**, 229.
90. V. Galasso, *Chem. Phys.*, 1987, **117**, 415.
91. V. Galasso, *Chem. Phys. Lett.*, 1988, **145**, 259.
92. V. Galasso and G. Fronzoni, *J. Chem. Phys.*, 1986, **84**, 3215.
93. P. Lazzeretti, E. Rossi and R. Zanasi, *J. Chem. Phys.*, 1984, **80**, 315.
94. J. Geertsen and J. Oddershede, *Chem. Phys.*, 1986, **104**, 67.
95. G. E. Scuseria, *Chem. Phys. Lett.*, 1986, **127**, 236.
96. J. Geertsen, J. Oddershede and G. E. Scuseria, *J. Chem. Phys.*, 1987, **87**, 2138.
97. G. E. Scuseria, J. Geertsen and J. Oddershede, *J. Chem. Phys.*, 1989, **90**, 2338.
98. M. T. Rayez, E. Neumann, J. Hoaran and F. Achard, *Chem. Phys.*, 1982, **69**, 323.
99. M. T. Rayez-Meaume and J. Hoaran, *Chem. Phys.*, 1978, **27**, 73.
100. J. A. Pople, J. W. McIver and N. S. Ostlund, *J. Chem. Phys.*, 1968, **49**, 2960, 2965.
101. A. C. Blizzard and D. P. Santry, *J. Chem. Phys.*, 1971, **55**, 950; 1973, **58**, 4714.
102. J. C. Facelli and R. H. Contreras, *Int. J. Quantum Chem.*, 1980, **18**, 1175.
103. J. C. Facelli and R. H. Contreras, *Int. J. Quantum Chem.*, 1981, **20**, 909.
104. J. C. Facelli and M. Barfield, *J. Am. Chem. Soc.*, 1984, **106**, 3407.
105. J. C. Facelli and M. Barfield, *J. Magn. Reson.*, 1984, **59**, 452.
106. (a) J. Del Bene and H. H. Jaffé, *J. Chem. Phys.*, 1968, **48**, 1807;
(b) K. Krogh-Jespersen and M. Rattnet, *J. Chem. Phys.*, 1976, **65**, 1305.
107. J. A. Pople and D. L. Beveridge, *Approximate Molecular Orbital Theory*. McGraw-Hill, New York, 1970.
108. G. E. Scuseria and R. H. Contreras, *Theor. Chim. Acta*, 1981, **59**, 437.
109. G. A. Webb and M. Jallali-Heravi, *Org. Magn. Reson.*, 1979, **12**, 174.
110. G. E. Scuseria, A. R. Engelmann and R. H. Contreras, *Theor. Chim. Acta*, 1982, **61**, 49.
111. J. M. S. Dewar and W. Thiel, *J. Am. Chem. Soc.*, 1977, **99**, 4899, 4907.

112. G. E. Scuseria and R. H. Contreras, *Chem. Phys. Lett.*, 1982, **93**, 425.
113. (a) J. Linderberg, P. Jorgensen and J. Oddershede, *J. Chem. Phys.*, 1972, **56**, 6213.
(b) P. Jorgensen and J. Oddershede, *J. Chem. Phys.*, 1972, **57**, 277.
(c) P. Jorgensen, J. Oddershede and M. Ratner, *J. Chem. Phys.*, 1974, **61**, 710.
114. J. Lambert and M. Klessinger, *Magn. Reson. Chem.*, 1987, **25**, 456.
115. R. Righini, C. G. Giribet, M. C. Ruiz de Azua and R. H. Contreras, *J. Mol. Struct. THEOCHEM*, 1990, **210**, 199.
116. A. D. C. Towl and Schaumburg, *Mol. Phys.*, 1971, **22**, 49.
117. H. Fukui, T. Tsuji and K. Miura, *J. Am. Chem. Soc.*, 1981, **103**, 3652.
118. H. Fukutone, *Int. J. Quantum Chem.*, 1981, **20**, 955.
119. (a) V. Galasso and A. Bigotto, *Org. Magn. Reson.*, 1974, **6**, 475.
(b) V. Galasso, *Theor. Chim. Acta*, 1974, **34**, 137.
(c) V. Galasso, *Chem. Phys. Lett.*, 1975, **32**, 108.
120. R. H. Contreras, H. O. Gavarini and M. A. Natiello, *J. Comput. Chem.*, 1987, **8**, 265.
121. F. A. A. A. M. De Leeuw, C. A. G. Haasnoot and C. Altona, *J. Am. Chem. Soc.*, 1984, **106**, 2299.
122. C. Barbier, H. Faucher and G. Berthier, *Theor. Chim. Acta*, 1971, **21**, 105.
123. L. L. Lohr and P. Pyykkö, *Chem. Phys. Lett.*, 1979, **62**, 333.
124. L. L. Lohr, M. Hotokka and P. Pyykkö, *Quantum Chemistry Program Exchange*, 1980, **12**, 387.
125. J. Jokisaari, P. Lazzeretti and P. Pyykkö, *Chem. Phys.*, 1988, **123**, 339.
126. P. Pyykkö, *Chem. Rev.*, 1988, **88**, 563.
127. M. Barfield, A. M. Dean, C. J. Fallick, R. J. Spear, S. Sternhell and P. W. Westerman, *J. Am. Chem. Soc.*, 1975, **97**, 1482.
128. M. Barfield, *J. Am. Chem. Soc.*, 1980, **102**, 1.
129. R. Laatikainen, *J. Magn. Reson.*, 1983, **52**, 293.
130. R. Laatikainen and E. Kolehmainen, *J. Magn. Reson.*, 1985, **65**, 89.
131. M. C. Ruiz de Azua and E. Diez, Unpublished results.
132. A. R. Engelmann, R. H. Contreras and J. C. Facelli, *Theor. Chim. Acta*, 1981, **59**, 17.
133. D. G. de Kowalewski, R. H. Contreras, A. R. Engelmann, J. C. Facelli and J. C. Durán, *Org. Magn. Reson.*, 1981, **17**, 199.
134. K. Yoshida, *Chem. Phys.*, 1977, **21**, 317.
135. A. R. Engelmann and R. H. Contreras, *QCPE Bull.*, 1982, **2**, 14.
136. R. Musio *QCPE Bull.*, 1990, **10**, 44: Program QCMP081.
137. A. R. Engelmann, G. E. Scuseria and R. H. Contreras, *J. Magn. Reson.*, 1982, **50**, 21.
138. R. Ditchfield, N. S. Ostlund, J. N. Murrell and M. A. Turpin, *Mol. Phys.*, 1970, **18**, 433.
139. H. Fukui, K. Miura, K. Ohta and T. Tsujki, *J. Chem. Phys.*, 1982, **76**, 5169.
140. H. Fukui, K. Miura and T. Sakurai, *J. Chem. Phys.*, 1988, **88**, 7040.
141. A. R. Engelmann and R. H. Contreras, *Int. J. Quantum Chem.*, 1983, **23**, 1033.
142. N. S. Verwoerd, *Chem. Phys.*, 1979, **44**, 151.
143. P.-O. Löwdin, *J. Math. Phys.*, 1962, **3**, 969.
144. M. A. Natiello and R. H. Contreras, *Chem. Phys. Lett.*, 1984, **104**, 568.
145. A. R. Engelmann, M. A. Natiello, G. E. Scuseria and R. H. Contreras, *Comput. Phys. Commun.*, 1986, **39**, 409.
146. R. H. Contreras, C. G. Giribet, M. C. Ruiz de Azua and A. C. Diz, *Recent Advances in Organic NMR Spectroscopy* (ed. J. Lambert and R. Rittner), p. 43. Norrel, Landisville, 1987.
147. G. E. Scuseria and R. H. Contreras, *Int. J. Quantum. Chem.*, 1986, **S20**, 603.
148. A. C. Diz, C. G. Giribet, C. C. Ruiz de Azua and R. H. Contreras, *Int. J. Quantum Chem.*, 1990, **37**, 663.
149. R. H. Contreras, M. C. Ruiz de Azua, C. G. Giribet and M. B. Ferraro, *Nuevas Tendencias en Química Cuántica*, Vol. 2 (ed. S. Fraga), p. 307. Consejo Superior de Investigaciones, Madrid, 1989.

150. R. H. Contreras, C. G. Giribet and M. C. Ruiz de Azua, *Proceedings of the VI Latin-American School in Theoretical Chemistry, Rio de Janeiro, 1988*, Vol. 1, p. 229.
151. R. H. Contreras, C. G. Giribet, M. C. Ruiz de Azua and M. B. Ferraro, *Structure, Interactions and Reactivity* (ed. S. Fraga), p. 212. Elsevier, Amsterdam, 1992.
152. L. B. Krivdin and G. A. Kalabin, *Usp. Khim.*, 1988, **57**, 3.
153. L. B. Krivdin and G. A. Kalabin, *Prog. NMR Spectrosc.*, 1989, **21**, 293.
154. L. B. Krivdin and E. W. Della, *Prog. NMR Spectrosc.*, 1991, **23**, 301.
155. J. L. Marshall, *Methods in Stereochemical Analysis*, Vol. 2 (ed. A. P. Marchand). Verlag Chemie, Deerfield Beach, Florida, 1983.
156. P. E. Hansen, *Prog. NMR Spectrosc.*, 1981, **14**, 175.
157. B. Wrackmeyer and Horchler, *Prog. NMR Spectrosc.* 1990, **22**, 209.
158. P. E. Hansen, *The Chemistry of Double Bonded Functional Groups* (ed. S. Patai), p. 81, Wiley, New York, 1989.
159. V. Mlynárik, *Prog. NMR Spectrosc.*, 1986, **18**, 277.
160. V. N. Chupakhin, V. N. Charushin and A. R. Cheryshev, *Prog. NMR Spectrosc.*, 1988, **20**, 95.
161. D. G. Gorenstein, *Prog. NMR Spectrosc.*, 1983, **16**, 1.
162. D. G. Gorenstein, *Phosphorus-31 NMR* (ed. D. G. Gorenstein), p. 37. Academic Press, Orlando, 198h.
163. L. D. Quin, *Phosphorus-31 NMR Spectroscopy in Stereochemical Analysis* (ed. J. G. Verkade and L. D. Quin). VCH, Deerfield Beach, Florida, 1987, p. 391.
164. H. Marsmann, *NMR: Basic Princ. Prog.*, 1981, **17**, 1.
165. K. M. Mackay and R. A. Thomson, *Main Group Metal Chem.*, 1987, **10**, 83.
166. B. Wrackmeyer, *Ann. Rep. NMR Spectrosc.*, 1985, **16**, 73.
167. B. Wrackmeyer and K. Horschler, *Ann. Rep. NMR Spectrosc.*, 1989, **22**, 249.
168. M. Minelli, J. H. Enemark, R. T. C. Brownlee, M. J. O'Connor and A. G. Wedd, *Coord. Chem. Rev.*, 1985, **68**, 169.
169. P. S. Pregosin, *Coord. Chem. Rev.*, 1982, **44**, 247.
170. P. S Pregosin, *Ann. Rep. NMR Spectrosc.*, 1986, **17**, 285.
171. J. F. Hinton, K. R. Metz and R. W. Briggs, *Prog. NMR Spectrosc.*, 1988, **20**, 423.
172. G. Anderegg, K. Popov and P. S. Pregosin, *Magn. Reson. Chem.*, 1987, **25**, 84.
173. W. von Philipsborn and R. Müller, *Angew. Chem. Int. Ed. Engl.*, 1986, **25**, 383.
174. (a) M. Witanowski, L. Stefaniak and G. A. Webb, *Ann. Rep. NMR Spectrosc.*, 1986, **18**, 1.
174. (b) M. Witanowski, L. Stefaniak and G. A. Webb, *Ann. Rep. NMR Spectrosc.* 1993, **25**, 2.
175. M. Witanowski, L. Stefaniak and G. A. Webb, *Ann. Rep. NMR Spectrosc.*, 1981, **11B**, 1.
176. V. I. Bakhmutov and M. V. Galakhov, *Russ. Chem. Rev.*, 1988, **57**, 1467.
177. N. M. Sergeyev, *NMR: Basic Princ. Prog.*, 1990, **22**, 32.
178. R. H. Contreras, M. A. Natiello and G. E. Scuseria, *Magn. Reson. Rev.*, 1985, **9**, 239.
179. C. J. Jameson, *Multinuclear NMR* (ed. J. Mason), Chap. 4. Plenum, New York, 1987.
180. P. Laszlo (ed.), *NMR of Newly Accessible Nuclei*. Academic Press, New York, 1983.
181. B. Wrackmeyer and H. Zhou, *Main Group Metal Chem.*, 1990, **13**, 99.
182. R. A. Shaw, *Phosphorus Sulfur*, 1987, **32**, 81.
183. J. Lounila and J. Jokisaari, *Prog. NMR Spectrosc.*, 1982, **15**, 249.
184. H. M. McConnell, *J. Mol. Spectrosc.*, 1957, **1**, 11.
185. J. N. Murrel, *Prog. NMR Spectrosc.*, 1970, **6**, 1.
186. M. Barfield and B. Chakrabarti, *Chem. Rev.*, 1969, **69**, 757.
187. H. Günther and G. Jikeli, *Chem. Rev.*, 1977, **77**, 599.
188. S. M. Susskind, G. E. Scuseria and R. H. Contreras, *Z. Phys. Chem.*, 1985, **266**, 395.
189. J. C. Facelli, C. G. Giribet and R. H. Contreras, *Int. J. Quantum Chem.*, 1984, **25**, 515.
190. M. A. Natiello, G. E. Scuseria and R. H. Contreras, *J. Mol. Struct. THEOCHEM*, 1983, **105**, 233.

191. R. Pachter, M. Woudenberg, D. Erorocritou and P. L. Wessel, *S. Afr. J. Chem.*, 1987, **40**, 172.
192. Th. Steiger, S. Gey and R. Radeglia, *Mol. Phys.*, 1975, **30**, 1729.
193. T. A. Holak, D. W. Aksnes and A. Sygula, *Org. Magn. Reson.*, 1983, **21**, 287.
194. S. Berger, *Org. Magn. Reson.*, 1984, **22**, 47.
195. A. N. Kook, S. L. Smith and E. V. Brown, *Org. Magn. Reson.*, 1984, **22**, 733.
196. L. Cassidei and G. Sciacovelli, *Spectrochim. Acta*, 1985, **41A**, 1459.
197. S. Biaqini, A. Lai, M. Monduzzi and G. Saba, *J. Chem. Soc. Faraday Trans. 2*, 1983, **79**, 491.
198. (a) N. E. Riggs, *Aust. J. Chem.*, 1985, **38**, 1575.
198. (b) V. A. Roznyatwoskii, and N. M. Sergeyeevand V. A. Chertkov, *Magn. Reson. Chem.*, 1991, **29**, 304.
199. S. Berger and K. P. Zeller, *J. Org. Chem.*, 1984, **49**, 3725.
200. J. C. Facelli and D. M. Grant, *Theor. Chim. Acta*, 1987, **71**, 277.
201. (a) M. A. Fox and D. Schultz, *J. Org. Chem.*, 1988, **53**, 4386.
(b) P. Sándor and L. Radics, *Magn. Reson. Chem.*, 1986, **24**, 607.
202. H. Bandmann, P. Heymanns, C. Siem and P. Rademacher, *Angew. Chem.*, 1984, **96**, 354.
203. P. Schmitt and H. Günther, *J. Magn. Reson.*, 1983, **52**, 497.
204. D. J. Sardella and E. Boger, *Magn. Reson. Chem.*, 1986, **24**, 287.
205. D. Vikic-Topic and Z. Meić, *J. Mol. Struct.*, 1986, **142**, 371.
206. P. Szczecinśki and A. Gyff-Keller, *Magn. Reson. Chem.*, 1988, **26**, 990.
207. R. A. Hoffman, *Mol. Phys.*, 1958, **1**, 326.
208. W. J. E. Parr and T. Schaefer, *Acc. Chem. Res.*, 1980, **13**, 400.
209. T. Schaefer and C. S. Takeuchi, *Can. J. Chem.*, 1989, **67**, 1022.
210. R. Laatikainen, E. Kolehmainen, T. Kuokkanen and K. Tuppurainen, *J. Mag. Reson.*, 1988, **78**, 9.
211. R. Laatikainen, K. Tuppurainen, Y. Hiltunen and S. Lotjonen, *Magn. Reson. Chem.*, 1990, **28**, 939.
212. T. Schaefer, G. H. Penner and R. Sebastian, 1985, *Can. J. Chem.*, 1985, **63**, 3219.
213. M. J. Collins, P. M. Hatton, S. Sternhell and C. W. Tansey, *Magn. Reson. Chem.*, 1987, **25**, 824.
214. J. C. Facelli, R. H. Contreras, D. G. de Kowalewski, V. J. Kowalewski and R. N. Piegaia, *J. Mol. Struct. THEOCHEM*, 1983, **94**, 163.
215. M. Barfield, C. J. Fallick, K. Hata, S. Sternhell and P. W. Westerman, *J. Am. Chem. Soc.*, 1983, **105**, 2178.
216. M. Barfield, M. J. Collins, J. E. Gready, S. Sternhell and C. W. Tansey, *J. Am. Chem. Soc.*, 1989, **111**, 4285.
217. P. Karuso and W. C. Taylor, *Magn. Reson. Chem.*, 1986, **24**, 739.
218. T. Schaefer, K. J. Cox and R. Sebastian, *Can. J. Chem.*, 1991, **69**, 908.
219. M. Barfield, R. J. Spear and S. Sternhell, *Chem. Rev.*, 1976, **76**, 593.
220. P. Diehl, J. Jokisaari, S. Müller and T. Väänänen, *Org. Magn. Reson.*, 1983, **21**, 143.
221. S. Gronowitz, A. B. Hörnfeldt, Y. Yang, U. Edlund, B. Eliasson and D. Johnels, *Magn. Reson. Chem.*, 1990, **28**, 33.
222. M. F. Tufró, R. H. Contreras and J. C. Facelli, *J. Mol. Struct. THEOCHEM*, 1992, **253**, 271.
223. V. J. Kowalewski and R. H. Contreras, *J. Magn. Reson.*, 1972, **8**, 101.
224. T. Schaefer, G. H. Penner and R. Sebastian, *Can. J. Chem.*, 1987, **65**, 873.
225. T. Schaefer, R. Sebastian and G. H. Penner, *Can. J. Chem.*, 1988, **66**, 1495.
226. T. Schaefer, C. Beaulieu and R. Sebastian, *Can. J. Chem.*, 1991, **69**, 503.
227. T. Schaefer, R. Sebastian and G. H. Penner, *Can. J. Chem.*, 1991, **69**, 496.
228. T. Schaefer, G. H. Penner, C. T. Takeuchi and C. Beaulieu, *Can. J. Chem.*, 1989, **67**, 1283.
229. R. Laatikainen, *Magn. Reson. Chem.*, 1986, **24**, 588.

230. R. Laatikainen and K. Tuppurainen, *J. Chem. Soc. Perkin Trans. 2*, 1987, 121.
231. T. Schaefer, R. Sebastian, J. Peeling, G. H. Penner and K. Koh, *Can. J. Chem.*, 1989, **67**, 1015.
232. T. Schaefer, R. Sebastian and G. H. Penner, *Can. J. Chem.*, 1986, **64**, 1372.
233. T. Schaefer and R. Sebastian, *Can. J. Chem.*, 1989, **67**, 2053.
234. T. Schaefer, J. Peeling and R. Sebastian, *Can. J. Chem.*, 1985, **63**, 3219.
235. T. Schaefer, R. Sebastian, T. A. Wildman and H. Dettman, *Can. J. Chem.*, 1982, **60**, 2274.
236. H. Nies and D. Rewicki, *J. Magn. Reson.*, 1982, **46**, 138.
237. H. A. Bent, *Chem. Rev.*, 1961, **61**, 275.
238. T. Schaefer and W. J. E. Parr, *J. Mol. Spectrosc.*, 1976, **61**, 479.
239. E. Kolehmainen, R. Laatikainen and V. Král, *Magn. Reson. Chem.*, 1986, **24**, 498.
240. T. Schaefer and C. S. Takeuchi, *Can. J. Chem.*, 1989, **67**, 827.
241. A. Otter, M. Neuenschwander and H. P. Kellerhals, *Magn. Reson. Chem.*, 1986, **24**, 353.
242. P. Bonzli and M. Neuenschwander, *Magn. Reson. Chem.*, 1991, **29**, 29.
243. T. Schaefer, J. Peeling and G. H. Penner, *Can. J. Chem.*, 1983, **61**, 2773.
244. T. Schaefer, G. S. Takeuchi and S. E. Sveison, *Can. J. Chem.*, 1988, **66**, 1490.
245. J. C. Facelli, C. G. Giribet and R. H. Contreras, *Org. Magn. Reson.*, 1982, **19**, 138.
246. T. Schaefer, W. Nienczura, C. Wong and K. Marat, *Can. J. Chem.*, 1979, **57**, 807.
247. R. J. Abraham, S. R. L. Ellison, M. Barfield and W. A. Thomas, *J. Chem. Soc. Perkin Trans. 2*, 1987, 977.
248. T. Schaefer, T. A. Wildman and R. Sebastian, *Can. J. Chem.*, 1982, **60**, 1924.
249. T. Schaefer, J. Peeling and T. A. Wildman, *Can. J. Chem.*, 1983, **61**, 2777.
250. T. Schaefer, R. Sebastian, R. P. Veregin and R. Laatikainen, *Can. J. Chem.*, 1983, **61**, 29.
251. T. Schaefer, K. Marat, J. Peeling and R. Veregin, *Can. J. Chem.*, 1983, **61**, 2779.
252. T. A. Wildman, PhD thesis, University of Manitoba, Winnipeg, 1982.
253. T. Schaefer, R. Laatikainen, T. A. Wildman, J. Peeling, G. H. Penner, J. Baleja and K. Marat, *Can. J. Chem.*, 1984, **62**, 1592.
254. T. Schaefer and R. Sebastian, *Can. J. Chem.*, 1989, **67**, 1148.
255. T. Schaefer and G. H. Penner, *Can. J. Chem.*, 1988, **66**, 1635.
256. T. Schaefer, G. H. Penner, R. Sebastian, J. Peeling and C. Beaulieu, *Can. J. Chem.*, 1991, **69**, 1047.
257. R. Benassi, U. Folli, D. Iarossi, A. Mucci, L. Schenetti and F. Taddei, *Magn. Reson. Chem.*, 1990, **28**, 702.
258. (a) T. Schaefer and G. H. Penner, *Can. J. Chem.*, 1988, **66**, 1229.
(b) T. Schaefer and J. D. Baleja, *Can. J. Chem.*, 1986, **64**, 1376.
259. T. Schaefer, G. H. Penner, C. Takeuchi and P. Tseki, *Can. J. Chem.*, 1988, **66**, 1647.
260. T. Schaefer and G. H. Penner, *Can. J. Chem.*, 1987, **65**, 2175.
261. T. Schaefer, J. Peeling, G. H. Penner, A. Lemire and R. Sebastian, *Can. J. Chem.*, 1985, **63**, 24.
262. G. H. Penner, *Can. J. Chem.*, 1987, **65**, 538.
263. T. Schaefer, R. Sebastian and G. H. Penner, *Can. J. Chem.*, 1988, **66**, 584.
264. T. Schaefer, J. Peeling and G. H. Penner, *Can. J. Chem.*, 1986, **64**, 2162.
265. R. K. Harris, A. Sebald, D. Furlani and G. Tagliavini, *Organometallics*, 1988, **7**, 388.
266. R. S. Matthews, *Org. Magn. Reson.*, 1982, **18**, 226.
267. W. J. P. Blonski, F. E. Hruska and T. A. Wildman, *Org. Magn. Reson.*, 1984, **22**, 505.
268. G. H. Penner, PhD thesis, University of Manitoba, Winnipeg, 1987.
269. T. Schaefer and G. H. Penner, *Can. J. Chem.*, 1988, **66**, 1641.
270. P. Diehl and J. Amrein, *Org. Magn. Reson.*, 1982, **19**, 148.
271. T. Schaefer, R. Sebastian and G. H. Penner, *Can. J. Chem.*, 1988, **66**, 1787.
272. A. Yu. Denisov, E. A. Tyshchishin, A. V. Trachev and V. I. Mamatyuk, *Magn. Reson. Chem.*, 1992, **30**, 886.
273. A. Pross, L. Radom and N. V. Rigss, *J. Am. Chem. Soc.*, 1980, **102**, 2253.

274. J. O. Williams, C. van Alsenoy, J. N. Scarsdale and L. Schäfer, *J. Mol. Struct. THEOCHEM*, 1981, **86**, 103.
275. C. Alvarez-Ibarra, M. S. Airas-Pérez, A. de Andres and J. L. Balcazarr, *Magn. Reson. Chem.*, 1986, **24**, 568.
276. L. Cazaux, C. Vidal and M. Pasdeloup, *Org. Magn. Reson.*, 1983, **21**, 190.
277. G. Cerichelli, G. Frachey and C. Galli, *Gazz. Chim. Ital.*, 1986, **116**, 683.
278. G. Saba, A. Lai, Monduzzi and G. Gelli, *J. Chem. Soc. Perkin Trans. 2*, 1983, 1569.
279. W. J. Hehre, L. Radom and J. A. Pople, *J. Am. Chem. Soc.*, 1972, **94**, 1496.
280. T. Schaefer and G. H. Penner, *Can. J. Chem.*, 1986, **64**, 2013.
281. R. E. Wasylishen and B. A. Pettitt, *Can. J. Chem.*, 1979, **57**, 1274.
282. W. Adcock and V. Sankar Tyer, *J. Org. Chem.*, 1985, **50**, 1538.
283. A. Lyčka, J. Jirman, A. Koloničny and J. Holeček, *J. Organomet. Chem.*, 1987, **333**, 305.
284. W. Kitching, G. Drew, W. Adcock and A. N. Abeywickrema, *J. Org. Chem.*, 1981, **46**, 2252.
285. E. Matarasso-Tchiroukhine and P. Cadiot, *Can. J. Chem.*, 1983, **61**, 2476.
286. L. A. Fedorov, *Zh. Strukt. Khim.*, 1984, **25**, 35.
287. J. Allwohn, R. Hunold, M. Pilz, R. G. Mueller, W. Massa and A. Brendt, *Z. Naturforsch.*, 1990, **45B**, 290.
288. B. Wrackmeyer, C. Bihlmayer and M. Schilling, *Chem. Ber.*, 1983, **116**, 3182.
289. B. Wrackmeyer, *J. Magn. Reson.*, 1980, **39**, 359.
290. T. N. Mitchell and C. Kummetat, *J. Organomet. Chem.*, 1978, **157**, 275.
291. M. Barfield and D. M. Grant, *J. Am. Chem. Soc.*, 1963, **85**, 1899.
292. M. J. Cook, G. Ghaen-Maghami, F. Kaberia and K. Bergesen, *Org. Magn. Reson.*, 1983, **21**, 339.
293. G. Nivon, S. Frank and D. Kaplan, *J. Chem. Soc. Perkin Trans 2*, 1984, 1145.
294. M. Barfield, V. J. Hruby and J.-P. Meraldi, *J. Am. Chem. Soc.*, 1976, **98**, 1308.
295. M. Barfield, *Recent Advances in Organic NMR Spectroscopy* (ed. J. B. Lambert and R. Rittner), Chap. 4. Norrel, Landisville, 1987.
296. T. C. Wong, W. Guo, M. Bohl, M. Hubner, G. Luck, T. Steiger and G. Reck, *J. Chem. Soc. Perkin Trans. 2*, 1988, 765.
297. C. Mahaim, P. A. Carrupt and P. Vogel, *Helv. Chim. Acta*, 1985, **68**, 2182.
298. G. Hunter, J. A. Miller, M. Moore and G. M. Ullah, *Org. Magn. Reson.*, 1983, **21**, 275.
299. P. Mohanakrisshnan and R. K. R. Easwaran, *Chem. Phys.*, 1986, **104**, 409.
300. (a) M. Karplus, *J. Chem. Phys.*, 1959, **30**, 11.
(b) V. F. Bystrov, *Prog. NMR Spectrosc.*, 1976, **10**, 41.
301. E. Kupče, B. Wrackmeyer and E. Lukevics, *Magn. Reson. Chem.*, 1991, **29**, 444.
302. R. H. Contreras, M. A. Natiello, M. F. Tufró and D. G. de Kowalewski, *Z. Phys. Chem.*, 1986, **267**, 289.
303. M. C. Vitorge, M. T. Chenon, C. Coupry and N. Lumbroso-Bader, *Org. Magn. Reson.*, 1983, **21**, 20.
304. F. H. A. Rummens, J. S. Lomas, B. Tiffon, C. Coupry and N. Lumbroso-Bader, *Org. Magn. Reson.*, 1982, **19**, 35.
305. D. Lentz and H. Oberhammer, *Inorg. Chem.*, 1985, **24**, 4665.
306. M. Barfield, F. A. Al-Obeidi, V. J. Hruby and S. R. Walter, *J. Am. Chem. Soc.*, 1982, **104**, 3302.
307. D. B. Davies and Md. A. Khaled, *J. Chem. Soc. Perkin Trans 2*, 1976, 1238.
308. M. L. Severson and G. E. Maciel, *J. Magn. Reson.*, 1984, **57**, 248.
309. M. Barfield, E. D. Canada, C. R. McDaniel, J. L. Marshall, S. R. Walter, *J. Am. Chem. Soc.*, 1983, **105**, 3411.
310. S. R. Walter, J. L. Marshall, C. R. McDaniel, E. D. Canada and M. Barfield, *J. Am. Chem. Soc.*, 1983, **105**, 4185.
311. M. Barfield and S. R. Walter, *J. Am. Chem. Soc.*, 1983, **105**, 4191.
312. L.-F. Kao and M. Barfield, *J. Am. Chem. Soc.*, 1985, **107**, 2323.

313. M. Barfield and W. B. Smith, *J. Am. Chem. Soc.*, 1992, **114**, 1574.
314. E. Diez, J. San Fabian, J. Guilleme, C. Altona and L. A. Donders, *Mol. Phys.*, 1989, **68**, 49.
315. J. San Fabian, J. Guilleme, E. Diez, L. A. Donders and C. Altona, private communication.
316. L. A. Donders, F. A. A. M. de Leeuw and C. Altona, *Magn. Reson. Chem.*, 1989, **27**, 556.
317. C. Altona, J. H. Ippel, J. A. W. Hoekzema, C. Erkelens, M. Groesbeek and L. A. Donders, *Magn. Reson. Chem.*, 1989, **27**, 564.
318. K. Imai and E. Osawa, *Magn. Reson. Chem.*, 1990, **28**, 668.
319. L. J. Smith, M. J. Sutcliffe, C. Redfield and C. M. Dobson, *Biochemistry*, 1991, **30**, 986.
320. R. J. Abraham and J. Fisher, *Magn. Reson. Chem.*, 1985, **23**, 856.
321. A. van Beuzekom, F. A. A. M. de Leeuw and C. Altona, *Magn. Reson. Chem.*, 1990, **28**, 68.
322. S. Hamman, C. Bequin, C. Charlton and C. Luu-duc, *Org. Magn. Reson.*, 1983, **21**, 361.
323. C. H. Hammer and S. Chandrasegaram, *J. Am. Chem. Soc.*, 1984, **106**, 1543.
324. P. E. Balonga, V. J. Kowalewski and R. H. Contreras, *Spectrochim. Acta*, 1988, **44A**, 819.
325. S. Hamman, T. Benaissa and C. G. Beguin, *Magn. Reson. Chem.*, 1988, **26**, 621.
326. M. Grignon-Dubois, M. Laguerre, B. Barbe and M. Pétraud, *Organometallics*, 1984, **3**, 359; 1984, **3**, 1060.
327. M. Grignon-Dubois and M. Laguerre, *Organometallics*, 1988, **7**, 1443.
328. T. G. Appleton, H. C. Clark and L. E. Manzer, *Coord. Chem. Rev.*, 1973, **10**, 335.
329. G. Grossman, R. Lang, G. Ohms and D. Scheller, *Magn. Reson. Chem.*, 1990, **28**, 500.
330. R. A. Shaw, *Phosphorus Sulfur*, 1987, **32**, 81.
331. C. Altona, *Theoretical Biochemistry and Molecular Biophysics* (eds. D. L. Beveridge and R. Lavery). Adenine Press, New York, 1990.
332. M. Hricorini, I. Tvaroška and J. Hirsh, *Carbohydr. Res.*, 1990, **198**, 193.
333. I. Tvaroška, *Carbohydr. Res.*, 1990, **206**, 55.
334. I. Tvaroška and F. R. Taravel, *Carbohydr. Res.*, 1991, **221**, 83.
335. A. B. Chopa, L. C. Koll, J. C. Podestá and T. N. Mitchell, *J. Organomet. Chem.*, 1989, **376**, 283.
336. N. Hertkorn and F. H. Köhler, *Z. Naturforsch.*, 1988, **43B**, 1405.
337. T. N. Mitchell, J. C. Podestá, A. Ayala and A. B. Chopa, *Magn. Reson. Chem.*, 1988, **26**, 497.
338. T. Lind and H. Toftlund, *Acta Chem. Scand.*, 1982, **36A**, 489.
339. P. F. Barron, *J. Organomet. Chem.*, 1982, **236**, 157.
340. F. Brady, R. W. Matthews, M. M. Thakur and D. G. Gillies, *J. Organomet. Chem.*, 1983, **252**, 1.
341. S. R. Salman, *Org. Magn. Reson.*, 1982, **20**, 151.
342. S. R. Salman, *Org. Magn. Reson.*, 1983, **22**, 385.
343. T. Schaefer, R. Sebastian and S. R. Salman, *Can. J. Chem.*, 1984, **62**, 113.
344. E. Kolehmainen, J. Knuutinen and P. J. Salovaara, *Org. Magn. Reson.*, 1982, **20**, 201.
345. T. Schaefer, G. H. Penner, R. Sebastian and C. S. Takeuchi, *Can. J. Chem.*, 1986, **64**, 158.
346. T. Schaefer, K. J. Cox and R. Sebastian, *Can. J. Chem.*, 1991, **69**, 1039.
347. M. Dandáková, D. Végh, J. Kováč, I. Goljer, N. Prónayová and K. Spirková, *Coll. Czech. Chem. Comm.*, 1986, **51**, 889.
348. R. Benassi, U. Folli, A. Mucci, L. Schenetti and F. Taddei, *Magn. Reson. Chem.*, 1987, **25**, 804.
349. R. Benassi, U. Folli, D. Iarossi, L. Schenetti and F. Taddei, *J. Chem. Soc. Perkin Trans. 2*, 1983, 911.
350. R. Laatikainen and V. Král, *J. Chem. Soc. Perkin Trans. 2*, 1985, 1091.

351. J. M. Schulman and W. S. Lee, *J. Magn. Reson.*, 1982, **50**, 142.
352. S. Duangthai and G. A. Webb, *Org. Magn. Reson.*, 1983, **21**, 199.
353. R. H. Contreras, G. A. Aucar, C. G. Giribet, M. C. Ruiz de Azua, C. N. Cavasotto and L. B. Krivdin, *J. Mol. Struct. THEOCHEM*, 1990, **210**, 175.
354. R. H. Contreras, M. C. Ruiz de Azua, C. G. Giribet, G. A. Aucar and R. Lobayan, *J. Mol. Struct. THEOCHEM*, in press.
355. A. Takasuka and Y. Torui, *J. Chem. Soc. Perkin Trans. 2*, 1984, 1545.
356. M. Witanowski, L. Stefaniak and G. A. Webb, *Ann. Rep. NMR Spectrosc.*, 1977, **7**, 118.
357. A. Fruchier, V. Pellegrin, R. S. Claramunt and J. Elguero, *Org. Magn. Reson.*, 1984, **22**, 473.
358. T. Axenrod, C. M. Watnick, M. J. Wieder, S. Duangthai, G. A. Webb, H. J. C. Yeh, S. Bulusu and M. M. King, *Org. Magn. Reson.*, 1982, **20**, 11.
359. Y. Kuroda, Y. Fujiwara and K. Matsushita, *J. Magn. Reson.*, 1985, **62**, 218.
360. N. S. Nudelman and S. B. Cerdeira, *Magn. Reson. Chem.*, 1986, **24**, 507.
361. W. Städeli, W. von Philipsborn, A. Wick and I. Kompis, *Helv. Chim. Acta*, 1980, **63**, 504.
362. E. Kupče and E. Lukevics, *J. Magn. Reson.*, 1988, **76**, 63.
363. E. Kupče, E. Liepins, O. Pudova and E. Lukevics, *J. Chem.Soc. Chem. Commun.*, 1984, 581.
364. E. Kupče, E. Lukevics, Yu. M. Varezhkin, A. N. Mikhailova and V. D. Sheludyakov, *Organometallics*, 1988, **77**, 1649.
365. J. D. Kennedy and W. McFarlane, *J. Chem. Soc. Chem. Commun.*, 1974, 983.
366. L. Paolillo and E. D. Becker, *J. Magn. Reson.*, 1970, **3**, 200.
367. B. Wrackmeyer and H. Zhou, *Magn. Reson. Chem.*, 1992, **28**, 1066.
368. D. W. Anderson, J. E. Bentham and D. W. H. Rankin, *J. Chem. Soc. Dalton Trans.*, 1973, 1215.
369. J. D. Kennedy, W. McFarlane and B. Wrackmeyer, *Inorg. Chem.*, 1976, **15**, 1299.
370. E. Kupče and B. Wrackmeyer, *Magn. Reson. Chem.*, 1991, **29**, 351.
371. G. Fritz and H. Schäfer, *Z. Anorg. Allg. Chem.*, 1974, **409**, 137.
372. W. McFarlane and D. S. Rycroft, *J. Chem. Soc. Dalton Trans.*, 1974, 1977.
373. B. Wrackmeyer and K. Horschler, *Magn. Reson. Chem.*, 1990, **28**, 56.
374. R. M. Lequan, M. J. Pouet and M.-P. Simonnin, *Org. Magn. Reson.*, 1974, **7**, 392.
375. B. W. Tattershall, *Polyhedron*, 1990, **9**, 553.
376. J. H. Nelson, S. Affandi, G. A. Gray and E. C. Alyea, *Magn. Reson. Chem.*, 1987, **25**, 774.
377. J. D. Kennedy, W. McFarlane, G. S. Pyne and B. Wrackmeyer, *J. Organomet. Chem.*, 1980, **195**, 285.
378. B. Wrackmeyer, K. Horschler and H. Zhou, *Spectrosc. Acta*, 1990, **46A**, 809.
379. V. Galasso, M. L. Martin, M. Trierweiler, F. Frinqueli and Taticchi, *J. Mol. Struct. THEOCHEM*, 1982, **90**, 53.
380. P. Sandor and L. Radics, *J. Mol. Struct. THEOCHEM*, 1985, **133**, 125.
381. R. H. Contreras, M. C. Ruiz de Azua and C. G. Giribet, *Magn. Reson. Chem.*, 1986, **24**, 675.
382. H. Duddeck, P. Wagner, D. Müller and J. C. Jászberényi, *Magn. Reson. Chem.*, 1990, **28**, 549.
383. W. Gombler, *Phosphorus Sulfur*, 1988, **38**, 231.
384. H. C. E. McFarlane and W. McFarlane, *Multinuclear NMR* (ed. J. Mason), Chap. 15. Plenum, New York, 1987.
385. J. A. Anderson and J. D. Odom, *Organometallics*, 1988, **7**, 267.
386. P. A. W. Dean and R. S. Srivastava, *Inorg. Chim. Acta*, 1985, **105**, 1.
387. B. Wrackmeyer, E. Kupče and A. Schmidpeter, *Magn. Reson. Chem.*, 1991, **29**, 1045.
388. B. Wrackmeyer, K. Horschler, A. Sebald and L. H. Merwin, *Magn. Reson. Chem.*, 1990, **28**, 465.
389. J. M. Schulman, J. Ruggio and T. J. Venanzi, *J. Am. Chem. Soc.*, 1977, **99**, 2045.

390. Y. Kuroda, Y. Fujiwara and K. Matsushita, *J. Chem. Soc. Perkin Trans. 2*, 1985, 1533.
391. Y. Kuroda, Y. Fujiwara, A. Kuwae and K. Matsushita, *J. Chem. Soc. Perkin Trans 2*, 1986, 675.
392. S. Duangthai and G. A. Webb, *Org. Magn. Reson.*, 1982, **20**, 33.
393. J. P. Albrand, A. Cogne and C. Taieb. *Org. Magn. Reson.*, 1983, **21**, 246.
394. M. Baudler and B. Makowka, *Z. Anorg. Allg. Chem.*, 1985, **528**, 7.
395. C. Stader and B. Wrackmeyer, *J. Magn. Reson.*, 1987, **72**, 544.
396. L. B. Krivdin, G. A. Kalabin, R. N. Nesterenko and B. A. Trofimov, *Tetrahedron Lett.*, 1984, **25**, 4817.
397. G. A. Kalabin, L. B. Krivdin, V. V. Shcherbakov and B. A. Trofimov, *J. Mol. Struct.*, 1986, **143**, 569.
398. M. C. Ruiz de Azua, A. C. Diz, C. G. Giribet, R. H. Contreras and I. D. Rae, *Int. J. Quantum Chem.*, 1986, **S20**, 585.
399. L. B. Krivdin, S. V. Zinchenko, V. V. Shcherbakov, G. A. Kalabin, R. H. Contreras, M. F. Tufró, M. C. Ruiz de Azua and C. G. Giribet, *J. Magn. Reson.*, 1989, **84**, 1.
400. L. B. Krivdin, S. V. Zinchenko, G. A. Kalabin, J. C. Facelli, M. F. Tufró, R. H. Contreras, A. Yu, Denisov, O. A. Gavrilyuk and V. I. Mamatyuk, *J. Chem. Soc. Faraday Trans.*, 1992, **88**, 2459.
401. W. Holzer and W. von Philipsborn, *Magn. Reson. Chem.*, 1989, **27**, 511.
402. V. K. Jain, J. Mason, R. C. Mehrotra and B. S. Saraswat, *Polyhedron*, 1985, **4**, 2089.
403. V. K. Jain, J. Mason, R. C. Mehrotra and B. S. Saraswat, *J. Organomet. Chem.*, 1986, **309**, 45.
404. R. R. Fraser and M. Bresse, *Can. J. Chem.*, 1983, **61**, 576.
405. N. De Kempe, R. Verhe, L. De Buyck and N. Schamp, *Can. J. Chem.*, 1984, **62**, 1812.
406. B. C. Chen, W. von Philipsborn and K. Nagarajan, *Helv. Chim. Acta*, 1983, **66**, 1537.
407. A. Römer, *Org. Magn. Reson.*, 1983, **21**, 130.
408. H. Goldwhite, D. Rowsell, L. E. Vertal, M. T. Bowers, M. A. Cooper and S. L. Manatt, *Org. Magn. Reson.*, 1983, **21**, 494.
409. W. B. Jennings, M. S. Tolley, *J. Chem. Soc. Perkin. Trans. 2*, 1984, 1207.
410. M. Baudler and F. Saykowski, *Z. Anorg. Allg. Chem.*, 1982, **486**, 39.
411. H. S. Hosseini, H. W. Kroto, J. F. Nixon and O. Ohashi, *J. Organomet. Chem.*, 1985, **296**, 351.
412. J. Mason and K. O. Christe, *Inorg. Chem.*, 1983, **22**, 1849.
413. G. Schatte, H. Willner and M. Willert-Porada, *Magn. Reson. Chem.*, 1992, **30**, 118.
414. D. J. Gulliver, E. G. Hope, W. Levason, S. G. Murray, D. M. Potter and G. L. Marshall, *J. Chem. Soc. Perkins Trans. 2*, 1984, 429.
415. T. Gasparis-Ebeling, H. Nöth and B. Wrackmeyer, *J. Chem. Soc. Dalton Trans.*, 1983, 97.
416. B. Wrackmeyer, *J. Magn. Reson.*, 1984, **59**, 141.
417. B. Wrackmeyer, T. Gasparis-Ebeling and H. Nöth, *Z. Naturforsch.*, 1989, **44B**, 653.
418. L. D. Quin, K. C. Caster, J. C. Kisalus and K. A. Mesch, *J. Am. Chem. Soc.*, 1984, **106**, 7021.
419. L. D. Quin and F. C. Bernhardt, *Magn. Reson. Chem.*, 1985, **23**, 929.
420. G. A. Aucar, C. G. Giribet, M. C. Ruiz de Azua and A. C. Diz, *J. Mol. Struct. THEOCHEM*, 1988, **164**, 1.
421. J. D. Roberts, D. R. Davies and R. P. Lutz, *J. Am. Chem. Soc.*, 1961, **83**, 246.
422. J. Hilton and L. H. Sutcliffe, *Prog. NMR Spectrosc.*, 1975, **10**, 27.
423. C. N. Cavasotto, C. G. Giribet, M. C. Ruiz de Azua and R. H. Contreras, *J. Comput. Chem.*, 1991, **12**, 141.
424. H. A. Gaur, J. Vriend and W. G. B. Huymans, *Tetrahedron Lett.*, 1969, **5**, 1999.
425. T. Schaefer and R. Laatikainen, *Can. J. Chem.*, 1983, **61**, 224.
426. T. Schaefer, S. R. Salman, T. A. Wildman, G. H. Penner, *Can. J. Chem.*, 1985, **63**, 782.
427. T. Schaefer, T. A. Wildman and J. Peeling, *J. Magn. Reson.*, 1984, **56**, 144.

428. T. Schaefer and R. Sebastian, *J. Magn. Reson.*, 1987, **73**, 541.
429. R. H. Contreras, D. G. de Kowalewski and J. C. Facelli, *J. Mol. Struct.*, 1982, **81**, 147.
430. M. A. Natiello, R. H. Contreras, J. C. Facelli and D. G. de Kowalewski, *J. Phys. Chem.*, 1983, **87**, 2603.
431. T. Schaefer and R. Sebastian, *Can. J. Chem.*, 1989, **67**, 1027.
432. A. Römer, *Org. Magn. Reson.*, 1982, **19**, 66.
433. D. A. Forsyth, V. M. Psterman and J. R. DeMember, *J. Am. Chem. Soc.*, 1985, **107**, 818.
434. W. J. Chazin and L. D. Colebrook, *Can. J. Chem.*, 1986, **64**, 2220.
435. T. Schaefer and J. D. Baleja, *J. Magn. Reson.*, 1984, **60**, 131.
436. T. Schaefer, R. Sebastian, S. R. Salman, J. D. Baleja, G. H. Penner and D. M. McKinnon, *Can. J. Chem.*, 1991, **69**, 620.
437. D. C. Spellmeyer, P. D. J. Grottenhuis, M. D. Miller, L. F. Kuyper and P. A. Kollman, *J. Phys. Chem.*, 1990, **94**, 4483.
438. T. Schaefer, R. Sebastian and S. R. Salman, *J. Magn. Reson.*, 1982, **46**, 325.
439. S. Carmely, M. Rotem and Y. Kashman, *Magn. Reson. Chem.*, 1986, **24**, 343.
440. T. Schaefer, J. Peeling and T. A. Wildman, *Org. Magn. Reson.*, 1984, **22**, 477.
441. T. Schaefer and J. Peeling, *J. Magn. Reson.*, 1985, **64**, 131.
442. G. Yamamoto and M. Oki, *J. Org. Chem.*, 1984, **49**, 1913.
443. D. J. Sardella and E. Boger, *Magn. Reson. Chem.*, 1989, **27**, 13.
444. F. B. Mallory, C. W. Mallory and W. M. Ricker, *J. Org. Chem.*, 1985, **50**, 457.
445. T. Schaefer and J. B. Rowbotham, *Chem. Phys. Lett.*, 1974, **29**, 633.
446. J. B. Rowbotham, M. Smith and T. Schaefer, *Can. J. Chem.*, 1975, **53**, 986.
447. T. Schaefer and W. J. Parr, *J. Chem. Phys.*, 1976, **65**, 1197.
448. T. Schaefer, K. Chum, K. Marat and R. E. Wasylishen, *Can. J. Chem.*, 1976, **54**, 800.
449. L. C. Hsee and D. J. Sardella, *Magn. Reson. Chem.*, 1990, **28**, 688.
450. W. Adcock and S. Q. A. Rizvi, *Aust. J. Chem.*, 1973, **26**, 2659.
451. T. Schaefer, S. R. Salman and T. A. Wildman, *Can. J. Chem.*, 1980, **58**, 2364.
452. M. Barfield, S. R. Walter, K. A. Clark, G. W. Gribble, K. W. Haden, W. J. Kelly and C. S. le Houiller, *Org. Magn. Reson.*, 1982, **20**, 92.
453. G. W. Gribble and W. J. Kelly, *Tetrahedron Lett.*, 1985, 3779.
454. W. Guo and T. C. Wong, *Magn. Reson. Chem.*, 1986, **24**, 75.
455. R. H. Contreras, C. G. Giribet, M. A. Natiello, J. Perez, I. D. Rae and J. A. Weigold, *Aust. J. Chem.*, 1985, **38**, 1779.
456. G. Yamamoto and M. Oki, *Tetrahedron Lett.*, 1985, **26**, 457.
457. T. Schaefer, G. H. Penner, T. A. Wildman and J. Peeling, *Can. J. Chem.*, 1985, **63**, 2256.
458. I. D. Rae, J. A. Weigold, R. H. Contreras and G. Yamamoto, *Magn. Reson. Chem.*, 1992, **30**, 1047.
459. T. N. Mitchell, K. Heesche-Wagner and H. J. Belt, *Magn. Reson. Chem.*, 1991, **29**, 78.
460. A. Albinati, C. Arz and P. Pregosin, *Inorg. Chem.*, 1987, **26**, 508.
461. C. G. Anklin and P. S. Pregosin, *Magn. Reson. Chem.*, 1985, **23**, 671.
462. B. V. Cheesman and R. F. M. White, *Can. J. Chem.*, 1984, **62**, 521.
463. F. B. Mallory, *J. Am. Chem. Soc.*, 1973, **95**, 7747.
464. F. B. Mallory and C. W. Mallory, *J. Am. Chem. Soc.*, 1985, **107**, 4816.
465. F. M. Mallory, C. W. Mallory and M. C. Fedarko, *J. Am. Chem. Soc.*, 1974, **96**, 3536.
466. F. B. Mallory, C. W. Mallory and M. B. Baker, *J. Am. Chem. Soc.*, 1990, **112**, 2577.
467. D. A. Burgess, M. F. Finn, D. Jordan, I. D. Rae and B. D. Walters, *Aust. J. Chem.*, 1984, **37**, 1769.
468. V. I. Bakhmutov, M. V. Galakhov and E. I. Fedin, *Magn. Reson. Chem.*, 1985, **23**, 971.
469. M. C. Ruiz de Azúa, Personal communication.
470. V. I. Bakhmutov and M. V. Galakhov, Personal communication.
471. (a) H. J. Jakobsen and W. S. Brey, *J. Chem. Soc. Chem. Commun.*, 1979, 478.
(b) H. J. Jakobsen and W. S. Brey, *J. Am. Chem. Soc.*, 1979, **101**, 774.
472. A. Costa, M. Tato and R. S. Matthews, *Magn. Reson. Chem.*, 1986, **24**, 547.

473. H. O. Gavarini, M. A. Natiello and R. H. Contreras, *Theor. Chim. Acta*, 1985, **68**, 171.
474. A. C. Diz, R. H. Contreras, M. A. Natiello and H. O. Gavarini, *J. Comput. Chem.*, 1985, **6**, 647.
475. E. A. V. Ebsworth, D. W. H. Rankin and J. G. Wright, *J. Chem. Soc. Dalton Trans.*, 1977, 2348.
476. E. A. V. Ebsworth, D. W. H. Rankin and J. G. Wright, *J. Chem. Soc. Dalton Trans.*, 1979, 1065.
477. R. B. King and T. W. Lee, *Inorg. Chem.*, 1982, **21**, 319.
478. T. R. Johnson and J. F. Nixon, *J. Chem. Soc. (A)*, 1969, 2518.
479. I. J. Colquhoun and W. McFarlane, *J. Chem. Soc. Dalton Trans.*, 1982, 1915.
480. R. R. Ford, B. L. Li, R. H. Neilson and R. J. Thoma, *Inorg. Chem.*, 1985, **24**, 1993.
481. J. Grobe, G. Lange and D. LeVan, *Z. Naturforsch.*, 1990, **45B**, 299.
482. T. Busch, W. W. Schoeller, E. Niecke, M. Nieger and H. Westermann, *Inorg. Chem.*, 1989, **28**, 4334.
483. S. Hetikamp and O. Stelzer, *Inorg. Chem.*, 1984, **23**, 258.
484. J. L. Bookham, W. McFarlane, I. J. Colquhoun and M. Thornton-Pett, *J. Organomet. Chem.*, 1988, **354**, 313.
485. A. J. Carty, D. K. Johnson and S. E. Jacobson, *J. Am. Chem. Soc.*, 1979, **101**, 5612.
486. H. Christina, E. McFarlane and W. McFarlane, *Polyhedron*, 1988, **7**, 1875.
487. A. L. Rheingold and M. E. Fountain, *Organometallics*, 1984, **3**, 1417.
488. L. Johannsen and H. Eggert, *J. Am. Chem. Soc.*, 1984, **106**, 1240.
489. I. Johannsen, L. Henriksen and H. Eggert, *J. Org. Chem.*, 1986, **51**, 1657.
490. R. S. Laitinen and T. A. Pakkanen, *Inorg. Chem.*, 1987, **26**, 2598.
491. H. Eggert, O. Nielsen and L. Henriksen, *J. Am. Chem. Soc.*, 1986, **108**, 1725.
492. I. D. Rae, A. Staffa, A. C. Diz, C. G. Giribet, M. C. Ruiz de Azúa and R. H. Contreras, *Aust. J. Chem.*, 1988, **40**, 1923.
493. A. C. Diz, C. G. Giribet, M. C. Ruiz de Azúa, R. H. Contreras and G. A. Aucar, *Magn. Reson. Chem.*, 1987, **25**, 883.
494. L. D. Quin, M. J. Gallagher, G. T. Cunkle and D. B. Chesnut, *J. Am. Chem. Soc.*, 1980, **102**, 3136.
495. M. Duncan and M. J. Gallagher, *Org. Magn. Reson.*, 1981, **15**, 37.
496. C. O. Meese and W. Walter, *Magn. Reson. Chem.*, 1985, **23**, 327.
497. S. L. Spassov, L. Markova, D. M. Mondeshka, C. N. Tancheva and C. M. Angelov, *Magn. Reson. Chem.*, 1985, **23**, 578.
498. R. Radeglia, R. Wolff, T. Steiger and S. Simova, *Z. Phys. Chem.*, 1984, **265**, 379.
499. A. Antoniads, U. Kunze and M. Moll, *J. Organomet. Chem.*, 1982, **235**, 177.
500. H. Kunzer, C. E. Cottrell and L. A. Paqquette, *J. Am. Chem. Soc.*, 1986, **108**, 8089.
501. J.-P. Bégué, D. Bonnet-Delpon, D. Mesureur and M. Ourévitch, *Magn. Reson. Chem.*, 1991, **29**, 675.
502. K. W. Rowland and R. D. Thomas, *Magn. Reson. Chem.*, 1985, **23**, 916.
503. M. Barfield, E. W. Della and P. E. Pigou, *J. Am. Chem. Soc.*, 1984, **106**, 5051.
504. M. Barfield, D. E. Della, P. E. Pigou and S. R. Walter, *J. Am. Chem. Soc.*, 1982, **104**, 3549.
505. G. E. Scuseria, J. C. Facelli, R. H. Contreras and A. R. Engelmann, *Chem. Phys. Lett.*, 1983, **96**, 560.
506. R. H. Contreras and G. E. Scuseria, *Org. Magn. Reson.*, 1984, **22**, 411.
507. G. A. Aucar, V. Zunino, M. B. Ferraro, C. G. Giribet, M. C. Ruiz de Azúa and R. H. Contreras, *J. Mol. Struct. THEOCHEM*, 1990, **205**, 63.
508. G. A. Olah, J. G. Shih, V. V. Krishnamurthy and B. P. Singh, *J. Am. Chem. Soc.*, 1984, **106**, 4492.
509. E. W. Della, E. Cotsaris and P. T. Hine, *J. Am. Chem. Soc.*, 1981, **103**, 413.
510. J. D. Goddard, A. W. Payne, N. Cook and H. R. Luss, *J. Heterocycl. Chem.*, 1988, **25**, 575.

511. P. R. Blake, J. B. Park, M. W. W. Adams and M. F. Summers, *J. Am. Chem. Soc.*, 1992, **114**, 4931.
512. A. V. Aonin, Z. V. Stepanova, V. K. Voronov and A. V. Vashchenko, *Khim. Geterosikl. Soedin.*, 1987, 1422.
513. T. Schaefer, R. Sebastian, R. Laatikainen and S. R. Salman, *Can. J. Chem.*, 1984, **62**, 326.
514. R. R. Biekofsky, A. B. Pomilio and R. H. Contreras, *J. Mol. Struct. THEOCHEM*, 1990, **210**, 211.
515. N Defay, R. Nasielski-Hinkens and J. Nasielski, *Magn. Reson. Chem.*, 1987, **25**, 87.
516. A. Yu. Denisov, V. P. Krivopalov, V. I. Mamatyuk and V. P. Mamaev, *Magn. Reson. Chem.*, 1988, **26**, 42.
517. R. E. Hess, C. D. Schaeffer and C. H. Yoder, *J. Org. Chem.*, 1971, **36**, 2202.
518. T. Angellotti, M. Krisko, T. O'Connor and A. S. Serianni, *J. Am. Chem. Soc.*, 1987, **109**, 4464.
519. D. B. Davies, M. MacCoss, S. S. Danyluk, *J. Chem. Soc. Chem. Commun.*, 1984, 536.
520. M. Hricovini and I. Tvaroška, *Magn. Reson. Chem.*, 1990, **28**, 862.
521. A. V. Afonin and M. A. Andriyankov, *Zh. Org. Khim.*, 1988, **24**, 1034.
522. A. V. Afonin, M. V. Sigalov, S. E. Korustova, I. A. Aliev, A. V. Vashchenko and B. A. Trofimov, *Magn. Reson. Chem.*, 1990, **28**, 580.
523. M. C. Vitorge, M. T. Chenon, C. Coupry and N. Lumbroso-Bader, *Org. Magn. Reson.*, 1987, **60**, 953.
524. H. Satonaka, K. Abe and M. Hirota, *Bull. Chem. Soc. Jpn*, 1988, **61**, 2031.
525. Th. Lectka and C. N. Hodge, *J. Am. Chem. Soc.*, 1989, **111**, 8867.
526. L. Kozerski, K. Kamienska-Trela, L. Kania and W. von Philipsborn, *Helv. Chim. Acta*, 1983, **66**, 2113.
527. N. M. Segeyev, *NMR: Basic Princ. Prog.*, 1990, **22**, 31.
528. R. Aydin and H. Günther, *Magn. Reson. Chem.*, 1990, **28**, 448.
529. M. W. Baum, M. Jones and U. Misslitz, Personal communication.
530. J. I. Musher, *Mol. Phys.*, 1963, **6**, 93.
531. P. Laszlo and P. von Ragué Schleyer, *J. Am. Chem. Soc.*, 1964, **86**, 1171.
532. F. A. A. M. de Leeuw, A. A. Beuzekom and C. Altona, *J. Comput. Chem.*, 1983, **4**, 438.
533. J. L. Marshall, S. R. Walter, M. Barfield, A. P. Marchand, N. W. Marchand and A. L. Segre, *Tetrahedron*, 1976, **32**, 537.
534. T. Schaefer, R. Sebastian, R. Laatikainen and S. R. Salman, *Can. J. Chem.*, 1984, **62**, 326.
535. T. Schaefer and K. J. Cox, *Can. J. Chem.*, 1991, **69**, 919.
536. T. Schaefer and C. S. Takeuchi, *Can. J. Chem.*, 1990, **68**, 339.
537. T. Schaefer and C. S. Takeuchi, *Can. J. Chem.*, 1989, **67**, 8727.
538. T. Schaefer, J. Peeling, G. H. Penner, A. Lemire and R. Laatikainen, *Can. J. Chem.*, 1986, **64**, 1859.
539. M. C. Salon, S. Hamman and C. G. Bequin, *Org. Magn. Reson.*, 1983, **21**, 265.
540. S. Prytulla, J. Lambert, J. Lauterwein, M. Klessinger and J. Thilm, *Magn. Reson. Chem.*, 1990, **28**, 888.
541. L. D. Quin, J. Szewczyk, K. Linehan and R. K. Harris, *Magn. Reson. Chem.*, 1987, **25**, 271.
542. W. Adcock and V. S. Iyer, *Magn. Reson. Chem.*, 1991, **29**, 381.
543. V. M. Kanagasabapathy, J. F. Sawer and T. T. Tidwell, *J. Org. Chem.*, 1985, **50**, 503.
544. V. V. Krishnamurthy, J. G. Shih and G. A. Olah, *J. Org. Chem.*, 1985, **50**, 1161.
545. (a) C. L. Khetrapal, *Specialist Periodical Report, Nuclear Magnetic Resonance*, Vol. 13 (ed. G. A. Webb), p. 298. The Royal Society of Chemistry, 1983.
(b) C. L. Khetrapal, *Specialist Periodical Report, Nuclear Magnetic Resonance*, Vol. 19 (ed. G. A. Webb), p. 437. The Royal Society of Chemistry, 1989.

546. Y. Hiltunen, J. Jokisaari, J. Lounila and A. Pulkkinen, *J. Am. Chem. Soc.*, 1989, **111**, 3217.
547. B. Haiping and R. K. Harris, *J. Magn. Reson.*, 1992, **96**, 24.
548. K. W. Zilm and D. M. Grant, *J. Am. Chem. Soc.*, 1981, **103**, 2913.
549. J. Manz, *J. Am. Chem. Soc.*, 1980, **102**, 180.
550. P. Lazzeretti, E. Rossi, F. Taddei and R. Zanasi, *J. Chem. Phys.*, 1982, **77**, 408.
551. P. Lazzeretti, E. Rossi, F. Taddei and R. Zanasi, *J. Chem. Phys.*, 1982, **77**, 2023.
552. P. Lazzeretti and R. Zanasi, *J. Chem. Phys.*, 1982, **77**, 2448.
553. P. Diehl, J. Jokisaari, J. Amrein, T. Vaanaenn and P. Pyykkö, *J. Magn. Reson.*, 1982, **48**, 495.
554. A. Pulkkinen, J. Jokisaari and T. Vaananen, *J. Mol. Struct.*, 1986, **144**, 359.
555. N. M. Peruchena, G. A. Aucar and R. H. Contreras, *J. Mol. Struct. THEOCHEM*, 1990, **210**, 205.
556. G. H. Penner, W. P. Power and R. E. Wasylishen, *Can. J. Chem.*, 1988, **66**, 1821.
557. J. Jokisaari, Y. Hiltunen and J. Lounila, *J. Chem. Phys.*, 1986, **85**, 3198.
558. D. C. Apperley, B. Haiping and R. K. Harris, *Mol. Phys.*, 1277, **68**, 1989.
559. C. J. Jameson and H. J. Osten, *J. Am. Chem. Soc.*, 1986, **108**, 2497.
560. W. T. Raynes, P. Lazzeretti, R. Zanasi and P. W. Fowler, *J. Soc. Chem. Commun.*, 1985, 1538.
561. P. Lazzeretti, R. Zanasi and Raynes, *J. Chem. Soc. Chem. Commun.*, 1986, 57.
562. M. Klessinger and P. Bolte, *J. Mol. Struct. THEOCHEM*, 1988, **169**, 119.
563. P. Lazzeretti, Personal communication.
564. W. T. Raynes, P. Lazzeretti and R. Zanasi, *Chem. Phys. Lett.*, 1986, **132**, 173.
565. J. Kowalewski, A. Laaksonen, B. Roos and P. Siegbahn, *J. Chem. Phys.*, 1979, **71**, 2896.
566. W. T. Raynes, J. Geertsen and J. Oddershede, *Chem. Phys.*, 1992, **197**, 516.
567. H. J. Osten and C. J. Jameson, *J. Chem. Phys.*, 1984, **81**, 4288.
568. H. J. Jakobsen, A. J. Zozulin, P. D. Ellis and J. D. Odom, *J. Magn. Reson.*, 1980, **38**, 219.
569. I. F. Leshcheva, V. N. Torochesnikov, N. M. Sergeyev, V. A. Chertkov and V. N. Khlopkov, *J. Magn. Reson.*, 1991, **94**, 9.
570. R. E. Wasylishen and N. Burford, *Can. J. Chem.*, 1987, **65**, 2707.
571. P. E. Hansen and J. J. Led, *Org. Magn. Reson.*, 1981, **15**, 288.
572. J. R. Wesener and H. Günther, *Tetrahedron Lett.*, 1982, **23**, 2845.
573. S. Berger, *NMR: Basic Princ. Prog.*, 1990, **22**, 1.
574. J. R. Everett, *Org. Magn. Reson.*, 1982, **19**, 169.
575. Yu. A. Strelenklo, V. N. Torochesnikov and N. M. Sergeyev, *J. Magn. Reson.*, 1990, **89**, 123.
576. E. Liepins, V. Gevorgyan and E. Lukevics, *J. Magn. Reson.*, 1989, **85**, 170.
577. K. L. Leighton and R. E. Wasylishen, *Can. J. Chem.*, 1987, **65**, 1469.
578. R. E. Wasylishen and J. D. Friedrich, *Can. J. Chem.*, 1987, **65**, 2238.
579. R. E. Wasylishen and N. Burford, *J. Chem. Soc. Chem. Commun.*, 1987, 1414.
580. R. E. Wasylishen and J. O. Friedrich, *J. Chem. Phys.*, 1984, **80**, 585.
581. R. H. Crabtree and A. Habib, *Inorg. Chem.*, 1986, **25**, 3698.
582. Z. Meić, D. Vikic-Topic and H. Güsten, *Org. Magn. Reson.*, 1984, **22**, 237.
583. L. Ernst, *Org. Magn. Reson.*, 1984, **22**, 789.
584. A. Laaksonen, J. Kowalewski and B. Jönsson, *Chem. Phys. Lett.*, 1982, **89**, 412.
585. G. Klopman, *Chem. Phys. Lett.*, 1967, **1**, 200.
586. S. N. Shargi and G. A. Webb, *Org. Magn. Reson.*, 1982, **19**, 126 and 216.
587. S. Watanabe, I. Ando and Y. Sakamoto, *J. Mol. Struct.*, 1983, **96**, 216.
588. S. N. Shargi, G. A. Webb, I. Ando and S. Watanabe, *J. Mol. Struct. THEOCHEM*, 1983, **91**, 325.
589. S. Watanabe and I. Ando, *J. Mol. Struct.*, 1983, **104**, 155.

590. I. Ando, Y. Inouie, S. Watanabe, Y. Sakamoto and G. A. Webb, *J. Mol. Liq.*, 1984, **27**, 179.
591. I. Ando, T. Sanefuji, T. Yamanobe, S. Watanabe and G. A. Webb, *J. Mol. Liq.*, 1985, **31**, 31.
592. M. Ruiz-López, D. Rinaldi, J. Rivail and A. Oliva, *J. Chem. Res.*, 1982, **12**, 329; *J. Chem. Res. (M)*, 1982, 3369.
593. J. L. Rivail and D. Rinaldi, *Chem. Phys.*, 1976, **18**, 233.
594. M. Barfield and M. D. Johnston, *Chem. Rev.*, 1973, **73**, 53.
595. A. G. Swanson, *Tetrahedron Lett.*, 1983, **24**, 1833.
596. M. Klessinger and J. H. Cho, *Angew. Chem. Int. Ed. Engl.*, 1982, **21**, 764.
597. M. Klessinger and J. H. Cho, *Org. Magn. Reson.*, 1983, **21**, 465.
598. J. H. Cho, M. Klessinger, U. Tecklenborg and K. Wilhelm, *Magn. Reson. Chem.*, 1985, **23**, 95.
599. R. Hübers, M. Klessinger and K. Wilhelm, *Magn. Reson. Chem.*, 1986, **24**, 1016.
600. M. Stöcker, *Org. Magn. Reson.*, 1982, **20**, 175.
601. E. W. Della, H. Gangodawila and P. E. Pigou, *J. Org. Chem.*, 1988, **53**, 592.
602. W. Adcock, A. N. Abeywickrema and G. B. Kok, *J. Org. Chem.*, 1984, **49**, 1387.
603. E. W. Della, B. Kasum and K. P. Kirkbride, *J. Am. Chem. Soc.*, 1987, **109**, 2746.
604. E. W. Della and J. Tsanaktsidis, *Organometallics*, 1988, **7**, 1179.
605. P. A. Lay and A. M. Sargeson, *Inorg. Chem.*, 1986, **25**, 4801.
606. G. E. Scuseria, J. C. Facelli, R. H. Contreras and A. R. Engelmann, *Chem. Phys. Lett.*, 1983, **96**, 560.
607. G. A. Aucar, M. C. Ruiz de Azúa, C. G. Giribet and R. H. Contreras, *J. Mol. Struct. THEOCHEM*, 1990, **205**, 79.
608. M. F. Tufró and R. H. Contreras, *Z. Phys. Chem.*, 1986, **267**, 873.
609. C. N. Cavasotto, C. G. Giribet, M. C. Ruiz de Azúa and R. H. Contreras, *J. Magn. Reson.*, 1990, **87**, 209.
610. T. N. Mitchell, R. Faust, B. Fabisch and R. Wickenkamp, *Magn. Reson. Chem.*, 1990, **28**, 82.

Index